Conference Proceedings of the Society for Experimental Mechanics Series

Brandon J. Dilworth
Timothy Marinone
Michael Mains *Editors*

Topics in Modal Analysis & Parameter Identification, Volume 9

Proceedings of the 41st IMAC, A Conference and Exposition on Structural Dynamics 2023

Springer

Conference Proceedings of the Society for Experimental Mechanics Series

Series Editor

Kristin B. Zimmerman
Society for Experimental Mechanics, Inc.,
Bethel, CT, USA

The Conference Proceedings of the Society for Experimental Mechanics Series presents early findings and case studies from a wide range of fundamental and applied work across the broad range of fields that comprise Experimental Mechanics. Series volumes follow the principle tracks or focus topics featured in each of the Society's two annual conferences: IMAC, A Conference and Exposition on Structural Dynamics, and the Society's Annual Conference & Exposition and will address critical areas of interest to researchers and design engineers working in all areas of Structural Dynamics, Solid Mechanics and Materials Research.

Brandon J. Dilworth • Timothy Marinone • Michael Mains
Editors

Topics in Modal Analysis & Parameter Identification, Volume 9

Proceedings of the 41st IMAC, A Conference and Exposition on Structural Dynamics 2023

Springer

Editors
Brandon J. Dilworth
Lincoln Laboratory
Massachusetts Inst of Technology
Lexington, MA, USA

Timothy Marinone
ATA Engineering
San Diego, CA, USA

Michael Mains
Modal Shop
Cincinnati, OH, USA

ISSN 2191-5644 ISSN 2191-5652 (electronic)
Conference Proceedings of the Society for Experimental Mechanics Series
ISBN 978-3-031-34941-6 ISBN 978-3-031-34942-3 (eBook)
https://doi.org/10.1007/978-3-031-34942-3

This Springer imprint is published by the registered company Springer Nature Switzerland AG
The registered company address is: Gewerbestrasse 11, 6330 Cham, Switzerland

Paper in this product is recyclable.

Preface

Topics in Modal Analysis and Parameter Identification represents one of ten volumes of technical papers presented at the 41st IMAC, a Conference and Exposition on Structural Dynamics, organized by the Society for Experimental Mechanics, held February 13–16, 2023. The full proceedings also include volumes on *Nonlinear Structures and Systems*; *Dynamics of Civil Structures*; *Model Validation and Uncertainty Quantification*; *Dynamic Substructures*; *Special Topics in Structural Dynamics and Experimental Techniques*; *Computer Vision and Laser Vibrometry*; *Dynamic Environments Testing*; *Sensors and Instrumentation and Aircraft/Aerospace Testing Techniques*; and *Data Science in Engineering*.

Each collection presents early findings from experimental and computational investigations on an important area within structural dynamics. *Topics in Modal Analysis and Parameter Identification* represents papers on enabling technologies for dynamic systems and applications of modal analysis in specific application areas.

The organizers would like to thank the authors, presenters, session organizers, and session chairs for their participation in this track.

Lexington, MA, USA — Brandon J. Dilworth
San Diego, CA, USA — Timothy Marinone
Cincinnati, OH, USA — Michael Mains

Contents

Chapter 1
Automated Operational Modal Analysis on a Full-Scale Wind Turbine Tower

Jens Kristian Mikkelsen, Esben Orlowitz, and Peter Møller Juhl

Abstract This chapter is concerned with the automated extraction of modal parameters (frequency and damping estimates) from accelerometer data measured on a full-scale wind turbine tower without its nacelle and blades installed. The proposed algorithm is based on an existing Operational Modal Analysis research software employing the Stochastic Subspace Identification algorithm for manual selection and extraction of modal parameters. The automatization of the algorithm is discussed in terms of the choices made and their consequences with respect to sensitivity and robustness. The algorithm is finally tested on a large experimental dataset consisting of 10 days of signals sampled at 25 Hz from two accelerometers mounted at the top of the tower in orthogonal directions. The automated algorithm is successful in time tracking the development of the first two modes with respect to frequency and damping despite the challenge posed by the fact that due to the high degree of symmetry in the setup the frequencies of the two modes are very similar.

Keywords Operational Modal Analysis · Modal parameter estimation · Automated method · Tracking of modes · Large structures

1.1 Introduction

In an experimental modal analysis, also including Operational Modal Analysis (OMA), a frequently used step for the Modal Parameter Estimation (MPE) is the utilization of the so-called stabilization diagram or consistency diagram. The stabilization diagram is a user-interactive tool used to sort out real/physical modes of the structure under test from the unavoidable computational/noise modes that will be present in most MPE methods (e.g., Stochastic Subspace Identification (SSI)). The basic idea of the stabilization diagram is to track mode estimates as a function of model order allowed in the MPE method. The modes of a real physical system will be unaffected by the model order, and they are stable. Computational/noise modes, however, will change as the model order changes, and they will be unstable. Via the stabilization diagram, an experienced user manually selects an estimate of the modes being observable to him/her, and hence this is a subjective decision which depends on the users experience and training. In addition, it is a time-consuming process which is too cumbersome for tracking modal parameters of a structure over long periods of time. Tracking the modal parameters of a structure over time could be relevant for several reasons like model validation, structural health monitoring, etc. Therefore, an automation of the MPE avoiding the manual step of inspecting the stabilization diagram is desirable. The aim of this chapter is to track the modal parameters of the two first-order bending modes of a wind turbine tower over a time period of 10 days. To accomplish this, a method for automatic OMA is proposed that removes the need for a user-interactive stabilization diagram. The method is as such independent of the MPE method employed as long as results for a stabilization diagram are produced. For the present work, the Stochastic Subspace Identification (SSI) method has been chosen [1] as implemented in Ref. [2]. The proposed method is finally tested on 10 days experimental data set from a full-scale wind turbine tower.

J. K. Mikkelsen · P. M. Juhl (✉)
The Faculty of Engineering, University of Southern Denmark, Odense, Denmark
e-mail: pmjuhl@sdu.dk; pmjuhl@sdu.dk

E. Orlowitz
Siemens Gamesa Renewable Energy, Brande, Denmark
e-mail: Esben.Orlowitz@siemensgamesa.com

B. J. Dilworth et al. (eds.), *Topics in Modal Analysis & Parameter Identification, Volume 9*, Conference Proceedings of the Society for Experimental Mechanics Series, https://doi.org/10.1007/978-3-031-34942-3_1

1.2 Background

1.2.1 The Tower and Acceleration Data

During the erection of a wind turbine prototype in Denmark,[1] the 116 m tower (without nacelle and rotor) was standing alone for 10 days. A sketch of the tower dimensions is presented in Fig. 1.1a. In this period, two accelerometers were mounted orthogonally at the top of the tower and measured the acceleration at a sampling frequency of 25 Hz. Figure 1.1b shows the root mean square (RMS) values of the acceleration in the two directions in 30 minutes averages. The data are presented in its raw format in Ref. [3].

1.2.2 COMSOL Model Tower

Before developing the automation algorithm, a simplified version of the wind turbine tower was set up in COMSOL Multiphysics 5.6 to obtain simulated values for the expected eigenfrequencies of the two first-order bending modes. The simplified model is based on a technical drawing and is illustrated in Fig. 1.1a. The tower is fixed at the base and free at the top, mimicking a cantilever problem. An eigenfrequency study of the tower was computed [4] and the eigenfrequencies of the two first-order bending modes, f_1, in both directions were found as $f_{1,x} = f_{1,y} = 0.57123\,\text{Hz}$ [5]. These two orthogonal modes are identical in frequency in this simulation since the tower has axial symmetry. In practice, there are imperfections in the tower and other effects leading to a separation of the eigenfrequencies of the modes. The shapes of the two bending modes are identical but in orthogonal direction. Because of this symmetry in the COMSOL model, it is expected that the two bending modes found in the data will be closely spaced in the frequency domain.

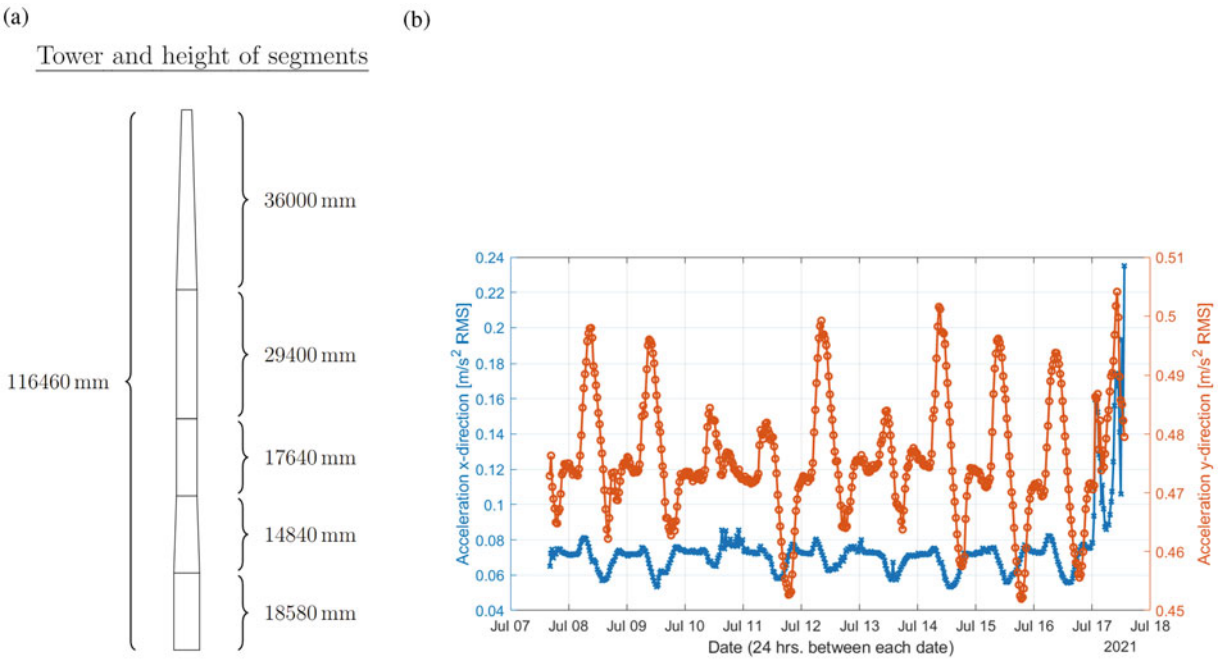

Fig. 1.1 (**a**) Illustrated overview of the wind turbine tower showing the longitudinal sections. (**b**) Averaged RMS acceleration data in both x- and y-direction. Each point shows the RMS average of the succeeding 30 minutes

[1] Danish National Test Center Østerild https://wind.dtu.dk/Facilities/oesterild.

1.2.3 Manual OMA algorithm

The input to the SSI algorithm employed [2] is a block of continuously sampled data from two accelerometers placed in the top of the tower in perpendicular directions. This allows for the identification of the two first-order modes of the tower only. Furthermore, the SSI algorithm requires user-set parameters such as the number of time lags and the maximum allowed model order, see, e.g., Ref. [6]. The SSI algorithm can result in a stabilization diagram. The stabilization diagram shows a graphical representation of the estimated modes by indicating the stable or unstable poles as a function of modal frequency and model order. Figure 1.2 shows a stabilization diagram of 30 minutes worth of data started at 40 hours into the time series. The range of the stabilization diagram has been truncated between 0.55 Hz and 0.65 Hz to better visualize the two closely spaced modes. In an earlier work [3], some damping estimates were found based on manually picked stable poles around the two first-order modes. One of the primary issues in picking poles manually is the consistency from the user as well as the time consumption. The supplied data set is about 240 hours long, and picking a data block length of 30 minutes for analysis purposes effectively results in 480 different frequency stabilization diagrams to manually sort and store. The two frequencies that can be extracted from the green stable poles in the stabilization diagram are $f_2 = 0.59614\,\text{Hz}$ and $f_1 = 0.59519\,\text{Hz}$, which are quite close to the eigenfrequencies found in COMSOL. Furthermore, the two modes are very closely spaced as seen in Fig. 1.2, where the difference in the two chosen frequencies is

$$\Delta f_{modes} = 0.00095\,\text{Hz}. \tag{1.1}$$

Thus, the frequency resolution needs to be finer than this resolution for the algorithm to properly discern the two modes.

One of the main purposes of this work is to automate this process, so a person does not have to manually interact with the graphical interface of the stabilization diagram 480 times, as mentioned. Instead of picking the poles manually and subjectively by the visual aid of the stabilization diagram, this work aims at automating the procedure by utilizing the Modal Assurance Criterion (MAC) to pick the optimal pole and mode shape for each 30-minute interval of data. The MAC is used to quantitatively compare modal vectors of mode shapes. It essentially compares the likeliness between modal vectors by calculating the normalized dot product of two complex modal vectors [7]. The MAC value evaluates between 0 and 1 wherein an indication of likeliness between modal vectors is given with 0 being a low likeliness and 1 being a high likeliness.

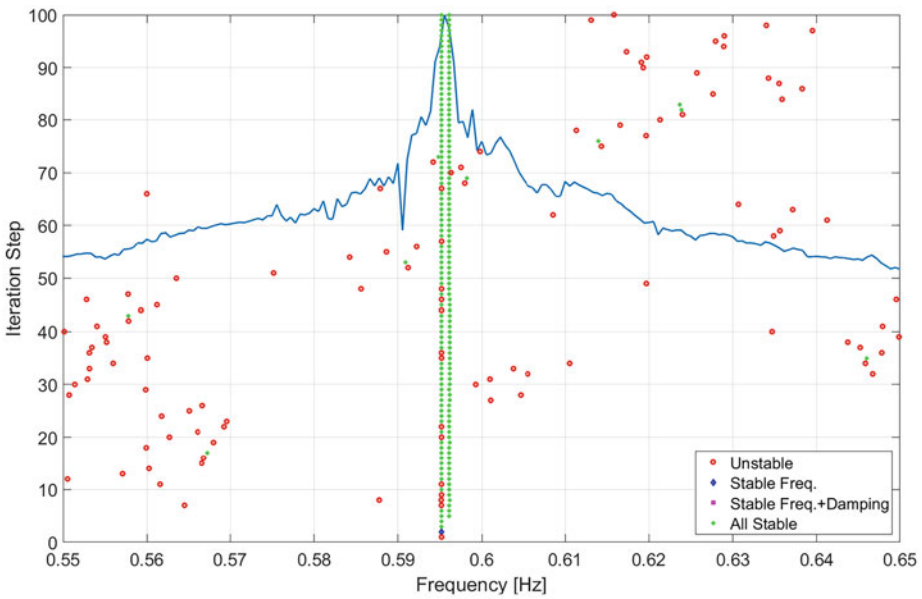

Fig. 1.2 Stabilization diagram of 30 minutes of data starting 40 hours into the acceleration data. The underlying blue line is a Power Spectral Density (PSD) estimate to visually identify the physical poles, the green points are the stable poles, the red points are all unstable poles, the blue point is a stable frequency, and the pink points are stable frequency and damping estimate

1.3 Analysis

1.3.1 Development of the Automated OMA

As mentioned by the input for the SSI algorithm, the Automated OMA (AOMA) algorithm uses similar inputs but a few additions for automation, herein an optional frequency range where in which the first mode is expected to be found and lastly an Auto MAC (AMAC) threshold for finding the most consistent model order. The output parameters of the method are two poles and two modal vectors for the first two modes, respectively. This algorithm is shown in the flowchart in Fig. 1.3. The flowchart shows when certain inputs are used throughout the algorithm and what processes are performed.

1.3.2 Algorithm Review and Choice of Thresholds

The list of poles and mode shapes from the SSI algorithm is extracted, circumventing the stabilization diagram graphical user interface, while the model order for each pole and the corresponding mode shapes are kept for later use. The complete list of poles is then converted to vectors of natural frequencies.

Next, the two modes need to be isolated in a histogram. Since the first modes are already expected inside the frequency range of $0.55 - 0.6$ Hz, a full histogram will not be created, only a truncated version. The width of histogram bins is determined by the frequency resolution which needs to be better than the difference between the two modes shown in Eq. (1.1) and is based on the frequency resolution which is dependent on the length of the signal as

$$\Delta f_{res} = \frac{1}{T_{30\,\text{minutes}}} = 0.00056\,\text{Hz}. \tag{1.2}$$

The first modes of the wind turbine tower will most often occur around 0.59 Hz in practice [3], so the algorithm will pick the two maximum bins inside this area. This is seen in Fig. 1.4. As in the flowchart, if the difference between the two bin counts

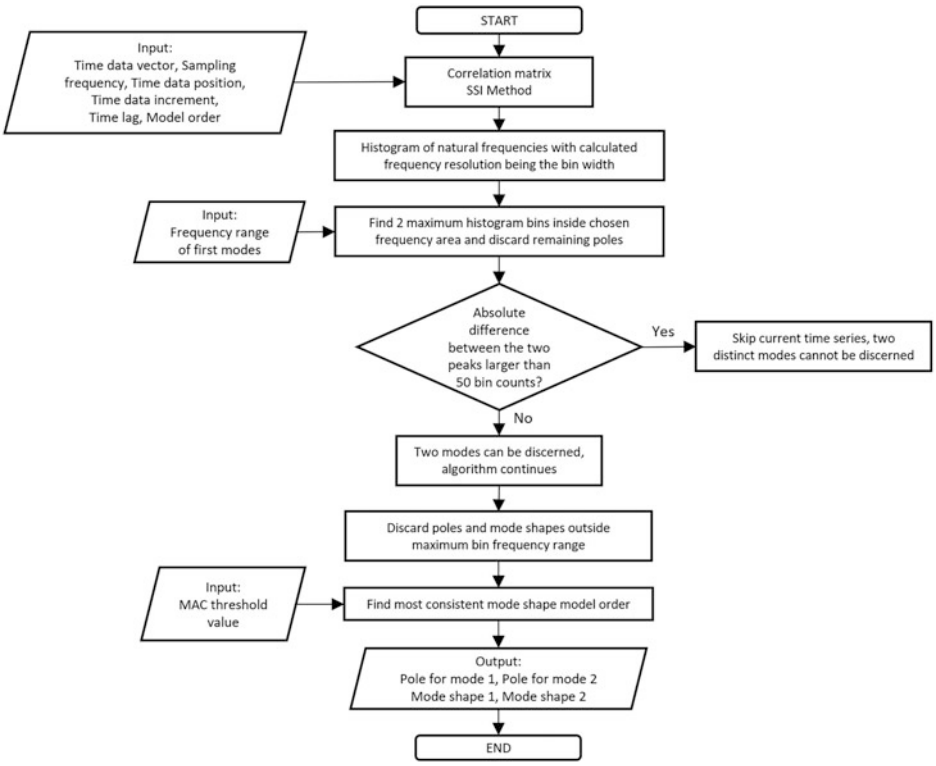

Fig. 1.3 Flowchart of the developed automation algorithm that illustrates picking a set of poles and modal vectors for a 30-minute long time series

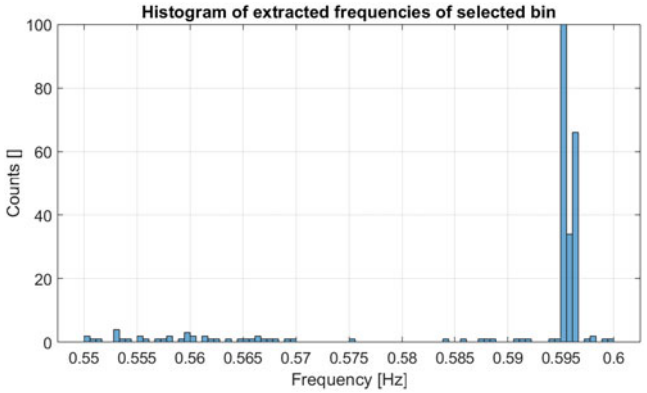

Fig. 1.4 Histogram of the frequencies inside the area of interest. Time series start point is 40 hours into the data and the time series length is 30 minutes

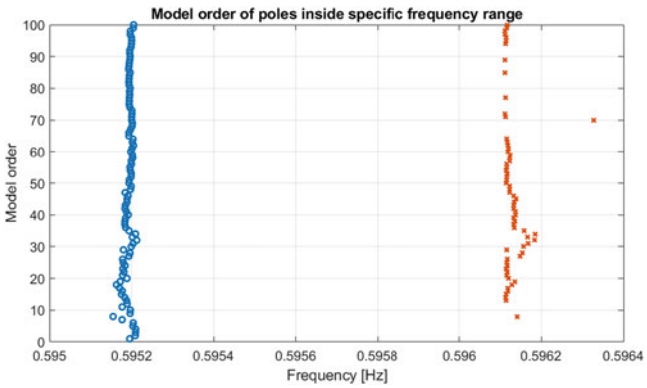

Fig. 1.5 Model order of each extracted natural frequency of the two closely spaced modes. Here, the time instance of 40 hours into the signal is still used

is larger than 50 in the case of this algorithm, the current time series is skipped as two modes cannot be discerned inside the frequency resolution. If two suspected physical modes can be discerned, the two bins of natural frequencies are isolated.

Optimally, there will now be two bins from the histogram, each with 100 natural frequencies of similar values because of the maximum chosen model order of 100, but in practice because of noise and frequency resolution there will be fewer poles left. The optimal two poles and two modal vectors have to be chosen, a set from the bin with the lowest frequency and a set from the bin with the highest frequency. Each model order corresponding to a pole is plotted against the natural frequency to visualize the two closely spaced modes in frequency. This is shown in Fig. 1.5.

To find the optimal pole and modal vector, an AMAC calculation is performed. In Fig. 1.5, each model order indicates a different pole and modal vector, and ideally all the blue points are the same mode shape and all the orange points are the same mode shape. Figure 1.6a shows each modal vector of the blue points in Fig. 1.5 compared to each other in the AMAC. This results in a contour plot where the color bar indicates the MAC value of each modal vector compared with the other modal vectors. The diagonal is unity since this is when a modal vector is compared to itself. To find the optimal modal vector—which determines the choice of the set of extracted poles and modal vectors—an acceptance threshold for the MAC value must be set where the number of model order's corresponding modal vectors in Fig. 1.6a that fulfill the threshold is summed for each model order. The acceptance threshold is set at

$$MAC_{threshold} \geq 0.9. \tag{1.3}$$

The model order with the most modal vectors that comply with the acceptance threshold is the most consistent model order and determines the set which is picked by the algorithm. The consistency plot of the model orders in Fig. 1.6a is shown in Fig. 1.6b. For this particular example, the most consistent model order is found to be 26, which is consistent with 24 other modes at the threshold set in Eq. (1.3).

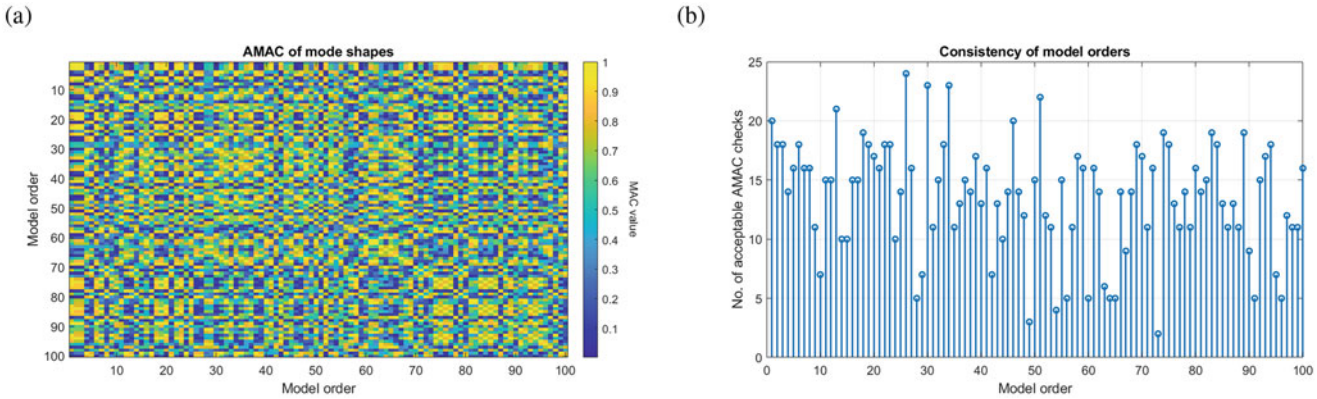

Fig. 1.6 (**a**) Contour plot where each modal vector from the blue points in Fig. 1.5 is compared to itself and all other modal vectors. The contour indicates the value of each MAC calculation of one model order's corresponding modal vector with the next. The diagonal is thus unity as expected. (**b**) Plot of consistent model orders. The MAC value threshold is set at 0.9, the value where a model order is accepted. For each model order, the number of accepted MAC checks between the modal vectors above the threshold is summed. The figure shows how consistently the model orders adhere to the MAC threshold. Here, the time series of 40 hours into the signal is still used

The MAC contour plot and the consistency check are to be performed for the orange points in Fig. 1.5 as well to get the second set of poles and modal vectors. Thus, the algorithm can continue to the next time increment where all the routines start over to pick the optimal poles and mode shapes.

1.3.3 Test of Thresholds

The developed algorithm has several criteria and thresholds throughout that discards or includes certain data based on the specific case of the wind turbine tower and the chosen OMA method. These choices are fitted to this case and should be refitted to other use cases where different frequency ranges, frequency resolutions, or MAC thresholds could be optimal instead. The most important of these choices and their effect on the algorithm will now be discussed.

In the case of this wind turbine tower, a threshold for the histogram of all extracted frequencies is chosen as to only include frequencies inside the area of 0.55 Hz to 0.6 Hz as this is where the first modes are expected to be found in this specific data set. This can be changed based on other use cases.

The frequency resolution is proportional to the reciprocal of the time series data length and is fixed in this case as the data length is constantly 30 minutes long. If the frequency resolution is worse than the difference in Eq. (1.1), the two modes cannot be separated which can lead to faulty damping estimates. However, the time series data length cannot be too long either since the SSI method assumes time-invariant data, and over longer time spans the recorded signal can become time dependent, a periodicity also observed in Fig. 1.1b. Thus, choosing between time dependency in the signal or greater frequency resolution is a fine balance.

In Fig. 1.4, two closely spaced modes in frequency were observed. If a large difference between the two most prominent bins is observed, the algorithm concludes that it cannot identify two excited modes and thus skips the time series. Several factors can result in the algorithm not being able to identify two excited modes: the first factor is the frequency resolution since a better resolution can discern bins better and a second reason can be MATLAB's histogram function that decides where the lines between histogram bins are drawn. Essentially, the algorithm cannot directly determine if a mode is excited in the data, but it can determine if two modes are insufficiently consistently present. The result of not being able the discern between the two modes can finally result in a wrong estimation of the damping if some frequencies are placed incorrectly in the histogram bins. The choice of a bin count difference of 50 being the threshold is based on the amount of extracted poles as well as the model order since a physical pole would ideally have 100 poles inside the bin if the maximum model order is chosen to be 100 as well. If the time series is shorter or the model order lower, one would have to change this bin difference threshold.

The AMAC acceptance threshold for picking the modal vector most frequently like the other modal vectors is set at the threshold value in Eq. (1.3) but can be changed based on the specific use case. In Ref. [5], the value was not picked at random, and a sweep of values were analyzed to showcase the optimal value by changing the MAC threshold value from 0.5 to 1. It was concluded that choosing a looser threshold value in the MAC essentially allows for the modal vectors to differ more from each other and that choosing a stricter threshold allows little change in the modal vectors.

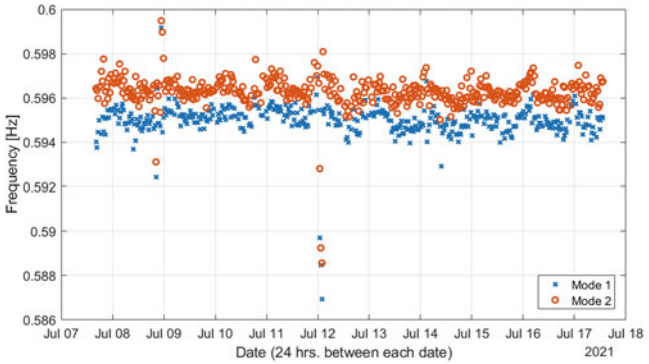

Fig. 1.7 Extracted natural frequencies of the first two modes as a function of time indicated by date. Each point indicates a 30-minute time series. Each vertical date line indicates midnight

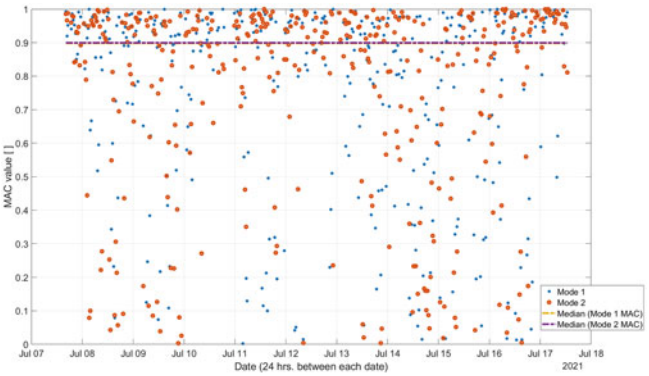

Fig. 1.8 CMAC values of modal vectors compared to succeeding modal vectors for the low frequency mode (blue dots), their median value (orange dashed line), CMAC values of modal vectors compared to succeeding modal vectors for the high frequency mode (orange dots), and lastly, their median value (purple dashed line)

1.4 Results of the Algorithm

The acceleration data seen in Fig. 1.1b in its raw format are used in the AOMA algorithm with the purpose of monitoring the change in the natural frequencies of the two closely spaced modes over time. The natural frequencies extracted for each 30 minutes of data over the 10 days of total data are shown as a function of time in Fig. 1.7. Here, a slight periodicity with respect to the time of day is observed, essentially showing an increase in the natural frequencies during midday and a decrease during the night. This is analyzed further in Ref. [5] but is not further relevant for this chapter.

One of the main challenges for this method is to circumvent the risk of two closely spaced modes overlapping in frequency or swapping places, so identification of individual modes becomes difficult. To potentially identify this, a Cross MAC (CMAC) check between the modal vector of the extracted mode shape from the current time instance is compared to the modal vector of the extracted mode shape from the succeeding time instance. This is performed for both modes and is plotted in Fig. 1.8 as a function of time with dates indicating time on the horizontal axis. The median value of the CMAC values is plotted as two overlaying lines on the plot indicating a strong congruence between the modal vectors over time, meaning a potential swap in mode shapes is unlikely, but still inconclusive.

1.5 Conclusion

The main purpose of the chapter was to develop an automation of the modal parameter estimation by operational modal analysis of a wind turbine tower. The automation is needed to avoid the time-consuming and subjective manual picking of modes from a stabilization diagram. Thus, the developed algorithm overall extracts two sets of poles and mode shapes for each time series serving as input to the program. The length of the time series and the sampling frequency can be altered by the user. The main use of the algorithm is monitoring of closely spaced modes over a lengthy period of time.

Thus, the use of the algorithm extends beyond an individual 30-minute measurement period. The primary way the algorithm has been developed is by analyzing the closely spaced natural frequencies as well as the similarity between modal vectors to determine the validity of two closely spaced modes being two different mode shapes. As a result of developing the algorithm, the measured acceleration data has been further analyzed after extraction, and the natural frequencies were plotted against the recorded time of day.

The change in the mode shapes has also been monitored over time where a cross-modal assurance criterion check has been performed between two modes with 30-minute increments between them with the purpose of checking if the modes swap at any instances in time. This analysis was deemed inconclusive, but the median of the cross-modal assurance criterion values indicate good conformity between the extracted mode shapes over time.

References

1. van Overschee, P., de Moor, B.: Subspace Identification For Linear Systems. Kluwer Academic Publishers, Dordrecht (1996)
2. Orlowitz, E.: Damping Estimation in Operational Modal Analysis. Ph.D. Thesis, 2015
3. Mikkelsen, J.K.: Damping estimation of a wind turbine. Technical report, University of Southern Denmark, Odense, 2022
4. COMSOL: Multiphysics cyclopedia: structural mechanics—eigenfrequency analysis (2018). https://www.comsol.com/multiphysics/eigenfrequency-analysis?parent=structural-mechanics-0182-212. Accessed 6 April 2022
5. Mikkelsen, J.K.: Comparison of modal parameters of a wind turbine by operational modal analysis and a finite element model. Master's Thesis, Odense, 2022
6. Orlowitz, E., Brandt, A.: Influence of noise in correlation function estimates for operational modal analysis. Topics Modal Anal. Testing **9**, 55–64 (2019)
7. Brandt, A.: Noise and Vibration Analysis: Signal Analysis and Experimental Procedures, 1st edn. Wiley, New York (2011)

Chapter 2
Combining Nontraditional Response Variables with Acceleration Data for Experimental Modal Analysis

P. M. Vinze, R. J. Allemang, A. W. Phillips, and R. N. Coppolino

Abstract Accelerometer data is the most commonly used data for experimental modal analysis of structures. Together with measuring applied force, it provides the basis for FRF estimation and subsequent modal parameter estimation and validation. As discussed in the paper by Dr. Coppolino (Experimental modal analysis using non-traditional response variables. In: IMAC Proceedings, 2021), there are situations where test analysis cross orthogonality is difficult to determine on inaccessible key regions of a test article. In that chapter, it is contended that it is in theory possible to augment data from accelerometers with data from other sensor sources at these key regions that have a proportionality to acceleration or displacement. This is important as strain and pressure have been shown to be useful measurements for modal analysis (Zienkiewicz et al., The finite element method: its basis and fundamentals, 6th edn. Butterworth-Heinemann, Oxford, p 563–584, 2005; Kranjc et al., J Sound Vib 332:6968, 2013; Kranjc et al., J Vib Control 22(2):371–381, 2016; Dos Santos et al., Strain-based experimental modal analysis: new concepts and practical aspects. In: Proceedings of ISMA. IEEE, Piscataway, p 2263–2277, 2016; Dos Santos et al., An overview of experimental strain-based modal analysis methods. In: Proceedings of the international conference on noise and vibration engineering (ISMA), Leuven, p 2453–2468, 2014). But they have not been used in augmentation with acceleration. Two specific examples discussed are fluid pressure and strain. Experimentally, this presents several problems. For example, in the most simple structures it is expected to have maximum acceleration at locations of 0 strain and vice versa. This makes it difficult to relate the modal information contained in acceleration variable to the strain variable at the location of maximum acceleration. Given that the FRF information will have to be uniform in units, this is another cause of concern when combining pressure, strain, and acceleration. Use of strain, pressure, and acceleration data all together for modal analysis purposes would reduce the need to place accelerometers in locations that are difficult to access. This chapter aims to present experimental results of strain and pressure FRF-based modal analysis on a rectangular steel plate and attempts to propose ways to combine these variables in the modal parameter estimation process.

Keywords Experimental modal analysis · Strain · Pressure · Augmentation · Non traditional variables

2.1 Introduction

In this research, two experiments were conducted on a rectangular steel place. The first experiment was an impact test with accelerometer and strain gauges as response measurements. The second experiment was another impact test with accelerometer, strain gauges, and microphones as the response measurements. Different ways of augmenting partial accelerometer data/results from partial accelerometer data were tried and MAC [2] values with full experimental data were checked. FRF synthesis from the modal vectors of the augmented data was also done and compared with measured acceleration FRF. Strain and pressure have been shown to be useful measurements for modal analysis [3–6] and [7]. But they have not been used in augmentation with acceleration. The aim of the MAC values and FRF synthesis comparisons was to show that augmenting accelerometer, pressure and strain data can give results that are close to results from accelerometer data.

P. M. Vinze (✉) · R. J. Allemang · A. W. Phillips
Department of Mechanical Engineering, College of Engineering and Sciences, University of Cincinnati, Cincinnati, OH, USA
e-mail: vinzepm@mail.uc.edu

R. N. Coppolino
Measurement Analysis Corporation, Torrance, CA, USA

B. J. Dilworth et al. (eds.), *Topics in Modal Analysis & Parameter Identification, Volume 9*, Conference Proceedings of the Society for Experimental Mechanics Series, https://doi.org/10.1007/978-3-031-34942-3_2

In the paper by Coppolino [1], the case that was considered was that of a rod that is modeled as a MDOF mass spring system. One of the major changes from that model to a system like a rectangular steel plate is that the strain (for all the modes in the frequency range of interest) is no longer due to extension and compression but due to bending. Another difference that is important to point out is that strain cannot be modeled as the ratio of difference of displacement at two neighboring points of response measurements and the length. The reason this does not work is that the plate is a continuous system, and the experimental strain measured will be the local measurement at the given point. In this way if measurements are made on n points, there will be n strain measurements, whereas in the theoretical model there will be $n - 1$ strains. These two factors are a big deviation from the model discussed in the referred paper but the general idea that measurements like strained pressure should give similar modal results is what served as motivation to attempt this work

2.2 Experimental Setup

The rectangular plate is rested on four rubber ball supports 6–8 inches inside of the four corners that approximate a free-free condition. The setup for the second experiment is shown in Fig. 2.1. For the first experiment, the setup was without the microphones and microphone stands. The strain gauges are placed next to the accelerometers and aluminum cubes were placed very close to provide a surface for X direction (along the long edge) impact (along the long edge on the plate). Figure 2.2 shows an image of the sensor placement. The numbers and circles etched on the plate are 160 equally spaced impact locations, a subset (40) of which have been used.

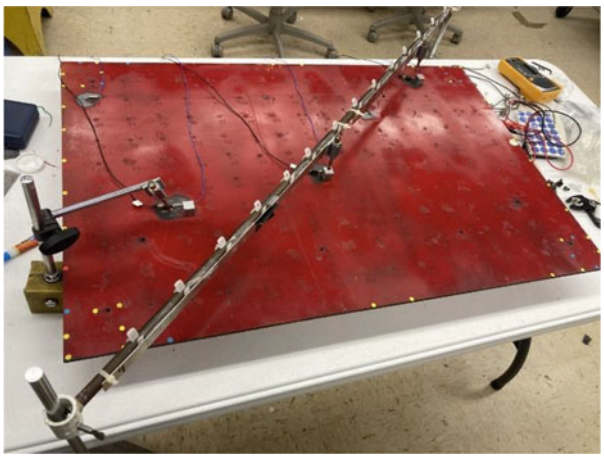

Fig. 2.1 Test setup

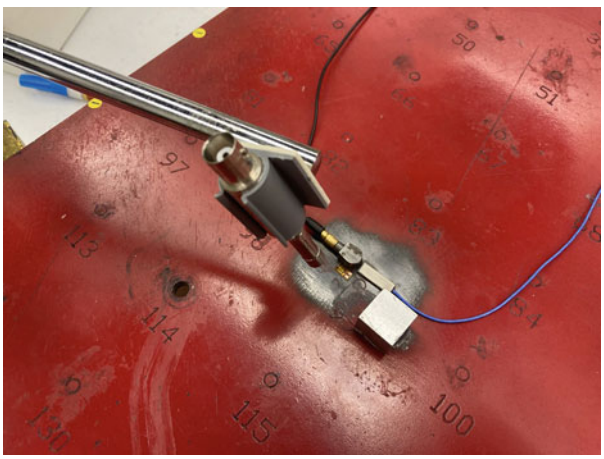

Fig. 2.2 Sensors on a plate

2.3 Analysis

A subset of the data gathered was used to get modal parameters. The idea was to work with several combinations of subsets to simulate a situation where different combinations of sensors on the structure could be worked with. This sieving of the full 9 × 40 FRF matrix was done in two ways:

1. Sieving by references only. This could be done before modal parameter estimation to create a new 3 × 40 FRF matrix that would contain one or two accelerometer reference points and the remaining reference points could be taken from the strain or pressure data for that reference points. When including pressure, it was important to scale the pressure in some way to a similar level of strain and acceleration.
2. Sieving by response as well as references. This means a subset of response points were chosen for acceleration references and another subset of response points for strain and in one case another subset of response points for pressure references. The choices are always made such that none of the 3 references or 40 response locations are completely missed out. Also some (3–5) response points are kept in common for all 3 reference locations. A composite modal vector is created by scaling the strain and pressure modal vectors based on the common response locations on the modal vectors and combining the scaled response at the locations that are not common between all three sensors.

These two methods were followed in different combination of selections and checked with a full set of accelerometer FRF-based results.

2.4 Sieving by References Only

The MACs were evaluated for strain and acoustic pressure-based modal vectors against the accelerometer-based modal vectors. The two MACs are shown in Figs. 2.3 and 2.4. This confirmed that pressure and strain data had the same modal information as acceleration data. Table 2.1 shows the modal frequencies and damping results for strain gauge and accelerometer-based modal analysis results and the percent difference between them. As can be seen the results agree expect for one damping result.

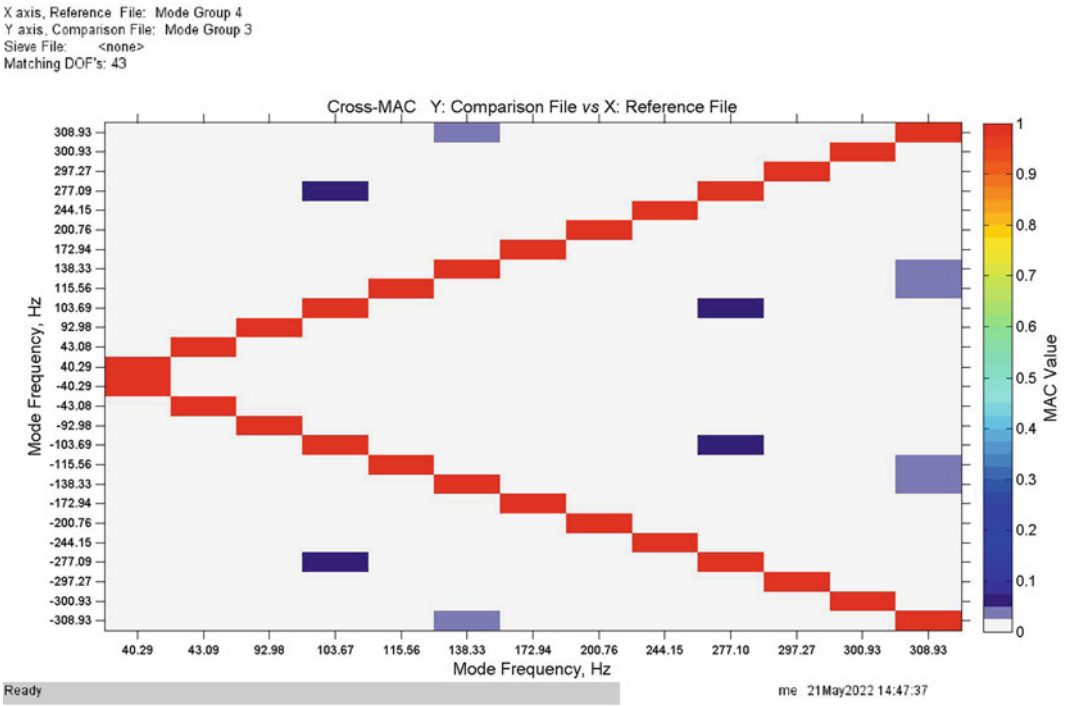

Fig. 2.3 Accelerometer-based versus strain-based modal vectors MACs

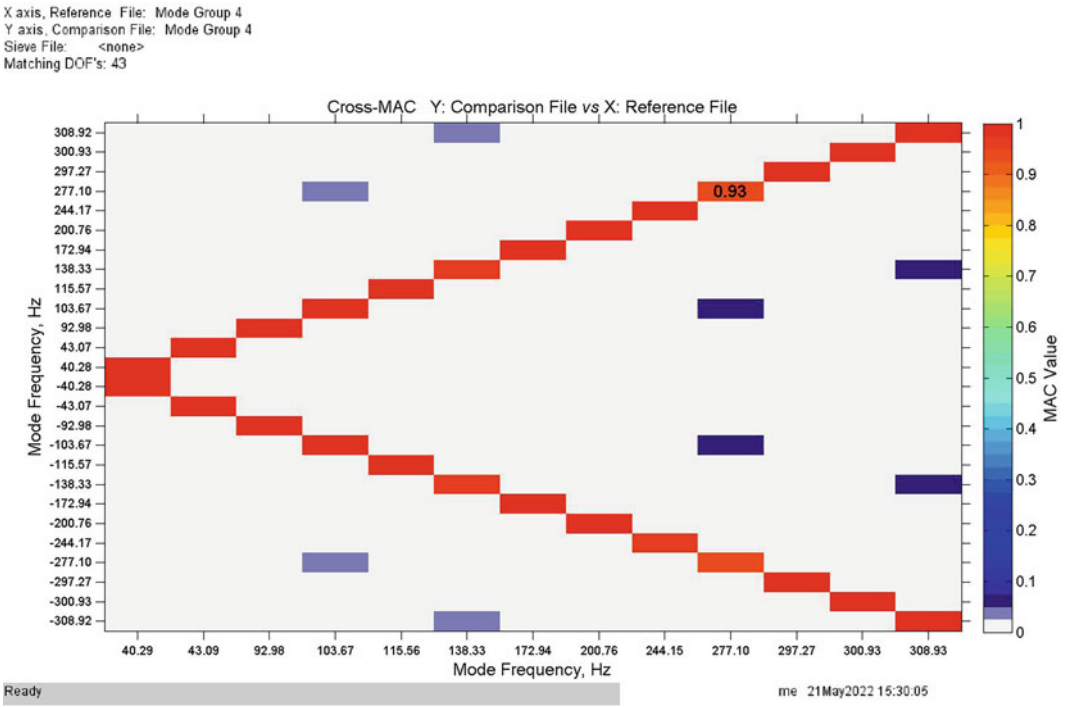

Fig. 2.4 Accelerometer-based versus microphone-based modal vectors MACs

Table 2.1 Accelerometer-based versus strain-based modal frequencies and damping results

S.No.	Strain frequency (Hz)	Strain damping (%)	Accelerometer frequency (Hz)	Accelerometer damping (%)	% diff frequency	% diff damping
1	40.2441	0.2488	40.255	0.2563	0.027077382	2.926258291
2	−40.2441	0.2488	−40.255	0.2563	0.027077382	2.926258291
3	43.0117	0.1258	43.0198	0.1401	0.018828539	10.206995
4	−43.0117	0.1258	−43.0198	0.1401	0.018828539	10.206995
5	92.931	0.0983	92.931	0.098	0	0.306122449
6	−92.931	0.0983	−92.931	0.098	0	0.306122449
7	103.679	0.029	103.6783	0.0284	0.000675165	2.112676056
8	−103.679	0.029	−103.6783	0.0284	0.000675165	2.112676056
9	115.5573	0.0274	115.5576	0.0275	0.000259611	0.363636364
10	−115.5573	0.0274	−115.5576	0.0275	0.000259611	0.363636364
11	138.3034	0.0331	138.2977	0.031	0.004121544	6.774193548
12	−138.3034	0.0331	−138.2977	0.031	0.004121544	6.774193548
13	172.9429	0.0206	172.9427	0.0199	0.000115645	3.51758794
14	−172.9429	0.0206	−172.9427	0.0199	0.000115645	3.51758794
15	200.731	0.0143	200.7539	0.0114	0.011407001	25.43859649
16	−200.731	0.0143	−200.7539	0.0114	0.011407001	25.43859649
17	244.1445	0.0264	244.1497	0.0246	0.002129841	7.317073171
18	−244.1445	0.0264	−244.1497	0.0246	0.002129841	7.317073171
19	277.0993	0.0257	277.0931	0.0265	0.002237515	3.018867925
20	−277.0933	0.0257	−277.0931	0.0265	7.21779E-05	3.018867925
21	297.2717	0.0353	297.2719	0.0351	6.72785E-05	0.56980057
22	−297.2717	0.0353	−297.2719	0.0351	6.72785E-05	0.56980057
23	300.9256	0.0148	300.9265	0.016	0.000299076	7.5
24	−300.9256	0.0148	−300.9265	0.016	0.000299076	7.5
25	308.9535	0.0356	308.9542	0.0351	0.000226571	1.424501425
26	−308.9535	0.0356	−308.9542	0.0351	0.000226571	1.424501425

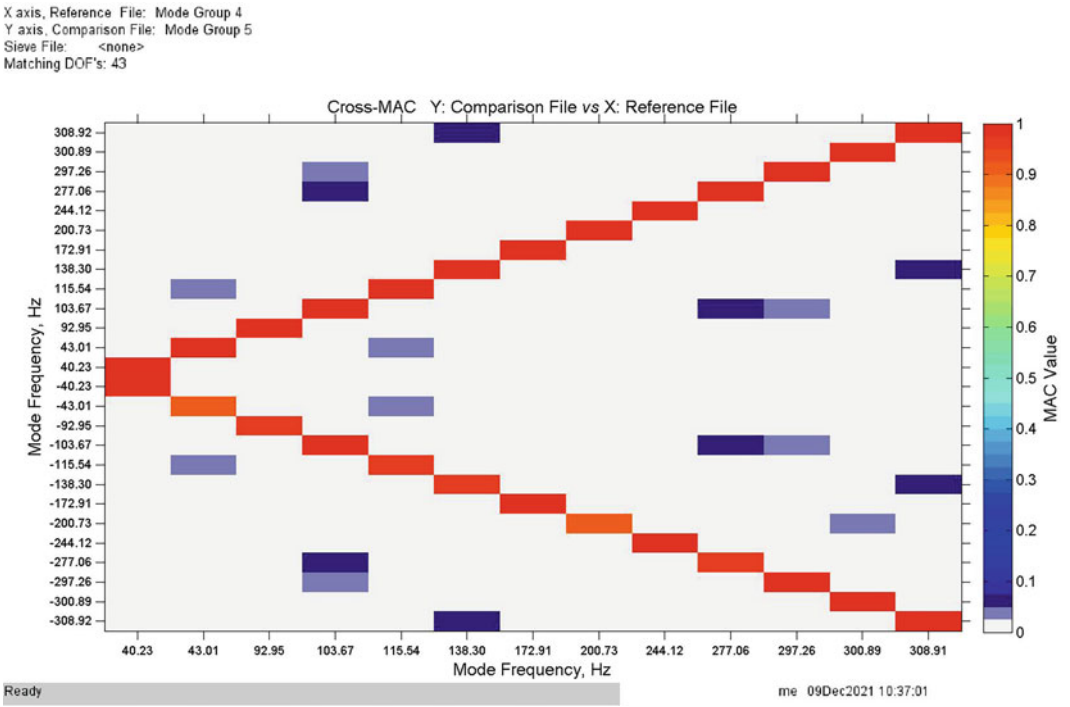

Fig. 2.5 MAC between 2 accelerometer and 1 strain versus 3 accelerometer

2.5 Accelerometers and One Strain Gauge

Modal vectors for data with two acceleration and one strain reference were compared with three acceleration modal vectors. The MAC comes out completely diagonal indicating that the modes are similar. MAC is shown in Fig. 2.5.

2.6 Accelerometer and Two Strain Gauges

Modal vectors for data with one acceleration and two strain references were compared with three acceleration modal vectors. The MAC comes out completely diagonal indicating that the modes are similar. MAC is shown in Figs. 2.6 and 2.7 for the two different acceleration references.

Another comparison that was done was to compare the density of pole estimates. There were differences in the density of the scatter plots, but it was different for different modes. There was not one set of data that gave better clusters of damping ratio values for all modes. This suggested that there was not any improvement in damping results from replacing accelerometers with strain gauges at some measurement locations.

2.7 Accelerometer and Microphones

To combine accelerometer data with microphone data, it was important to consider the fact that there was a large difference in their magnitudes. The microphone data was observed to be around 6 orders of magnitude larger. An equation was set up such that modified pressure FRF data was expressed as

$$\text{Hpm} = R3 * \text{Hp} + R2/\omega^2 + R1$$

where Hpm is the modified pressure data, Hp is measured pressure FRF, and $R1$, $R2$ and $R3$ are the terms determined in the least square sense by comparing Hpm to the displacement FRF on the same location. The average of all $R3$ values for all

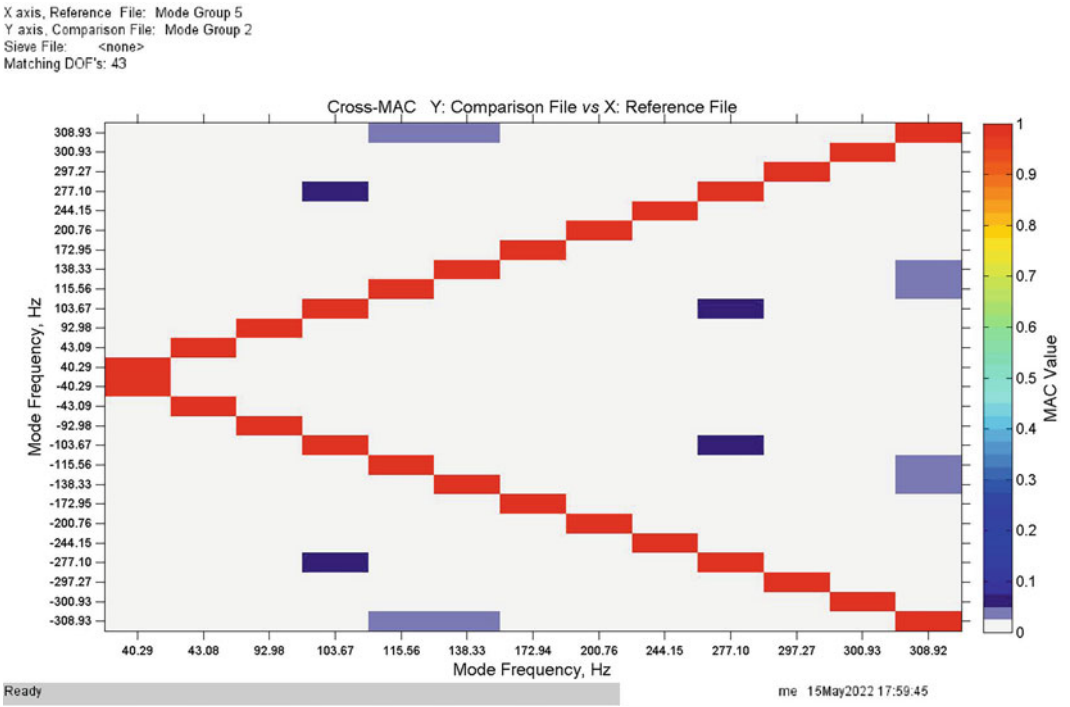

Fig. 2.6 MAC between 1 accelerometer (location14) and 2 strain versus 3 accelerometer

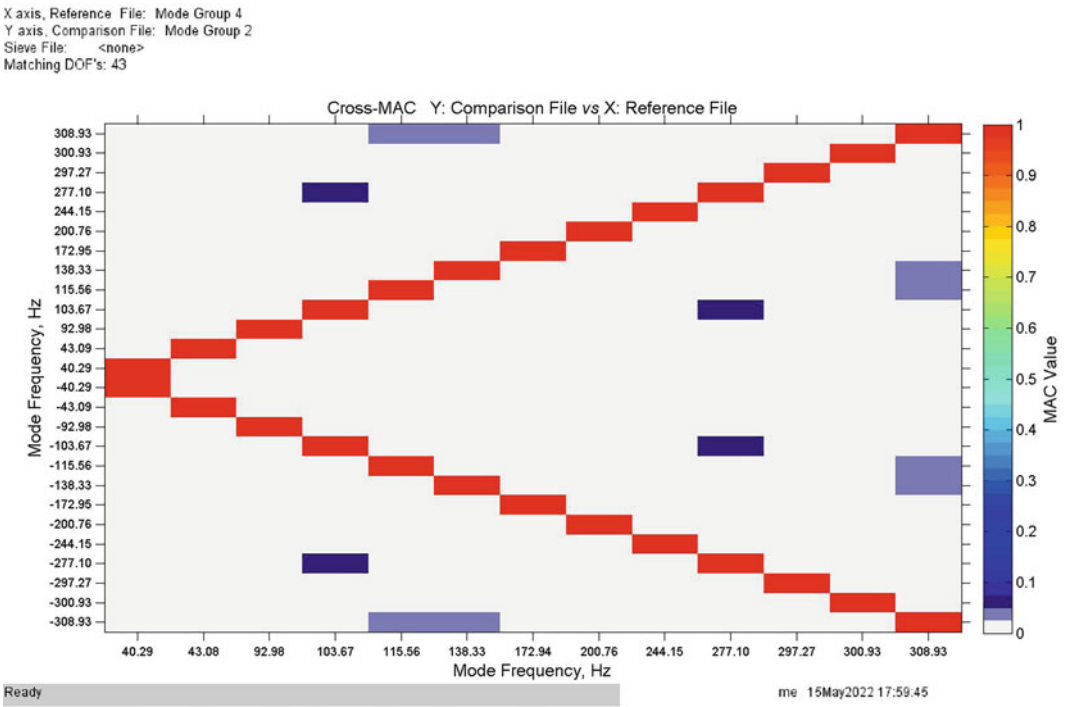

Fig. 2.7 MAC between 1 accelerometer (location99) and 2 strain versus 3 accelerometer

FRFs is calculated and used as the multiplier. The combining of pressure and displacement FRFs is only possible with the modified pressure because of the significant difference of scale of pressure and displacement data. Figures 2.8 and 2.9 show that the modal vectors obtained from combining pressure with acceleration measurements result in diagonal MAC values.

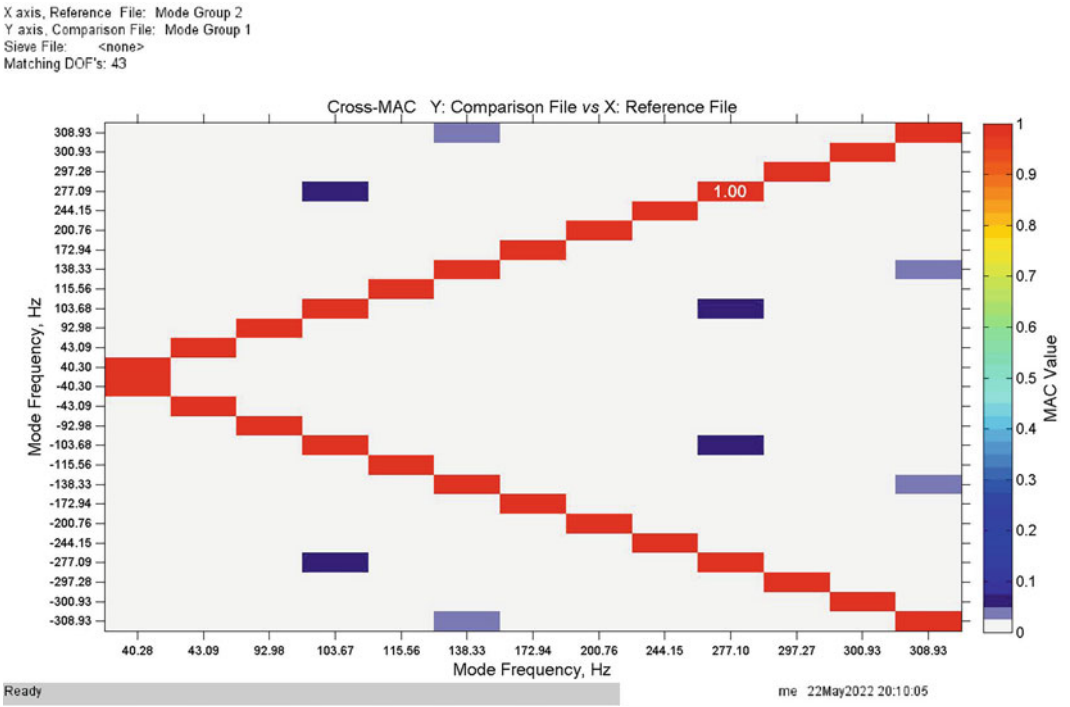

Fig. 2.8 MAC for 2 accelerometer 1 pressure modes versus 3 accelerometer modes

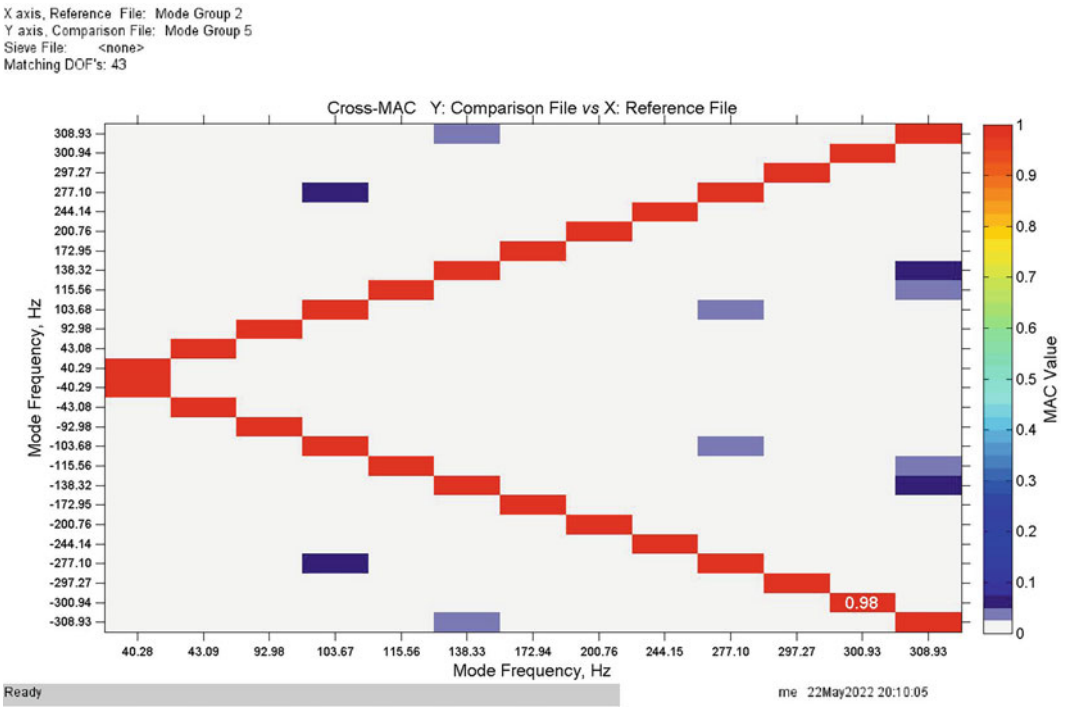

Fig. 2.9 MAC for 1 accelerometer 2 pressure modes versus 3 accelerometer modes

2.8 Sieving by References and Responses

2.8.1 Acceleration and Strain

Two different modal parameter estimation processes were carried out on two different sets of sieved FRF data. Seventeen response locations with 3 acceleration references were selected and modal vectors were extracted for first 13 modes. Twenty-eight response locations with 3 strain references were selected and modal vectors were extracted for first 13 modes. The 28 locations selected were such that there were exactly 5 locations in common with the 13 points selected for accelerometer data. Three out of these 5 locations on the two modal vectors (strain based and accelerometer based) were used to scale the strain modal vector upto the accelerometer modal vector. This was done by taking the point-by-point ratio of each of the 3 locations for the 13 modal vectors and averaging this value across the 3 ratio values. This yielded one multiplier for each strain based modal vector. Except for the 2 entries (corresponding to the 5th mode) in column 2, the ratio values are consistent across the three columns.

The MAC between the composite vectors and modal vectors found from 40 $\times$ 3 accelerometer data also comes diagonal showing that the sets of vectors match. The crossMAC is shown in Fig. 2.10. Residuals were calculated for these modal vectors based on the Modal A values obtained from X-Modal and synthesized displacement FRFs were compared to measured FRFs. Some example comparisons are shown in Fig. 2.11 in magnitude and phase format. It can be seen that the FRFs compare well. Another variation tried was when doing the acceleration MPE, and one of the references were removed. The FRF data for this reference was then synthesized from the composite modal vector. The results obtained were also consistent with the measured acceleration FRF of the selected reference.

2.8.2 Acceleration, Strain, and Pressure

Three different modal parameter estimation processes were carried out on three different sets of sieved FRF data. Seventeen responses with 3 acceleration references, 17 responses with 3 strain references, and 16 responses with 3 pressure references were taken such that 5 of the response locations were common. The acceleration response from these locations was used to scale the other two modal vectors to the acceleration modal vector magnitude. Similar to the data in Table 2.1, a ratio was evaluated between the common location modal vectors elements strain and acceleration and pressure and acceleration. The ratios were found to be generally consistent across 5 locations. This ratio was averaged and used to scale the strain and pressure-based modal vectors. A composite modal vector was then assembled using the three partial modal vectors. MAC was evaluated for the composite modal vector versus a full accelerometer-based modal vector. This MAC is shown in Fig. 2.12. Synthesized FRFs from these composite modal vectors were compared with measured FRFS and were observed to compare well as shown in Fig. 2.13. Synthesis of an absent reference has not been tried in this combined method yet.

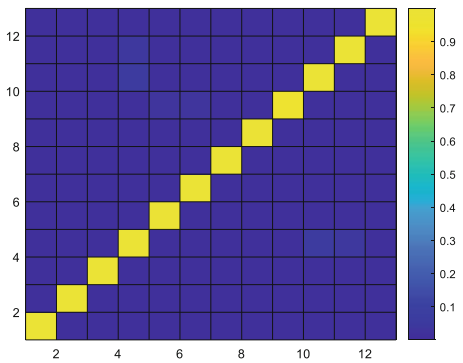

Fig. 2.10 MAC composite (acceleration and strain) modal vector versus normal modal vector

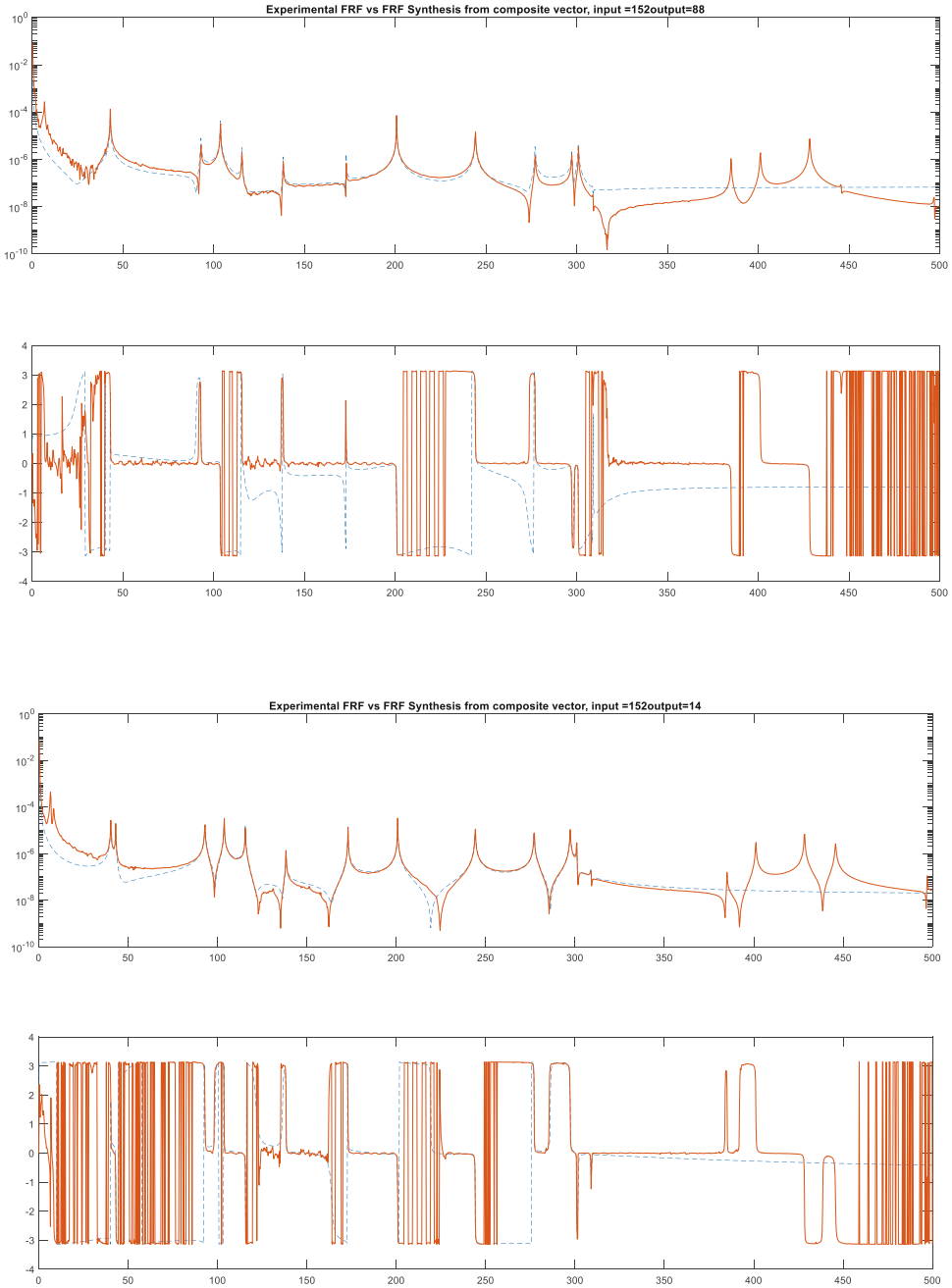

Fig. 2.11 Experimental (solid orange) versus synthesized (dotted blue) FRFs from composite vector (acceleration and strain)

2.9 Conclusion

Substituting acceleration reference with strain yielded close modal vector results as well as modal frequencies and damping. The difference in modal frequencies and damping is close to what is shown in Table 2.1 in all cases. There is variation in terms of how much of a scatter is observed in the damping estimates. But no consistent improvement due to adding strain data was observed across all modes. Substituting acceleration reference with acoustic pressure was not as simple. The pressure data had to be modified to bring it to a similar scale as the acceleration and strain data. Once that was done, the modal vector results did have a good MAC with full acceleration-based modal vectors.

When data was filtered through references as well as responses, it was done post modal parameter estimation of both strain and acceleration reference subsets. The ratio of modal contributions at the common locations for strain and acceleration came

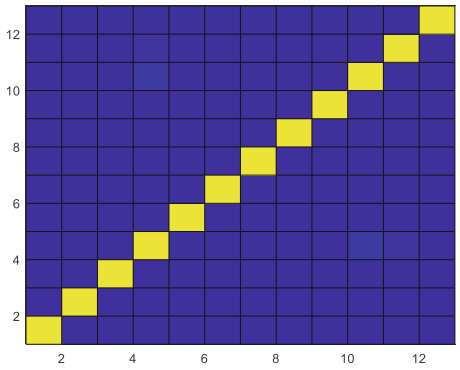

Fig. 2.12 MAC composite (acceleration, strain and pressure) modal vector versus normal modal vector

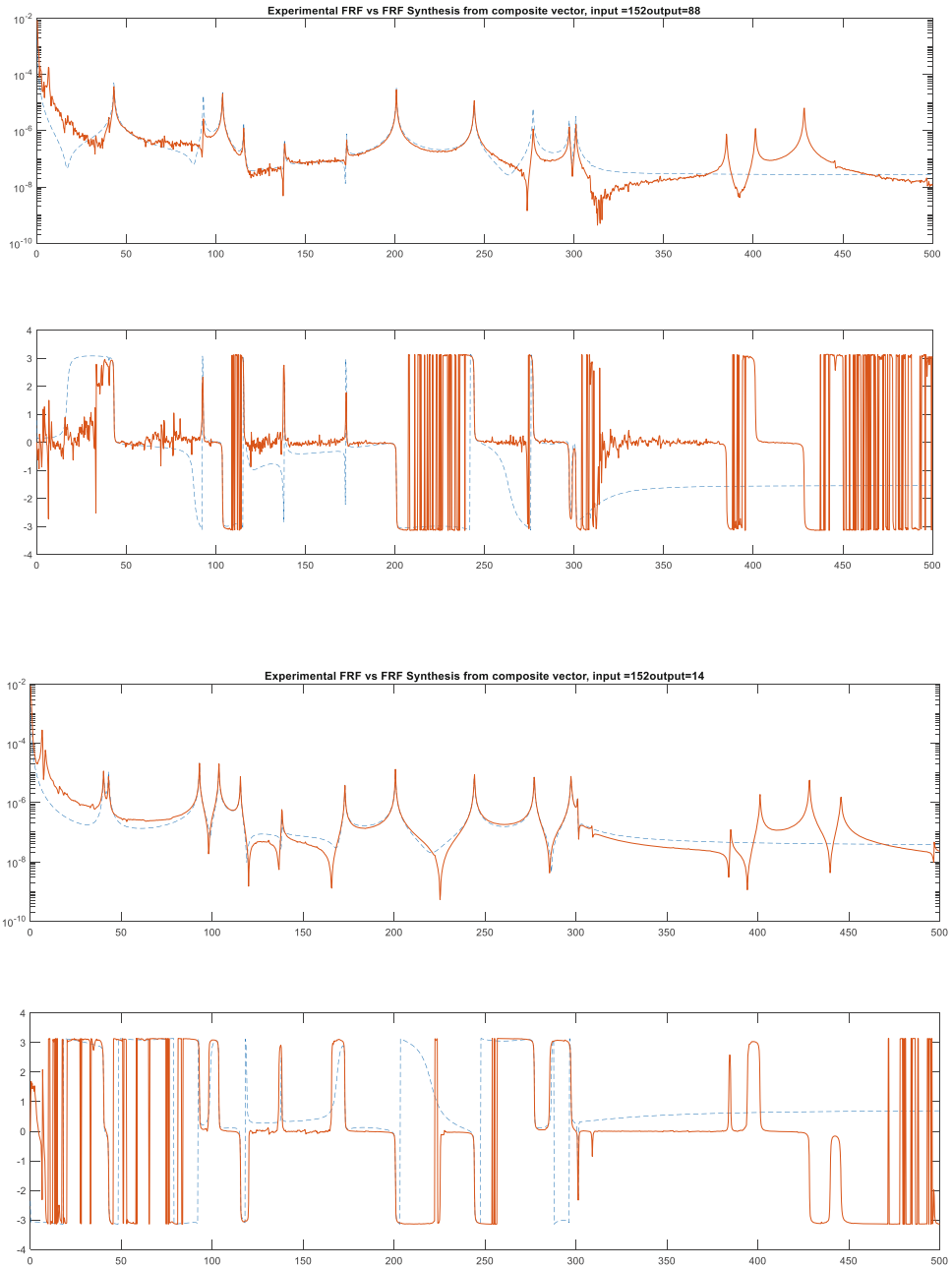

Fig. 2.13 Experimental (solid orange) versus synthesized (dotted blue) FRFs from composite vector (acceleration, strain and pressure)

out very close to −1 and 1 except for the 5th mode. The composite modal vector MAC with accelerometer-based modal vector came out diagonal. FRF data synthesized based on the composite modal vector compared generally well with the measured FRF. Composite modal vector evaluated with pressure data included with acceleration and strain also had a good MAC with accelerometer-based modal vectors. FRF synthesized compared well with acceleration-based modal vector.

The modal parameters obtained are the same or very close to what was obtained with the same amount of accelerometers, which brings up the question of whether replacing accelerometer data with other sensor data has yielded any improvements. It may be that due to its simplicity three accelerometers prove to be enough for the modal analysis of a rectangular plate. In that case, it might be useful to have a similar experiment of a structure that does not yield great results with three accelerometers. It will be worthwhile to also test a cylindrical container as originally discussed in the paper by Coppolino [1].

References

1. Coppolino, R.N.: Experimental modal analysis using non-traditional response variables. In: IMAC Proceedings. Springer, Cham (2021)
2. Allemang, R.J., Brown, D.L.: A correlation coefficient for modal vector analysis. In: Proceedings, International Modal Analysis Conference, pp. 110–116. Union College/Society for Experimental Mechanics/International Society for Optical Engineering Springer, Schenectady/Bethel/New York (1982)
3. Zienkiewicz, O.C., Taylor, R.L., Zhu, J.H.: The Finite Element Method: Its Basis and Fundamentals, 6th edn, pp. 563–584. Butterworth-Heinemann, Oxford (2005)
4. Kranjc, T., Slavic, J., Boltezar, M.: The mass normalization of the displacement and strain mode shapes in a strain experimental modal analysis using the mass-change strategy. J. Sound Vib. **332**, 6968 (2013)
5. Kranjc, T., Slavič, J., Boltežar, M.: A comparison of strain and classic experimental modal analysis. J. Vib. Control. **22**(2), 371–381 (2016)
6. Dos Santos, F.L.M., Peeters, B., Desmet, W., Góes, L.C.S.: Strain-based experimental modal analysis: new concepts and practical aspects. In: Proceedings of ISMA, pp. 2263–2277. IEEE, Piscataway (2016)
7. Dos Santos, F.L.M., Peeters, B., Lau, J., Desmet, W., Góes, L.C.S.: An overview of experimental strain-based modal analysis methods. In: Proceedings of the International Conference on Noise and Vibration Engineering (ISMA), pp. 2453–2468, Leuven (2014)

Chapter 3
A Somewhat Comprehensive Critique of Experimental Modal Analysis

Robert N. Coppolino

Abstract Over the past 70 years, the US aerospace community has maintained a standard for verification and validation of experimentally determined, real structural dynamic modes and mathematical models based on mass-weighted orthogonality criteria. This standard fundamentally contradicts observable physical aspects associated with the mechanical behavior of structures. Specifically, (a) energy dissipation (damping) forces are most often concentrated in joints, rather than nearly uniformly distributed throughout the structure; (b) structural modes are mathematically complex, yet often approximately real except when successive modal frequencies are closely spaced; and (c) complex structural modes, while often are approximately real, do not strictly satisfy mass-weighted orthogonality criteria. A bottom-up approach, based on the Simultaneous Frequency Domain Technique (SFD-2018), employs left-hand eigenvectors to (1) isolate individual complex measured modes and (2) guarantee mathematical orthogonality of complex measured modes (completely independent of a theoretical mass matrix and model expectations). In addition, (3) complex modes deduced from virtually all experimental modal analysis techniques are classified in terms of a complex mode index parameter that indicates each mode's level of "complexity," and (4) conventional experimental mode orthogonality and experimental-to-theoretical mode cross-orthogonality metrics are adapted via replacement of the transform operator with the Hermitian operator permitting direct employment of complex experimental modes. A welcome surprise, due to review of a specific real experimental mode approximation extends the useful life of established US aerospace community standards for verification and validation of modal test data and correlation and reconciliation of modal test results and mathematical model predictions.

Keywords Complex · Modes · Verification · Validation · Standards

3.1 Nomenclature

$[A]$	State-space plant matrix
$[B]$	Damping matrix
COH	Coherence
[COR]	Cross-orthogonality matrix
$\{F_e\}$	Applied force array
K	Stiffness matrix
$[M]$	Mass matrix
[OR]	Orthogonality matrix
$[V]$	SVD orthogonal that vector matrix
f	Frequency (Hz)
f_{n}	Natural frequency (Hz)
$\{q\}$	Modal displacement array
$\{u\}$	Displacement array
$\{v\}$	Velocity array
$[\Phi]$	Modal (eigenvector) matrix

R. N. Coppolino (✉)
Measurement Analysis Corporation, Torrance, CA, USA

B. J. Dilworth et al. (eds.), *Topics in Modal Analysis & Parameter Identification, Volume 9*, Conference Proceedings of the Society for Experimental Mechanics Series, https://doi.org/10.1007/978-3-031-34942-3_3

$[\Phi_{\mathrm{L}}]$	Left-hand eigenvector matrix
$[\Gamma_e]$	Applied force allocation matrix
$[I]$	Identity matrix
$[\varphi_u]$	Displacement partition of state-space modal matrix
$[\varphi_{u\mathrm{L}}]$	Displacement partition of left hand state-space modal matrix
$[\varphi_v]$	Velocity partition of state-space modal matrix
$[\varphi_{v\mathrm{L}}]$	Velocity partition of left-hand state-space modal matrix
λ	Eigenvalue
ω	Frequency (radian/s)
ω_{n}	Natural frequency (radian/s)
$\{\xi\}$	SVD generated displacement array
ζ_n	Modal damping

3.2 Introduction

Over the past 60+ years, the US aerospace community has developed, refined, and standardized an integrated approach to structural dynamic model verification and validation. One name for this overall approach is the Integrated Test Analysis Process (ITAP) for structural dynamic systems. ITAP consists of seven sequential steps, namely, (1) development of a system dynamic model, (2) development of a modal test plan, (3) measured data acquisition, (4) measured data analysis, (5) experimental modal analysis, (6) test-analysis correlation, and (7) model updating (reconciliation). Steps (1) and (2) focus primarily on finite element modeling and specialized matrix analysis techniques. Steps (3) and (4) employ time history data and correlation and spectral analysis techniques that ultimately provide estimated frequency response data required for Step (5) experimental modal analysis operations (the primary focus of this paper).

Experimental modal analysis, as viewed by the US aerospace community, consists of two sub-components, namely, (5a) estimation of test modes, natural frequencies, and modal damping factors associated with a subject modal test article, and (5b) verification and validation of estimated test modes employing modal orthogonality criteria. Established US aerospace community standards presently require satisfaction of real mode based orthogonality goals, which presents a challenge in situations involving test modes that are strongly complex (typically occurring when modal frequencies are closely spaced). Moreover, test mode orthogonality is always dependent on accuracy of a theoretical test-analysis model (TAM) mass matrix. The established approach to satisfaction of orthogonality goals involves conversion of mathematically complex test modes to an approximate real form; one particularly reliable approach to that conversion has been in use by several US aerospace organizations for many years. That being said, effectiveness of test mode verification and validation is dependent on accuracy of the TAM mass matrix, rendering the process a blend of theoretical FEM and laboratory efforts. Relief to the "blend" issue is uniquely offered by an experimental modal analysis procedure, namely SFD-2018, which estimates automatically orthogonal state-space experimental modes that are completely independent of a FEM-based TAM mass matrix. Reliance on SFD-2018 completely separates experimental mode estimation and verification and validation from FEM inaccuracies.

Getting back to the "post-test" challenges associated with (6) test-analysis correlation and (7) model updating (reconciliation), it appears that application of the Aerospace Corporation's technique for approximation of real test modes permits effective use of procedures that operate on undamped test article modal characteristics. In many modal test situations, this extends utility of established techniques for generation of high-quality post-test dynamic models.

It should be noted here that this chapter's title adjective "somewhat comprehensive" alludes to a deliberately limited class of test articles that behave as linear systems. Nonlinearity is the subject of future "comprehensive" studies.

3.3 Overview of the Integrated Test-Analysis Process

Over the past 60+ years, the US aerospace community has developed, refined, and standardized an integrated approach to structural dynamic model verification and validation. One name for this overall approach is the Integrated Test Analysis Process (ITAP) for structural dynamic systems, which is summarized in Fig. 3.1.

The yellow colored steps are associated with analytical-centric disciplines, while the aqua colored steps are associated with laboratory-centric disciplines. The mixed colored steps involve a blend of analytical and laboratory disciplines. Within the US aerospace community, two particular standards [1, 2] provide specifications related to the ITAP process.

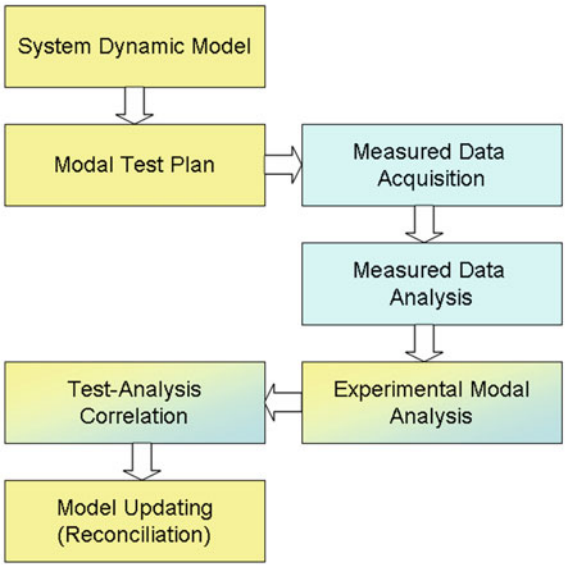

Fig. 3.1 Overview of the integrated test analysis process

3.3.1 System Dynamic Model

An appropriate finite element *system dynamic* model (FEM) requires adherence to several practical, well-documented guidelines [3, 4]. In summary, the most important guidelines that are sometimes missed in practice are as follows:

1. Strictly enforced consistency of the FEM with engineering drawings (CAD).
2. Selection of component sufficiently refined grid spacing to appropriately capture relevant frequency band dynamics.
3. Inclusion of quasi-static effects (differential stiffness) due to gravity or steady acceleration and hydrostatic pressure loads.
4. Provision for localized joint flexibilities to permit subsequent model updating (reconciliation).
5. Inclusion of nonlinear features, when significant, especially at component interfaces (early Space Shuttle experiences) [5–7].

3.3.2 Modal Test Plan

The commonly accepted practice for modal test planning focuses on development of a test-analysis model (TAM) employing Guyan reduction [8] of a detailed FEM that is consistent with a selected set of test accelerometer degrees of freedom (DOF). Moreover, "residual kinetic energy" strategies for selection of appropriate TAM degrees of freedom [9, 10] are widely accepted today. The most important products of the modal test planning step are the TAM mass matrix, which is used for validation of experimental modes through an orthogonality check [1, 2], FEM natural frequencies, and (real) mode shapes (in particular, the TAM DOF order partition).

3.3.3 Measured Data Acquisition and Measured Data Analysis

Measured data acquisition, the technical discipline of highly experienced laboratory personnel, involves selection and verification and validation of excitation and response measurement resources to be used in a modal test. On the other hand, measured data analysis is a discipline that requires both (a) measured data acquisition expertise and (b) utilization of advanced mathematical tools [4, 11, 12] and associated personnel (who are ideally experienced in both data acquisition and analysis). Key products of these ITAP steps are as follows:

1. Determination of linear or nonlinear modal test article behavior (nonlinear behavior is beyond the scope of this chapter).
2. Estimation of MI/MO frequency response arrays and associated coherence arrays required for experimental modal analysis.

Close attention must be paid to coherence array data to establish high signal-to-noise qualities of estimated frequency response arrays and accurate experimentally determined system modes.

3.3.4 *Experimental Modal Analysis*

The discipline of experimental modal analysis, from the viewpoint of this chapter, may be divided into three distinct eras:

(a) The "analog" era (pre-1970 and later), which focused on experimental techniques to isolate individual (real) modes often employing multi-shaker sine-dwell tuning [13].
(b) The "digital" era (1970-present), which focuses primarily on mathematical techniques to estimate real or complex modes from MI/MO frequency response arrays [14, 15].
(c) The Simultaneous Frequency Domain or "SFD" era (1979-present), a subdivision of the "digital" era, which focuses on mathematical techniques employing singular value decomposition (SFD) and linear least-squares tools to estimate real or complex modes from MI/MO frequency response arrays [3, 4].

Across all three above noted eras, the dominant emphasis in the US aerospace community has focused on "real" experimental modes [13] in spite of strong evidence beyond the "analog" era indicating the actuality of "complex" experimental modes [3, 4, 15]. As a result, NASA [1] and the US Air Force Space Command [2] established standardized (TAM mass matrix weighted) orthogonality criteria for validation of "real" experimental modes. Since the TAM mass matrix is based on a theoretical finite element model, the US aerospace community's experimental mode validation criteria are not entirely objective; that is, failure to satisfy standardized orthogonality criteria may be due to inaccuracies in the test article's FEM, "real" experimental modes, or both sources. More recently developed methodology [4], to be discussed in a later section of this chapter, defines a more objective (experimental data based) approach for validation of "complex" experimental modes.

3.3.5 *Test-Analysis Correlation*

Correlation of the results of experimental modal analysis with a test article's FEM is necessarily a process straddling experimental and analytical data sources. Within the US aerospace community, NASA [1], and the US Air Force Space Command [2] established standardized (TAM mass matrix weighted) cross-orthogonality criteria for comparison of "real" experimental modes and natural frequencies and FEM undamped modes and natural frequencies. Effectiveness and relevance of the standardized cross-orthogonality criteria are legitimately challenged by the actuality of (sometimes strongly) complex experimental modes and widely employed "real" experimental mode approximations.

3.3.6 *Test-Analysis Reconciliation*

Reconciliation of the test article's FEM with experimental modal analysis results focuses on parametric alteration of the pre-test FEM to minimize differences between corresponding modal test and FEM modal characteristics. Within the US aerospace community, reconciliation is typically governed by satisfaction of (a) "real" test mode mass-weighted orthogonality, and (b) "real" test mode to FEM undamped mode mass-weighted cross-orthogonality including "real" test mode to FEM undamped mode natural frequency correspondence criteria [1, 2]. The variety of algorithms currently employed to achieve reconciliation include (a) efficient FEM parametric sensitivity analysis via residual mode augmentation [16], (b) minimization (optimization) of defined cost functions employing Simplex [17], Monte-Carlo [18], and genetic [19] strategies.

3.4 Damping and Parametric Uncertainties in Structural Assemblies

It appears that enduring misconceptions regarding damping are based on Lord Rayleigh's 1877 statement [20], "The first case occurs frequently, *in books at any rate*, when motion of each part of the system is resisted by a retarding force, proportional

both to the mass and velocity of the part. The same exceptional reduction is possible when F (*the dissipation force*) is a linear function of T (*kinetic energy*) and V (*strain energy*)." This statement is believed responsible for the concept of "proportional damping," which is described by the symmetric damping matrix for a damped linear structural dynamic system,

$$[M]\{\ddot{u}\} + [B]\{\dot{u}\} + [K]\{u\} = [\Gamma_e]\{F_e\}, \tag{3.1}$$

where following Lord Rayleigh's 1877 speculation,

$$[B] = \alpha[M] + \beta[K], \tag{3.2a}$$

or based on Caughey and O'Kelly's extension [21],

$$[B] = [M]\sum_{j=0}^{N-1}\left[M^{-1}K\right]^j \tag{3.2b}$$

Employing unit mass normalized system modes, $[\Phi]$, defined by,

$$[K][\Phi] = [M][\Phi][\lambda], [\Phi]^{\mathrm{T}}\ [M][\Phi] = [\mathrm{I}], \tag{3.3}$$

The modal damping matrix (based on either Eqs. 3.2a or 3.2b) is uncoupled, that is,

$$[\Phi]^{\mathrm{T}}\ [B][\Phi] = \left[\text{diagonal}\right] \tag{3.4}$$

While the concept of proportional damping is mathematically elegant and widely employed in structural dynamics practice, a wealth of empirical data [22] indicates that damping in many structural assemblies is non-proportional and concentrated in joints. Moreover, (difficult to predict and model) localized flexibility appears to be concentrated in structural joints and other discontinuities [23]. Two uncomfortably clear facts result from the above empirical evidence (supported by extensive results of experimental modal analyses [14, 15]) specifically,

1. Parametric stiffness and damping uncertainties in appropriately modeled structural assemblies tend to be localized in joints and other discontinuities.
2. Vibration modes for (linearly behaving) structural assemblies are mathematically complex (although often approximately real).

3.5 Real and Complex Structural Dynamic Modes

The matrix equations describing dynamics of a linearly behaving structural dynamic system (see Eq. 3.1), that is not strongly interacting with other media (e.g., flowing fluids, propulsion systems, rotating turbo-machinery, control systems), are described by symmetric, positive-definite mass, and positive-semi-definite damping and stiffness matrices. It is instructive at this point to review and summarize modal relationships for two general situations, specifically (a) real normal modes and (b) complex modes.

3.5.1 Real Modes

Modes associated with the undamped, symmetric matrix system satisfy the following algebraic eigenvalue problem,

$$[K][\Phi] = [M][\Phi]\left[\omega_n^2\right], \tag{3.5}$$

where the matrix of eigenvalues, $[\omega_n^2]$, is real and diagonal. In addition, the real modes, $[\Phi]$ (when they are unit modal mass normalized) satisfy the following orthogonality conditions:

$$[\Phi]^{\mathrm{T}}[M][\Phi] = [I], [\Phi]^{\mathrm{T}}[K][\Phi] = \left[\omega_n^2\right]. \tag{3.6}$$

Employing the real mode displacement transformation,

$$\{u\} = [\Phi]\{q\}, \tag{3.7}$$

the system's dynamic response may be described in terms of the uncoupled modal equations,

$$\ddot{q}_n + 2\zeta_n\omega_n\dot{q}_n + \omega_n^2 q_n = \left[\Phi_n^{\mathrm{T}}\Gamma_e\right]\{F_e\}, \tag{3.8a}$$

where,

$$2\zeta_n\omega_n = \{\Phi_n\}^{\mathrm{T}}[B]\{\Phi_n\}. \tag{3.8b}$$

An important additional (theoretical) decoupling transformation resulting from the Eq. 3.6 orthogonality property is

$$\{\ddot{q}\} = \left[\Phi^{\mathrm{T}}M\right]\{\ddot{u}\}. \tag{3.9}$$

The above relationship forms the basis of the SMAC algorithm [24]; however, it does not satisfactorily decouple experimentally estimated modal responses when the measured system dynamics are more consistent with empirically estimated complex modes.

3.5.2 *Complex Modes*

The matrix equations describing dynamics of a linearly behaving structural dynamic system (see Eq. 3.1) are now described in state-space form by introduction of the velocity array,

$$\{v\} = \{\dot{u}\}, \tag{3.10}$$

ultimately resulting in the (unsymmetric) state-space matrix equation set,

$$\begin{Bmatrix}\dot{v}\\ \dot{u}\end{Bmatrix} = \begin{bmatrix}-M^{-1}B & -M^{-1}K\\ I & 0\end{bmatrix}\begin{Bmatrix}v\\ u\end{Bmatrix} + \begin{bmatrix}M^{-1}\Gamma_e\\ 0\end{bmatrix}\{F_e\}. \tag{3.11}$$

It should be noted here that various (two coefficient matrix) symmetric forms of the state-space equations are possible [3]; however, the above single coefficient matrix form suits the purposes of the present discussion. Complex state-space modes associated with the algebraic eigenvalue problem [25],

$$\begin{bmatrix}-M^{-1}B & -M^{-1}K\\ I & 0\end{bmatrix}\begin{bmatrix}\varphi_v\\ \varphi_u\end{bmatrix} + \begin{bmatrix}\varphi_v\\ \varphi_u\end{bmatrix}[\lambda] \Rightarrow [A][\Phi] = [\Phi][\lambda], \tag{3.12}$$

are mutually orthogonal via definition of the left-hand eigenvectors (employing the full set of state-space eigenvectors or modes),

$$[\Phi]^{-1} = [\Phi_{\mathrm{L}}] = [\varphi_{v\mathrm{L}}\ \ \varphi_{u\mathrm{L}}]. \tag{3.13}$$

Therefore, the "left-hand" and "right-hand" eigenvectors satisfy the following orthogonality conditions:

$$[\Phi_{\mathrm{L}}]\,[\Phi] = [\varphi_{v\mathrm{L}}\varphi_v + \varphi_{u\mathrm{L}}\varphi_u] = [\mathrm{I}] \tag{3.14a}$$

$$[\Phi_{\mathrm{L}}]\,[A]\,[\Phi] = [\lambda]\,. \tag{3.14b}$$

Note that the above state-space orthogonality conditions are neither mass-weighted nor necessarily "normalized." Employing the state-space modal transformation,

$$\left\{ \begin{matrix} v \\ u \end{matrix} \right\} = [\Phi]\,\{q\}\,, \tag{3.15}$$

and the above orthogonality relationships, the state-space orthogonality conditions to Eq. 3.11 results in the uncoupled modal state-space dynamic equations,

$$\dot{q}_n - \lambda_n q_n = \left[\varphi_{v\mathrm{L}} M^{-1} \Gamma_e \right] \{F_e\}\,. \tag{3.16}$$

Finally, employing state-space orthogonality a more general (theoretical) decoupling transformation,

$$\{\dot{q}\} = [\Phi_{\mathrm{L}}] \left\{ \begin{matrix} \dot{v} \\ \dot{u} \end{matrix} \right\} = [\varphi_{v\mathrm{L}}]\,\{\dot{v}\} + [\varphi_{u\mathrm{L}}]\,\{\dot{u}\}\,, \tag{3.17}$$

that is not compromised by the presence of complex modes (as is the case for Eq. 3.9) is realized.

3.6 Experimental Modal Analysis with a Focus on the SFD Method

Challenges associated with experimental modal analysis within the context of the integrated test-analysis process (ITAP) and established US aerospace community standards [1, 2] were the topic of two recent IMAC papers [26, 27] and a book [4]. Those same publications offer a complete discussion on the topic experimental modal analysis and SFD, which will be outlined in the following sections.

3.6.1 Experimental Modal Analysis Overview

Continuing the discussion initiated in Sect. 3.4 of this chapter, the experimental modal analysis process associated with the "digital" era (1970-present), of which the "SFD" era (1979-present) is a sub-category, can be summarized in the flow chart provided in Fig. 3.2.

Excepting the important category of ambient or operational modal analysis [28–30], "digital" era experimental modal analysis (identification) involves processing of frequency response function (FRF) arrays associated with quality (high signal-to-noise), linear dynamic system measured data. It is important to note that quality and linearity of FRFs are verified by established data acquisition and data analysis practices and procedures [4]; questionable quality and linearity of FRF data often produces misleading experimental modal analysis results.

A wide variety of techniques have been developed for estimation of modal parameters (mode shapes, natural frequencies, damping parameters) from FRF data [14, 15]. The vast majority of experimental modal analysis techniques produce complex (rather than real) modes, which are "inconvenient" with respect to generally accepted US aerospace community standards [1, 2] that rely on TAM mass-weighted orthogonality criteria for experimental mode validation. An alternative approach to experimental mode validation, specifically computation of uncoupled modal frequency responses, reminiscent of "analog" era (pre-1970 and later) techniques [13], circumvents inconveniences associated with complex experimental modes. The alternative validation approach, however, is a unique capability of the SFD-2018 technique that is summarized in the next section.

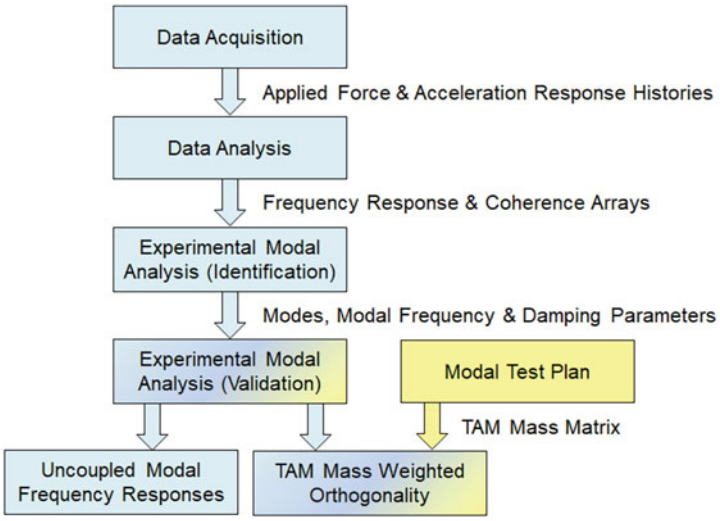

Fig. 3.2 Experimental modal analysis (1970-present) overview

3.6.2 Overview of the Simultaneous Frequency Domain (SFD-2018) Method

A thorough exposition of the SFD method [4, 26, 27] is not repeated in this chapter. Instead, an overview of the features, options, and new opportunities offered by the latest version of the method, namely SFD-2018, is provided herein.

The SFD method assumes that FRFs associated with a series of "N" excitations may be expressed in terms of the "Ritz natural condensation" (RNC) transformation described by

$$\left[\ddot{U}_1(f)\ \ddot{U}_2(f)\ \ldots\ \ddot{U}_N(f)\right] = [V]\left[\ddot{\xi}_1(f)\ \ddot{\xi}_2(f)\ \ldots\ \ddot{\xi}_N(f)\right] \Rightarrow \left[\ddot{U}(f)\right] = [V]\left[\ddot{\xi}(f)\right], \tag{3.18}$$

By performing singular value decomposition (SVD) analysis [31] of the FRF collection, a dominant set of RNC vectors, $[V]$, and complex generalized FRFs, $\left[\ddot{\xi}(f)\right]$, is obtained. Unit normalization of the SVD trial vectors is expressed as

$$[V]^{\mathrm{T}}[V] = [I]\,. \tag{3.19}$$

Theoretically, the generalized FRF array describes the following dynamic system equations associated with the individual applied forces,

$$\left[\ddot{\xi}(f)\right] + \left[\tilde{B}\right]\left[\dot{\xi}(f)\right] + \left[\tilde{K}\right][\xi(f)] = \left[\tilde{\Gamma}\right][F(f)]\,, \text{ where } \left[\tilde{B}\right] = \left[M^{-1}\right][B] \text{ and } \left[\tilde{K}\right] = \left[M^{-1}\right][K]\,. \tag{3.20}$$

The real, effective dynamic system matrices, $\left[\tilde{B}\right]$, $\left[\tilde{K}\right]$, and $\left[\tilde{\Gamma}\right]$, are estimated by linear least-squares analysis [32].

Estimation of experimental modal parameters is performed by complex eigenvalue analysis of the state variable form of the effective dynamic system,

$$\begin{Bmatrix} \ddot{\xi}(f) \\ \dot{\xi}(f) \end{Bmatrix} = \begin{bmatrix} -\tilde{B} & -\tilde{K} \\ I & 0 \end{bmatrix} \begin{Bmatrix} \dot{\xi}(f) \\ \xi(f) \end{Bmatrix} + \begin{bmatrix} \tilde{\Gamma} \\ 0 \end{bmatrix} \{F(f)\}\,. \tag{3.21}$$

The effective dynamic system is of the same type described previously in Sect. 5.2 of this chapter. And its complex modal solution possesses the same orthogonality properties, specifically,

$$\begin{bmatrix} -\tilde{B} & -\tilde{K} \\ I & 0 \end{bmatrix} \begin{bmatrix} \varphi_{\dot{\xi}} \\ \varphi_{\xi} \end{bmatrix} = \begin{bmatrix} \varphi_{\dot{\xi}} \\ \varphi_{\xi} \end{bmatrix} [\lambda] \Rightarrow \left[\tilde{A}\right]\left[\tilde{\Phi}\right] = \left[\tilde{\Phi}\right][\lambda]\,, \tag{3.22}$$

$$\left[\tilde{\Phi}\right]^{-1} = \left[\tilde{\Phi}_{\mathrm{L}}\right] = \left[\varphi_{\dot{\xi}\mathrm{L}}\ \varphi_{\xi\mathrm{L}}\right], \left[\tilde{\Phi}_{\mathrm{L}}\right]\left[\tilde{\Phi}\right] = \left[\varphi_{\dot{\xi}\mathrm{L}}\varphi_{\dot{\xi}} + \varphi_{\xi\mathrm{L}}\varphi_{\xi}\right] = [I], \left[\tilde{\Phi}_{\mathrm{L}}\right]\left[\tilde{A}\right]\left[\tilde{\Phi}\right] = [\lambda]. \tag{3.23}$$

$$\{\dot{q}(f)\} = \left[\varphi_{\dot{\xi}\mathrm{L}}\right]\left\{\dot{\xi}(f)\right\} + \left[\varphi_{\xi\mathrm{L}}\right]\{\xi(f)\}\ \text{(uncoupled modal frequency responses)}. \tag{3.24}$$

An important experimental modal analysis "modal coherence" metric [4, 26, 27] is defined based on comparison of uncoupled modal responses based on Eq. 3.24 and direct analytical solutions of Eq. 3.20.

Recovery of (analytically orthogonal, complex) state-space experimental modes in terms of the physical DOFs involves back transformation employing the trial vector matrix, $[V]$, specifically,

$$[\Phi] = \begin{bmatrix}\varphi_v \\ \varphi_u\end{bmatrix} = \begin{bmatrix}V & 0 \\ 0 & V\end{bmatrix}\begin{bmatrix}\varphi_{\dot{\xi}} \\ \varphi_{\xi}\end{bmatrix}, [\Phi_{\mathrm{L}}] = \left[\varphi_{v\mathrm{L}}\ \varphi_{u\mathrm{L}}\right] = \left[\varphi_{\dot{\xi}\mathrm{L}}\ \varphi_{\xi\mathrm{L}}\right]\cdot\begin{bmatrix}V^{\mathrm{T}} & 0 \\ 0 & V^{\mathrm{T}}\end{bmatrix}, [\mathrm{OR}] = [\Phi_{\mathrm{L}}][\Phi] \equiv [I]. \tag{3.25}$$

3.6.3 Linear Least-Squares Refitting of Experimental Modes

A widely used strategy for estimation of experimental modes, regardless of the specific technique employed to estimate a modal test article's complex eigenvalues, involves linear least-square fitting of measured frequency response functions, $\left[\ddot{U}(f)\right]$. Two strategies appear to be employed for (a) constrained estimation of mathematically real experimental modes and (b) unconstrained estimation of mathematically complex experimental modes.

Constrained estimation of real experimental modes operates on the relationship,

$$\left[\ddot{U}(f)\right] = [\varphi_v]\left[\ddot{\xi}(f)\right], \tag{3.26}$$

where for each mode,

$$\ddot{\xi}_n(f) = \frac{-(f/f_n)^2}{1 + 2i\zeta_n\,(f/f_n) - (f/f_n)^2}. \tag{3.27}$$

Unconstrained estimation of complex experimental modes operates on the relationship,

$$\left[\ddot{U}(f)\right] = -\,(2\pi\cdot f)\cdot\sum_{n=1}^{N}\left(\frac{\varphi_{vn}}{\lambda_n - i\,(2\pi\cdot f)} + \frac{\varphi_{vn}^*}{\lambda_n^* - i\,(2\pi\cdot f)}\right), \tag{3.28}$$

where for each positive frequency mode,

$$\lambda_n = -\zeta_n\omega_n + i\omega_n\ (\omega_n = 2\pi f_n) \tag{3.29}$$

3.6.4 Experimental Mode Rectification and the Complex Mode Index Metric

Complex experimental mode estimates possess characteristics that require an understanding that extends beyond more familiar real experimental mode estimates. Note that all references to experimental modes in the present context refer to the "velocity" partition, $\{\varphi_V\}$, of the complex state-space mode, $\{\Phi\}$ (see Eq. 3.25). Specifically, similar to the case of real modes, complex modes may be expressed in terms of arbitrary phase in the complex plane (note that real modes are expressible with arbitrary "±" phase in the real plane). An effective rectification method for complex modes involves minimization of the mean phase angle of a complex mode's real and imaginary components using a linear least-squares algorithm [32]. Typical complex experimental mode rectification results associated with the ISPE (SFD-2018) experimental mode 26 [26, 27], rotated by ~25°, are shown in Fig. 3.3.

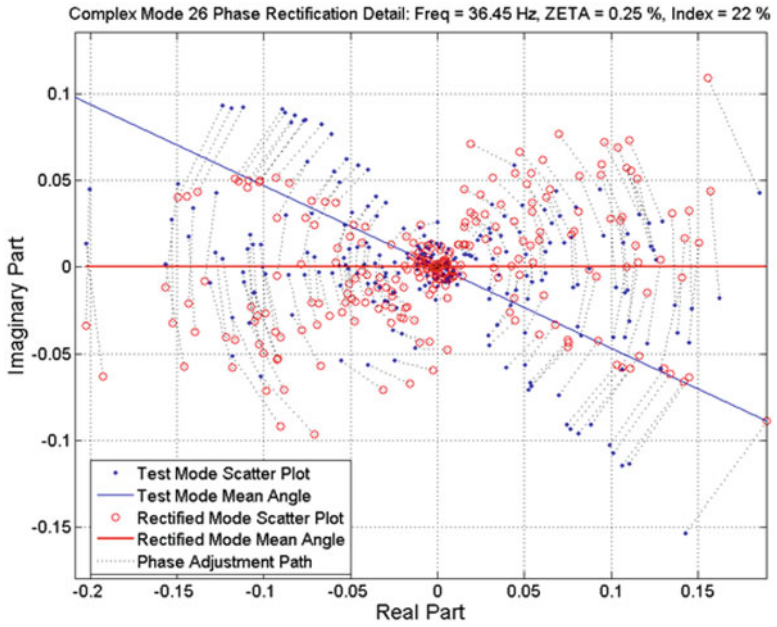

Fig. 3.3 Illustrative example of ISPE complex mode rectification results

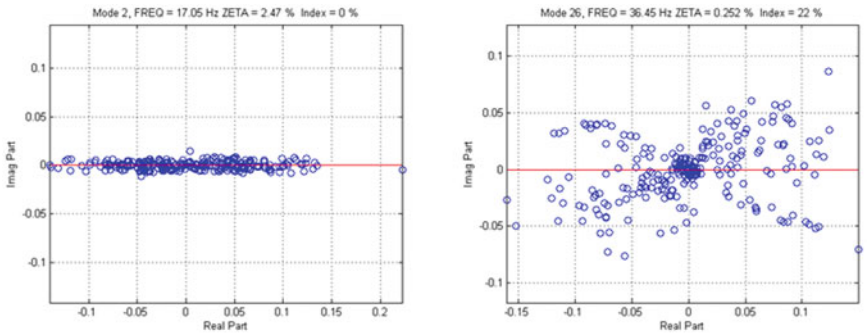

Fig. 3.4 Illustrative example of ISPE complex mode scatter plots and complex mode indices

Two (unit length normalized) estimates for the rectified experimental mode are now formed, specifically (a) normalized rectified complex mode, $\{\varphi_{V,\,\mathrm{CN}}\}$, and (b) normalized real mode, $\{\varphi_{V,\,\mathrm{RN}}\}$ (from real part of the rectified experimental mode). Further consideration of the collection of normalized real modes, $[\varphi_{V,\,\mathrm{RN}}]$, is the subject of the next section of this chapter.

The complex mode index for each experimental mode is defined in percentage units as

$$\text{Index} = 100 \cdot \left(1 - \left|\{\varphi_{V,\mathrm{RN}}\}^{\mathrm{T}} \cdot \{\varphi_{V,\mathrm{CN}}\}\right|^2\right). \tag{3.30}$$

When Index ~ 0, an experimental mode is approximately real; increased magnitudes indicate an increased level of "mode complexity." Typical ISPE rectified complex experimental mode scatter plots, shown in Fig. 3.4, illustrate the role played by the complex mode index metric.

3.7 Experimental Mode Validation

As indicated in Fig. 3.2, there are two options for experimental mode validation, specifically (a) a novel SFD-2018-specific uncoupled complex modal frequency response coherence metric [26, 27], which is objective since it does not require a TAM mass matrix and (b) the established US aerospace industry standard [1, 2], which is not entirely objective due to the need for

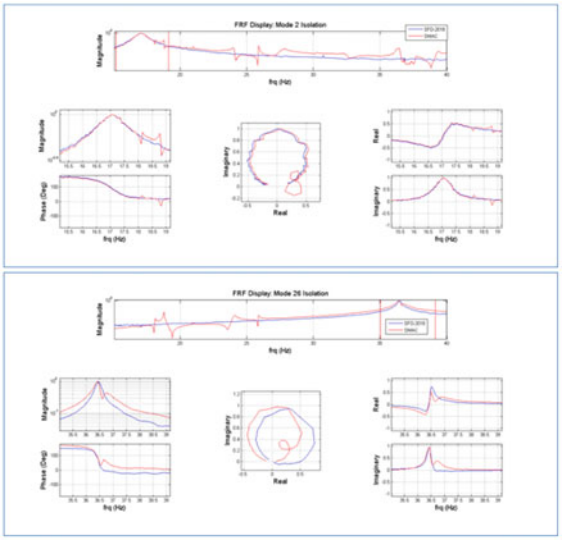

Fig. 3.5 Performance of SFD-2018 and SMAC FRF decoupling transformations

an analytical TAM mass matrix. Regarding the second case, an extension of the established standard to account for complex experimental modes is useful.

3.7.1 Uncoupled SFD-2018 Modal Frequency Responses and the Modal Coherence Metric

The superior FRF uncoupling properties of SFD-2018 (blue curves), following Eqs. 3.17 and 3.24, over the SMAC [24] based uncoupling attempt (red curves) based on real experimental modes (rectified real part of the SFD-2018 modes), following Eq. 3.9, are illustrated in results of ISPE test data analyses for modes 2 and 26, respectively, in Fig. 3.5.

Both SFD-2018 and SMAC decoupling transformations for ISPE mode 2 appear to be effective, since that complex experimental mode is approximately real (Index ~ 0%). However for the case of ISPE mode 26, the SMAC decoupling transformation is not effective, while the SFD-2018 transformation is quite effective, due to the prominent complexity (Index ~ 22%) of that experimental mode. It should be pointed out that the SFD-2018 decoupling transformation achieves a key goal associated with "analog" era techniques [13], without their associated mode-by-mode laboratory tuning inefficiencies.

A reality of all modal testing techniques is the fact that not all test article modes (especially for structures with many closely spaced modes) are well excited. The level of clarity and quality of estimated test modes, identified by SFD-2018, has been found to be judged on the basis of comparison of uncoupled FRF approximations (based on Eq. 3.24 and exact FRF solution of Eq. 3.21), which are used to define the modal coherence metric [4, 26],

$$\text{coh}_n = \frac{\left|[\dot{q}_n(f)]_A^* \cdot [\dot{q}_n(f)]_E\right|^2}{\left|[\dot{q}_n(f)]_A^* \cdot [\dot{q}_n(f)]_A\right| \cdot \left|[\dot{q}_n(f)]_E^* \cdot [\dot{q}_n(f)]_E\right|}, \tag{3.31}$$

where the "A" subscript designates the Eq. 3.21 modal FRF and the "E" subscript designates the Eq. 3.24 modal FRF for experimental mode "n."

A useful tabular summary of SFD-2018 estimated ISPE test modes in the base frequency band up to 40 Hz is provided in Table 3.1 (note in the table that "h" refers to $[\dot{q}_n(f)]_E$ functions).

The rows colored in light blue are judged to be predominantly "real" based on a value of complex index < 5%, and the rows colored in yellow are judged to be "complex" based on a value of complex index ≥ 5%. The rows colored in gray are subjectively judged to be of questionable quality based on a number of considerations including modal coherence, reduced modal FRF magnitude, and interpretation of uncoupled modal FRF graphics (illustrated in Figs. 3.6, 3.7, and 3.8).

It should be noted that all of the SFD-2018 estimated complex modes are perfectly orthogonal based on the fact that they were computed for an estimated state-space dynamic system (see Eqs. 3.22 and 23).

Table 3.1 Summary of SFD-2018 estimated ISPE experimental modes

					|h| (%)				coh (%)			
Mode	Freq (Hz)	Zeta (%)	Index (%)	Δ(Ang) (deg)	1.0	2.0	3.0	4.0	1.00	2.00	3.00	4.00
1	16.761	2.403	0	-1	3.0	2.2	1.7	0.6	99.59	99.37	99.03	93.24
2	17.045	2.467	0	1	0.7	1.6	2.3	2.6	94.41	98.90	99.56	99.74
3	18.125	0.110	0	0	4.3	2.8	6.4	11.1	86.32	68.88	72.69	96.36
4	18.160	0.116	0	2	10.3	4.2	4.4	2.3	97.01	79.10	86.40	60.16
5	18.793	0.113	0	0	24.1	24.8	22.7	21.4	93.75	86.73	97.34	94.85
6	20.048	3.447	19	-7	1.1	0.6	1.6	1.2	92.30	66.14	94.99	93.95
7	20.268	2.063	1	0	1.6	0.8	1.6	0.8	96.23	91.93	93.63	90.11
8	20.956	0.107	0	0	6.6	10.9	11.8	7.8	88.22	96.99	93.74	92.53
9	21.011	0.083	0	0	13.7	14.1	15.4	10.8	95.45	91.14	88.52	87.94
10	24.042	0.207	15	6	3.0	1.4	1.4	5.4	98.93	91.79	94.91	99.31
11	24.067	0.451	0	-1	1.8	14.8	14.3	24.4	73.75	99.40	99.47	99.87
12	24.264	0.416	0	0	22.1	14.3	17.5	1.1	99.81	99.57	99.77	55.01
13	25.817	0.137	0	0	20.0	9.7	6.1	6.4	99.41	97.46	95.09	95.45
14	25.888	0.120	0	0	7.2	8.5	12.3	25.6	75.53	97.07	90.19	98.72
15	27.635	1.504	7	-1	3.4	0.9	1.0	3.6	99.82	95.00	94.26	99.77
16	27.783	1.670	7	9	1.1	4.0	4.1	1.3	95.25	99.20	99.19	95.10
17	30.151	0.132	0	0	9.8	5.2	5.3	8.0	98.89	98.44	91.22	99.22
18	32.429	0.984	8	2	0.3	0.8	0.9	1.7	68.73	81.26	92.67	98.02
19	33.324	2.341	14	2	2.0	7.8	5.3	2.5	84.54	97.90	95.64	85.60
20	33.423	0.192	2	-3	2.8	9.0	8.1	3.3	94.88	98.51	97.99	96.79
21	33.752	2.568	19	-5	3.5	3.9	2.2	4.0	97.72	97.86	94.56	98.64
22	34.774	4.197	38	-13	0.9	1.3	0.8	1.2	86.59	90.79	82.47	94.66
23	35.176	1.567	13	12	1.7	3.2	3.2	4.7	56.91	87.15	85.36	92.26
24	35.385	0.726	12	0	5.6	6.1	2.7	13.5	98.27	97.45	94.02	99.79
25	36.148	0.368	4	-1	11.8	13.4	4.2	4.4	90.00	89.26	58.28	40.48
26	36.454	0.252	22	25	80.3	57.4	71.8	87.1	99.63	99.25	99.41	99.62
27	36.625	0.528	8	2	93.8	82.9	82.1	100.0	99.94	99.91	99.93	99.96
28	37.050	0.308	1	-1	27.8	31.6	15.3	22.8	99.15	99.63	97.98	99.19
29	37.364	0.339	3	-2	23.2	9.9	56.7	11.5	99.68	98.06	99.94	99.40
30	37.661	0.349	1	-1	21.8	41.9	16.5	22.2	99.51	99.90	99.26	99.81
31	37.677	2.550	26	4	3.1	3.1	3.3	3.1	98.93	98.99	99.24	99.31
32	38.511	0.893	7	8	1.3	1.4	2.3	6.8	79.00	88.31	94.09	99.76
33	38.794	0.393	4	0	5.7	3.7	7.6	3.5	91.09	89.67	87.93	88.73
34	39.282	0.270	17	-14	4.3	5.0	3.7	10.5	67.39	87.36	74.52	95.44
35	39.554	0.209	0	1	5.8	17.3	17.3	4.5	28.84	94.39	91.81	52.78

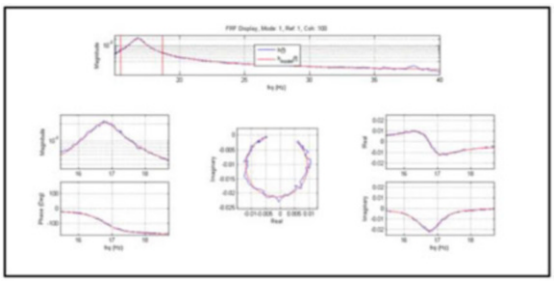

Fig. 3.6 SFD-2018 estimated ISPE Mode 1 (complex index ~0%)

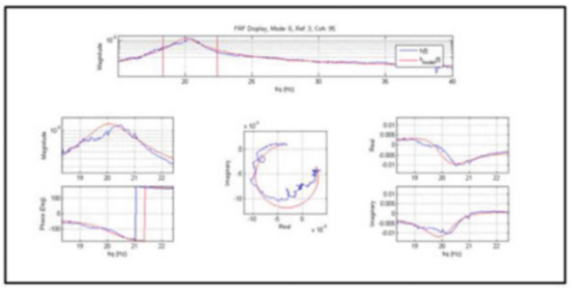

Fig. 3.7 SFD-2018 estimated ISPE Mode 6 (complex index ~ 19%)

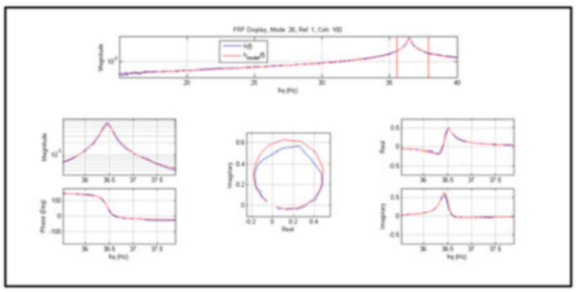

Fig. 3.8 SFD-2018 estimated ISPE Mode 26 (complex index ~ 22 %)

3.7.2 Extension of Mass-Weighted Orthogonality and Cross-Orthogonality Definitions

Due to the fact that modal test article experimental modes (and theoretical modes for the case of non-proportional damping) are sometimes substantially complex (see Table 3.1), the well-established mass-weighted orthogonality and cross-orthogonality definitions may be modified by substitution of the complex "Hermitian" operator for the real "transpose" operator. Therefore, the following modified quantities are defined:

$$[\mathrm{OR}_{11}] = [\varphi_{V1}]^{*}\,[M]\,[\varphi_{V1}] \qquad \text{(Self-orthogonality, } [\varphi_{V1}] = \text{unit mass normalized complex or real modes)} \qquad (3.32a)$$

Table 3.2 Mass-weighted self-orthogonality (absolute values) of SFD-2018 complex experimental modes

				|Orthogonality| (%)																						
Mode	Freq (Hz)	Zeta (%)	Index (%)	1	2	3	4	5	8	9	10	11	12	13	14	15	16	17	18	24	26	27	28	29	30	31	32
1	16.76	2.40	0	**100**	8	1	4	3	1	2	10	2	4	4	2	4	4	1	**11**	2	2	3	1	3	1	4	2
2	17.05	2.47	0	8	**100**	9	5	6	1	2	8	1	3	1	4	8	4	1	4	1	1	1	0	1	1	4	1
3	18.13	0.11	0	1	9	**100**	8	1	1	6	3	6	3	3	1	1	2	2	1	2	5	2	5	0	8	1	2
4	18.16	0.12	0	4	5	8	**100**	3	5	2	1	2	4	2	9	2	1	5	3	7	3	2	8	9	6	4	2
5	18.79	0.11	0	3	6	1	3	**100**	1	4	1	1	6	0	6	0	1	3	1	2	**11**	**13**	3	5	2	5	5
8	20.96	0.11	0	1	1	1	5	1	**100**	5	1	3	2	2	0	2	0	3	2	9	3	1	1	2	2	3	3
9	21.01	0.08	0	2	2	6	2	4	5	**100**	1	1	3	2	1	2	1	1	1	10	2	1	4	4	4	6	3
10	24.04	0.21	15	10	8	3	1	1	1	1	**100**	**56**	5	1	1	**18**	8	2	2	2	3	0	5	4	2	3	2
11	24.07	0.45	0	2	1	6	2	1	3	1	**56**	**100**	4	2	3	1	2	5	2	2	7	2	10	7	4	4	1
12	24.26	0.42	0	4	3	3	4	6	2	3	5	4	**100**	3	7	1	1	3	1	7	3	4	5	4	2	4	5
13	25.82	0.14	0	4	1	3	2	0	2	2	1	2	3	**100**	5	1	1	4	1	1	3	2	1	3	2	4	4
14	25.89	0.12	0	2	4	1	9	6	0	1	1	3	7	5	**100**	1	1	5	1	3	6	3	1	1	0	0	1
15	27.64	1.50	7	4	8	1	2	0	2	2	**18**	1	1	1	1	**100**	**53**	2	5	2	2	2	3	3	1	2	3
16	27.78	1.67	7	4	4	2	1	1	0	1	8	2	1	1	1	**53**	**100**	2	4	2	3	4	2	1	0	3	0
17	30.15	0.13	0	1	1	2	5	3	3	1	2	5	3	4	5	2	2	**100**	2	1	4	2	1	0	0	5	1
18	32.43	0.98	8	**11**	4	1	3	1	2	1	2	2	1	1	1	5	4	2	**100**	4	3	1	3	3	0	3	2
24	35.39	0.73	12	2	1	2	7	2	9	10	2	2	7	1	3	2	2	1	4	**100**	8	2	3	**15**	1	**13**	6
26	36.45	0.25	22	2	1	5	3	**11**	3	2	3	7	3	3	6	2	3	4	3	8	**100**	**65**	4	7	3	**13**	2
27	36.63	0.53	8	3	1	2	2	**13**	1	1	0	2	4	2	3	2	4	2	1	2	**65**	**100**	7	**12**	7	**21**	4
28	37.05	0.31	1	1	0	5	8	3	1	4	5	10	5	1	1	3	2	1	3	3	4	7	**100**	1	1	8	5
29	37.36	0.34	3	3	1	0	9	5	2	4	4	7	4	3	1	3	1	0	3	**15**	7	**12**	1	**100**	3	**33**	**11**
30	37.66	0.35	1	1	1	8	6	2	2	4	2	4	2	2	0	1	0	0	0	1	3	7	1	3	**100**	**20**	4
31	37.68	2.55	26	4	4	1	4	5	3	6	3	4	4	4	0	2	3	5	3	**13**	**13**	**21**	8	**33**	**20**	**100**	**26**
32	38.51	0.89	7	2	1	2	2	5	3	3	2	1	5	4	1	3	0	1	2	6	2	4	5	**11**	4	**26**	**100**

Table 3.3 Mass-weighted self-orthogonality (absolute values) of SFD-2018 "Rectified, Real" experimental modes

				|Orthogonality| (%)																						
Mode	Freq (Hz)	Zeta (%)	Index (%)	1	2	3	4	5	8	9	10	11	12	13	14	15	16	17	18	24	26	27	28	29	30	31	32
1	16.76	2.40	0	**100**	6	0	2	3	1	2	**11**	2	4	4	2	5	4	1	10	1	3	3	0	4	0	5	0
2	17.05	2.47	0	6	**100**	6	3	5	1	2	10	1	3	1	4	9	4	1	4	0	1	1	0	1	1	2	1
3	18.13	0.11	0	0	6	**100**	3	1	1	6	2	6	3	3	1	1	2	2	1	2	5	1	5	1	8	2	2
4	18.16	0.12	0	2	3	3	**100**	3	5	2	1	2	4	2	9	2	0	5	3	8	2	2	8	10	6	2	2
5	18.79	0.11	0	3	5	1	3	**100**	1	4	1	1	6	0	6	0	2	3	1	2	**11**	**14**	2	5	1	4	5
8	20.96	0.11	0	1	1	1	5	1	**100**	4	0	3	2	2	0	2	0	3	1	9	3	1	1	2	2	4	3
9	21.01	0.08	0	2	2	6	2	4	4	**100**	0	1	3	2	1	2	1	1	1	10	2	2	4	4	4	3	3
10	24.04	0.21	15	**11**	10	2	1	1	0	0	**100**	**20**	1	0	0	**21**	9	0	2	2	0	1	1	3	1	2	2
11	24.07	0.45	0	2	1	6	2	1	3	1	**20**	**100**	4	2	1	1	1	5	0	2	7	1	10	7	4	3	1
12	24.26	0.42	0	4	3	3	4	6	2	3	1	4	**100**	1	7	1	1	3	1	8	3	3	5	4	2	3	5
13	25.82	0.14	0	4	1	3	2	0	2	2	0	2	1	**100**	1	1	1	4	0	1	3	2	1	3	2	1	4
14	25.89	0.12	0	2	4	1	9	6	0	1	0	1	7	1	**100**	2	0	5	0	4	6	2	1	1	0	0	1
15	27.64	1.50	7	5	9	1	2	0	2	2	**21**	1	1	1	2	**100**	**26**	2	5	1	1	1	3	3	1	3	3
16	27.78	1.67	7	4	4	2	0	2	0	1	9	1	1	1	0	**26**	**100**	2	1	1	2	4	2	1	0	1	0
17	30.15	0.13	0	1	1	2	5	3	3	1	0	5	3	4	5	2	2	**100**	1	1	4	1	1	0	0	4	1
18	32.43	0.98	8	10	4	1	3	1	1	1	2	0	1	0	0	5	1	1	**100**	3	3	1	3	3	0	7	1
24	35.39	0.73	12	1	0	2	8	2	9	10	2	2	8	1	4	1	1	1	3	**100**	4	3	1	**13**	0	2	5
26	36.45	0.25	22	3	1	5	2	**11**	3	2	0	7	3	3	6	1	2	4	3	4	**100**	**28**	4	7	3	**19**	2
27	36.63	0.53	8	3	1	1	2	**14**	1	2	1	1	3	2	2	1	4	1	1	3	**28**	**100**	7	6	7	**17**	3
28	37.05	0.31	1	0	0	5	8	2	1	4	1	10	5	1	1	3	2	1	3	1	4	7	**100**	0	0	1	4
29	37.36	0.34	3	4	1	1	10	5	2	4	3	7	4	3	1	3	1	0	3	**13**	7	6	0	**100**	2	**24**	10
30	37.66	0.35	1	0	1	8	6	1	2	4	1	4	2	2	0	1	0	0	0	0	3	7	0	2	**100**	**18**	4
31	37.68	2.55	26	5	2	2	2	4	4	3	2	3	3	1	0	3	1	4	7	2	**19**	**17**	1	**24**	**18**	**100**	**24**
32	38.51	0.89	7	0	1	2	2	5	3	3	2	1	5	4	1	3	0	1	1	5	2	3	4	10	4	**24**	**100**

$$[\mathrm{COR}_{21}] = [\varphi_{V2}]^{*}\,[\mathrm{M}]\,[\varphi_{V1}] \qquad \text{(Cross-orthogonality, } [\varphi_{V1}] \;\&\; [\varphi_{V2}] = \text{unit mass normalized complex or real modes)} \tag{3.32b}$$

Employing the modified definition for self-orthogonality, the mass-weighted (using the ISPE TAM mass matrix) self-orthogonality of the SFD-2018 "credible" complex experimental modes (previously summarized in Table 3.1) is provided in Table 3.2.

It is interesting to note that the predominantly real experimental modes (colored in light blue) satisfy US aerospace community orthogonality criteria [1, 2], that is, off-diagonal term magnitudes $\leq 10\%$.

Employing the real part of rectified SFD-2018 modes, following a practice adopted by several US aerospace organizations for "real test mode" approximation (RTMA) [3], the orthogonality matrix (originally complex mode) terms exhibit closer compliance with respect to orthogonality criteria, as shown in Table 3.3.

Finally, orthogonality of linear least-squares refitted (real) SFD-2018 modes, computed according to Eqs. 3.26 and 3.27, a common practice in many experimental modal analysis applications, regardless of particular modal estimation technique [15], is provided in Table 3.4.

Table 3.4 Mass-weighted self-orthogonality (absolute values) of linear least-squares refitted (Real) SFD-2018 modes

				|Orthogonality| (%)																					
Mode	Freq (Hz)	Zeta (%)	Index (%)	1	2	3	4	5	8	9	10	11	12	13	14	15	16	17	18	24	26	27	28	29	30	31	32
1	16.76	2.40	0	**100**	6	0	2	3	1	2	**11**	2	4	4	2	5	4	1	10	2	3	3	0	4	0	6	1
2	17.05	2.47	0	6	**100**	6	3	5	1	2	10	1	3	1	4	9	4	1	4	0	1	1	0	1	1	3	1
3	18.13	0.11	0	0	6	**100**	3	1	1	6	2	6	3	3	1	1	2	2	1	2	5	1	5	1	8	2	2
4	18.16	0.12	0	2	3	3	**100**	3	5	2	0	2	4	2	9	2	0	5	3	8	2	2	8	10	6	2	2
5	18.79	0.11	0	3	5	1	3	**100**	1	4	1	1	6	0	6	0	2	3	1	2	**13**	**14**	2	5	1	4	5
8	20.96	0.11	0	1	1	1	5	1	**100**	4	0	3	2	2	0	2	0	3	1	9	3	1	1	2	2	4	3
9	21.01	0.08	0	2	2	6	2	4	4	**100**	0	1	3	2	1	2	1	1	1	10	2	1	4	4	4	3	3
10	24.04	0.21	15	**11**	10	2	0	1	0	0	**100**	**14**	2	0	0	**22**	8	0	2	2	1	1	1	2	0	2	2
11	24.07	0.45	0	2	1	6	2	1	3	1	**14**	**100**	4	2	1	**1**	1	5	0	2	6	1	10	7	4	3	1
12	24.26	0.42	0	4	3	3	4	6	2	3	2	4	**100**	1	7	1	1	3	1	8	3	3	5	4	2	3	5
13	25.82	0.14	0	4	1	3	2	0	2	2	0	2	1	**100**	1	1	1	4	0	1	3	2	1	3	2	1	3
14	25.89	0.12	0	2	4	1	9	6	0	1	0	1	7	1	**100**	2	0	5	0	4	5	2	1	1	0	0	1
15	27.64	1.50	7	5	9	1	2	0	2	2	**22**	1	1	1	2	**100**	**30**	2	5	1	1	1	3	3	1	3	3
16	27.78	1.67	7	4	4	2	0	2	0	1	8	1	1	1	0	**30**	**100**	2	0	1	3	4	2	1	0	2	1
17	30.15	0.13	0	1	1	2	5	3	3	1	0	5	3	4	5	2	2	**100**	1	1	3	1	1	0	0	3	1
18	32.43	0.98	8	10	4	1	3	1	1	1	2	0	1	0	0	5	0	1	**100**	3	3	1	3	3	0	7	1
24	35.39	0.73	12	2	0	2	8	2	9	10	2	2	8	1	4	1	1	1	3	**100**	2	3	1	**13**	1	2	4
26	36.45	0.25	22	3	1	5	2	**13**	3	2	1	6	3	3	5	1	3	3	3	2	**100**	**46**	6	8	4	**24**	2
27	36.63	0.53	8	3	1	1	2	**14**	1	1	1	1	3	2	2	1	4	1	1	3	**46**	**100**	7	7	7	**18**	3
28	37.05	0.31	1	0	0	5	8	2	1	4	1	10	5	1	1	3	2	1	3	1	6	7	**100**	0	0	1	4
29	37.36	0.34	3	4	1	1	10	5	2	4	2	7	4	3	1	3	1	0	3	**13**	8	7	0	**100**	2	**23**	10
30	37.66	0.35	1	0	1	8	6	1	2	4	0	4	2	2	0	1	0	0	0	1	4	7	0	2	**100**	**17**	4
31	37.68	2.55	26	6	3	2	2	4	4	3	2	3	3	1	0	3	2	3	7	2	**24**	**18**	1	**23**	**17**	**100**	**25**
32	38.51	0.89	7	1	1	2	2	5	3	3	2	1	5	3	1	3	1	1	1	4	2	3	4	10	4	**25**	**100**

Orthogonality of the linear least-squares refitted test modes does not exhibit the overall level of improvement noted for the case of modes approximated by the Aerospace Corporation practice (particularly for test modes 26 and 27). This issue warrants further examination in the next section of this chapter.

3.7.3 Further Analysis of the Aerospace Corporation Real Test Mode Approximation

The practice adopted by the Aerospace Corporation for "real test mode" approximation warrants further analysis through study of analytically simulated modal test data for which exact, unreduced modal solutions are known. The simulated data selected for further examination relates to the 5616 DOF shell structure FEM (and simulated test mode summary) depicted in Fig. 3.9.

The blue and green colored grid points denote locations associated with axisymmetric shell (mass and stiffness) elements, the green colored grid points denote locations associated with localized damping elements, and the red colored grid points denote locations associated with localized non-axisymmetric added mass coefficients. Three separate applied excitation forces, denoted in Fig. 3.9, are intended to stimulate lateral and axial responses.

The (a) complex mode self-orthogonality and (b) RTMA self-orthogonality summaries are provided in Tables 3.5 and 3.6, respectively.

Cross-orthogonality between real, undamped FEM modes and (a) complex test modes and (b) RTMA results are provided in Tables 3.7 and 3.8, respectively.

The results summarized in Tables 3.5, 3.6, 3.7, and 3.8 indicate that the Aerospace Corporation real test mode approximation yields (a) the self-orthogonality matrix that satisfies US aerospace community orthogonality criteria, and (b) improved cross-orthogonality between simulated test and undamped FEM modes with respect to the simulated complex test mode results. The fact that the Aerospace Corporation method's real test modes do not produce an "identity" cross-orthogonality matrix indicates that the approximation does not exactly correspond to the "true" real modes. Moreover, while the approximation improves test-FEM cross-orthogonality, complete reliance on the approximation may not be universally appropriate for model updating and reconciliation operations.

3.7.4 Why the Real Test Mode Approximation (RTMA) Works (A Heuristic Reliability Proof)

While RTMA has been employed by that organization for many years, an analytical "proof" of its appropriateness is unavailable in a key reference document [3]. This section of this chapter offers a heuristic proof of the approximation's accuracy.

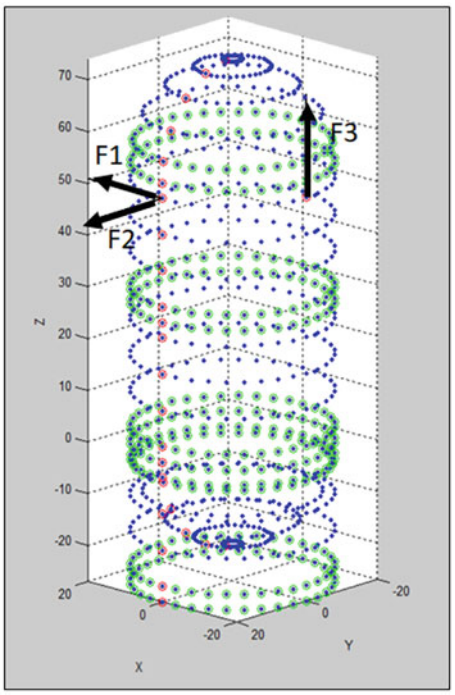

Mode	KE Body (%)	KE (%)Shell	Freq (Hz)	Zeta (%)	Index (%)	Δ(Ang) (deg)	|h1| (%)	|h2| (%)	|h3| (%)
1-TY	98	2	121.14	2.14	0.0	0	23.0	0.1	0.0
2-TX	98	2	121.23	2.49	0.2	0	0.0	20.9	5.5
3	0	100	174.32	5.83	13.0	12	0.0	2.1	1.7
4	0	100	175.78	1.04	0.2	0	15.8	0.5	0.0
5	0	100	183.36	1.94	11.5	5	0.0	3.3	2.3
6	0	100	187.48	0.83	0.1	1	11.5	12.0	0.0
7	0	100	237.11	2.43	5.6	10	0.0	0.7	5.1
8	0	100	240.19	0.91	0.1	3	29.1	28.0	0.0
9	0	100	255.63	1.58	3.5	4	0.0	3.5	1.5
10	0	100	260.36	0.55	0.1	0	14.6	2.7	0.0
11-RZ	98	2	312.35	0.80	0.1	1	80.7	83.9	0.0
12	5	95	361.39	6.13	2.1	6	0.0	1.0	0.9
13	7	93	367.52	1.67	0.8	-2	0.0	1.8	6.8
14-TX	90	10	374.13	0.76	1.6	1	13.3	4.7	0.0
15-TY	84	16	374.72	0.72	0.5	0	0.0	7.9	42.2
16	5	95	375.48	0.36	0.4	-1	19.5	16.9	0.0
17	3	97	377.52	1.99	2.4	-1	7.3	2.5	0.0
18	1	99	378.27	1.84	0.6	1	0.3	4.2	0.8
19	1	99	378.41	1.80	1.6	-2	4.2	6.0	0.0
20	0	100	436.12	3.12	2.2	1	0.0	5.1	2.7
21	0	100	449.47	1.79	0.2	1	5.9	4.9	0.0
22	0	100	451.55	1.62	0.9	-1	0.0	10.0	2.0
23	0	100	452.89	1.31	0.0	0	12.7	0.6	0.0
24-TZ	98	2	463.47	0.61	0.1	0	0.0	2.6	100.0
25	0	100	487.77	4.90	5.9	6	0.0	0.8	0.4

Fig. 3.9 Simulated shell modal test structure

Table 3.5 Shell complex mode self-orthogonality (absolute values) summary

						|Orthogonality| (%)																				
Mode	KE Body (%)	KE (%)Shell	Freq (Hz)	Zeta (%)	Index (%)	1	2	3	4	5	6	7	8	9	10	11	12	13	14	15	16	17	18	19	20	21	22	23	24	25
1-TY	98	2	121.14	2.14	0.0	100		3		2		2		1	2															
2-TX	98	2	121.23	2.49	0.2		100	12		5		4		3			1	2		1				1						
3	0	100	174.32	5.83	13.0		12	100		63		20		12			1	7							1					
4	0	100	175.78	1.04	0.2	3			100		7		2		1	1			1									1		
5	0	100	183.36	1.94	11.5		5	63		100		12		7			1	4					1				1			
6	0	100	187.48	0.83	0.1	2			7		100		2		1	1						1		1						
7	0	100	237.11	2.43	5.6		4	20		12		100		35			1	7					1							1
8	0	100	240.19	0.91	0.1	2			2		2		100		4	4			1											
9	0	100	255.63	1.58	3.5		3	12		7		35		100			2	6		1			2		1					
10	0	100	260.36	0.55	0.1	1			1		1		4		100	2			1			2		1						
11-RZ	98	2	312.35	0.80	0.1	2			1		1		4		2	100			3		1									
12	5	95	361.39	6.13	2.1		1	1		1		1		2			100	6		9			1		26		3			1
13	7	93	367.52	1.67	0.8		2	7		4		7		6			6	100		6					2		2			
14-TX	90	10	374.13	0.76	1.6				1				1		1	3			100		10	23	1	14		2		1		
15-TY	84	16	374.72	0.72	0.5		1							1			9	6		100			12	1	1		3		2	4
16	5	95	375.48	0.36	0.4											1			10		100	5		3		4		1		
17	3	97	377.52	1.99	2.4						1				2				23		5	100	2	18		1		1		
18	1	99	378.27	1.84	0.6					1		1		2			1	1	1	12		2	100	6	1		1			2
19	1	99	378.41	1.80	1.6						1				1				14	1	3	18	6	100				1		
20	0	100	436.12	3.12	2.2		1							1			26	2		1			1		100		2		1	2
21	0	100	449.47	1.79	0.2														2		4	1				100				
22	0	100	451.55	1.62	0.9			1		1							3	2		3			1		2		100		3	19
23	0	100	452.89	1.31	0.0				1										1		1	1		1				100		
24-TZ	98	2	463.47	0.61	0.1															2					1		3		100	4
25	0	100	487.77	4.90	5.9							1					1			4			2		2		19		4	100

The algebraic Eigenvalue problem described in Eq. 3.22 may be recast into the second-order form (for each mode, dropping brackets)

$$\varphi_{\dot{\xi}}\lambda^2 + \tilde{B}\varphi_{\dot{\xi}}\lambda + \tilde{K}\varphi_{\dot{\xi}} = 0. \tag{3.33}$$

Explicit description of the complex eigenvalues and eigenvectors in terms of real and imaginary components

$$\varphi_{\dot{\xi}} = \varphi_R + i\varphi_I, \qquad \lambda = \lambda_R + i\lambda_I, \qquad \lambda^2 = \left(\lambda_R^2 - \lambda_I^2\right) + i\left(2\lambda_R\lambda_I\right) \tag{3.34}$$

results in the following real part of Eq. 3.33:

$$\left\lfloor \varphi_R\left(\lambda_R^2 - \lambda_I^2\right) + \tilde{K}\varphi_R \right\rfloor + \left\lfloor \tilde{B}\varphi_R\lambda_R - \tilde{B}\varphi_I\lambda_I - 2\varphi_R\lambda_R\lambda_I \right\rfloor = 0. \tag{3.35}$$

Table 3.6 Shell Aerospace Corporation real test mode self-orthogonality (absolute values) summary

						|Orthogonality| (%)																						
Mode	KE Body (%)	KE (%)Shell	Freq (Hz)	Zeta (%)	Index (%)	1	2	3	4	5	6	7	8	9	10	11	12	13	14	15	16	17	18	19	20	21	22	23	24	25
1-TY	98	2	121.14	2.14	0.0	100																								
2-TX	98	2	121.23	2.49	0.2		100	1		2				1																
3	0	100	174.32	5.83	13.0		1	100						3						1										
4	0	100	175.78	1.04	0.2				100																					
5	0	100	183.36	1.94	11.5		2			100		4		1						1										
6	0	100	187.48	0.83	0.1						100																			
7	0	100	237.11	2.43	5.6					4		100		1																
8	0	100	240.19	0.91	0.1								100																	
9	0	100	255.63	1.58	3.5		1	3		1		1		100						1										
10	0	100	260.36	0.55	0.1										100															
11-RZ	98	2	312.35	0.80	0.1											100														
12	5	95	361.39	6.13	2.1												100													
13	7	93	367.52	1.67	0.8			1		1				1						100										
14-TX	90	10	374.13	0.76	1.6																100			1		1				
15-TY	84	16	374.72	0.72	0.5																	100					1			
16	5	95	375.48	0.36	0.4																		100			1				
17	3	97	377.52	1.99	2.4																1			100		1				
18	1	99	378.27	1.84	0.6																				100	1				
19	1	99	378.41	1.80	1.6																1		1	1	1	100				
20	0	100	436.12	3.12	2.2																	1					100			
21	0	100	449.47	1.79	0.2																							100		
22	0	100	451.55	1.62	0.9																								100	1
23	0	100	452.89	1.31	0.0																									
24-TZ	98	2	463.47	0.61	0.1																								100	
25	0	100	487.77	4.90	5.9																									100

Table 3.7 Shell undamped FEM mode to complex "Test" mode cross-orthogonality (absolute values) summary

			|Cross-Orthogonality| (%)																								
Mode			1	2	3	4	5	6	7	8	9	10	11	12	13	14	15	16	17	18	19	20	21	22	23	24	25
	Freq (Hz)	Index (%)	120.97	121.13	172.06	175.76	184.94	187.47	237.31	240.17	256.59	260.31	312.43	359.94	367.98	373.97	374.65	375.36	377.43	378.13	378.31	436.99	449.06	450.89	452.78	463.45	485.96
1-TY	121.14	0.0		100		1		1		1			1														
2-TX	121.23	0.2	100		5		2		1		1																
3	174.32	13.0	7		93		36		8		5			1	2												
4	175.78	0.2		2		100		3		1																	
5	183.36	11.5	3		38		92		5		3				1												
6	187.48	0.1		1		4		100		1																	
7	237.11	5.6	3		11		8		97		17			1	3												
8	240.19	0.1		1		1		1		100		2	2			1											
9	255.63	3.5	2		7		5		19		98			1	3					1							
10	260.36	0.1								2		100	1						1								
11-RZ	312.35	0.1		2		1		1		2		1	100			1											
12	361.39	2.1	1		1		1		1		1			99	5		7					12		1			
13	367.52	0.8	1		4		3		4		4			6	99		3					1		1			
14-TX	374.13	1.6								1			2			98		7	18		10		1		1		
15-TY	374.72	0.5												7	4		99			10		1		1		1	2
16	375.48	0.4														6		100	7		3		2				
17	377.52	2.4										1				19		8	97	1	9						
18	378.27	0.6					1				1			1			10		1	99	5	1						1
19	378.41	1.6						1				1				9	1	3	11	5	99						
20	436.12	2.2												14	1		1			1		99					1
21	449.47	0.2														1		2					100		1		
22	451.55	0.9												1	1		1					1		99		2	10
23	452.89	0.0				1										1		1					1		100		
24-TZ	463.47	0.1															1							1		100	3
25	487.77	5.9							1					1			3			1		1		11		3	97

Table 3.8 Shell undamped FEM mode to Aerospace Corporation real test mode cross-orthogonality (absolute values) summary

			|Cross-Orthogonality| (%)																								
Mode			1	2	3	4	5	6	7	8	9	10	11	12	13	14	15	16	17	18	19	20	21	22	23	24	25
	Freq (Hz)	Index (%)	120.97	121.13	172.06	175.76	184.94	187.47	237.31	240.17	256.59	260.31	312.43	359.94	367.98	373.97	374.65	375.36	377.43	378.13	378.31	436.99	449.06	450.89	452.78	463.45	485.96
1-TY	121.14	0.0		100																							
2-TX	121.23	0.2	100		1																						
3	174.32	13.0	2		98		19																				
4	175.78	0.2				100																					
5	183.36	11.5	2		20		98		4		2				1												
6	187.48	0.1						100																			
7	237.11	5.6							100		5																
8	240.19	0.1								100	0																
9	255.63	3.5	1		2		2		4		100				1												
10	260.36	0.1										100															
11-RZ	312.35	0.1											100														
12	361.39	2.1												100	4		5					1					
13	367.52	0.8												5	100		2					1					
14-TX	374.13	1.6														99		3	15		7						
15-TY	374.72	0.5												6	2		99			8		1					
16	375.48	0.4														4		100	6		3						
17	377.52	2.4														15		7	98		5						
18	378.27	0.6															8		1	99	4						
19	378.41	1.6														7		3	5	3	99						
20	436.12	2.2																				100		1			
21	449.47	0.2																					100		1		
22	451.55	0.9															1					1		100			5
23	452.89	0.0																					1		100		
24-TZ	463.47	0.1																						1		100	2
25	487.77	5.9															1							6		2	99

In the case of a lightly damped system, the eigenvalues are expressed as

$$\lambda_I = \sqrt{\lambda_I^2 - \lambda_R^2} \approx \omega_n, \qquad \lambda_R \approx -\zeta_n \omega_n. \tag{3.36}$$

Substitution of the above result into Eq. 3.35 results in

$$\left\lfloor -\omega_n^2 \varphi_R + \tilde{K}\varphi_R \right\rfloor + \left\lfloor -\tilde{B}\varphi_R \xi_n \omega_n - \tilde{B}\varphi_I \omega_n + 2\varphi_R \xi_n \omega_n^2 \right\rfloor \approx 0. \tag{3.37}$$

Investigation of Euclidian norms of the coefficient matrices and numerical analysis of the above matrix terms associated with ISPE experimental data and shell simulated data indicates that the Eq. 3.37 terms are in the following order of magnitude relationship:

$$\left\lfloor -\omega_n^2 \varphi_R + \tilde{K}\varphi_R \right\rfloor + 0\left(\zeta_n \tilde{K}\varphi_R, \zeta_n \tilde{K}\varphi_I\right) \rightarrow \left\lfloor -\omega_n^2 \varphi_R + \tilde{K}\varphi_R \right\rfloor \approx 0. \tag{3.38}$$

This completes the heuristic reliability proof of RTMA. That being said, it must be emphasized that the real mode approximation does not amount to exact replication of undamped system modes.

3.8 Recapitulation and Conclusions

The recapitulation and conclusions to this "somewhat comprehensive" critique of experimental modal analysis are stated with respect to the seven key steps of the Integrated Test Analysis Process (ITAP) for structural dynamic systems.

3.8.1 System Dynamic Model (Covered in Previous Publications)

An appropriate finite element (FEM) system dynamic model requires adherence to several practical, well-documented guidelines, specifically:

(a) Strictly enforced consistency of the FEM with engineering drawings (CAD).
(b) Selection of component sufficiently refined grid spacing to appropriately capture relevant frequency band dynamics.
(c) Inclusion of quasi-static effects (differential stiffness) due to gravity or steady acceleration and hydrostatic pressure loads.
(d) Provision for localized joint flexibilities to permit subsequent model updating (reconciliation).
(e) Inclusion of nonlinear features, when significant, especially at component interfaces (early Space Shuttle experiences).

3.8.2 Modal Test Plan (Covered in Previous Publications)

The commonly accepted practice for modal test planning focuses on development of a test-analysis model (TAM) employing Guyan reduction of a detailed FEM that is consistent with a selected set of test accelerometer degrees of freedom (DOF). Moreover, "residual kinetic energy" strategies for selection of appropriate selection of TAM degrees of freedom are widely accepted today. The most important products of the modal test planning step are the TAM mass matrix, which is used for validation of experimental modes through an orthogonality check, FEM natural frequencies, and (real) mode shapes (in particular, the TAM DOF order partition).

3.8.3 Measured Data Acquisition and Measured Data Analysis (Covered in Previous Publications)

Measured data acquisition, the technical discipline of highly experienced laboratory personnel, involves selection and verification and validation of excitation and response measurement resources to be used in a modal test. On the other hand, measured data analysis is a discipline that requires both (a) measured data acquisition expertise and (b) utilization of advanced mathematical tools and associated personnel (who are ideally experienced in both data acquisition and analysis). Key products of these ITAP steps are as follows:

(a) Determination of linear or nonlinear modal test article behavior (nonlinear behavior is beyond the scope of this chapter).
(b) Estimation of MI/MO frequency response arrays and associated coherence arrays required for experimental modal analysis.

Close attention must be paid to coherence array data to establish high signal-to-noise qualities of estimated frequency response arrays and accurate experimentally determined system modes.

3.8.4 Experimental Modal Analysis

(a) Estimated modes based on virtually all "digital" era experimental modal analysis algorithms are sometimes highly complex.
(b) The SFD-2018 technique produces "analog" era type decoupled modal FRFs (without the burden of an excessive laboratory timeline, a unique feature of SFD-2018).
(c) The SFD-2018 technique produces state-space complex experimental modes that automatically satisfy US aerospace community orthogonality standards, independent of an analytical TAM mass matrix.
(d) The Aerospace Corporation's approximate real modes (formed by the real part of "rectified" complex experimental modes) produce a mass-weighted orthogonality matrix that produces generally acceptable satisfaction of US aerospace community standards (provided the TAM mass matrix is based on an appropriately defined system dynamic model).

3.8.5 Test-Analysis Correlation

The RTMA modes (formed by the real part of "rectified" complex experimental modes) produce a mass-weighted cross-orthogonality matrix (correlating analytical and experimental modes) that produces generally acceptable satisfaction of US aerospace community standards (provided the TAM mass matrix is based on an appropriately defined system dynamic model).

3.8.6 Test-Analysis Reconciliation

(a) Reconciliation of the test article's FEM with experimental modal analysis results may be accomplished on the basis of the RTMA technique and parametrically varied system dynamic modes. This is the basis for virtually all modern test-analysis reconciliation strategies.
(b) In exceptional situations, for example, high modal damping and highly complex modes, it may become necessary to perform test-analysis reconciliation using complex experimental and analytical modes.

It is finally noted that this chapter represents yet another step toward establishment of an improved ITAP process. Continued efforts in the academic and industry communities are absolutely encouraged.

References

1. Load Analysis of Spacecraft and Payloads, NASA-STD-5002 (1996)
2. Independent Structural Loads Analysis. U.S. Air Force Space Command, SMC-S-004 (2008)
3. Kabe, A.M., Sako, B.H.: Structural Dynamics Fundamentals and Advanced Applications, vol. 1 & 2. Academic Press, London (2020)
4. Coppolino, R.N.: The Integrated Test Analysis Process for Structural Dynamic Systems. Morgan & Claypool Publishers, San Rafael (2020)
5. Hunt, D., Adams, W., Bock, T.: Dynamic analysis of structures with friction forces at sliding joints. J. Spacecr. Rockets. **21**(2) (1984)
6. Henkel, E.E., Misel, J.E., Frederick, D.H.: A methodology to include static and kinetic friction effects in space shuttle payload transient loads analysis. In: Shuttle Environment and Operations Meeting. AIAA, Washington, DC (1983)
7. A friction methodology for space shuttle/payload transient loads analysis. In: Proc. Shuttle Payload Dynamics Loads Prediction Workshop, JPL-D-1347, vol. 2 (1984)
8. Guyan, R.J.: Reduction of stiffness and mass matrices. AIAA J. **3**, 380–381 (1965)
9. Coppolino, R.: Automated response DOF selection for mapping of experimental normal modes. In: IMAC XVI (1998)
10. Tuttle, R.E., Cole, T.R., Lollock, J.A.: An automated method for identification of efficient measurement degrees-of-freedom for modal survey testing. In: 46th AIAA/ASME/ASCE/AHS/ASC SDM Conference (2005)
11. Bendat, J.S., Piersol, A.G.: Random Data Analysis and Measurement Procedures, 4th edn. Wiley, Hoboken (2010)
12. Bendat, J.S.: Nonlinear Systems Techniques and Applications, 2nd edn. Wiley, New York (1998)
13. Bishop, R.E.D., Gladwell, G.M.L.: An investigation into the theory of resonance testing. Philos. Trans. Royal Soc. Lond. Ser. A. **225**, A-1055 (1963)
14. Brown, D.L., Allemang, R.J.: The modern era of experimental modal analysis. Sound Vib. Mag., 85 (2007)
15. Allemang, R.J., Brown, D.L.: Chapter 21: experimental modal analysis. In: Piersol, A.G., Paez, T.L. (eds.) Harris' Shock and Vibration Handbook, 6th edn. McGraw-Hill, New York. (2010)
16. Coppolino, R.: Methodologies for Verification and Validation of Space Launch System (SLS) Structural Dynamic Models, vol. 1, NASA CR-2018-219800 (2018)
17. Nelder, J., Mead, R.: A simplex method for function minimization. Comput. J. **7**(4), 308–313 (1965)
18. Metropolis, N., Ulam, S.: The Monte Carlo Method. J. Am. Stat. Assoc. **44**(247), 335–341 (1949)
19. Zimmerman, D.C., Jorgensen, S.S.F.: Parallel multispecies genetic algorithm for physics and parameter estimation in structural dynamics. AIAA J. **43**, 2224 (2005)
20. Rayleigh, J.W.S.: The Theory of Sound, 1st American edn. Dover Publications, New York (1945)
21. Caughey, T.K., O'Kelly, M.E.J.: Classical normal modes in damped linear dynamic systems. ASME J. Appl. Mech. **32**, 583–588 (1965)
22. Cremer, L., Heckl, M., Ungar, E.: Structure Borne Sound. Springer-Verlag, New York (1973)
23. Coppolino, R.N.: Structural dynamics modeling–tales of sin and redemption. Sound Vib. Mag. **50**(1), 7–11 (2016)
24. Mayes, R., Klenke, S.: The SMAC modal parameter extraction package. In: IMAC XVII (1999)
25. Wilkinson, J.H.: The Algebraic Eigenvalue Problem. Oxford University Press, New York (1965)
26. Coppolino, R.N.: The integrated test-analysis process (2020 challenges). In: IMAC XXXVIII (2020)
27. Coppolino, R.N.: Roadmap to a highly improved modal test process. In: IMACXXXVIII (2020)
28. Ibrahim, S.R., Mikulcik, E.C.: A method for the direct identification of vibration parameters from the free response. Shock Vib. Bull. **47**, 183–196 (1977)
29. Juang, J., Pappa, R.S.: An eigensystem realization algorithm for modal parameter identification and model reduction. J. Guid. Control Dyn. **8**, 620–627 (1985)
30. Brincker, R., Ventura, C.E.: Introduction to Operational Modal Analysis. Wiley, Chichester (2015)
31. Golub, G.H., Reinsch, C.: Singular value decomposition and least squares solutions. Numer. Math. **14**, 403–420 (1970)
32. Miller, K.: Complex linear least squares. SIAM Rev. **15**(4), 706–726 (1973)

Chapter 4
OMA of a High-Rise TV Tower Using the Novel Poly-reference Complex Frequency Modal Identification Technique Formulated in Modal Model

Sandro D. R. Amador, Liga Gaile, Emmanouil Lydakis, and Rune Brincker

Abstract When it comes to multi-dataset Operational Modal Analysis (OMA) of large civil structures, the main goal is to clearly identify the global vibration modes in a very accurate and robust manner. In this chapter, a new frequency domain identification technique is applied to the vibration responses of an outstanding 363-m high television and radio transmission tower, i.e., the Riga TV Tower located at the city of Riga, Latvia. The vibration data was collected during a 3-day testing campaign where a total of 6 datasets were collected at different storeys of the structure by means of two independent measurement systems consisting of two 3D vibration sensors each. The main advantage of the identification technique applied to the tower's vibration data with regard to the existing approaches is that the former provides clearer stabilization diagrams, facilitating the identification of the physical modes of the tested structures. The application of the novel modal identification technique to tower's response records led to a clear diagram, from which the most important global vibration modes were easily identified.

Keywords OMA · Multi-dataset · Modal identification · TV tower · Clear stabilization

4.1 Introduction

When it comes to multi-patch vibration test of large civil engineering structures, the main challenge is to merge the different datasets acquired over course of output-only vibration test campaigns and extract the global modal properties of the tested structure from the merged data. The modal properties' extraction can be carried out by means of non-parametric or parametric modal identification techniques' single dataset identification. The former comprise the so-called **F**requency **D**omain **D**ecomposition (**FDD**) [1], whereas the latter category consists of time and frequency domain techniques such as the **p**oly-reference **L**east **S**quares **C**omplex **E**xponential (**pLSCE**) [2, 3], the **I**brahim **T**ime **D**omain (**ITD**) [4, 5, 6, 7], and the **p**oly-reference **L**east **S**quares **C**omplex **F**requency (**pLSCF**) [8, 9].

The key step in extracting the global modal properties from the various recorded datasets consists of merging these data together. This can be carried either before or after the modal parameter extraction takes place, as described, for instance, in [10, 11]. The accuracy of the extracted global modal properties from the merged vibration data depends on the performance and robustness of the used modal identification technique. In this chapter, the new poly-reference **C**omplex **F**requency technique formulated in **M**odal **M**odal (**pCF-MM**) is applied to the data acquired in a multi-dataset vibration test. The underlying idea behind the formulation of the pCF-MM approach is to consider two adjacent samples of the frequency domain function, i.e., the **F**requency **R**esponse **F**unction (**FRF**) of the **H**alf **S**pectrum (**HS**) to formulate an eigenvalue problem, which can then be subsequently solved to yield the experimental modal properties of the tested structural systems. In this chapter, the pCF-MM is applied to the vibration data of the Riga TV Transmission Tower shown in Fig. 4.1.

S. D. R. Amador (✉) · E. Lydakis
Department of Civil and Mechanical Engineering (CONSTRUCT), Technical University of Denmark (DTU), Kgs. Lyngby, Denmark
e-mail: sdio@dtu.dk; elysi@dtu.dk

L. Gaile
Institute of Structural Engineering, Riga Technical University, Riga, Latvia
e-mail: liga.gaile_1@rtu.lv

R. Brincker
Brincker Monitoring ApS, Copenhagen K, Denmark
e-mail: rune@brincker-monitoring.com

B. J. Dilworth et al. (eds.), *Topics in Modal Analysis & Parameter Identification, Volume 9*, Conference Proceedings of the Society for Experimental Mechanics Series, https://doi.org/10.1007/978-3-031-34942-3_4

(a) (b)

Fig. 4.1 Riga TV and Radio Transmission Tower: whole tower viewed from a distance (**a**) and detail of one of the boxed legs (**b**)

The structure is located at the City of Riga, Latvia, and it was built between 1979 and 1989 during the occupation of Latvia (one of the three Baltic states, alongside with Lithuanian and Estonia) by the then Soviet Union. Nowadays, the structure is owned and maintained by a State Joint Stock Company, the "**L**atvian **S**tate **R**adio and **T**elevision **C**enter" (**LVRTC**). The Tower is the tallest civil structure in the European Union and the third tallest in the whole Europe, measuring 368.5 m high from the ground level to the highest point of the antenna. In addition to being regarded as Riga's most prominent landmark, the structure plays an important role to the Latvian cultural identity and society since it is used as an antenna by Riga Radio and TV station to broadcast several TV and radio channels locally and nation-wise.

The vibration data of the Riga Tower is used to assess the accuracy and robustness of the novel pCF-MM technique when it is applied to a multi-dataset OMA. In the first part of the chapter, a brief description of the technique is made, whereas in the second part, the key steps undertaken to analyze the tower's vibration data and the results in terms of modal properties estimates are presented.

4.2 Background Theory

In an experimental modal analysis, the main goal is to extract the modal properties from the vibration measurements collected in vibration tests of structural systems. The modal properties extraction (or modal identification) can be carried out either in the time domain or in the frequency domain. In the former, a free decay function is normally used as primary data. In this case, the modal properties are computed basically by fitting an analytical model to the free decay measurements. The free decay matrix of a structural system with general viscous damping in discrete time containing the information of N_i inputs and N_o outputs and sampled with sampling interval Δt can be modeled by the so-called time domain modal model as

$$\mathbf{Y}_k = \sum_{i=1}^{n_c} \boldsymbol{\phi}_i \boldsymbol{\gamma}_i^T e^{\lambda_i k \Delta t} + \boldsymbol{\phi}_i^* \boldsymbol{\gamma}_i^H e^{\lambda_i^* k \Delta t} \tag{4.1}$$

where $(\bullet)^T$ and $(\bullet)^H$ denote the transpose and the complex conjugate transpose (Hermitian), respectively, and $(\bullet)^*$ the complex conjugate; $k \in \mathbb{N}$ denotes a discrete time instant $t = k\Delta t$; n_c is the number of vibration modes occurring in complex conjugate pairs, $\boldsymbol{\phi}_r \in \mathbb{C}^{N_o \times 1}$ and $\boldsymbol{\gamma}_r \in \mathbb{C}^{N_i \times 1}$ are, respectively, the mode shape and the modal participation factor vectors, and $\lambda_r \in \mathbb{C}$ the continuous-time poles, which are related to the natural frequencies in rads/s, ω_i, and damping ratios, ξ_i as

$$\lambda_i, \lambda_i^* = -\xi_i \omega_i \pm j\sqrt{1-\xi_i^2}\omega_i \tag{4.2}$$

with $j = \sqrt{-1}$ designating the imaginary unit, and $\omega_i = 2\pi f_i$ the circular natural frequency in rad/s as function of the natural frequency in hertz (cycles/s) f_i. Equation (4.1) can be rewritten in matrix form as

$$\mathbf{Y}_k = \boldsymbol{\Phi}\boldsymbol{\Lambda}^k\boldsymbol{\Gamma}^T \tag{4.3}$$

where $\boldsymbol{\Phi} \in \mathbb{C}^{N_o \times 2n_c}$ is the mode shape matrix, $\boldsymbol{\Lambda} \in \mathbb{C}^{2n_c \times 2n_c}$ is a diagonal matrix containing the discreet time poles, $\mu_i = e^{\lambda_i \Delta t} \in \mathbb{C}$, and $\boldsymbol{\Gamma} \in \mathbb{C}^{N_i \times 2n_c}$ is the modal participation matrix. By comparing (4.1) and (4.3), it is straightforward to prove that such matrices are given by

$$\begin{aligned}
\boldsymbol{\Phi} &= \left[\boldsymbol{\phi}_1\ \boldsymbol{\phi}_1^* \cdots \boldsymbol{\phi}_n\ \boldsymbol{\phi}_n^*\right] \in \mathbb{C}^{N_o \times 2n_c} \\
\boldsymbol{\Gamma} &= \left[\boldsymbol{\gamma}_1\ \boldsymbol{\gamma}_1^* \cdots \boldsymbol{\gamma}_n\ \boldsymbol{\gamma}_n^*\right] \in \mathbb{C}^{N_i \times 2n_c} \\
\boldsymbol{\Lambda} &= \mathrm{diag}\left(\left[\mu_1\ \ \mu_1^*(t) \cdots \mu_{n_c}\ \mu_{n_c}^*\right]\right) \in \mathbb{C}^{2n_c \times 2n_c}
\end{aligned} \tag{4.4}$$

where diag (•) denotes the diagonal matrix operator. The free decay (4.3) in discrete time can be written in a more general form, for an arbitrary time advance $\tau \geq 0$ as

$$\mathbf{Y}_{k+r} = \boldsymbol{\Phi}\boldsymbol{\Lambda}^r\boldsymbol{\Lambda}^k\boldsymbol{\Gamma}^T \tag{4.5}$$

where $r \in \mathbb{N}$ denotes an arbitrary forward time shift ($\tau = r\Delta t$) in continuous time. The free decay model in discrete time with an arbitrary time advance as in Eq. (4.5) can be converted from time to frequency domain by means of the Laplace Transform or Z-Transform. Though both transforms can be used in the formulation of the pCF-MM described in the next section, the derivation of the system matrices becomes more obvious if the latter is used. Taking the Z-Transform of Eq. (4.5) gives

$$\mathbf{H}(z)z^r = \boldsymbol{\Phi}\boldsymbol{\Lambda}^r\left[\mathbf{I}z - \boldsymbol{\Lambda}\right]^{-1}\boldsymbol{\Gamma}^T \tag{4.6}$$

where $\mathbf{I}$ is the identity matrix and $z^r = e^{jr\omega\Delta t} \in \mathbb{C}$ is the Z-domain variable, with $\omega = 2\pi f$ standing for the angular frequency in radians/s which is expressed as function of the frequency, f, in cycles/s (Hz).

4.3 The New Poly-Reference Complex Frequency formulated in Model Model (pCF-MM)

Equation (4.6) can be written down for a set of time shifts, r, ranging from 0 to n, and combining the obtained equations into a single matrix expression, giving

$$\mathbf{H}_0(z) = \boldsymbol{\Phi}\left(\mathbf{I}z - \boldsymbol{\Lambda}\right)^{-1}\boldsymbol{\Psi}^T \tag{4.7}$$

with

$$\mathbf{H}_0(z) = \left[\mathbf{H}(z)\ z\mathbf{H}(z) \cdots z^n\mathbf{H}(z)\right] \in \mathbb{C}^{N_o \times (n+1)N_i} \tag{4.8}$$

and

$$\boldsymbol{\Psi}^T = \left[\boldsymbol{\Gamma}^T\ \boldsymbol{\Lambda}\boldsymbol{\Gamma}^T \cdots \boldsymbol{\Lambda}^n\boldsymbol{\Gamma}^T\right] \in \mathbb{C}^{(n+1)N_i \times (n+1)N_i} \tag{4.9}$$

Equation (4.7) can be written for two discrete consecutive frequency lines ω_a and ω_b ($\forall\omega_b > \omega_a$) spaced from each other by a single discrete frequency step $\Delta\omega$ as

$$\begin{aligned}\mathbf{H}_0(z_a) &= \boldsymbol{\Phi}\left(\mathbf{I}z_a - \boldsymbol{\Lambda}\right)^{-1}\boldsymbol{\Psi}^T \\ \mathbf{H}_0(z_b) &= \boldsymbol{\Phi}\left(\mathbf{I}z_b - \boldsymbol{\Lambda}\right)^{-1}\boldsymbol{\Psi}^T\end{aligned} \tag{4.10}$$

Isolating $\boldsymbol{\Phi}^T$ in both equations and combining the obtained expressions yield

$$\boldsymbol{\Psi}^{-1}\left[\mathbf{H}_1(z_b) - \mathbf{H}_1(z_a)\right]^T = \boldsymbol{\Lambda}\boldsymbol{\Psi}^{-1}\left[\mathbf{H}_0(z_b) - \mathbf{H}_0(z_a)\right]^T \tag{4.11}$$

with

$$\mathbf{H}_1(z) = \left[z\mathbf{H}(z)\ z^2\mathbf{H}(z)\ \cdots\ z^{n+1}\mathbf{H}(z)\right] \in \mathbb{C}^{N_o\times(n+1)N_i} \tag{4.12}$$

Writing down (4.11) for all the N_f discrete frequency lines available in the frequency band, i.e., for ω_a and ω_b ranging, respectively, from ω_0 to ω_{N_f-1} and from ω_1 to ω_{N_f}, and combining the equations corresponding to each pair of evaluated frequency values in a single matrix equation yield

$$\boldsymbol{\Psi}^{-1}\mathbf{B}^T = \boldsymbol{\Lambda}\boldsymbol{\Psi}^{-1}\mathbf{A}^T \tag{4.13}$$

where

$$\begin{aligned}\mathbf{A} &= \begin{bmatrix}\mathbf{H}_0(z_1) - \mathbf{H}_0(z_0)\\ \mathbf{H}_0(z_2) - \mathbf{H}_0(z_1)\\ \vdots \\ \mathbf{H}_0(z_{N_f}) - \mathbf{H}_0(z_{N_f-1})\end{bmatrix} \in \mathbb{C}^{N_o(N_f-1)\times(n+1)N_i} \\ \mathbf{B} &= \begin{bmatrix}\mathbf{H}_1(z_1) - \mathbf{H}_1(z_0)\\ \mathbf{H}_1(z_2) - \mathbf{H}_1(z_1)\\ \vdots \\ \mathbf{H}_1(z_{N_f}) - \mathbf{H}_1(z_{N_f-1})\end{bmatrix} \in \mathbb{C}^{N_o(N_f-1)\times(n+1)N_i}\end{aligned} \tag{4.14}$$

An eigenvalue problem can be formulated from (4.13) using the **D**ouble **L**east **S**quares approach (**DLS**) [6, 1], giving

$$\frac{1}{2}\left(\mathbf{B}^T\mathbf{A}^*\left(\mathbf{A}^T\mathbf{A}^*\right)^{-1} + \mathbf{B}^T\mathbf{B}^*\left(\mathbf{A}^T\mathbf{B}^*\right)^{-1}\right) = \boldsymbol{\Psi}\boldsymbol{\Lambda}\boldsymbol{\Psi}^{-1} \tag{4.15}$$

Once the eigenvalue problem Eq. (4.15) is solved, the modal participation factors can be retrieved as the 1st N_o rows of $\boldsymbol{\Psi}$, and the natural frequencies and damping ratios are computed from diagonal elements of $\boldsymbol{\Lambda}$. The eigenvalue problem as in Eq. (4.15) gives eigenvalues and eigenvectors not occurring in complex conjugate pairs. If modal participation factor vectors and continuous time poles occurring in conjugate pairs are desired, the following eigenvalue problem should be used instead.

$$\frac{1}{2}\left(\mathfrak{Re}\left(\mathbf{B}^T\mathbf{A}^*\right)\left(\mathfrak{Re}\left(\mathbf{A}^T\mathbf{A}^*\right)\right)^{-1} + \mathfrak{Re}\left(\mathbf{B}^T\mathbf{B}^*\right)\left(\mathfrak{Re}\left(\mathbf{A}^T\mathbf{B}^*\right)\right)^{-1}\right) = \boldsymbol{\Psi}\boldsymbol{\Lambda}\boldsymbol{\Psi}^{-1} \tag{4.16}$$

where $\mathfrak{Re}\,(\bullet)$ stands for the real part of a complex number.

4.4 Application to the Multi-dataset Vibration Test of the Riga TV and Radio Broadcast Tower

In order to illustrate the practical application of the pCF-MM described in the previous section, a case study consisting of the multi-dataset output-only vibration test of the Riga TV and Radio Broadcast Tower is presented. The vibration test campaign to measure the vibration responses in 6 different datasets was carried out over the course of two days, a period within which mild wind velocities were observed. The acceleration response time series of each dataset were acquired for one hour and

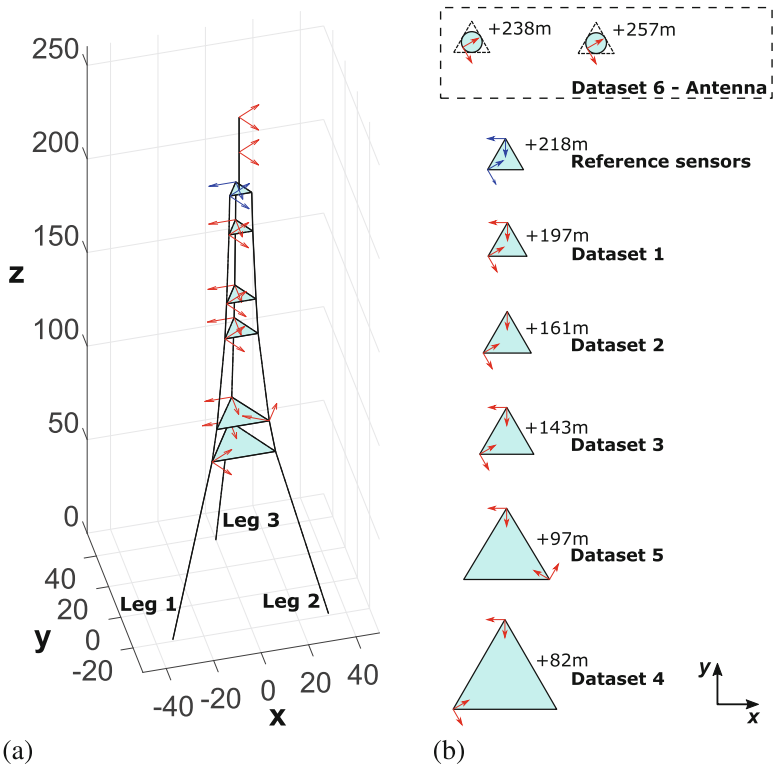

Fig. 4.2 Sensors' locations and directions: measured DOFs (**a**) and position of each dataset (**b**). The blue arrows indicate the reference sensors, whereas the red ones denote the moving sensors

thirty minutes due to the very low fundamental frequency suited around 0.2 Hz. The acquisition of such responses was done with a sampling rate, f_s, of 10 Hz.

Due to the dimensions of the tower, two independent (un-synchronized) acquisition systems were used to record the vibration responses: one used as reference and the other as roving system, being both comprising two 3D nodes with each node consisting of three geophone sensors. The sensors' locations and directions of each dataset are shown in Fig. 4.2. Figure 4.2a shows all **D**egrees **O**f **F**reedoms (**DOF**s) measured in the test campaign, whereas Fig. 4.2b indicates the locations and measurement directions of the sensors in each measured dataset, with the blue arrows designating the reference and red arrows the moving sensors. During the testing campaign, a total of 6 datasets were measured along the height of the tower, being the 1st five measured at the tower itself, whereas the sixth and last dataset was measured at the bottom part of the antenna, as indicated in Fig. 4.2b.

Since the reference and roving acceleration responses were acquired with two independent systems, the acceleration time series recorded with the roving system had to be synchronized with regard to those of the reference system. The synchronization of each dataset was accomplished by, first, calculating the average phase angle of the transfer function between the 1st reference and 1st roving channel and subsequently by removing the time shift corresponding this phase from all the roving channels. Afterward, the synchronized times series were de-trended and decimated with a factor of 4, leading to time series with a sampling frequency of 2.5 Hz. Once synchronized, filtered, de-trended, and down-sampled, the time series of each dataset was used to compute the HS matrix with a resolution of 513 frequency lines. Afterward, the HS matrix of each dataset was prescaled and stacked on the top of each other to form a global spectrum following the approach described in [11, 10].

Finally, the formed global HS matrix was used as primary data by the pCF-MM technique from which the natural frequencies, damping rations, and operational factor vectors were extracted with the aid of a stabilization diagram. Figure 4.3 shows the stabilization diagram constructed with pCF-MM by identifying models with order ranging from 1 to 70. The vertical red lines in such diagram indicate the natural frequencies of the physical vibration modes automatically identified by means of a Hierarchical Cluster Algorithm [10]. It is worth highlighting that the peak suited to around 0.7 Hz corresponds to poorly excited modes and, therefore, could not be clearly identified as physical. The details of the closed–spaced modes around 0.2, 0.5, and 0.82 Hz are shown in Fig. 4.3b, c, and d, respectively.

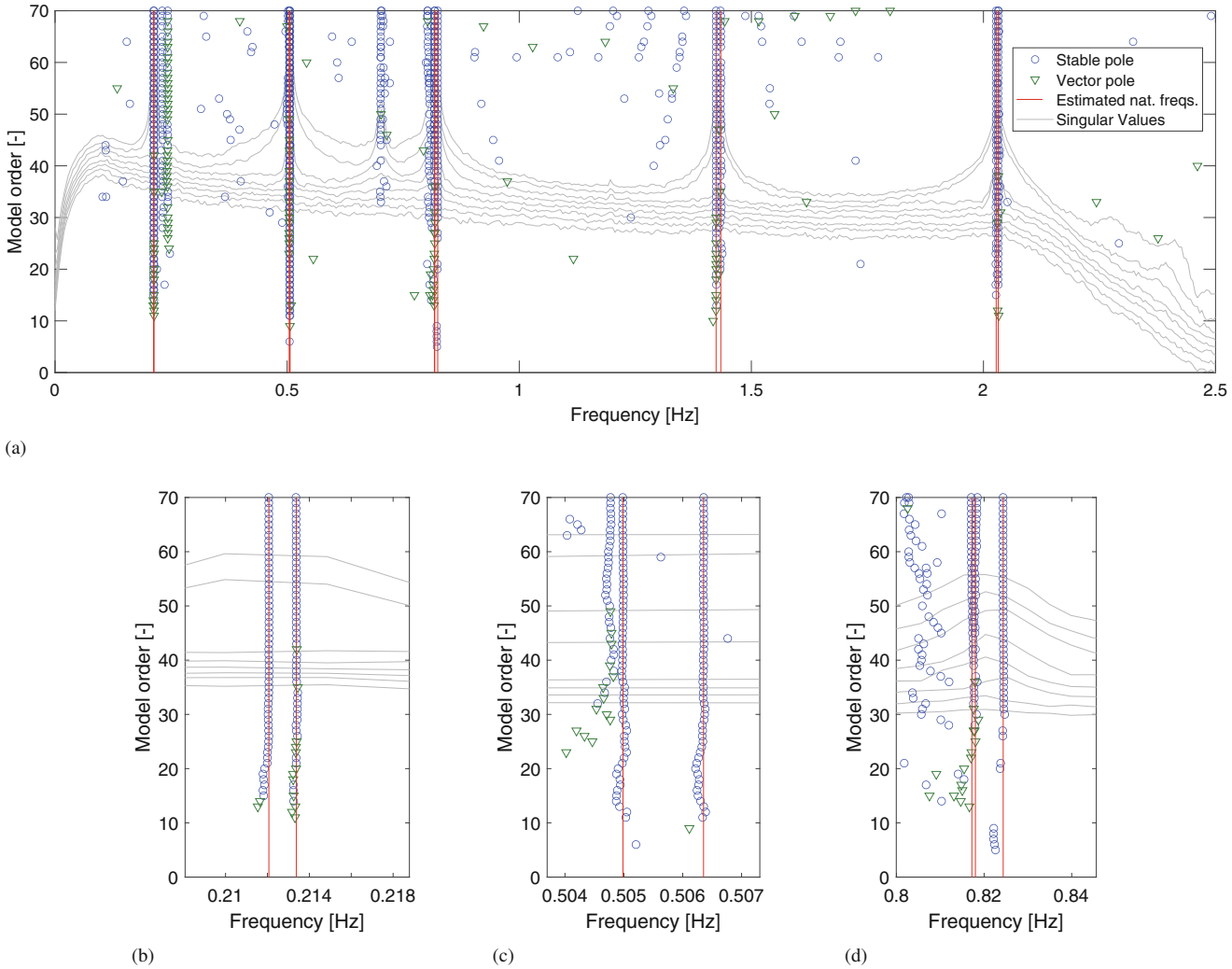

Fig. 4.3 Stabilization diagram constructed with the novel pCF-MM by the identifying models with order ranging from 1 to 70 (**a**), and details of the closed spaced modes automatically identified with HC algorithm around 0.2 Hz (**b**), 0.5 Hz (**c**), and 0.82 Hz (**d**)

After automatically identifying the operation factor vectors, the mode shape vectors were estimated in a subsequent step by means of the so-called **L**east **S**quares **C**omplex **F**requency (**LSFD**) algorithm [12]. The summary of the identification results obtained for the TV tower with the novel pCF-MM technique is shown in Fig. 4.4.

4.5 Conclusion

This chapter shows the results of a multi-dataset modal identification performed on the Riga TV and Radio transmission tower to the estimate the global modal properties of the structure. The vibration responses of the tower measured at different storeys underwent a comprehensive signal processing to (i) remove the phase between reference and roving responses and (ii) estimate the global HS matrix used as primary data in the identification process. The novel pCF-MM was then applied to the prescaled global HS matrix to estimate the tower's natural frequencies, damping ratios, and operational factor vectors in the frequency range of 0.0 to 2.5 Hz in a first step of the identification process. In a subsequent step, the mode shape vectors were estimated by making use of the so-called LSFD algorithm. The application of the pCF-MM to the Riga TV Tower vibration data led to the construction of a clear stabilization diagram from which eleven vibration modes were clearly and accurately identified. The accuracy and robustness provided by the pCF-MM algorithm were particularly observed in the estimation of the very closed–spaced modes around 0.2, 0.5, and 0.82 Hz.

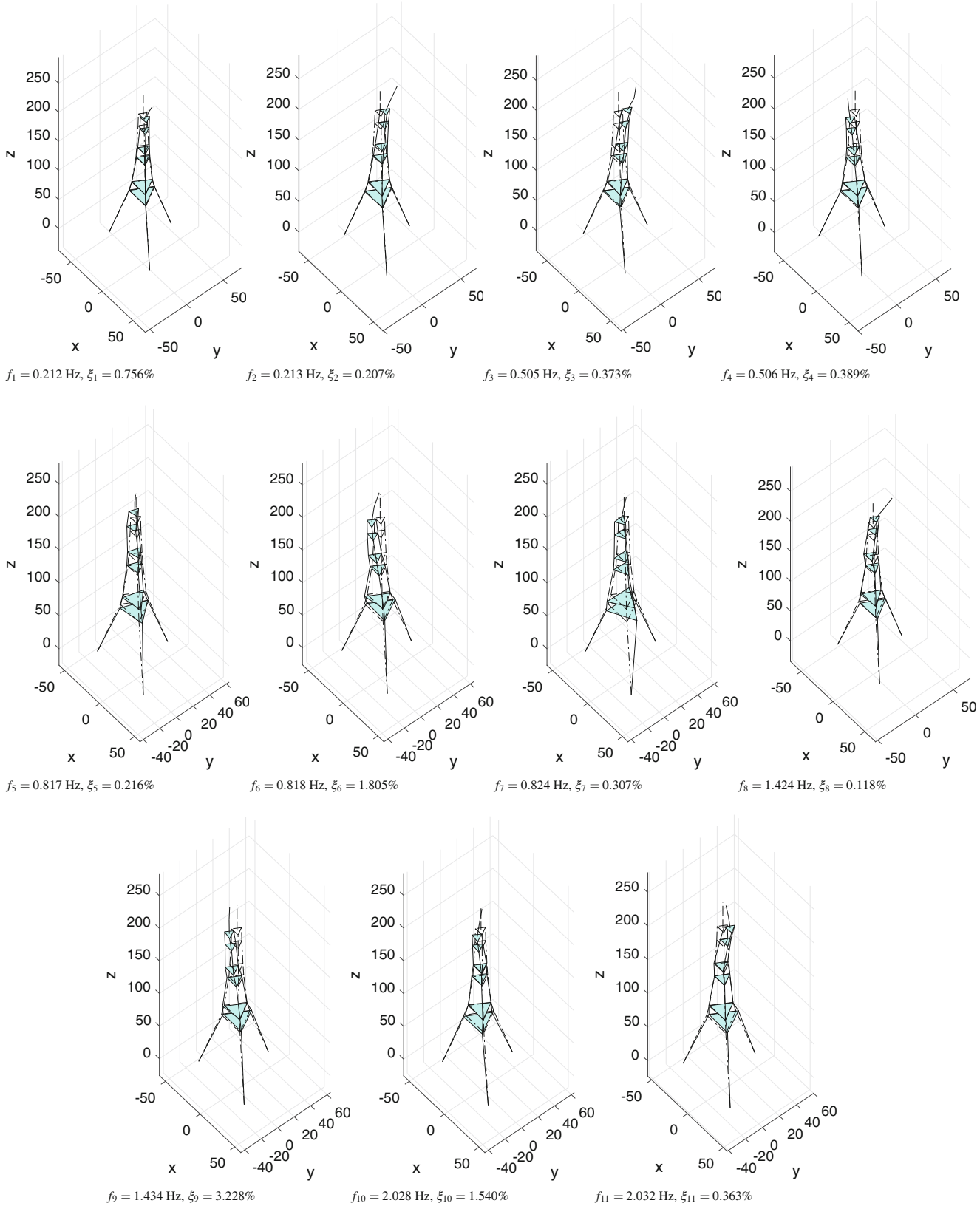

$f_1 = 0.212$ Hz, $\xi_1 = 0.756\%$ $f_2 = 0.213$ Hz, $\xi_2 = 0.207\%$ $f_3 = 0.505$ Hz, $\xi_3 = 0.373\%$ $f_4 = 0.506$ Hz, $\xi_4 = 0.389\%$

$f_5 = 0.817$ Hz, $\xi_5 = 0.216\%$ $f_6 = 0.818$ Hz, $\xi_6 = 1.805\%$ $f_7 = 0.824$ Hz, $\xi_7 = 0.307\%$ $f_8 = 1.424$ Hz, $\xi_8 = 0.118\%$

$f_9 = 1.434$ Hz, $\xi_9 = 3.228\%$ $f_{10} = 2.028$ Hz, $\xi_{10} = 1.540\%$ $f_{11} = 2.032$ Hz, $\xi_{11} = 0.363\%$

Fig. 4.4 Global mode shapes of the Riga TV and Radio Transmission Tower identified with the novel pCF-MM technique

Acknowledgments The raw data for the publication is a courtesy of the Latvia state-owned company LVRTC. The authors especially acknowledge (i) the funding received from DTU Offshore—Danish Offshore Technology Centre—to develop the pCF-MM technique, (ii) the technicians—high climbers of LVRTC Normunds Patmalnieks and Eduards Putilins for their valuable support and assistance in the dynamic testing of the structure, (iii) Julija Batalauska for excellent organizational help, and (iv) the technicians Klaus Myndal and Ian Rasmussen of the Civil and Mechanical Engineering Department (CONSTRUCT) at the Technical University of Denmark (DTU) for their assistance in the preparation and testing of the measurement system used in the multi-dataset vibration test of the Riga TV and Radio Transmission Tower.

References

1. Brincker, R., Ventura, C.: Introduction To Operational Modal Analysis, 1st edn. Wiley, New York (2015)
2. Vold, H., Kundra, J., Thomas Rocklin, G., Russel, R.: A multi-input modal estimation algorithm for mini-computers. SAE Trans. **91**, 815–821 (1982)
3. Vold, H., Thomas Rocklin, G., Russel, R.: The numerical implementation of a multi-input modal estimation algorithm for mini-computers. In: Proceedings of IMAC 1 (1982)
4. Ibrahim, S.R., Mikulcik, E.C.: A method for the direct identification of vibration parameters from the free response. In: Shock and Vibration Bulletin, pp. 183–196 (1977)
5. Ibrahim, S.R.: Modal confidence factor in vibration testing. J. Spacecraft **15**, 313–316 (1978)
6. Ibrahim, S.R.: A modal identification algorithm for higher accuracy requirements. In: AIAA paper, in: Proceedings of the 25th Structures, Structural Dynamics and Materials, pp. 117–122. AIAA (1984)
7. Fukozono, K.: Investigation of multiple-reference Ibrahim time domain modal parameters estimation technique. Master's Thesis, Department of Mechanical and Industrial Engineering, University of Cincinnati, 1986
8. Peeters, B., Van der Auweraer, H., Guillaume, P., Leuridan, J.: The polymax frequency–domain method: a new standard for modal parameter estimation? Shock Vib. **11**, 395–409 (2004)
9. Peeters, B., Van der Auweraer, H., Vanhollebeke, F. and Guillaume, P.: Operational modal analysis for estimating the dynamic properties of a stadium structure during a football game. Shock Vib. **14**, 283–303 (2007)
10. Amador, S.D.R., Magalhães, F., Matos, Á., Caetano, E.: High spatial resolution modal identification of a stadium suspension roof: Assessment of the estimates uncertainty and of modal contributions. Eng. Struct. **135**, 117–135 (2017)
11. Amador, S.D.R., Brincker, R.: Robust multi-dataset identification with frequency domain decomposition. J. Sound Vib. **508**, 116207 (2021)
12. Amador, S.D.R.: Uncertainty Quantification in Operational Modal Analysis and Continuous Monitoring of Special Structures. Ph.D. Thesis, Department of Civil Engineering, Faculty of Engineering of University of Porto, Porto, Portugal, 2015

Chapter 5
The New Poly-reference Complex Frequency Formulated in Modal Model (pCF-MM): A New Trend in Experimental Modal Analysis

Sandro D. R. Amador and Rune Brincker

Abstract In Experimental and Operational Modal Analysis (EMA and OMA), the main challenge is to extract the experimental modal properties of the tested structures from the vibration measurements in a very accurate and robust manner. The EMA and OMA can be carried out in time or frequency domain by fitting a parametric model to time or frequency domain measurements, so that the modal properties can be subsequently extracted for the obtained normal matrices. In this chapter, a novel poly-reference modal identification technique formulated in the frequency domain is proposed. The advantage of the proposed approach with regard to the existing techniques is that it yields numerical (non-physical) modes with negative damping, making it easier to distinguish the physical modes. The accuracy and robustness of such an approach is demonstrated by means of an application example at last part of the chapter.

Keywords OMA · Modal analysis · System identification · Vibrations

5.1 Introduction

Over the last five decades, there have been ground breaking advancements in modern experimental structural dynamics, namely in **EMA** and **OMA**. In the late 70s, the **I**brahim **T**ime **D**omain (**ITD**) [1, 2] was introduced to the modal analysis community as the first single-reference **L**east **S**quares (**LS**) modal identification technique capable of handling multiple output measurements at once. Later on, the **p**oly-reference **LS** **C**omplex **E**xponential (**pLSCE**) [3, 4] was proposed to estimate the modal properties by fitting an **A**uto-**R**egressive (**AR**) model to the measured free decay functions.

The **pLSCE** algorithm consists of a poly-reference **LS** modal identification technique, meaning that it is capable of taking into account multiple input and multiple output measurements at once in the identification process. Shortly after the invention of the **pLSCE**, the **ITD** was reformulated into a poly-reference **LS** technique [5]. Though the **ITD** and the **pLSCE** were the first poly-reference modal analysis algorithms ever invented, to this day, they are still regarded by many as some of the most robust modal analysis algorithms available. In the 90s, other model identification techniques like the **S**tochastic **S**ubspace **I**dentification (**SSI**) technique [6, 7] and the **F**requency **D**omain **D**ecomposition (**FDD**) [8] were proposed, entailing a revolution in OMA.

Recently, around the mid-2000s, the frequency domain poly-reference technique known as **p**oly-reference **L**east **S**quares **C**omplex **F**requency domain (**pLSCF**) [9, 10, 11] was proposed to perform broadband frequency domain modal identification. In this chapter, a novel poly-reference modal identification technique is proposed. Such an approach is formulated in the frequency domain using the z-domain modal model, hence the name **p**oly-reference **C**omplex **F**requency formulated in **M**odal **M**odel (**pCF-MM**). Similar to the ITD technique, the idea behind the pCF-MM is to formulate an eigenvalue problem by comparing the two different samples of the measured vibration data.

The advantages of the pCF-MM with regard to the existing techniques include, for instance, increased robustness in sorting the physical modal properties from the numerical ones. In order to illustrate these benefits from a practical perspective, the performance of the novel **pCF-MM** technique is assessed by means of a real OMA of two steel platform specimens.

S. D. R. Amador (✉)
Department of Civil and Mechanical Engineering (CONSTRUCT), Technical University of Denmark (DTU), Kgs. Lyngby, Denmark
e-mail: sdio@dtu.dk; rune@brincker-monitoring.com

R. Brincker
Brincker Monitoring ApS, Copenhagen K, Denmark

B. J. Dilworth et al. (eds.), *Topics in Modal Analysis & Parameter Identification, Volume 9*, Conference
Proceedings of the Society for Experimental Mechanics Series, https://doi.org/10.1007/978-3-031-34942-3_5

5.2 Background Theory

In an experimental modal analysis, the main goal is to extract the modal properties from the vibration measurements collected in vibration tests of structural systems. The modal properties extraction (or modal identification) can be carried out in either time domain or frequency domain. In the former, a free decay function is normally used as primary data. In this case, the modal properties are computed basically by fitting an analytical model to the free decay measurements. The free decay matrix of a structural system with general viscous damping in discrete time containing the information of N_i inputs and N_o outputs and sampled with sampling interval Δt can be modeled by the so-called time domain modal model as

$$\mathbf{Y}_k = \sum_{i=1}^{n_c} \boldsymbol{\phi}_i \boldsymbol{\gamma}_i^T e^{\lambda_i k \Delta t} + \boldsymbol{\phi}_i^* \boldsymbol{\gamma}_i^H e^{\lambda_i^* k \Delta t} \tag{5.1}$$

where $(\bullet)^T$ and $(\bullet)^H$ denote the transpose and the complex conjugate transpose (Hermitian), respectively, and $(\bullet)^*$ the complex conjugate; $k \in \mathbb{N}$ denotes a discrete time instant $t = k\Delta t$; n_c is the number of vibration modes occurring in complex conjugate pairs, $\boldsymbol{\phi}_r \in \mathbb{C}^{N_o \times 1}$ and $\boldsymbol{\gamma}_r \in \mathbb{C}^{N_i \times 1}$ are, respectively, the mode shape and the modal participation factor vectors, and $\lambda_r \in \mathbb{C}$ the continuous-time poles, which are related to the natural frequencies in rads/sec, ω_i, and damping ratios, ξ_i as

$$\lambda_i, \lambda_i^* = -\xi_i \omega_i \pm j\sqrt{1-\xi_i^2}\omega_i \tag{5.2}$$

with $j = \sqrt{-1}$ designating the imaginary unit, and $\omega_i = 2\pi f_i$ the circular natural frequency in rad/sec as function of the natural frequency in hertz (cycles/sec) f_i. Equation (5.1) can be rewritten in matrix form as

$$\mathbf{Y}_k = \boldsymbol{\Phi} \boldsymbol{\Lambda}^k \boldsymbol{\Gamma}^T \tag{5.3}$$

where $\boldsymbol{\Phi} \in \mathbb{C}^{N_o \times 2n_c}$ is the mode shape matrix, $\boldsymbol{\Lambda} \in \mathbb{C}^{2n_c \times 2n_c}$ is a diagonal matrix containing the discreet time poles, $\mu_i = e^{\lambda_i \Delta t} \in \mathbb{C}$, and $\boldsymbol{\Gamma} \in \mathbb{C}^{N_i \times 2n_c}$ is the modal participation matrix. By comparing (5.1) and (5.3), it is straightforward to prove that such matrices are given by

$$\begin{aligned}
\boldsymbol{\Phi} &= \left[\boldsymbol{\phi}_1 \ \boldsymbol{\phi}_1^* \cdots \boldsymbol{\phi}_n \ \boldsymbol{\phi}_n^*\right] \in \mathbb{C}^{N_o \times 2n_c} \\
\boldsymbol{\Gamma} &= \left[\boldsymbol{\gamma}_1 \ \boldsymbol{\gamma}_1^* \cdots \boldsymbol{\gamma}_n \ \boldsymbol{\gamma}_n^*\right] \in \mathbb{C}^{N_i \times 2n_c} \\
\boldsymbol{\Lambda} &= \text{diag}\left(\left[\mu_1 \ \ \mu_1^*(t) \cdots \mu_{n_c} \ \mu_{n_c}^*\right]\right) \in \mathbb{C}^{2n_c \times 2n_c}
\end{aligned} \tag{5.4}$$

where diag $(\bullet)$ denotes the diagonal matrix operator. The free decay (5.3) in discrete time can be written in a more general form, for an arbitrary time advance $\tau \geq 0$ as

$$\mathbf{Y}_{k+r} = \boldsymbol{\Phi} \boldsymbol{\Lambda}^r \boldsymbol{\Lambda}^k \boldsymbol{\Gamma}^T \tag{5.5}$$

where $r \in \mathbb{N}$ denotes an arbitrary forward time shift ($\tau = r\Delta t$) in continuous time. The free decay model in discrete time with an arbitrary time advance as in Eq. (5.5) can be converted from time to frequency domain by means of the Laplace Transform or Z-Transform. Though both transforms can be used in the formulation of the pCF-MM described in the next section, the derivation of the system matrices becomes more obvious if the latter is used. Taking the Z-Transform of Eq. (5.5) gives

$$\mathbf{H}(z) z^r = \boldsymbol{\Phi} \boldsymbol{\Lambda}^r \left[\mathbf{I} z - \boldsymbol{\Lambda}\right]^{-1} \boldsymbol{\Gamma}^T \tag{5.6}$$

where $\mathbf{I}$ is the identity matrix and $z^r = e^{j\omega\Delta t} \in \mathbb{C}$ is the Z-domain variable, with $\omega = 2\pi f$ standing for the angular frequency in radians/sec which is expressed as function of the frequency, f, in cycles/sec (hertz).

5.3 The New Poly-Reference Complex Frequency formulated in Model Model (pCF-MM)

Equation (5.6) can be written down for a set of time shifts, r, ranging from 0 to n, and combining the obtained equations into a single matrix expression, giving

$$\mathbf{H}_0(z) = \boldsymbol{\Psi}\,(\mathbf{I}z - \boldsymbol{\Lambda})^{-1}\,\boldsymbol{\Gamma}^T \tag{5.7}$$

with

$$\mathbf{H}_0(z) = \begin{bmatrix} \mathbf{H}(z) \\ z\mathbf{H}(z) \\ \vdots \\ z^n\mathbf{H}(z) \end{bmatrix} \in \mathbb{C}^{N_o(n+1)\times N_i} \tag{5.8}$$

and

$$\boldsymbol{\Psi} = \begin{bmatrix} \boldsymbol{\Phi} \\ \boldsymbol{\Phi}\boldsymbol{\Lambda} \\ \vdots \\ \boldsymbol{\Phi}\boldsymbol{\Lambda}^n \end{bmatrix} \in \mathbb{C}^{(n+1)N_o\times(n+1)N_o} \tag{5.9}$$

Equation (5.7) can be written for two discrete consecutive frequency lines ω_a and ω_b ($\forall\omega_b > \omega_a$) spaced from each other by a single discrete frequency step $\Delta\omega$ as

$$\begin{aligned} \mathbf{H}_0(z_a) &= \boldsymbol{\Psi}\,(\mathbf{I}z_a - \boldsymbol{\Lambda})^{-1}\,\boldsymbol{\Gamma}^T \\ \mathbf{H}_0(z_b) &= \boldsymbol{\Psi}\,(\mathbf{I}z_b - \boldsymbol{\Lambda})^{-1}\,\boldsymbol{\Gamma}^T \end{aligned} \tag{5.10}$$

Isolating $\boldsymbol{\Gamma}^T$ in both equations and combining the obtained expressions yield

$$\boldsymbol{\Psi}^{-1}\,[\mathbf{H}_0(z_b) - \mathbf{H}_0(z_b)] = \boldsymbol{\Lambda}\boldsymbol{\Psi}^{-1}\,[\mathbf{H}_1(z_b) - \mathbf{H}_1(z_b)] \tag{5.11}$$

with

$$\mathbf{H}_1(z) = \begin{bmatrix} z\mathbf{H}(z) \\ z^2\mathbf{H}(z) \\ \vdots \\ z^{n+1}\mathbf{H}(z) \end{bmatrix} \in \mathbb{C}^{N_o(n+1)\times N_i} \tag{5.12}$$

Writing down (5.11) for all the N_f discrete frequency lines available in the frequency band, i.e., for ω_a and ω_b ranging, respectively, from ω_0 to ω_{N_f-1} and from ω_1 to ω_{N_f}, and combining the equations corresponding to each pair of evaluated frequency values in a single matrix equation yield

$$\boldsymbol{\Psi}^{-1}\mathbf{B} = \boldsymbol{\Lambda}\boldsymbol{\Psi}^{-1}\mathbf{A} \tag{5.13}$$

where

$$\begin{aligned} \mathbf{A} &= \left[\mathbf{H}_0(z_1) - \mathbf{H}_0(z_0)\ \mathbf{H}_0(z_2) - \mathbf{H}_0(z_1)\ \cdots\ \mathbf{H}_0(z_{N_f}) - \mathbf{H}_0(z_{N_f-1})\right] \in \mathbb{C}^{N_o(n+1)\times N_i(N_f-1)} \\ \mathbf{B} &= \left[\mathbf{H}_1(z_1) - \mathbf{H}_1(z_0)\ \mathbf{H}_1(z_2) - \mathbf{H}_1(z_1)\ \cdots\ \mathbf{H}_1(z_{N_f}) - \mathbf{H}_1(z_{N_f-1})\right] \in \mathbb{C}^{N_o(n+1)\times N_i(N_f-1)} \end{aligned} \tag{5.14}$$

An eigenvalue problem can be formulated from (5.13) using the **D**ouble **L**east **S**quares approach (**DLS**) [12, 8], giving

$$\frac{1}{2}\left(\mathbf{B}\mathbf{A}^H\left(\mathbf{A}\mathbf{A}^H\right)^{-1}+\mathbf{B}\mathbf{B}^H\left(\mathbf{A}\mathbf{B}^H\right)^{-1}\right)=\boldsymbol{\Psi}\boldsymbol{\Lambda}\boldsymbol{\Psi}^{-1} \tag{5.15}$$

Once the eigenvalue problem (5.15) is solved, the modal shape vectors can be retrieved as the 1st N_o rows of $\boldsymbol{\Psi}$, and the natural frequencies and damping ratios are computed from the diagonal elements of $\boldsymbol{\Lambda}$. The eigenvalue problem as in Eq. (5.15) gives eigenvalues and eigenvectors not occurring in complex conjugate pairs. If mode shape vectors and continuous time poles occurring in conjugate pairs are desired, the following eigenvalue problem should be used:

$$\frac{1}{2}\left(\mathfrak{Re}\left(\mathbf{B}\mathbf{A}^H\right)\left(\mathfrak{Re}\left(\mathbf{A}\mathbf{A}^H\right)\right)^{-1}+\mathfrak{Re}\left(\mathbf{B}\mathbf{B}^H\right)\left(\mathfrak{Re}\left(\mathbf{A}\mathbf{B}^H\right)\right)^{-1}\right)=\boldsymbol{\Psi}\boldsymbol{\Lambda}\boldsymbol{\Psi}^{-1} \tag{5.16}$$

where $\mathfrak{Re}(\bullet)$ stands for the real part of a complex number.

5.4 Application to the Output-only Modal Analysis of the Steel Platform Specimen

In order to illustrate the practical application of the pCF-MM described in the previous section, a case study consisting of two independent steel platforms is considered. The specimens were used in a previous study to investigate the coupled dynamic behavior of offshore oil platforms when they are connected by a bridge [13]. A photo of the platform specimens is shown in Fig. 5.1a. The platform specimens consist of 0.0025 m thick steel plates, which are supported by four steel columns placed 0.05 m from the edges of the top steel plates. The steel plates are square with dimensions of 0.3 × 0.3 and 0.4 × 0.4 m, respectively. The columns, which are clamped to the steel plates at the top and to a stiff wooden box at the bottom, have a square cross section of 0.005 m and are 0.6 m high. The vibration responses in acceleration were measured at a total of 6 **D**egrees **O**f **F**reedoms (**DOF**s), three of which measured on the platform with smaller plate and three on the bigger one as indicated in Fig 5.1b.

The two steel platforms were randomly excited at six different positions by a pneumatic actuator whose air flow was instantaneously adjusted by valves actively controlled by an algorithm. The excitation signal used to control each valve independently in the algorithm was designed with flat spectral density ranging from 2 up to 20 Hz to secure the excitation of the first five modes. The vibration responses due to the air flow excitation were measured in acceleration with HBK accelerometers (piezoelectric CCLD with TEDS, with a sensitivity of 100 mV/g) with a sampling rate of 1652.9 Hz. A total of 164,993 time samples were acquired in the output-only vibration test, which corresponds to a measurement duration of, approximately, 1 min and 40 seconds. Afterward, the acceleration time series underwent a signal processing step to estimate the HS matrix $\mathbf{S}_{yy}^{+}$. To achieve this goal, they were de-trended, filtered with an eighth-order lowpass Chebyshev Type I filter,

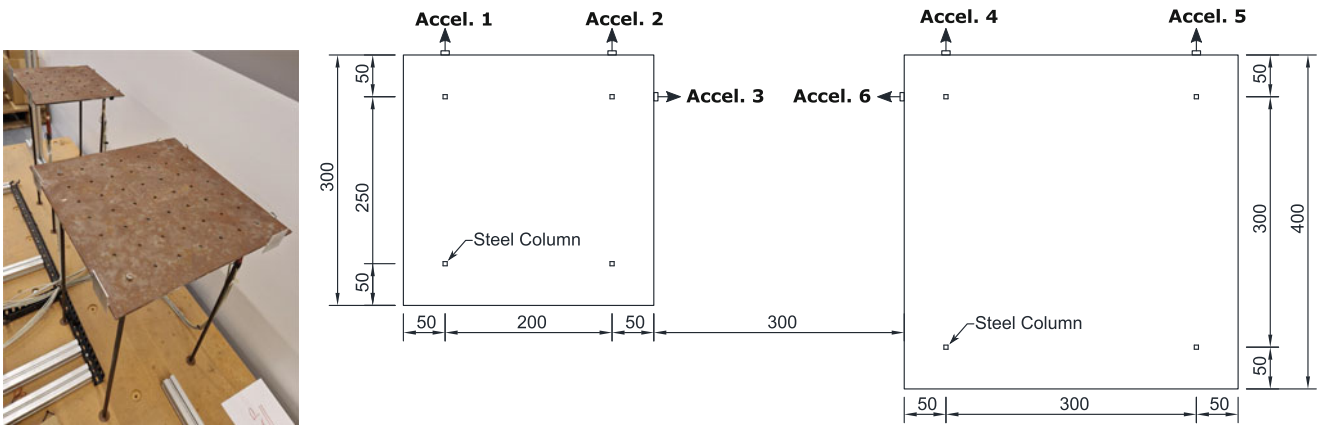

(a) (b)

Fig. 5.1 Steel platform specimen: (**a**) photo of the real platform specimen and (**b**) dimensions (in millimeters) of the top site of the steel platform specimens, sensors' positions, and measurement directions (**b**)

and resampled with a sampling frequency of 68.8705 Hz. Finally, the HS matrix was computed with a frequency resolution, N_f, of 513 frequency lines. Once computed, the HS matrix with dimension $6 \times 6 \times 513$ was used as primary data by the pCF-MM algorithm.

In order to facilitate the identification of the physical modes of the platforms, a stabilization diagram was constructed with the pCF-MM by identifying models with order, n, ranging from 1 to 80. Fig. 5.2 shows the stabilization diagram constructed with the pCF-MM and details of the close–spaced modes around 6.7 and 8.5 Hz. The identification of the physical poles in such a diagram was carried out by using a **H**ierarchical **C**lustering (**HC**) algorithm [14, 15]. The physical modes identified with such an approach are indicated by vertical red solid lines in Fig. 5.2. After automatically identifying the mode shape vectors, the operational factor vectors were estimated in a subsequent step by means of the so-called **L**east **S**quares **C**omplex **F**requency (**LSFD**) algorithm [14] and then used to synthesize the HS matrix from the estimated modal properties.

As seen in Fig. 5.2, the pCF-MM provided clear stable poles that matched precisely the peaks of the Power Spectral Density singular values (estimated with the FDD technique) shown in the background of the diagram solely for comparison purposes. Aiming at assessing the accuracy of the modal parameter estimation obtained with the pCF-MM, the trace of synthesized HS matrix is compared to that of the measured HS in Fig. 5.3. By comparing the synthesized trace with its measured counterpart in such a figure, it is clear that the pCF-MM provided very accurate estimates for the modal properties of the platform specimens.

The summary of the identification results obtained with the novel pCF-MM technique is shown in Fig. 5.4. The mode shapes represented in such a figure were the plotted with the aid of slave DOFs under the assumption that the top plates on both platforms behave as rigid bodies.

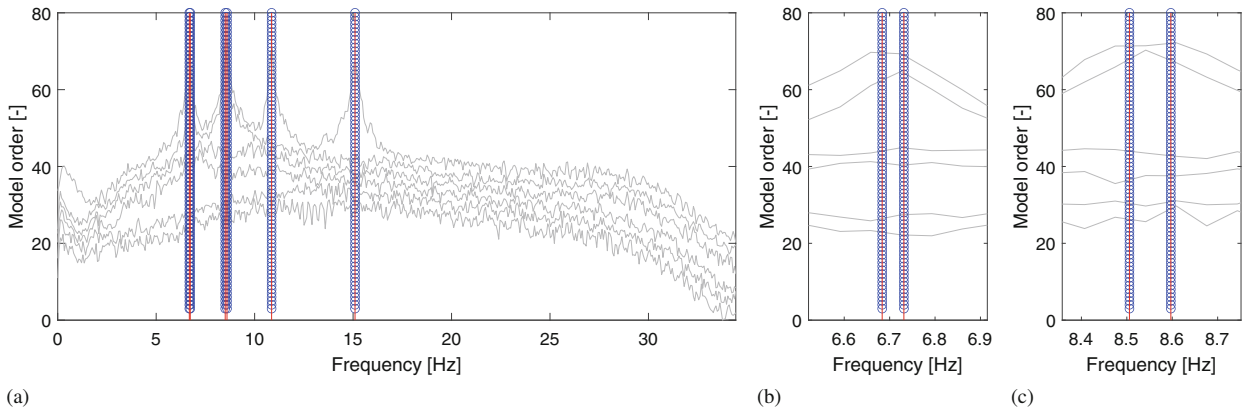

Fig. 5.2 Stabilization diagram constructed with the novel pCF-MM by the identifying models with order ranging from 1 to 80 (**a**) and the details of the closed spaced modes automatically identified with HC algorithm around 6.7 Hz (**b**) and 8.5 Hz (**c**)

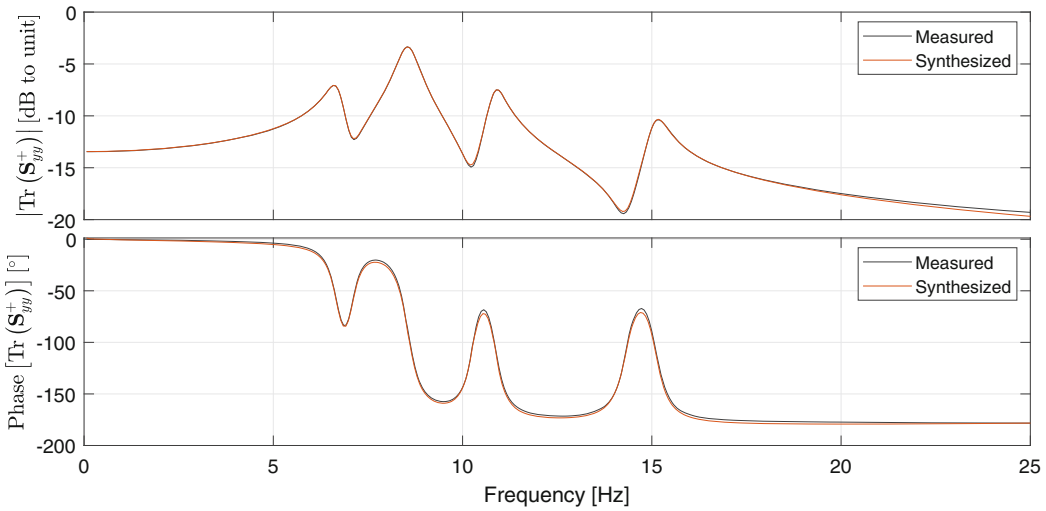

Fig. 5.3 Trace of the measured (black solid line) and pCF-MM synthesized HS matrix $\mathbf{S}_{yy}^{+}$ (red solid line): the top plot shows the magnitude, whereas the bottom shows the phase of the trace of the HS matrix

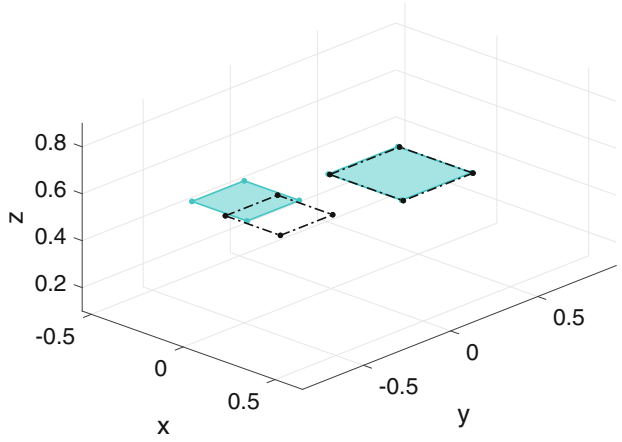

$f_1 = 6.684$ Hz, $\xi_1 = 0.590\%$

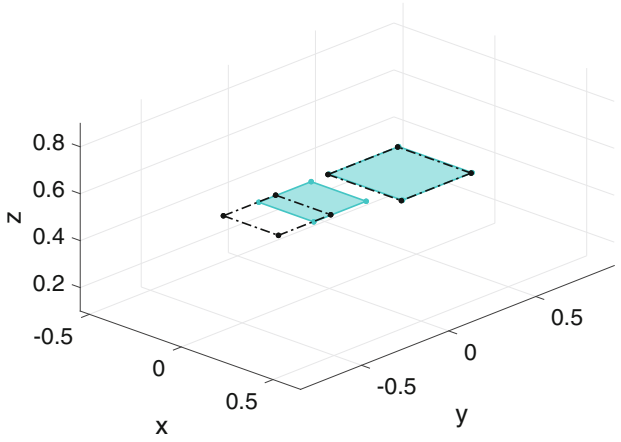

$f_2 = 6.731$ Hz, $\xi_2 = 0.445\%$

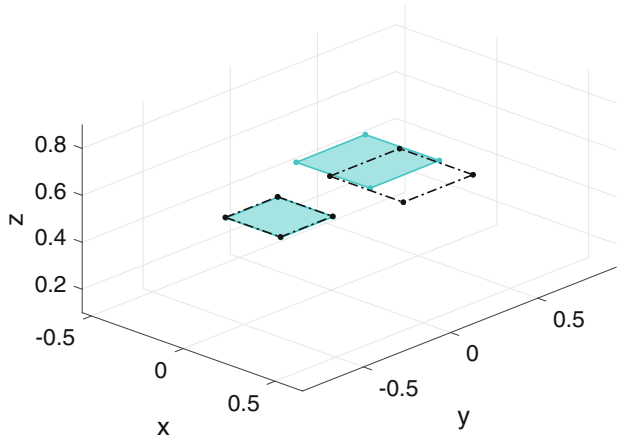

$f_3 = 8.506$ Hz, $\xi_3 = 0.554\%$

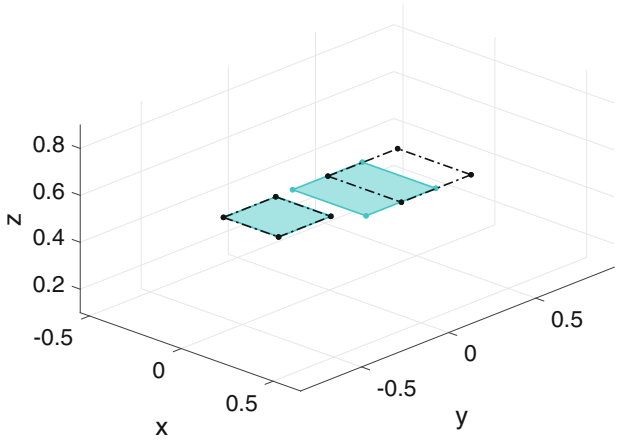

$f_4 = 8.597$ Hz, $\xi_4 = 0.526\%$

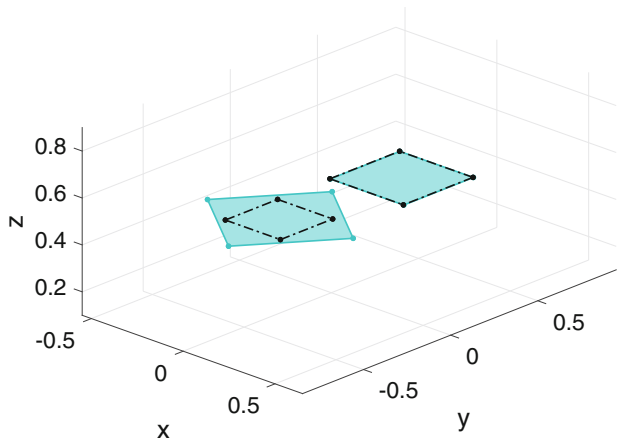

$f_5 = 10.862$ Hz, $\xi_5 = 0.379\%$

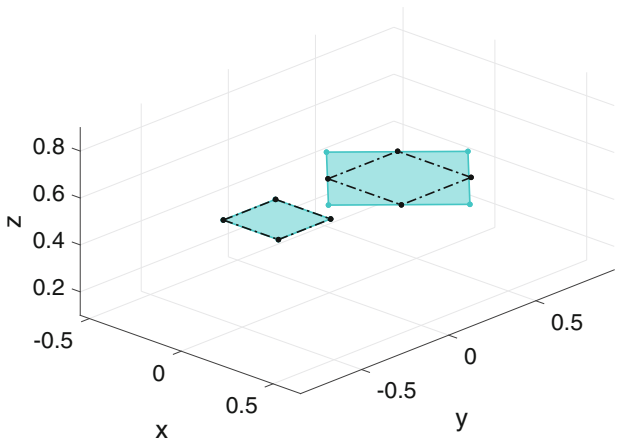

$f_6 = 15.098$ Hz, $\xi_6 = 0.509\%$

Fig. 5.4 Natural frequencies, damping ratios, and mode shapes of the two platforms identified with the novel pCF-MM technique

5.5 Conclusion

This chapter introduces and describes a new modal identification technique formulated in z-domain modal model. The underlying idea behind this novel approach is to formulate a high-order eigenvalue problem by comparing the measured frequency domain function (FRF or HS) at two adjacent spectral lines and by using different forward time shifts. The formulation of the pCF-MM herein described is meant for estimating the continuous-time poles and modal shape vectors but can be modified to estimate the modal participation factors, making it more suitable for classic EMA. In order to assess the performance of the proposed pCF-MM, the technique was applied to a practical OMA example. The results obtained from this analysis showed that the novel pCF-MM was capable of accurately and clearly identifying the first five vibration modes of the tested specimens. The accuracy and robustness provided by the pCF-MM algorithm was particularly observed in the estimation of the very closed–spaced vibration modes around 6.7 and 8.5 Hz.

Acknowledgments The authors acknowledge the funding received from DTU Offshore—Danish Offshore Technology Centre—to develop the pCF-MM technique.

References

1. Ibrahim, S.R., Mikulcik, E.C.: A method for the direct identification of vibration parameters from the free response. In: Shock and Vibration Bulletin, pp. 183–196 (1977)
2. Ibrahim, S.R.: Modal confidence factor in vibration testing. J. Spacecraft **15**, 313–316 (1978)
3. Vold, H., Kundra, J., Thomas Rocklin, G., Russel, R.: A multi-input modal estimation algorithm for mini-computers. SAE Trans. **91**, 815–821 (1982)
4. Vold, H., Thomas Rocklin, G., Russel, R.: The numerical implementation of a multi-input modal estimation algorithm for mini-computers. In: Proceedings of IMAC 1, Orlando (1982)
5. Fukozono, K.: Investigation of multiple-reference Ibrahim time domain modal parameters estimation technique. Master's Thesis, Department of Mechanical and Industrial Engineering, University of Cincinnati, 1986
6. Van Overschee, P., De Moor, B.: Subspace algorithm for the stochastic identification problem. Automatica **29**(3), 649–660 (1993)
7. Peeters, B., De Roeck, G.: Reference-based stochastic subspace identification for output-only modal analysis. Mech. Syst. Signal Process. **13**(6), 855–878 (1999)
8. Brincker, R., Ventura, C.: Introduction To Operational Modal Analysis, 1st edn. Wiley, New York (2015)
9. Guillaume, P., Verboven, P., Vanlanduit, S., Van Der Auweraer, H., Peeters, B.: A poly-reference implementation of the least-squares complex frequency-domain estimator. In: Proceedings of the 21st International Modal Analysis Conference (IMAC 21), Kissimmee. Society for Experimental Mechanics (2003)
10. Peeters, B., Van der Auweraer, H., Guillaume, P., Leuridan, J.: The polymax frequency–domain method: a new standard for modal parameter estimation? Shock Vib. **11**, 395–409 (2004)
11. Peeters, B., Van der Auweraer, H., Vanhollebeke, F., Guillaume, P.: Operational modal analysis for estimating the dynamic properties of a stadium structure during a football game. Shock Vib. **14**, 283–303 (2007)
12. Ibrahim, S.R.: A modal identification algorithm for higher accuracy requirements. In: AIAA paper, in: Proceedings of the 25th Structures, Structural Dynamics and Materials, pp. 117–122, Palm Springs, California (1984). AIAA
13. Rokne, A.G., Orfanos, A.: Experimental model testing of offshore platform models due to random loading. Master's Thesis, Department of Civil Engineering, Technical University of Denmark, Denmark, 2017
14. Amador, S.D.R.: Uncertainty Quantification in Operational Modal Analysis and Continuous Monitoring of Special Structures. PhD Thesis, Department of Civil Engineering, Faculty of Engineering of University of Porto, Porto, Portugal, 2015
15. Amador, S.D.R., Magalhães, F., Matos, Á., Caetano, E.: High spatial resolution modal identification of a stadium suspension roof: assessment of the estimates uncertainty and of modal contributions. Eng. Struct. **135**, 117–135 (2017)

Chapter 6
Mode Shape Identification Using Drive-by Monitoring: A Comparative Study

Kultigin Demirlioglu, Semih Gonen, and Emrah Erduran

Abstract The structural system identification technique referred to as *drive-by* health monitoring has recently become popular for the dynamic investigation of bridges. Drive-by monitoring enables extracting dynamic characteristics of bridges such as modal frequencies, damping, and mode shapes by using vibration responses measured on sensors mounted on a passing vehicle. Due to the mobility of the vehicle, the sensor receives the dynamic information of each point along the bridge and allows for acquiring higher resolution in the mode shapes compared to the conventional direct monitoring where a limited number of sensors can be mounted on a bridge. Therefore, theoretically, drive-by monitoring systems promise better resolution in constructing mode shapes, which will, in turn, yield better accuracy in many engineering applications such as damage detection, model updating, and calibration. To this end, this chapter aims at investigating two of the most used drive-by identification methodologies to obtain mode shapes of bridges. In this numerical study, the mode shapes of a single-span bridge are computed from the dynamic response of the instrumented vehicle by applying (i) variational mode decomposition together with the amplitude histories of the Hilbert transform and (ii) a system identification algorithm, namely, the reference-based Stochastic Subspace Identification. The efficacy of the two methods in mode shape identification is investigated using a parametric study, where the sensitivity of the results to different vehicle speeds, sampling rates, and road surface roughness is evaluated.

Keywords Bridge · Drive-by monitoring · Mode shapes · Variational mode decomposition · Reference-based SSI · Hilbert transform

6.1 Introduction

Bridge infrastructures are continuously exposed to various environmental conditions, natural hazards, and excessive loads. This exposure can lead to structural degradation and failure, as evidenced by recent bridge collapses. Therefore, bridge health monitoring is crucial for maintaining and evaluating transportation infrastructure. The conventional bridge health monitoring requires numerous sensors directly mounted on the structure to identify its modal parameters [1–5]. However, when it comes to the need to monitor the entire transportation network, the conventional approach leads to very high costs. Yang et al. [6] introduced a novel idea for extracting the dynamic parameters of the bridge *indirectly* from the acceleration response of a moving vehicle. The indirect approach, which is recently referred to as *drive-by monitoring* or *indirect monitoring*, promises efficient and low-cost inspection for the condition assessment of bridges without the requirement of instrumentation of each bridge.

Several researchers worked on mode shape identification using indirect measurements as bridge mode shapes are particularly useful for structural engineering purposes such as Finite Element (FE) modal updating and damage detection [7]. Zhang et al. [8] proposed an approach for constructing the mode shapes of bridges by the amplitude history of the Short-time Fourier transform (STFT) applied to the acceleration response of the vehicle. To make the vibration amplitudes larger, the vehicle was excited by tapping force with different frequencies close to the natural frequency of the bridge. Yang et al. [9] introduced a method using a signal decomposition technique to extract the bridge's modal components from the vehicle's acceleration response and determine the mode shapes by applying the Hilbert transform (HT) to the obtained components. Several researchers employed STFT [10, 11] and HT [7, 12, 13] to extract the mode shapes from the response

K. Demirlioglu (✉) · S. Gonen · E. Erduran
Department of Civil Engineering and Energy Technology, Oslo Metropolitan University, Oslo, Norway
e-mail: kultigin@oslomet.no

B. J. Dilworth et al. (eds.), *Topics in Modal Analysis & Parameter Identification, Volume 9*, Conference Proceedings of the Society for Experimental Mechanics Series, https://doi.org/10.1007/978-3-031-34942-3_6

of vehicle. In addition to these, Yang et al. [14] revealed that the contact-point (CP) response does not contain vehicle frequencies that hamper identifying the bridge frequencies. This observation was verified by numerical simulations [14] and later by conducting an in-situ test [15]. Yang et al. [16] indicated that using the CP response enables extracting more bridge frequencies and constructing mode shapes more accurately than the ones obtained from the vehicle response. Also, some researchers have developed a different concept for mode shape identification [17–20]. In their approach, the acceleration signal measured on the vehicle is separated into a number of equal segments along the bridge deck to form a data set at each segment that carries information on the mode shapes of that segment. Then, the mode shapes of the bridge can be obtained by applying an Operational Modal Analysis (OMA) to each data record. These studies made substantial contributions to the mode shape identification of bridges using indirect measurements. However, there is still a lack of studies that objectively evaluate the accuracy of these methodologies under varying conditions. This article aims at assessing the efficacy of two of the most commonly employed methods that apply (i) variational mode decomposition together with the amplitude histories of the Hilbert transform [16] and (ii) the reference-based Stochastic Subspace Identification (SSI) [19] in extracting bridge mode shapes. These methods will be referred to as Method 1 [16] and Method 2 [19], respectively, for brevity. They could be considered representatives of two different approaches in drive-by monitoring. In order to investigate their performance in estimating the bridge mode shapes, this chapter uses the application of these two distinct methods on the same single-span bridge that has similar properties to the ones used in [9, 16, 19]. For a proper comparison, the same quarter-car is employed in the numerical simulations of both methods. However, the CP response is adopted for Method 1 as proposed by [16], while the vehicle response is utilized for Method 2 [19]. Finally, their sensitivity to different parameters is evaluated using a parametric study that considers the effects of vehicle speed, sampling rate, and road roughness profile on constructing the mode shapes of the bridge.

6.2 Numerical Simulations

A simply supported bridge with a total span length of 25 m is modeled using ABAQUS software and Euler-Bernoulli beam elements as shown in Fig. 6.1. The bridge is discretized into 50 equal-length elements of 0.5 m. The elasticity modulus of the bridge is assumed to be $E = 30$ GPa, the moment of inertia of its cross-section is $I = 0.20$ m^4, and its mass per length $\rho = 2000$ kg/m. The first three vertical modal frequencies of the bridge are computed as 4.35, 17.23, and 38.06 Hz, respectively, through Eigen-value analysis. The vehicle moving over the bridge is simulated with a quarter-car model, i.e., using a lumped-mass spring model as shown in Fig. 6.1. The vehicle's characteristic mass, stiffness coefficient, and damping coefficient are adopted as m_v =2000 kg, k_v =550,000 N/m, and $c_v = 2000$ N.s/m, respectively. The frequency of the vehicle is 2.63 Hz.

The acceleration responses of the vehicle and the contact point (CP) are obtained during the crossing of the vehicle over the bridge with a velocity of 5 m/s using a sampling rate of 1000 Hz (Fig. 6.2a, b). The measured responses are processed using the Fast Fourier transform (FFT) to obtain the frequency spectra; see Fig. 6.2c, d. Figure 6.2c indicates that the spectrum obtained from the vehicle response consists of four main frequencies: the vehicle frequency f_v =2.63 Hz; the driving frequency f_d =0.2 Hz, which is computed as the ratio of the vehicle velocity to the length of the bridge; and the two frequencies for each modal frequency of the bridge which are shifted ($f_b \pm f_d/2$) due to the Doppler's effect [21]. As a result, the first, second, and third frequencies of the bridge are identified as 4.40, 17.20, and 37.80 Hz, respectively, by taking the average of their corresponding shifted frequencies [21]. Moreover, Fig. 6.2c also demonstrates that the bridge frequencies become less visible in the FFT spectrum for the higher modes [16]. However, using the CP's response completely eliminates the vehicle frequency from the FFT spectrum, as demonstrated in Fig. 6.2d. It significantly enhances the amplitudes of the second and third modal frequencies of the bridge and make them more detectable in the FFT spectrum, as seen in Fig. 6.2d.

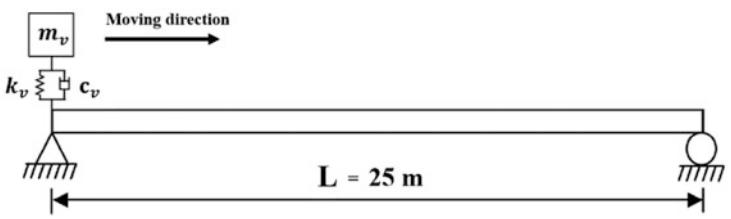

Fig. 6.1 The single-span bridge

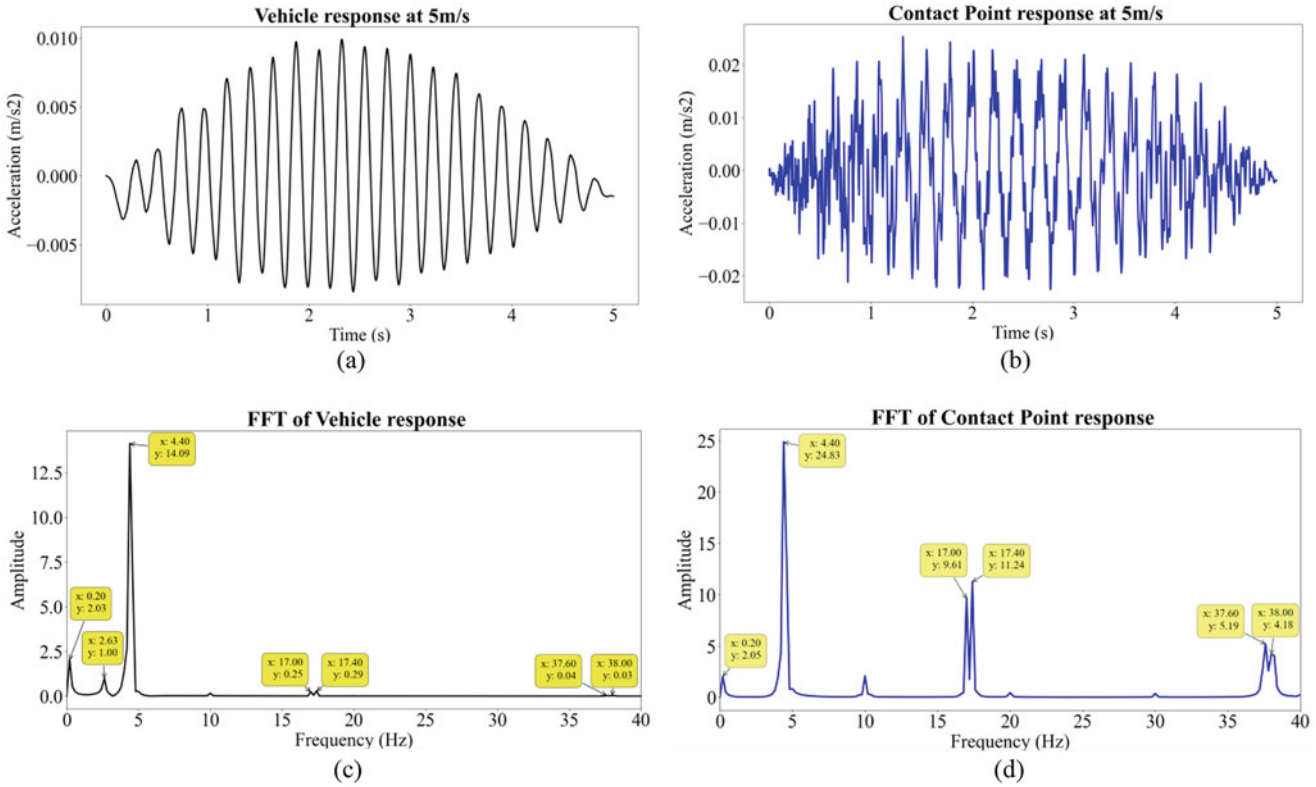

Fig. 6.2 (**a**) Vehicle response; (**b**) CP response; (**c**) FFT spectrum of vehicle response; (**d**) FFT spectrum of CP response

Regarding the slight differences observed between the identified and numerical bridge frequencies, it should be noted that the actual modal frequencies of bridges can be obtained under ambient vibrations. However, the dynamic response of the vehicle-bridge interaction (VBI) system is a nonstationary problem due to the moving vehicle that causes the bridge to behave under the forced vibrations [22]. Therefore, observing the variation between the identified bridge frequencies extracted from the nonstationary response and the theoretical ones is reasonable.

The configurations used to describe the system and the moving vehicle analysis, which are explained above, are referred to as the benchmark model in the rest of this chapter. In the following sections, various simulations are carried out with the same bridge and vehicle properties to investigate the effects of vehicle speeds, sampling rates, and road surface roughness on mode shape identification using two approaches proposed by Yang et al. [9, 16] and Li et al. [19], respectively. These two methods are briefly introduced in the following sections. For further details, the readers are recommended to refer to the Refs. [9, 16, 19].

6.2.1 Method 1

Method 1 proposed by Yang et al. [9, 16] utilizes the same VBI system as presented in Fig. 6.1. This method is principally based on signal decomposition to identify the modal information of the bridge and processing the decomposed signals to construct the mode shapes. First, the vertical acceleration response of CP recorded during the passage of the vehicle over the bridge at a constant velocity is used to filter the vehicle frequency out as described [16] and depicted in Fig. 6.2d. Second, the component responses associated with the modal frequencies of the bridge can be extracted by implementing a feasible signal decomposition tool to the recorded signal, such as the band-pass filter, singular spectrum analysis, and empirical modal decomposition. In this study, the variational mode decomposition (VMD) method is applied as a signal decomposition tool to extract the first three modal components [23]. Finally, the obtained components are processed by the Hilbert transform (HT) to provide the instantaneous amplitude history for constructing the mode shape of the given mode [24]. For instance, when the acceleration response of CP in Fig. 6.2b is processed by VMD and HT, the components related to the first three modes and their amplitude histories are plotted in Fig. 6.3.

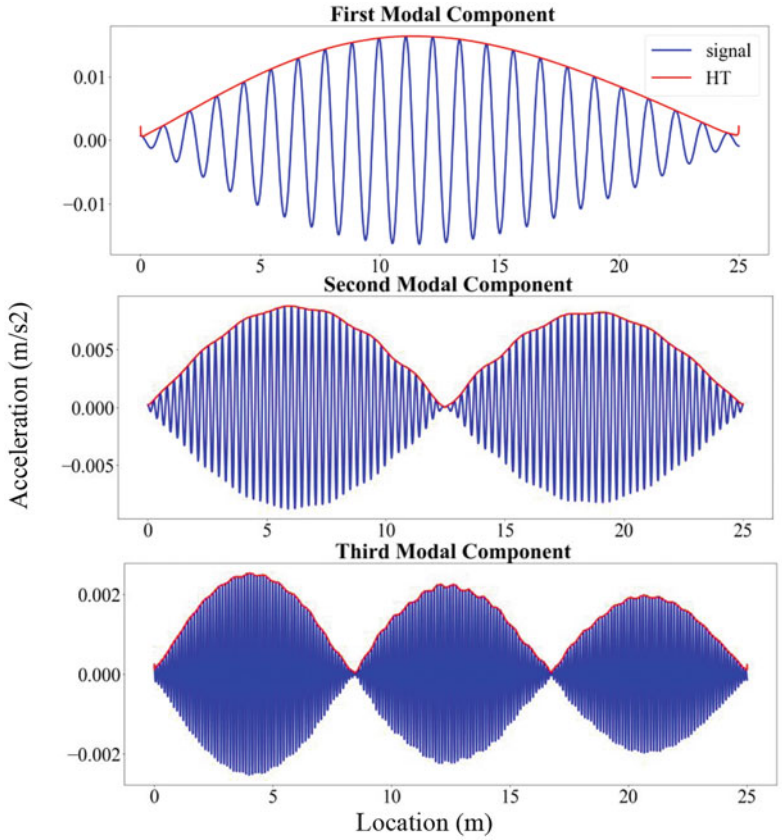

Fig. 6.3 The first three modal components obtained from the CP response in the benchmark model at 5 m/s

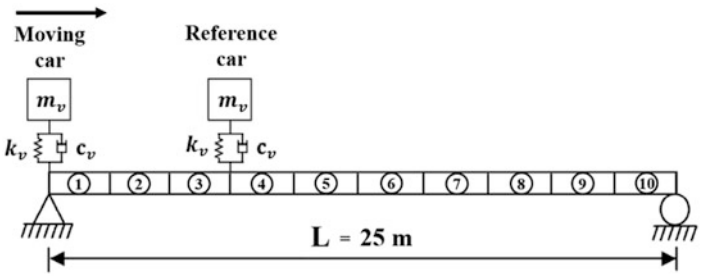

Fig. 6.4 Method 2's VBI model

6.2.2 Method 2

Method 2 proposed by Li et al. [19] uses the acceleration responses measured on two cars, one stationary (reference) and one moving (see Fig. 6.4). The reference car is positioned at a fixed location, while the other drives over the deck at a constant velocity. The reference car is stationed at the mid-span and the quarter-span to identify the first and second mode shapes, respectively, to capture the maximum modal amplitudes. The measurements from the two cars for each analysis are separated into ten equal segments based on the time range of the moving car corresponding to that segment. Therefore, the two acceleration responses in each segment form one pair of the data record. The local mode shape values at the mid-point of each segment are obtained by applying the reference-based SSI method to each data record [25], such that each segment is individually processed by the SSI algorithm. Finally, a progressive rescaling procedure in Eq. 6.1 is applied to the local mode shape values to obtain the global mode shape.

$$\mathbf{\Phi}_i = \frac{\mathbf{\Phi}_{\text{ref}}}{\varphi_{i,\text{ref}}} \varphi_{i,i}, \, (i = 1, 2 \ldots 10) \tag{6.1}$$

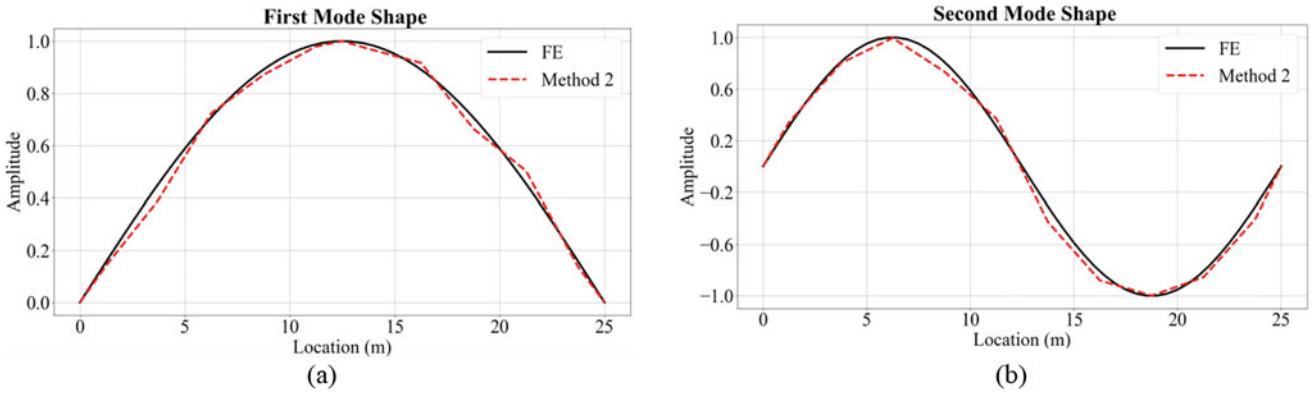

Fig. 6.5 (**a**) The first and (**b**) the second mode shapes of the bridge

where $\mathbf{\Phi}_i$ is the global mode shape value for the ith segment, $\mathbf{\Phi}_{\text{ref}}$ is the mode shape value obtained from the response of the reference car during the passage of moving car over the same segment where the reference car is stationed, $\varphi_{i,\,i}$ is the local mode shape value obtained from the response of the moving car measured in the ith segment, and $\varphi_{i,\,\text{ref}}$ is the local mode shape value obtained from the response of the reference car during the passage of the moving car over the ith segment. When the procedure is applied using a sampling rate of 1000 Hz and the moving car speed of 2.5 m/s, the first two mode shapes of the bridge are constructed, as shown in Fig. 6.5.

6.3 Parametric Study

The accuracy of the methods in estimating the mode shapes for varying vehicle speed, sampling rate, and road surface roughness is investigated using a parametric study.

6.3.1 Effect of Vehicle Speed

The effect of the vehicle speed on the extracted mode shapes of the bridge employing the two methods is evaluated using a sampling rate of 1000 Hz and three different vehicle speeds: 2.5 m/s, 5 m/s, and 10 m/s. The first two mode shapes of the bridge are constructed using both methods (Fig. 6.6). On the other hand, the third mode shape of the bridge could only be retrieved by Method 1, as presented in Fig. 6.7. It can be seen from Fig. 6.6a, c that the first two mode shapes can be identified with good precision using Method 1. The results show that increasing the vehicle velocity from 2.5 to 10 m/s improves the accuracy of mode shapes gradually since the vehicle traversing at higher speeds can induce larger excitation on the bridge [16]. Note that this statement is valid for the maximum speed limit of 10 m/s in this study and cannot be generalized for the use of speeds higher than 10 m/s, which may result in insufficient data for mode shape identification due to the relatively short travel time of the vehicle. It is also observed that as velocity increases, the edge effects of HT, which result from insufficient signal information, cause the HT amplitudes to fluctuate more at the locations near the bridge boundaries [12, 26]. Therefore, the edge effects worsen the mode shape estimation close to the bridge ends. In addition to these, Fig. 6.7 shows that the accuracy in extracting the third mode shape using Method 1 visibly decreases with decreasing speed. Particularly, the amplitudes of the mode shape along final two-thirds of the bridge length, i.e., the last two peaks of the mode shape, reduce, and remarkably become distanced from the theoretical mode shape with a decrease in the vehicle speed.

The mode shapes obtained using Method 2 (Fig. 6.6b, d) demonstrate that the performance of the method in extracting mode shapes is highly sensitive to the vehicle speed. The accuracy of mode shapes obtained at 2.5 m/s considerably reduces when the velocity is set as 5 m/s. As the vehicle speed increases, the travel time of the vehicle at each segment (see Fig. 6.4) relatively shortens. This influences the amount of data collected on the vehicle and leads to less dynamic information about the vibrations of the deck. Therefore, the SSI algorithm does not yield any stable modes in the stabilization diagram to recover mode shapes at 10 m/s due to insufficient amount of input signal measured at each segment. Additionally, to identify the third mode shape from the vehicle response using Method 2, a third configuration where the reference car is stationed at one-sixth

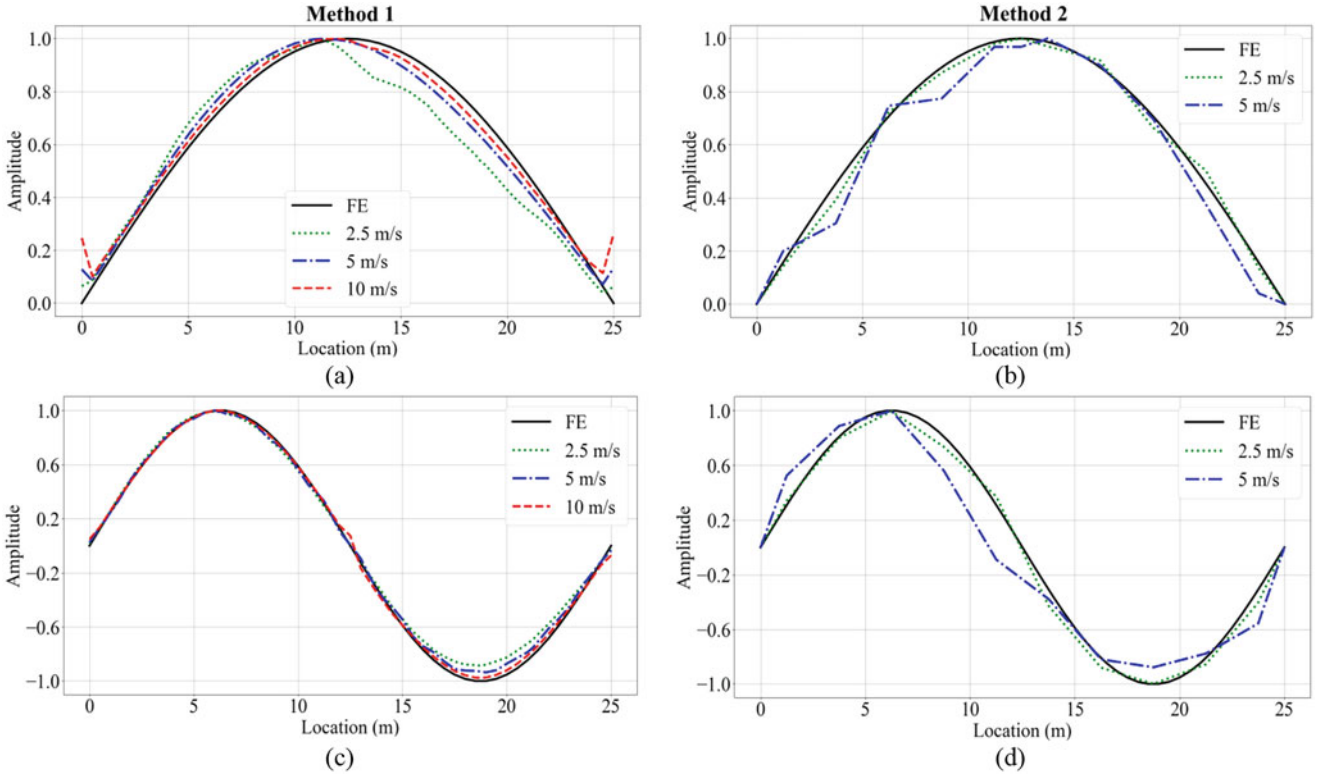

Fig. 6.6 At the range of vehicle speeds (**a**) the first mode shape of the bridge by Method 1; (**b**) the first mode shape of the bridge by Method 2; (**c**) the second mode shape of the bridge by Method 1; (**d**) the second mode shape of the bridge by Method 2

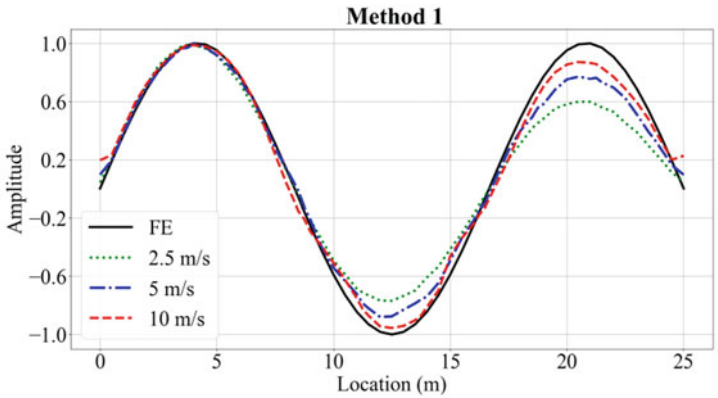

Fig. 6.7 Third mode shape of the bridge at the range of vehicle speeds

of the bridge length, where the third mode shape has its maximum amplitude, is performed for capturing the maximum modal amplitudes of the third mode. However, the SSI algorithm does not provide sufficient stable modes to recover the third mode shape in all three cases considered where the reference car is placed at the one-sixth bridge length, quarter-span, and mid-span. When the efficacy of the methods is considered for mode shape identification, it can be concluded that Method 2 outperforms Method 1 in constructing the mode shapes at 2.5 m/s; however, Method 1 is more robust to the velocity change.

6.3.2 Effect of Sampling Rates

The effect of sampling rate on the mode shape identification is assessed by employing three sampling rates of data acquisition: 250, 500, and 1000 Hz. In all the numerical simulations, the vehicle velocity is set as 2.5 m/s. The constructed mode shapes

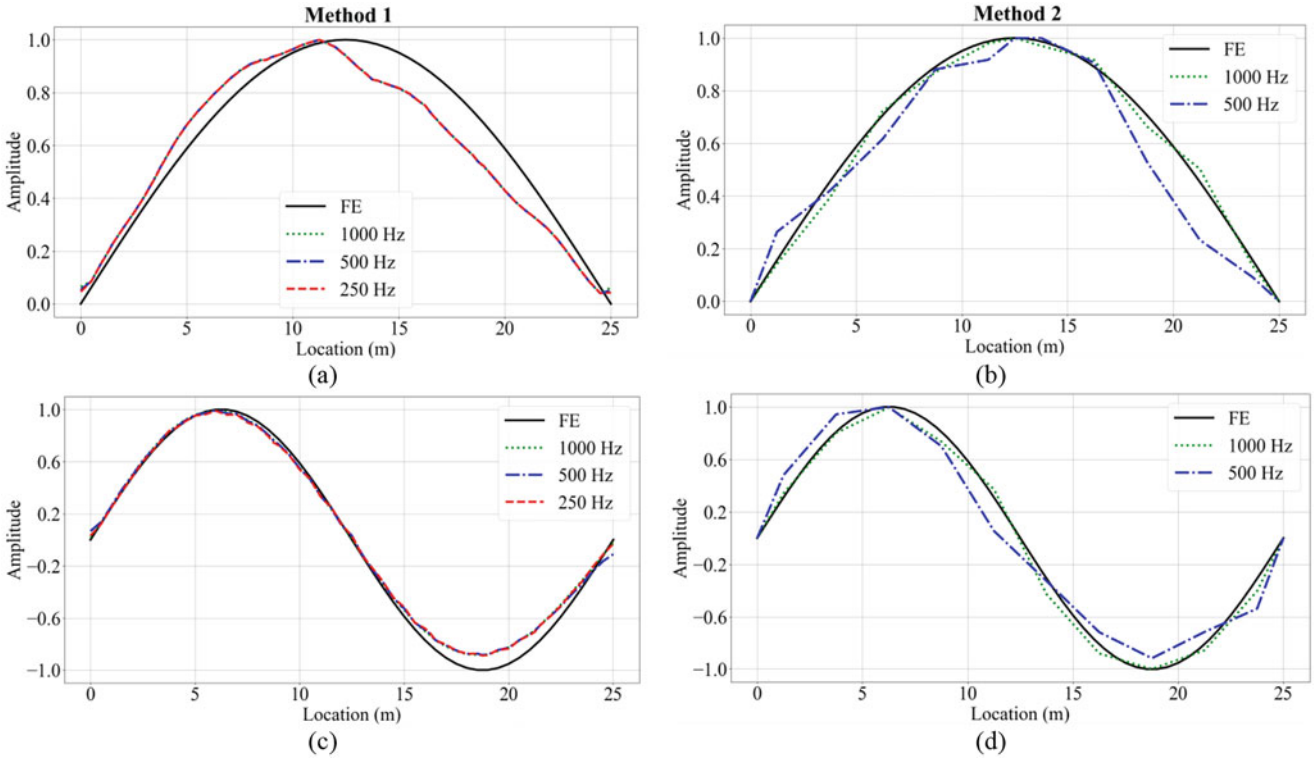

Fig. 6.8 Using the range of sampling rates (**a**) the first mode shape of the bridge by Method 1; (**b**) the first mode shape of the bridge by Method 2; (**c**) the second mode shape of the bridge by Method 1; (**d**) the second mode shape of the bridge by Method 2

of the bridge are presented in Fig. 6.8. The results show that Method 1 yields the mode shapes with almost the same accuracy at all sampling rates. However, the obtained mode shapes using Method 2 have been substantially distorted as the sampling rate decreases from 1000 Hz to 250 Hz. That stems from the fact that the effectiveness of the SSI algorithm is directly associated with the length of the acquired data, which is influenced by the sampling rate. As a result, Method 1 is highly robust to a decrease in the sampling rate of the signal, whereas the efficacy of Method 2 in estimating the mode shapes is significantly affected.

6.3.3 Effect of Road Roughness

Finally, the impact of road roughness on the FFT spectrum and the extracted mode shapes of the bridge is evaluated. The roughness profile is generated by the power spectral density (PSD) function of ISO-8608 for Class A [27] using the one-sided power spectral densities for the reference spatial frequency (0.1 m^{-1}), 16×10^{-6} m^3, which accounts for a *good* profile in the road classification. In generating this road profile, the lower and upper limits for spatial frequency are set as 0.01 m^{-1} and 10 m^{-1}, respectively. The road surface irregularity is simulated in the FE model at 0.1 m intervals along the bridge, as shown in Fig. 6.9.

The acceleration responses of the vehicle and the CP are processed using FFT. The obtained frequency spectra are presented in Fig. 6.10 as three subfigures for separate frequency ranges to account for the significant variation in the amplitudes. Figure 6.10a reveals that the road surface roughness significantly affects the dynamic response of the vehicle, amplifying the vehicle's frequency in the FFT spectrum at 2.63 Hz. Since using the CP response eliminates the vehicle-related frequency content, it makes the first modal frequency of the bridge more visible. It is also observed from Fig. 6.10b, c that the amplified vehicle response due to the roughness completely masks the visibility of the bridge-related dynamic information for higher modes. However, the second and third frequencies of the bridge can be clearly detected in the FFT spectrum when the CP response is used.

The performance of both methods in mode shape identification is also evaluated for Class A road roughness, setting the velocity of vehicles as 2.5 m/s and using a sampling rate of 1000 Hz in all the numerical simulations. The constructed mode shapes of the bridge are presented in Fig. 6.11. The results show that Method 2 performs better than Method 1 in extracting

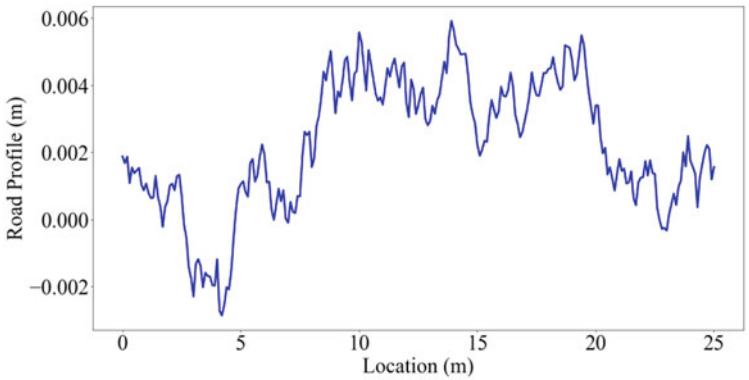

Fig. 6.9 The road roughness profile generated for Class A

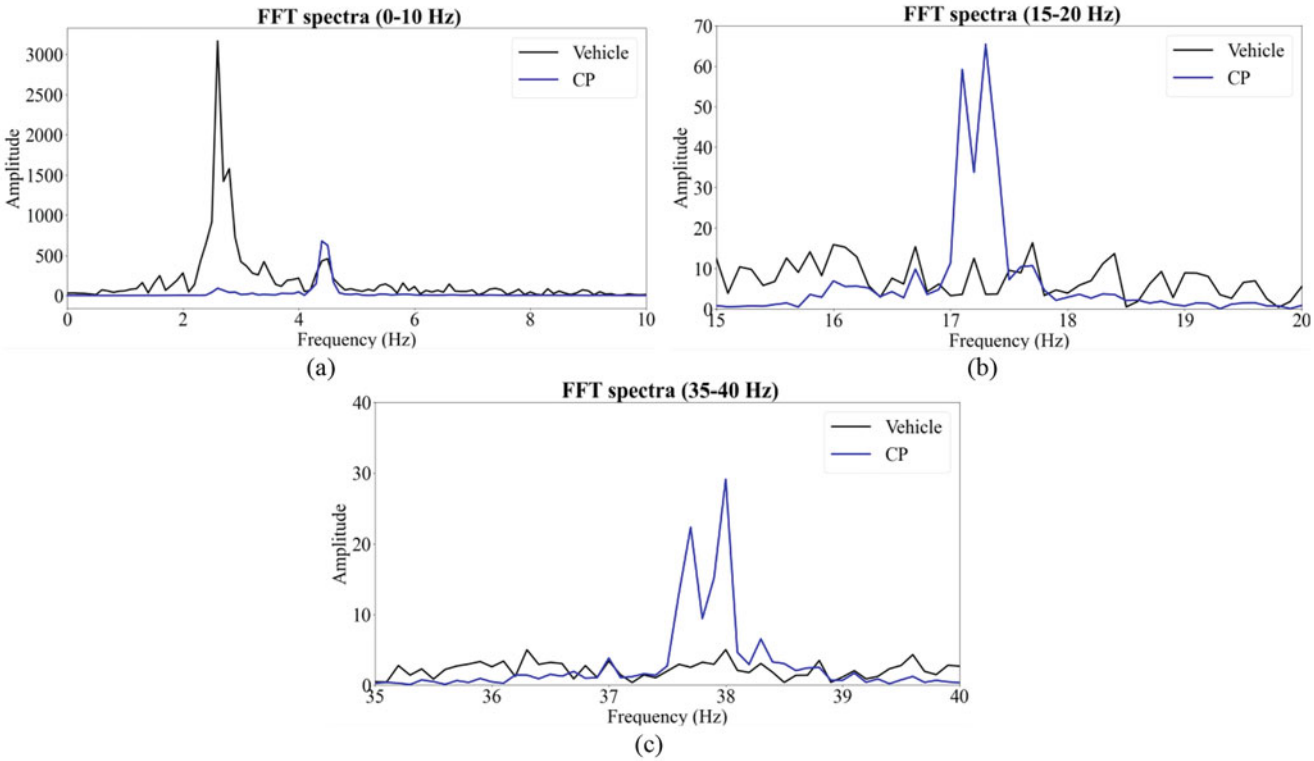

Fig. 6.10 FFT spectra of the benchmark model, including the road roughness profile (**a**) 0–10 Hz; (**b**) 15–20 Hz; (**c**) 35–40 Hz

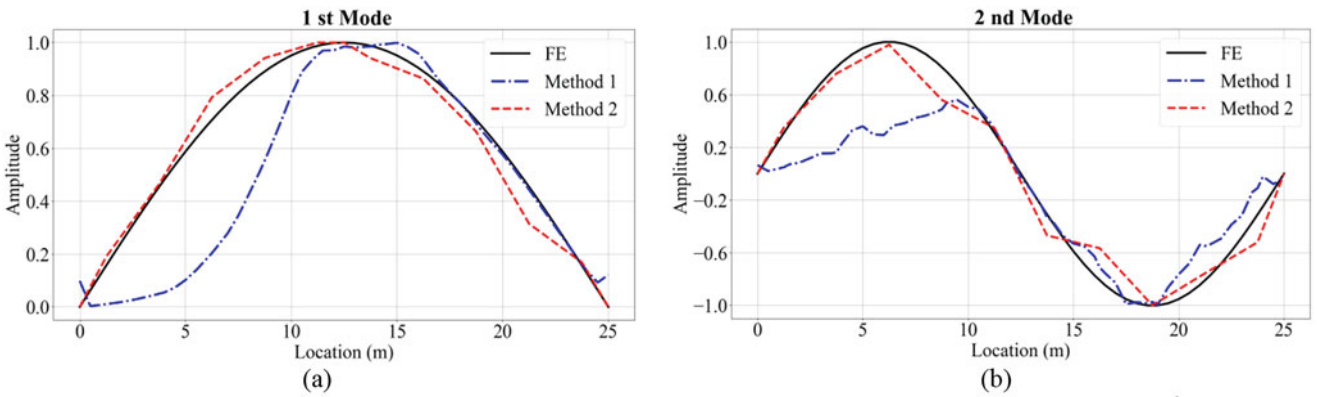

Fig. 6.11 Comparison of mode shapes in the presence of road surface roughness (**a**) 1 st mode; (**b**) 2 nd mode

the mode shapes. It is observed that the bridge components extracted in Method 1 are highly polluted due to the roughness effect. However, the stationary reference car used in Method 2 is not influenced by road roughness. Thus, it enables yielding stable modes in the stabilization diagram of the reference-based SSI and helps construct mode shapes better compared to Method 1.

6.4 Conclusions

This work investigated the efficacy of the modal identification of bridges using drive-by monitoring methods and their sensitivity to different parameters via a numerical study. Two of the most commonly employed methods in the literature to extract bridge modal frequencies and mode shapes through drive-by monitoring were used. Method 1 [9, 16] and Method 2 [19] were investigated in detail, and the results were compared to each other with the aim of providing guidance in their use. Based on the results of this study, the following conclusions are drawn:

- The accuracy of Method 1 in estimating mode shapes improves gradually as the vehicle velocity increases since the vehicle traversing at higher speeds can induce larger excitation on the bridge.
- Method 2 is highly affected by the length of the input signal, which is directly associated with the variations in sampling rates and vehicle speeds. This method provides the best results for lower vehicle speeds and high sampling frequencies.
- Method 2 is robust against the effect of road roughness in retrieving mode shapes, while the accuracy of the first method decreases significantly once road roughness is introduced.

The results presented in this study highlight the need for further research to develop a methodology that is more robust against changing parameters and conditions such as the vehicle speed and road roughness. In addition, the accuracy of methods should be investigated by a comparative study in different road roughness classes applying road roughness elimination approaches.

References

1. Demirlioglu, K., Gonen, S., Erduran, E.: On the selection of mode shapes used in optimal sensor placement. Conf. Proc. Soc. Exp. Mech. Ser., 85–92 (2023). https://doi.org/10.1007/978-3-031-05415-0_8/COVER
2. Erduran, E., Gonen, S., Alkanany, A.: Parametric analysis of the dynamic response of railway bridges due to vibrations induced by heavy-haul trains. (2022). https://doi.org/10.1080/15732479.2022.2090582
3. Gonen, S., Demirlioglu, K., Erduran, E.: Modal identification of a railway bridge under train crossings: a comparative study. Conf. Proc. Soc. Exp. Mech. Ser., 33–40 (2023). https://doi.org/10.1007/978-3-031-05449-5_4/COVER
4. Gonen, S., Soyoz, S.: Dynamic identification of masonry arch bridges using multiple methodologies. Conf. Proc. Soc. Exp. Mech. Ser., 37–47 (2021). https://doi.org/10.1007/978-3-030-47709-7_4/FIGURES/9
5. Salehi, M., Demirlioglu, K., Erduran, E.: Evaluation of the effect of operational modal analysis algorithms on identified modal parameters of railway bridges. In: IABSE Congr. Ghent 2021 Struct. Eng. Futur. Soc. Needs, pp. 441–449 (2021). https://doi.org/10.2749/ghent.2021.0441
6. Yang, Y.B., Lin, C.W., Yau, J.D.: Extracting bridge frequencies from the dynamic response of a passing vehicle. J. Sound Vib. **272**, 471–493 (2004). https://doi.org/10.1016/S0022-460X(03)00378-X
7. Malekjafarian, A., O'Brien, E.J.: On the use of a passing vehicle for the estimation of bridge mode shapes. J. Sound Vib. **397**, 77–91 (2017). https://doi.org/10.1016/j.jsv.2017.02.051
8. Zhang, Y., Wang, L., Xiang, Z.: Damage detection by mode shape squares extracted from a passing vehicle. J. Sound Vib. **331**, 291–307 (2012). https://doi.org/10.1016/j.jsv.2011.09.004
9. Yang, Y.B., Li, Y.C., Chang, K.C.: Constructing the mode shapes of a bridge from a passing vehicle: A theoretical study. Smart Struct. Syst. **13**, 797–819 (2014). https://doi.org/10.12989/sss.2014.13.5.797
10. Zhang, Y., Lie, S.T., Xiang, Z.: Damage detection method based on operating deflection shape curvature extracted from dynamic response of a passing vehicle. Mech. Syst. Signal Process. **35**, 238–254 (2013). https://doi.org/10.1016/j.ymssp.2012.10.002
11. Kong, X., Cai, C.S., Kong, B.: Numerically extracting bridge modal properties from dynamic responses of moving vehicles. J. Eng. Mech. **142**, 1–12 (2016). https://doi.org/10.1061/(asce)em.1943-7889.0001033
12. Tan, C., Uddin, N., O'Brien, E.J., McGetrick, P.J., Kim, C.-W.: Extraction of bridge modal parameters using passing vehicle response. J. Bridg. Eng. **24**, 1–15 (2019). https://doi.org/10.1061/(asce)be.1943-5592.0001477
13. Tan, C., Zhao, H., O'Brien, E.J., Uddin, N., Fitzgerald, P.C., McGetrick, P.J., Kim, C.W.: Extracting mode shapes from drive-by measurements to detect global and local damage in bridges. Struct. Infrastruct. Eng. **17**, 1582–1596 (2021). https://doi.org/10.1080/15732479.2020.1817105
14. Yang, Y.B., Zhang, B., Qian, Y., Wu, Y.: Contact-point response for modal identification of bridges by a moving test vehicle. Int. J. Struct. Stab. Dyn. **18**, 1–24 (2018). https://doi.org/10.1142/S0219455418500736
15. Yang, Y.B., Xu, H., Zhang, B., Xiong, F., Wang, Z.L.: Measuring bridge frequencies by a test vehicle in non-moving and moving states. Eng. Struct. **203**, 109859 (2020). https://doi.org/10.1016/j.engstruct.2019.109859

16. Yang, Y.B., Xu, H., Wang, Z.L., Shi, K.: Using vehicle–bridge contact spectra and residue to scan bridge's modal properties with vehicle frequencies and road roughness eliminated. Struct. Control Heal. Monit., 1–25 (2022). https://doi.org/10.1002/stc.2968
17. Oshima, Y., Yamamoto, K., Sugiura, K.: Damage assessment of a bridge based on mode shapes estimated by responses of passing vehicles. Smart Struct. Syst. **13**, 731–753 (2014). https://doi.org/10.12989/sss.2014.13.5.731
18. Malekjafarian, A., O'Brien, E.J.: Identification of bridge mode shapes using Short Time Frequency Domain Decomposition of the responses measured in a passing vehicle. Eng. Struct. **81**, 386–397 (2014). https://doi.org/10.1016/j.engstruct.2014.10.007
19. Li, J., Zhu, X., Seong Law, S., Samali, B.: Indirect bridge modal parameters identification with one stationary and one moving sensors and stochastic subspace identification. J. Sound Vib. **446**, 1–21 (2019). https://doi.org/10.1016/j.jsv.2019.01.024
20. Mei, Q., Shirzad-Ghaleroudkhani, N., Gül, M., Ghahari, S.F., Taciroglu, E.: Bridge mode shape identification using moving vehicles at traffic speeds through non-parametric sparse matrix completion. Struct. Control Heal. Monit. **28**, 1–21 (2021). https://doi.org/10.1002/stc.2747
21. Yang, Y.B., Yang, J.P.: State-of-the-Art Review on Modal Identification and Damage Detection of Bridges by Moving Test Vehicles (2018). https://doi.org/10.1142/S0219455418500256
22. Cantero, D., Hester, D., Brownjohn, J.: Evolution of bridge frequencies and modes of vibration during truck passage. Eng. Struct. **152**, 452–464 (2017). https://doi.org/10.1016/j.engstruct.2017.09.039
23. Dragomiretskiy, K., Zosso, D.: Variational mode decomposition. IEEE Trans. Signal Process. **62**, 531–544 (2014). https://doi.org/10.1109/TSP.2013.2288675
24. Huang, N.E., Shen, Z., Long, S.R., Wu, M.C., Snin, H.H., Zheng, Q., Yen, N.C., Tung, C.C., Liu, H.H.: The empirical mode decomposition and the Hubert spectrum for nonlinear and non-stationary time series analysis. Proc. R. Soc. A Math. Phys. Eng. Sci. **454**, 903–995 (1998). https://doi.org/10.1098/RSPA.1998.0193
25. Peeters, B., De Roeck, G.: Reference-based stochastic subspace identification for output-only modal analysis. Mech. Syst. Signal Process. **13**, 855–878 (1999). https://doi.org/10.1006/mssp.1999.1249
26. Rato, R.T., Ortigueira, M.D., Batista, A.G.: On the HHT, its problems, and some solutions. Mech. Syst. Signal Process. **22**, 1374–1394 (2008). https://doi.org/10.1016/j.ymssp.2007.11.028
27. ISO 8608, Mechanical vibration—road surface profiles—reporting of measured data, E (2016) 44. https://us.v-cdn.net/6030008/uploads/editor/83/oyhfu0i29vek.pdf

Chapter 7
Tips, Tricks, and Obscure Features for Modal Parameter Estimation

William Fladung and Kevin Napolitano

Abstract A good piece of advice for those who engage in modal parameter estimation is "Don't use data that doesn't help your cause." Selecting the frequency range of interest and down-selecting the references and responses are common features in all commercial modal analysis software packages. While these procedures are usually sufficient for producing acceptable results, there are some supplemental techniques available that go beyond just defining the temporal and spatial boundaries of the dataset. This chapter discusses some of these more obscure features that could be helpful in improving your modal parameter estimation results.

Keywords Modal parameter estimation · Normal modes · Orthogonality

Nomenclature

CMIF Complex mode indicator function
FRF Frequency response function
PSMIF Power spectral mode indicator function
QMIF Quadrature mode indicator function
ZDOP Z-domain orthogonal polynomial

7.1 Introduction

In the early days of modal testing, measurement channels were precious and few, and often the data had to be acquired in subsets of channels (or "patches" in the parlance of the time), which was a time-consuming process. Collecting a complete dataset could take several hours, and over this extended test duration, inconsistencies might creep into the data, which could cause troubles for the modal parameter estimation results. Nowadays, we have data acquisition systems with hundreds of channels at a reasonable price that allows us to acquire all of the measurements together, which takes much less time and produces more-consistent datasets.

Having all of these consistently acquired frequency response functions (FRFs), the general consensus is to use all of them in the parameter estimation process, and often this en masse approach produces acceptable results in one pass through the software. Of course, you can redefine the temporal and spatial boundaries of the dataset by narrowing the frequency range of interest and sieving the references and responses to concentrate on a particular component or subset of modes. However, there are some less common techniques that can be utilized to further segregate and prioritize the data within the dataset boundaries that can have beneficial effects on the results. These novelties can be particularly relevant when test self-orthogonality metrics are part of the requirements for a successful modal test. A goal of many aerospace modal tests is to ensure that the off-diagonal terms of the test self-orthogonality matrix are less than or equal to 10%. High off-diagonal terms can signify testing errors, which could have been caused by nonfunctional sensors, mislabeling of the channel table, analysis model errors, or modal extraction errors.

W. Fladung (✉) · K. Napolitano
ATA Engineering, Inc., San Diego, CA, USA
e-mail: bfladung@ata-e.com

B. J. Dilworth et al. (eds.), *Topics in Modal Analysis & Parameter Identification, Volume 9*, Conference Proceedings of the Society for Experimental Mechanics Series, https://doi.org/10.1007/978-3-031-34942-3_7

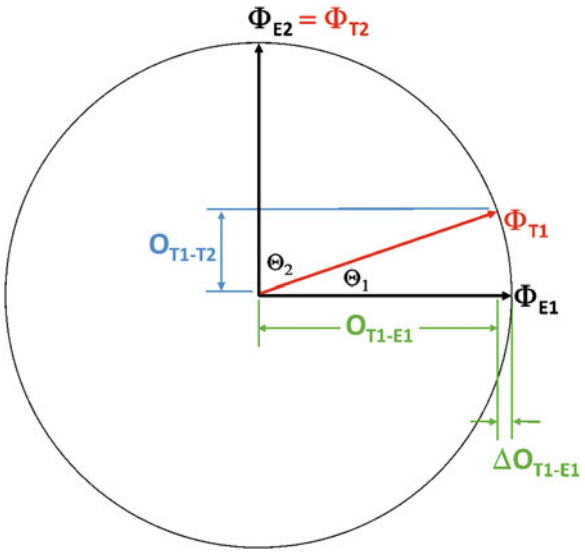

Fig. 7.1 Idealized representation of two orthogonal shapes and an imperfectly extracted shape that is a mass-weighted linear combination of the two exact shapes

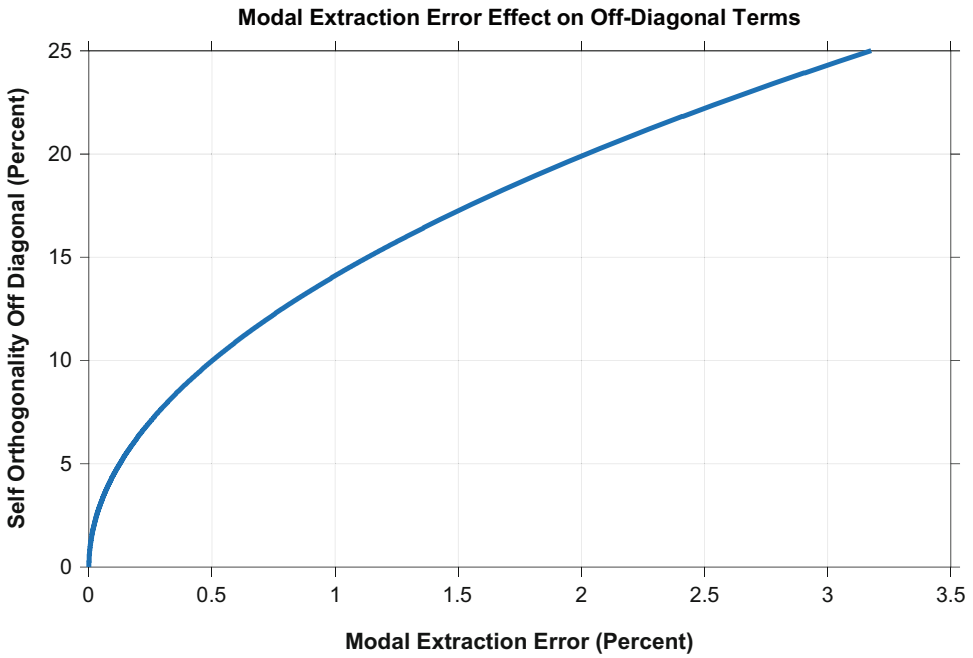

Fig. 7.2 Off-diagonals of test self-orthogonality matrix are very sensitive to small errors in modal extraction

Test self-orthogonality is defined as $O_{ij} = \Phi_i^{\mathrm{T}} M \Phi_j$, where M is the mass matrix and the magnitudes of the shapes are defined such that $\Phi_i^{\mathrm{T}} M \Phi_i = 1$.In an idealized case with a perfect mass matrix, $\Phi_i^{\mathrm{T}} M \Phi_j = 1$ for $i = j$, and $\Phi_i^{\mathrm{T}} M \Phi_j = 0$ for $i \neq j$. Thus, orthogonality can be thought of as a mass-weighted dot product used to calculate the projection of one shape onto another. In the ideal case, as shown in Fig. 7.1, two "exact" shapes, Φ_{E1} and Φ_{E2}, can be represented on a unit circle as being perpendicular to each other. Assume that an "imperfect" shape, Φ_{T1},can be represented as being rotated from the exact shape Φ_{E1} and that Φ_{T2} is a perfect modal extraction for Φ_{E2}. The orthogonality between Φ_{T2} and Φ_{T1}, O_{T1-T2}, is the projection of Φ_{T2} onto Φ_{T1}. The orthogonality between Φ_{T1} and Φ_{E1} is O_{T1-E1}, which would be 1 if the modal extraction of Φ_{T1} had been perfect, but is less than 1 by the amount ΔO_{T1-E1}.

The error for the first shape (ΔO_{T1-E1}) versus the orthogonality for the second shape (O_{T1-T2}) is depicted graphically as $1 - \cos\Theta_1$ and $\cos\Theta_2$ in Fig. 7.2, which shows that small percentage errors in modal extraction can lead to large off-diagonals in orthogonality. For example, a 1% error in a test mode (Φ_{T1}) can lead to an off-diagonal term of 14%.

7.2 Excluding Frequency Ranges

In a selected frequency range of interest (as indicated by the vertical cursors with triangular end-markers in Fig. 7.3), there will typically be several hundred to a few thousand spectral lines, which is plenty to generate an overdetermined least-squares solution for the matrix polynomial coefficients from which the poles are computed. By default, all of the spectral lines are used, and some software packages may allow the user to decimate the spectral lines to alleviate the computational burden (but this may just be a remnant of a past when computers were slower and had less memory). Rather, what we are advocating here is instead of using some evenly spaced subset of spectral lines, is to exclude *certain* spectral lines or frequency ranges, as indicated by the pink regions in Fig. 7.3, that may be detrimental to the estimation process—to exclude "data that doesn't help your cause."

In the conceptual examples in Fig. 7.3, there are no modes in the noisy region between 310 and 420 Hz, and that data will not contribute anything constructive to the parameter estimation. To omit this region, you could do one frequency range for all the modes below 310 Hz and a second frequency range for the one mode above 420 Hz, or you could do the entire frequency range from 30 to 450 Hz and just exclude all of the spectral lines between 310 and 420 Hz. Electrical line noise relentlessly shows up in our measurements at predictable spectral lines and can usually be ignored, but if it happens to interfere with mode identification (e.g., as at 240 Hz in Fig. 7.3), those specific frequencies could be excluded. A more serious noise problem is leakage, which can split a peak, as evident for the 50 Hz mode in Fig. 7.3, where it is known that there is only one mode. In this case, the parameter estimation algorithm is not going to be able to provide a reliable solution. However, the leakage error is localized to a few spectral lines near the peak, which can be excluded to get a better estimate of the pole for that mode.

In the example shown in Fig. 7.4, leakage was induced in the FRFs (green) by extending the burst length such that the response did not decay within the time period while the FRFs without leakage (blue) were measured using a more appropriate burst length. The estimated poles for these two modes from the baseline without leakage, leakage without excluded frequency ranges, and leakage with excluded frequency ranges are listed in Table 7.1. Also plotted in Fig. 7.4 are the synthesized FRFs for the two leakage cases, and the excluded frequency ranges are designated by the gray patches. Even though the split peaks in the FRF may give the appearance of more than one mode at both of these peaks, the z-domain orthogonal polynomial (ZDOP) algorithm [1] found only one mode for each of them. The leakage had little effect on the frequency estimates but caused an overestimation of the damping due to the apparent broadening of the peak, as evident by the synthesized FRFs.

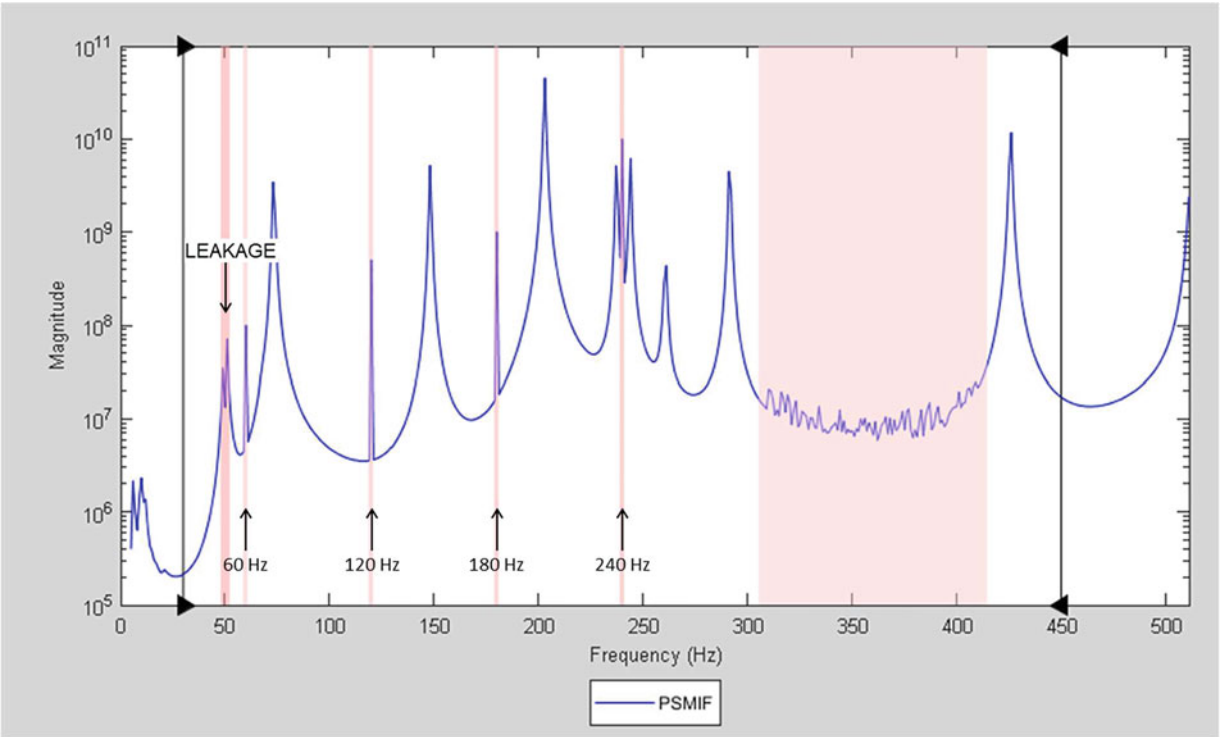

Fig. 7.3 Power spectral mode indicator function (PSMIF) showing excluded frequency ranges

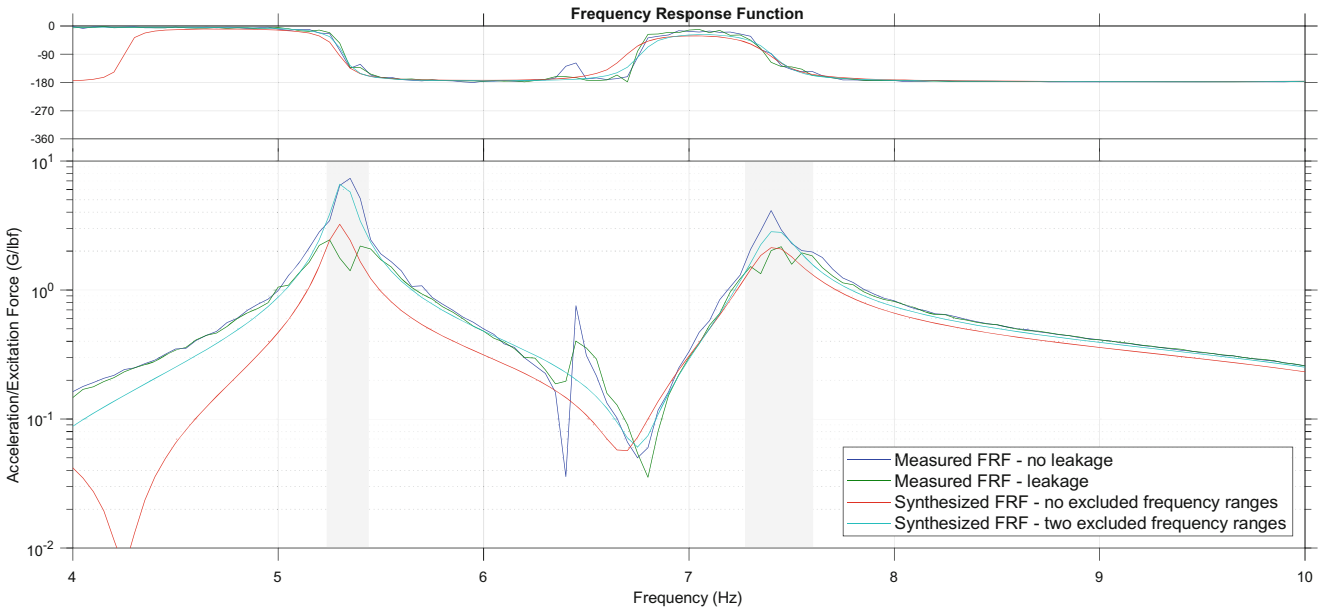

Fig. 7.4 Measured and synthesized FRFs with and without excluding frequency ranges at peaks with leakage

Table 7.1 Frequency and damping estimates for the FRFs in Fig. 7.4

No leakage		Leakage—no excluded frequency ranges		Leakage—two excluded frequency ranges	
Frequency (Hz)	Damping (%)	Frequency (Hz)	Damping (%)	Frequency (Hz)	Damping (%)
5.31	0.70	5.30	1.07	5.32	0.84
7.40	1.38	7.40	1.60	7.41	1.29

While not a panacea for all of the ills caused by leakage, excluding the leakage-contaminated spectral lines at these two peaks can at least make the best out of a bad situation.

The derivation of the rational fraction polynomial algorithm, which is the base model of the frequency-domain methods, arrives at a matrix form for generating an overdetermined least-squares solution for the polynomial coefficients as something similar to Eq. (7.1), which is valid for *all* frequencies—for *all* frequencies, with no conditions that they must be contiguous, which means we are free to choose the frequencies that are included in or excluded from the algorithm. This is also true for orthogonal polynomial algorithms [1, 2], which place no restrictions on the evenness of the frequency spacing when constructing the basis functions. However, for discrete-time-domain algorithms, which rely on the inverse Fourier transform, evenly spaced frequencies are required, and excluding frequency ranges or spectral lines is not a viable option.

$$\begin{bmatrix} H(\omega) & j\omega H(\omega) & \cdots & (j\omega)^{m-1} H(\omega) & |-1 & -(j\omega) & \cdots & -(j\omega)^{m-2} \end{bmatrix} \begin{bmatrix} \alpha_0 \\ \alpha_1 \\ \vdots \\ \frac{\alpha_{m-1}}{\beta_0} \\ \beta_1 \\ \vdots \\ \beta_{m-2} \end{bmatrix} = -(j\omega)^m H(\omega) \tag{7.1}$$

7.3 Selecting Frequency Bands for Residues

Modern modal parameter estimation is a two-step process, with estimation of the poles being the first step and estimation of the residues being the second step. Expert and novice curve-fitters alike spend most of their time on the first step selecting

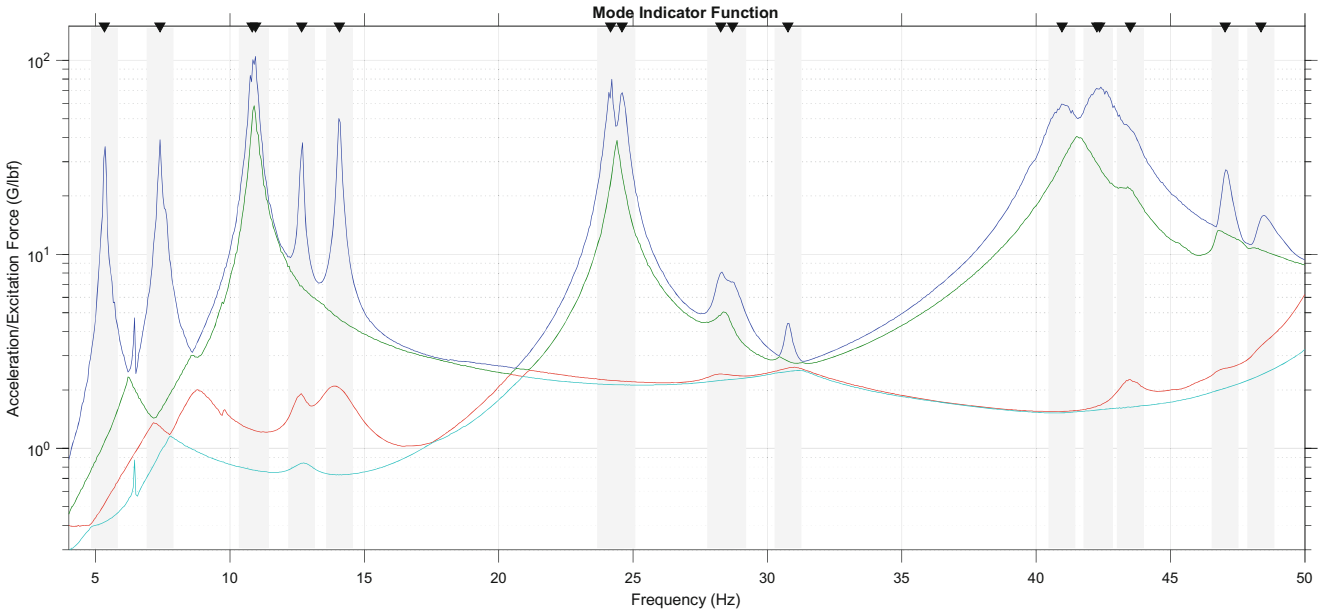

Fig. 7.5 Complex mode indicator function (CMIF) showing constant frequency bands for residue estimation

a good group of poles from a stability, or consistency, diagram, while the second step is generally considered the easy part with not much more to do except sometimes moving the frequency range cursors and maybe changing the default selection for the residuals to include in the solution for the residues. However, there are some other, obscure features available that may lead to better results in the residue-estimation process.

The frequency range to include in the residue-estimation process should naturally encompass the span of the frequencies of the selected poles, (e.g., from 10% below the lowest frequency to 10% above the highest frequency). Of course, any frequency ranges or spectral lines excluded from the pole estimation should also be excluded from the residue estimation. While the default might be to include all other spectral lines between the frequency range cursors, there may be wide valleys between the peaks not containing any modes (i.e., not containing any response that would help the cause of estimating residues). Several of these regions can be found in Fig. 7.3, and at least two more in Figs. 7.5 and 7.6. So instead of using everything, a more judicious approach might be to use only frequency bands in the vicinity of the selected poles, which are designated by the triangular markers in Fig. 7.6. There are several ways to define these bands: as a number of spectral lines, as a frequency bandwidth in Hz, or as a percentage of the frequency of each pole. For the first two options, the frequency band will have a constant width, but for the third, the frequency band will be wider for higher-frequency modes, which are typically less densely spaced, and will be narrower for lower-frequency modes, which may yield too few spectral lines. In this case, there needs to be some minimum number of spectral lines to ensure a credible solution. In the example shown in Fig. 7.5, the gray patches represent the ± 0.5 Hz (± 10 spectral lines) frequency bands, where for closely spaced modes the bands may overlap. In the example shown in Fig. 7.6, the gray patches represent the $\pm 5\%$ frequency bands, where there is more overlap of the higher-frequency bands.

In the example shown in Fig. 7.7, the mode at 7 Hz and the modes between 11 and 14 Hz were not well excited by whatever set of inputs were chosen for this dataset. While these frequency ranges do not necessarily contain "bad data" that should be excluded entirely, no viable modes are found in them, so including those spectral lines is not going to help get better estimates of the residues for the four selected modes designated by the triangular markers. In this case, an alternative would be to use the 5% frequency bands represented by the gray patches.

7.4 Solving for Normal Modes

Residue estimation starts with the partial fraction form of a displacement-over-force FRF as in Eq. (7.2), where H is the FRF, A_r are the residues, λ_r are the poles, $2N$ in the upper limit of the summation indicates conjugate pairs of modes, and the standard, single-term upper and lower residuals (R_{L} and R_{U}) have been added to account for out-of-band modes.

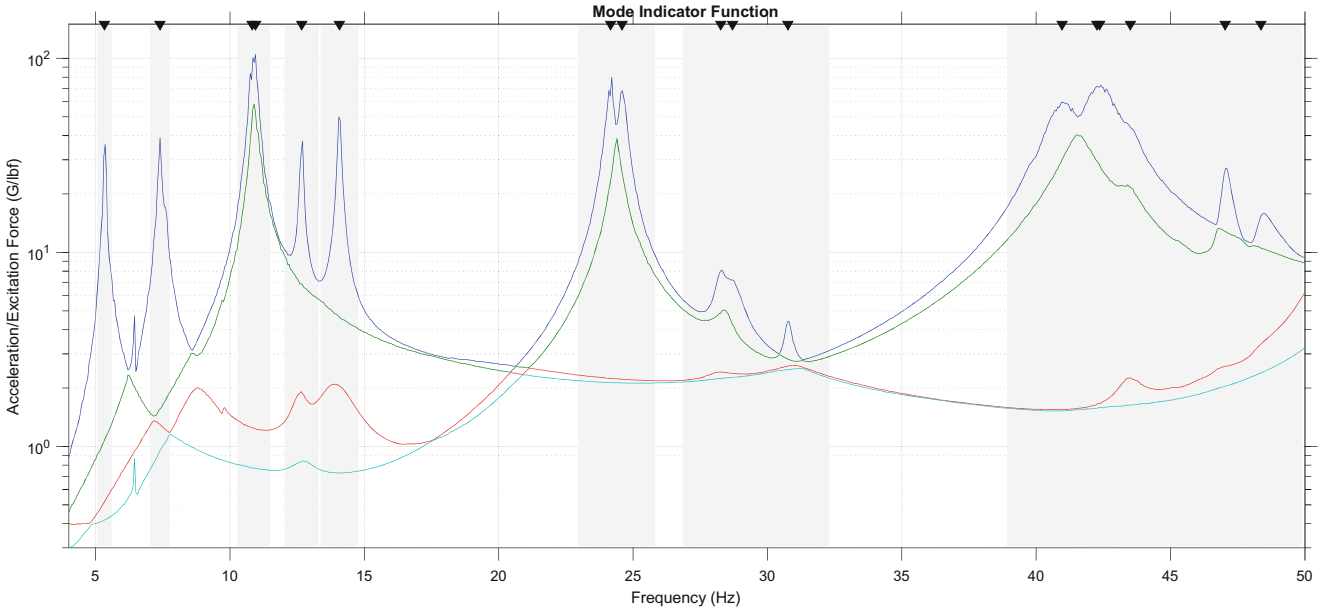

Fig. 7.6 CMIF showing proportional frequency bands for residue estimation

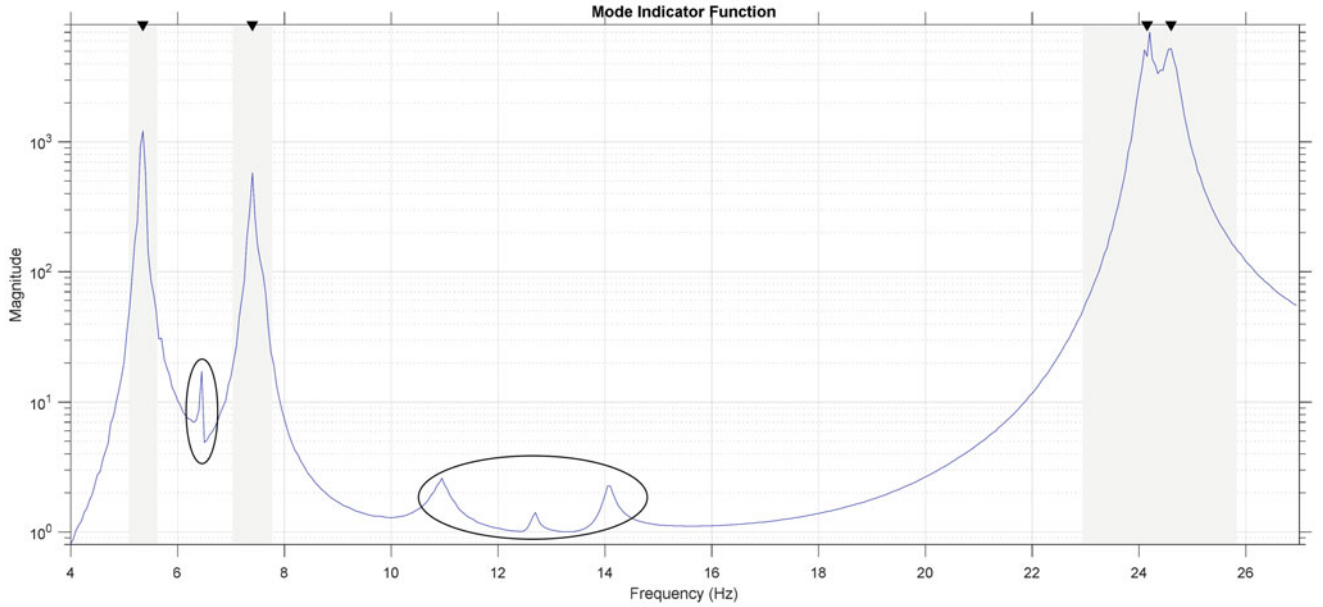

Fig. 7.7 PSMIF showing when to use frequency bands to ignore regions without selected modes

The summation is reassembled into matrix form, and a least-squares solution for the residues and residuals is generated by evaluating Eq. (7.3) with any and all frequencies we choose.

$$H(\omega) = \sum_{r=1}^{2N} \frac{A_r}{j\omega - \lambda_r} - \frac{R_L}{\omega^2} + R_U = \begin{bmatrix} \Lambda_1(\omega) & \cdots & \Lambda_{2N}(\omega) & -\omega^{-2} & 1 \end{bmatrix} \begin{bmatrix} A_1 \\ \vdots \\ A_{2N} \\ R_L \\ R_U \end{bmatrix}, \quad \text{where} \quad \Lambda_r(\omega) = \frac{1}{j\omega - \lambda_r} \tag{7.2}$$

$$\begin{bmatrix} H(\omega_1) \\ H(\omega_2) \\ H(\omega_3) \\ \vdots \end{bmatrix} = \left[\begin{array}{ccc|cc} \Lambda_1(\omega_1) & \dots & \Lambda_{2N}(\omega_1) & -\omega_1^2 & 1 \\ \Lambda_1(\omega_2) & \dots & \Lambda_{2N}(\omega_2) & -\omega_2^2 & 1 \\ \Lambda_1(\omega_3) & \dots & \Lambda_{2N}(\omega_3) & -\omega_3^2 & 1 \\ \vdots & & \vdots & \vdots & \vdots \end{array}\right] \begin{bmatrix} A_1 \\ \vdots \\ \frac{A_{2N}}{R_L} \\ R_U \end{bmatrix} \quad \text{or} \quad Ax = b \tag{7.3}$$

In general, the residues are (or can be) complex, but for many structures and for some end uses, real (or normal) mode shapes are expected. In this case, we could solve for the general, complex residues and normalize them to be real vectors, or we could separate the complex parts of $Ax = b$ into what is known as a phase-constrained least-squares solution. This starts with partitioning Eq. (7.3) as

$$\hat{A}\hat{x} + c_L R_L + c_U R_U = b, \quad \text{where } \hat{x} = \left\{ A_1 \cdots A_{2N} \right\}^T, \quad c_L = \frac{-1}{\omega^2}, \quad c_U = 1, \tag{7.4}$$

$\hat{A}$ is the left partition of A, b is the FRF, and R_L and R_U are real such that the residual terms are purely real. Then expand the complex terms into their real and imaginary parts as

$$\left(\hat{A}_r + j\hat{A}_i\right)\left(\hat{x}_r + j\hat{x}_i\right) + c_L R_L + c_U R_U = b_r + jb_i, \quad \text{where } \hat{A}_r = \text{Re}\left(\hat{A}\right), \quad \hat{A}_i = \text{Im}\left(\hat{A}\right), \tag{7.5}$$

and likewise for $\hat{x}$ and b. Next, expand the product of the two complex terms and collect the real and imaginary components into separate equations as

$$\begin{aligned} \hat{A}_r\hat{x}_r - \hat{A}_i\hat{x}_i + c_L R_L + c_U R_U &= b_r \\ \hat{A}_i\hat{x}_r + \hat{A}_r\hat{x}_i &= b_i \end{aligned} \tag{7.6}$$

For a normal mode, the residue is purely imaginary, which means that $\hat{x}_r = 0$. Removing those terms and combining into matrix form gives the phase-constrained least-squares solution for the imaginary part of the residues and the real-valued residuals as

$$\begin{bmatrix} -\hat{A}_i & c_L & c_U \\ \hat{A}_r & 0 & 0 \end{bmatrix} \begin{Bmatrix} \hat{x}_i \\ R_L \\ R_U \end{Bmatrix} = \begin{Bmatrix} b_r \\ b_i \end{Bmatrix} \tag{7.7}$$

Thus by an algebraic manipulation of the complex data, a real solution for the residues can be formulated directly. Of course, the formulation above can be extrapolated for multiple references and multiple responses and generalized for velocity- and acceleration-over-force FRFs.

7.5 Ignoring Residual Effects in Residue Estimation

One method of removing residual effects of out-of-band modes is to use just the quadrature part of the FRF (i.e., the imaginary part of an acceleration-over-force FRF) since the quadrature part of a mode is active over a much smaller frequency range than its coincident part. Figure 7.8 compares the singular values of an FRF matrix using the complex values, i.e., the complex mode indicator function (CMIF), to the singular values of the quadrature part of the FRF matrix, which is called the quadrature mode indicator function (QMIF). Note that the residual terms associated with the coincident part of the FRF matrix are activate across the entire frequency band, whereas the quadrature part is activate mainly at just the resonant frequencies. For example, there are some resonant frequencies, such as those near 65 Hz, that are barely noticeable in the CMIF but clearly observable in the QMIF.

To ignore the residual effects embedded in the complex FRFs and estimate the residues from only the imaginary part of the FRF, $b_r = 0$ in Eq. (7.7) and no residuals are included in the model since those terms are purely real, which leaves the nontrivial solution as $\hat{A}_r\hat{x}_i = b_i$.

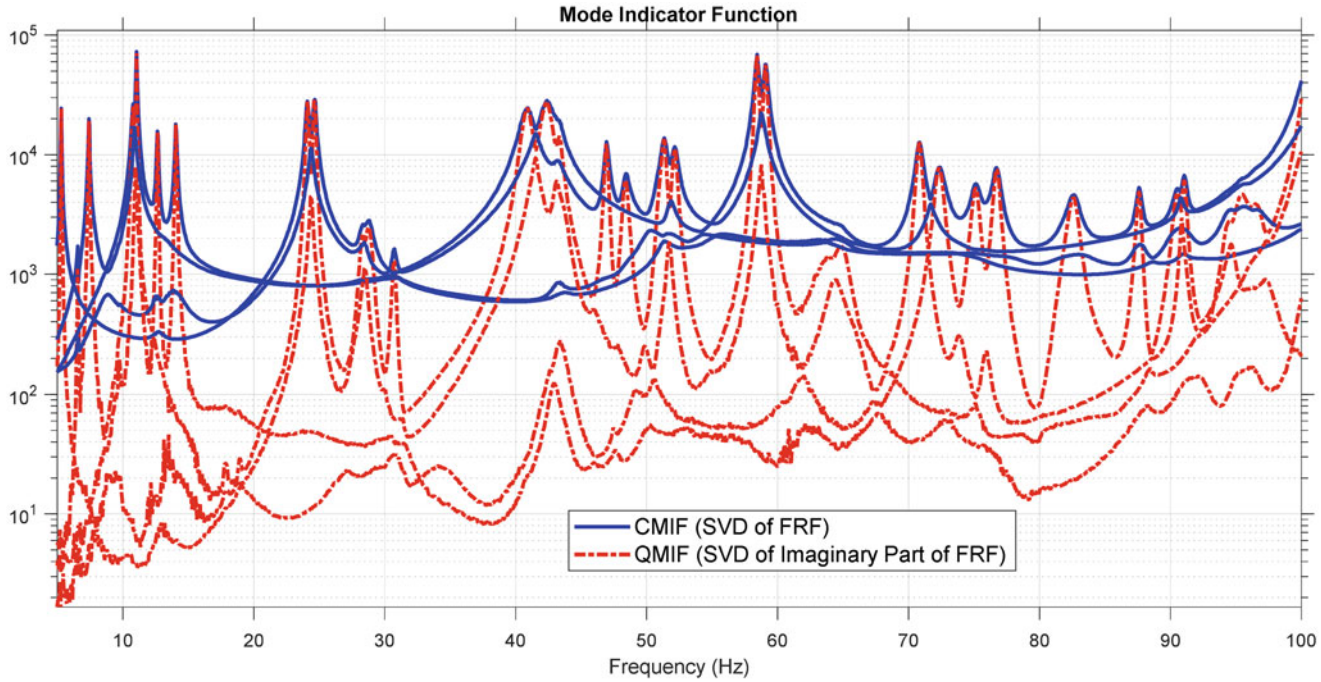

Fig. 7.8 Singular values of the imaginary part of an FRF matrix (QMIF) versus singular values of the complex FRF matrix (CMIF)

7.6 Conclusions

With the current state of data acquisition and computer capabilities, we can acquire and process large volumes of data without waiting too long for the results. And while it might be tempting to use all the data all the time for parameter estimation, a recurring theme in this chapter has been "Don't use data that doesn't help your cause." Excluding frequency ranges containing noise (be it of the variance, periodic, or bias variety) is a simple yet effective way to heed this advice. In addition, selecting frequency bands around the poles that only use data that constructively contributes to estimating their residues is another. Although residues are, in their most general form, complex—and some software packages may use vector complexity as a quality-of-fit metric—you can also solve directly for normal modes using the quadrature part of the FRF. In doing so, modal parameters can oftentimes be more accurately estimated.

The tips, tricks, and obscure features described in this chapter are based on actual events that necessitated their development over the years for real-world test data. However, due to the nature of the authors' business, these data belong to our customers and cannot readily be shared in an open forum (at least not without a lot of paperwork). Although the data presented herein are taken from nonproprietary laboratory test articles (e.g., "iron birds"), the contrived examples are meant to be representative of the types of situations in which these techniques have proven useful.

Bibliography

1. Fladung, W., Vold, H.: An orthogonal view of the polyreference least-squares complex frequency modal parameter estimation algorithm. In: Proceedings of the 33rd International Modal Analysis Conference, pp. 171–182. Springer, Cham (2015)
2. Fladung, W., Vold, H.: An improved implementation of the orthogonal polynomial modal parameter estimation algorithm using the orthogonal complement. In: Proceedings of the 33rd International Modal Analysis Conference, pp. 157–170. Springer, Cham (2015)

Chapter 8
Modal Analysis Using a UAV-Deployable Wireless Sensor Network

Joud N. Satme, Ryan Yount, Jacob Vaught, Jason Smith, and Austin R. J. Downey

Abstract In structural health monitoring, wireless sensor networks are favorable for their minimal invasiveness, ease of deployment, and passive monitoring capabilities. Wireless vibration sensor nodes have been implemented successfully for frequency domain analysis in ambient vibration detection. To leverage advances in structural damage quantification techniques, which require modal information, nodes in a wireless sensor network must operate with a near-synchronous clock to enable the collection of the signal phase. The non-deterministic timing nature of wireless systems raises a significant challenge when trying to accurately determine the phase of a signal. In particular, the trigger time delay of the various nodes on the structure cannot be differentiated from a true phase caused by the examined system. This study investigates the reliability and error-handling capabilities of the ShockBurst 2.4 GHz wireless protocol in triggering and data transfer. Building on an open-source UAV-deployable sensor node, mode shapes from a 2-meter test specimen are experimentally determined. An optimization technique that enhances time domain accuracy for non-deterministic wireless triggers is presented. This work quantifies latency and error management effects that contribute to enhancing the modal extraction capabilities of wireless systems in structural health monitoring applications.

Keywords SHM · Sensors · Modal analysis · Vibrations · Dynamic

8.1 Introduction

Structural Health Monitoring (SHM) is a Nondestructive Inspection process carried out by measuring the parameters of a given system to infer the current structural state. This process relies on damage identification and quantification algorithms [1]. Furthermore, SHM is used to monitor changes (i.e., damage) in the system through its life cycle to make actionable decisions such as structural repairs. SHM is crucial in extending infrastructures' operational lifespan and maintaining safety following extreme weather conditions. Its purpose is highly dependent on the system in question. For example, the goal for SHM is drastically different between a railroad bridge and a naval ship. Continuing, SHM for infrastructure primarily assesses changes that take place on a long timescale (i.e., fatigue) while SHM for naval ships is used for various damage types that occur on short and long time scales such as impact, fatigue, and corrosion. While SHM for both structures assesses fatigue damage, the actionable decisions conducted for each structure are different.

Vibration-oriented damage detection for structural components is used to evaluate the dynamic and structural property changes as damage indicators. A common vibration-based damage detection technique is modal analysis, where the modes of the structure's ground truth state are analytically and experimentally determined. These modes are then compared to future states in the structure's life cycle to quantify differences between each state, and any differences detected signify damage in the structure.

Damage detection methods such as acoustic emission analysis are a passive Non-Destructive Testing Techniques (NDTs) that have been successively used on structures such as bridges, tunnels, pipes, and buildings. This method is superior at

J. N. Satme · R. Yount · J. Vaught · J. Smith
Department of Mechanical Engineering, University of South Carolina, Columbia, SC, USA
e-mail: Jsatme@email.sc.edu; RJYOUNT@email.sc.edu; jvaught@sc.edu; JMS32@email.sc.edu

A. R. J. Downey (✉)
Department of Mechanical Engineering, University of South Carolina, Columbia, SC, USA

Department of Civil and Environmental Engineering, University of South Carolina, Columbia, SC, USA
e-mail: austindowney@sc.edu

B. J. Dilworth et al. (eds.), *Topics in Modal Analysis & Parameter Identification, Volume 9*, Conference Proceedings of the Society for Experimental Mechanics Series, https://doi.org/10.1007/978-3-031-34942-3_8

detecting and localizing damage such as cracking, deformation, and crushing. However, its downside is that the energy emitted by the acoustic emission is very small in comparison to the structure and ambient noise conditions. This leads to interference between the Acoustic Emission and noise signals. Another approach would be numerical modeling. FEA is a good alternative when the system is expensive or difficult to test. However, it is limited by the user's experience, modeling accuracy, and computational resources. If the model is extremely accurate, then the analysis time and computational resources will be high or realistically unachievable, so a middle ground should be found.

8.2 Background

A single vibration sensor can provide information about a structure's vibration signature, and however, in structural health monitoring and experimental modal analysis, a single sensor fails to provide the adequate information required to carry out such processes. Sensor networks are typically used in this case to offer more observation points. Using multiple points on the structure gives information on how vibrations propagate through the material and where mode shapes lie [2]. Using a small number of high-mobility compact sensing nodes, which can be spread throughout a given structure, offers the flexibility needed for rapid modal analysis [3]. Moving sensor packages to scan across a given structure can be done easily and with minimal invasiveness. With strides in computer vision, autonomous aerial vehicles, and swarm algorithms, such systems can offer high-mobility rapid infrastructure assessment capability [4]. In this work, an improvement on a previously designed UAV-deployable sensing node will be covered. Utilizing electropermanent magnets (EPMs) and radio frequency (RF) communication, this sensing node demonstrated the ability to gather vibration signatures from remote infrastructures in inaccessible terrain, given an external excitation. Via a drone, those standalone sensors can be rapidly deployed across a structure where the accelerometer onboard collects data according to a preset schedule to later be sent back for analysis. The developed open-source sensing system breakdown is made available in a public repository [5]. When deploying a network of those sensors across a large structure certain challenges arise, one of the most significant is trigger synchronization [3]. Without the ability to start collecting data simultaneously, phase data, or the measure of how vibration propagates is hindered useless as differentiating between trigger delay and vibration phase cannot be done. With the addition of a real-time clock, an accurate time reference can be set between all sensors, and the trigger delay can be minimized to an acceptable tolerance dictated by the sampling rate and a structure's natural frequencies.

The sensor package utilized in this work is an embedded system-based device with the processing core being an ARM Cortex-M7 onboard a Teensy 4.0 microcontroller (Fig. 8.1). With the goal being long-term deployment, the sensor package is fitted with a 1500 mAh 2-cell lithium polymer battery and a power management board to regulate the voltage to the various subsystems. The sensor onboard is a Murata SCA 3300-d01 high-performance MEMS accelerometer on the Serial Peripheral Interface (SPI) protocol to enable high sampling rates. For deployment with minimal invasiveness, an EPM V3R5C NicaDrone electropermanent magnet is used. Electropermanent magnets are favorable for such applications for their low power consumption. A one-second pulse of approximately 5 W is required only when switching the magnet's state which is typically done twice per deployment. For data transfer and IO commands, a Nordic Semiconductors NRF24L01 module is used. Operating at 2.4 GHz ShockBurst protocol, connection with multiple sensor nodes at once is made possible which is desirable for sensor triggering applications. Additionally, a real-time clock is included for data logging and trigger time reference as those devices are reliable and have minimal drift. Finally, nonvolatile memory (SD card module) is added to the sensor package, so data is not lost in case of low power or shutdown. The system is fitted into a protective 3D-printed PLA shell to shield delicate electronics from harsh conditions during field deployments. The footprint and weight of the sensor package were optimized for UAV deployment [6]. Shown in Fig. 8.2 is a high-level block diagram of the various subsystems onboard.

To validate the sensor network's ability to determine the mode shapes of a given structure, a model of a simple square beam pinned at each end is adopted. The goal of the modeling phase is to provide an estimate of the optimal location to position the sensing nodes. In an experimental modal analysis, the sensors should be mounted at the antinodes of the mode desired to be measured which ensures the highest signal strength. In SHM, this can be a challenge as structures can have complex geometries where using a model can significantly aid in the process [7]. For this work, the model was constructed using a finite-element modal analysis where the output of the model was the mode shapes and their accompanying frequencies. Utilizing this information, the sampling rate and sensors' location are determined. The model determined the first three modal frequencies of the structure to be 46.2 Hz, 133.7 Hz, and 316.3 Hz, respectively, with the mode shapes shown in Fig. 8.3.

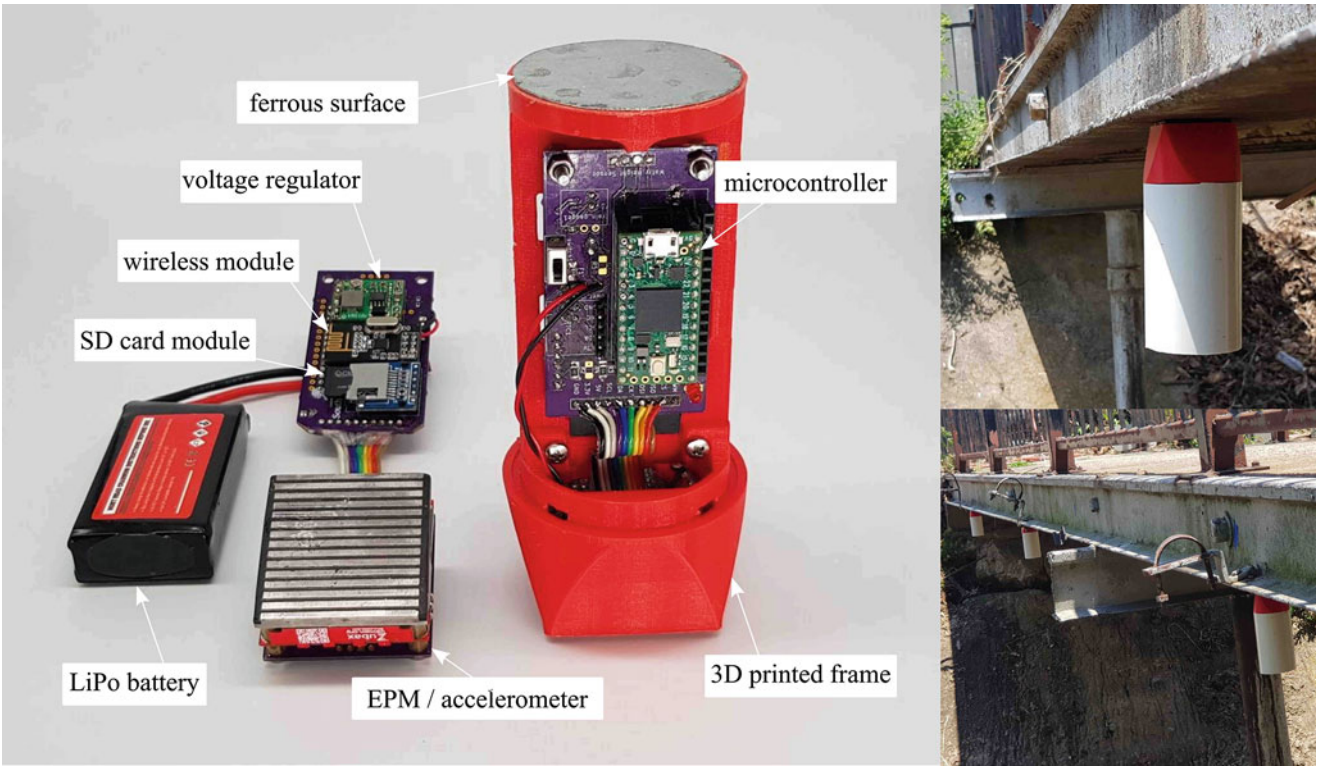

Fig. 8.1 Vibration sensor package with key components annotated along with a field deployment on a test bridge

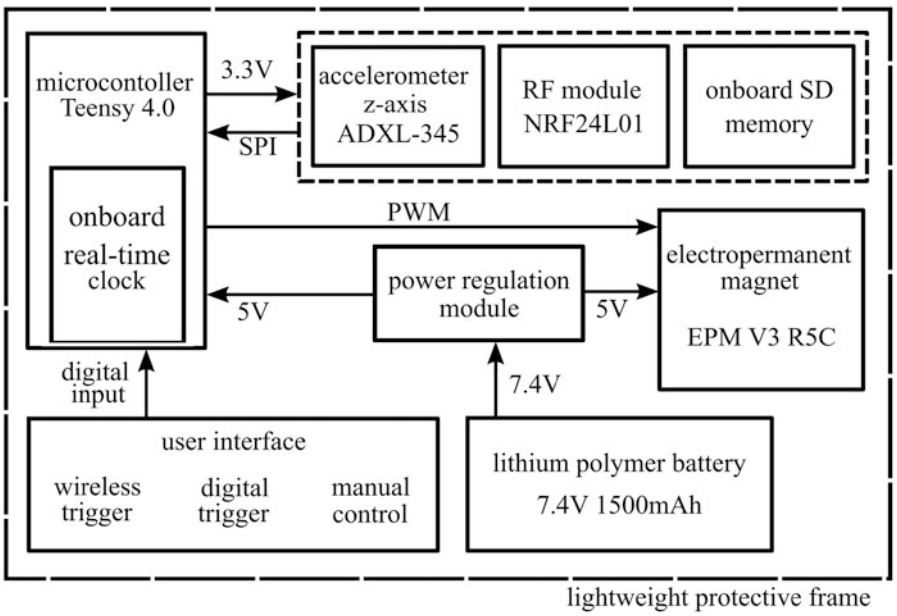

Fig. 8.2 Block diagram of sensor package with the various modules onboard

8.3 Analysis

The goal of this section is to characterize the sensor package parameters. Experiments are constructed to quantify the power consumption of the various subsystems onboard. Additionally, an investigation into the length of deployment is reported.

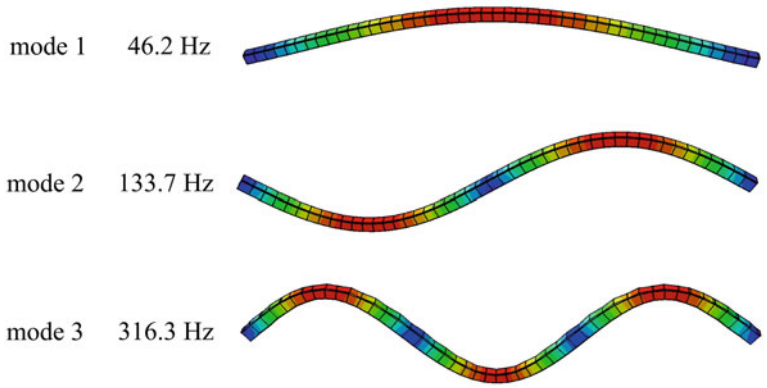

Fig. 8.3 FEA modal simulation results indicating the first three mode shapes of the bench top experimental beam

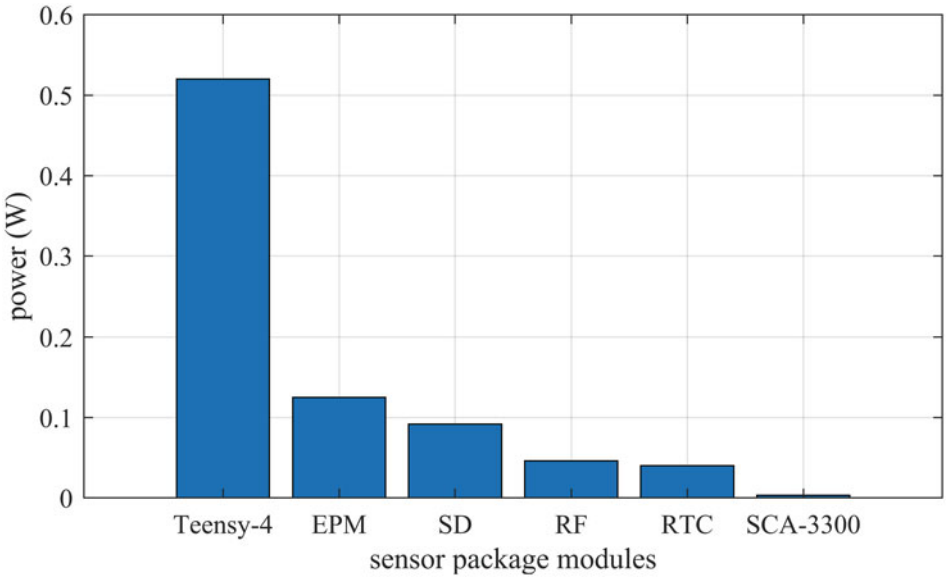

Fig. 8.4 Power consumption of the various modules onboard the sensor package

For the wireless system, the latency of triggering between two deployed packages is presented along with an experimental modal analysis test to measure the first three mode shapes of a beam.

With longer deployment periods in mind, a standalone power subsystem is used. A lithium polymer battery was chosen as it has desirable power density per footprint, optimal for areal deployment applications where the payload is a significant concern. Solid-state voltage regulators and a power conditioning circuit are also added to step down voltage and deliver it to the various subsystems onboard. An experiment is constructed to measure each module's power consumption. As indicated in Fig. 8.4, the Teensy 4.0 microcontroller has the highest steady-state power consumption at 0.52 W. For extended deployment (>10 hours), a strict power-saving mode can be deployed where the microcontroller along with non-vital modules is turned off, when not in use, further preserving power. Temperature dependencies were observed in this phase as lithium polymer's charge output can degrade in low temperatures causing voltage drops. This problem was partially rectified by adding conditioning capacitors to the package to compensate for the temperature-related voltage swings. furthermore, increasing the number of cells in the battery can ensure the voltage regulators receive adequate voltage regardless of temperature.

As for battery life, the capacity of the battery chosen for this work was a 1500 mAh 2-cell lithium polymer, and this was chosen for medium-length deployment (<10 hours). An experiment is constructed to measure the possible deployment period before the battery voltage gets critical. A safety system with an alarm is added during this stage to prevent the battery from over draining which can decrease the lifespan and cause deformation to the battery itself. The experiment was run at a constant room temperature to construct a linear model of the power system. Temperature variations can introduce high nonlinearities in the battery's state of charge making it challenging to model. In this case, only the voltage of the battery was observed as an indicator of the discharge rate. As shown in Fig. 8.5, the experiment ran for over 8.3 hours with the voltage

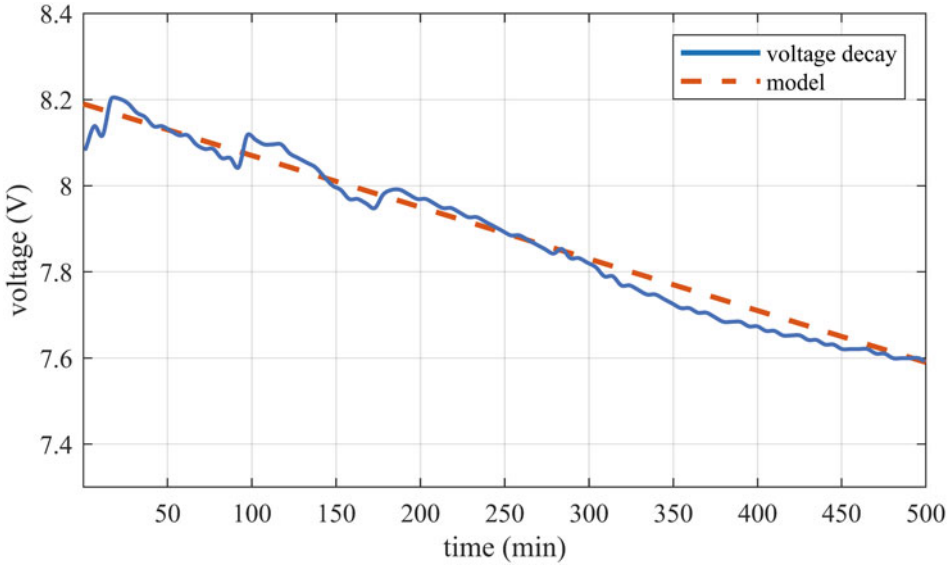

Fig. 8.5 Voltage decay of lithium polymer battery during sensor package deployment

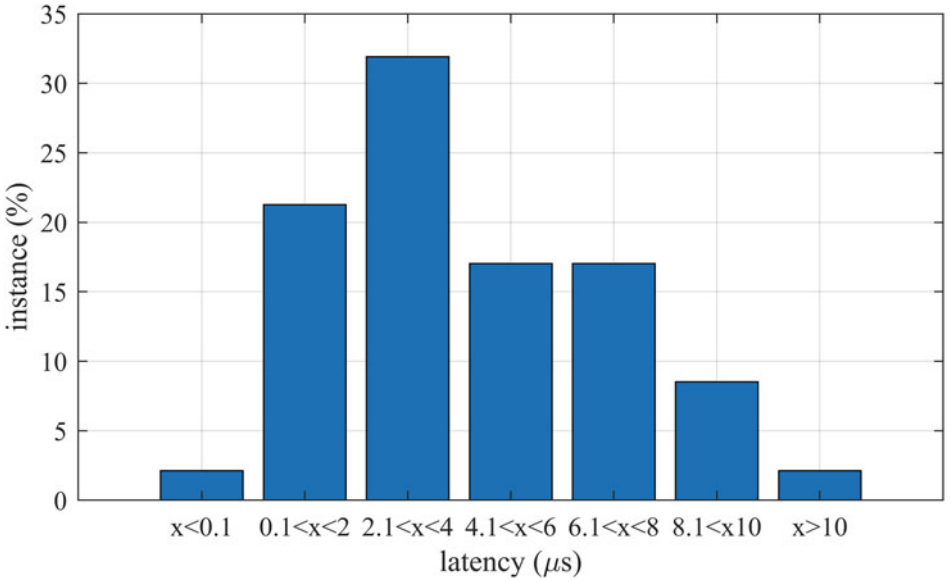

Fig. 8.6 Timing instance of trigger latency between wireless receivers onboard two sensor packages

decay linear model shown in Eq. 8.1.

$$V = -2 * 10^{-5}(t) + 8.19 \tag{8.1}$$

To investigate trigger latency, an experimental setup was constructed to measure the time it takes for two packages to receive a wireless trigger and initiate data collection. A high-resolution oscilloscope is connected to a digital pin of both packages, and a transmitter is then used to send a wireless trigger command. The time difference (trigger latency) between the two sensor packages is recorded over multiple iterations with the data normalized as a percentage. While varying the distance between the transmitter (TX) and the two receiver sensor packages (RX1, RX2), a better understanding of how antenna orientation and distance influence the sensor delay is deduced. As shown in Fig. 8.6, the system's latency lies mainly below 10 microseconds.

In this experiment, the simulated beam from the finite element analysis is constructed. The structure of choice was adopted for its simplicity and well-known behavior. Three sensor nodes were used as shown in Fig. 8.7. A wireless transmitter was

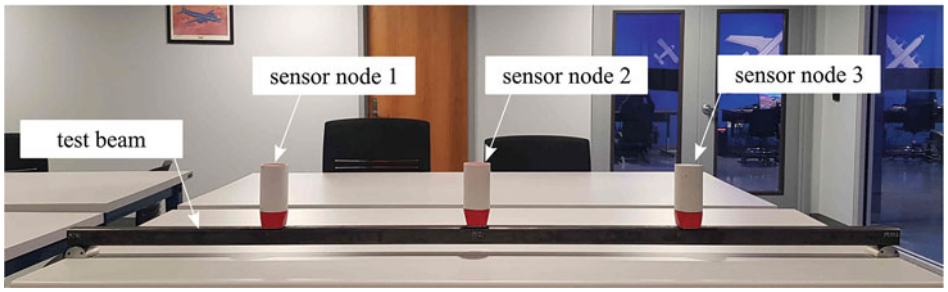

Fig. 8.7 Benchtop experimental setup for the sensor package network deployment

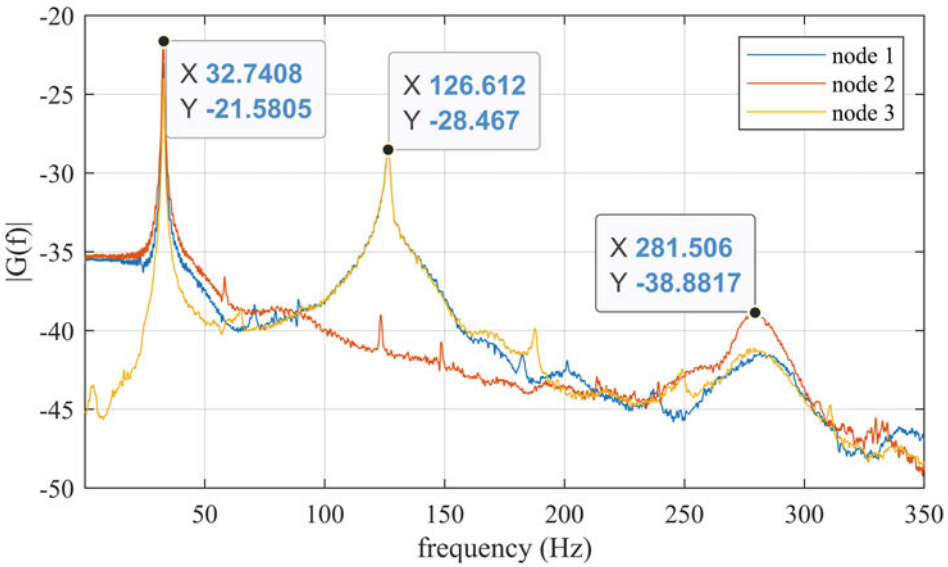

Fig. 8.8 Frequency domain analysis of the beam impulse response test with the first three modes annotated

used to initiate all sensors within an acceptable tolerance. The beam was then excited with an impulse response using a hammer at various positions on the beam. This ensured that all mode shapes are excited. With the data of interest being the frequencies of the first three mode shapes, the time domain data extracted from the test is converted to the frequency domain using the Fast Fourier Transform (FFT). In Fig. 8.8, the first three frequency peaks are observed. The peaks at 32.74 Hz, 126.62 Hz, and 281.50 Hz are of the first three modes, respectively. This was compared to the FEA model presented prior. A maximum error margin of 11% was found between modal frequencies extracted from the model when compared to experimental results. This is attributed to boundary conditions and material property inconsistencies. Using mode shapes from the simulation, the sensor packages were positioned at the mode's antinodes where the vibration signal was at its highest. For mode 1, it was shown that the three sensors peak together as they all experience vibration in the same direction at 32.7 Hz. When observing mode 2 at 126.6 Hz, it is shown that sensor node 2 (middle package) does not detect any peak which correlates to a node of mode 2. Finally, peaks are observed as mode 3 at a frequency of 281.5 Hz indicating that all three sensors are on antinodes of the third mode.

8.4 Conclusion

In this work, an embedded system-based high-mobility sensor network is examined. During system characterization tests, the network has shown the potential to be a reliable tool in structural health monitoring and experimental modal analysis applications. The ease of use and compact footprint, along with the magnetic mounting capability, makes these sensors optimal for UAV deployment where human access is challenging or dangerous. For rapid assessment of infrastructure following extreme weather conditions, such systems can be widely deployed in a very short time providing the first

responders with preliminary data about the infrastructure state. Experimentation has also shed the light on some system limitations. Although the wireless system ensures relatively low latency, the time non-determinism of the latency makes it challenging to accurately determine the phase. This will be further rectified by basing the trigger not only on a wireless signal but also on a real-time clock onboard the package, where all sensors would collect data on a preset schedule. That will enable all sensors to have an accurate time reference further minimizing latency-related error. The future work will also include error-handling capabilities with the wireless system to allow rapid data transfer and real-time monitoring capabilities.

Acknowledgments This material is based upon work supported by the Air Force Office of Scientific Research (AFOSR) through award no. FA9550-21-1-00832. This work is also partly supported by the National Science Foundation Grant number 1850012. The support of these agencies is gratefully acknowledged. Any opinions, findings, and conclusions, or recommendations expressed in this material are those of the authors and do not necessarily reflect the views of the National Science Foundation or the United States Air Force.

References

1. Worden, K., Farrar, C.R., Manson, G., Park, G.: The fundamental axioms of structural health monitoring. Proc. R. Soc. A: Math. Phys. Eng. Sci. **463**(2082), 1639–1664 (2007)
2. Bocca, M., Eriksson, L.M., Mahmood, A., Jäntti, R. and Kullaa, J.: A synchronized wireless sensor network for experimental modal analysis in structural health monitoring. Comput.-Aided Civil Infrastruct. Eng. **26**(7), 483–499 (2011)
3. Nguyen, T., Chan, T.H.T., Thambiratnam, D.P.: Effects of wireless sensor network uncertainties on output-only modal analysis employing merged data of multiple tests. Adv. Struct. Eng. **17**(3), 319–329 (2014)
4. Sim, S.H., Spencer, B.F. Jr., Zhang, M., Xie, H.: Automated decentralized smart sensor network for modal analysis. In: Tomizuka, M. (ed.) Sensors and Smart Structures Technologies for Civil, Mechanical, and Aerospace Systems 2009, vol. 7292, p. 72920W. International Society for Optics and Photonics, SPIE (2009)
5. Satme, J., Downey, A.: Drone delivered vibration sensor (2022). https://github.com/ARTS-Laboratory/Drone-Delivered-Vibration-Sensor
6. Carroll, S., Satme, J., Alkharusi, S., Vitzilaios, N., Downey, A., Rizos, D.: Drone-based vibration monitoring and assessment of structures. Appl. Sci. **11**(18), 8560 (2021)
7. Stinemates, D.W., Farrar, C.R., Sohn, H., Bennett, J.G.: Structural health monitoring system design using finite element analysis. In Kundu, T. (ed.) Smart Nondestructive Evaluation for Health Monitoring of Structural and Biological Systems, vol. 4702, pp 169–178. International Society for Optics and Photonics, SPIE (2002)

Chapter 9
Vibration-Based Approach for Identifying Closely Spaced Modes in Space Frame Structures and Derivation of Member Axial Forces

Mena Abdelnour and Volkmar Zabel

Abstract It has become evident that climate change is an escalating situation requiring societies to act to prevent a nearby climate crisis. Preservation of existing infrastructures to withstand material deterioration and the current increase in loadings does not lead only to reducing dismantling debris but also less consumption of resources, leading to the protection of the environment. Space frame structures were and are still a widely used structural solution for many infrastructures due to their considerable lightweight and ease of erection. The structural stress status of space frame structures is an important step in the preservation process. Assessing the load-bearing capacity of space frame structures gives an insight into the stress status, which is possible through identifying axial forces inside various members. The determination of axial forces of a single tension cable has been intensively investigated based on vibration methods. In addition, as a part of a two-dimensional truss, the identification of stress status in tension members has been studied. However, far less attention has been put so far on the consideration of compression members and more complex systems. This chapter adopts a previously developed methodology to identify tension forces in a two-dimensional truss and extends it to include compression forces identification and application to three-dimensional systems. The approach includes the identification of members' axial forces based on a numerical model and experimentally determined modal parameters, particularly natural frequencies and mode shapes. This chapter uses a relatively simple space frame structure as a case study. Numerical models of the simple space frame structure give an insight into the natural frequencies and mode shapes to be expected from the physical model. The closely spaced local and global modes of vibration obtained from the numerical model are discussed and explained, and a criterion to distinguish between them is introduced. From the experimental side, applying parametric modal identification is a reliable tool to extract modal parameters by considering different model orders concerning the identification of local and global modes. With the help of experimental results, axial forces are derived based on a numerical model of the structure. The numerical model does not give only a priori information about the modal parameters but also about the minimal model order needed for the identification of global and local modes.

Keywords Force estimation · Local/global modes · Space truss

9.1 Introduction

The determination of the actual load-bearing capacity of space frame structures is a challenging task. Because accurate information about external loads, characteristics of the structure skeleton, connections and supports are usually unknown. Over the past decades, space frame structures have been suitable as lightweight structural solutions especially for long-span roof structures. Not only due to their low weight-to-area ratio but also because of the production of standardized cross-sections and connecting nodes, which promoted the ease of erection concerning cost and time, space frame structures can be found all over the world today. Due to the increase of design loads in previous years and the modification of further criteria, such as serviceability limits, in the codes of practice also existing structural systems have to be re-assessed by engineers with respect to their load-bearing capacity. In case that the proofs cannot be satisfied by means of common calculations, experimental investigations can be performed to identify the current stress state of structural members.

A traditional method to obtain the actual load-bearing capacity of a space frame structure is static load tests. An alternative approach to determine the axial forces of single members of a truss system, which then gives information about the actual

M. Abdelnour (✉) · V. Zabel
Institute of Structural Mechanics, Faculty of Civil Engineering, Bauhaus-University, Weimar, Germany
e-mail: mena.abdelnour@uni-weimar.de

B. J. Dilworth et al. (eds.), *Topics in Modal Analysis & Parameter Identification, Volume 9*, Conference Proceedings of the Society for Experimental Mechanics Series, https://doi.org/10.1007/978-3-031-34942-3_9

load-bearing capacity of critical elements, is related to the identification of the local modal behavior. The derivation of axial forces inside a single rod/cable, based on vibration methods has been intensively considered in literature [1–3]. The actual axial forces are obtained by analytical derivations, using identified modal parameters. So far, the identification of axial tension forces in members of a two-dimensional truss structure of average complexity could be achieved with reliable accuracy [4]. This chapter presents the determination of modal parameters for space frame structures as the first step toward actual force derivation.

9.2 Background

In [5], the authors investigated local and global vibrations of space frame structures. Local vibrations are usually referred to a single or member members' vibrations while the rest of the system is almost at rest. On the other hand, global vibrations represent the dynamic behavior of the complete structure similar to beam or surface systems. To distinguish between local and global vibrations of a truss structure, the authors of [5] proposed an approach that is based on the calculation of modal strain energies. According to their definition, a mode with high axial strain energies correlates to global structure vibration. For local member vibrations, the bending strain energy is supposed to be a dominant component in the total modal strain energy of the mode.

Another aspect in the context discussed here is the correct automatic pairing of numerical and experimental mode shapes during the model updating procedure, in which the calculation of the modal assurance criterion (MAC) is insufficient. To tackle this issue, an energy-based modal assurance criterion (EMAC) has been introduced in [6]. The EMAC uses the modal strain energy for a selected cluster of degrees of freedom as a weighting factor multiplied by the MAC values.

From the experimental point of view, identifying modal parameters of a space frame structure using a parametric identification technique such as the stochastic subspace identification (SSI) requires the exploration of chosen analysis parameters for the respective method. Due to the high number of degrees of freedom and the fact that not all modes are excited equally, an examination of different model orders in stabilization diagrams is necessary to identify the modal parameters of solutions related to physical modes. As suggested in [7], the model order and the number of block rows influence the identified accuracy of the modes. Yet, in the case of a space frame structure, underestimating these parameters leads to fewer modes after analyzing the measurements.

9.3 Methodology

In the following, a procedure is suggested that allows for a correct identification of modal parameters of a space frame structure in steps: (1) creation of a numerical model using beam elements to describe the dynamic behavior of the members; (2) selection of degrees of freedom to be chosen in the experimental modal analyses, based on the numerical modal parameters; (3) performance of modal tests and acquisition of measurement data; (4) analysis of the SSI analysis parameters in particular the required minimal model order to identify all desired modes; (5) system and modal identification; and finally (6) correct pairing of experimentally identified and numerical mode shapes using the EMAC criterion, followed by the calculation of the MAC values.

This procedure has been implemented and tested on the relatively simple space frame structure, shown in Fig. 9.1. The laboratory structure contains standardized elements with circular-cross sections of 0.5 and 0.7 m lengths. For the connections, standardized spherical steel nodes were applied. Finally, a tension rod (shown in red in Fig. 9.1) connects the two nodes at the inverted pyramids of the structure, to allow for the application of different levels of pre-stressing in the members.

9.4 Numerical Analysis

To prepare the experimental investigations, first the space frame structure shown in Fig. 9.1 has been modeled numerically. The truss members were modeled by means of finite beam elements based on Timoshenko beam theory. Each of the members was divided into six beam elements, such that in the numerical model always five intermediate nodes occur between the structural connection nodes. To avoid undesired effects during the tests due to uncertain boundary conditions at the supports,

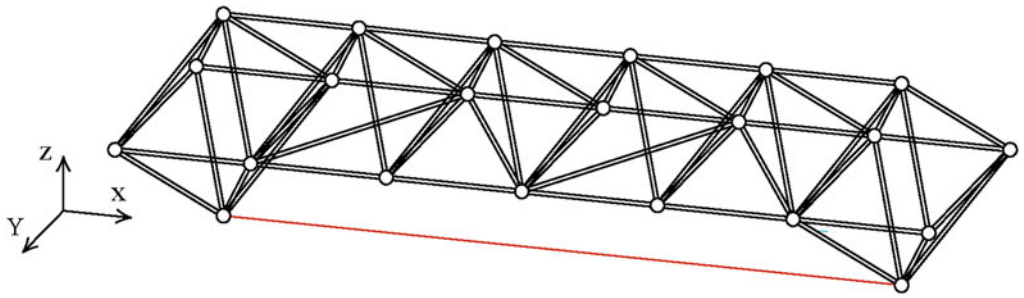

Fig. 9.1 Physical model of a space frame structure with circular cross-section and MERO connecting nodes, threaded tension rod in red

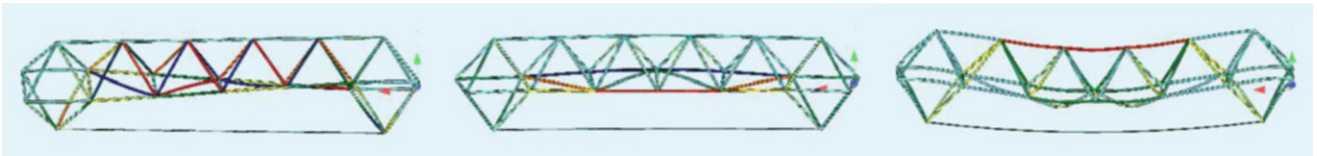

Mode 1: Torsion 92.40 Hz | Mode 2: Lateral bending 126.12 Hz | Mode 3: Vertical bending 143.59 Hz

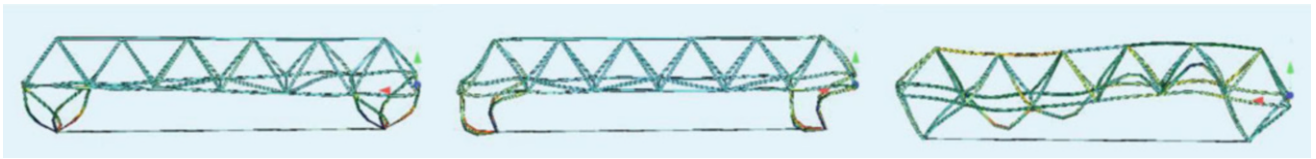

Mode 4: Local member bending and torsion 162.44 Hz | Mode 5: Local member bending 173.84 Hz | Mode 6: Local member bending and vertical bending 191.20 Hz

Fig. 9.2 First six numerical mode shapes with their corresponding frequencies

Table 9.1 Quantification of percentages of axial and bending strain energies to the total modal strain energy of the first six modes

Mode	Axial modal strain energy [%]	Bending modal strain energy [%]	Type of vibration	
			Local	Global
1	90.7	5.9		x
2	93.3	4.5		x
3	85.3	13.1		x
4	5.3	75.7	x	
5	2.2	62.5	x	
6	47.3	43.7		x

it was decided to simulate free-free support conditions what has also been taken into account, respectively, in the numerical model. Figure 9.2 shows the first six mode shapes of the numerical model with their frequencies.

The numerical results show two types of modes indication: both global and local vibrations in conjunction with the results presented in [5]. A mode shape is considered as global if the complete structure is deforming in a way comparable to a continuum structure. For instance, the first three mode shapes in Fig. 9.2 are classified as global: torsion, lateral bending, and vertical bending. In other words, the global displacement is higher than any local member displacement. On the other hand, local modes show member vibrations with no or minimal global deformation. In other words, the deformations of vibrating members are dominating the respective mode shape. Furthermore, it is in some cases difficult to distinguish clearly between only these two types of vibration, as also mentioned in [5]. For example, mode shape six is a combination between global vibration and local member vibration.

Considering that the global vibration of a space frame structure, one can conclude that they are related to longitudinal deformations of the members, while in the case of local member vibration, the bending deformation of the members is dominant. Thus, a distinction between these two types of vibration is possible based on the percentage of participation of the axial and bending strain energies to the total modal strain energy of the structure, as illustrated in Table 9.1.

9.5 Experimental Analyses

For the sake of a better distinction of global and local member modes in the identification, the sensors were arranged in respective setups. In the first setup, the sensors were only placed at the structural connection nodes of the structure for the identification of global vibration modes. The second and third setups aimed to capture local member vibration, one for tension members and another for compression members. The sensors were arranged such that accelerations could be measured simultaneously in vertical and lateral directions. The acquired time series were analyzed by means of the covariance-driven stochastic subspace identification (SSI-COV).

To investigate the influence of different analysis parameters for the SSI-COV, in particular, the maximum model order and the number of block rows of the block Hankel or Toeplitz matrix, an analysis according to the approach proposed in [7] was performed. In a parametric modal analysis, the order of a system to be identified is usually unknown. Underestimating the model order leads to failure to capture actual modal parameters for a given structure. Yet, an overestimation would result in spurious modes: (1) noise modes, (2) mathematical modes, and (3) vibration modes of other single members that were not instrumented. The last type can be also considered as noise modes. Further problems may arise in the case that the natural frequencies of local member modes interfere with the frequency range of global modes of the space frame structure, as it is also the case in the study described here.

The common tool for the selection of solutions within a parametric modal identification that are related to physical modes is the stabilization diagram. As the mathematical system to be identified in the first step of the analysis is related not only to a modal model but also to a model of a mechanical system with a certain number of physical degrees of freedom, there is a dependency between the identifiable modes on the order or dimension of the system model. In case of this study, this means, for example, that a model that is able to represent also modes that include deformations of the truss members requires the inclusion of degrees of freedom between the connection nodes. In consequence, the minimal model order for the identification of local modes of space frame structures is considerably higher than the one that is needed to represent the global modal behavior for which only degrees of freedom at the structural connection nodes would be sufficient. At the same time, of course, the different modal contributions to the analyzed signals have the well-known influence on the minimal model order necessary to identify modes that are hardly contributing to the response at the instrumented degrees of freedom. The relation between the required system model order and the number of identifiable modes is illustrated in Fig. 9.3.

As illustrated in Fig. 9.3, the use of a higher model order leads to more identifiable modes in this case study as expected. In the modal identification of civil engineering structures, the maximal model order is commonly limited to 100 or 200. However, for the space frame structure considered here, this would not be sufficient as shown in Fig. 9.4. There one can well extract that one can only identify five or six modes in a frequency range up to 300 Hz if the maximal model order is chosen to be 100. If higher model orders are included in the analyses, the number of identifiable modes increases significantly as can be seen in Fig. 9.4 as well. The additional stable poles appearing in the stabilization diagram at model orders greater than 100 are almost all related to physical modes in this case. This is an observation that is different from the situation one usually faces in the modal identification of continuous structures such as bridges, towers, or floor where it is sufficient to consider a smaller maximal model order within the frequency range of interest.

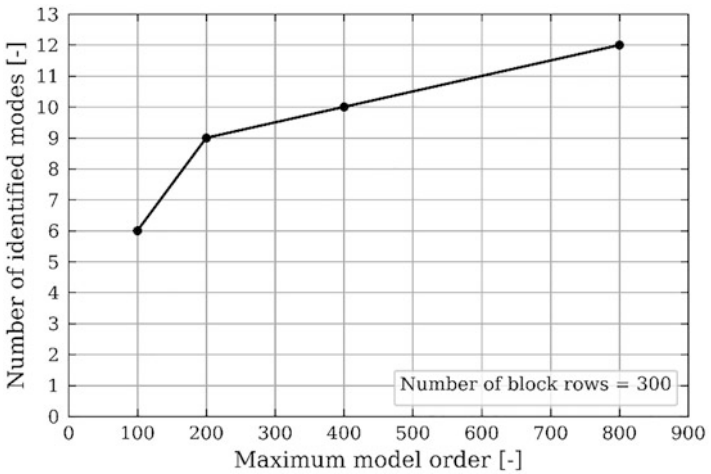

Fig. 9.3 Parameter study on the relation between maximal model order and number of identifiable modes

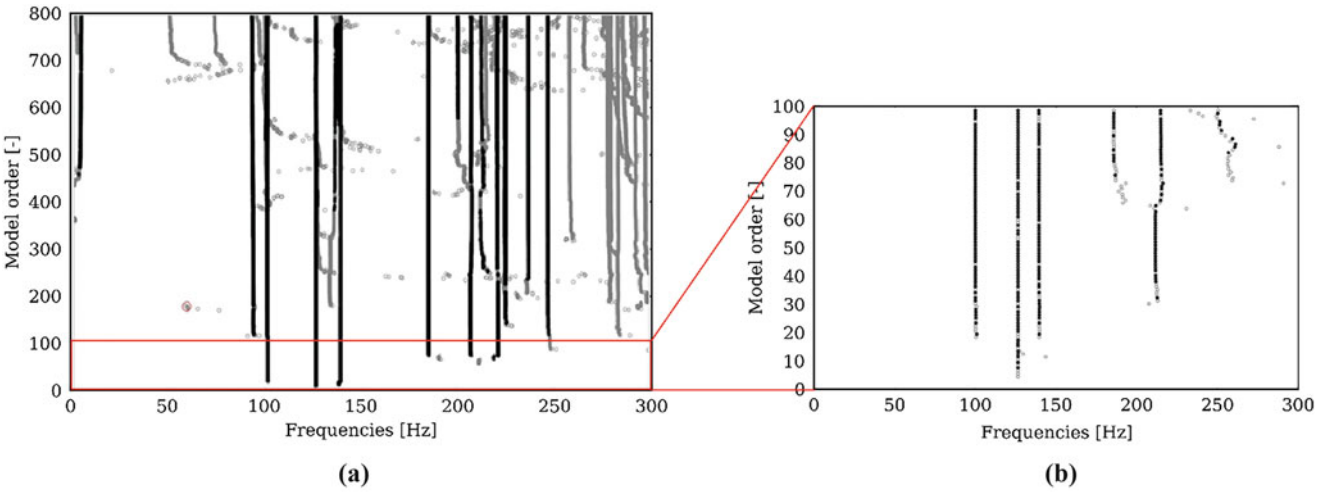

Fig. 9.4 Stabilization diagrams of the identified modal parameters: (**a**) using 300 number of block rows and model order of 800, (**b**) 50 block rows is used and a model order of 100

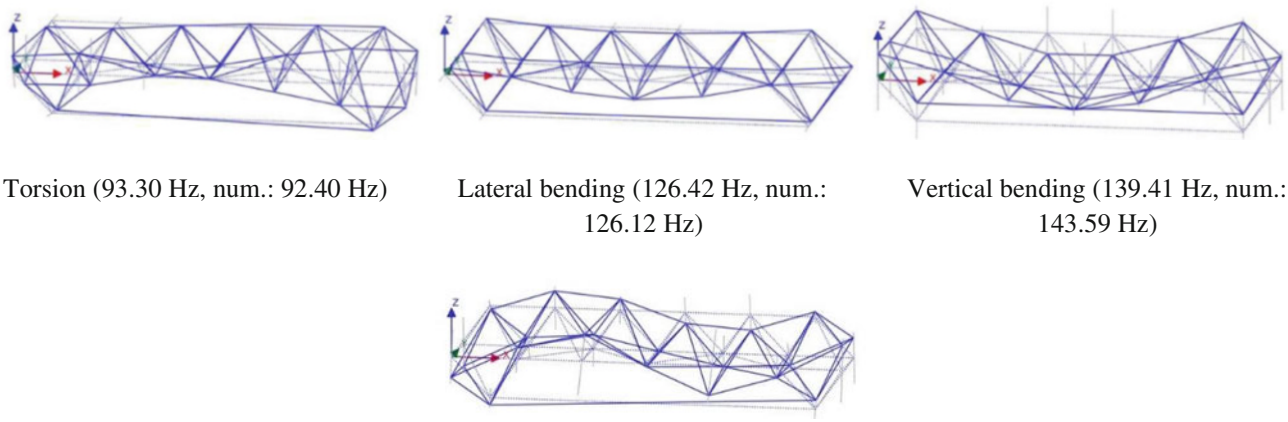

Torsion (93.30 Hz, num.: 92.40 Hz)

Lateral bending (126.42 Hz, num.: 126.12 Hz)

Vertical bending (139.41 Hz, num.: 143.59 Hz)

Vertical bending (185.04 Hz, num.: 191.20 Hz)

Fig. 9.5 Identified global mode shapes and corresponding frequencies

Figure 9.5 shows the first four identified global mode shapes and respective natural frequencies that show good agreement with the numerical results. These mode shapes were obtained by using data that was exclusively measured at the structural nodes. From the tests with instrumented truss members, also the local behavior related to these modes could be identified well as indicated in Figs. 9.6 and 9.7. In this study, the data acquired with sensors installed at the connection nodes and those that were placed on selected truss elements were analyzed separately. This procedure made the modal identification in this case by far more feasible compared to a combined analysis including a mixed instrumentation both on the connection nodes and on truss members. Close natural frequencies of modes related to global and local vibrations made this approach necessary.

9.6 Conclusion

For identifying global and local modal parameters of a space frame structure, numerical modeling is vital to have information about the expected frequencies and mode shapes. Additionally, the calculation of modal strain energies helps in the distinction between global and local vibrations. Moreover, to select relevant degrees of freedom for identifying the mode shapes of

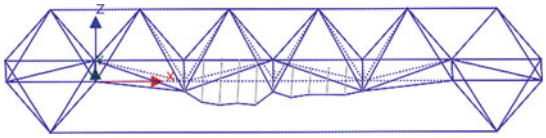

Lateral member bending of the bottom chord related to global lateral bending (125.93 Hz, num. 126.12 Hz)

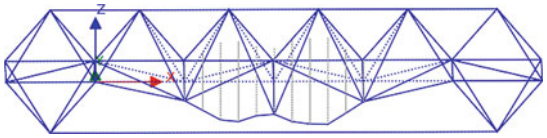

Vertical member bending of the bottom chord related to global vertical bending (140.75 Hz, num.: 143.59 Hz)

Fig. 9.6 Identified local vibrations that are coupled to global mode shapes of selected compression members and corresponding frequencies

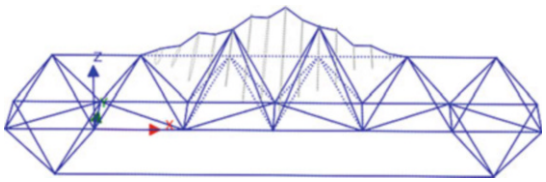

Lateral member bending of the top chord related to global lateral bending (127.46 Hz, num. 126.12 Hz)

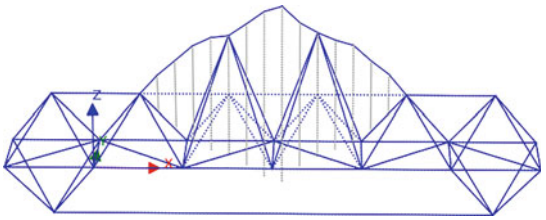

Vertical member bending of the top chord related to global vertical bending (139.72 Hz, num.: 143.59 Hz)

Fig. 9.7 Identified local vibrations that are coupled to global mode shapes of selected tension members and corresponding frequencies

local members, the modal strain energy is used to choose which frequencies to consider where the bending deformation is activated. The high number of degrees of freedom of a space frame structure, reflected in the numerical model, indicates that a higher maximal model order should be considered in a parametric modal identification than commonly necessary if continuous systems such as bridges, towers, or floors are investigated.

Acknowledgments The authors would like to express sincere gratitude to the Priority Program SPP 2255 “Kulturerbe Konstruktion” for the initiation of the research project “DENKRAUM” with special thanks to the German Research Foundation (DFG) for the financial support.

References

1. Maes, K., Peeters, J., Reynders, E., Lombaert, G., De Roeck, G.: Identification of axial forces in beam members by local vibration measurements. J. Sound Vib. **332**, 5417–5432 (2013)
2. Li, S., Reynders, E., Maes, K., De Roeck, G.: Vibration-based estimation of axial force for a beam member with uncertain boundary conditions. J. Sound Vib. **332**(4), 795–806 (Feb. 2013). https://doi.org/10.1016/j.jsv.2012.10.019
3. Rebecchi, G., Tullini, N., Laudiero, F.: Estimate of the axial force in slender beams with unknown boundary conditions using one flexural mode shape. J. Sound Vibr. (2013)., [Online]. Available: https://doi.org/10.1016/j.jsv.2013.03.018
4. Luong, T.M.H.: Identification of the State of Stress in Iron and Steel Truss Structures by Vibration–Based Experimental Investigations. BTU Cottbus-Senftenberg/Bauhaus University in Weimar, Cottbus/Weimar (2018)
5. Warnaar, D.B., Mcgowan, P.E.: Effects of local vibrations on the dynamics of space truss structures. In: Proc. of AIAA Dynamics Specialists Conf., pp. 868–875, Monterey (1987)
6. Brehm, M., Zabel, V., Bucher, C.: An automatic mode pairing strategy using an enhanced modal assurance criterion based on modal strain energies. J. Sound Vib. **329**, 5375–5392 (2010)
7. Rainieri, C., Fabbrocino, G.: Influence of model order and number of block rows on accuracy and precision of modal parameter estimates in stochastic subspace identification. Int. J. Lifecycle Perform. Eng. **1**(4), 317–334 (2014)

Chapter 10
A Technique for Minimizing Robot-Induced Modal Excitations for On-Orbit Servicing, Assembly, and Manufacturing Structures

Cory J. Rupp

Abstract Robot-driven on-orbit servicing, assembly, and manufacturing (OSAM) promises to enable and enhance a wide range of space technologies in the coming decades. Supporting technologies, however, are still nascent and must still be developed to manage the unique characteristics of this upcoming construction paradigm. Robotic operation on OSAM structures will introduce modal excitations that, if not controlled, may damage or fatigue the structure. This chapter develops a method for planning robot motions such that modal excitations are minimized, thereby reducing induced loads and risk to the structure. An example is presented using a relevant exemplary OSAM structure.

Keywords Structural dynamics · Vibration · OSAM · Robotics · Path planning

10.1 Introduction

On-orbit servicing, assembly, and manufacturing (OSAM) is an upcoming in-space operation and construction paradigm enabled by autonomous and semi-autonomous robotic systems. It offers significant advantages for both government and commercial entities over current single-launch solutions in terms of lower risk and cost as well as enabling missions with repairability, life extension, and larger structures. Examples of structures that would benefit from this technology include very large diameter space telescopes and antennas and persistent space platforms [1, 2]. Although the concept of OSAM is decades old, relevant technologies in robotic autonomy have only recently matured to the point where extensive use of OSAM is possible. Nevertheless, several technological needs must still be developed in order to fully realize the promise of OSAM. Among these needs are techniques for performing in-space modal testing to capture the varying nature of the mode shapes and frequencies as an under-construction OSAM structure changes in size and shape [3], new adaptive control architectures for robotic and spacecraft stationkeeping systems that will take into account such modal changes [4], and, as to be described in this chapter, a way of minimizing modal excitations of the structure (which may cause damage or fatigue) during robotic operations. While this chapter focuses on OSAM structures, the technique described herein is equally applicable to terrestrial, lunar, or other gravity-bound situations in which a robot is operating while attached to a flexible structure.

Many different types of robotic systems are envisioned for OSAM, including free-flyers, long-reach robotic arms, and traversing robots. Regardless of design, a robotic system attached to an OSAM structure will necessarily introduce structural dynamic excitations as the robot performs its tasks. As described in Ref. [3], there exists an intricate relationship between a robot's design, how it is actuated, its attachment location on the OSAM structure, and the OSAM structure's modal response. With this in mind, it is natural to conclude that the *manner* in which the robot moves (i.e., the motions it makes during operations) will affect the manner in which the modal response is manifest. In most cases, and in particular for robotic arms, some form of path planning is necessary to define such motions. It is in this activity that we have the opportunity to tailor the robot motion with the intent of minimizing modal excitations.

The generic robot path-planning or trajectory-planning problem can be described as defining the motions of the actuated robot degrees of freedom that will move the robot from one pose (or combination of joint angles) to another. Standard practice for solving this problem for robotic arms is to formulate an optimization problem that minimizes the duration of the motion under the constraints of the joint actuation limits. In some situations, it is beneficial to minimize a different quantity,

C. J. Rupp (✉)
ATA Engineering, Inc., Lakewood, CO, USA
e-mail: cory.rupp@ata-e.com

B. J. Dilworth et al. (eds.), *Topics in Modal Analysis & Parameter Identification, Volume 9*, Conference Proceedings of the Society for Experimental Mechanics Series, https://doi.org/10.1007/978-3-031-34942-3_10

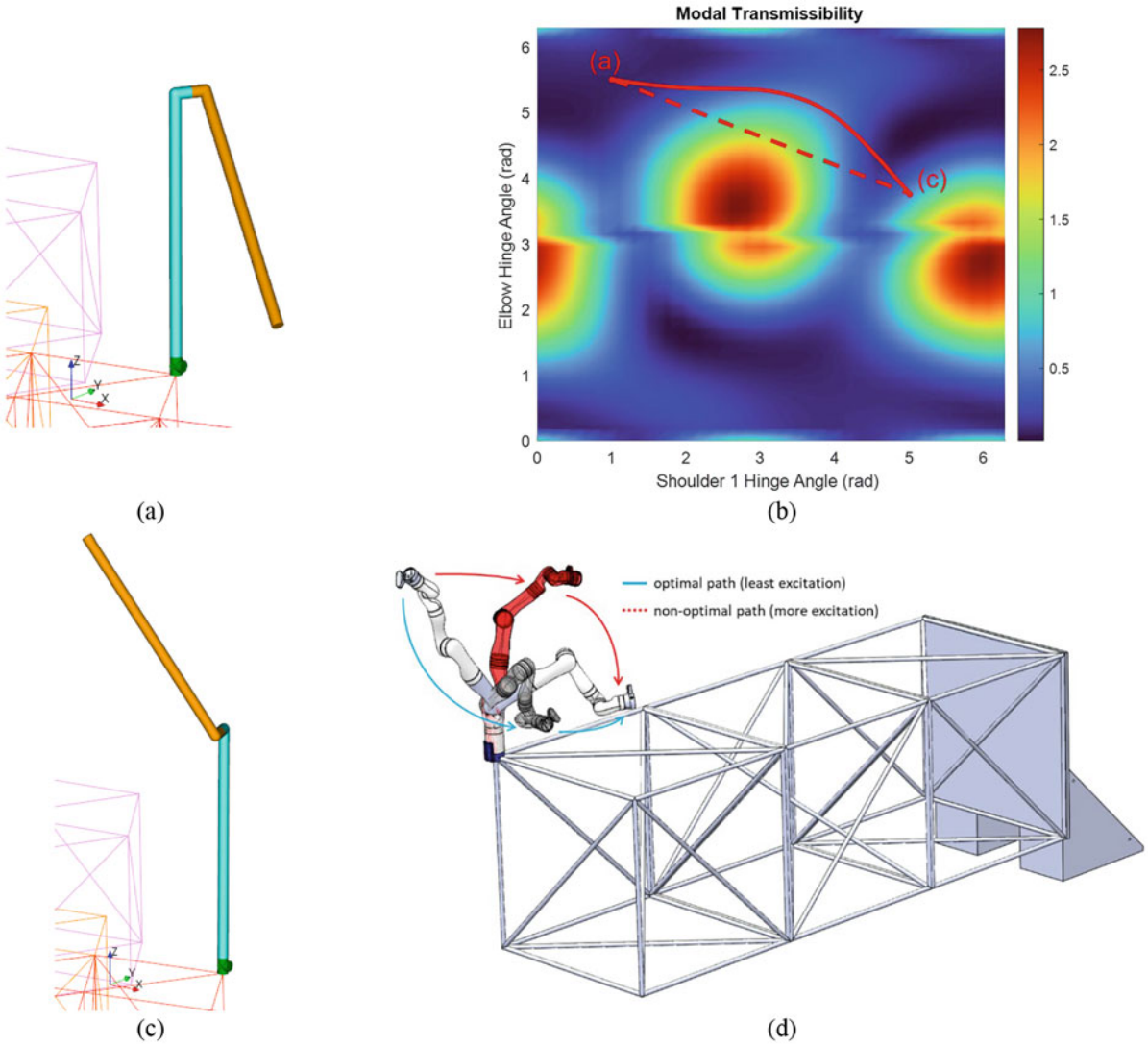

Fig. 10.1 If a robot needs to move from pose (**a**) to pose (**c**), there are many different paths it could take, some better than others, as shown in (**b**), where high modal transmissibility (for a single mode) can be avoided through different motions, as conceptually depicted in (**d**)

such as peak jerk, power, or even energy [5]. Constraints on the motion can be further added to the problem to enable considerations such as collision avoidance, which can be implemented using a variety of methods [6, 7]. Unexplored to date is the consideration of how to design robot trajectories that minimize dynamic excitations external to the robotic system itself (i.e., excitations generated by the robot through interactions with its environment). This consideration is of particular concern for robots operating while attached to flexible structures (as opposed to the more typical scenario of robots operating while hard-mounted to ground). While the use of specialized controllers for OSAM structures that reduce modal excitation has been shown [4], it is arguably more prudent to avoid excessive excitation in the first place, and for this, an excitation minimization technique is needed.

The idea of designing motion paths for robotic systems that also minimize modal excitations is conceptualized in Fig. 10.1. For a two-degree-of-freedom robot starting at pose (a) and tasked with moving to pose (c), there are a number of paths that would suffice. By overlaying the robot configuration or pose-space with a map of modal transmissibility as a function of robot pose (Fig. 10.1b), we can see that while a straight-line path is most expedient, it would inadvertently pass through a high-transmissibility region and excite the structure to which it is attached more than necessary. By instead choosing a path that avoids high-transmissibility regions, the modal excitation can be reduced. It is the goal of this chapter to develop a method and demonstrate that excitation reduction can be achieved by considering the relationship between the robot pose and modal transmissibility.

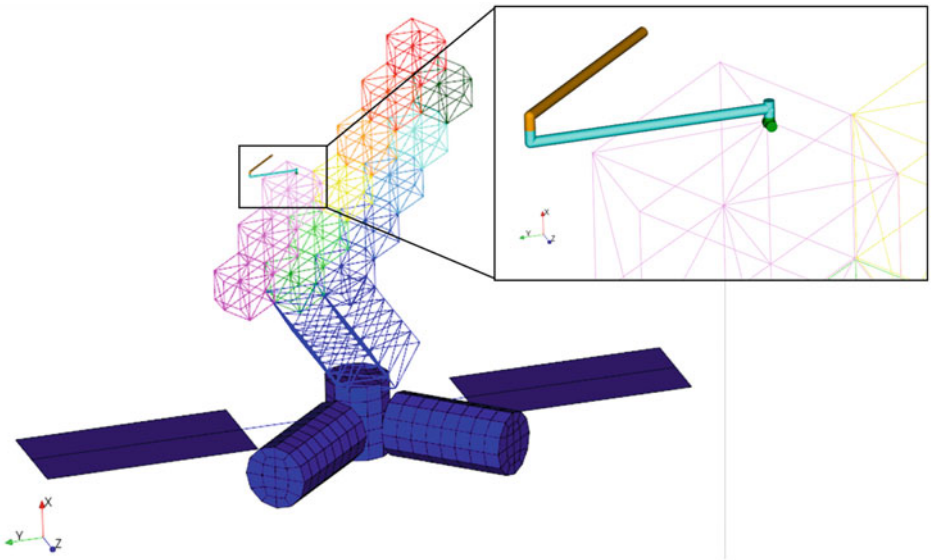

Fig. 10.2 Partially assembled OSAM telescope example model with attached notional assembly robot; each different-colored hexagonal backplane segment represents an assembly unit

Table 10.1 Frequencies of the first eight flexible modes of the partially assembled OSAM telescope

#	Mode description	Frequency (Hz)	#	Mode description	Frequency (Hz)
1	Forward bend	3.18	5	System yaw twist	8.42
2	Base truss roll twist	3.43	6	Second roll twist	9.48
3	Fwd bend w/ storage	3.49	7	Truss bend + backplane yaw	10.8
4	Mixed backplane twist and fwd bend	7.07	8	Backplane yaw	12.1

10.2 Demonstration Model

For evaluation and demonstration purposes, a mobile robot arm based on those found on the International Space Station and envisioned for the lunar gateway [8] is used in conjunction with an exemplary OSAM structure based on the in-space astronomical telescope (iSAT) reference design [9]. A partially assembled version of the iSAT telescope was developed and consists of a space platform and several hexagonal truss segments that constitute the telescope mirror backplane (Fig. 10.2). During construction, the robotic arm will assemble the backplane segments before mounting mirror segments. Analytical modal characteristics of this model obtained via Nastran and substructuring routines within IMAT™ [10] are provided in Table 10.1. Modal damping of 1% is applied to the assembled structure. The robotic arm is modeled as a set of three rigid bodies and simulated via a multibody dynamics solver coupled to the iSAT model within IMAT. The angle of two joints of the robotic arm (one elbow joint and one shoulder joint near the connection to the iSAT structure) are independently controlled to follow defined trajectory profiles via PD controllers implemented within MathWorks' Simulink. More details about this combination of iSAT and robotic arm models can be found in Refs. [3, 4].

10.3 Selection of Minimal Excitation Poses

Our goal in this chapter is to define a technique that allows for selecting robot poses and trajectory motions that minimize robot-induced modal excitations. We start by exploring the relationship between modal excitation and robot actuation. Then we develop a metric that can be used to guide robot path and trajectory planning. Finally, we verify our findings through an analytical demonstration of two otherwise equivalent robotic motions that induce different modal responses, with one clearly preferred over the other.

As discussed in detail in Ref. [3], there exists an intricate relationship between robot pose and transmissibility between the robot actuator torque and the structural modes. In short, as the robot arm changes orientation, its ability to excite a given

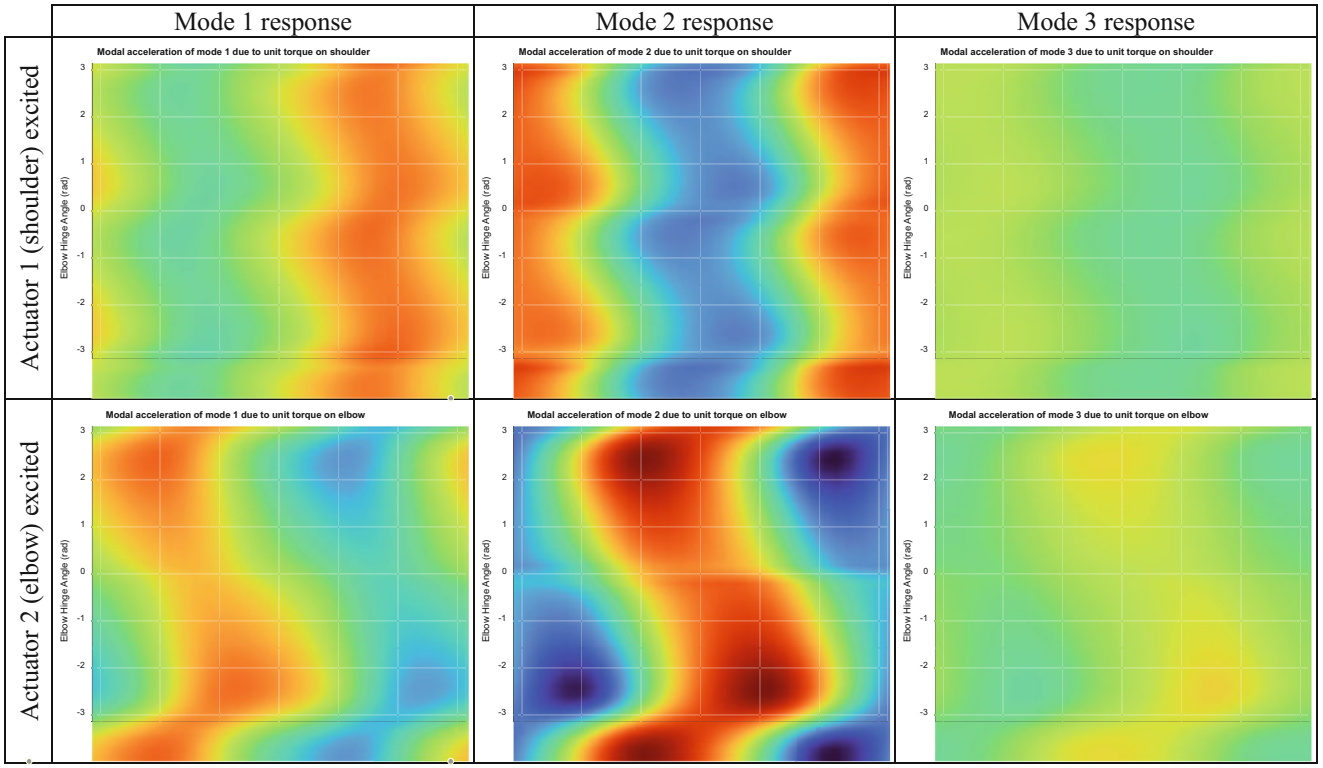

Fig. 10.3 Actuator-to-modal acceleration transfer functions as a function of robot arm pose; red indicates high in-phase excitation, blue indicates high out-of-phase excitation, and green indicates low excitation (all plots have the same color scale)

mode will change in a deterministic but nontrivial way. We explore this relationship for our demonstration model by varying the actuator angles throughout the entire pose- or configuration-space of the robot and solving for the modal amplitude excited by a unit torque on an actuator. Figure 10.3 shows this relationship via parameter sweeps of joint angles for motor torque-to-modal acceleration amplitude transfer functions (evaluated at the modal frequency). One plot for each combination of actuator joint and the first three modes of the structure is shown. These data show that mode 2 is generally more excitable at the robot attachment location and actuator 1 excites the structure differently than actuator 2 such that it is not necessarily clear how combined motion will excite the structure. With these data at our disposal, we must now combine it into a useful metric for designing robot motion paths that minimize modal excitations.

In the general case, we may be interested in capturing specific effects, such as stress concentrations or joint forces, that would be relevant to engineered structures. These responses are calculated by weighting the transfer function by the relevant stress or force mode shape coefficients for a given location of interest on the structure and summing the response over the modes. However, since we do not know the phasing between the modal responses, we must use a conservative measure to ensure that we capture the worst-case scenario. As such, we choose as our excitation metric to take the root-sum-square (RSS) of the transfer function data on a pose-by-pose basis (i.e., RSSing among the plots above). Since stress, force, and other mode shape coefficients vary throughout the structure, we can use arbitrary weighting to perform the following analysis without losing generality. We thus choose equal weighting, focusing on the magnitude of the modal acceleration rather than any specific response quantity.

Figure 10.4 shows the results of RSSing between modes for each actuator and then further RSSing across the actuated responses (with equal weighting between the actuation magnitudes) to define a metric for combined actuation response. Also depicted in this figure is a pair of arm motion paths starting at a common point equidistant from two poses that result in the same position in space for the end effector at the tip of the second arm link. The starting pose and two final poses are shown in Fig. 10.5. As robot path planning is almost always concerned with placement of the end effector, these two paths and final poses represent equivalent solutions to the path-planning problem. We chose these paths in particular because they end at distinctly different response magnitudes, as shown in Fig. 10.4c. As such, we expect that the modal responses of the structure will be different, with the leftward path exhibiting lower response than the rightward path.

To evaluate our hypothesis, a transient simulation of the robotic arm traversing the described paths is performed. The actuator trajectories are defined as straight-line paths between the starting and ending joint angles. The simulation is

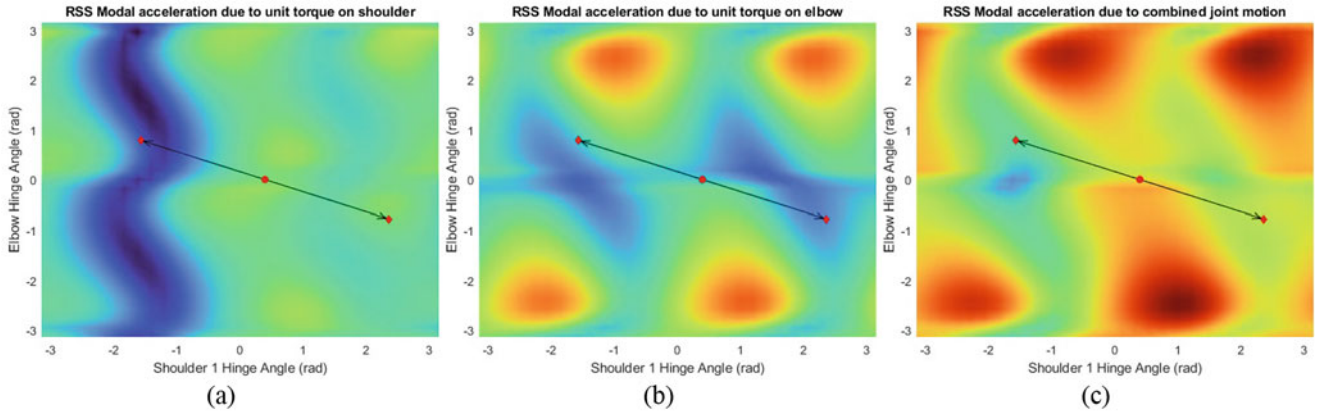

Fig. 10.4 RSS of modal acceleration responses to unit actuator torque for the (**a**) elbow and (**b**) shoulder actuators and (**c**) RSS of (**a**) and (**b**) to provide a metric of combined actuation response (all plots have the same color scale with blue showing low response and red showing high response)

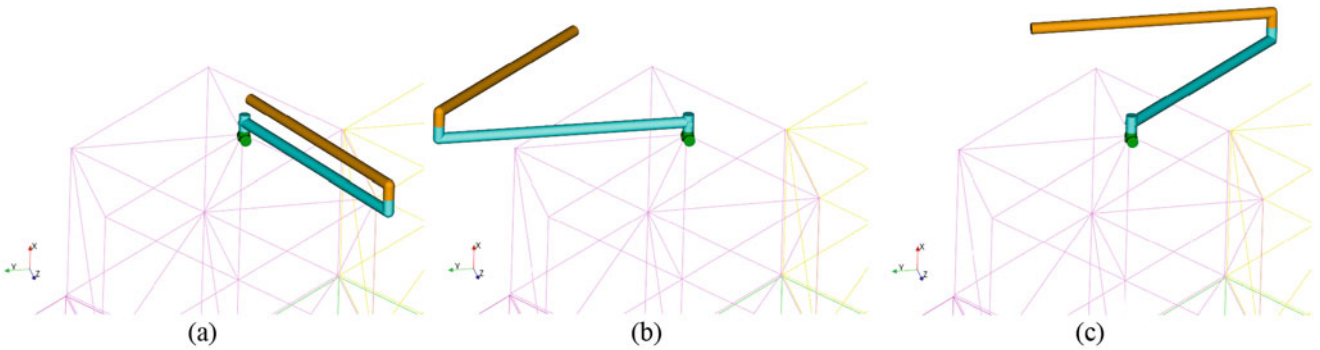

Fig. 10.5 (**a**) Starting pose for the robotic arm motion, which ends at the final pose for the leftward (**b**) and rightward (**c**) paths; the final poses achieve the same placement of the end effector

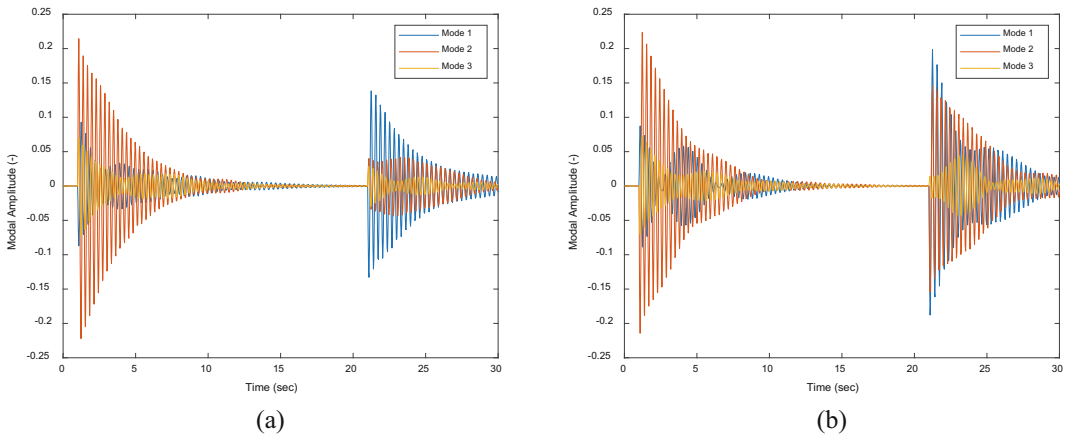

Fig. 10.6 Modal responses of the structure due to robotic motion for the leftward (**a**) and rightward (**b**) paths

performed for 30 s, with the actuation starting at 1 s and ending 20 s later. Note that due to the final poses being equidistant from the starting pose, the two motion profiles and resulting actuator torques are identical apart from sign. This is important so that differences between the dynamic responses can be attributed to dynamic coupling with the structure and not to differences in actuator output.

Modal responses induced by the two robotic arm motion paths are shown in Fig. 10.6. As expected, initial transients at the start and end of motion, which coincide with significant engagement of the actuators, are present. The relatively quiet

response during traversal is also expected for the specifically applied motion profile, as the motors are effectively coasting without introducing much torque; this may not be the case for other motion profiles. The response during motion start is largely similar between the two cases, although there are some minor differences that reflect how the combination of actuator torque signs comes into play. The response at motion stop, however, is of most interest, and we see that the leftward path exhibits a lower response magnitude than the rightward path, both overall and particularly in the response of mode 2. These results confirm our hypothesis and our use of a modal response metric to identify optimal poses and path plans that reduce modal excitations under robotic motion.

10.4 Conclusions

This chapter has developed and demonstrated a technique for identifying robotic motion paths and trajectories that reduce robot-induced modal excitations of structures. We find that not all robot poses are created equal when it comes to modal excitation, since movement to/from one pose may induce more excitation than another. Extension of the technique to robotic systems with more degrees of freedom is straightforward, but it will produce more complex multidimensional response spaces that may require the development of new techniques for them to be efficiently explored. Direct application of the technique within path-planning algorithms is possible, wherein the identified modal response metric could be used to augment the associated optimization problem. This technique continues paving the way toward the use of robots for construction and operation on OSAM structures by providing a means to minimize robot-induced structural vibrations.

References

1. Boyd, I.D., et al.: On-Orbit Manufacturing and Assembly of Spacecraft. Institute for Defense Analyses Science and Technology Policy Institute, Alexandria (2017)
2. Piskorz, D., Jones, K.L.: On-Orbit Assembly of Space Assets: A Path to Affordable and Adaptable Space Infrastructure. Center for Space Policy and Strategy. Aerospace Corporation (2018)
3. Rupp, C.J., Hunt, T.: Robot-driven modal testing for on-orbit servicing, assembly, and manufacturing. In: IMAC XL, Orlando (2022)
4. Rupp, C.J., Clemen, L.A.: Modal Compensation for OSAM Control Systems. SciTech Forum, San Diego, CA & Virtual (2022)
5. Clemen, L., Rupp, C.J.: Single- and multi-degree of freedom servo trajectory generation: an optimization framework, implementation, and examples. In: Proceedings of the IEEE/ASME International Conference on Advanced Intelligent Mechatronics (2023)
6. Liu, S., Liu, P.: A review of motion planning algorithms for robotic arm systems. In: Proceedings of the 8th International Conference on Robot Intelligence Technology and Applications. Springer, Singapore (2020)
7. Dai, Y., et al.: A review of spatial robotic arm trajectory planning. Aerospace. **9**, 361 (2022)
8. Canadian Space Agency. "Canadarm, Canadarm2, and Canadarm3 – A Comparative Table." 2019. https://www.asc-csa.gc.ca/eng/iss/canadarm2/canadarm-canadarm2-canadarm3-comparative-table.asp
9. Mukherjee, R., Siegler, N., Thronson, H.: The future of space astronomy will be built: results from the in-space astronomical telescope (iSAT) assembly design study. In: 70th International Astronautical Congress. Curran Associates, Inc, Red Hook (2019)
10. ATA Engineering, Inc.: IMAT User's Guide v7.8.0. (2021). http://www.ata-e.com/downloads/imat/all_doc/doc/index.html

Chapter 11
Design Optimization of 3D Printed Chiral Metamaterials with Simultaneous High Stiffness and High Damping

Wei-Chun Lu, Othman Oudghiri-Idrissi, Hrishikesh Danawe, and Serife Tol

Abstract For vibration mitigation and impact resistance, energy dissipation is desired in mechanical and aerospace structures to ensure their required loading capacity and dynamic performance. However, designing a structure with simultaneously high dissipation and high stiffness simultaneously is challenging due to the inherent tie between the material damping and stiffness. In this work, a tetra-chiral metamaterial beam design, which possesses enhanced damping thanks to local resonance, is proposed and optimized for simultaneously high stiffness, high dissipation, and high mass efficiency. Various designs with different geometric configurations are explored, and a design optimization framework is developed with stiffness, damping, and mass as the main metrics. Finally, the optimized dissipative tetra-chiral metamaterial beam designs that achieve high dissipation performance with consistent stiffness and mass efficiency are presented and compared to the initial one.

Keywords Elastic metamaterials · Metadamping · Chirality · Design optimization · Neural network

11.1 Background and Motivation

The traditional design of mechanical and aerospace structures requires a careful selection of materials to ensure their load-bearing capacity and desired dynamic performance. In general, material damping is desired in the structural system for vibration attenuation and stabilization. However, a trade-off between the material damping and stiffness should be achieved [1]. Designing a structure with high dissipation and high stiffness is a challenge in the field of vibration mitigation and precision control of lightweight structures. Locally resonant metamaterials (LRMs) can remedy this problem by exploiting their unconventional behavior. Locally resonant metamaterials are periodic structures that include locally resonating substructures on the subwavelength scale. "Metadamping," the unconventional damping property of LRM, is the phenomenon of enhanced damping due to the local resonance of the unit cells, which also manifests in stiff periodic structures [2, 3]. Researchers proposed different types of locally resonant metamaterial designs, such as phononic resonators that present high metadamping by combining features of acoustic metamaterials and phononic crystals [4], and the scissor-like electromechanical metamaterial that possesses high dissipation and tunable metadamping [5]. On the other hand, chiral metamaterials are a class of metastructures commonly adopted in vibration absorption [6]. For instance, a beam design composed of an aluminum frame and chiral rubber inclusions with heavy mass resonators was designed and proved to have significant vibration mitigation compared to a baseline aluminum frame [7]. The optimization of the chiral metamaterial bandgap was also investigated by varying the design parameters of the chiral substructure [8].

Most of the studies on chiral metamaterials mainly focus on bandgaps and seldom consider the viscoelastic material in the design or explore their damping, stiffness, and mass efficiency properties. Furthermore, metadamping studies mostly investigate local resonators of LRM with simple lumped mass models. This work proposes a tetra-chiral metamaterial beam design with 3D printable viscoelastic materials and chiral substructures and analyzes its dissipation property along with its stiffness and mass efficiency using the finite element method (FEM). The chiral beam design is then optimized to achieve high stiffness, high dissipation, and high mass efficiency simultaneously, with the ultimate goal of integrating the proposed chiral designs into a high-precision and lightweight space structures.

W.-C. Lu · O. Oudghiri-Idrissi · H. Danawe · S. Tol (✉)
Department of Mechanical Engineering, College of Engineering, University of Michigan, Ann Arbor, MI, USA
e-mail: wclu@umich.edu; stol@umich.edu

B. J. Dilworth et al. (eds.), *Topics in Modal Analysis & Parameter Identification, Volume 9*, Conference Proceedings of the Society for Experimental Mechanics Series, https://doi.org/10.1007/978-3-031-34942-3_11

11.2 Analysis and Discussion

In our work, chiral designs with local rotation and deformation of internally resonating elements are leveraged along with viscoelastic materials to dissipate energy. The proposed tetra-chiral metamaterial beam made of 3D printable materials is shown in Fig. 11.1a. The stiff material, VeroClear, forms the main chiral structure, and a viscoelastic coating material, Agilus30, is introduced for passive dissipation. The ring radius r_c, ligament angle ϕ, thickness of VeroClear ligament t_{vc}, and thickness of Agilus30 ligament t_{ag}, are the main four parameters that characterize the geometry of the unit cell design. For a stiff, highly damped, and lightweight beam structural element, (a) the fundamental frequency f_1 of the beam (in a cantilever setting) that characterizes its stiffness to mass ratio, (b) the corresponding damping ratio ξ_1, and (c) the mass m of the beam are the three selected metrics to assess the performance of the beam design. By conducting a parametric study of the tetra-chiral beam design via FEM, it is noted that: (i) the fundamental frequency and mass of the beam increase and damping decreases as the internal ring radius, ligament angle, and VeroClear thickness increase in the design, and (ii) the damping and mass of the beam increase and the fundamental frequency decreases with the thickness of Agilus30 ligament. It is concluded from the preliminary study that the variation of the internal ring radius and ligament angle has a relatively larger effect on the fundamental frequency and damping of the beam, while the change of the ligament thicknesses affects mainly the beam's mass.

Next, an optimization framework is constructed to achieve a highly stiff, highly damped, and mass-efficient chiral beam design. To this end, a design parameter space is defined with consistent parameter ranges and geometrical constraints. Additionally, in order to improve the processing time of the optimization, neural networks are leveraged as a surrogate model, which maps the design parameters to the three metrics. Four thousand various designs are randomly sampled from the design space, and FEM is used to evaluate the fundamental frequency and corresponding damping ratio of the beam designs. The results are then collected as the dataset for network training, with 85% of the data for training and 15% of the data for validation. The regression factors of the FEM results and predictions from the trained neural nets are evaluated at 0.99, indicating a good accuracy for the surrogate model. In the second stage, two approaches for multi-objective optimization are considered. First, a scalarization of the three metrics into a single combined objective function F is considered, such that

$$F = -w_1 \frac{f_1}{f_0} - w_2 \xi_1 + w_3 \frac{m}{m_0} \tag{11.1}$$

where w_1, w_2, and w_3 are the weights, and f_0 and m_0 are the fundamental frequency and mass of a reference VeroClear solid beam of the same outer dimensions. By minimizing the composite objective function, an optimal design based on the user-defined weights can be obtained. In this work, the weights are set to an equal value (1/3), and 100 random designs with the lowest objective function values are chosen as initial designs for optimization to avoid convergence to a local optimum. The second approach optimizes the three metrics simultaneously by identifying a set of optimal solutions called the Pareto-optimal set. In this setting, the three objective functions are defined as

$$F_1 = \frac{-f_1}{f_0}, F_2 = -\xi_1, F_3 = \frac{m}{m_0} \tag{11.2}$$

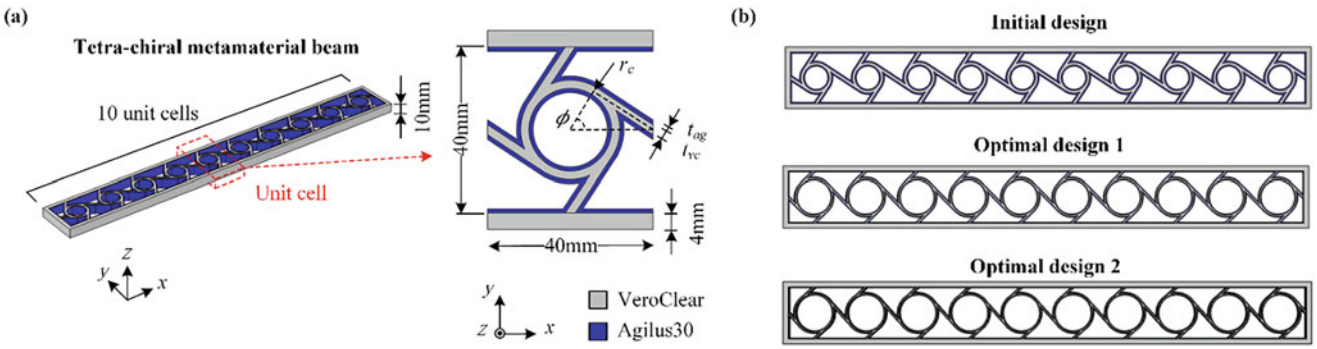

Fig. 11.1 (**a**) Tetra-chiral viscoelastic metamaterial beam and its unit cell with four design parameters. (**b**) Comparison of the initial, optimal design 1, and optimal design 2 of the tetra-chiral beam

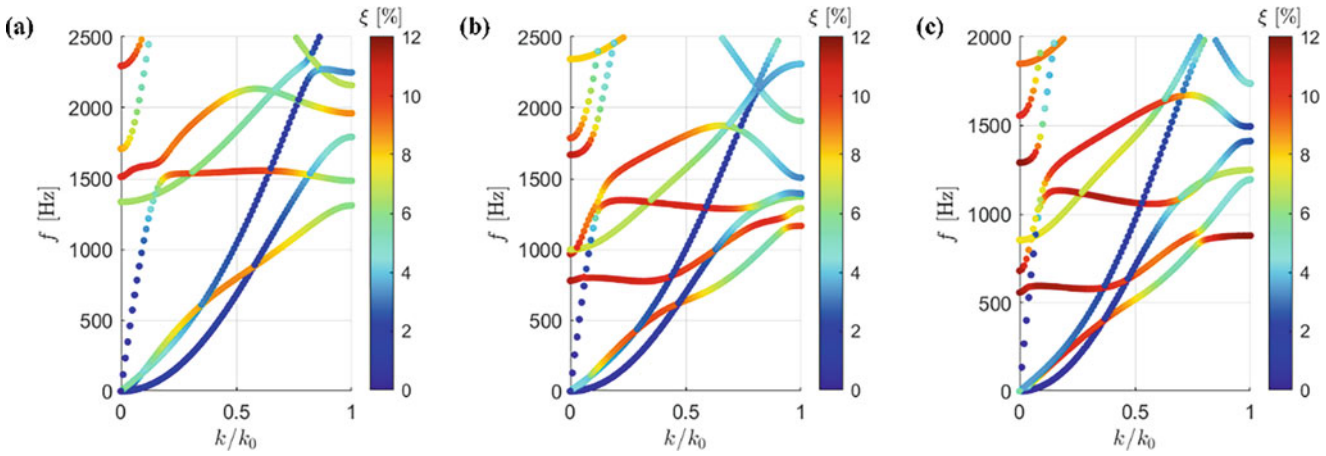

Fig. 11.2 Dispersion plots for the unit cells of (**a**) initial, (**b**) optimal design 1, and (**c**) optimal design 2 of the tetra-chiral beam. The color of the markers represents damping ratios. The masses of the chiral beams formed by the three unit cells are 0.101, 0.083, and 0.076 kg, respectively

The solution that has the closest distance from the Pareto front (the hypersurface in the criteria (metric/objective) space mapped from the Pareto-optimal set) to the Utopia point (whose coordinates are the respective minima of all the metrics in the criteria space) is chosen as the second optimal solution. The optimal designs of the two approaches are compared in Figs. 11.1b and 11.2 to the initial chiral beam design. It is noted that the two optimal designs have a larger internal ring radius and thinner thickness of the ligaments (including VeroClear and Agilus 30 materials). The optimal design obtained from the first method has a similar fundamental frequency to the initial design, with a damping increase of 69% and a mass reduction of 18%. On the other hand, the optimal design obtained from the second approach presents a damping increase of 156% and a mass reduction of 25%, with a reduction of the fundamental frequency of 18% compared to the initial design. It is also noted that the design parameters of the two optimal designs are close to each other, indicating that designs with similar configurations present a good performance by satisfying high stiffness, high damping, and high mass efficiency.

11.3 Conclusion

A tetra-chiral beam design with viscoelastic material is proposed and optimized for simultaneously high stiffness, high dissipation, and high mass efficiency. A proper design space is defined, and two approaches are adopted for multi-objective optimization. The optimal designs present significant improvement compared to the initial design. The optimal design from the first method shows 69% increase in damping and 18% reduction in mass, and the second optimal design presents a damping increase of 156% and a mass reduction of 25% with 18% reduction of the fundamental frequency. Our goal is to integrate the optimal chiral metamaterial beams into the structural design of next-generation space structures with high precision, high damping, and lightweight.

Acknowledgments This material is based upon work supported by the Defense Advanced Research Projects Agency (DARPA) under Contract No. HR001121C0241.

References

1. Ashby, M.F.: Materials Selection in Mechanical Design, 4th edn, pp. 57–96. Butterworth-Heinemann, Oxford (2011)., ch. 4
2. Hussein, M.I., Frazier, M.J.: Metadamping: an emergent phenomenon in dissipative metamaterials. J. Sound Vib. **332**(20), 4767–4774 (2013)
3. Bacquet, C.L., Ba'ba'a, H.A., Frazier, M.J., Nouh, M., Hussein, M.I.: Metadamping: dissipation emergence in elastic metamaterials. Adv. Appl. Mech. **51**, 115–164 (2018)
4. DePauw, D., Ba'ba'a, H.A., Nouh, M.: Metadamping and energy dissipation enhancement via hybrid phononic resonators. Extreme Mech. Lett. **18**, 36–44 (2018)
5. Al Ba'ba'a, H., Lin, Z., Tol, S.: Metadamping enhancement and tunability via scissor-like electromechanical metamaterials. J. Appl. Phys. **130**(18), 184901 (2021)

6. Wu, W., Hu, W., Qian, G., Liao, H., Xu, X., Berto, F.: Mechanical design and multifunctional applications of chiral mechanical metamaterials: a review. Mater. Des. **180**, 107950 (2019)
7. Baravelli, E., Ruzzene, M.: Internally resonating lattices for bandgap generation and low-frequency vibration control. J. Sound Vib. **332**(25), 6562–6579 (2013)
8. Abdeljaber, O.A., Inman, D.J.: Optimization of chiral lattice based metastructures for broadband vibration suppression using genetic algorithms. J. Sound Vib. **369**, 50–62 (2016)

Chapter 12
Modal Analysis of a Coilable Composite Tape Spring Boom with Parabolic Cross Section

Deven Mhadgut, Sheyda Davaria, Minzhen Du, Rob Engebretson, Gustavo Gargioni, Tyler Rhodes, and Jonathan Black

Abstract The need for using extendable booms to deploy payloads, solar sails, and antennas is ever increasing. Their inclusion in future space missions can provide a viable alternative to massive truss-like structures as well as significantly reduce fuel mass requirements for attitude control systems. Over the last few decades, various designs of these have been developed and studied. However, at the present, flight heritage booms are considered inadequate in terms of both bending and torsional stiffness. Booms with conic cross sections have not been studied in the past and we believe they might have certain advantages in these aspects in their deployed configuration. This chapter aims to investigate the dynamic characterization of a composite tape spring boom with a parabolic cross section. This boom sample is also planned to be the primary payload on a 3 U cubesat at Virginia Tech, Ut ProSat-1. The cubesat mission aims to collect acceleration data from the tip of the deployed boom. This data will then be validated using the test data from the ground experiments. Finally, this chapter discusses the setup of a finite element analysis in Abaqus as well as future plans for the ground vibration experiments.

Keywords Tapespring boom · Modal · Acceleration · Deployable · Cubesat

12.1 Introduction

Coilable composite booms serve as the prominent structural element of many large deployable structures in space. These structures have played an important role in a large number of NASA missions over the past several decades due to their high reliability and low costs. Not only are they ultra lightweight, but they also provide high packaging efficiencies for the launch vehicles. Because of all these advantages, they have been used in a plethora of applications from massive solar sails for spacecraft propulsion and precision antennas for communication satellites to payload isolation mechanisms for cubesats. Various designs of these booms have been developed and studied in the past. The basic tape spring with uniform curvature is the simplest one of them all. More examples of booms with open cross sections include the Storable Tubular Extensible Member (STEM) [1] and the Triangular Rollable and Collapsible (TRAC) [2] boom. These are usually very cheap to manufacture and exhibit good mechanical performance. However, closed cross section booms such as the Collapsible Tubular Mast (CTM) [3] are preferred due to their increased axial and torsional stiffness. With the advent of large-scale structures such as the James Webb Space Telescope and projects such as the Starshade, the need for more robust booms is ever increasing.

Here, we will be talking about the dynamic analysis of a bistable composite tape spring boom with a parabolic cross section [4]. Also, it is to be noted that the terms, tape spring and boom, will be used interchangeably henceforth. The geometry and material properties are based on the boom sample that will fly as the primary payload on a 3 U cubesat at Virginia Tech, Ut ProSat-1 [5]. This tapespring boom was manufactured at the NASA Langley Research Center and will be coiled inside a novel deployer [6] designed by the student team. The boom can be deployed passively via its own strain energy and then retracted actively using a stepper motor. It also exhibits bistability by virtue of the specific layup geometry and materials of the composite, allowing for a more controllable self-deployment. It is widely accepted that modal analysis is a powerful tool for improving the reliability of a system at its design stage. Here, we talk about the modal analysis of this boom using the PSV-400 scanning laser vibrometer from Polytec. We also talk about some finite element analysis that we did in order to validate the experimental results.

D. Mhadgut (✉) · S. Davaria · M. Du · R. Engebretson · G. Gargioni · T. Rhodes · J. Black
Aerospace and Ocean Engineering Department Virginia Tech, Blacksburg, VA, USA
e-mail: devenmhadgut@vt.edu

B. J. Dilworth et al. (eds.), *Topics in Modal Analysis & Parameter Identification, Volume 9*, Conference Proceedings of the Society for Experimental Mechanics Series, https://doi.org/10.1007/978-3-031-34942-3_12

This chapter is organized as follows. The importance of modal analysis as a test as well as the literature review has been presented in Sect. 12.2. Then, the design and material properties of the parabolic composite boom are presented in Sect. 12.3. The results and discussions on the modal analysis experiments, finite element analysis, and preliminary on-ground deployment experiments are introduced in Sect. 12.4. This chapter is concluded in Sects. 12.5 and 12.6, where the plan for future work is discussed.

12.2 Background

Experimental modal analysis can be used to determine parameters such as the natural frequencies, modal damping effects as well as the mode shapes of a structure. This technique predicts potential issues and can help engineers address them early in the design process. Apart from this, the most important application of modal analysis is that it helps to validate any future finite element analyses and ground test experiments for more complex phenomenon such as buckling and full deployment. Therefore, it was decided to start with modal analysis as a first step toward dynamic characterization of the boom sample under study.

Previously, Seffen and Pellegrino [7] have discussed the behavior of these tape springs in terms of predicting the motion of folds during their self-actuated deployment. Further, Kwok and Pellegrino [8] investigated the effect of viscoelasticity on the folding and deployment behavior of composite tape springs. The bistability phenomenon was further explored by Lee and Fernandez [9], where they developed an analytical model for bending of two-shelled composite booms and devised the criterion for inducing bistability in them. Recently, Mallol et al. [10] carried out experiments, focusing on the deployment of these bistable booms suspended in gravity off-loaded systems. They report the deployment times and the strain energy values. However, not much work has been done on studying the effect of deployment shock on the spacecraft chassis. Also, there is a knowledge gap between the acceleration prediction from ground tests and actual on-orbit measurements. We intend to fill that gap via repeated deployment tests in the lab while simulating on-orbit conditions and then comparing the data.

As mentioned earlier, this tape spring boom will fly on a 3 U cubesat, Ut ProSat-1(UPS-1) onboard the NG-19 flight mission of the Cygnus spacecraft in February 2023 (tentative). UPS-1 aims to collect dynamic characteristic data of the payload boom through the use of Inertial Measurement Units (IMUs). The tip of the boom will have an enclosed IMU attached to it. A second IMU will be fastened to the cubesat chassis near the root of the boom. These will measure the acceleration at these specific locations and will help compute the overall frequency response function (FRF) of the boom. The boom will not be excited by any active vibration source but the IMUs will essentially measure the effect of the tape spring deployment on the cubesat chassis. The boom tip IMU will be oriented so as to measure the transverse vibrations generated due to the shock wave at the end of the boom deployment. The experimental data presented here, will help validate and verify the data that we get on-board during and at the end of deployment (Fig. 12.1).

The boom is 1.22 m long and 70 mm wide in the coiled configuration. The thickness of the boom is 0.16 mm. The tape spring has a symmetric composite laminate, and it consists of three plies oriented in the [45PW$_c$/0$_c$/45PW$_c$] configuration. The layup is as follows: two carbon fiber/epoxy (M30S/PMT-F7) plain weave (PWc) plies (at $\pm 45^{\circ}$) on the outside and one carbon fiber/epoxy (MR60H/PMT-F7) unidirectional (UD) ply (0°) in the middle. It is noted that this design of the laminate gives it sufficient strain energy for self-extension through bistability even after the development of creep effects. This boom also has four embedded copper traces [11] co-located with the central UD layer on one side of the parabolic cross section (shown in Fig. 12.2). However, it is to be noted that the final version of the boom will have eight traces on each side of the parabola. These traces run along the entire length of the boom and carry power and data to and from the tip of the boom. An IMU is mounted on a flexible circuit (shown in Fig. 12.2 and this circuit collects and transmits the end-of-deployment acceleration data back to the payload control module (PCM) board located inside the cubesat chassis.

12.3 Experimental Setup

The modal analysis tests were performed by exciting the boom using an impulse hammer and a shaker. Three strips of reflective tape were adhered to the convex surface of the boom through its full length, one along the centerline of the boom and two on the “arms” of the parabola. The boom was suspended vertically downward by fixing the deployer system to a rigid stand and the laser was directed perpendicular to the boom axis (shown in Fig. 12.3).

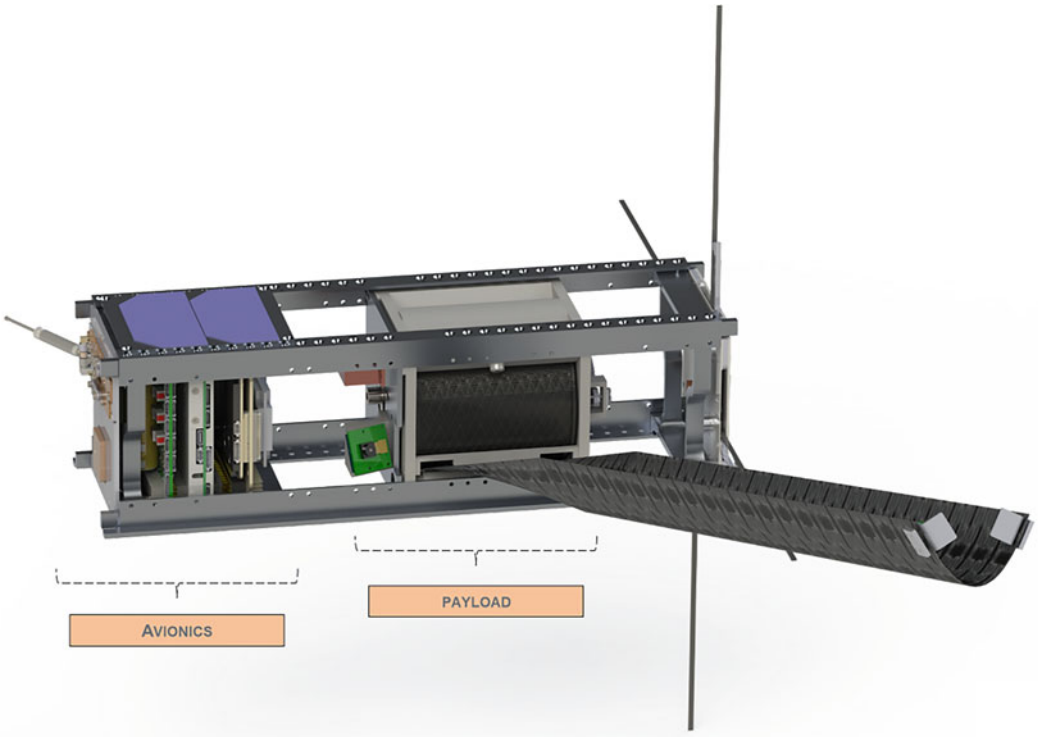

Fig. 12.1 CAD model of Ut ProSat-1 showing the fully deployed boom

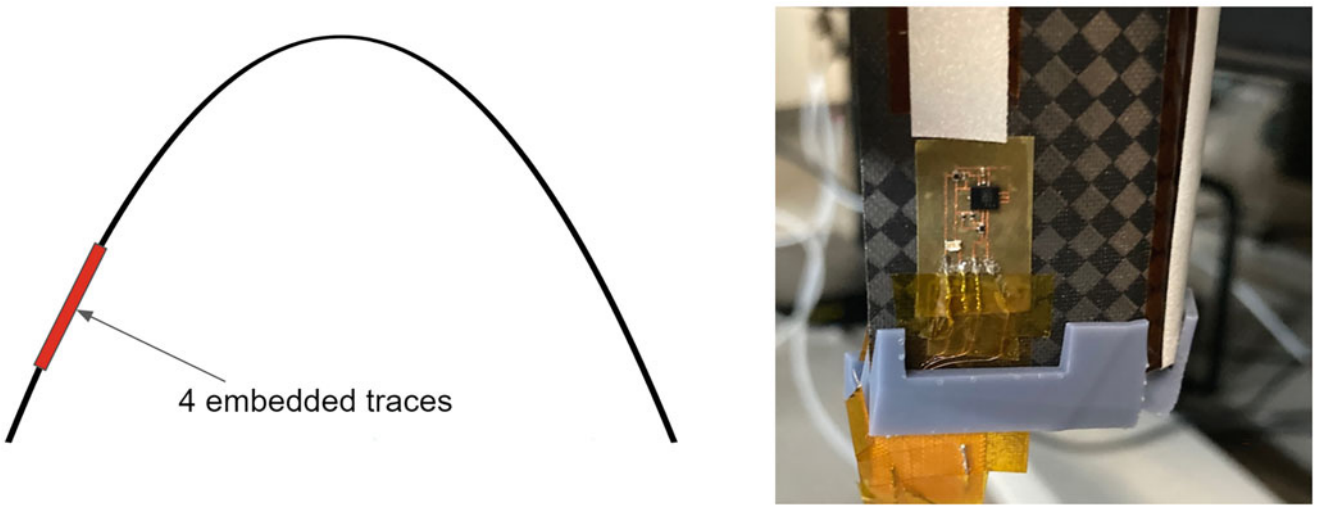

Fig. 12.2 Boom profile with embedded cables (left), first specimen of the boom (right)

First, the velocity and force response of the boom was measured at different locations along the boom by hitting it with an impulse hammer. The hammer has a load cell attached to its tip, which generates a voltage signal proportional to the excitation force. Multiple points were selected for obtaining the frequency response function (FRF) of the boom and then the fast Fourier transform (FFT) of the FRF was plotted in the Polytec data acquisition software, giving us the mode shapes and the natural frequencies of the boom (shown in Fig. 12.5).

A similar setup was created for exciting the boom with a modal shaker (Fig. 12.4). A nylon stinger was used to connect the shaker to the boom surface. A load cell was placed at the point of excitation at one end of this stinger. This load cell would report the input force for calculating the transfer function. The shaker is driven by a digital to analog converter (DAC)

Fig. 12.3 Setup for the impulse hammer test

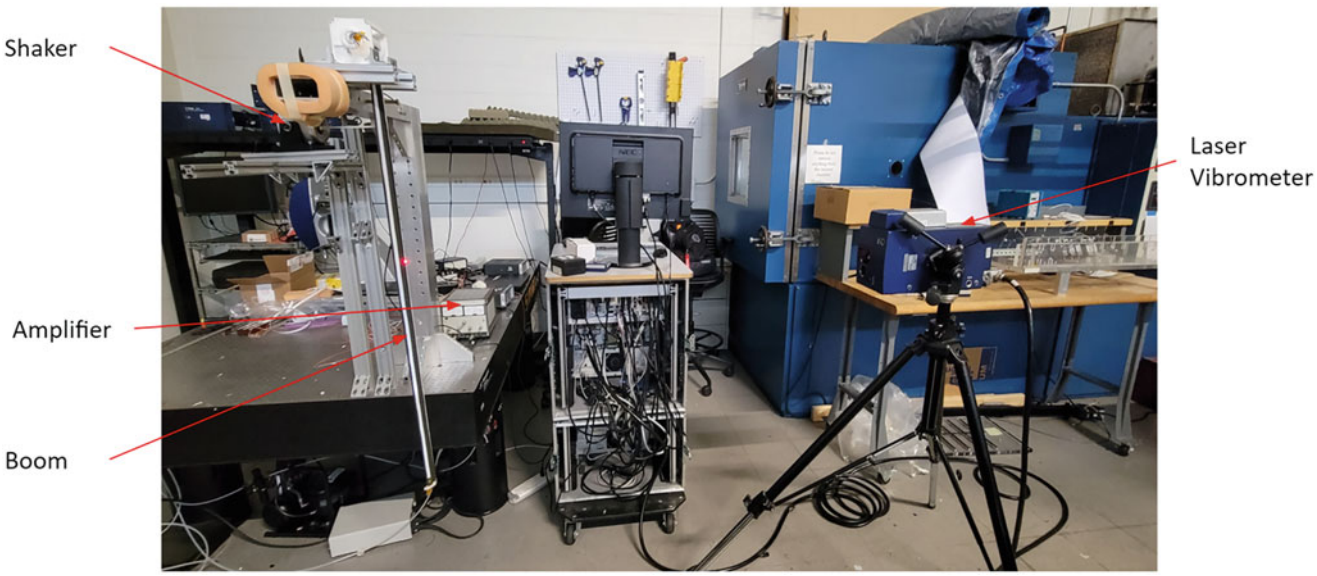

Fig. 12.4 Setup for the modal shaker test

and a burst chirp signal is used to excite the boom. Burst chirp is basically a sine signal starting at low frequency and then quickly sweeping to a high frequency in a time period of less than a second. The DAC is programmed to produce this signal repeatedly to collect data at all points of interest on the boom surface.

We also performed some deployment tests in the same vertically suspended configuration where we rolled up the boom inside the deployer and released it. The acceleration of the boom was measured using an accelerometer attached to the tip of the boom. Data was collected at the end of each deployment sequence.

12.4 Analysis and Results

12.4.1 Experimental Results

The relative velocity/force frequency response function (measured in dB) has been plotted against the frequency for both the impact hammer and modal shaker tests in Figs. 12.5 and 12.6, respectively. Theoretically, it is expected that there should be no difference between the results of the two tests. However, this is only true if we assume that the force transducers used in the experiment are massless and there is no interaction between the applied periodic force and the structure itself. This is definitely not true in practice and therefore, we see a clear shift in the modes of the tapespring boom between the two tests.

The acceleration profile obtained from the accelerometer attached to the boom tip has been shown in Fig. 12.7. Two separate measurements were reported, one where we collect data throughout the deployment (blue) and then one at the very end of deployment (orange). One can notice the pattern in the orange curve repeating at the end of the blue curve. A peak transverse acceleration value of -11.7 m/s^2 was noted.

12.4.2 Finite Element Analysis

An implicit finite element analysis (FEA) was conducted in Abaqus/Standard 2022 to verify the results from the modal analysis tests presented in Figs. 12.5 and 12.6. The boom profile was measured at different locations along the boom to make a CAD part that could be imported directly into Abaqus as a 3D deformable shell part. The material properties were defined and inserted via the material manager, based on the paper from Lee and Fernandez [4] on parabolic booms. The composite layup editor was then used to enter the ply information for the boom. The discrete option was selected for defining the

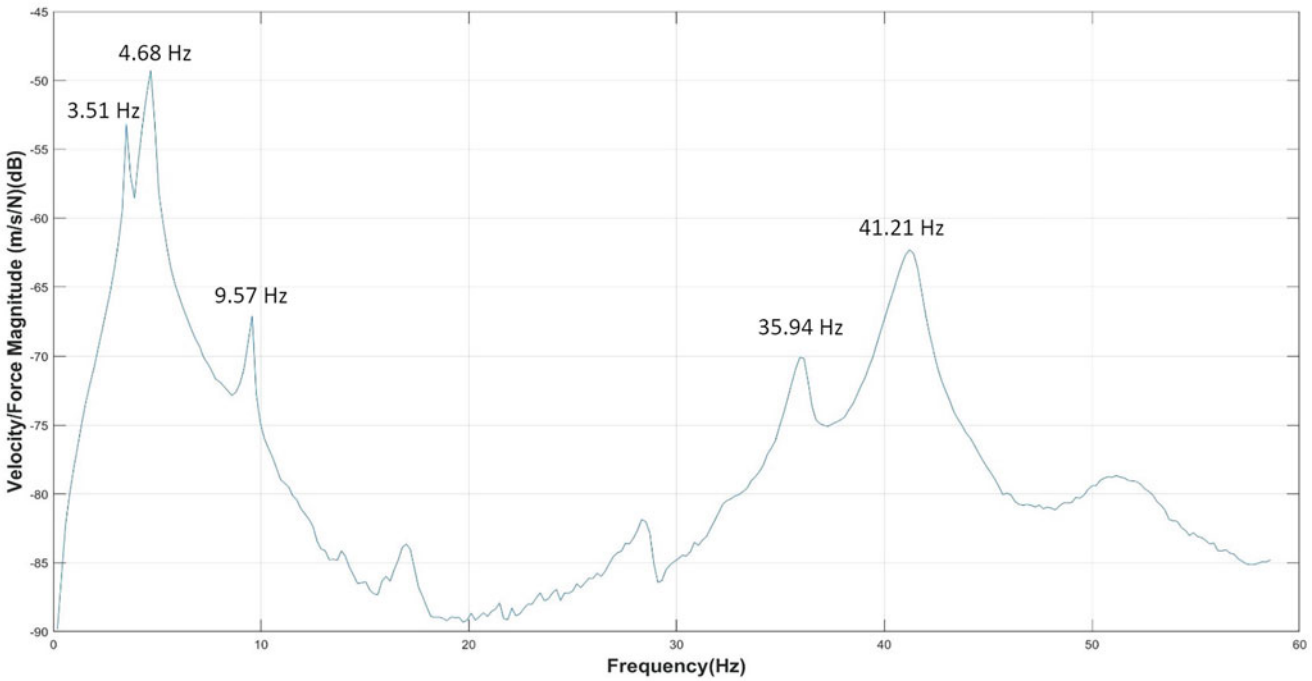

Fig. 12.5 Modal analysis of boom using impulse hammer

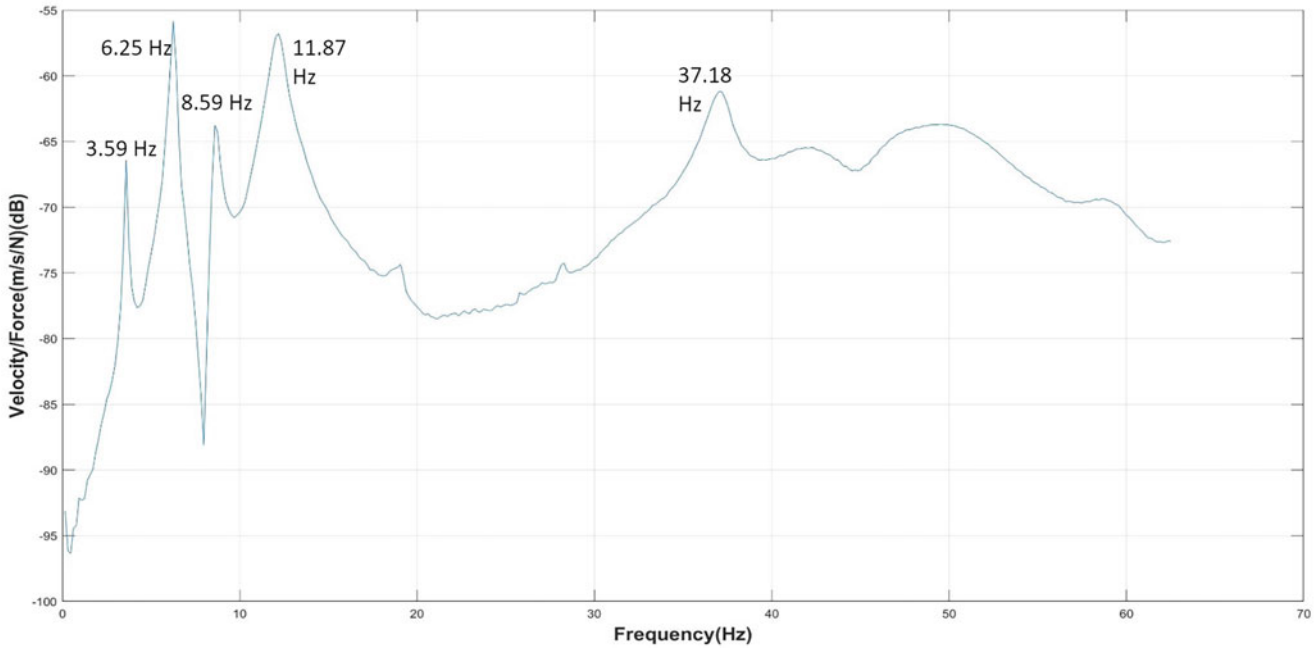

Fig. 12.6 Modal analysis of boom using shaker

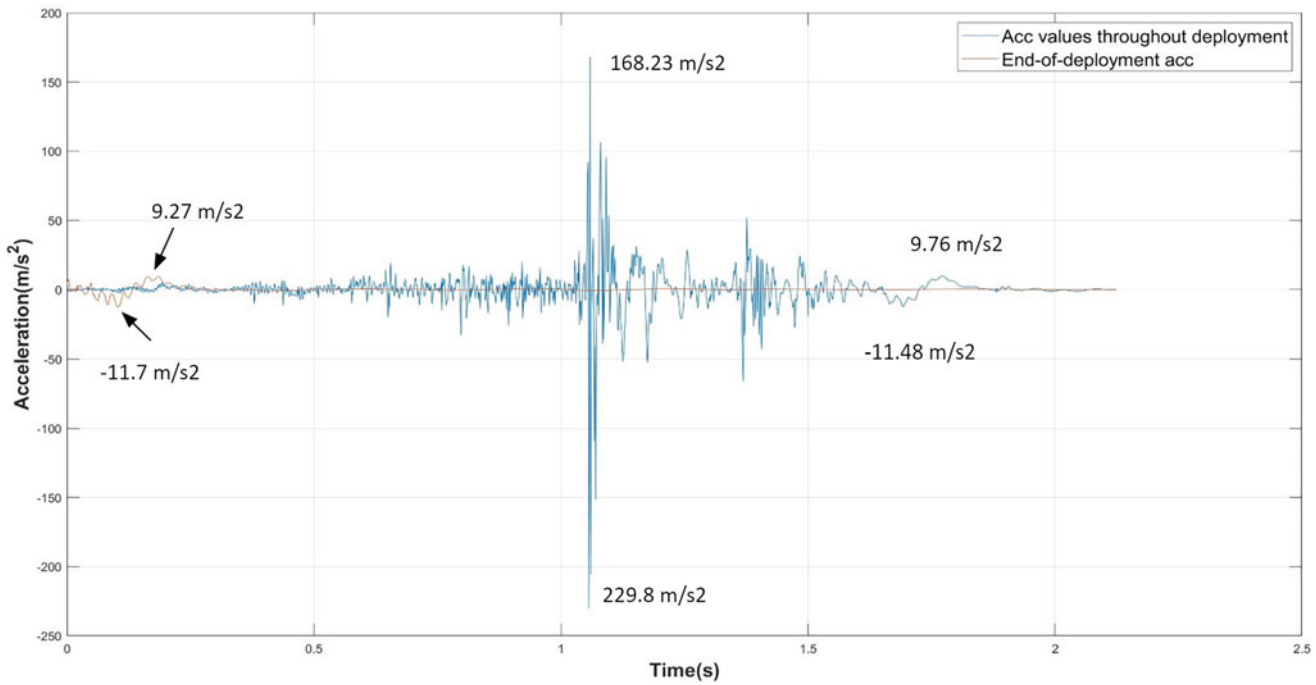

Fig. 12.7 Measurement of deployment acceleration during (blue) and at the end of deployment (orange)

layup orientation and the appropriate shell normal and primary axes were chosen accordingly. The next step was setting up a linear perturbation/frequency analysis to output the first six frequency modes based on the Lanczos eigensolver. Finally, the tape spring part was meshed with conventional 4-node thin shell elements (S4R). Preliminary modal analysis results show promising results for the first few frequency modes. Non-linear behavior of the boom was not considered in this model but will be examined in the subsequent studies.

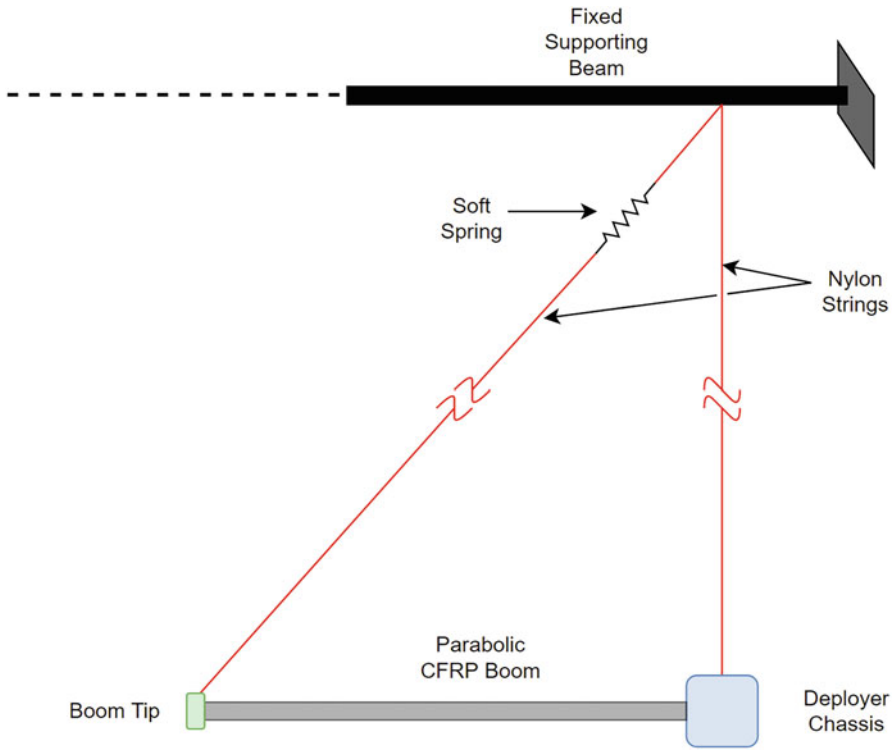

Fig. 12.8 Gravity off-loading system with single-point suspension

12.5 Future Work

Although vertical suspension of the boom mitigates the effect of gravity on its transverse vibrations at the end of each deployment sequence, an innovative gravity off-loading system (GOLS) would be necessary in order to simulate the on-orbit conditions. Previously, Mallol and Tibert [12] have done this using single point suspension based on the marionette paradigm [13]. Single point suspension of the boom-deployer system (shown in Fig. 12.8) allows for rotation in both the vertical and horizontal planes. Furthermore, soft extensional springs attached to the boom tip result in a smooth deployment. Suspension is done using nylon strings which also reduces the overall mass of the GOLS, reducing its inertia and any obstruction to the free movement of the boom during the deployment process. The same setup could also be used to observe the vibration modes using a laser vibrometer based on the procedure described earlier.

12.6 Conclusion

Modal analysis was performed using both an impulse hammer and a shaker and the results were compared. The preliminary setup for the finite element analysis in Abaqus was also discussed. Second, the next steps for the ground testing were mentioned. It was noted that during these tests using the laser vibrometer, we were not able to capture the surface curvature of the tape spring. Therefore, an important step in this direction would be scanning the boom using three laser heads aligned along three different directions. Apart from that, future studies would involve suspension of the boom using a gravity off-loading system so as to simulate on-orbit conditions. It would also involve the use of the IMUs for measuring the deployment acceleration. Finally, it is noted that temperature will play an important role in the deployment dynamics of the boom, and, therefore, thermal vacuum tests will play an integral role in the future.

Acknowledgments Mr. Deven Mhadgut and Dr. Sheyda Davaria gratefully acknowledge the support from the Center for Space Science and Engineering Research at Virginia Tech. We would like to thank NASA Langley Research Center and Dr. Juan M. Fernandez for providing us the boom samples for testing.

References

1. Groskopfs, E.: Storable tubular extensible member device. Patent US3434674A, registered (1967)
2. Murphey, T.W., Turse, D.E., Adams, L.G.: TRAC^{TM} Boom structural mechanics. In: 4th AIAA Spacecraft Structures Conference, 2017, pp. 1–13 (2017). https://doi.org/10.2514/6.2017-0171
3. Fernandez, J.M.: Bistable Collapsible Tubular Mast Boom. US Patent 201916503663 (2020)
4. Lee, A.J., Fernandez, J.M.: Bistable Deployable Composite Booms with Parabolic Cross-Sections, pp. 1–16 (1840)
5. Whited, D., Angle, N., Engebretson, R., Gargioni, G., Kenyon, S., Black, J.: Ut ProSat-1: a platform for testing lightweight deployable composite structures. In: 36th Annual Small Satellite Conference (2023)
6. Engebretson, R., Du, M., Mhadgut, D., Rhodes, T., Spinetta, A., Gargioni, G., Whited, D., Black, J.: A Hybrid Deployer Mechanism for Active and Passive Deployment of a Parabolic Bistable Tape Spring for Space Deployable Structures, pp. 1–9 (2022). https://doi.org/10.2514/6.2022-4338
7. Seffen, K.A., Pellegrino, S.: Deployment dynamics of Tape Springs. Proc. R. Soc. A: Math. Phys. Eng. Sci. **455**(1983), 1003–1048 (1999). https://doi.org/10.1098/rspa.1999.0347
8. Kwok, K., Pellegrino, S.: Folding, stowage, and deployment of viscoelastic tape springs. AIAA J. **51**(8), 1908–1918 (2013). https://doi.org/10.2514/1.J052269
9. Lee, A.J., Fernandez, J.M.: Mechanics of bistable two-shelled composite booms. In: AIAA Spacecraft Structures Conference, 2018, vol. 210019, pp. 1–24 (2018). https://doi.org/10.2514/6.2018-0938
10. Mallol, P., Mao, H., Tibert, G.: Experiments and simulations of the deployment of a bistable composite boom. J. Spacecr. Rocket. **55**(2), 292–302 (2018). https://doi.org/10.2514/1.A33906
11. Yao, Y., Ambruso, A., Fernandez, J.M., Bilén, S.G., Ning, X.: A Multifunctional Bistable Ultrathin Composite Boom for In-Space Monitoring of Deployment Dynamics, pp. 1–10. AIAA Scitech (2023). https://doi.org/10.2514/6.2023-2400
12. Mallol, P., Tibert, G.: Deployment modeling and experimental testing of a bi-stable composite boom for small satellites. In: 54th AIAA/ASME/ASCE/AHS/ASC Structures, Structural Dynamics, and Materials Conference, pp. 1–23 (2013). https://doi.org/10.2514/6.2013-1672
13. Greschik, G.: Marionette suspension in the testing of long light structures. In: Collection of Technical Papers – AIAA/ASME/ASCE/AHS/ASC Structures, Structural Dynamics and Materials Conference, vol. 2, pp. 1419–1430 (2007). https://doi.org/10.2514/6.2007-1821

Chapter 13
On the Behavior of Superimposed Orthogonal Structure-Borne Traveling Waves in Two-Dimensional Finite Surfaces

William C. Rogers and Mohammad I. Albakri

Abstract Wave-driven motion is a phenomenon that has been observed in nature as a method for propulsion. Earlier studies replicated these traveling waves in finite structures to propel the structures itself or particles across the surface of the structure. Two-mode excitation has been introduced as an effective method to generate steady-state structure-borne traveling waves (SBTW). Two-mode excitation generates SBTW in finite structures by superimposing two standing waves in a structure with a prescribed phase offset. While the generation of STBW for propulsion and particle motion has been a topic of study for some time, most research has examined SBTW propagating along a single axis.

This chapter expands on this method by using two pairs of actuators to simultaneously excite two SBTW orthogonal to one another. The superposition of these orthogonal waves results in a net SBTW that propagates in any desired direction. By controlling the direction of SBTW using only two pairs of actuators, an active surface could be made to drive motion in any direction without the need for a large number of actuators. It is shown that while the excitation frequency will determine the mode shapes that dominate the behavior of the SBTW, it is the geometry, boundary conditions, and the locations of actuators that will determine the possible combinations of SBTW that can be excited in the plate. It is found that adjusting the relative amplitude and phase between the two SBTW will influence the quality of the wave, in addition to affecting the overall direction of the superimposed SBTW. This motion is studied using simulations in a 2D Finite Element model that represents a plate using first-order shear deformation theory. The quality of the SBTW is calculated using a traveling index defined by the complex orthogonal decomposition of the wavefront. The direction of the wavefront in this study is interpreted by calculating a weighted average of the structural intensity (SI) field over the plate.

Keywords Traveling waves · Finite element · Two-mode excitation · Structural intensity · Two-dimensional traveling waves

13.1 Introduction

In nature traveling waves are used as a form of locomotion. This characteristic is seen on land in the case of snakes and snails, but also in the ocean in the case of rays or eels [1–3]. Traveling waves are a low-profile method of driving the motion of a structure using the structure itself. These traveling waves have been studied by researchers and have been replicated to generate wave-driven motion in cylinders, beams, and plates [4–7]. Previous research has examined wave propagation behavior in structures and their ability to drive particle motion on the surface of structures [8–10]. One method of generating wave-driven motion uses an active sink which requires two actuators. One actuator would be used to initiate a wave on a structure and another actuator to cancel out the propagating wave by working as an active sink [11]. Another method uses an actuator to excite a traveling wave and another to match the impedance of the beam. In this case, the beam to behaves as though it were semi-infinite with a wave being initiated and passing through the boundary without reflection [12]. The method used in this work is referred to as two-mode excitation. This method uses the modal properties of the structure to

W. C. Rogers (✉)
Fusion of Analysis, Simulation, and Testing Laboratory (FAST), Department of Mechanical Engineering, Texas A&M University, College Station, TX, USA
e-mail: wcrogers42@tamu.edu

M. I. Albakri
Smart Materials and Structures Laboratory (SMSL), Department of Mechanical Engineering, Texas A&M University, Education City, Doha, Qatar

B. J. Dilworth et al. (eds.), *Topics in Modal Analysis & Parameter Identification, Volume 9*, Conference Proceedings of the Society for Experimental Mechanics Series, https://doi.org/10.1007/978-3-031-34942-3_13

generate a SBTW by exciting the structure with two actuators excited at the same frequency but with a phase offset between them [13–17]. While the individual excitation of the actuators will generate standing waves, selecting a suitable phase offset will cause the operating deflection shapes of the standing waves to become complex, and this is what drives the traveling wave behavior. If the phase offset between actuators is non-ideal or the excitation frequency is a natural frequency of the structure, then two-mode excitation will produce either a combination of standing and traveling waves or pure standing waves. To find the ideal phase offset, metrics have been developed that look at the complexity of the wave motion. This Method utilizes a circle-fit approach where the SBTW is plotted on the complex plane and fitted to a circle using the Fourier transform [14, 18]. On the complex plane, pure traveling waves will appear as a circle, a combination of standing and traveling waves will appear as an ellipse, and a pure standing wave will appear as a line or a disordered scattered set of points. For 2D SBTW, a method referred to as complex orthogonal decomposition (COD) can be used to evaluate the quality without the need for a line fit [19]. Feeny's COD compares the real and imaginary parts of the complex mode that contributes to the wave motion over time. Musgrave presented a procedure for the generation of high-quality 2D SBTW in finite plates [17]. The focus of this work was concentrated on the generation of high-quality SBTW, but this work was focused on exciting only one SBTW. Later work by Musgrave showed empirically that superimposing the excitation conditions related to two separate SBTW will generate a SBTW that is the superposition of the constituent SBTW [20]. Rogers noted that waves described by COD as high quality can have inconsistent quality in local regions on the surface of the plate and showed that the quality of SBTW in local regions can be improved by superimposing SBTW [21].

While earlier work has shown several methods for the generation of SBTW that are suited for wave-driven motion, controlling wave propagation direction has not yet been investigated. This work examines the potential for combining SBTW to drive wave motion in a prescribed direction. The SBTW behavior is examined using a finite element model that has been validated experimentally in previous work by Musgrave [17]. The direction of wave propagation is a difficult metric to define for these superimposed cases and for different applications such as driving particle motion or propulsion, the operating force that would drive motion will be different. For particle motion applications, the trajectory of the particle would be dependent on the motion of the plate in the region where the particle is located. When a SBTW is used to drive the motion of a plate suspended in a fluid, the overall waveform would need to be under consideration to determine the trajectory of the plate. A method of approximating the direction of wave propagation using a single constant value would be useful in predicting the trajectory of a plate suspended in fluid. Calculation of a single constant value representing the propagation direction of a SBTW requires a compromise. Information will be lost in averaging over time and space, but this is necessary to condense the overall wave motion into a single constant. The direction of wave propagation has been approximated using a heuristic method, wherein a weighted average of the SI field over the plate is used. In the literature, SI is typically used to examine the wave flow based on the direction of energy propagation in a structure to study wave localization in plates [22–26]. This work uses SI as a tool to determine the overall direction of wave propagation, using the magnitude of the SI to determine the weight of the SI vectors. This is important because the direction of wave propagation is a local phenomenon, which can appear to change over time. By using the SI, the direction the overall waveform can be determined without potential error that can arise from attempting to determine the direction visually.

13.2 Background

In this section, the model and boundary conditions for this work will be described. Following this, the methods for defining the quality of the SBTW using COD and the direction of the SBTW with SI will be described.

13.2.1 Finite Element Model and Boundary Conditions

The finite element model for this work approximates a thin plate using first-order shear deformation theory. The piezo-actuators are assumed to be perfectly bonded on the surface of the plate and are included in the model using classical lamination theory, ignoring bending-extensional coupling. The model used in this work has been validated in previous work by Musgrave. For a full derivation of the model, interested readers are directed to [17]. Fixed boundary conditions are used in this study because this focuses the energy of the wave to the middle of the plate. A free boundary will cause large deflections away from the center of the plate and reduce the ability for the wave propagation to be adjusted. Malladi noted that when all boundaries of the plate are free then waves can be generated that rotate around the edges of the plate [15]. While this wave behavior would be useful for driving the motion of a plate suspended in fluid, this behavior would not be as useful for particle motion applications where a larger active area is more useful. Fixed boundary conditions are also more convenient for the

weighted average SI method to be representative of the wave propagation behavior. A square plate is used because of the convenient nodal line locations. This is explained in detail in Sect. 2.3. Figure 13.1 shows the spatially averaged frequency response function (FRF) of the plate and the mode shapes associated with the natural frequencies of the plate. Mode 4 does not have a peak in the FRF because both pairs of actuators lie on nodal lines of this mode. The regions ($R1$, $R2$, ..., $R5$) shown in Fig. 13.1 are bounded by the natural frequencies. SBTW generated using frequencies within each region will have the same mode shapes making up the SBTW, but different frequencies will have different optimal phase offsets between actuators [17]. The excitation used in this study will use an excitation frequency $f = 225.8$ Hz. The primary mode shapes that are excited when the x and y SBTW are excited separately are modes 2 and 5 for the x-SBTW and modes 3 and 5 for the y-SBTW. When both pairs of actuators are excited, the mode shapes that are combined are modes 2 and 6 for the x-SBTW and modes 3 and 6 for the y-SBTW. This change is due to the peaks in mode 5 that are out of phase, leading it to be canceled out when both actuator pairs are excited.

13.2.2 Complex Orthogonal Decomposition

The excitation frequency used for the individual SBTW have been identified using complex orthogonal decomposition (COD), which was developed by Feeny and was first used to evaluate the quality of 2D SBTW by Musgrave [19, 27]. The reader is referred to [16, 19, 27] for procedures related to identifying high-quality SBTW using COD. COD quantifies the quality of a traveling wave by comparing the real and complex parts of the first complex eigenvector of a complex correlation matrix that is developed using the time history of the SBTW. This complex eigenvector is used to calculate a traveling index, T_i. A traveling index $T_i \approx 1$ is indicative of a pure traveling wave, while $T_i \approx 0$ is indicative of a pure standing wave. Any value of $0 < T_i < 1$ corresponds to a combination of standing and traveling waves. The traveling index is included in Table 13.1 for each of the cases under study.

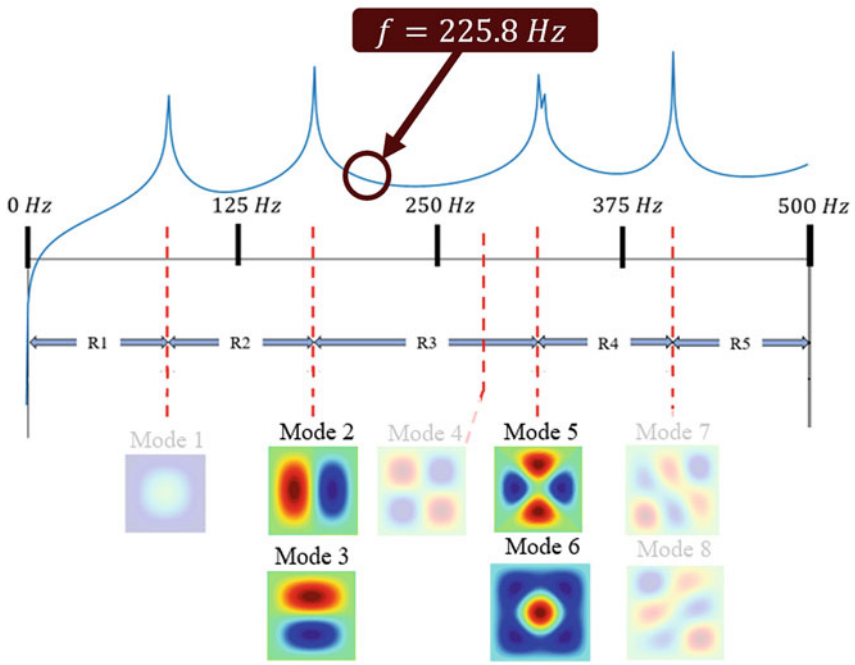

Fig. 13.1 Spatially averaged FRF for the plate with the dominant mode shapes of the SBTW in this study highlighted

Table 13.1 Excitation conditions for the cases

Case	λ_x	ϕ_A [°]	$\overline{\theta}$ [°]	T_i
x-STBW	–	–	180	0.95
y-STBW	–	–	270	0.95
(1)	1	0	225	0.87
(2)	0.53	0	258.2	0.90
(3)	1	95	250.8	0.84

13.2.3 Relative Amplitude and Relative Phase

The equation of motion is defined for the k-th actuator in Eq. (13.1).

$$\boldsymbol{M}\ddot{\boldsymbol{z}}_k + \boldsymbol{K}\boldsymbol{z}_k = \boldsymbol{F}_k e^{j\omega t} \tag{13.1}$$

where M and K are the mass and stiffness matrices and d_k and F_k are the k-th displacement field and forcing vector where $k = 1, 2, 3, 4$. Assuming $z_k(t) = \boldsymbol{d}_k e^{j\omega t}$, the operating deflection shapes $\boldsymbol{d}_k$ is used to define the SBTW in Eqs. (13.2) and (13.3).

$$z_y(t) = \left(\boldsymbol{d}_1 + \boldsymbol{d}_2 e^{j\phi_y}\right) e^{j\omega_y t} \tag{13.2}$$

$$z_x(t) = \left(\boldsymbol{d}_3 + \boldsymbol{d}_4 e^{j\phi_x}\right) e^{j\omega_x t} \tag{13.3}$$

Where ϕ_x and ϕ_y are phase offsets between actuators within each pair. The actuators corresponding to the $\boldsymbol{d}_k$'s are identified in Fig. 13.2. The vectors z_y and z_x are the y and x propagating SBTW, respectively. In the next section, the SI will require the out-of-plane velocity. This is calculated as the time derivative of Eqs. (13.2) and (13.3) and is given in (13.4) and (13.5).

$$\boldsymbol{v}_y(t) = j\omega_y \left(\boldsymbol{d}_1 + \boldsymbol{d}_2 e^{j\phi_y}\right) e^{j\omega_y t} \tag{13.4}$$

$$\boldsymbol{v}_x(t) = j\omega_x \left(\boldsymbol{d}_3 + \boldsymbol{d}_4 e^{j\phi_x}\right) e^{j\omega_x t} \tag{13.5}$$

The direction of wave propagation can be influenced by the excitation frequencies, the relative amplitude of the two SBTWs, and the relative phase between the two SBTWs. Adjusting the excitation frequencies (ω_x, ω_y) will change what mode shapes of the plate will dominate the individual SBTW. An excitation frequency ω_x can be selected such that nodal lines of its most dominant mode shapes align with the positions of the actuators associated with the y-SBTW. Additionally, the excitation frequency has been chosen such that the dominant mode shapes of the SBTW propagating in the x direction have nodal lines along the horizontal and vertical midlines of the plate. This allows the actuators acting in the y direction to drive an SBTW without affecting the x-SBTW behavior that the y actuators are unable to affect the SBTW in the x direction and vice versa. Square plate chosen for this study has symmetric dimensions along the two directions of wave travel; hence, the same SBTW can be excited orthogonal to one another. For all three cases considered in this study, the excitation frequencies

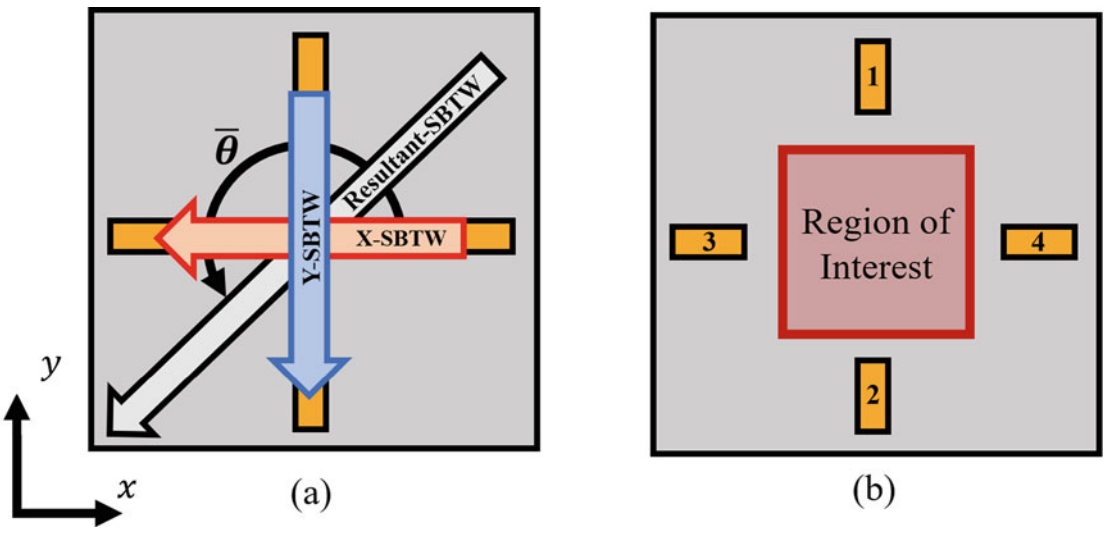

Fig. 13.2 (**a**) Directions of the SBTW and the definition of $\bar{\theta}$, (**b**) Region of interest defined on the plate

will be the same, and the analysis will be focused on the effect of the relative amplitude and phase. Table 13.1 shows the cases of relative amplitude and phase considered in this study. The excitation conditions of each of the actuators will have $f_x = f_y = 225.8\ Hz$ and $\phi_x = \phi_y = 50.56°$. The relative amplitude can be thought of physically as adjusting the relative peak voltage used to excite the pairs of actuators. The relative amplitude will be adjusted with a scalar factor $\lambda_x \in [0, 1]$. Because the geometry and SBTW in the examples presented here are symmetrical, adjusting the relative amplitude of the x and y SBTW would yield the same results.

While the relative amplitude affects the direction of wave propagation by directly influencing which of the constituent SBTW dominates the superposition, adjusting the phase between SBTW adjusts how the two superimposed SBTW interact over time. This additional phase offset is represented by ϕ_A. Including the scale factor λ_x and ϕ_A in the SBTW expressions is shown in Eq. (13.6). In the analysis of this work, the relative amplitude (λ_x) and phase (ϕ_A) will be adjusted separately.

$$\boldsymbol{v}_x(t) = j\omega_x\lambda_x\left(\boldsymbol{d}_3 + \boldsymbol{d}_4 e^{j\phi_x}\right)e^{j(\omega_x t+\phi_A)} \tag{13.6}$$

13.2.4 Structural Intensity

One of the problems associated with superimposed orthogonal SBTW is the difficulty of determining the overall direction of wave propagation. Often the superimposed orthogonal SBTW propagation behavior is intricate, and the direction of propagation behavior appears to change over time depending on the predominant mode shapes and the phase offset between the consultant SBTW. In the interest of describing the direction of wave propagation with a single direction, a heuristic method using a weighted temporal and spatial average of the SI has been developed. SI has been used in previous research to study the behavior of wave propagation and how the energy flows through a structure. SI is a vector that shows the direction of energy flow in a structure over time [22–26]. Based on this, the SI is calculated at M locations within the region of interest on the plate. To give a visual representation of the wave propagation with a single image, the SI will be averaged over a period T. Equation (13.7) is the definition of the i-th component of the SI at the m-th point on the plate.

$$[I_i(t)]_m = -\frac{1}{2}\sum_{l=1}^{3}[\sigma_{il}(t)v_l(x_m, y_m, t)]_m \tag{13.7}$$

Where σ_{il} and v_l are the il-th component of the stress tensor and the l-th component of the velocity, respectively. To account for the contribution, all four actuators (13.7) will be rewritten in terms of the model. To rewrite the equation in terms of the model, let the velocity of the k-th actuator at the m-th point on the plate be defined $(v_l(x_m, y_m, t))_k = (v_l(x_m, y_m))_k e^{j(\omega_k t+\phi_k)}$. The SI is then summed for the four actuators at the m-th point considered on the surface of the plate. The plate has been modeled as thin; hence, the SI in the z direction has been ignored. Structural intensity at the point (x_m, y_m) in the x direction is given in Eq. (13.8) and in the y direction is given in Eq. (13.9).

$$I_x(x_m, y_m, t) = -\frac{1}{2}\sum_{k=1}^{4}\sum_{l=1}^{3}(\sigma_{xl})_k(v_l(x_m, y_m))_k e^{j(\omega_k t+\phi_k)} \tag{13.8}$$

$$I_y(x_m, y_m, t) = -\frac{1}{2}\sum_{k=1}^{4}\sum_{l=1}^{3}\left(\sigma_{yl}\right)_k(v_l(x_m, y_m))_k e^{j(\omega_k t+\phi_k)} \tag{13.9}$$

To get the temporal average of the SI, Eqs. (13.8) and (13.9) are average for N points, which account for two periods of excitation. The temporal average renditions of Eqs. (13.8) and (13.9) are written in Eqs. (13.10) and (13.11), respectively.

$$[I_{xt}]_m = \sum_{i=1}^{N}\mathrm{Re}\left[\frac{[I_x\ (t_i)]_m}{N}\right] \tag{13.10}$$

$$\left[I_{yt}\right]_m = \sum_{i=1}^{N}\mathrm{Re}\left[\frac{\left[I_y\ (t_i)\right]_m}{N}\right] \tag{13.11}$$

The SI field of a plate generated with these SBTW will often have regions (see Fig. 13.4) where the direction of the SI does not appear to follow the direction of wave propagation based on visual inspection. To prevent these outlier SI vectors

from corrupting the average SI, the spatial average will be weighted by the magnitude of the SI at these locations. For this calculation, the magnitude of the SI at the m-th point is calculated in Eq. (13.12). The spatially weighted average of the SI in the x and y directions is then calculated in Eqs. (13.13) and (13.14), respectively. The approximate average direction of wave propagation is then defined as the angle between $\overline{I}_x$ and $\overline{I}_y$ in Eq. (13.15).

$$|I|_m = \left((I_{xt})^2{}_m + \left(I_{yt}\right)^2{}_m \right)^{1/2} \tag{13.12}$$

$$\overline{I}_x = \frac{\sum_{m=1}^{M} (|I|_m I_{xt})}{M \sum_{m=1}^{M} |I|_m} \tag{13.13}$$

$$\overline{I}_y = \frac{\sum_{m=1}^{M} (|I|_k I_{xt})}{M \sum_{m=1}^{M} |I|_m} \tag{13.14}$$

$$\overline{\theta} = \tan^{-1}\left(\frac{\overline{I}_y}{\overline{I}_x}\right) \tag{13.15}$$

The directions of the SBTW without adjustment of the relative amplitude or phase are shown in Fig. 13.2a. The region where the SI field is calculated is shown in Fig. 13.2b. The direction of SI for the average is only considered for a region in the middle of the plate that does not include the actuators. This is because for fixed boundary conditions most of the energy of the SBTW will be focused in the middle of the plate; hence, the behavior in these outer regions is not of interest. Additionally, the direction of have propagation around the piezo-actuators and the fixed edges of the SBTW are ignored because SI values in these regions can influence the $\overline{\theta}$ value and cause it to deviate from the value at the middle of the plate, which is of primary interest. By defining this spatially and temporally averaged SI, a single direction can be used to approximately describe the direction of wave propagation in these complex overall waveforms. Because this method describes the direction of propagation using a single angle, this method is only useful when examining SBTW that appear to propagate in a single direction. For example, in [15, 17] it was shown that a single SBTW can be generated such that the wave propagates in opposite directions on either side of the nodal lines. In such cases, this $\overline{\theta}$ value would fail to accurately represent the direction of wave propagation. This method is best used for cases where the overall SBTW is expected to propagate in a single direction; otherwise, the structure needs to be divided into separate regions where a local propagation direction is calculated. The time-averaged SI can be shown as a vector field over the surface of the plate.

13.3 Analysis and Discussion

13.3.1 Case 1

When the two SBTWs are combined with equal amplitude and phase, the resulting waveform propagates at an angle exactly between the constituent SBTW. Figure 13.3c shows the wave propagation behavior over fourths of a period. This SBTW has been chosen to show that when the constituent SBTW has been carefully selected, the resulting SBTW appears to propagate in a direction that is different from the propagation direction of the separate SBTW. The weighted SI average is applied to the superimposed SBTW. The approximate direction of wave propagation is calculated to be $\overline{\theta}_1 = 225°$, which shows the time-averaged SI field over the plate. The complete SI field is plotted, but only the SI values within the boxed region were used in the calculation of the weighted SI average. In the SI field, the magnitude of the SI has been normalized by the maximum value so that values appearing more in red are larger while values in blue correspond to smaller values.

The SI values have been normalized because in presenting this plot only the relative values are important in understanding the energy flow in the SBTW. The plot of the SI shows that there are many regions in the SI field where the magnitude of the SI is small, and the direction of SI appears to be spreading outward radially (circled in black dotted lines). These are the regions where the amplitude of the wave is small. The SI magnitude in these regions is notably small; hence, the contribution to $\overline{\theta}$ is low. From Fig. 13.3c, we can surmise that the SBTW's overall propagation direction is accurately represented by $\overline{\theta}$. It is worth noting that the SI field shown in Fig. 13.4c is symmetrical along the diagonal path that the SBTW travels, but not along the diagonal perpendicular to the propagation direction. This is related to the phase offset between pairs of actuators

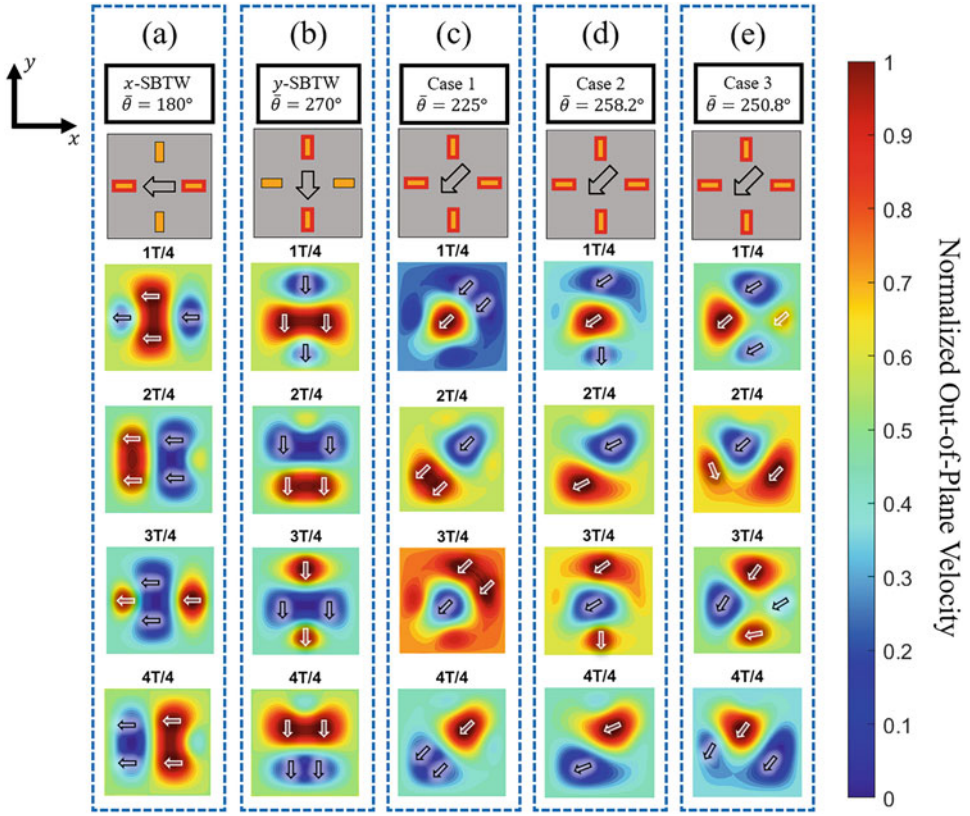

Fig. 13.3 Wave propagation patterns for (**a**) *x*-SBTW, (**b**) *y*-SBTW, (**c**) Case 1, (**d**) Case 2, (**e**) Case 3

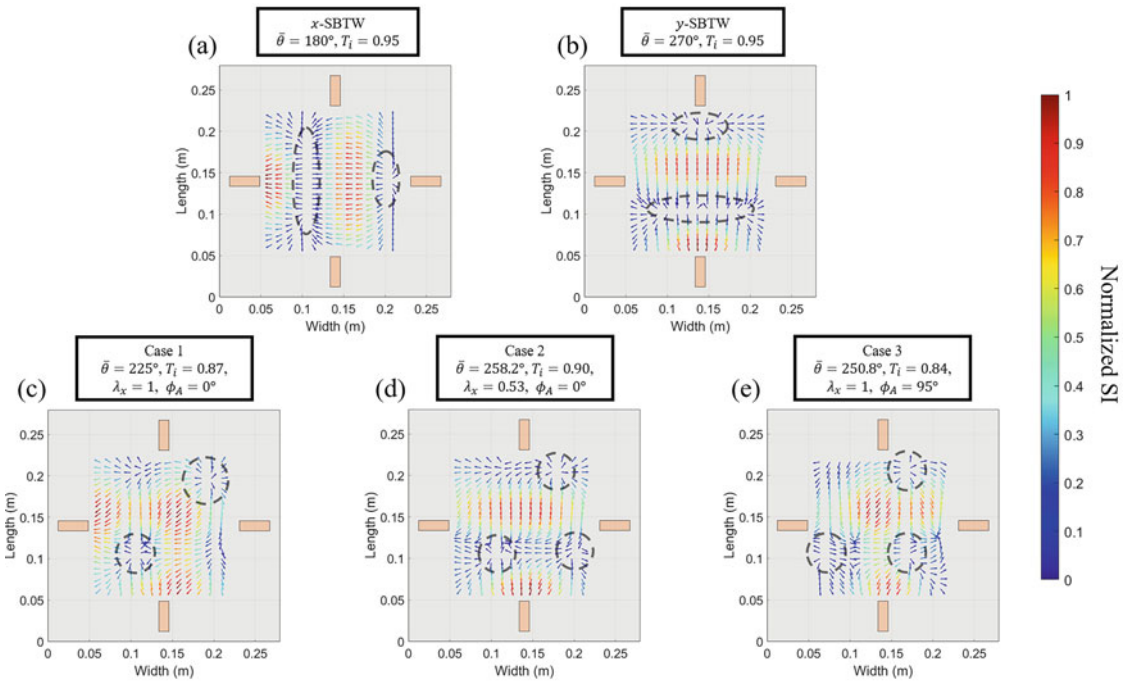

Fig. 13.4 SI field individual for (**a**) x-SBTW, (**b**) y-SBTW, (**c**) Case 1, (**d**) Case 2, (**e**) Case 3. Regions where SI appears to emanate from are circled

and the excitation frequency. We can also note that mode 5 does not contribute to the Case 1 motion because the actuator pairs are in phase, leading to the SBTW being dominated by modes 2, 3, and 6.

The traveling index of the SBTW for this case is $T_i = 0.87$,which indicates a slightly larger standing wave component to the SBTW than the individual x and y SBTWs that have $T_i = 0.95$. This lower quality is likely due to the change in the contributing mode shapes to the overall SBTW. As is the case with all excitation configurations, excluding excitation frequencies equal to natural frequencies, there are some phase offsets $\phi_x = \phi_x'$ and $\phi_y = \phi_y'$ that would optimize the quality of the Case 1 SBTW. Adjusting the phase offset to optimize the quality of Case 1, would then change the quality of the constituent SBTW. For this reason, the phase offset between actuators has been left at $\phi_x = \phi_y = 50.56°$ for all three cases despite the reduction in quality.

13.3.2 Case 2

Case 1 is encouraging for wave-driven motion applications because of the consistent wave propagation direction and the intuitive way that the SBTW combines. Case 2 examines the effect of adjusting the relative amplitude, $\lambda_x = 0.53$, on the wave propagation direction. Figure 13.3d shows the wave propagation behavior over fourths of a period for Case 2. The constituent SBTWs have not changed leading to the Case 2 superimposed SBTW to still be composed of the same mode shapes, but due to the change in relative amplitude, they have not combined symmetrically. Figure 13.4d shows the time-averaged SI field and the approximate propagation direction for this case is $\overline{\theta} = 258.2°$. The traveling index for Case 2 is $T_i = 0.90$ which is slightly higher than Case 1. This is expected because by reducing the magnitude of the x-SBTW, the y-SBTW is able to contribute more to the overall waveform. Figure 13.4d shows that the direction of the wave motion is more consistent in direction although the regions with the greatest amplitude are similar in size. The SI field in Fig. 13.4d has three locations where wave motion appears to emanate from, while Fig. 13.4c shows that the SI field for Case 1 only has two of these emanation points. When the STBW is redirected by adjusting the relative amplitude (λ_x), a new emanation point is introduced which in effect pushes the wave into the prescribed direction.

13.3.3 Case 3

While the resulting propagation behavior of Case 2 is intuitive, Case 3 shows that the relative phase between the SBTW can also affect the overall propagation direction of the waveform. Figure 13.3e shows the wave propagation behavior of the SBTW when $\phi_A = 95°$. While in the other cases, the dominant mode shapes in the SBTW were modes 2, 3, and 6, the adjusted phase of the x-SBTW has caused mode 5 to be more prominent in the overall waveform. While it is not initially clear from Fig. 13.3e, the averaged SI field yields $\overline{\theta} = 250.8$. Figure 13.4e shows the time averages SI field, which is not as consistent as the SI fields shown in Fig. 13.4c, d. Because adjusting the phase offset introduces a timing lag between the constituent SBTW, the peaks of each SBTW coincide at contrasting times than when the pairs of actuators are in phase. This causes the maximum energy of the SBTW to occur while the SBTW is propagating in different directions depending on ϕ_A. The traveling index for this case is $T_i = 0.84$,which is the lowest of the cases considered here. The additional phase offset does not affect the x-SBTW's quality, but the superimposed case does have a slightly lower quality traveling wave. This low quality is from the additional phase offset introducing standing wave components to the overall SBTW by causing a disruptive interaction between the x and y SBTW. Figure 13.4e shows that the SI field like in Case 2 has three points that appear to function as sources.

13.4 Conclusion

This work has shown that the orthogonal SBTW can be superimposed to generate an overall SBTW that propagates in a different direction. A method for approximating the direction of complex waveforms using a weighted average of the SI field is presented. It was further shown that the propagation direction of these superimposed SBTW can be redirected by adjusting the relative amplitude or the relative phase of the constituent SBTW. With the propagation direction being adjusted by superposition, the motion is driven with only two pairs of actuators. This is more convenient than alternative methods where a large array of actuators would be needed to generate a SBTW to travel in each desired direction. This

work introduces an additional dimension to current wave-driven motion applications. Where previous work has focused on wave-driven motion along a single axis or rotational waves traveling along the boundaries of a structure, this is the first investigation into quantifying these two-dimensional traveling waves by defining a dominant direction of wave propagation in a complex traveling wave.

While the superposition of orthogonal SBTW shows promise as a method for generating controlled wave-driven motion in 2D, there are several factors in the SBTW combination that have not been considered in this work. The geometry of the plate and the boundary conditions will present more possibilities by introducing different mode shapes and introducing a new order of appearance for the mode shapes of the plate. Because of the vast potential of SBTW combinations possible, a set of metrics need to be developed to evaluate the effectiveness of SBTW combinations so that combinations can be compared. Additionally, it can be seen from the SI plots that the direction of the wave is not completely propagating in the approximate direction decided by the SI. This indicates a need for quantifying the accuracy of the approximate propagation direction. Metrics for comparing SBTW pairs and the quality of the approximate propagation direction will be investigated in future work.

References

1. Blevins, E.L., Lauder, G.V.: Rajiform locomotion: three-dimensional kinematics of the pectoral fin surface during swimming by freshwater stingray *Potamotrygon orbignyi*. J. Exp. Biol. **215**, jeb.068981 (2012). https://doi.org/10.1242/jeb.068981
2. Cui, Z., Gu, X., Li, K., Jiang, H.: CFD studies of the effects of waveform on swimming performance of Carangiform fish. Appl. Sci. **7**(2), 149 (2017). https://doi.org/10.3390/app7020149
3. Sfakiotakis, M., Lane, D.M., Davies, J.B.C.: Review of fish swimming modes for aquatic locomotion. IEEE J. Ocean. Eng. **24**(2), 237–252 (1999). https://doi.org/10.1109/48.757275
4. Gabai, R., Bucher, I.: Spatial and temporal excitation to generate traveling waves in structures. J. Appl. Mech. **77**(2), 021010 (2010). https://doi.org/10.1115/1.3176999
5. Hariri, H., Bernard, Y., Razek, A.: A traveling wave piezoelectric beam robot. Smart Mater. Struct. **23**(2), 025013 (2014). https://doi.org/10.1088/0964-1726/23/2/025013
6. Malladi, V.V.N.S., Albakri, M., Musgrave, P., Tarazaga, P.A.: Investigation of propulsive characteristics due to traveling waves in continuous finite media. In: Presented at the SPIE Smart Structures and Materials + Nondestructive Evaluation and Health Monitoring, p. 101620O, Portland (2017). https://doi.org/10.1117/12.2260156
7. Mace, B.R., Manconi, E.: Modelling wave propagation in two-dimensional structures using finite element analysis. J. Sound Vib. **318**(4–5), 884–902 (2008). https://doi.org/10.1016/j.jsv.2008.04.039
8. Viswarupachari, C., DasGupta, A., Pratik Khastgir, S.: Vibration induced directed transport of particles. J. Vib. Acoust. **134**(5), 051005 (2012). https://doi.org/10.1115/1.4006412
9. Fleishman, D., Asscher, Y., Urbakh, M.: Directed transport induced by asymmetric surface vibrations: making use of friction. J. Phys. Condens. Matter. **19**(9), 096004 (2007). https://doi.org/10.1088/0953-8984/19/9/096004
10. Daniel, S., Chaudhury, M.K., de Gennes, P.-G.: Vibration-actuated drop motion on surfaces for batch microfluidic processes. Langmuir. **21**(9), 4240–4248 (2005). https://doi.org/10.1021/la046886s
11. Tanaka, N., Kikushima, Y.: Active wave control of a flexible beam: proposition of the active sink method. JSME Int. J. Ser 3 Vib. Control Eng. Eng. Ind. **34**(2), 159–167 (1991). https://doi.org/10.1299/jsmec1988.34.159
12. Kuribayashi, M., Ueha, S., Mori, E.: Excitation conditions of flexural traveling waves for a reversible ultrasonic linear motor. J. Acoust. Soc. Am. **77**(4), 1431–1435 (1985). https://doi.org/10.1121/1.392037
13. Tomikawa, Y., Adachi, K., Hirata, H., Suzuki, T., Takano, T.: Excitation of a progressive wave in a flexurally vibrating transmission medium. Jpn. J. Appl. Phys. **29**(S1), 179 (1990). https://doi.org/10.7567/JJAPS.29S1.179
14. Mallidi, S., Inman, D.J., Kurdila, A.J., Philen, M.K., Embree, M.P.: Continual Traveling Waves in Finite Structures: Theory, Simulations, and Experiments, p. 204, Virginia Tech University, Blacksburg, Virgina (2016)
15. Malladi, V.V.S., Albakri, M., Tarazaga, P.A.: An experimental and theoretical study of two-dimensional traveling waves in plates. J. Intell. Mater. Syst. Struct. **28**(13), 1803–1815 (2017). https://doi.org/10.1177/1045389X16679284
16. Malladi, V.V.N.S., Avirovik, D., Priya, S., Tarazaga, P.: Characterization and representation of mechanical waves generated in piezo-electric augmented beams. Smart Mater. Struct. **24**(10), 105026 (2015). https://doi.org/10.1088/0964-1726/24/10/105026
17. Musgrave, P.F., Albakri, M.I., Tenney, C., Tarazaga, P.A.: Generating and tailoring Structure-Borne Traveling Waves on two-dimensional surfaces. J. Sound Vib. **480**, 115417 (2020). https://doi.org/10.1016/j.jsv.2020.115417
18. Bucher, I.: Estimating the ratio between travelling and standing vibration waves under non-stationary conditions. J. Sound Vib. **270**(1–2), 341–359 (2004). https://doi.org/10.1016/S0022-460X(03)00539-X
19. Feeny, B.F.: A complex orthogonal decomposition for wave motion analysis. J. Sound Vib. **310**(1–2), 77–90 (2008). https://doi.org/10.1016/j.jsv.2007.07.047
20. Musgrave, P.F., Malladi, V.V.N.S., Tarazaga, P.A.: Investigation into the superposition of multiple mode shape composed traveling waves. In: Presented at the SPIE Smart Structures and Materials + Nondestructive Evaluation and Health Monitoring, p. 1016408, Portland (2017). https://doi.org/10.1117/12.2260323
21. Rogers, W.C., Albakri, M.I.: Tailoring Structure-Borne Traveling Waves in Targeted Areas of a Two-Dimensional Plate for Particle Motion Applications, in *ASME 2021 Conference on Smart Materials, Adaptive Structures and Intelligent Systems*, Virtual, Online: American Society of Mechanical Engineers, p. V001T07A004 (2021). https://doi.org/10.1115/SMASIS2021-67804

22. Wang, C.Q., Ong, E.H., Qian, H., Guo, N.Q.: On the application of B-spline approximation in structural intensity measurement. J. Sound Vib. **290**(1–2), 508–518 (2006). https://doi.org/10.1016/j.jsv.2005.04.011
23. Pires, F., Muyshondt, P.G.G., Keustermans, W., Vanlanduit, S., Roozen, N.B., Dirckx, J.J.J.: Structural intensity analysis of flat plates based on digital stroboscopic holography measurements. J. Sound Vib. **428**, 168–178 (2018). https://doi.org/10.1016/j.jsv.2018.05.010
24. Gavric, L., Carlsson, U., Feng, L.: Measurement of structural intensity using a normal mode approach. J. Sound Vib. **206**(1), 87–101 (1997). https://doi.org/10.1006/jsvi.1997.1077
25. Pavić, G.: Measurement of structure borne wave intensity, part I: formulation of the methods. J. Sound Vib. **49**(2), 221–230 (1976). https://doi.org/10.1016/0022-460X(76)90498-3
26. Wang, Y., Du, J., Cheng, L.: Power flow and structural intensity analyses of Acoustic Black Hole beams. Mech. Syst. Signal Process. **131**, 538–553 (2019). https://doi.org/10.1016/j.ymssp.2019.06.004
27. Musgrave, P.F., Albakri, M.I., Phoenix, A.A.: Guidelines and procedure for tailoring high-performance, steady-state traveling waves for propulsion and solid-state motion. Smart Mater. Struct. **30**(2), 025013 (2021). https://doi.org/10.1088/1361-665X/abd3d7

Chapter 14
Comparative Assessment of Force Estimation in MIMO Tests

Odey Yousef, Fernando Moreu, and Arup Maji

Abstract Dynamic testing of systems is most realistic of real-world conditions when multiple input and multiple output (MIMO) techniques are used. To replicate measured environmental conditions, a series of desired outputs on the system must be realized by inverting the frequency response functions (FRF) matrix for force estimation. Depending on the number of inputs and outputs, the type and number of solutions can vary significantly. Depending on the objective of the test, defining the target response can also vary, such as matching accelerations, stresses, or strains at various locations. In MIMO testing, both the auto spectra and cross spectra of the outputs affect the auto spectra of the inputs. Defining the most relevant outputs and the optimal input spectra is an ongoing challenge and has attracted recent attention.

This research evaluates the errors associated with these variables on a linear multi-story frame fixed at the base. Three inputs are provided uniaxially with the use of suspended electrodynamic shakers, and up to nine output locations are instrumented with accelerometers. Results of tests are analyzed to guide improved MIMO testing.

Keywords MIMO · Vibration testing · Structural dynamics

14.1 Introduction

Recreating target responses on a test article is desirable to understand its behavior under other conditions, such as different boundary conditions, loads, or changes in the system. To do so, the system frequency response functions (FRFs) must be inverted using the Moore-Penrose pseudoinverse. The FRF matrix may then be used for force estimation, then iterated on using measured error to the reference spectrum. This process is described in Fig. 14.1. This work deals with the quantification of system uncertainty and its implications on the convergence of errors in the iterative force estimation. Challenges are encountered throughout the entire process, with some listed here.

- System identification may be uncertain, and measured FRFs may deviate from the true FRFs in terms of magnitude, phase, and frequency [1].
- Filling in the reference matrix is difficult. Popular methods include extreme inputs/outputs and independent drives [2]. The cross terms are selected to optimize an objective according to each method.
- Generating a random multivariate time series from a cross-spectral density is known to be imprecise [3].
- FRF matrix inversion is strongly dependent on system ID and choice of regularization parameters [4].

Sandia National Laboratories is a multimission laboratory managed and operated by National Technology & Engineering Solutions of Sandia, LLC, a wholly owned subsidiary of Honeywell International Inc., for the U.S. Department of Energy's National Nuclear Security Administration under contract DE-NA0003525.

This chapter describes objective technical results and analysis. Any subjective views or opinions that might be expressed in this chapter do not necessarily represent the views of the U.S. Department of Energy or the United States Government.

O. Yousef (✉) · F. Moreu
Department of Civil, Construction, and Environmental Engineering, University of New Mexico, Albuquerque, NM, USA
e-mail: yousefo@unm.edu; fmoreu@unm.edu

A. Maji
Sandia National Laboratories, Albuquerque, NM, USA

B. J. Dilworth et al. (eds.), *Topics in Modal Analysis & Parameter Identification, Volume 9*, Conference Proceedings of the Society for Experimental Mechanics Series, https://doi.org/10.1007/978-3-031-34942-3_14

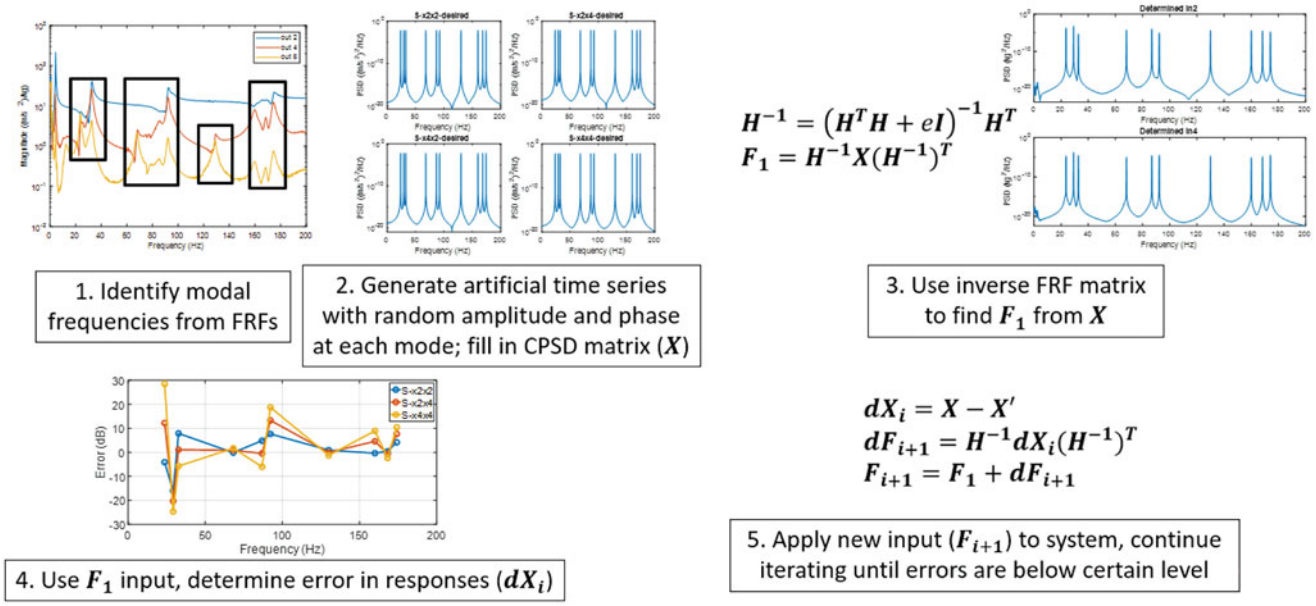

Fig. 14.1 FRF inversion and iterative force estimation process

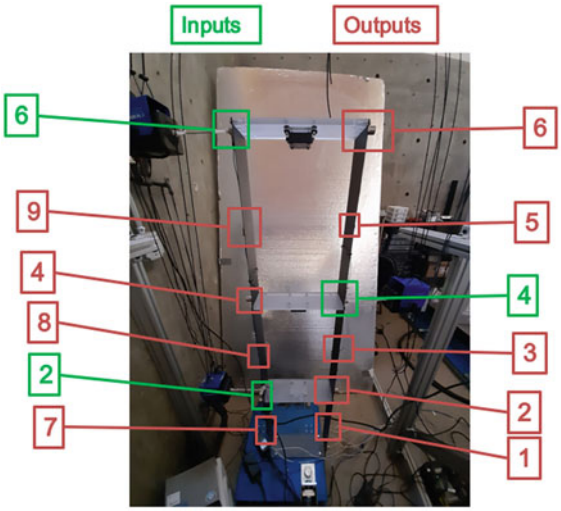

Fig. 14.2 System and instrumentation

Table 14.1 Absolute average 3 standard deviations as a percentage of mean of FRFs, 20–200 Hz

	Out1	Out2	Out3	Out4
In2 magnitude	9.63%	5.84%	11.20%	3.66%
In2 phase	0.63%	0.29%	18.64%	0.95%
In4 magnitude	27.56%	15.69%	59.56%	100.78%
In4 phase	1.79%	1.64%	1.30%	2.08%

14.2 Analysis

The system analyzed is shown in Fig. 14.2. It is a 3-story frame fixed at its base with inputs applied at each floor level with suspended electrodynamic shakers. A total of 9 accelerometers are distributed throughout the structure, although not all are used for target response replication.

Test-to-test variation in FRF magnitude and phase was quantified as 3 standard deviations of the mean, based off of multiple tests for system ID. Average values from 20 to 200 Hz for input locations 2 and 4 with outputs locations 1–4 are given in Table 14.1.

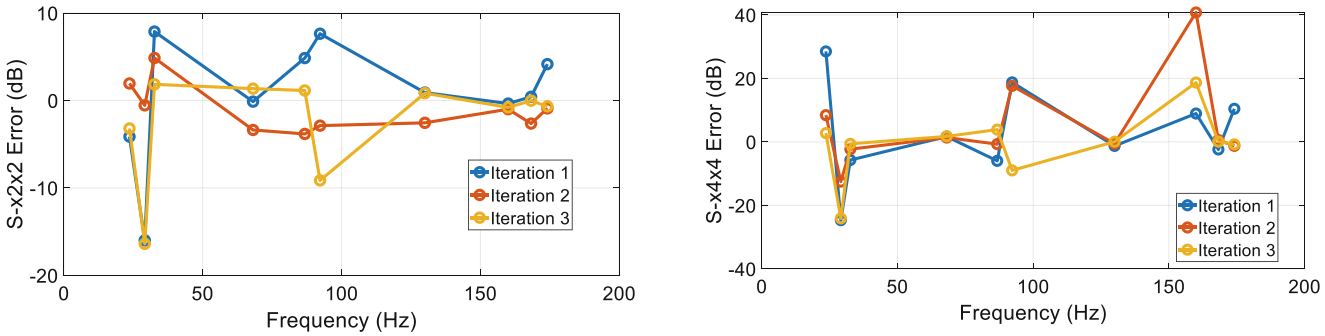

Fig. 14.3 Autospectral density (ASD) error over 3 iterations. Left: Location 2. Right: Location 4

The process in Fig. 14.1 was followed to generate the desired reference spectrum for a 2 × 2 system (inputs and outputs at locations 2 and 4), with frequency content at each modal frequency. FRF matrix inversion was done with a Tikhonov regularization parameter of 10^{-5}. Three iterations were conducted to attempt error convergence. Results are shown in Fig. 14.3 with the ASD error at locations 2 and 4.

14.3 Conclusion

Convergence of the 2 × 2 case was effective at certain modes, but not over the entire spectrum. Test-to-test variation in FRFs was found to be at a maximum at antiresonances, but also higher at certain resonances than others. Closely spaced, highly local modes were observed due to the symmetry of the structure, and their interaction may cause some error.

Further research should be conducted to assess the issues with test-to-test variation in modal analysis, namely, mode shapes and damping factors. Continued work will quantify the uncertainty and attribute associated errors for the remaining steps in the inverse process and a greater variety in the number of input and output locations used in the system.

Acknowledgments The financial support of this research is provided by Sandia National Laboratories Grant 1985700, under Project Manager Dr. John Pott, Manager, Environments Engineering, to whom the authors are grateful.

Conflict of Interest The authors declare that they have no conflict of interest.

References

1. Woodall, J., Hossain, M., Maji, A., Pott, J., Moreu, F.: Exploring uncertainties in multi-input-multi-output (MIMO) testing. In: Special Topics in Structural Dynamics & Experimental Techniques, vol. 5, pp. 197–204. Springer, Cham (2021)
2. D'Elia, G., Musella, U., Mucchi, E., Guillaume, P., Peeters, B.: Analyses of drives power reduction techniques for multi-axis random vibration control tests. Mech. Syst. Signal Process. **135**, 106395 (2020)
3. Smallwood, D.O.: Generation of stationary non-Gaussian time histories with a specified cross-spectral density. Shock Vib. **4**(5–6), 361–377 (1997)
4. Maji, A.: Evaluation of MIMO input derivations and their physical context. In: Topics in Modal Analysis & Testing, vol. 9, pp. 217–226. Springer. https://doi.org/10.1007/978-3-319-74700-2_23

Chapter 15
Online Implementation of the Local Eigenvalue Modification Procedure for High-Rate Model Assimilation

Alexander B. Vereen, Emmanuel A. Ogunniyi, Austin R. J. Downey, Jacob Dodson, Adriane G. Moura, and Jason D. Bakos

Abstract High-rate structural health monitoring of active structures operating in high-rate dynamic environments empowers the execution of preventative behavior in response to structural degradation or external stimuli. Examples of structures operating in high-rate dynamic environments include hypersonic vehicles, space crafts, and ballistic packages. The effective selection of reactive actions to be taken in real time requires an up-to-date model of the structure's state. Importantly, the short timescale of relevance to these structures means that the model must be continuously updated with a time step of 1 millisecond or less. However, traditional frequency-based methods for updating the finite element model online require solving the generalized eigenvalue problem, which becomes more complex as the number of nodes or FEA model increases, thereby increasing computational time. In this work, the local eigenvalue modification procedure is put forward to accelerate the extraction of natural frequencies from finite element models updated online. The local eigenvalue modification procedure works by precomputing the eigenvalue solution to a reference state of the system and then computes the single (i.e., local) change in the modal domain from the reference state to the current state online. The modal domain update in the local eigenvalue modification procedure bypasses the general eigenvalue problem, which is the most expensive computational step. For the online implementation of the state estimation, the Dynamic Reproduction of Projectiles in Ballistic Environments for Advanced Research testbed is used. The testbed allows for the controlled movement of a pinned condition attached to an otherwise free cantilever beam. In previous studies, the testbed has been used with the generalized eigenvalue solver in a frequency-based model assimilation approach to infer the most likely position of the pinned condition (i.e., state of the structure). This work reports the effectivity of the local eigenvalue modification procedure compared to the generalized eigenvalue solution of the system for inference accuracy while varying the nodes dedicated to the analysis. The optimal efficiency of the system's approach is explored for the testbed-based health assessments. Timing results and effects of sensor noise on the system are discussed in detail.

Keywords High rate · Modal analysis · FEA · Eigenvalue · LEMP

A. B. Vereen (✉) · E. A. Ogunniyi
Department of Mechanical Engineering, University of South Carolina, Columbia, SC, USA
e-mail: avereen@email.sc.edu; OGUNNIYI@email.sc.edu

A. R. J. Downey
Department of Mechanical Engineering, University of South Carolina, Columbia, SC, USA

Department of Civil and Environmental Engineering, University of South Carolina, Columbia, SC, USA
e-mail: austindowney@sc.edu; jacob.dodson.2@us.af.mil

J. Dodson
Air Force Research Laboratory, Munitions Directorate, Eglin Air Force Base, Eglin, FL, USA
e-mail: adriane.moura.ctr@us.af.mil

A. G. Moura
Applied Research Associates, Emerald Coast Division, Niceville, FL, USA
e-mail: JBAKOS@cse.sc.edu

J. D. Bakos
Department of Computer Science and Engineering, University of South Carolina, Columbia, SC, USA

B. J. Dilworth et al. (eds.), *Topics in Modal Analysis & Parameter Identification, Volume 9*, Conference Proceedings of the Society for Experimental Mechanics Series, https://doi.org/10.1007/978-3-031-34942-3_15

15.1 Introduction

Active control can provide critical intervention to reduce or negate damage to a structure in situ; however, it requires the acquisition of the state of the structure as a prerequisite to the decision and implementation of an intervention [1]. In high-rate systems, estimating the structure's state through modal analysis allows sparse networks of sensors to be used to attain the natural frequencies of the structure [2]. The natural frequencies of a structure can be helpful despite the non-unique description of the structure given its shape and boundary conditions. Acquiring the natural frequencies of a structure and then proposing an explanatory model of the system can ascertain the system's state using sparse sensor networks [2, 3].

Candidate models are evaluated for their natural frequencies by solving the eigenvalue problem of the proposed models. State acquisition by way of modal analysis and candidate model testing is broken into three major tasks [2]. The first task entails system excitation followed by hardware acquisition and digitization. Second, frequency analysis is performed. Third, candidate models are proposed and evaluated for their similarity to the observed frequency response. The most time-consuming procedure is solving the eigenvalue problem for the frequencies of a candidate model. This step scales in $O(n^3)$ time by traditional mode extraction methods [4–7].

For high-rate state estimation, attaining estimations of the system's state in less than one millisecond can enable responsive interventions in active aerospace structures [1]. Modal analysis can be used in all structural geometries; however, the complexity required for a minimally accurate solution can increase the required computations. The Dynamic Reproduction of Projectiles in Ballistic Environments for Advanced Research (DROPBEAR) testbed is used to explore a functional implementation of a high-rate dynamic system. The testbed allows for the controlled movement of a pinned condition attached to an otherwise free cantilever beam. This system is useful as it can be modeled as a 1D finite element formulation and can instate a repeatable change to its boundary condition.

A myriad of known algorithms can attain the eigenvalue solution, each responding in a worst case of $O(N^3)$, where N is the finite element mesh size, and a best case of $O(N^2)$ [6]. However, in the high-rate state estimation problem, there is only a requirement to retrieve the eigenvalues of a proposed model. The Local Eigenvalue Modification Procedure (LEMP) avoids incurring the operational complexity of a mode extraction algorithm by obtaining the eigenvalues of a modified state through modification of known eigenvalues and eigenvectors of the system [3, 8]. The central proposal of this work is to avoid solving the eigenvalue problem online by approximating the eigenvalues from a reference state and a single added change to the state. In a timing investigation of LEMP's online update step vs. a general eigen solution method for the eigenvalue problem, the implementation of LEMP provided an approximately 100× reduction in time. Furthermore, it showed operational complexity to be directly proportional to the mesh size of the finite element model. In an implementation of the algorithm in hardware, the speed of LEMP was shown to reliably provide good estimates of the state while achieving the 1 millisecond time target, which was out of reach for the mode extraction algorithms. The merit of this work is in exploring and quantifying the result of a direct algorithmic comparison between LEMP and traditional mode extraction methods and showing the full state estimation implementation loop in hardware and the resulting time per estimate.

15.2 Background

For the online implementation of the state estimation, the Dynamic Reproduction of Projectiles in Ballistic Environments for Advanced Research (DROPBEAR) testbed is used. The testbed allows for the controlled movement of a pinned condition attached to an otherwise free cantilever beam and is shown in Fig. 15.1, and specifications for the system are provided in

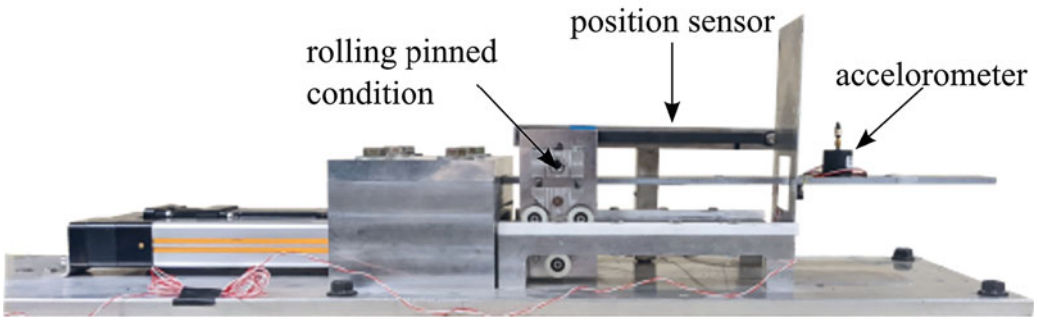

Fig. 15.1 Dynamic Reproduction of Projectiles in Ballistic Environments for Advanced Research (DROPBEAR) testbed

Table 15.1 Specifications for the configuration of the DROPBEAR testbed used in this work

Beam properties		Actuator properties	
Beam length	501 mm	Roller travel	84 mm
Beam width	51 mm	Roller max velocity	3.32 m/s
Beam thickness	6.66 mm	Roller start position	57.73 mm
Beam Young's modulus	209.5 GPa		
Beam density	7900 $\frac{\text{kg}}{\text{m}^3}$		

Table 15.1. The sensors utilized in the Hardware in the Loop (HIL) implementations were the Honeywell position sensor (model SPS-L075-HALS) and a PCB Piezotronics accelerometer (model 393B05) at the end of the beam. Data from the trial recordings on the beam were played back for all HIL tests in this study to eliminate as much potential noise from the physical process allowing a fair comparison between algorithms. Computations were carried out using an eight-core Intel® Xeon® E5-2618L v3 processor mounted in a PXIe-8880 manufactured by National Instruments processing acceleration data digitized using a 14-bit ADC module (PXI-6133) mounted in a common PXI chassis (PXIe-1082).

For this work, a previously developed 1D FEA model describes the beam, and localized sub-sampling was implemented [3]. Subsampling allows a reduction in the number of scenarios tested at each estimation. Instead of testing every location along the beam each time step as a likely position, sampling a normal distribution around the last known position is used. The selected samples in the distribution are referred to as particles in this work. Subsampling within the scenario space is a necessary trade-off for speed in high-rate state estimation. For a 1D model of the beam with a mesh size of N, convergence to the most likely position pinned location to exactly one step would take solving for the frequencies of that beam in N models. Subsampling at least the current position, a minimally forward position, and a minimally backward position guarantee convergence in at most N steps testing three models per step. If, however, the pinned condition is local to its last known location, as is a safe assumption in tracking problems, then, on average, the convergence will only take the difference of minimal steps between them. Allowing for a large reduction in calculations to achieve convergence quicker than the overhead of testing each of N points each step would allow.

Modal analysis requires solving the eigenvalue problem; however, in the general case, a matrix inversion is required where the operational complexity of solving the inversion grows proportionally as a square of the size of the matrices. For example, an Euler–Bernoulli beam formulation is $(2N)^2$, where N is the number of nodes in the beam. LEMP avoids solving the eigenvalue problem and instead updates the solution as a change to the modal space representation [8]. The algorithmic implementation of LEMP for the online configuration used in this work is shown in Fig. 15.2. As a result, solving for the frequencies of each model becomes a linear time problem in the state estimation. Therefore, a 1-dimensional system only requires three solutions to the eigenvalue problem, and a P-dimensional tracking requires only $2P$ orthogonal models as a minimum subsample. In terms of big O notation, LEMP allows a time complexity of $O(PN)$ P being the dimensionality and the N the size of the mesh of describing the structure while solving the eigenvalue problem incurs a time complexity of $O(PN^3)$. The authors have also previously demonstrated the viability of the LEMP algorithm [3] and a corresponding real-time solver [9].

15.3 Analysis

Two timing studies were implemented. First, a timing study on an algorithm in each simulation step is carried out. LEMP was used to update a base cantilever beam model to a beam with a pinned condition, in comparison to the general eigen solution, both solving the same system. This was done for mesh sizes 20 through 200 at each multiple of 10, 1000 times per unique combination of parameters. The second study was on the full online implementation using the HIL setup. The parameters varied over this study were the mesh size, the number of particles solved for, and the FFT window size. Increasing the window size allows more frequency resolution at the cost of less time resolution and more computational time. Increasing the mesh size allows for more positional resolution resulting in increased computational time. Similarly, sampling more particles allows quicker convergence to a given position at the cost of computational time.

The first timing study shows that LEMP managed to be consistently solved in less time than the general eigen solution algorithm, as shown in Fig. 15.3. Note that the y-axis is in $\log_{10}$. The diagrams from the timing study show the variations in timing that are an artifact of implementing the proposed method on a non-real-time operating system. This variation comes from the Windows operating system having to que operations alongside running of the LEMP and a LabVIEW native generalized eigenvalue solver. In Table 15.2, it is shown in detail that for this first algorithmic study that a 100× reduction in

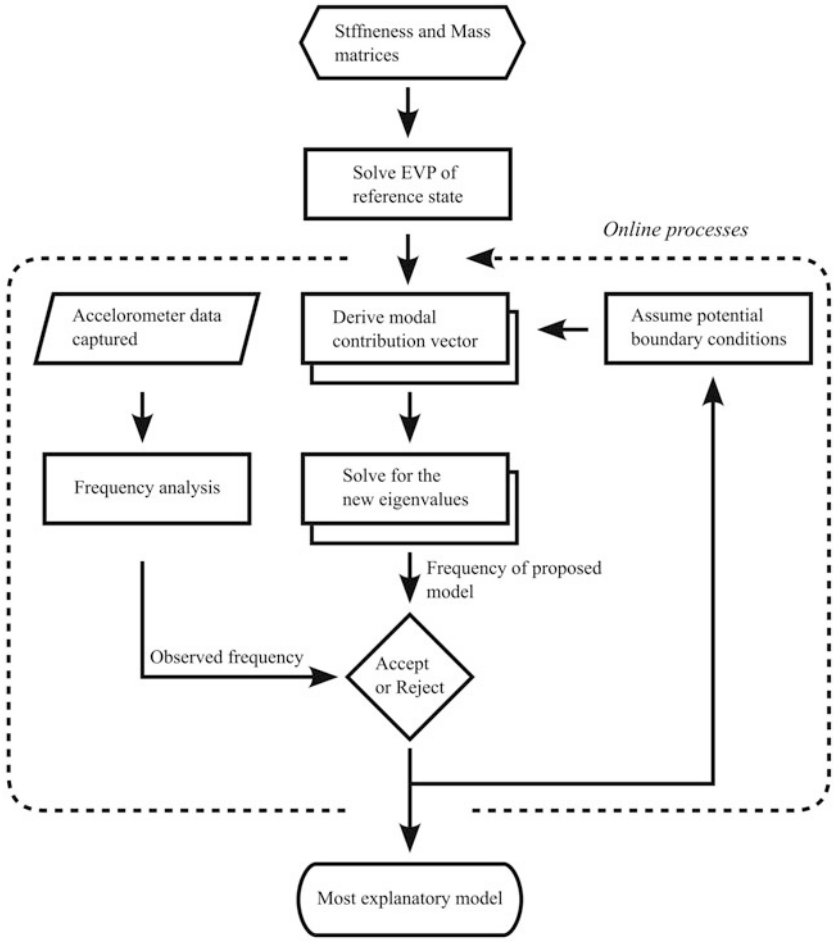

Fig. 15.2 Data flow for the online LEMP algorithm used in this work

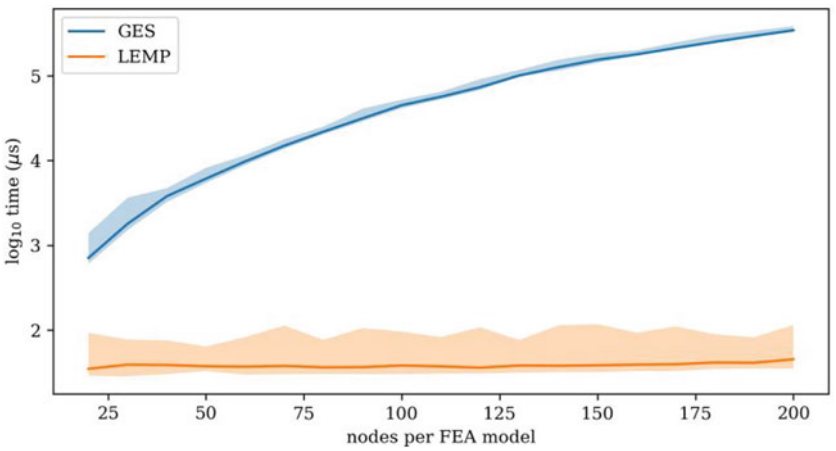

Fig. 15.3 Time execution vs mesh size vs nodes for Local Eigenvalue Modification Procedure (LEMP) and General Eigenvalue Solver (GES)

Table 15.2 Selected timing values extracted from Fig. 15.3

	Nodes				
	40	80	120	160	200
LEMP (μs)	38.90	36.51	36.16	39.26	45.39
GES (μs)	3804	21,974	73,593	179,314	344,519

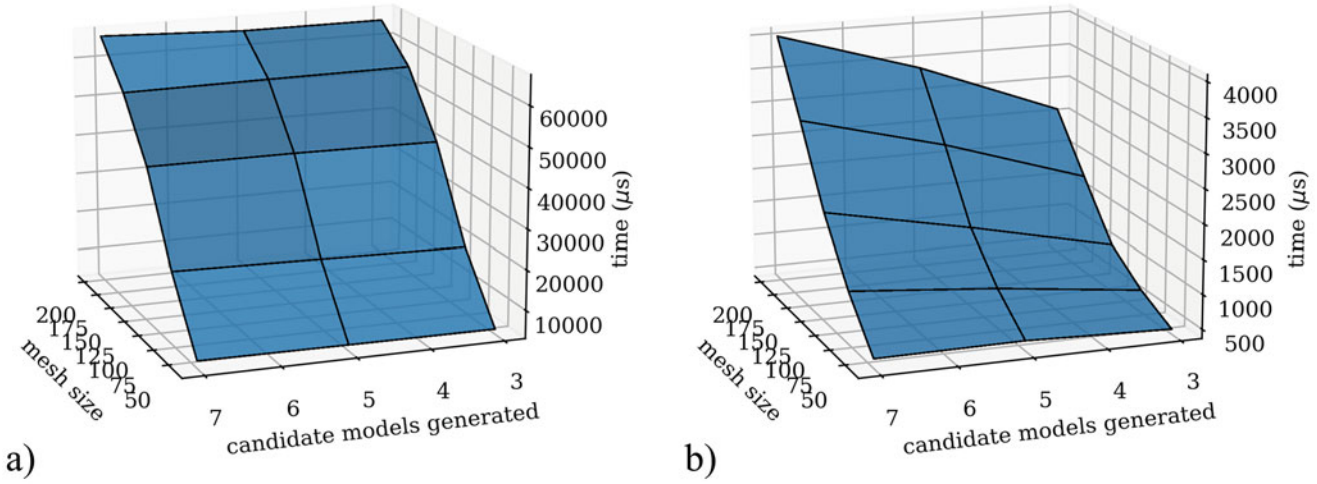

Fig. 15.4 Time for FEA execution versus nodes for (**a**) GES and (**b**) LEMP each using an FFT window of 5000 points (0.02 s)

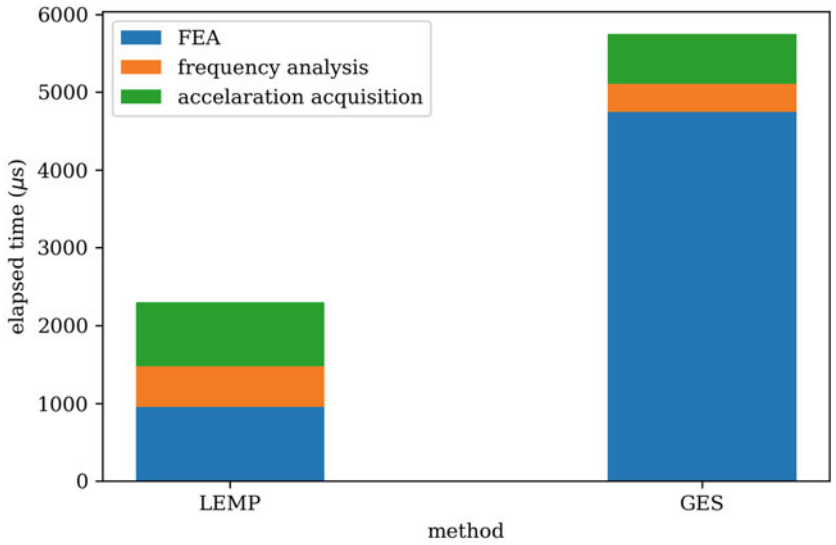

Fig. 15.5 Time execution for Local Eigenvalue Modification Procedure (LEMP) vs a General Eigenvalue Solver (GES)

execution time was found a 40-node mesh size on average over 1000 trials. Notably, this gap in performance grows with the mesh size.

In the second timing study, the HIL implementation is investigated. Figure 15.4 shows the mean completion times for the LEMP algorithm over relevant parameters, namely the model size and the number of candidate models tested. In addition, it is observed that there are large time savings to be had using the LEMP model updating method. With the hardware in the loop, it was found that the implementation using LEMP required considerably more time than the pure algorithmic study pointing to there being room for optimization in the implementation to reach the same performance.

Figure 15.5 shows the time allocation of each step of the processes for a configuration with a mesh size of 40, testing 5 models, and an FFT window of length 5000 data points (0.02 s). The time saving provided by LEMP is seen in the time required to solve the FEA analysis. It is seen that with LEMP solving the FEA model for the considered problem requires a similar time to that for the data acquisition and frequency analysis steps.

Results for the second timing study focused are on HIL implementation are reported in Figs. 15.6 and 15.7. Figure 15.6 reports a typical time response obtained using the LEMP model updating method compared to the measured boundary condition change instated by the pin. For these results, an FEA model with 80 nodes and an FFT window size of 15000 (0.06 s) was utilized.

Figure 15.7 reports performance metrics for the HIL implementation of LEMP as a function of mesh size and FFT window length. The Time Response Assurance Criterion (TRAC) is used to gauge the similarity between time traces by comparing

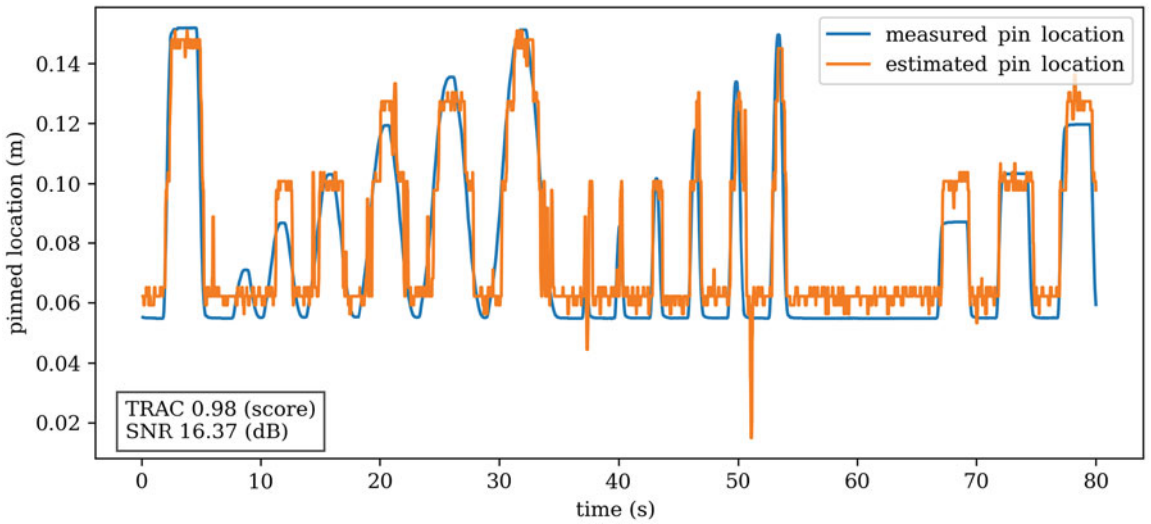

Fig. 15.6 HIL position tracking implementation using LEMP with a mesh size of 120 nodes, testing 5 candidate models, and using an FFT window size of 5000 points (0.02 s)

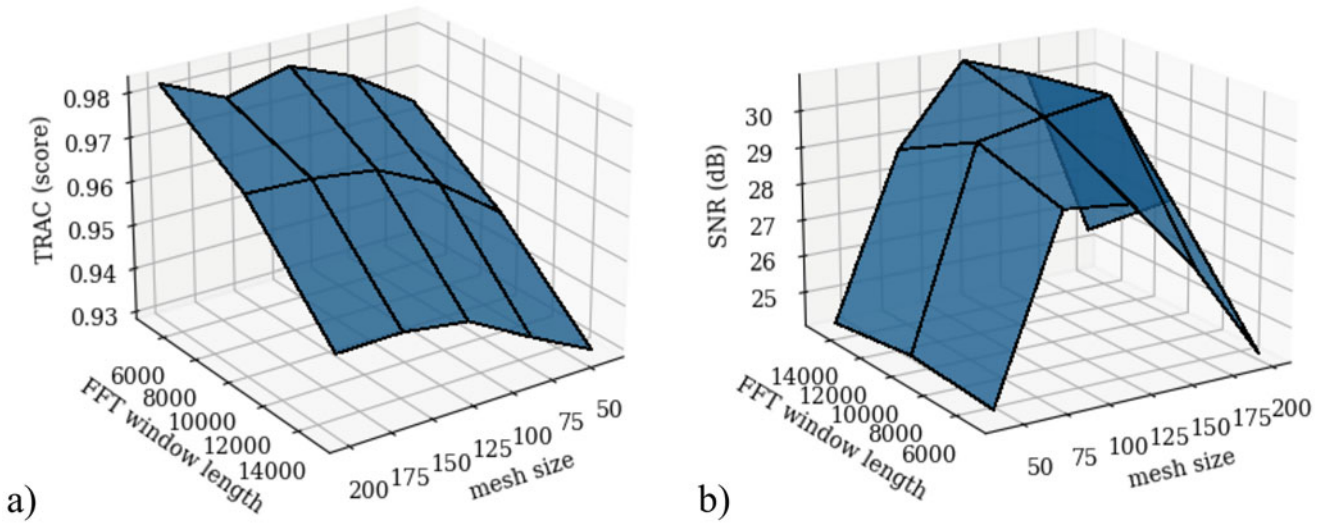

Fig. 15.7 Performance metrics for HIL implementation shown in (**a**) TRAC and (**b**) the SNR of LEMP as a function of mesh size and FFT window length

the numerical error and time delay of each estimation on a scale from 0 to 1 [10]. To expand, TRAC shows how well the signals replicate each other, disregarding the amplitude of each signal. As TRAC is sensitive to changes in phase, it shows the penalty for extending the FFT window size, indicating a phase lag incurred in the state estimation. Due to LEMP's high speed, latency from the mesh size was shown to have a limited impact on the TRAC score in comparison. The Signal-to-Noise Ratio (SNR) performance metric shows a trade-off between mesh size and the FFT window length. While obtaining the optimal mesh size was found to be an important parameter to consider, the relative improvement from 24 to 31 dB shows that the LEMP solver is still useful even at less-than-optimal parameter selections.

15.4 Conclusion

In this work, the local eigenvalue modification procedure (LEMP) is demonstrated to accelerate the extraction of natural frequencies from finite element models updated online with real-time constraints on real-time hardware. LEMP's linear time cost makes it ideal for further extensions and studies into high-rate state estimations. For the online implementation of the

state estimation, the Dynamic Reproduction of Projectiles in Ballistic Environments for Advanced Research (DROPBEAR) testbed is used. Timing reports for LEMP in comparison to the generalized eigenvalue method were reported showing speedups of 10× in the HIL implementation. This is shown to not necessarily be a ceiling for the approach as in the algorithmic study the for meshes of the same size a 100× speed up was shown. Performance metrics for the HIL implementation of LEMP were also discussed in detail. In future work, the algorithm will be extended to a working prototype of a 2D implementation of this system.

Acknowledgments This material is based upon work supported by the United States Air Force through the Air Force Research Lab Summer Faculty Fellowship Program and by the Air Force Office of Scientific Research (AFOSR) through award no. FA9550- 21-1-0083. This work is also partly supported by the National Science Foundation Grant numbers 1850012, 1956071, and 1937535. The support of these agencies is gratefully acknowledged. Any opinions, findings, and conclusions, or recommendations expressed in this material are those of the authors and do not necessarily reflect the views of the National Science Foundation or the United States Air Force.

References

1. Dodson, J., Downey, A., Laflamme, S., Todd, M.D., Moura, A.G., Wang, Y., Mao, Z., Avitabile, P., Blasch, E.: High-rate structural health monitoring and prognostics: an overview. Data Sci. Eng. **9**, 213–217 (2022)
2. Downey, A., Hong, J., Dodson, J., Carroll, M., Scheppegrell, J.: Millisecond model updating for structures experiencing unmodeled high-rate dynamic events. Mech. Syst. Signal Process. **138**, 106551 (2020)
3. Hong, S.H., Drnek, C., Downey, A., Wang, Y., Dodson, J.: Real-time model updating algorithm for structures experiencing high-rate dynamic events. In: ASME 2020 Conference on Smart Materials, Adaptive Structures and Intelligent Systems. American Society of Mechanical Engineers (2020)
4. Feeny, B.F., Farooq, U.: A nonsymmetric state-variable decomposition for modal analysis. J. Sound Vib. **310**(4-5), 792–800 (2008)
5. Dhillon, I.: A new o (n^2) algorithm for the symmetric tridiagonal eigenvalue. Eigenvector Problem (1997)
6. Coakley, E.S., Rokhlin, V.: A fast divide-and-conquer algorithm for computing the spectra of real symmetric tridiagonal matrices. Appl. Comput. Harmon. Anal. **34**(3), 379–414 (2013)
7. Imachi, H., Hoshi, T.: Hybrid numerical solvers for massively parallel eigenvalue computations and their benchmark with electronic structure calculations. J. Inform. Process. **24**(1), 164–172 (2016)
8. Avitabile, P.: Twenty years of structural dynamic modification-a review. Sound Vib. **37**(1), 14–27 (2003)
9. Ogunniyi, E.A., Downey, A.R.J. Jr., Bakos, J.D.: Development of a real-time solver for the local eigenvalue modification procedure. In: Sensors and Smart Structures Technologies for Civil, Mechanical, and Aerospace Systems 2022, vol. 12046, pp. 253–267. SPIE (2022)
10. Avitabile, P., Pingle, P.: Prediction of full field dynamic strain from limited sets of measured data. Shock Vib. **19**(5), 765–785 (2012)

Chapter 16
Modal Correlation Is Required to Reduce Uncertainty in Shock Analysis and Testing

Monty Kennedy and Jason Blough

Abstract The average aerospace structural analyst is very familiar with performing various types of dynamics analysis (sine vibration, random vibration, transient) but much less familiar with dealing with shock analysis defined by SRS (shock response spectrum) dealing with very high acceleration levels (1000–2000 g's) and high frequency content (10 kHz). Likewise, the average aerospace engineer performs a lot of sine and random vibration testing at the system and subsystem levels and feedback from those tests are readily compared to analysis predictions.

In contrast, typically very little SRS-related analysis and subsequent shock testing is performed either at the system or subsystem level and rarely would shock analysis predictions be compared with shock test results. Typically going into sine and random vibration test, a structural analyst will know expected responses at accelerometer locations. For a typical shock test, many times a dynamics engineer is a bystander and watches the test lab use their shock test method to achieve the SRS tolerance levels in each axis and typically no shock analysis predictions of the shock test setup are performed.

Sine and random vibration tests at the system level are common, but shock testing at the system level is much rarer (sometimes the customer will waive the system shock test requirement – that cannot happen!) as it is much more difficult test to perform. Shock loads are much more complex and more difficult to analyze than sine and random vibration loads and thus more engineering is required to get more accurate predictions. Thus, to reduce uncertainty in shock analysis predictions:

- It is essential that shock testing at the system level become as common as sine and random vibration testing and much less difficult to do.
- It is necessary to feed back the shock testing responses at the system level into a system-level shock FEM such that reasonable correlation is achieved between shock testing and shock analysis predictions accounting for structural dynamics effects, shock propagation, and shock attenuation with distance from the shock source and through joints.

Keywords Shock · SRS · FEM · Testing · Correlation

16.1 Introduction

The purpose of this presentation is to provide clear guidelines on the process of correlating FEM to shock test results. To accomplish this objective will require more shock analysis and testing knowledge a commitment and more attention to address shock analysis and testing throughout the development program. Then shock predictions and proposed testing at the system level and subsystem levels can be routinely addressed at CDR (Critical Design Review) and thus it will become readily apparent to the customer that shock analysis and testing is being properly addressed. This type of engineering detail required for shock analysis and testing is currently not being done – and is one of the reasons why there is still significantly more uncertainty in shock analysis predictions than sine and random analysis predictions.

M. Kennedy (✉)
MK Engineering and Michigan Tech University, Houghton, MI, USA
e-mail: montyk@mtu.edu

J. Blough
Department of Mechanical Engineering/Engineering Mechanics, Michigan Technological University, Houghton, MI, USA

B. J. Dilworth et al. (eds.), *Topics in Modal Analysis & Parameter Identification, Volume 9*, Conference Proceedings of the Society for Experimental Mechanics Series, https://doi.org/10.1007/978-3-031-34942-3_16

16.2 Discussion

MTU has created a shock resonant plate (a shock fixture) for testing individual electronic boards. The shock testing results on this plate using a calibrated hammer will be used to calibrate this FE model shock predictions.

Siemens Simcenter 3D software will be used to perform the correlation, which is based upon both FRF (frequency response function) and modal correlation.

For this test, one triax accelerometer was mounted at the reference location and two uniaxial accelerometers were mounted on the outer edge. A Crystal Instrument CR-80X Spider 8 channel data acquisition system was used to acquire the test data. Various standard digital signal processing checks are made on the test data to verify the validity of the test data. Enough tap locations were used to capture the modal characteristics of this test setup to about 8 kHz. To do this, 43 tap locations on the shock resonant plate were used.

The procedure involved in correlation analysis is to import into Simcenter 3D the FEM and the FEM mode shapes and test tap and accelerometer locations and associated test mode shapes and FRFs from all of the tap locations.

For modal correlation, Simcenter 3D will then pair the FEM and test mode shapes and calculate MAC (modal assurance criteria) and frequency errors. Based upon selected allowable error criteria, the FEM can then be updated based upon the design variables selected and allowed to be adjusted within tolerance ranges for each variable. Simcenter 3D will then update the FEM, and then modal correlated shock predictions can be made and compared with uncorrelated shock predictions.

Similarly, FRF correlation can be performed and FRF amplitude and frequency errors associated with all modes of interest can be determined. However, Simcenter 3D only updates the FEM only based upon modal correlation.

Based upon both the modal and correlation results, it became immediately apparent that there the initial FEM did not match the test setup. Specifically, the Nastran glued interfaces between the strike plate and the round plate and the electronic board cavity and the round plate did not properly model these joints correctly. The other issue is with the ground springs, and they also were modified. So FEM adjustments were made and the modal and FRF correlation between FEM and test data were much closer. This allowed correlation up to a much higher frequency – up to 8 kHz in this case. In SRS the goal would be to get modal correlation to 10 kHz, but that involves a lot of modes, even for a simple shock subsystem like this MTU shock resonant plate, and thus difficult to do.

This presentation will present the FRF and modal correlation results, showing the effects of the correlation on the SRS over the entire frequency band from 100 to 10,000 Hz. This is done by converting shock transient response versus time predictions and creating a SRS from those time predictions. The goal is to stay within the ± 3 dB tolerance bands from 100 to 10,000 Hz of the tap test shock response at the reference accelerometer.

Modal and FRF correlation on a small shock subsystem like this MTU shock resonant plate will also be much easier than performing correlation at the system level, like an entire spacecraft. For such a system, there will be hundreds of modes involved to 10 kHz, and it will not be possible to correlate to that upper frequency. However, there should not be a need to since the spacecraft will act as a low pass filter for the higher frequencies thus spacecraft structural dynamic effects on shock responses will less than about 3 kHz.

FE models have significant limitations when performing shock transient analysis and can only be expected to provide accurate responses up to perhaps 1 kHz, which is typically where the SRS knee frequency is based upon many launch vehicle loads documents. However, this is probably acceptable since it is desirable to determine the structural dynamics effects of a base shock transient input that is synthesized from a SRS. Most of the significant structural dynamics effects will be less than 1 kHz and will allow shock margins to be determined for small parts, brittle parts, and electronics that are most vulnerable to shock transients that only last for about 20 ms.

This will also allow the user to define shock zones within a spacecraft that can be used to determine appropriate spacecraft subsystem shock levels. FE analysis does not take into account the shock energy dissipation that occurs from a shock pulse applied to the base of a spacecraft. Therefore, the resulting shock levels for the various shock zones will have to be modified by using the shock attenuation empirical curves that are used in the aerospace industry. In addition, the attenuation through joints needs to be accounted for. It is recommended that the ESA [1] and NASA [2] empirically derived attenuation rules be used with caution as there will be order of magnitude type errors at some frequencies.

The word “initially” is used because the goal would be to perform spacecraft shock level testing and feedback the results into the FEM such that the FEM shock analysis predictions match the spacecraft shock testing responses. If spacecraft shock testing is not possible, then a minimum tap testing should be done, which will provide invaluable test information that will help define shock zones.

16.3 Conclusion

If spacecraft level testing and FEM correlation become more commonplace, it is expected that the uncertainty associated with performing complex shock analysis will be significantly reduced. To reduce this uncertainty will require more engineering effort – much more than any other type of vibration analysis and testing. It will require more knowledge for the average aerospace engineer. Such knowledge is typically not obtained in any college vibration or structural dynamics class. Shock analysis and testing is a specialized field and is often overlooked or just briefly discussed in college curriculums. This is one of the reasons that shock predictions are typically met with much skepticism even today.

References

1. European Space Engineering Mechanical Shock Design and Verification Handbook (2015)
2. NASA-STD-7003A, Pyroshock Test Criteria for NASA Spacecraft, Payload, and Launch Vehicle Hardware (2011)

Chapter 17
Modal Analysis of a Time-Variable Ropeway System: Model Reduction and Vibration Instability Detection

Hugo Bécu, Claude-Henri Lamarque, and Alireza Ture Savadkoohi

Abstract Reliable, safe, and sustainable form of mobility is an important issue in their engineering designs. Ropeways have been used for century for different purposes: their advantages in terms of cost, footprint, and energy efficiency make it as one of the solutions to meet the need for urban mobility. Nevertheless, because of the presence of moving cables and the time-varying modification of the mass repartition and stiffness properties of the system, ropeways are sensitive to the effects of dynamic perturbation and self-sustaining oscillations. So far, the analytical models are generally restricted to a cable span between two supports and are too simple to account for different existing phenomena. From this observation, the present chapter proposes a dynamic analysis based on an original definition of the vibration modes of the ropeway considered in its entirety according to an analytical–numerical approach. The modes are defined for several successive positions of the vehicles along the cable established on a linearized dynamics around a nonlinear static equilibrium state, using an equivalent parametric vision of the modal evolution of the system. Then, a model reduction by projection on a mode identified as problematic for the vibratory behavior is conducted. From the results given by the calculation of the quasi-static evolutions, a Mathieu–Hill type equation with a parametric excitation is obtained. A stability analysis of the reduced model is carried out in order to identify design rules that allow to avoid unstable operating zones likely to generate strong vibrations.

Keywords Cable · Multi-body · Ropeway · Dynamics · Parametric excitation

17.1 Introduction

The first step to approach the modelling of a cable system is to know which level of point of view to adopt to address the problem. There are several possible approaches to represent the cable. On the one hand, by going into a level of detailed considerations of interaction between each part of the cable with a model which accounts for the influence of contact between the strands and the friction. On the other hand, by adopting a more macroscopic point of view of the cable at the scale of a cable span and considering it as a line that reduces each section to a point.

In the case of cable transport systems, a global point of view is suitable to represent the system in its entirety given the scales involved. Many authors have approached the cable as a one-dimensional curvilinear medium, bathed in a 3D physical space, to study its static and dynamic equilibria. One of the particularities of cables is that deformed configuration under the effect of a loading is not initially known. A geometrical nonlinear problem must therefore be treated, which can be done analytically with the catenary equations [1] in the specific case of a homogeneous loading. On the other hand and for more generality on the nature of the external load, finite element methods are problematic given the poor numerical conditioning [2]. The vibration modes can be obtained in an analytical form under certain assumptions neglecting the effects of large deflection and the influence of longitudinal dynamic motion with respect to horizontal displacement [3].

The bibliography dedicated to ropeway mechanics modelling and simulation is more limited. In France, the technical publication from the beginning of the twentieth century are from Cretin [4] and Rebuffel [5], following by Lehanneur [6]

H.Bécu (✉)
Tribology and System Dynamics Laboratory, École nationale des travaux publics de l'État, Lyon, France

Design Office Department, DCSA, Grenoble & Chamonix, Chamonix, France
e-mail: hugo.becu@gadz.org

C.-H. Lamarque · A. T. Savadkoohi
Tribology and System Dynamics Laboratory, École nationale des travaux publics de l'État, Lyon, France
e-mail: claude.lamarque@entpe.fr; alireza.turesavadkoohi@entpe.fr

B. J. Dilworth et al. (eds.), *Topics in Modal Analysis & Parameter Identification, Volume 9*, Conference Proceedings of the Society for Experimental Mechanics Series, https://doi.org/10.1007/978-3-031-34942-3_17

Fig. 17.1 A picture of aerial tramway: mobile and fixed cables, vehicle, and tower (photo: Doppelmayr website)

and Goirand [7] who have published technical materials using analytical and approximate methods to treat static equilibrium. At the same time, other authors published works mainly focused on cable statics [8, 9]. More recently, the advent of numerical methods has allowed us to build numerical model of ropeway for statics and transient simulation [10, 11].

The models generally encountered in the state of the art are restricted to the study of a portion of cable alone, with a coupling with a suspended mass [12]. However, the static and dynamic model of a cable loop with suspended masses and contact to intermediate supports, pulleys, driving, and tensioning device is not studied. The main issues in modelling cable transportation systems arise from the following characteristics (see Fig. 17.1):

- Multi-body: cable is in interaction with its supports at towers and end stations via contact interfaces (saddle, pulley, roller battery) and vehicles via grip or rolling carriage [13].
- Multi-physics: mechanical behavior of the cable line and its components is coupled with electromechanical devices controlling cable movement (electrical motor and kinematic chain regulation, hydraulic tensioning regulation [14]).
- Multi-scale: cable span can range more than a kilometer while contacts are realized on lengths of the order of a meter [15].
- Flexible body: cable is a flexible body changing its form according to the loading and which has nonlinear geometrical behavior.
- Time-variant: cable loop and vehicles attached to it are moving, the mass and stiffness properties of the system are therefore time-dependent.

Thus, there is a need to model the entire cable loop as well as its interaction with vehicles, intermediate towers, and end stations to perform dynamic calculations that take into account the nonlinear and time-varying nature of the system. The objective is to understand the dynamic behavior of the steady-state movement and provide a tool able to predict strong vibrations according to parameters to be optimized.

17.2 Assembly of the Multi-body System Model

System modelling consists in defining working hypotheses for each of the elements that make up the system and then establishing an assembly strategy to couple each of the parts together (see Fig. 17.2). The cable is considered as a homogeneous medium with constant properties along it: linear mass μ, section A, and Young's modulus E. A curvilinear vision is adopted: the cable is condensed into a line described by curvilinear abscissa S and a local frame $(\underline{t}, \underline{n}, \underline{e}_z)$ with only tension T neglecting flexural stiffness and torsion effects (Fig. 17.3). A hyper-elastic behavior law is chosen to tackle with statics elongation in finite displacement,

$$T(S) = EA\hat{\varepsilon}(S) \tag{17.1}$$

with $\hat{\varepsilon}$ the Green–Lagrange strain measure, while a linear elastic one is retained in the dynamic framework involving ε the linearized Green–Lagrange strain measure. The initial length of the cable loop L_0 is given as an input in the model.

Under such assumptions, the balance of a cable defined by its position vector $\underline{X}(S, t)$ for each $(S, t) \in [0, L_0] \times [0, +\infty[$ provides

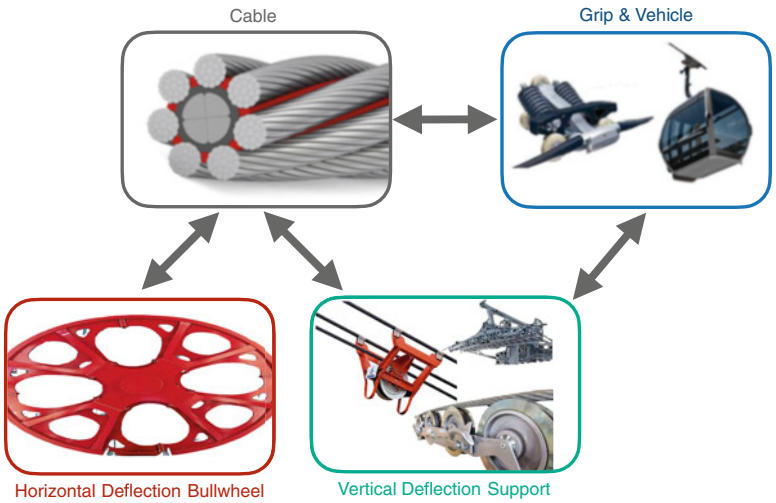

Fig. 17.2 Interactions between each mechanical part of a ropeway

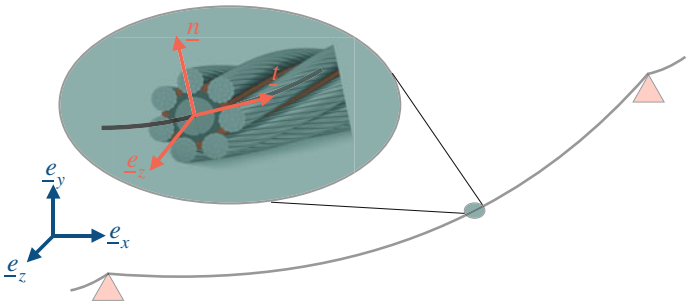

Fig. 17.3 Cable model with local frame $(\underline{t}, \underline{n}, \underline{e}_z)$

$$\frac{\mathrm{d}}{\mathrm{d}S}\left(T(S,t)\frac{\mathrm{d}}{\mathrm{d}S}\underline{X}(S,t)\right) + \underline{f}(S,t) = \mu\frac{\partial^2\underline{X}(S,t)}{\partial t^2}, \tag{17.2}$$

where $\underline{T}(S,t) = T(S,t)\ \underline{t}$ is the tension vector and $\underline{f}$ the external linear load along the cable.

In the specific case of the static (time t independent) and uniform (space S independent) external load due to gravity $\underline{f} = -\mu g\ \underline{e}_y$, the resolution of Eq. (17.2) leads to catenary analytical solution for the cable shape $y(x)$ and the tension $T(x)$ depending on $x \in [x_A, x_B]$ Cartesian parameter given in the global frame $(\underline{e}_x, \underline{e}_y, \underline{e}_z)$,

$$y(x) = \tau\cosh\left(\frac{x}{\tau} + K_1\right) + K_2, \tag{17.3}$$

$$T(x) = \mu g\tau\cosh\left(\frac{x}{\tau} + K_1\right), \tag{17.4}$$

where τ, K_1, and K_2 depend on the boundary conditions at the ends of the cable. An additional equation accounts for the effect of the behavior law on the current cable length L

$$L = L_0 + \int_{x_A}^{x_B}\hat{\varepsilon}(x)\,\mathrm{d}x = L_0 + \int_{x_A}^{x_B}\frac{T(x)}{EA}\,\mathrm{d}x. \tag{17.5}$$

The linearization of Eq. (17.2) in the local frame $(\underline{t}, \underline{n}, \underline{e}_z)$, see Fig. 17.3, around an in-plane static configuration $\underline{X}_s(S) = x\ \underline{e}_x + y\ \underline{e}_y$ calculated above is given as a dynamic displacement $\underline{U}(S,t) = u(S,t)\ \underline{t} + v(S,t)\ \underline{n} + w(S,t)\ \underline{e}_z$ given in the framework of small dynamic displacement with a linear ε strain measure,

$$-\mu\ddot{u}(S,t) - \Delta^2\kappa[v(S,t)' + \kappa u(S,t)] = 0, \tag{17.6}$$

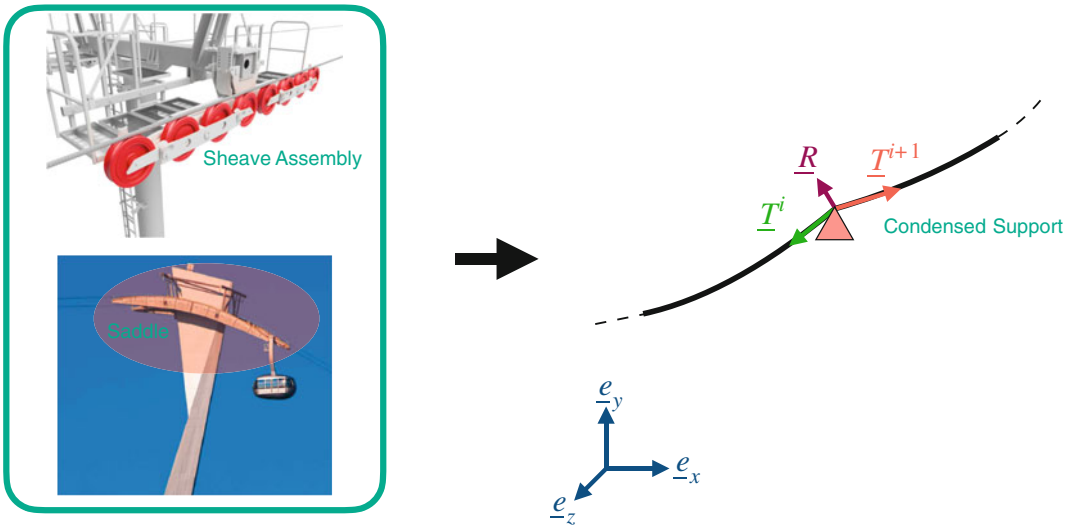

Fig. 17.4 The support condensed model

$$-\mu\ddot{v}(S,t) + \Delta^2[v(S,t)' + \kappa u(S,t)]' + \kappa T_d = 0, \tag{17.7}$$

$$-\mu\ddot{w}(S,t) + \Delta^2 w(S,t)'' = 0, \tag{17.8}$$

where $\dot{\bullet}$ denotes the time t derivative, $\bullet'$ denotes the space S derivative,

$$\Delta^2 = EA\frac{\varepsilon}{1+\epsilon} \tag{17.9}$$

a static elastic effort quantity and κ the static configuration curvature which are both assumed to be constant with respect to S,

$$T_d = EA[u(S,t)' - \kappa v(S,t)] \tag{17.10}$$

the dynamic tension increment.

Cable and support contact interface i is supposed to be reduced to a fixed point and bilateral (Fig. 17.4): cable remains in contact with its support. Dynamic displacement of the support is not taken into account in the proposed model because characteristic vibration mode frequencies of the tower-type support (first mode around 1 Hz, see Fig. 17.5) are outside the band of interest for the vibration frequencies of the cable lines of ropeways (around 10^{-1} Hz) in steady-state movement of the cable translation. An equivalent friction Coulomb's law of coefficient $c_{f,l}$ in the limit case of sliding is adopted to represent the combined effect of friction and rolling resistance of the moving parts of the interface, with a sign depending of the translation direction of the cable loop along the support,

$$\left\|\underline{T}^{i+1}\right\| = \left\|\underline{T}^{i}\right\| \pm c_{f,l}\left\|\underline{R}\right\| \tag{17.11}$$

with $\underline{T}^i$ and $\underline{T}^{i+1}$ left and right cable tensions and $\underline{R}$ the resulting force of the support on the cable.

Vehicles k are represented as point masses m_k equivalent to a punctual load (Fig. 17.6)

$$\underline{P}_k = -m_k g\ \underline{e}_y \tag{17.12}$$

acting on the cable without any flexural stiffness at the hanging point (only tension is acting on it) and neglecting pendular movement around the rotation axis.

The equilibrium of the vehicle in the position $\underline{X}(S_v^k, t) = \underline{X}_v^k(t)$ is given with respect to its weight $\underline{P}^k$, the left $\underline{T}^k$ and right $\underline{T}^{k+1}$ side cable tension,

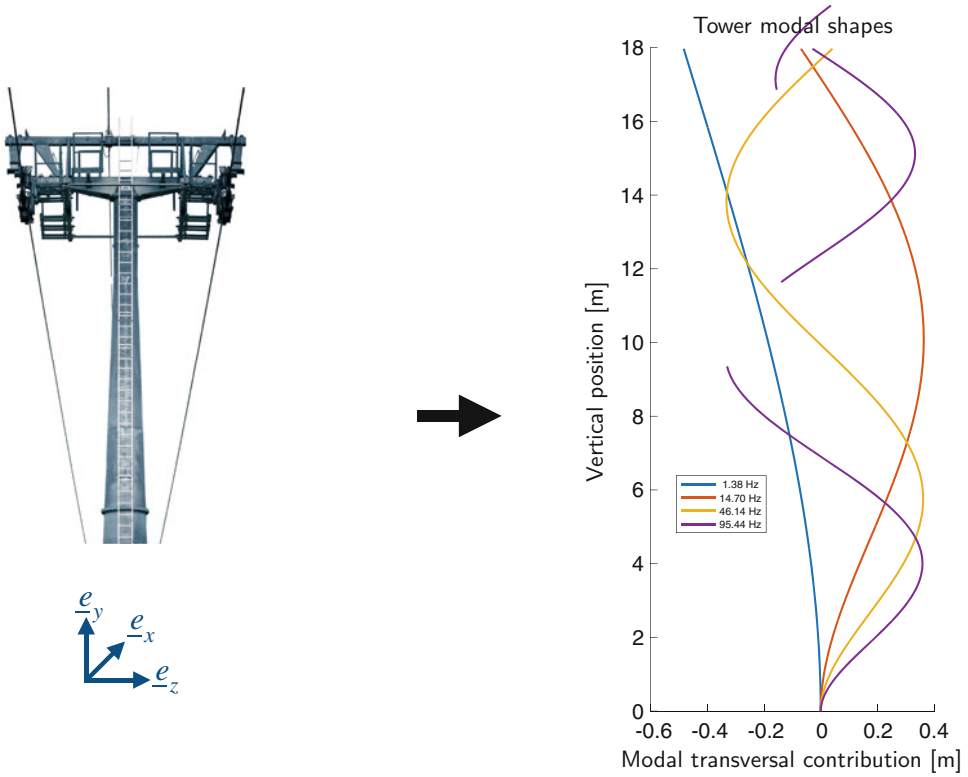

Fig. 17.5 Example of a typical tower vibration modes along $\underline{e}_x$ and $\underline{e}_z$ with effect of the cable static as a vertical preload

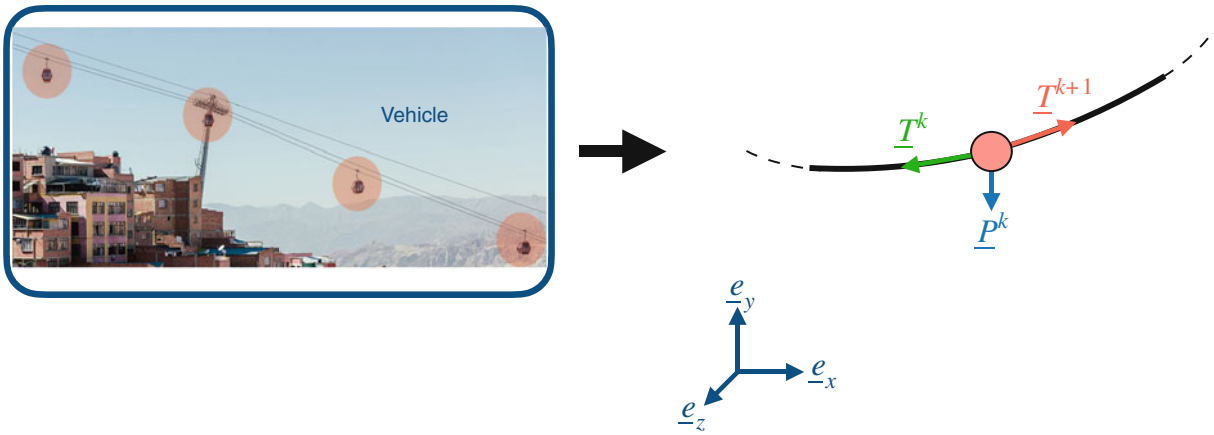

Fig. 17.6 The vehicle model

$$m_k \, \ddot{\underline{X}}_v^k = \underline{T}^k(S,t) + \underline{T}^{k+1}(S,t) + \underline{P}^k. \tag{17.13}$$

Bullwheels close the cable loop at each station extremity. Bullwheel body is assumed to be infinitely rigid, while the cable–rubber contact interface is supposed to be described by an equivalent friction Coulomb's law of coefficient $c_{f,s}$, in the limit case of sliding to represent the friction combined with the rolling resistance of the moving parts (bearings), with a sign depending of the rotation direction of the bullwheel

$$\left\| \underline{T}^+ \right\| = \left\| \underline{T}^- \right\| \pm c_{f,s} \left\| \underline{R} \right\| \tag{17.14}$$

with $\underline{T}^+$ and $\underline{T}^-$ the cable tensions in bullwheel input and output and $\underline{R}$ the resulting force of the bullwheel on the cable.

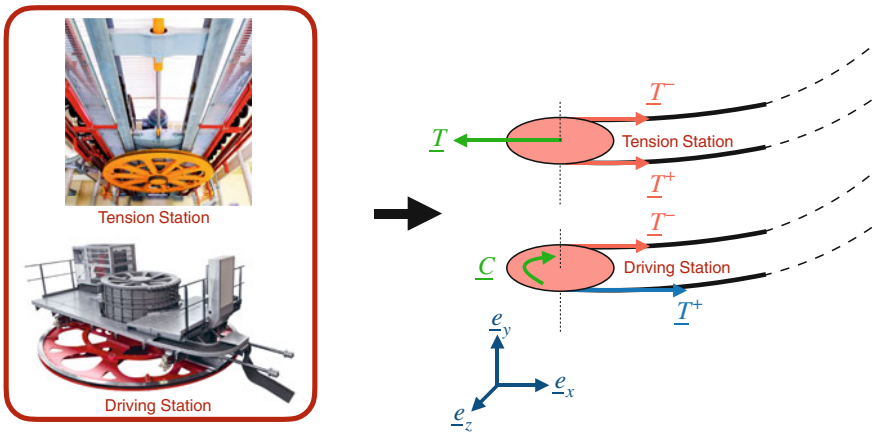

Fig. 17.7 End station model

The end stations considered here are of two types (Fig. 17.7): either a driving system which acts on the cable loop to set it in motion with a torque C applied at the driving bullwheel axis,

$$C = r(\|\underline{T}^+\| - \|\underline{T}^-\|), \tag{17.15}$$

where r the is bullwheel radius and $\underline{T}^+$ and $\underline{T}^-$ the cable tensions in bullwheel input and output or a tensioning station where a mechanical device stretches the cable line with a force $\underline{T}$ applied to the carriage

$$\|\underline{T}\| = \|\underline{T}^-\| + \|\underline{T}^+\|, \tag{17.16}$$

where $\underline{T}^+$ and $\underline{T}^-$ are the cable tensions in bullwheel input and output.

Once the mechanical model of each component is written, the next step is the assembly of the elements together. Only the cable is represented as a continuous element described by its static shape (x, y) in-plane position and the dynamic displacement $\underline{U}(S,t) = u(S,t)\ \underline{t} + v(S,t)\ \underline{n} + w(S,t)\ \underline{e_z}$ around the statics. The other components of the system act as point conditions at the edges of each cable portion. The supports, vehicles, and stations constitute nodes that divide the cable loop into successive continuous portions linked together by applying:

- Equations (17.11), (17.13), (17.14), (17.15), and (17.16) describing the mechanical equilibrium at each link and depending on the type of element
- Static position and dynamics displacement continuity at each link

Figures 17.8 and 17.9 are given as an example of a global static calculation for a complete cable line of real ropeway system. We can notice angle discontinuities on the cable shape at vehicles and supports associated with tension jump due to vehicle weight and friction at supports.

17.3 Definition of a Vibration Mode for the Time-Variant System

When the system is in operation, the cable loop moves and the vehicles occupy different positions at each time t. Thus, one of the modelling issues is to account for this time-varying aspect by using classical tools available in dynamics analysis for time-invariant linear system. A possible approach of the problem would be to assimilate the cable loop to a continuous homogeneous medium between two supports and to represent the vehicles as moving external forces acting on the system, as can be done to deal with the interaction between a catenary cable and a pantograph in the railway field [16]. Thus, system vibration modes $\underline{\Phi}$ such as

$$\underline{U}(S,t) = q(t)\ \underline{\Phi}(S) \tag{17.17}$$

could be defined for any position of the vehicles, which removes the difficulty of the time-variable aspect.

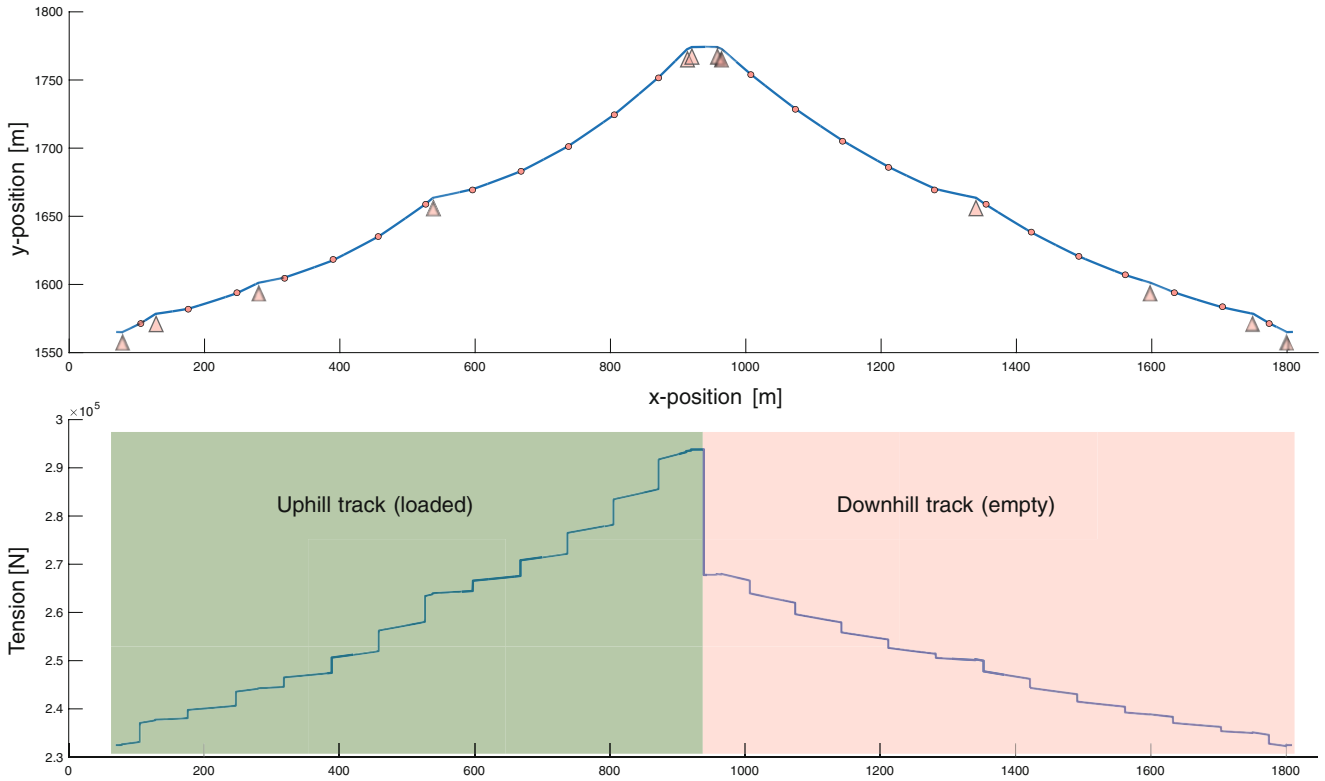

Fig. 17.8 Static equilibrium of a cable loop for a ropeway line

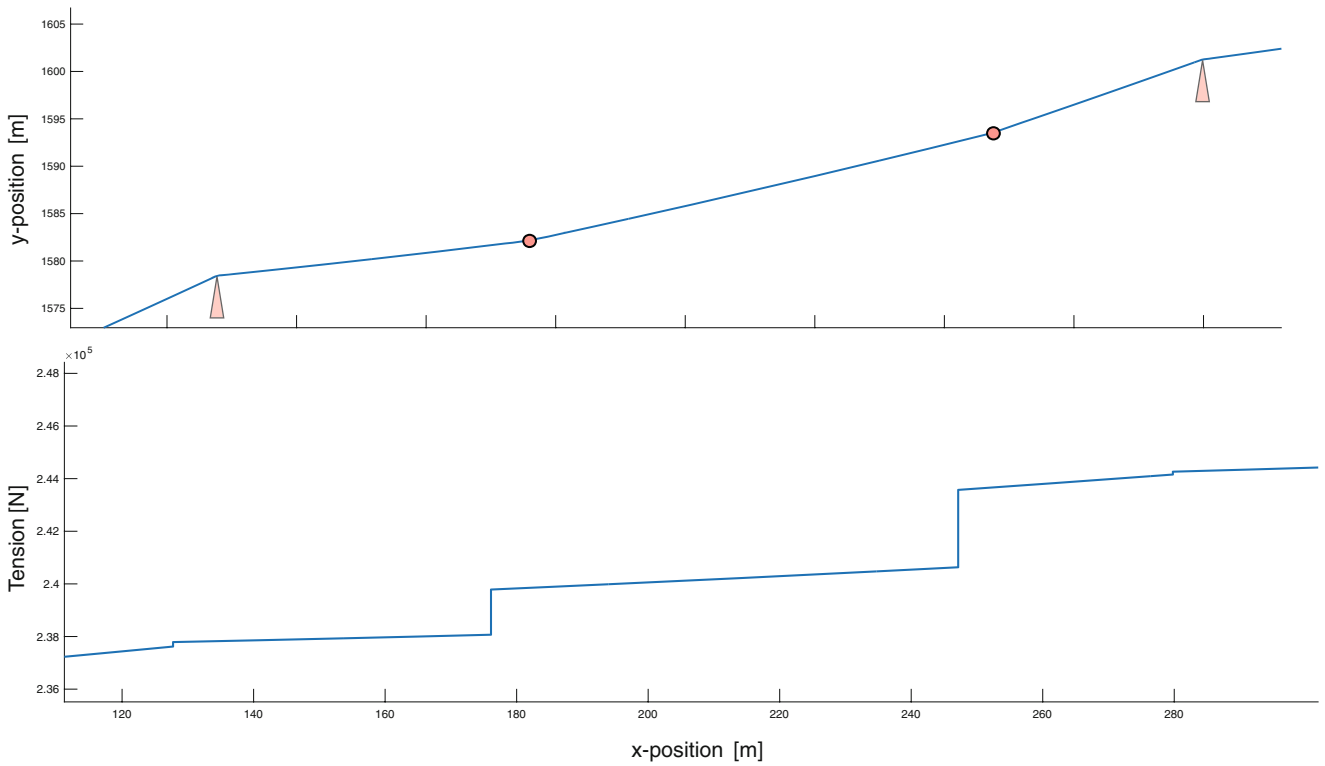

Fig. 17.9 Zoom on a specific span for $x \in [125, 280]$ m

But the presence of the vehicles introduces a singularity with a discontinuity of the cable static shape and tension. The role of the static correction $\underline{X}_s$ is therefore important for the dynamic calculation. It is expected that this singularity of the contact points between the cable and the vehicles introduces a strong dependence of the modal subspace.

Therefore, the strategy followed is to define parametric vibration modes $\underline{\Phi}(S, l_c)$ given as a function of the quantity $l_c \in [0, l_d]$, which describes the length between the last vehicle closest to the driving station and the driving bullwheel, where l_d is the distance between two consecutive vehicles. l_c is a geometric control parameter. Thus, modes $\underline{\Phi}(S, l_c)$ describe an instantaneous state of the dynamics around a static position defined by l_c.

By searching for harmonic solutions of the cable dynamics in the form

$$\underline{U}(S, t, l_c) = \underline{\Phi}(S, l_c)\, e^{j\omega t} = (\Phi_u(S, l_c)\, \underline{t} \;+\; \Phi_v(S, l_c)\, \underline{n} \;+\; \Phi_w(S, l_c)\, \underline{e}_z)\, e^{j\omega t} \tag{17.18}$$

and injecting into Eqs. (17.6), (17.7), and (17.8), one has the following shape analytical expression for the parametric modes:

$$\Phi_u(S, l_c) = A_v\, \frac{\kappa(l_c)\Delta(l_c)}{\sqrt{\mu}\omega}\, \sin\left(\frac{\sqrt{\mu}\omega}{\Delta(l_c)}S\right) \;-\; B_v\, \frac{\kappa(l_c)\Delta(l_c)}{\sqrt{\mu}\omega}\, \cos\left(\frac{\sqrt{\mu}\omega}{\Delta(l_c)}S\right) \;+\; \left(\frac{1}{EA} - \frac{\kappa(l_c)^2}{\mu\omega^2}\right)T_d S \;+\; A_u, \tag{17.19}$$

$$\Phi_v(S, l_c) = A_v\, \cos\left(\frac{\sqrt{\mu}\omega}{\Delta(l_c)}S\right) \;+\; B_v\, \sin\left(\frac{\sqrt{\mu}\omega}{\Delta(l_c)}S\right) \;-\; \frac{\kappa(l_c)}{\mu\omega^2}\, T_d \tag{17.20}$$

$$\Phi_w(S, l_c) = A_w\, \cos\left(\frac{\sqrt{\mu}\omega}{\Delta(l_c)}S\right) \;+\; B_w\, \sin\left(\frac{\sqrt{\mu}\omega}{\Delta(l_c)}S\right) \tag{17.21}$$

depending on A_u, A_v, B_v, A_w, B_w, T_d constants. The mode shape can then be rewritten

$$\left\{\Phi(S, l_c)\right\} = \left[\phi(S, l_c)\right]_{[6\times 6]} \left\{X\right\}_{[6\times 1]}, \tag{17.22}$$

where

$$\left\{X\right\} = \begin{Bmatrix} A_u \\ A_v \\ B_v \\ A_w \\ B_w \\ T_d \end{Bmatrix}. \tag{17.23}$$

Applying boundary conditions of the system assembly for each continuous portion of cable $S \in [S_i, S_{i+1}]$, one can obtain a $6n_{cable} \times 6n_{cables}$ system, where n_{cable} is the total number of cable portions in the loop,

$$\left[H(\omega, l_c)\right]_{[6n_{cable}\times 6n_{cable}]} \left\{X\right\}_{[6n_{cable}\times 1]} = \left\{0\right\}. \tag{17.24}$$

By imposing

$$\det(\left[H(\omega, l_c)\right]) = 0, \tag{17.25}$$

one can find the modal pulsation ω_k of the mode number k associated with the k mode shape

$$\left\{\Phi_k(S, l_c)\right\} = \left[\phi(S, l_c)\right] \left\{X_k\right\}, \tag{17.26}$$

where

$$\left[H(\omega_k, l_c)\right] \left\{X_k\right\} = \left\{0\right\}. \tag{17.27}$$

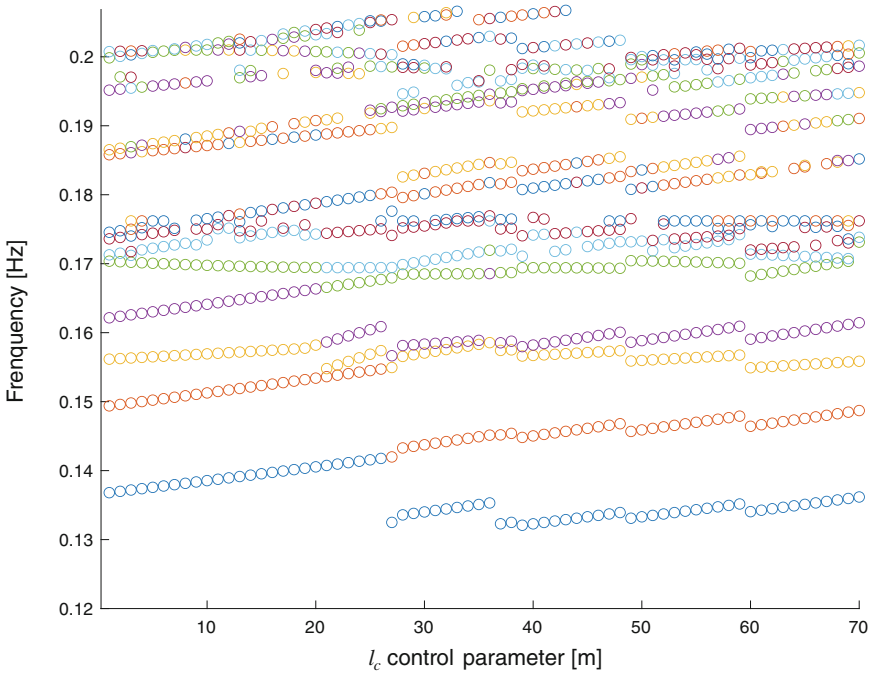

Fig. 17.10 First parametric modal frequencies of a ropeway line for $l_c \in [0, l_d]$ with $l_d = 70$ m

Then, mode shape is normalized. Figure 17.10 shows the evolution of the instantaneous modal frequencies with respect to the geometric control length l_c. A high modal density can be observed. Figure 17.11 represents an in-plane vibration mode shape with the coupled longitudinal Φ_u and Φ_v vertical contribution as a function of the curvilinear abscissa S along the cable line.

17.4 Reduced Model and Parametric Excitation

A well-known behavior to the skilled man is the sudden appearance of strong oscillations of the cable line localized between two successive supports for a specific load and speed case. One of the challenges is to understand the mechanism of appearance of these oscillations and to set up a strategy to avoid at the design stage the system operating points for which these oscillations appear.

Once a collection of N normalized modes $(\underline{\Phi}_k, \omega_k)$ has been computed, one can select a mode $(\underline{\Phi}_p, \omega_p)$ able to localize the vibrational energy within a cable span and then project the dynamic equations on this mode searching for a dynamic displacement solution

$$\underline{U}(S,t) = q(t)\ \underline{\Phi}_p(S). \tag{17.28}$$

System dynamics is then reduced to one equation of a 1 dof parametric oscillator in the form of Mathieu's equation,

$$\ddot{q} + c\dot{q} + [\omega_p^2 + a(t)]q = 0. \tag{17.29}$$

The particularity of Mathieu's equation is the possibility of an amplification of a small parametric excitation $a(t)$ if the frequency of the excitation source is close to twice the frequency of one of the modes of the system [17]. On ropeway line working at constant velocity V_0 and with evenly spaced vehicles with an l_d distance (Fig. 17.12), parametric excitation $a(t)$ arises from the periodic modification of the mass distribution and stiffness properties of the system with a fundamental frequency $f_{qs} = \frac{V_0}{l_d} = \frac{\Omega}{2\pi}$ when the cable loop is moving. A stability analysis of Mathieu's equation by a multiple scale method gives the boundary of the instability zones expressed as a function of the amplitude of parametric forcing term in

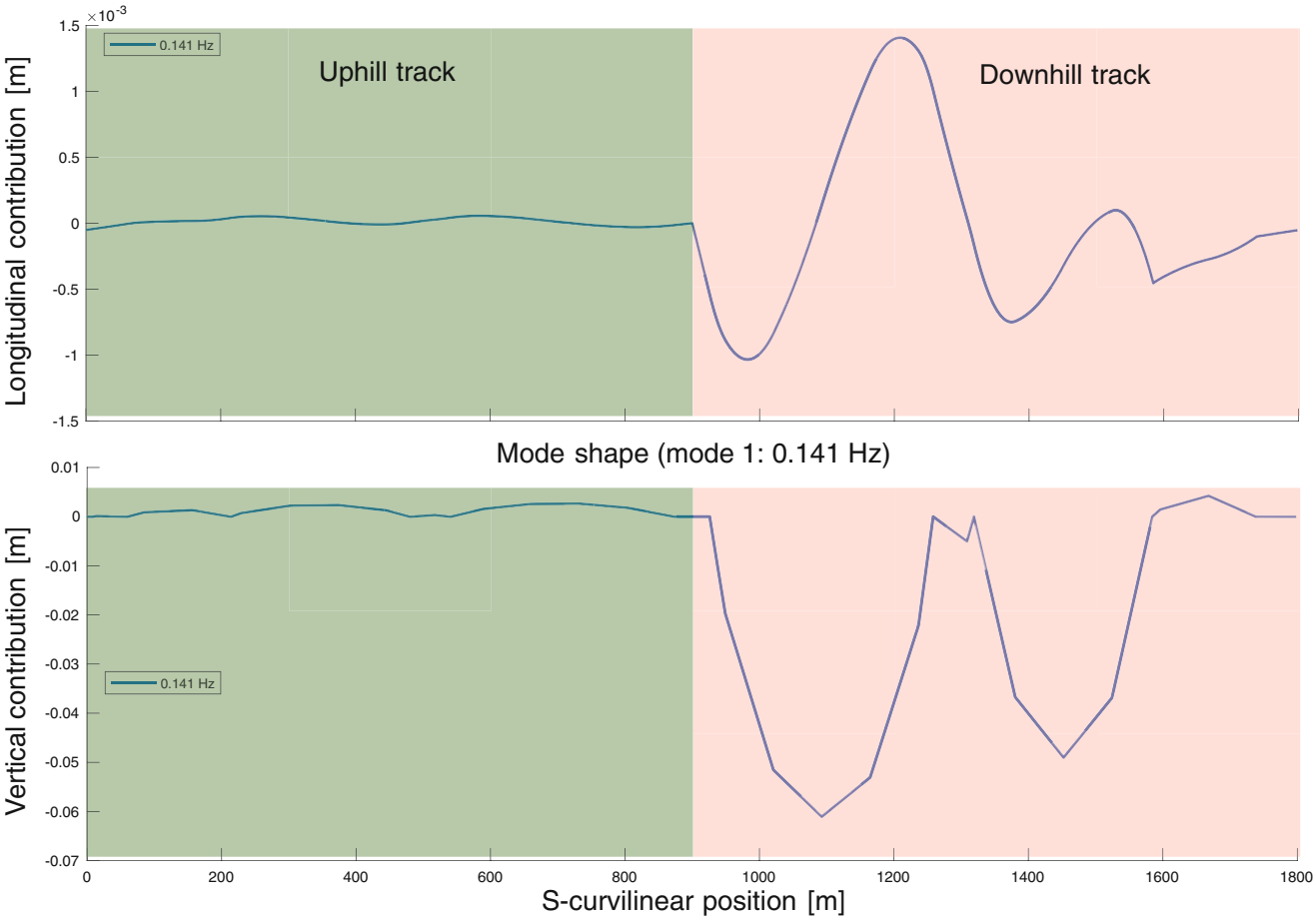

Fig. 17.11 First in-plane mode shape of a ropeway line

Fig. 17.12 Periodic pattern in space on a ropeway cable loop (photo: Doppelmayr website)

dimensionless form tension T_p, the modal damping coefficient c, and a small parameter ϵ introduced in the development to the different orders [17],

$$n^2 = \frac{\omega_p^2}{\Omega^2} \pm \sqrt{\epsilon^2 T_p^2 - c^2 n^2}, \tag{17.30}$$

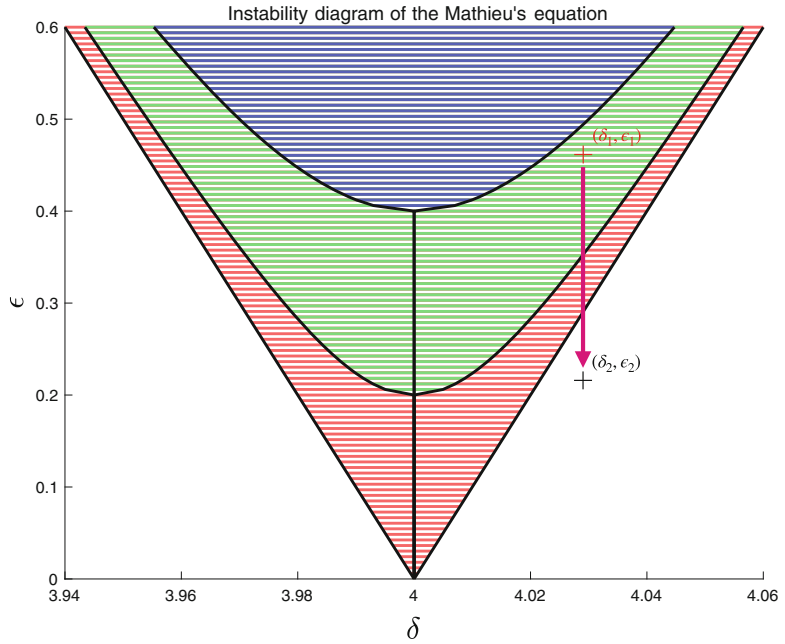

Fig. 17.13 Stability diagram of Mathieu's equation for $n = 2$ for three levels of modal damping (red : $c = 0\%$, green : $c = 1\%$, and blue = $c = 2\%$)

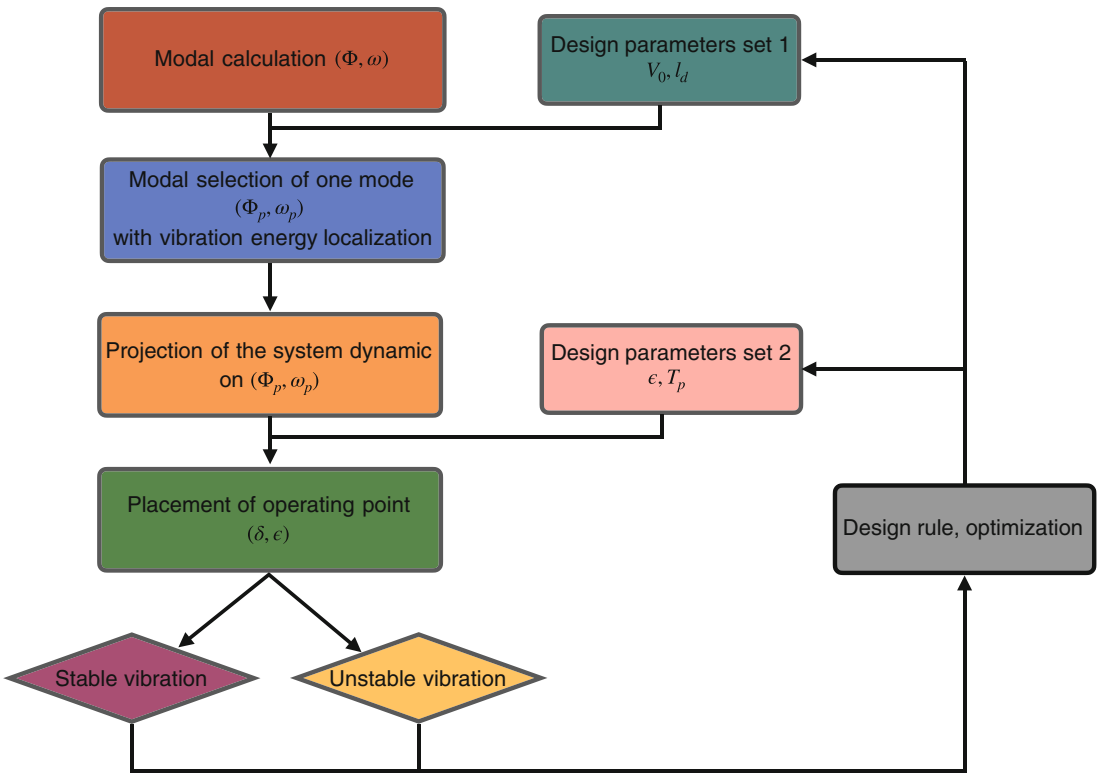

Fig. 17.14 Design process

where $n \in \mathbf{N}^*$. The case $n = 2$ is represented in Fig. 17.13. An optimal design strategy to avoid unstable vibration zones is then possible following the procedure described in Fig. 17.14 and illustrated in the stability diagram in Fig. 17.13: an unstable operating point (δ_1, ϵ_1) is moved to (δ_2, ϵ_2) in a stable region by changing design parameters.

17.5 Conclusion and Perspectives

A model taking into account the entire ropeway cable line as well as its interactions with the supports and the vehicles has been proposed. The dynamic problem is formulated with a parametric vision of the time evolutionary nature of the system and a vibration mode of the line is defined. A reduction of the model on a specific vibration mode is carried out to serve as a model for the study of the oscillation stability and to propose design strategy in order to improve the robustness of the dimensioning. An extension of the work could be focused in the addition of nonlinear contributions in the Mathieu type equation due to geometrical nonlinearities that appear for large dynamic displacements, leading to

$$\ddot{q} + c\dot{q} + [\omega_p^2 + a(t)]q + bq^2 + dq^3 = 0. \tag{17.31}$$

Then, it permits calculation of the amplitude of the response of the line in unstable zones (saturation effect of the limit cycle with nonlinearities). The information on the amplitude and jerk of the oscillations will allow to define comfort zones for the users.

Acknowledgments The authors thank DCSA company and ANRT (CIFRE 2019/1376) for supporting this work.

References

1. Marigo, J.J.: Mécanique des milieux continus, lecture notes. École Polytechnique (2014)
2. Bertrand, C., Acary, V., Lamarque, C.-H., Ture Savadkoohi, A.: A robust and efficient numerical finite element method for cables. Int. J. Numer. Methods Eng. **121**(18), 4157–4186 (2020)
3. Irvine, H.M., Max, H.: Cable structures. (1981)
4. Cretin, F.: Les transporteurs aériens à câbles. Génie civil, LXXVIII (1921)
5. Rebuffel, A.: Les transporteurs aériens par câbles. Techniques Modernes (1929)
6. Lehanneur, L.: Conférences sur les téléphériques à voyageurs, lecture notes. École nationale des ponts et chaussées (1962)
7. Goirand, P.: Transporteurs aériens sur câbles. Techniques de l'Ingénieur **A972**, 1–19
8. Czitary, E.: Seilschwebahnen. Springer, Berlin (1962)
9. Schneigert, Z.: Téléphériques et transporteurs aériens. Eyrolles (1964)
10. Portier, B.: Dynamic phenomena in ropeways after a haul rope rupture. Earthquake Eng. Struct. Dyn. **12**, 433–449 (1984)
11. Hurel, G., Laborde, J., Jézéquel, L.: Simulation of the dynamics behavior of a bi-cable ropeway with modal bases. In: In Topics in Modal Analysis Testing: Proceedings of the 36th IMAC, A Conference and Exposition on Structural Dynamics, vol. 9, pp. 43–54 (2018)
12. Babaz, M., Jezequel, L., Perrard, P.: Original expression of tension of a cable. Dynamics of Civil Structures: Proceedings of the 33rd IMAC, A Conference and Exposition on Structural Dynamics, vol. 2, pp. 553–557 (2015)
13. Knawa, M., Bryja, D.: Computational model of an inclined aerial ropeway and numerical method for analyzing nonlinear cable-car interaction. Comput. Struct. **89**, 1895–1905 (2011)
14. Wenin, M., Ladurner, S., Reiterer, D., Bertotti, M.L., Modanese, G.: Validation of the velocity optimization for a ropeway passing over a support. Sustainability **13**, 2986 (2021)
15. Arena, A., Carboni, B., Angeletti, F., Babaz, M.: Ropeway roller batteries dynamics: modeling, identification, and full-scale validation. Eng. Struct. **180**, 793–808 (2019)
16. Van, O.V., Massat, J.-P., Balmes, E.: Waves, modes and properties with a major impact on dynamic pantograph-catenary interaction. J. Sound Vib. **402**, 51–69 (2017)
17. Nayfeh, A.H., Mook, D.T.: Nonlinear Oscillations. Wiley, New York (1979)

Chapter 18
Investigation of Rotating Structures' Modal Response by Using DIC

Davide Mastrodicasa, Emilio Di Lorenzo, Bart Peeters, and Patrick Guillaume

Abstract Modal analysis of rotating structures is a challenging field of structural analysis research. In the case of a rotating structure, the major difficulty is applying a known excitation to the system, which is crucial for frequency domain modal analysis. Another obstacle is installing and connecting enough sensors (such as strain gauges or accelerometers) to the rotating blades in order to fully characterize the system. Slip rings are used to transmit electrical signals between the rotating and non-rotating frames, complicating the installation. They can also change the actual response by shifting the natural frequencies and introducing external damping. As a result, the number of experimental modal analyses of rotating structures under operating conditions is limited. DIC and other optical methods are appealing for measuring deformations because they do not require electrical wiring or slip rings and can be easily configured to measure large test articles. While setting up an experimental setup with DIC is easier than setting up a contact measurement test setup, there are several challenges to overcome when using DIC with rotating structures. The main challenge is compensating for rigid body motion caused by structure rotation motion to evaluate deformation displacements rather than absolute displacements. This chapter uses DIC to measure deformations on a rotating structure to characterize its modal behavior in operational conditions.

Keywords Digital image correlation · Full-field deformations · Optical methods · Image processing · Rotating structure

18.1 Introduction

Tire noise is currently one of the most difficult challenges for tire manufacturers as well as automobile OEMs. This is related to new strong regulation constraints as well as high NVH standards aimed by car manufacturers. With the current trend of vehicle electrification, vehicles are significantly heavier, which has an impact on the required tire designs. Furthermore, when the engine noise is removed, the predominant noise contribution is from the tires up to 300 Hz [1]. This indicates that understanding how tire noise is generated is critical in order to improve our present knowledge of tires and develop more silent vehicles. These phenomena are not yet fully understood since they involve complex material characterization. As a result, it is critical to investigate tire vibrations and provide a reliable characterization of tire dynamics. Tire deformations are usually measured using pointwise sensors such as accelerometers and strain gauges. They are relatively cheap and can provide data in real time. They do, however, only provide data at discrete points and can induce mass loading effects, and placing accelerometers might be challenging due to the shape of the structure. Optical techniques, such as LDV, have recently gained huge interest in the structural dynamics field due to their ability to produce full-field measurements and their sensitivity in measuring a wide variety of vibrations. However, when dealing with tire vibrations, it has some limitations. If the number of points to measure is very high, the measurement duration is very long and there could be variations in material

D. Mastrodicasa (✉)
Siemens Industry Software NV, Leuven, Belgium

Vrije Universiteit Brussel, Brussels, Belgium
e-mail: davide.mastrodicasa@siemens.com

E. Di Lorenzo · B. Peeters
Siemens Industry Software NV, Leuven, Belgium
e-mail: emilio.dilorenzo@siemens.com; bart.peeters@siemens.com

P. Guillaume
Vrije Universiteit Brussel, Brussels, Belgium
e-mail: patrick.guillaume@vub.be

B. J. Dilworth et al. (eds.), *Topics in Modal Analysis & Parameter Identification, Volume 9*, Conference Proceedings of the Society for Experimental Mechanics Series, https://doi.org/10.1007/978-3-031-34942-3_18

properties due to the variation of temperature, as well as wear effects that might change the tire structural behavior from point to point during the test [2]. DIC is another non-contact optical technique that provides full-field displacement and strain of the object under inspection. Several research groups have used this technique to measure vibrations of helicopter blades [3], wind turbines [4, 5, 6], automotive tires [2, 7], and infrastructures [8]. The contactless characteristic of DIC makes it suitable for modal analysis on lightweight and/or rotating structures.

18.2 Measurement Campaigns and Results

DIC technique has been used here to perform a full-field modal analysis on a free–free spinning tire. The idea behind this study is to investigate the capability of using DIC for the modal parameter estimation on rotating structures. In this experimental setup, a Siemens electric vehicle (SimRod) was lifted using some supports to approach the free–free boundary conditions, Fig. 18.1. In this condition, the tire is free to spin and the rotational speed was imposed by using directly the electric vehicle motor.

To excite the structure, a normal hammer was used to hit the structure and induce some detectable vibrations. The tire was speckled by using a white marker in order to use DIC, as shown in Fig. 18.2. The experimental setup includes two iX i-SPEED 5 Series high-speed cameras, two high-intensity lights, and a laptop for managing camera settings. The camera settings and the DIC parameters are shown in Table 18.1.

The pictures were processed by using the MatchID DIC software, and the results in Fig. 18.3 were obtained. An incremental DIC algorithm was used to track the points during the tire rotation. This algorithm allows changing the reference picture when the displacement becomes too high to be correlated with the reference picture. This is applied by changing the reference picture when the number of iterations for the correlation passes a certain threshold. In this picture, just a subset of the acquired time history is shown.

Fig. 18.1 Experimental setup

Fig. 18.2 Speckled structure

Table 18.1 iX i-SPEED 5 camera and DIC settings

Parameters	Values
Resolution	1920 × 1080 pixel
Exposure time	15000 μs
Fps	2000 fps
Subset size	31
Step size	15
Interpolation function	Bicubic splines
Shape function	Quadratic
Matching criterion	ZNSSD
DIC algorithm	Incremental DIC

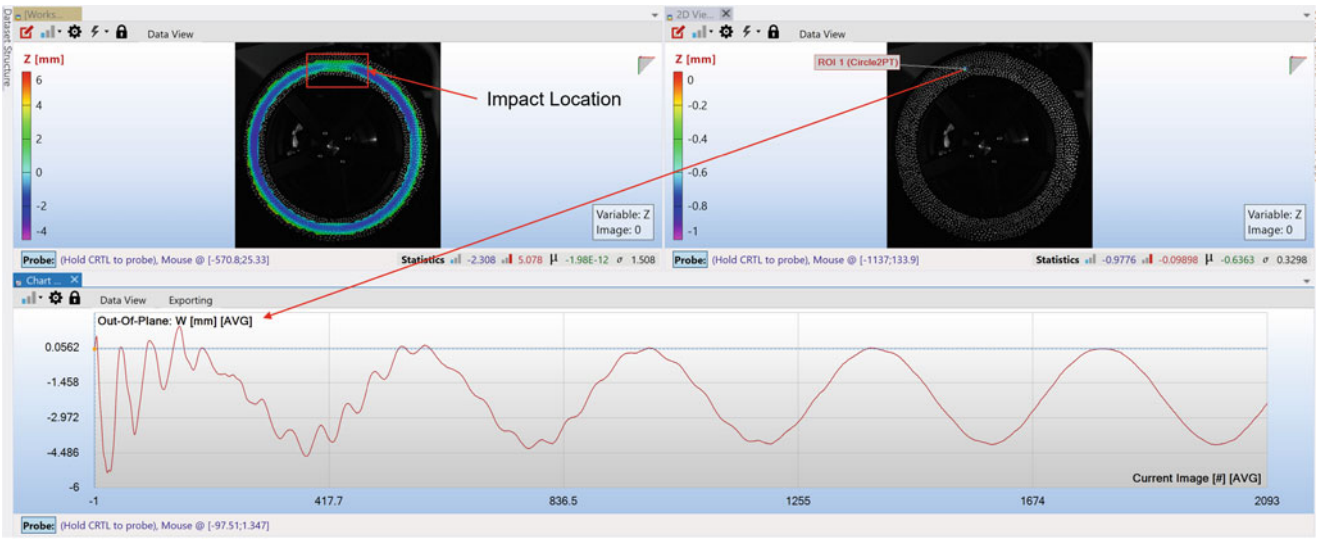

Fig. 18.3 DIC results

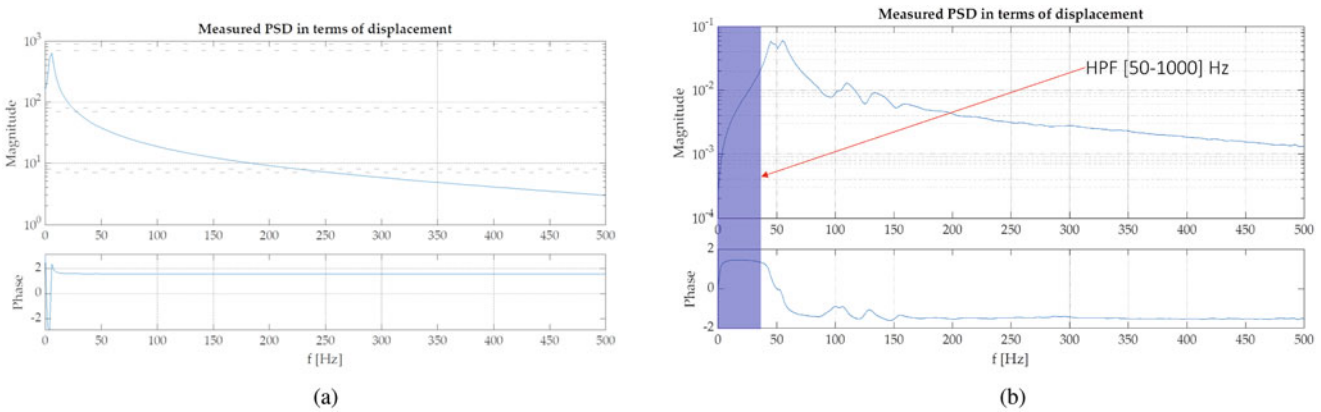

Fig. 18.4 Original and filtered PSDs. (**a**) Original PSD. (**b**) Filtered PSD

The first picture considered in the analysis is the one acquired just after the hammer impact, as it is possible to see from the out-of-plane geometry reconstruction in the top left part of Fig. 18.3.

Due to the nature of the excitation, measuring the force applied to the structure is quite challenging. Therefore, an operational modal analysis approach was used to investigate the dynamic of the structure. A point nearby the excitation location was used as a reference point for the calculation of the PSD matrix. Considering one of the structure points, the PSD shown in Fig. 18.4 was obtained.

By processing directly the original PSDs, it is possible to note that all the structure dynamic is hidden under the peak at low frequency (≈5 Hz), Fig. 18.4a. To improve the results, a frequency filter between 50 and 1000 Hz was used to cut out

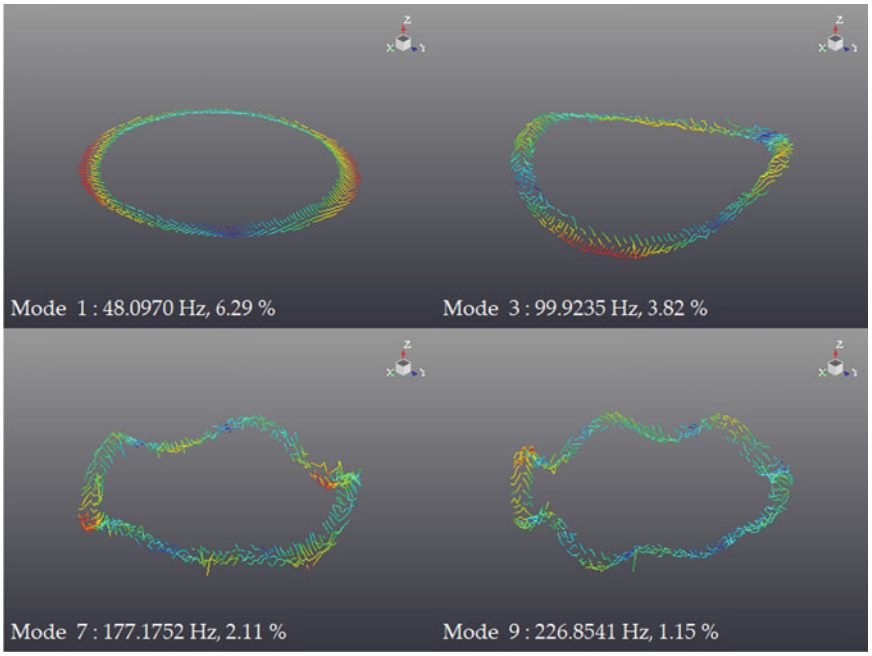

Fig. 18.5 Operational mode shapes

Table 18.2 Operational modal parameters

Mode	f_n (Hz)	ζ_n (Hz)
1	48.10	6.29
2	54.63	5.85
3	99.92	3.82
4	108.26	3.81
5	128.98	3.04
6	152.62	2.28
7	177.18	2.11
8	199.99	1.74
9	226.85	1.15
10	299.86	2.57

the low-frequency part and reveal the dynamics of the structure at a higher frequency. The effect of the filter is shown in Fig. 18.4b.

The calculated PSDs were processed by using Operational PolyMAX. The modal parameters and mode shapes shown in Fig. 18.5 and Table 18.2 were obtained.

18.3 Conclusion

The study's findings demonstrate that it is possible to measure a rotating tire's response using the DIC technique. The vibration properties of a tire in rolling conditions can be obtained using the non-contact DIC technique, whereas this would be challenging to accomplish with the traditional modal analysis method. The suggested non-contact technique is an innovative replacement for the existing measurement methods. This methodology not only removes the influence of mass loading but also offers full-field information about the test structure. This work successfully investigates the sidewall vibrations of a rolling tire, demonstrating the capabilities of using DIC to investigate the structural behavior of the tire under operational conditions. However, some limitations need to be considered:

- More advanced frequency filters have to be tried and used for filtering out the low-frequency influence. The high-frequency mode shapes are hidden below the tail of the first mode shapes.

- The excitation was not easily repeatable and reliable. A more reliable excitation should be found and investigated.
- A streamlined solution covering the full measurement and processing chain is needed.
- A validation of the DIC obtained results should be done by using reference results from either simulation or proven measurement methodologies (accelerometers, LDV).

The next steps will include a new measurement campaign on a rotating tire to overcome these limitations.

Acknowledgments The authors gratefully acknowledge Flanders Innovation and Entrepreneurship for its support of the Baekeland project "Digital Image Correlation For Structural Dynamics Full-field Analysis" [nr. HBC.2019.2595].

References

1. Bank, G., Hathaway, G.T.: A revolutionary 3-d interferometric vibrational mode display. J. Audio Eng. Soc. (1980)
2. Galeazzi, S., Chiariotti, P., Martarelli, M., Tomasini, E.P.: 3d digital image correlation for vibration measurement on rolling tire: procedure development and comparison with laser doppler vibrometer. J. Phys. Confer. Series **1149**(1), 012010 (2018)
3. Mastrodicasa, D., Lorenzo, E.D., Manzato, S., Peeters, B., Guillaume, P.: Full-field modal analysis by using digital image correlation technique. In: Di Maio, D., Baqersad, J. (eds.) Rotating Machinery, Optical Methods & Scanning LDV Methods, vol. 6, pp. 105–112. Springer, Cham (2022)
4. Poozesh, P., Baqersad, J., Niezrecki, C., Avitabile, P., Harvey, E., Yarala, R.: Large-area photogrammetry based testing of wind turbine blades. Mech. Syst. Signal Process. **86**, 98–115 (2017). Full-field, non-contact vibration measurement methods: comparisons and applications
5. Poozesh, P., Sabato, A., Sarrafi, A., Niezrecki, C., Avitabile, P.: A multiple stereo-vision approach using three dimensional digital image correlation for utility-scale wind turbine blades (2018)
6. Baqersad, J., Carr, J., Lundstrom, T., Niezrecki, C., Avitabile, P., Slattery, M.: Dynamic characteristics of a wind turbine blade using 3d digital image correlation. In: Proceedings of SPIE - The International Society for Optical Engineering, vol. 8348, p. 74 (2012)
7. Mange, A., Srivastava, V., More, J.: Using digital image correlation to measure dynamics of rolling tires (2018)
8. Yang, Y., Dorn, C., Farrar, C., Mascarenas, D.: Full-field imaging and modeling of structural dynamics with digital video cameras (2017)

Chapter 19
Increasing Multi-Axis Testing Confidence Through Finite Element and Input Control Modeling

Kaelyn Fenstermacher, Sarah Johnson, Aleck Tilbrook, Peter Fickenwirth, John Schultze, and Sandra Zimmerman

Abstract Testing devices multi-axially can be a better approximation of a device's operational conditions compared to single-axis testing. However, multi-axis environmental tests involve a more complicated test setup that is often determined by a test engineer's judgment. Some of the complexities the engineer must determine include where to locate shakers on intricate geometries, how much input is required to excite the structure, how many control channels are necessary, and how well the environmental test boundary conditions replicate the operational environment. Any one of these things can lead to the device under test's (DUT) response differing greatly from the desired response. Often there is no indication of whether the environmental test setup appropriately replicates field conditions prior to the start of the test. The ability to simulate a test on a finite element model (FEM) would allow the engineer to have insight into the predicted response of the DUT prior to performing an environmental test. This study uses Sandia National Laboratories Rattlesnake control software to conduct virtual tests on an FEM of the base section from a Box Assembly with Removable Component (BARC) and aims to determine if virtual testing can be used to predict optimal environmental test setup accurately and achieve the desired response from the DUT. Including a virtual test as a step in the procedure for multi-axis vibration testing could provide test engineers with the necessary information for a reliable test such as input controls and locations, equipment requirements, and sensor placement prior to performing a test, reducing the time required in the lab, and improving test results.

Keywords Virtual testing · Input modeling · MIMO testing

19.1 Introduction

The purpose of experimental vibration testing is to recreate operational environments and analyze the dynamic response a structure might experience when it is in service. Traditionally, vibration testing has been conducted by connecting a device under test to a single-axis shaker table and recording the response in one direction then reconfiguring it to be tested along the other axes of interest. This single-input, multi-output method of vibration testing is time intensive and is not an accurate representation of distributed loads DUTs will experience in operation. A more realistic representation of operational loads is multi-input, multi-output (MIMO) excitation [1]. This involves exciting the DUT along multiple axes simultaneously to excite more degrees of freedom and allows more flexibility to recreate environmental conditions. One way to conduct MIMO testing is through multi-axis testing which involves many relatively small shakers that are strategically placed on the DUT to excite it from multiple locations simultaneously [2]. The concept of multi-input testing has been around for over four decades, but at the time of its initial applications, the computational power required to create a useable test range and analyze the results was not readily available. It has become more common in the last 20 years that MIMO testing has been conducted and used to predict system behavior [3]. Now that multi-axis testing is becoming more common, the intricacies of a successful test are being realized.

In this approach, the DUT must have an appropriate number of inputs and outputs that are strategically located to produce the desired response. Optimizing input and output placement allows finding the minimum amount of input required to produce the maximum response of a structure, which is especially important when input capability is the limiting factor in a test. One method for choosing the best locations for input is Impedance Matched Multi-Axis Testing (IMMAT). The goal of IMMAT is to establish a system impedance that is as similar as possible to the impedance in the field test, and this includes

K. Fenstermacher · S. Johnson · A. Tilbrook · P. Fickenwirth · J. Schultze · S. Zimmerman (✉)
Los Alamos National Laboratory, Los Alamos, NM, USA
e-mail: szimmerman@lanl.gov

B. J. Dilworth et al. (eds.), *Topics in Modal Analysis & Parameter Identification, Volume 9*, Conference Proceedings of the Society for Experimental Mechanics Series, https://doi.org/10.1007/978-3-031-34942-3_19

added impedance from boundary conditions and force transmission. One example of reducing impedance added by force transmission and boundary conditions is shaker input being transmitted through stingers instead of attaching the DUT to a rigid shaker table, where the shaker table can change the system response greatly [2, 4]. IMMAT has been shown to recreate field power spectral densities (PSD) better with small shakers compared to large single-axis shakers, but has not been used extensively outside of Atomic Weapons Establishment in the UK [4, 5]. Attempts have been made to use brute force and iterative calculations to optimize number of shakers, shaker location, and amplification voltage required [6]. While these methods do create better responses from the DUT, they are computationally expensive and often do not consider practical limitations such as part geometry and hardware attachment, which renders some of the proposed experimental setups useless. A common test structure in multi-axis testing is the BARC. This was developed at Sandia National Laboratories and Kansas City National Security Campus to create a common test structure for investigating how component dynamics affect each other and how modification of test boundary conditions affects the structures response [7]. The BARC base is representative of an operational mounting structure and the removable component is representative of a unit under test [5]. To avoid modeling bolted interfaces, this study will focus on the BARC base.

Daborn [2] and Banwell et al. [8] have shown finite element analysis (FEA) is a powerful tool in analyzing a part or structure's frequency response. To use FEMs to run simulations, they must first be examined to ensure they are representative of the system of interest. Typically, difficulties lie in trying to model boundary conditions, connections, and certain material properties, which can have large effects on the system dynamics. Modal analysis is a common way to refine FEMs where natural frequencies and mode shapes are compared between the analytical model and the physical device. Once updated, FEMs can be used with more confidence in design modeling [8]. A robust FEM can also be used to perform virtual vibration tests to establish system response predictions, test feasibility, and effective test setups [2]. Establishing a predicted response can drastically reduce the time cost of setting up an environmental test.

This study aims to explore virtual, multi-axis vibration testing on an FEM to determine test feasibility, especially when boundary conditions differ between the field and environmental tests, and to establish an appropriate test setup prior to attempting a test on the DUT. The virtual tests will be performed via Sandia National Labs' Rattlesnake Control Software on the Eigen solution of a validated FEM. This virtual test will allow any configuration of sensor locations, control locations and quantity, shaker location and input, and boundary conditions to be considered without the risk of damaging costly hardware [9]. Adding virtual testing to a vibration test procedure can reduce the amount of time required in the lab to prepare and perform testing. Unlike many other shaker location optimization methods, this strategy aims to allow the test engineer to use his or her judgment to evaluate optimal locations and inputs while also considering the true environmental conditions. Based on the results achieved, the simulated test setup can be applied to the DUT in an environmental test. The virtual test and environmental test will both be performed using Rattlesnake Control Software, which will allow consistency in input controls between the tests. This could greatly reduce the time and resources required to set up environmental test conditions and improve accuracy of testing by allowing test engineers to see shortcomings in their models, test setups, and test equipment much faster.

19.2 Modal Testing

19.2.1 Testing

To use an FEM of the BARC base for virtual testing, it first needed to be refined. This was done through two sets of modal testing, an impact hammer modal test, and a multi-shaker modal test. Simcenter TestLab software was used as the data acquisition system. Initially, 9 response channels were placed at locations where preliminary FEM frequency analysis of the BARC base showed high amounts of displacement. The BARC base was hung by fishing line from a rigid structure in order simulate free-free boundary conditions. To ensure the full frequency response up to 2000 Hz was captured, and the test was sampled at 5120 Hz.

For impact testing, the BARC base was partitioned throughout with a 1″ grid as well as a centerline across the bottom and sides, as shown in Fig. 19.1, to have enough resolution for comparison with the FEM. A nylon hammer tip was shown to excite the frequency range of interest and used for testing. Using a roving hammer technique, each of the 119 experimental nodes was impacted and the response recorded on the 9 output channels. To reduce leakage at low frequencies, a 1% exponential window was used. The exponential window reduced leakage so that the low frequency system modes to be observed in the frequency response. The suspension modes (shown in Fig. 19.2) were observed to be below 8 Hz, a factor of 10 below the first recorded flexural mode of the BARC base, indicating the modes of the fishing line had minimal interference with the modes of the BARC base, and it is sufficient to assume free-free boundary conditions.

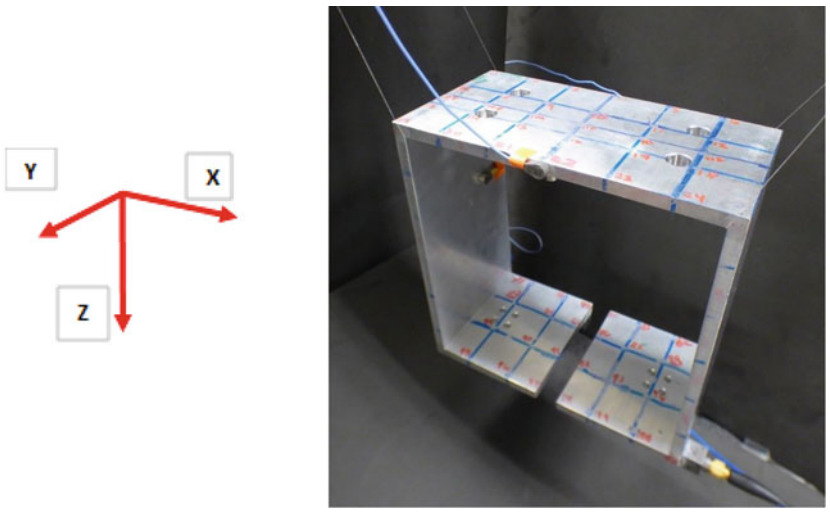

Fig. 19.1 Experimental setup, mesh, coordinate system, and boundary conditions

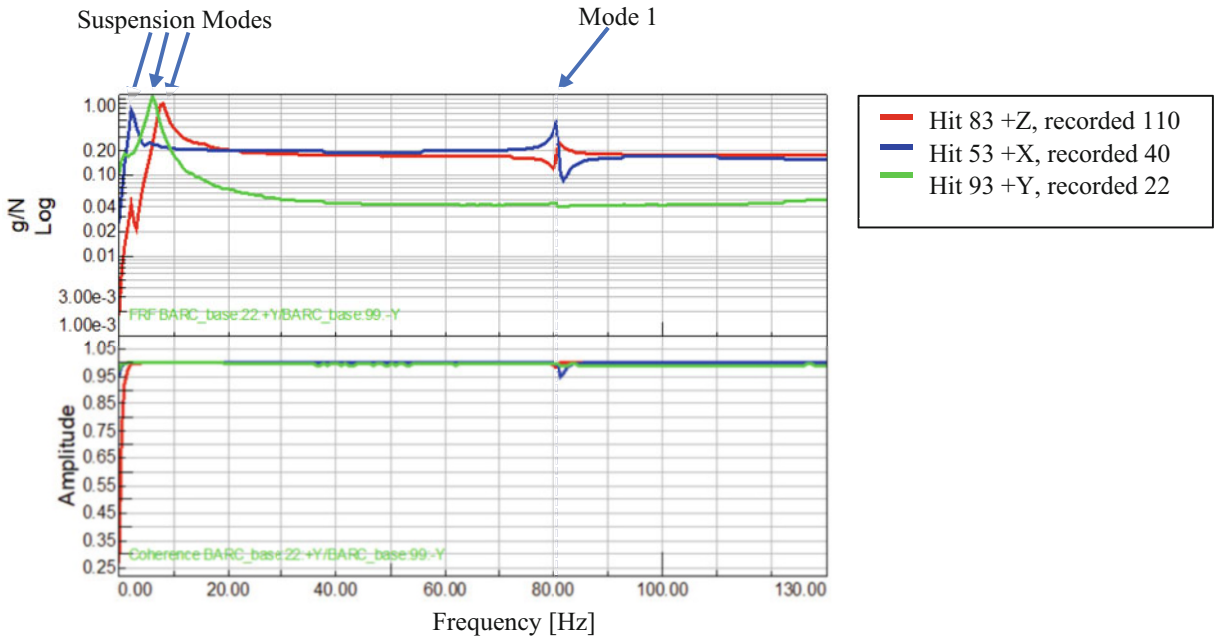

Fig. 19.2 FRF and coherence from impact test with visible suspension modes

To gain a better understanding of how the system response might change with the addition of stingers for force transmission, multi-shaker modal tests were conducted as well. These involved a shaker at the middle of the bottom face (Node 110) in the Z direction; the second shaker was placed 1″ from the base edge and half an inch from the centerline on the sidewall (Node 40) shown in Fig. 19.3. Because the BARC is a thin structure (0.25″), the driving point accelerometers were placed on the inner surface of the BARC base, coaxially with the load cells. Because the structure was lightly damped, the burst random vibration was not appropriate; therefore, a continuous random excitation with a 50% overlap and a Hanning window was applied.

In an FEM, it is assumed that the system has linearity and reciprocity. For a physical system, this must be checked experimentally. To examine linearity, the response was recorded at several input levels and compared. Testing confirmed that no nonlinearities were identified in the voltage range tested (50–200 mV), as shown in Fig. 19.4. To evaluate reciprocity and path dependencies, the input at one driving point was compared to the response at the other and vice versa. The responses were the same until about 1600 Hz, as shown in Fig. 19.5, indicating that the system obeyed the assumption of reciprocity until that point. Due to the drop off in reciprocity at 1600 Hz, it was decided to revise the frequency band of interest to be 0–1600 Hz, which included the first 10 modes of the BARC base.

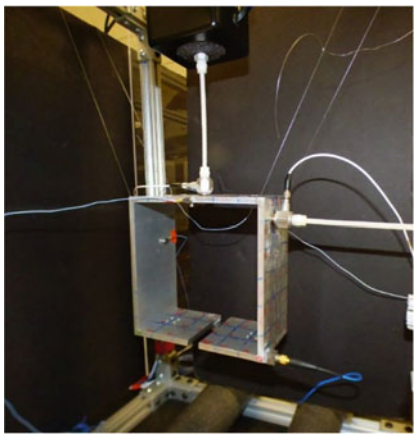

Fig. 19.3 Multi-axis shaker test setup with shakers at Node 110 and Node 40

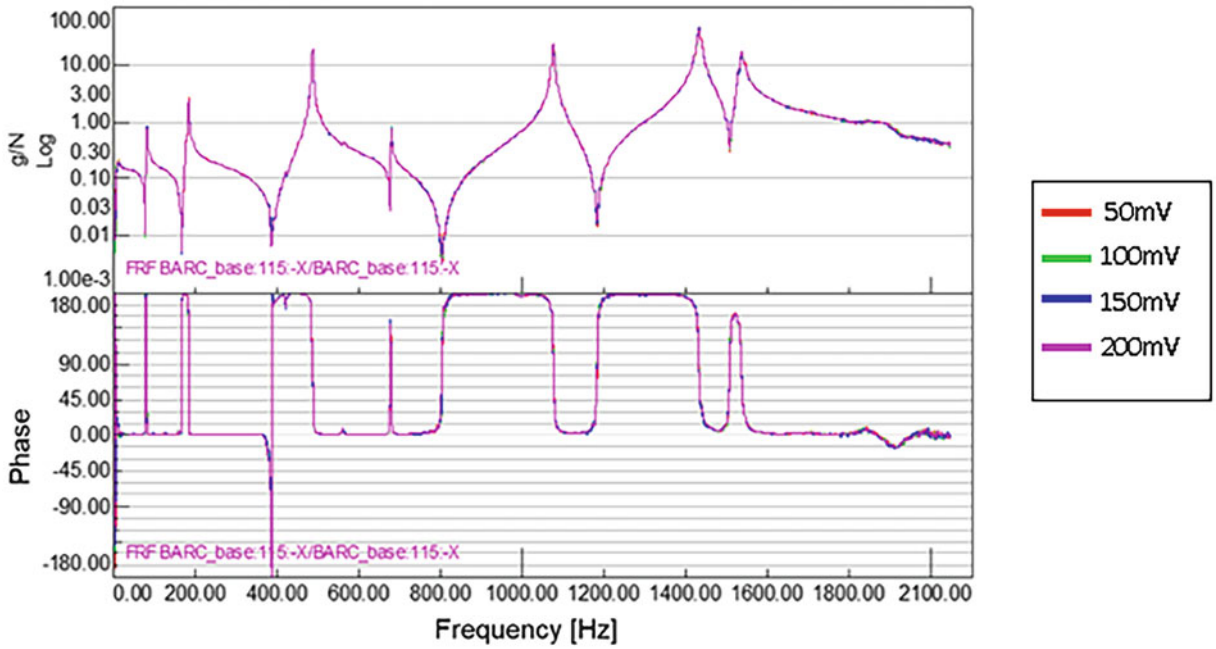

Fig. 19.4 Linear frequency response of the DUT to different input voltages

19.2.2 Results

To determine the natural frequencies of the modal tests, the frequency response functions (FRFs) were analyzed in IMAT (a MATLAB toolbox produced by ATA Engineering). Using complex mode indicator functions, the driving points, in-line response, out-of-line response, and total response were checked; each of these had smooth frequency response with minimal noise at the frequency band of interest and no leakage of low frequencies present, confirming that the constraints to use of a Fourier transform were met.

At each resonance peak, the frequency, damping, and modal order of the system were recorded. These frequencies selected where then used to create synthesized response in IMAT. This simulated response was compared to the actual response of the system to check that the natural frequencies chosen captured its full response. Because the simulated response coincided with the physical response as seen in Fig. 19.6, it was determined those frequencies corresponded to the natural frequencies and modes of the system. This method was used to analyze the natural frequencies and mode shapes for both the impact test and multi-shaker test.

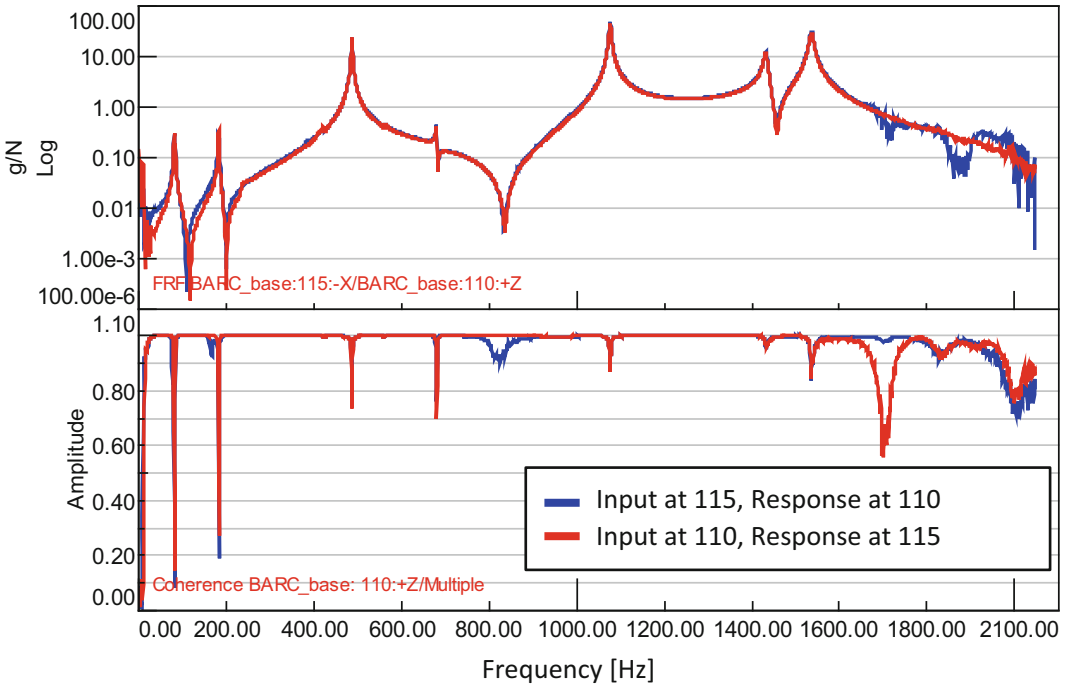

Fig. 19.5 Reciprocal frequency response of DUT indicated a 1600 Hz frequency bandwidth

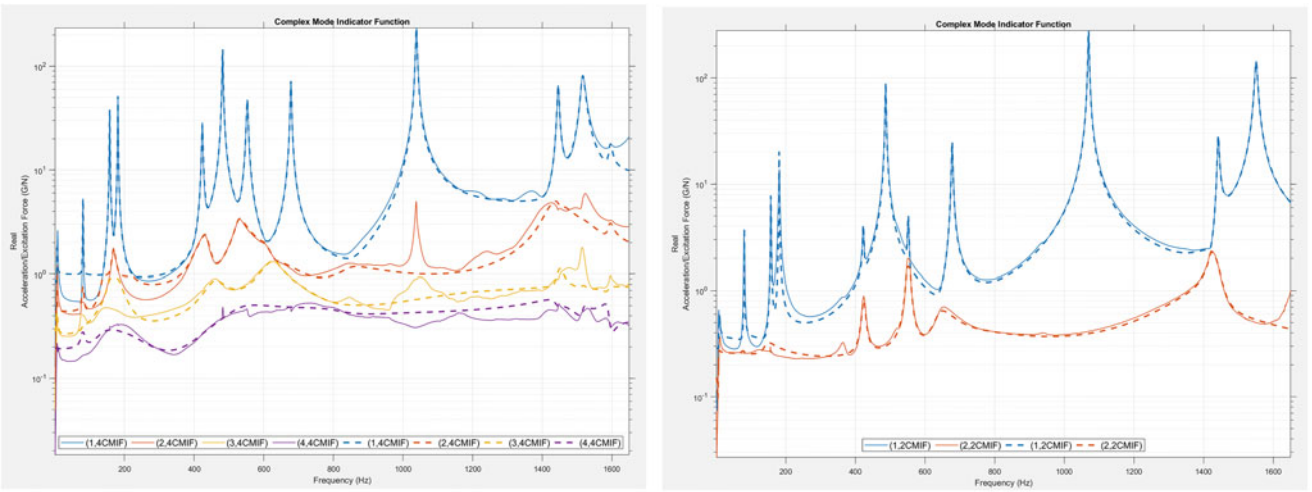

Fig. 19.6 The simulated response based on the chosen natural frequencies in curve fitting for (**a**) impact testing and (**b**) multi-shaker modal testing

19.2.3 Comparison and Refinement of FEM

The FEM was originally created in Abaqus CAE based on a drawing of the BARC base. The BARC base was modeled using solid elements, no boundary conditions, and no damping. A step frequency analysis on the model was performed within the Abaqus CAE software. The first 10 natural frequencies after the 6 rigid body modes were recorded between 0 and 1600 Hz, and these were compared to the modal test results. To better match the modal testing results, several different models were generated and compared to find the model that most accurately represented the physical system that was tested. One included modeling the BARC base with the additional added mass of the accelerometers. Another included modeling the BARC base

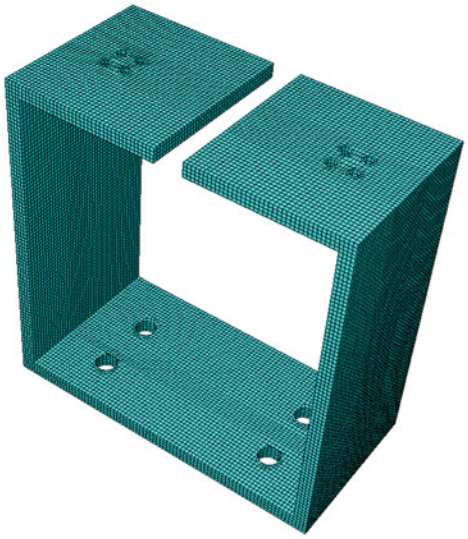

Fig. 19.7 FEM mesh for test article

Table 19.1 Comparison of natural frequencies from numerical analysis and modal testing in Hz

Natural frequencies [Hz]	FEM	Impact test	Multi-shaker test	Maximum % difference
Mode 1	81.7	80.7	80.8	**1.23%**
Mode 2	157.6	157.5	157.3	**0.19%**
Mode 3	184.7	181.1	181.3	**1.97%**
Mode 4	433.0	423.2	422.7	**2.42%**
Mode 5	500.7	481.8	486.9	**3.86%**
Mode 6	570.7	555.5	551.9	**3.36%**
Mode 7	629.3	678.1	677.9	**7.37%**
Mode 8	1124.8	1038.9	1071.0	**7.97%**
Mode 9	1480.2	1445.5	1442.2	**2.61%**
Mode 10	1589.9	1516.2	1550.5	**4.75%**

as a shell because its thickness is in between a solid and a shell. Ultimately, refining the mesh yielded the results that most closely matched the natural frequencies of the modal tests. A mesh of global size 1.8 was applied using hex elements shown in Fig. 19.7, and it was within 10% of all modal analysis frequencies (see Table 19.1) and determined to be an appropriate model to use in virtual testing.

In addition to comparing the natural frequencies of the system to determine mode similarity, the mode shapes obtained in the modal test and the FEM frequency analysis were compared. These were compared using the modal assurance criterion (MAC) to determine the orthogonality and uniqueness of the mode shapes from each test. The MAC was also used to determine if modal switching had occurred in the FEM and if the modes observed in the FEM and physical systems were symmetric. Figure 19.8 shows high correlation along the diagonal and low correlation on the off diagonal, indicating that the FEM mode shapes were directly comparable to those observed in physical testing.

19.3 Vibration Testing

19.3.1 Field Test Environment

The full BARC assembly was instrumented with several accelerometers and strain gauges and placed in a High Operation Tempo Shot (HOTSHOT) rocket launch. In the rocket, the BARC was bolted to a sounding rocket base. The rocket was fired, and the response was recorded. The best responses were recorded on the accelerometers shown in Fig. 19.9 and yielded the response in Fig. 19.10.

A random environment was selected as the specification, in this case, the first burn. The spectral densities of the accelerometer response were extracted and used to create a power spectral density specification for testing. This was created in MATLAB as a $2 \times 2 \times 2048$ 3D array. However, the cross powers from the two control locations were specific to the

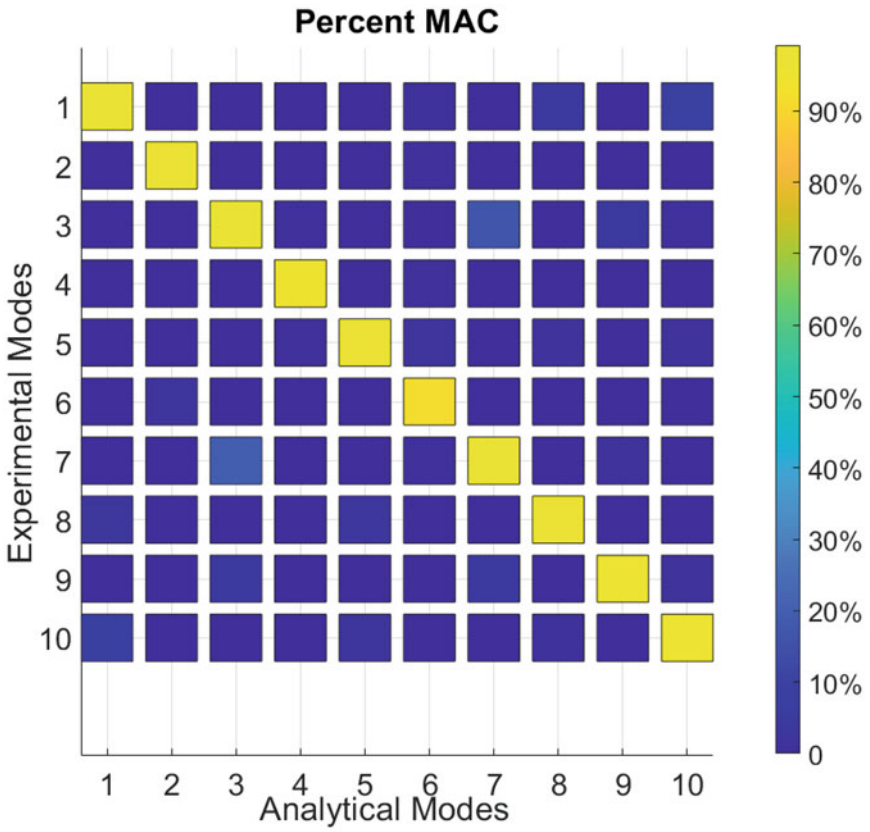

Fig. 19.8 The MAC for the first ten modes is above 90%

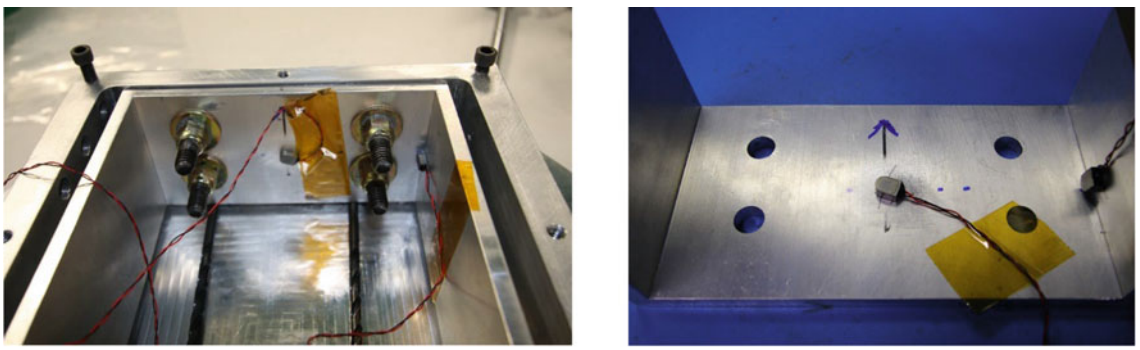

Fig. 19.9 The BARC base was secured to in the hot shot rocket (**a**) by being bolted to a sounding rocket base with (**b**) response locations in the middle of the base plate and side wall

relationship between the accelerometers in the HOT shot configuration. The BARC base was left suspended by fishing line for the environmental test, which is a drastically different boundary condition from the field test. As a result, the physical test configuration did not replicate the field test specification, specifically the cross-power terms. To address this, a modified buzz test was performed to establish the cross-power relationship of the free-free boundary condition of the physical test. To create a specification for the environmental test setup, the auto-power and cross-power terms were scaled by a factor of 20 for hardware safety. With the scaled specification and the built-in "buzz_control" law in Rattlesnake, the modified buzz test was performed by inputting low-level excitation to the structure and recording the new relationship between the input locations at the current boundary conditions. Additionally, the locations of the controls where set in the Rattlesnake channel table. Inputs were assigned to control response locations through specified fields within Rattlesnake. This test yielded new cross-power terms that reflected the experimental setup.

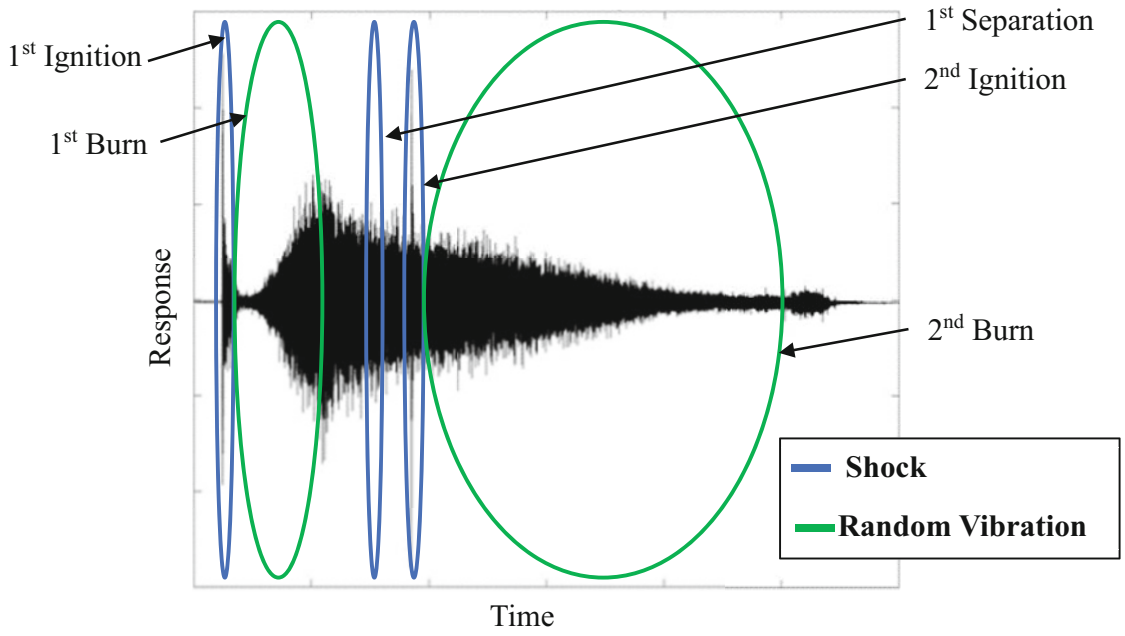

Fig. 19.10 Response of the rocket launch, the first burn is to be replicated in an environmental test

The buzz control law first performed a buzz test in the "system identification" portion of Rattlesnake then a pseudoinverse control with the newly developed specification for the "run test" portion. For the safety of the lab equipment, the specification determined in the system identification was scaled by a factor of −10 decibels [dB]. This was determined to be an appropriate target excitation level that would not result in damage due to over testing.

19.3.2 Virtual Testing

To compare the physical test, the FEM needed to include only the 11 nodal degrees of freedom present in the physical test to be considered for input and response locations that would be tested virtually. To reduce the FEM degrees of freedom, a static Guyan reduction was applied. This was done using a substructure within Abaqus that consisted of the 11 degrees of freedom corresponding with the sensors in the physical system. Damping was also added to the model so the virtual DUT was as close as possible to the physical DUT and the Eigen solution was valid to be used with Rattlesnake. Equation (19.1) was used to convert the modal damping recorded in the multi-shaker modal test to physical damping in order to be consistent with the physical mass and stiffness outputs from the FEM.

$$[\phi]^{\mathrm{T}}[C][\phi] = [2\zeta\omega_n] \tag{19.1}$$

where Φ is the shape matrix, C is the physical damping matrix, ζ is the modal damping, and ω_n is the natural frequency matrix.

The reduced, damped FEM Eigen solution was uploaded to Rattlesnake (for more guidance see [10]), and the virtual test used the same test specification, control law, and scaling as the physical test.

19.4 Results and Analysis

19.4.1 Comparing Virtual and Physical Tests

When comparing the virtual and physical responses to the desired response, the shapes of the PSD profiles were largely similar as seen in Fig. 19.11, with excursions in the physical response around 500 Hz. This could be due to natural frequencies

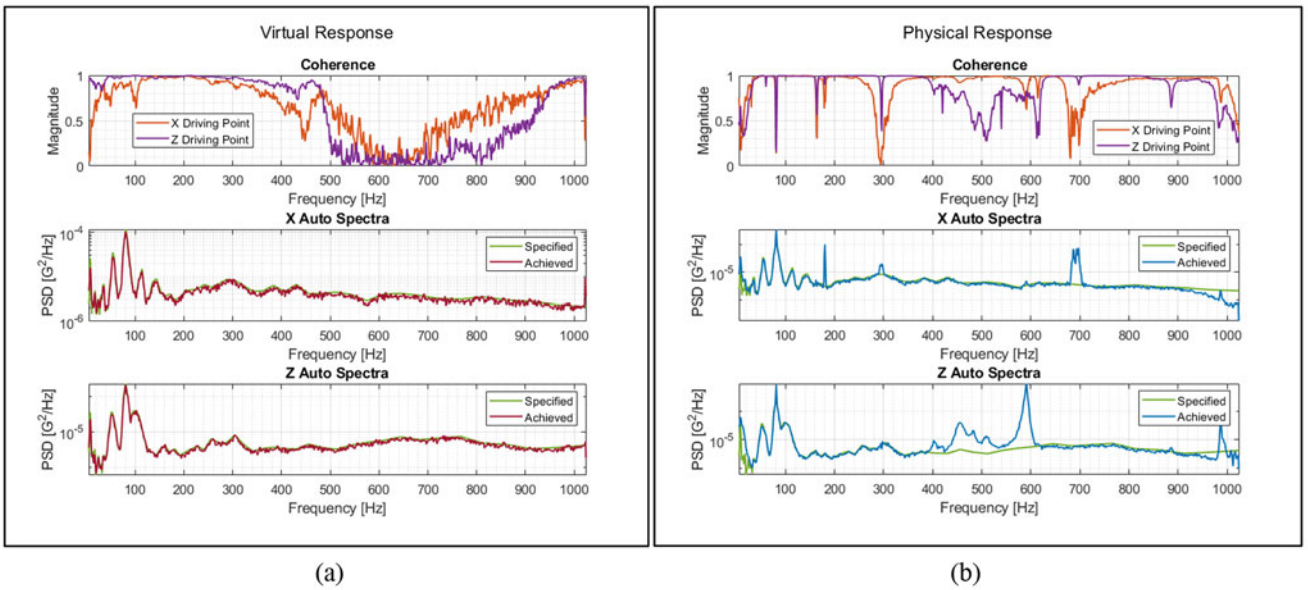

Fig. 19.11 The result of the virtual test (**a**) and physical test (**b**) at each control location were compared to the desired response (input specification)

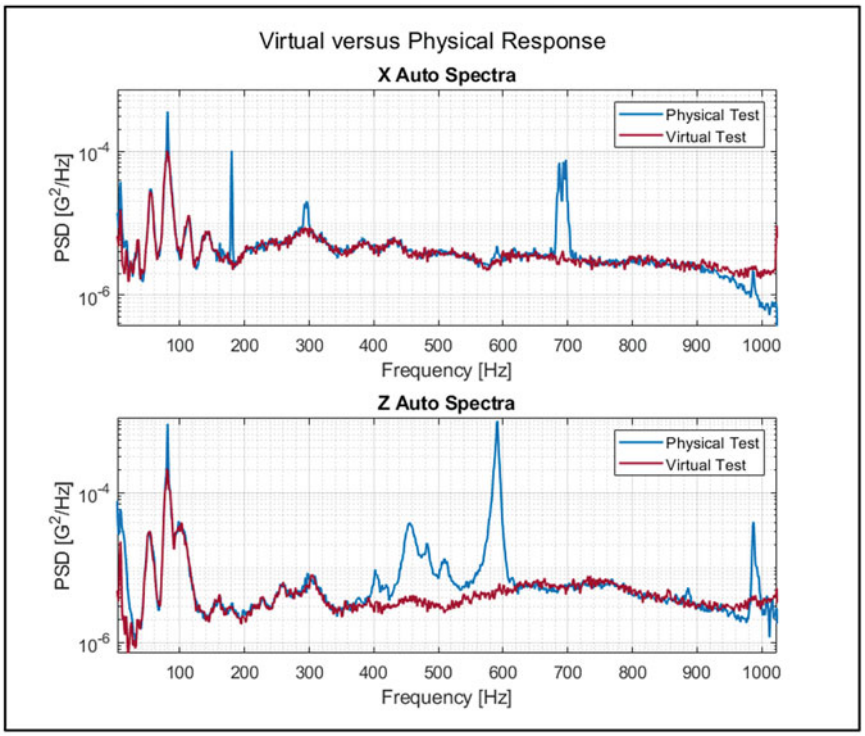

Fig. 19.12 The physical response has several excursions not accounted for in the virtual response

the BARC base experiences in the "free-free" boundary condition that were shifted up to higher frequencies in the field test due to the added stiffness of the bolted boundary condition. However, the excursions noted in the physical test were not present in the virtual model shown in Fig. 19.12. Further exploration into the FEM is required to determine why the excursions did not occur. The multiple coherence taken at the driving points of the two tests was not as expected and requires further investigation.

To determine the difference in the virtual, physical, and desired responses, the root mean square (RMS) of the response was determined. The RMS was used because it is a reliable check of the difference in the predicted and recorded energy input into the DUT, which is a parameter of great interest in vibration testing. Based on the achieved RMS values shown

Table 19.2 Desired and achieved RMS values

Control location	Specification (desired)	Virtual		Physical		Virtual to physical
–	RMS	RMS	% Error from desired	RMS	% Error from desired	% Error
X	0.0738	0.0702	4.88%	0.0801	8.5%	3.48%
Z	0.0850	0.0806	5.18%	0.1236	45.4%	16.0%

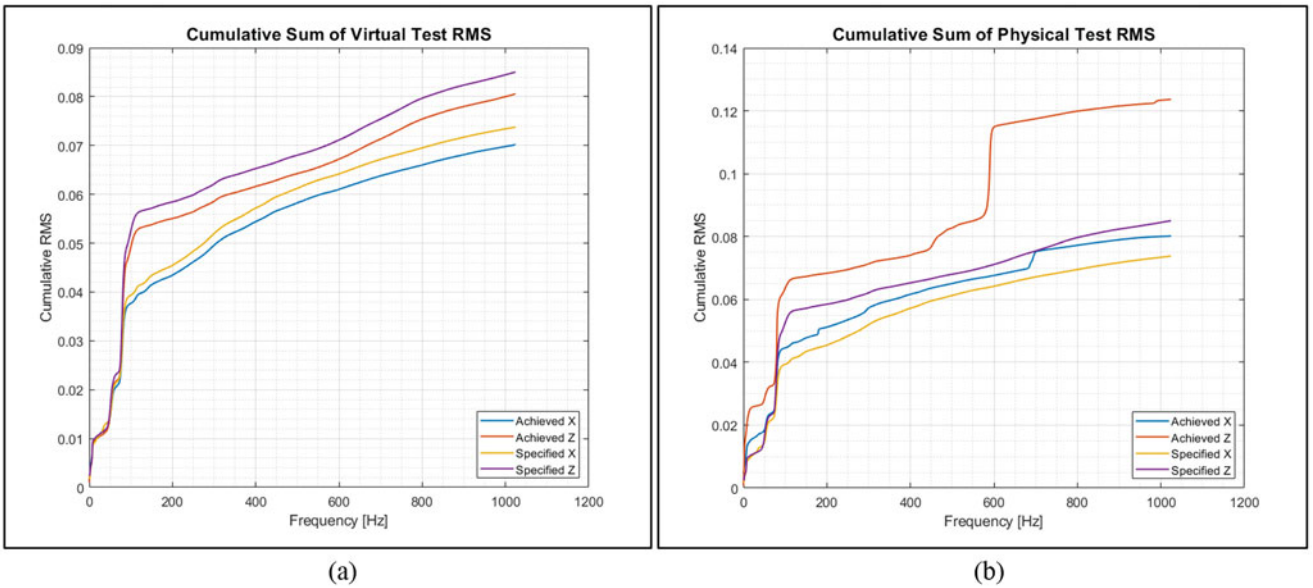

Fig. 19.13 The cumulative sum of the RMS for the virtual test (**a**) and physical test (**b**) at each control location was used to determine the appropriate bandwidth of consideration for these tests

in Table 19.2, the virtual test was approximately a 5% underestimation of the specification. The physical test was an over test within 10% for one control location but nearly 50% in the other. However, in vibration testing, an over test by 50% can be considered acceptable in limited frequency bands, indicating both tests predicted the vibrations experienced in the HOTSHOT.

The cumulative sum of the RMS values was used to determine an appropriate bandwidth for the consideration in these tests. The areas of Fig. 19.13 where the values for desired and achieved are nearly matching, represents a bandwidth in which the test systems could be a good representation of the specification, and the results could be further analyzed. Outside of this band, the input energy deviated enough that further refinement of the physical and virtual test systems would need to be considered to analyze the results. For the virtual test, an appropriate bandwidth for analysis is 0 to 1000 Hz while the physical test is appropriate from 0 to 600 Hz.

19.5 Conclusion

Because this study was an initial investigation, RMS values within 50% of the desired RMS values can be considered a success. It can be concluded that the virtual test reasonably accounts for the actual vibrations of the BARC base aboard the HOTSHOT rocket. As a result, performing a virtual vibration test on an FEM prior to conducting a multi-axis vibration test can be a reasonable way to estimate the system response and testing requirements to achieve a specification. Adding virtual testing as a step to vibration testing procedures could increase testing confidence and determine test feasibility before the test is performed, which reduces the risk of over testing the DUT that could potentially break equipment. It is desired to continue this testing to determine if this method could also be used to find ideal test setups and ideal control laws in a virtual setting, allowing the test engineer to know exactly how a multi-axis vibration test should be performed before ever setting foot in the lab. To do this, there are a few aspects of the testing that will require further research. This includes the excursions seen in the coherence at the driving points and the excursions seen in physical but not virtual response. It would be useful to explore different methods to reduce the FEM to find the best way to capture the full mass and stiffness matrices of model for virtual

testing. Using different methods to capture the FEM relationship would allow additional degrees of freedom to be added to the virtual test so that each node in the experimental mesh can be considered as a potential input and response locations.

Acknowledgments This research was funded by Los Alamos National Laboratory (LANL) through the Engineering Institute's Los Alamos Dynamics Summer School. The Engineering Institute is a research and education collaboration between LANL and the University of California San Diego's Jacobs School of Engineering. This collaboration seeks to promote multidisciplinary engineering research that develops and integrates advanced predictive modeling, novel sensing systems, and new developments in information technology to address LANL mission relevant problems.

References

1. Rohe, D.P., Nelson, G.D., Schultz, R.A.: Strategies for shaker placement for impedance-matched multi-axis testing. In: Proceedings of the 37th IMAC, A Conference and Exposition on Structural Dynamics 2019, Orlando, FL (2019)
2. Daborn, P.: Scaling up of the Impedance Matched Multi-Axis Test (IMMAT) technique. In: Proceedings of the 35th IMAC, A Conference and Exposition, Garden Grove, CA (2015)
3. Underwood, M., Keller, T., Ayres, R.: Multi-Shaker Control: A Review of the Evolving State-of-the-Art. Spectral Dynamics Inc., San Jose (2017)
4. Mayes, R., Ankers, L., Daborn, P., Moulder, T., Ind, P.: Optimization of shaker locations for multiple shaker environmental testing. Exp. Tech. **44**, 283–297 (2020)
5. Musella, U., Blanco, M.A., Mastrodicasa, D., Monco, G., Emilio, D.L., Simone, M., Peeters, B., Mucchi, E., Guillaume, P.: Combining test and simulation to tackle the challenges derived from boundary conditions mismatches in environmental testing. In: Proceedings of the 37th IMAC, A Conference and Exposition on Structual Dynamics 2019, Orlando, FL (2019)
6. Beale, C., Schultz, R.: Sensor Selection for MIMO Vibration. Sandia National Laboratories, Albuquerque (2020)
7. Soine, D.E., Jones, R.J., Harvie, J.M., Skounsen, T.J., Schoenherr, T.F.: Designing hardware for the boundary condition round robin challenge. In: Topics in Modal Analysis & Testing, Volume 9. Conference Proceedings of the Society for Experimental Mechanics Series (2018)
8. Banwell, G., Mohr, S., Rothenberg, S., Roberts, J.: Using experimental modal analysis to validate a finite element model of a tennis racket. In: 9th Conference of the International Sports Engineering Association (2012)
9. Rohe, D.P., Schultz, R.: A Custom Multi-Axis Vibration Controller with Flexible Control Strategies. Sandia National Laboratories, Albuquerque (2020)
10. Rohe, D.P., Schultz, R., Hunter, N.: Rattlesnake User's Manual. Sandia National Laboratories, Albuquerque (2021)

Chapter 20
Vibration-Based Damage Detection of a Monopile Specimen Using Output-Only Environmental Models

Emmanouil Lydakis, Sandro D. R. Amador, Holger Koss, and Rune Brincker

Abstract The field of vibration-based Structural Health Monitoring (SHM) relies on the evolution of the dynamic characteristics to identify the current health state of a monitored structure. In reality, these parameters are influenced either by a potential degradation of the structural integrity or by the varying environmental conditions. Therefore, a robust SHM scheme must clearly distinguish the different sources of changes in the monitored modal parameters. Along these lines, this study aims to identify structural changes in a monitored structure subjected to ambient vibrations and varying environmental conditions. The investigated structure consists of a wooden mast with a steel frame topside and is clamped to a concrete block at the bottom. During the monitoring campaign, the vibration response is acquired by a measurement system with four 3D sensors placed at strategic locations on the topside.

Keywords SHM · OMA · Modal identification · Environmental influence · Damage detection

20.1 Introduction

One of the main challenges in vibration-based SHM lies in the fact that the modal parameters of civil structures are heavily influenced by the varying environmental and operational conditions (e.g., temperature, humidity, wind speed). In fact, even though changes in the modal parameters can reflect a potential structural degradation, they can also be caused by the aforementioned environmental variability [1–8]. As a result, to ensure reliable damage detection of structures exposed to different environmental conditions, it is of significant importance to identify and separate the different environmental and operational effects from the modal parameters. To accomplish that, numerous statistical methods have been proposed in literature over the years, such as but not limited to principal component analysis (PCA), multivariate linear regression (MLR), and autoregressive (AR) models [1–3]. Especially when it comes to environmental variability, it is common to consider that a full year of monitoring is essential to develop a robust environmental model, suitable to describe the changing environmental factors as well as the seasonal variability. Nevertheless, there are various cases that a faster evaluation of the structural integrity is required; thus, the monitored modal parameters need to be obtained much sooner [2, 3]. In recent studies, for instance [1, 2], an environmental model was developed based on a monitoring campaign of only few months (3 and 1 months, respectively), leading to remarkable results in terms of damage detection of a wooden mast specimen. Consequently, an efficient environmental model is a solid basis where the corrected modal parameters can be assessed in the context of a vibration-based damage detection technique, to investigate whether structural changes are present in the monitored structures.

Based on the above, this study aims to eliminate the varying environmental effects from the modal parameters of a medium-sized monopile structure. This is achieved by an output-only environmental model utilizing the PCA approach. Moreover, the performance of a damage detection scheme based on statistical tools, namely control charts, is evaluated. Last but not least, it is worth noting that this investigation is carried out based on experimental data obtained during a previous monitoring campaign of the same specimen, conducted by [1].

E. Lydakis (✉) · S. D. R. Amador · H. Koss
Department of Civil and Mechanical Engineering, Technical University of Denmark, Lyngby, Denmark

R. Brincker
Brincker Monitoring ApS, Copenhagen, Denmark

B. J. Dilworth et al. (eds.), *Topics in Modal Analysis & Parameter Identification, Volume 9*, Conference Proceedings of the Society for Experimental Mechanics Series, https://doi.org/10.1007/978-3-031-34942-3_20

20.2 Methodology

In this section, the fundamental theoretical background utilized in this study is briefly discussed. First, the main principles of the PCA approach are presented, while a short description of control charts for damage detection follows. Principal component analysis is an output-only statistical approach to estimate a lower-dimensional representation of a data set, while retaining most of its variance [1, 4–6]. The application of PCA is based on the initial data matrix Y containing N observations of n observed features. A singular value decomposition (SVD) of the covariance matrix $Y^{\mathrm{T}}Y$ is performed as

$$Y^{\mathrm{T}}Y = US^2U^{\mathrm{T}} \tag{20.1}$$

where U is an $n \times n$ matrix containing the singular vectors and S is a diagonal matrix including the n singular values. The diagonal terms of S are organized in ascending order and are associated with the so-called principal components, which represent the directions of the data that explain the maximum amount of variance. Therefore, the first principal components are associated with the physical information, while the last ones include residual contributions related to noise effects. Along these lines, a robust PCA model lies in the optimal selection of $m(<n)$ singular values that represent sufficient amount of the data's variance. Once this condition is fulfilled, the loading matrix T is formed by taking into account only the first m number of features (i.e., columns) from U. Based on that, an estimate of the observed features is expressed as

$$Y = YTT^{\mathrm{T}} \tag{20.2}$$

The loss of information between the initial data matrix Y and the estimate $\hat{Y}$ obtained from PCA is estimated in terms of the residual error matrix $\hat{E}$ as [1].

$$\hat{E} = Y - \hat{Y} \tag{20.3}$$

The performance and efficiency of PCA in modeling environmental effects can be assessed, for instance, by means of control charts, which are tools of statistical quality control to detect whether a process is out of control. When an unexpected event occurs, the variability of this event in terms of an outlier index exceeds the range of predefined control limits. In this study, the Shewhart or T^2-chart is utilized, where structural changes are detected by means of the novelty index T^2-statistic, given by the expression

$$T^2 = \frac{N_k}{N_{k+1}} \left(x - \bar{\bar{x}}\right) R^{-1} \left(x - \bar{\bar{x}}\right)^{\mathrm{T}} \tag{20.4}$$

where N_k is the number of observations when the process is in control, meaning in this case the reference period where the investigated structure is in its undamaged condition. Moreover, x denotes the observations over the monitoring period, while $\bar{\bar{x}}$ and R designate the subgroup average and the covariance matrix of the observations during the reference period, respectively. To control the deviation of T^2-statistic, an upper and a lower control limit are estimated. The lower control limit (LCL) coincides with the x-axis, while the upper control limit (UCL) is given by

$$\mathrm{UCL} = \frac{(N_k - 1)\, n}{N_k - n} \, F_{n,n-m}\,(\alpha) \tag{20.5}$$

where $F_{n,\,n\,-\,m}$ denotes the α percentage point of the F distribution with n and $n - m$ degrees of freedom [4, 5].

20.3 Experimental Study

The theoretical framework described above is implemented to assess induced damage cases in a medium-sized monopile structure, exposed to ambient vibrations and varying environmental conditions. In a previous study by [1], a 3-month monitoring campaign has been carried out in the same structure to apply a vibration-based SHM scheme. Based on the same collected data, this work aims to further assess the efficiency of the PCA-based model created to remove the varying environmental conditions from the observed (i.e., estimated) natural frequencies and apply a damage detection scheme.

Fig. 20.1 Left: Medium-sized monopile specimen. Top middle: Two sensors clamped on the upper plate of the topside. Bottom middle: Steel topside with the four sensors clamped on different corners. Right: Cuts on the wooden mast [1]

The experimental model consists of a 3.6-m wooden mast with a square cross section of 0.1 × 0.1 m. A steel topside is placed at the top of the mast, while its bottom part is founded on a concrete block. The vibration responses are collected by four 3D geophone nodes, vibration sensors that are selected due to their high sensitivity and low noise floor. The monitoring campaign initiated on November 30, 2021, and lasted until March 4, 2022. Several damage cases are introduced to the experimental model over a 10-day time span, starting from February 15, 2022. The induced damages are practically 11 cuts on the wooden mast, as illustrated in the right pane of Fig. 20.1. In the X direction, the depth of each cut is initiated at 2 mm and is gradually increasing by 2 mm, until it reaches the maximum depth of 10 mm. On the contrary, the Y direction of the mast is only damaged once by inflicting a cut of 10 mm.

The measured vibration responses are utilized to apply OMA and more specifically, the Eigensystem Realization Algorithm (ERA) is used to estimate the modal parameters [9]. In this study, a shorter time window of 1 month is investigated, to assess whether that period is sufficient to develop a robust environmental model and identify the structural changes. The evolution of the natural frequencies over the 1-month monitoring period for the first two modes is presented in Fig. 20.2, where the different damage scenarios are indicated with vertical lines.

20.4 Environmental Model

As previously discussed, a PCA model is developed to describe the varying environmental conditions over the monitoring period. This model is built using two principal components (PCs), as they are capable of explaining the 99.99% of the data's variance. The monitoring period is split into training, validation, and prediction periods, where the PCA model is trained and subsequently validated through the reference (i.e., undamaged) period. Based on this training, the model is extrapolated and provides an estimate for the remaining period, where the state of the structure is considered unknown. The training, validation, and prediction periods of the PCA model are presented in Fig. 20.3, where a comparison is made with the actual natural frequency observations.

According to this figure, it is concluded that even though the PCA model provides an efficient estimate for the reference period, it can no longer represent the actual evolution of the natural frequencies over the damage period, especially for the first mode. Obviously, this is the case as the model is trained over the reference state where no structural changes are apparent; thus, it cannot predict the damage cases that followed. In fact, the environmental model seems to work as a damage indicator itself, since the actual frequency decrease compared to the PCA estimate reflects a potential structural degradation.

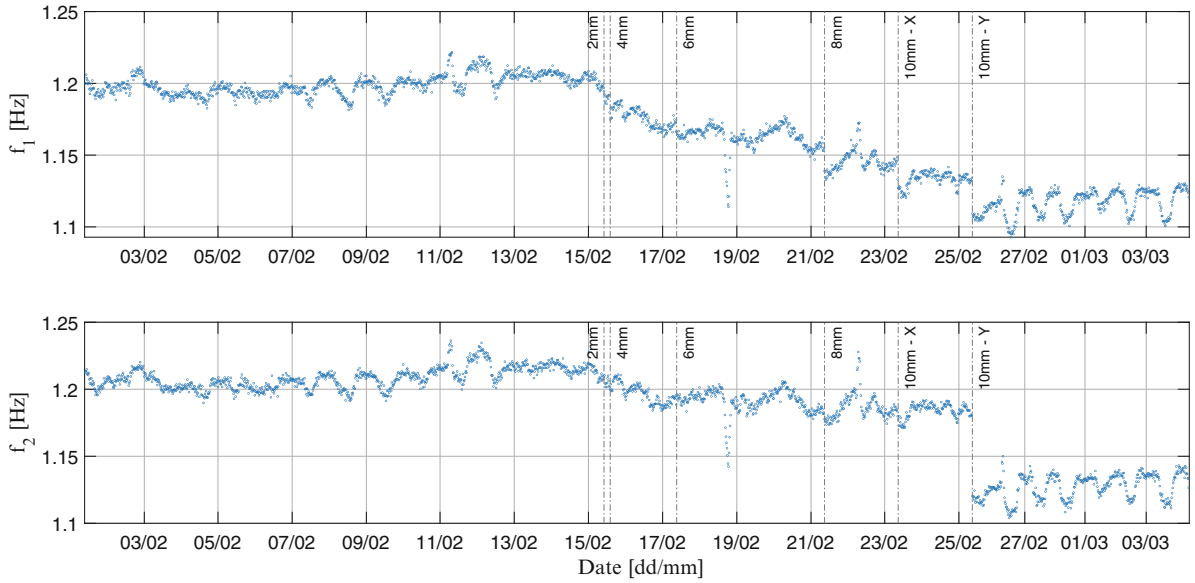

Fig. 20.2 Natural frequency evolution over the monitoring campaign for the first two modes. The induced damage cases are indicated with vertical lines [1]

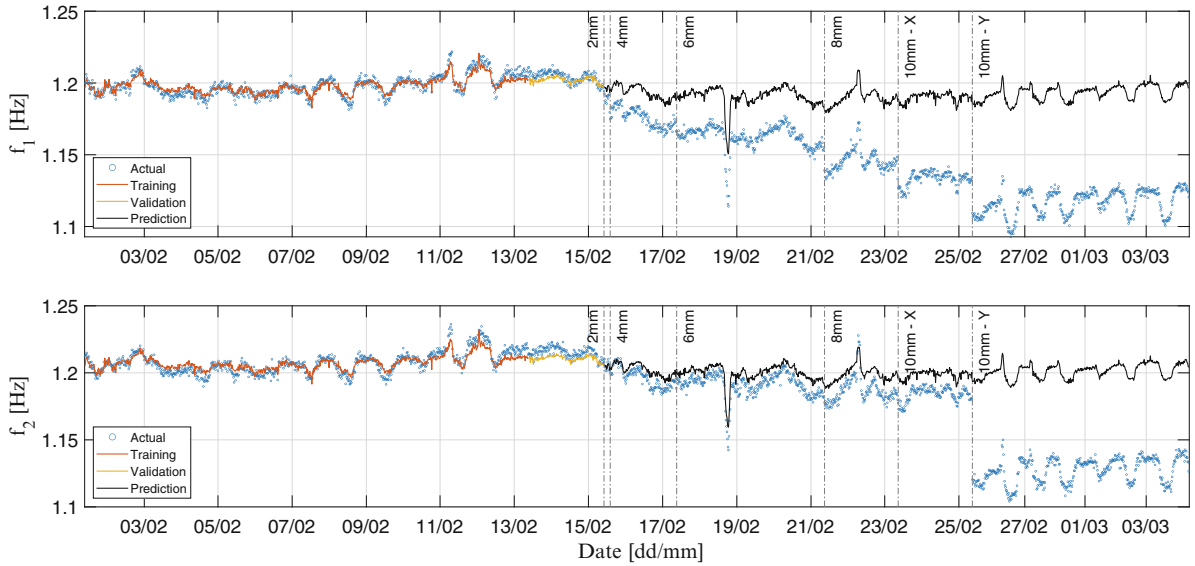

Fig. 20.3 Comparison between the PCA estimate with the actual natural frequencies. The PCA estimate is split into training (orange), validation (yellow), and prediction (black) periods

Furthermore, the corrected values of the natural frequencies are estimated based on the residual error, defined in Eq. (20.3). The PCA estimate including the environmental effects is subtracted from the observed values; thus, it provides a clearer picture of the structural degradation. In this way, the fluctuation due to the varying environmental conditions is eliminated, leading to a steadier evolution of the frequencies over time. On top of that, the damage presence becomes even more apparent, as the different damage cases are identified as sharper discontinuities in the evolution of the corrected natural frequencies. Specifically, in Fig. 20.4, six discontinuities are observed in the natural frequencies of the first mode, while only one significant offset is observed in the second mode.

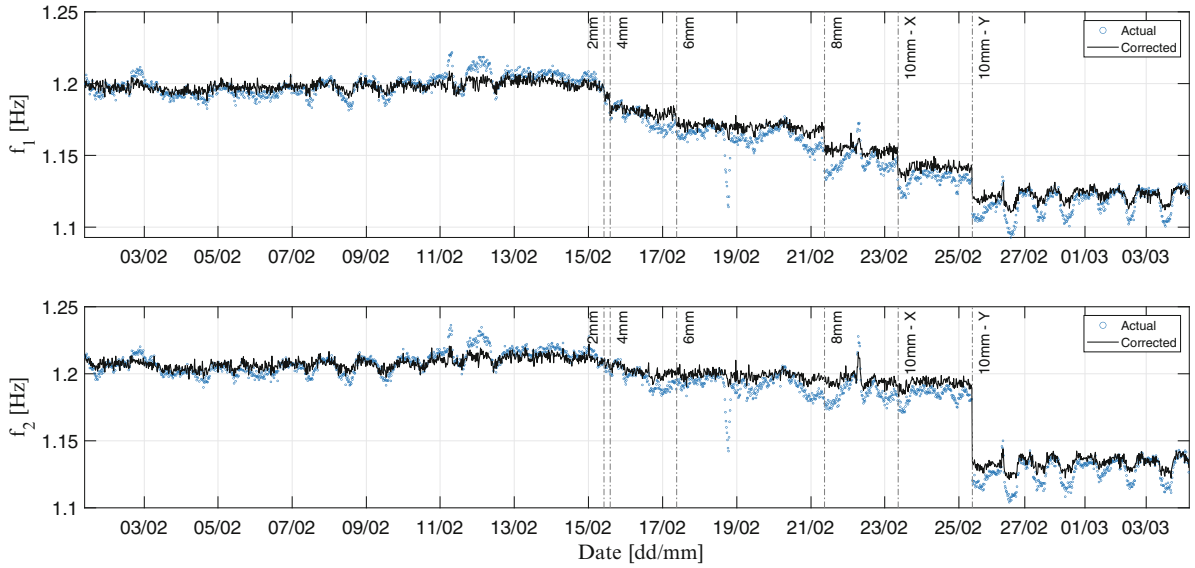

Fig. 20.4 Actual and corrected (from the PCA model) values of the natural frequencies for the first two modes. After removing the environmental effects, the corrected values show smaller variability and sharper discontinuities

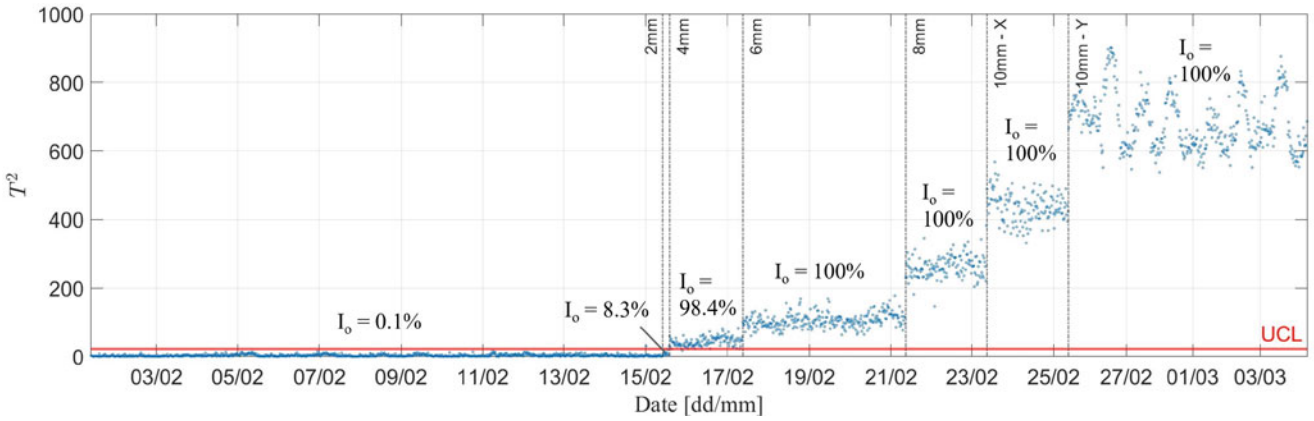

Fig. 20.5 T^2-chart and outlier index I_o over the monitoring period. The gradual increase in damage depth causes a remarkable increase of the T^2-statistic values, far above UCL

20.5 Damage Detection Based on Control Charts

Despite that the structural degradation is already apparent based on the environmental model described above, this section presents the performance of the T^2-chart for damage detection. The T^2-chart identifies the structural changes by means of the novelty index T^2-statistic, illustrated in Fig. 20.5 over the monitoring period. To control the deviation of this index, the UCL is estimated by considering an F distribution with $m = 2$, $n - m = 3$ degrees of freedom and a confidence interval of 95%. According to Fig. 20.5, it is clearly observed that the T^2-index follows the same increasing trend as the damage depth increases, leading it to far exceed the UCL. This can also be verified by the outlier rate I_o, estimated for the different periods of the monitoring campaign. In Fig. 20.5, it is observed that even a 2 mm cut on the wooden mast is enough to raise I_o from 0.1% to 8.3%. Moreover, it becomes obvious that the more the cut depth increases, the more T^2-statistic values exceed the UCL, leading to an outlier rate of 100% after the cut of 6 mm and above.

20.6 Conclusions

To sum up, this study focused on the damage detection of a medium-sized monopile specimen, exposed to ambient vibrations and varying environmental conditions. More specifically, the output-only PCA approach was used to eliminate the environmental effects from the observed natural frequencies, while the T^2 control chart was utilized as the main damage detection technique. Overall, this investigation showed the following:

- The induced damage scenarios on the experimental model caused a reduction of the natural frequencies of the first two vibration modes.
- The gradually increased damage depth in the X direction of the mast resulted in a gradual frequency decrease in the first mode, while the cut in the Y direction is mainly associated with the sharp reduction of the corresponding frequencies in the second mode.
- After eliminating the environmental variability, the structural degradation became significantly more apparent, as the different damage cases were identified as sharper discontinuities in the time evolution of the natural frequencies.
- The T^2-chart proved to be a robust damage detection scheme, as the T^2 index clearly indicated the induced damage cases as outlier observations that exceeded the control limit UCL.

Acknowledgments The authors acknowledge the funding received from DTU Offshore – Danish Offshore Technology Centre.

References

1. Lydakis, E., Amador, S.D.R., Brincker, R.: Structural health monitoring of a wooden mast structure based on OMA techniques. In: Proceedings of the 9th International Operational Modal Analysis Conference, pp. 352–360 (July 2022)
2. Andersen, P.L., Amador, S.D.R., Nielsen, S.T., Katsanos, E., Brincker, R.: Vibration-based damage detection using input-output and output-only environmental models: a comparison. Dyn. Civil Struct. **2**, 29–38 (2020)
3. Andersen, P.L., Nielsen, S.T., Amador, S.D.R., Katsanos, E., Brincker, R.: OMA-based structural health monitoring of a wooden mast structure exposed to ambient vibrations. In: Proceedings of the 8th International Operational Modal Analysis Conference, pp. 195–204 (May 2019)
4. Diord, S., Magalhães, F., Cunha, Á., Caetano, E., Martins, N.: Automated modal tracking in a football stadium suspension roof for detection of structural changes. Struct. Control. Health Monit. **24**, e2006 (2017)
5. Deraemaeker, A., Reynders, E., De Roeck, G., Kullaa, J.: Vibration-based structural health monitoring using output-only measurements under changing environment. Mech. Syst. Signal Process. **22**, 34–56 (2008)
6. Magalhães, F., Cunha, Á., Caetano, E.: Vibration based structural health monitoring of an arch bridge: from automated OMA to damage detection. Mech. Syst. Signal Process. **28**, 212–228 (2012)
7. Rainieri, C., Gargaro, D., Fabbrocino, G.: Statistical tools for the characterization of environmental and operational factors in vibration-based SHM. Struct Health Monit. Damage Detect. **7**, 175–184 (2015)
8. Gaile, L., Amador, S.D.R., Brincker, R.: Initial results from the continuous monitoring campaign of a wooden frame specimen. In: Proceedings of the 9th International Operational Modal Analysis Conference, pp. 352–360 (July 2022)
9. Brincker, R., Ventura, C.: Introduction to Operational Modal Analysis. Wiley (2015)

Chapter 21
Analysis of Traveling Wave Properties of Mechanical Metamaterial Structures: Simulation and Experiment

Hannes Fischer and Sebastian Tatzko

Abstract The steady-state response of harmonically excited structures can exhibit a significant traveling wave ratio. Local excitation of structures with locally increased damping or even structures that are proportionally damped, for example, lead to wave propagation phenomena. Since damping distribution plays a key role in formation of traveling waves, it needs to be considered in the dynamic analysis. In this chapter, we analyze the steady-state vibration behavior of 3D printed metamaterial structures. The investigated parts are made of resin and steel by laser sintering. The dynamic analysis with special attention to traveling wave effects is simulated based on finite element method and experimentally validated. Due to the complex geometry of the metamaterial structure, fine meshing is necessary for accurate results, making reduction techniques inevitable. A combination of modal reduction and dynamic condensation is used to obtain the simulated results. In the laboratory, laser scanning vibrometry is used to measure the entire structure and validate the simulations. We show in both simulation and experiment that the studied structures exhibit both standing waves with locally fixed nodal lines and traveling nodal lines with significant traveling wave content, depending on the excitation frequency.

Keywords Local damping · Modal damping · Traveling waves · Dynamic condensation · Metamaterial

21.1 Introduction

Harmonic excitation on a mechanical structure will create structural waves [1]. Typically, these waves are reflected at structural boundaries, and superposition of waves leads to a standing wave pattern. However, these standing waves, which at resonance are close to eigenmodes of the structure, are only a special solution to the general wave form of vibrations. Especially, with non-negligible damping, the reflected wave will not match the original wave in amplitude resulting in a significant traveling wave portion.

Formation of traveling waves is not restricted to a certain type of damping, but the combination of excitation and damping is crucial. Even proportional damping that is often used due to its diagonalization property leads to traveling waves when the excitation is applied by a local force [2]. Furthermore, local damping will generate energy transfer from excitation source to the damper with a characteristic phase shift in the steady-state vibration response. Complex phenomena associated with waves can already be observed in two degree of freedom mechanical systems [3] and vibrating strings with just one local dissipative attachment [4]. Indeed, traveling wave motion has been used for some time in technical applications, such as ultrasonic motors [5] or granular transportation [6]. Today, the researchers are concerned with wave propagation and its manipulation to create waveguides and bandgaps passively through metamaterial structures [7]. Thus, the fundamental mechanical theories on periodic waves combined with efficient numerical methods for model reduction and substructuring are utilized to design and analyze structures with specific properties [8].

H. Fischer (✉) · S. Tatzko
Institute of Dynamics and Vibration Research, Department of Mechanical Engineering, Leibniz University Hannover, Garbsen, Germany
e-mail: fischer@ids.uni-hannover.de; tatzko@ids.uni-hannover.de

B. J. Dilworth et al. (eds.), *Topics in Modal Analysis & Parameter Identification, Volume 9*, Conference Proceedings of the Society for Experimental Mechanics Series, https://doi.org/10.1007/978-3-031-34942-3_21

21.2 Modeling

In this chapter, two metamaterial beams with local resonators are analyzed, see Fig. 21.1. The structures are both 3D-printed. One resin beam built in an SLA printer and one steel beam additively manufactured in an SLS printer. Since both beams are linear vibration structures, the different materials can be referred to as a change in the distributed damping.

In the first step, the beam structures are analyzed theoretically regarding their traveling wave characteristics. Later, experiments will be performed in the lab to validate the theoretical findings. In the following, the numerical analysis is described and results are discussed. The geometry is modeled using finite elements to capture the periodic shape with local resonators precisely. To keep computational effort low while maintaining a high accuracy of dynamic properties, dynamic condensation is applied. The discretized equation of motion system reads

$$\mathbf{M}\ddot{\vec{x}} + \mathbf{C}\dot{\vec{x}} + \mathbf{K}\vec{x} = \vec{b}^T \hat{F} \cos \Omega t, \tag{21.1}$$

where $\mathbf{M}$, $\mathbf{C}$, and $\mathbf{K}$ are the mass, damping, and stiffness matrix, respectively, $\vec{x}$ contains displacements of all degrees of freedom (DoF), and $\vec{b}$ is a Boolean vector to project the harmonic excitation on a certain structural DoF. Applying a modal transformation with modal damping ratios D_i for each mode, Eq. 21.1 can be written as

$$\hat{\vec{x}} = \mathbf{H}\vec{b}^{\mathrm{T}} \hat{F} \cos \Omega t \quad \text{with} \quad \mathbf{H} = \sum_{i=1}^{n} \frac{\vec{\varphi}_i \vec{\varphi}_i^T}{\omega_{0i}^2 - \Omega^2 + \mathrm{j}2D_i\omega_{0i}\Omega}, \tag{21.2}$$

where $\mathbf{H}$ is the dynamic compliance matrix which can be obtained as a sum over all modes computing the dyadic product of eigenvectors φ_i [2]. A modal truncation is now possible by limiting the sum to $n < m$ with m the number of modes. Furthermore, dynamic condensation is easily performed by using a reduced eigenvector φ^* containing only DoF of interest, e.g., excitation and response DoF as well as DoF to analyze the spatial vibration form. In this case, the finite element model with over 158000 DoFs was reduced to 63 equally distributed degrees of freedom along the beam. The dynamic accuracy is guaranteed because the eigenvectors and eigenfrequencies were calculated with the full system. The excitation is applied on one end (Fig. 21.1 point A) of the beam with free-free boundary condition. Additionally, to modal damping, a local damping element is applied (Fig. 21.1 point B), which is implemented by adding a corresponding column to the compliance matrix $\mathbf{H}$ in Eq. 21.2 (Fig. 21.2).

Fig. 21.1 Metamaterial beams made of different types of base material

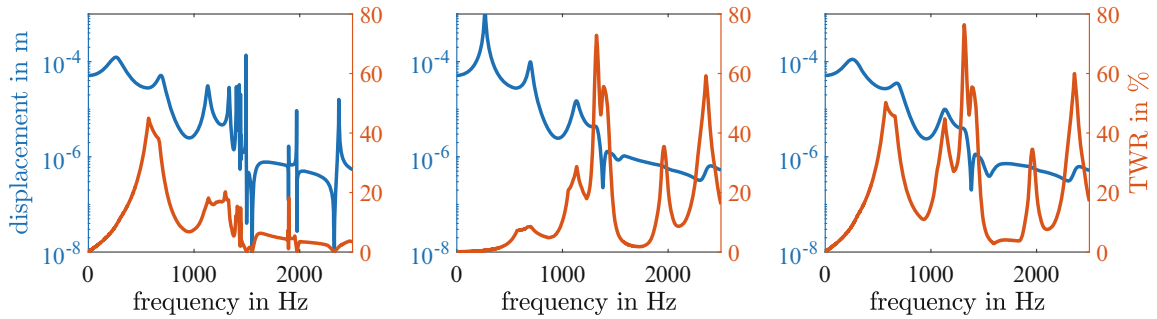

Fig. 21.2 Mode shapes of the metamaterial beam: (**a**) 697.9 Hz, (**b**) 1445.3 Hz, and (**c**) 1970.6 Hz

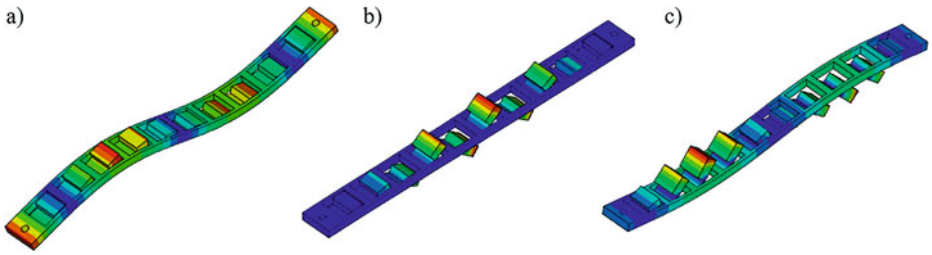

Fig. 21.3 Damping comparison: local damping (left), modal damping (middle), and local+modal damping (right)

21.3 Results

In Fig. 21.3, simulation results for different damping setups of the metamaterial beam are presented. The FRFs from point A to B are shown (Fig. 21.3). The traveling wave ratio (TWR) is here defined as the inverse of the standing wave ratio known from the field of radio engineering. Only the nodes of the frame structure were used to calculate the TWR. Local resonators were not considered in TWR calculation. Typical mode shapes of the metamaterial are shown in Fig. 21.2 with different amounts of participation by the resonators. Modal and local damping have different effects on the TWR. With local damping, higher TWRs can be realized at lower frequencies, while modal damping leads to a high TWR at higher frequencies but lower amplitudes. By combining local and modal damping, higher TWRs can be achieved over a wider frequency range. These findings have to be validated by experiments in the future by using the 3D-printed structures.

Acknowledgments This work was funded by the Deutsche Forschungsgemeinschaft (DFG, German Research Foundation)—462650249.

References

1. Doyle, J.F.: Wave propagation in structures. In: Wave Propagation in Structures, pp. 126–156. Springer, New York (1989)
2. Gasch, R., Knothe, K., Liebich, R.P: Strukturdynamik. Springer, Berlin (2021)
3. Krack, M. Bergman, L.A., Vakakis, A.F.: Motion complexity in a non-classically damped system with closely spaced modes: from standing to traveling waves. Proc. Inst. Mech. Eng. Part K: J. Multi-Body Dyn. **230**(2), 178–190 (2016)
4. Cheng, X., Blanchard, A., Tan, C.A., Lu, H., Bergman, L.A., McFarland, D.M., Vakakis, A.F.: Separation of traveling and standing waves in a finite dispersive string with partial or continuous viscoelastic foundation. J. Sound Vib. **411**, 193–209 (2017)
5. Hagedorn, P., Wallaschek, J.: Travelling wave ultrasonic motors, part I: working principle and mathematical modelling of the stator. J. Sound Vib. **155**(1), 31–46 (1992)
6. Mracek, M., Wallaschek, J.: A system for powder transport based on piezoelectrically excited ultrasonic progressive waves. Mater. Chem. Phys. **90**(2–3), 378–380 (2005)
7. Hussein, M.I., Leamy, M.J., Ruzzene, M.: Dynamics of phononic materials and structures: historical origins, recent progress, and future outlook. Appl. Mech. Rev. **66**(4), 040802 (2014)
8. Van Belle, L., Claeys, C., Deckers, E., Desmet, W.: On the impact of damping on the dispersion curves of a locally resonant metamaterial: modelling and experimental validation. J. Sound Vib. **409**, 1–23 (2017)

Chapter 22
Data Sampling Frequency Impact on Automatic Operational Modal Analysis Application on Long-Span Bridges

Anno C. Dederichs and Ole Øiseth

Abstract Bridge monitoring projects based on vibration data analysis tend, since the early 2010s, to process vibration acceleration data using a time-domain system identification method use an automatic operational modal analysis (AOMA) algorithm to extract the modal properties, without the involvement of an operator. This work highlights the impact that the acceleration data sampling frequency has on the outcome of some of the AOMA algorithms. Acceleration datasets, downsampled to different frequencies, from the Hardanger Bridge are processed by the Magalhaes 2009, Neu 2017, and Kvåle 2020 AOMA algorithms. It is shown that that the best results in terms of modal detection rates and number of errors are obtained for sampling frequencies between 10 and 20 Hz. Additionally, no algorithm is more impacted than another by the different sampling frequencies.

Keywords Automatic operational modal analysis (AOMA) · Long-span bridge · Sampling frequency · OMA · cov-SSI

22.1 Introduction

There is an increasing interest in deploying structural monitoring systems in road brides, both in new construction projects and retrofitting existing structures. To make these systems commercially viable, it is necessary that the analysis software upon which they rely functions in an automated fashion. This requires automatic operational modal analysis (AOMA) algorithms to extract the modal properties from vibration measurements made on the structure. Since the early 2010s, many such algorithms have been proposed for bridge applications ([1–6], among others). Although some of these algorithms are better than others, it is impossible to conclusively declare one single one as the best because a compromise between detection consistency, errors made, automation level, and computational complexity has to be made [7]. Regardless of which algorithm, and how automatic it is, is chosen, some initial setup is required when starting a new monitoring project. When using covariance-driven stochastic subspace identification (cov-SSI) as a system identification method, these setup values are the model orders to be analysed and the maximum number of time-lag steps for correlation analysis. Ballpark values, rule-of-thumb methods, and studies on the impact of these values are well established. However, the input data also needs to be discretised. There is no well-established guidance on what sampling frequency should be selected, neither for traditional operational modal analysis nor for automatic operational modal analysis. Information theory dictates that the sampling frequency must be at least twice as high as the highest modal frequency to be detected. In the authors' experience, when selecting the sampling frequency to be as low as possible, the outcomes of AOMA algorithms tend to generally not be satisfying, and it is necessary to select a higher sampling frequency than is strictly necessary to achieve good results. This study is interested in understanding the performance characteristics of AOMA algorithms when subjected to different sampling frequencies of the same input data and in inferring some rules-of-thumb for the choice of sampling frequency when working with long-span bridge monitoring projects. Data from the Hardanger Bridge case study is analysed at different sampling frequencies using three of the best-performing AOMA algorithms, Magalhaes 2009 [1], Neu 2017 [4], and Kvåle 2020 [6], with a particular interest in the modal detection consistency and error rates made by each algorithm at the different sampling frequencies.

A. C. Dederichs (✉) · O. Øiseth
Department of Structural Engineering, Structural Mechanics Group, Norwegian University of Science and Technology (NTNU), Trondheim, Norway
e-mail: anno.c.dederichs@ntnu.no

B. J. Dilworth et al. (eds.), *Topics in Modal Analysis & Parameter Identification, Volume 9*, Conference Proceedings of the Society for Experimental Mechanics Series, https://doi.org/10.1007/978-3-031-34942-3_22

22.2 Theory

System identification and operational modal analysis for civil engineering structures and long-span bridges is a well-documented subject without the need for a major introduction or theoretical explanation. However, as this study concerns the impact of sampling frequency of input data on (automatic) modal detections, which is a core element of any operational modal analysis algorithm, a concise introduction of covariance-driven stochastic subspace identification (cov-SSI) is provided for the convenience of the reader. A second brief theoretical part is dedicated to introducing the automatic modal detection algorithms used as part of this research, using the cov-SSI system identification outputs to extract the structural modes and their properties.

22.2.1 System Identification

System identification is the process of extracting core behavioural information of a process from experimental measurements. In the case of bridge engineering and monitoring, one is interested in extracting structural mode information from vibration acceleration data measured simultaneously at multiple points along a bridge. Many different system identification procedures are available to work with output-only information [8, 9], both in the frequency and time domains. Cov-SSI, a time-domain method assuming that the structure is modelled by a state-space model, is chosen as the system identification method for this research.

The discrete acceleration measurements are sampled at a given frequency f_s; $\boldsymbol{y}_n$ is the vector containing the acceleration values at time sample n across all l sampling locations. Cov-SSI relies on the construction and analysis of a block-Hankel matrix $H_{k,i}$ containing the time-lagged cross-correlations R_j of all acceleration components. The time lag is determined by $\Delta t = \frac{j}{f_s}$.

$$R_j = E\left(\left(\boldsymbol{y}_{n+j}\right)\left(\boldsymbol{y}_n\right)\right) \tag{22.1}$$

$E(\cdot)$ is the expectancy operator. The block-Hankel matrix will consist of $2i + 1$ time lags, and k indicates the smallest time lag included.

$$H_{k,i} = \begin{bmatrix} R_k & R_{k+1} & \cdots & R_{k+i} \\ R_{k+1} & R_{k+2} & \cdots & R_{k+i+1} \\ \vdots & \vdots & \ddots & \vdots \\ R_{k+i} & R_{k+i+1} & \cdots & R_{k+2i+1} \end{bmatrix} \tag{22.2}$$

The block-Hankel matrix can also be written as an observability matrix O_i and a controllability matrix Γ_i. These matrices are products of the state-space model state A and output C matrices; therefore, A and C can be determined from the block-Hankel matrix, given that it is transformed into a "more workable" format. This is achieved through a singular value decomposition (SVD).

$$H_{0,i} = \begin{bmatrix} U_\mathrm{o} & U_\mathrm{d} \end{bmatrix} \begin{bmatrix} \Sigma_\mathrm{o} & 0 \\ 0 & \Sigma_\mathrm{d} \end{bmatrix} \begin{bmatrix} V_\mathrm{o} \\ V_\mathrm{d} \end{bmatrix} \widetilde{=} U_\mathrm{o} \Sigma_\mathrm{o} V_\mathrm{o}^\mathrm{T} \tag{22.3}$$

The structure is assumed to have a finite number of modes participating in its movement; hence, only these o modes are detectable. The SVD of the block-Hankel matrix allows for this to be considered by only retaining the o largest singular values. The other singular values represent measurement noise and should ideally be zero. The observability and controllability matrices are then found as

$$O_i = U_\mathrm{o} \Sigma_\mathrm{o}^{1/2} \tag{22.4}$$

$$\Gamma_i = \Sigma_\mathrm{o}^{1/2} V_\mathrm{o}^\mathrm{T} \tag{22.5}$$

Finally, cov-SSI uses the analytical structure of the observability matrix to determine A as

$$A = O_i^{\uparrow\,\dagger} O_i^{\downarrow} \tag{22.6}$$

where $O_i^{\uparrow}$ is the observability matrix without its last l rows and $O_i^{\downarrow}$ is the same matrix without its first l rows. $(\cdot)^{\dagger}$ dentoes the pseudo inverse. C is simply the first l rows of O_i. Eigenvalue decomposition of A returns the eigenvalues λ_{d} and eigenvectors ψ of the system. They need to be transformed to continuous-time values through

$$\lambda_{\mathrm{c}} = \frac{\ln(\lambda_{\mathrm{d}})}{f_{\mathrm{s}}} \tag{22.7}$$

$$\phi = C\psi \tag{22.8}$$

λ_{c} is a complex value containing information about the frequency and damping of the detected system pole, and the corresponding column in the matrix ϕ contains the mode shape of the pole.

22.2.2 Automatic Operational Modal Analysis

Operational modal analysis is interested in extracting the modal features of the bridge structure. In an ideal world, this is already achieved once cov-SSI method has finished its processing. However, it is generally not possible to know the model order o to include in cov-SSI process in advance because the exact number of exited modes in the structure is not known in advance and measurement noise also leads to non-zero singular values. The system identification is performed for multiple model orders to counteract this problem, and their outcomes are compared. If a pole repeatedly appears with similar characteristics (frequency, damping, mode shape,) at many different model orders, the pole is likely a physical mode. However, a pole with no (or few) similar poles at other model orders is a mathematical artefact from the system identification process, which does not represent anything physical. Such artefacts are disregarded.

Traditionally, this process has been performed manually using a stabilisation diagram (a plot of model orders versus detected pole frequencies), as vertical lines forming in the diagram indicate a physical mode. This process is time- and resource-consuming because it requires an operator to analyse the outcome of each dataset. In the context of permanent structural monitoring, it is not feasible to perform this task by hand. Since the early 2010s, multiple algorithms relying on machine learning have been proposed to solve this task automatically. The automatic operational modal analysis algorithms are based on the same core three-step process:

1. The results from the system identification are further analysed to extract additional information – for example, the mode shape collinearity (MPC) or the mean phase deviation (MPD) – about the mode shape complexity and complex behaviour of each pole. A preliminary analysis to determine if a pole likely is a physical occurrence or a spurious mathematical object is performed to remove as many of the latter as possible. This is often done using a partition clustering algorithm such as k-means to separate the poles into two groups.
2. The potentially physical poles are grouped into clusters with high internal homogeneity. Ideally, a cluster would contain only poles from different model orders representing the same structural mode. This clustering step is usually performed with an agglomerative method, such as hierarchical clustering. There are differences between algorithms on how the similarity between two poles should be measured and how to determine the cut-off distance to find the different clusters. Most algorithms agree that a combination of relative distance in frequency and mode shape between two poles is a good base for the similarity measure. Statistical analysis of all these distances can provide a good estimate of the cut-distance.
3. The clusters resulting from step two are generally of two types. Large and homogenous clusters represent structural modes, and smaller and less homogenous clusters are groupings of spurious poles that made it past the initial filtering at step one. These smaller clusters need to be removed, as they are not relevant. This step is automated by either selecting a deterministic minimal number of poles to be in a cluster for it to be considered representative of a structural mode, or through another partition clustering method (i.e. k-means) automatically separating the detected clusters into structural and non-structural modes based on the number of elements within the cluster. The first method may be considered semi-automatic, as the threshold needs to be manually chosen. Finally, each retained cluster is generally filtered to remove any outliers which it may still contain, and representative mode features are derived from the poles within the cluster.

This work focuses on three algorithms: Magalhaes 2009 [1], the first AOMA algorithm to be proposed for bridge engineering, which can reasonably claim to be automatic. Neu 2017 [4], an algorithm based on multiple predecessors to represent state of the art in k-means and hierarchical clustering combination algorithms. Kvåle 2020 [6] is the first algorithm to use HDBSCAN – an agglomerative density-based clustering algorithm capable of performing steps one and two simultaneously and with low computational costs. Full details of the algorithms can be found in their original publications.

22.2.2.1 Magalhaes 2009

The clearing step in this algorithm is performed with a traditional stabilisation diagram analysis, which relies on removing any pole which varies more than a set amount in frequency, damping, or mode shape from its nearest neighbour at the next lowest model order. This type of analysis is historically part of the manual analysis workflow. Its downside is that the maximal relative variation acceptable for each feature needs to be determined manually, reducing the level of automation of the algorithm. The second clustering step is performed with hierarchical clustering with a distance measure between two poles defined as

$$d_{i,j} = \left| \frac{f_i - f_j}{f_j} \right| + \left(1 - \mathrm{MAC}_{i,j}\right) \tag{22.9}$$

The cut-off distance to determine two clusters apart is user selected and suggested to be $d_c = 0.02$. The n-largest clusters (a value predetermined by the user) are retained as structural modes. A box-and-whisker outlier detection method is used to remove any spurious poles still found within the clusters. The representative features of the detected mode are determined as the average value of all poles located within the cluster.

22.2.2.2 Neu 2017

The clearing step is performed using k-means partition clustering to separate the poles into two groups of potential physical and certainly mathematical poles. The clustering is performed on a feature vector associated with each pole based on as many values as possible, all characterising the relative difference from the given pole to its nearest neighbour at the next lowest model order. A box-cox transform of each feature is performed to make its distribution more normal-like, increasing the performance of k-means clustering.

The second step uses hierarchical clustering with a distance between two poles measured as

$$d_{\mathrm{c}i,j} = d\lambda_{i,j} + \left(1 - \mathrm{MAC}_{i,j}\right) \tag{22.10}$$

The cut-off value is determined by fitting a Weibull distribution to the distances between each pole and its nearest neighbour using Eq. (22.10) and selecting the value corresponding to the 95% percentile of the fitted distribution.

All resulting clusters with more than 25–75% (user selected) of the number of elements of the largest cluster are retained as structural modes. These clusters are filtered using a Thompson-Tau method on frequency and damping values within the cluster. Finally, the representative values for each mode are chosen as the average value of all the poles constituting it.

22.2.2.3 Kvåle 2020

The first step is performed using a traditional stabilisation diagram analysis. The clustering step is performed using hierarchical density-based spatial clustering for applications with noise (HDBSCAN), a combination of an agglomerative and density-based clustering method. The distance between two poles is defined by

$$d_{\mathrm{c}i,j} = \sqrt{\alpha_\lambda \left(d\lambda_{i,j}\right)^2 + \alpha_{\mathrm{MAC}} \left(d\mathrm{MAC}_{i,j}\right)^2} \tag{22.11}$$

Contrary to hierarchical clustering, it is not necessary to specify a cut-off level, but a minimal number of poles per cluster $n_{\min} = 20$ needs to be chosen to be able to separate clusters from one another. HDBSCAN automatically detects outliers and removes them from the clusters. Once the clusters are found, the algorithm retains only one pole per model order with each cluster before returning the detected modal features as the average of the features of all the poles in each cluster.

22.2.3 Sampling Frequency

The Nyquist-Shannon sampling theorem dictates that the vibration data must be sampled at least twice that of the highest modal frequency of interest. As vibration data is usually recorded at a frequency much higher than strictly necessary, it is downsampled to an adequate frequency to reduce computational complexity and time.

However, in the case of automatic operational modal analysis, where there is a lot of measurement and process noise which must be removed to reach good results, it is beneficial if some of the noise occurs outside the frequency range of interest for the structure. One way to achieve this is to increase the sampling frequency, as the noise will have the opportunity to settle in a frequency range above the low frequencies of interest. It is then simple to disregard this noise by ignoring the higher frequencies. The major downside of this method is that it also increases the frequency range in which modal detections are made, and with a maximum number of detectable modes (determined through the mode order), the number of modal detections made within the range of interest is generally diminished, with the less exited modes not being detected by the system identification. Figure 22.1 illustrates the lower amounts of detected poles for higher sampling frequencies in the frequency range of interest.

22.3 Experimental Case

The Hardanger Bridge is a suspension bridge with a main span of 1310 m located in the southwest of Norway. It is a slender structure composed of two driving lanes and a pedestrian walkway, leading to large displacements mostly due to environmental loading. In counterpart, the natural modal frequencies of the bridge are low, ranging from around 0.05 Hz for the first mode to around 0.420 Hz for the fourteenth deck mode. Table 22.1 shows the numerically expected frequencies of the first 14 modes of the bridge, their previously experimentally detected frequency [10], a description of their main deflection shapes, and the tolerance range used to accept an automatic detection represents the given mode. The bridge has been equipped since 2013 with 20 triaxial accelerometers, recording the ambient vibrations of the bridge. The recorded data is openly available [11].

One hundred datasets randomly selected from 2015 are used in this work. The datasets are downsampled to six sampling rates of 1 Hz, 2 Hz, 5 Hz, 10 Hz, 20 Hz, and 100 Hz. Each dataset is processed with all three AOMA algorithms, which return a list of detected structural modes for all sampling rates. The modal detections of the AOMA algorithms are then compared to the experimentally expected frequency values of the Hardanger Bridge to determine the consistency rate and the number of errors of each algorithm at each sampling frequency. The consistency rate is defined as the number of modal detections found within the tolerance range of a known mode divided by the total number of known modes. The number of errors is composed of two different types of errors: first, detections that an algorithm makes which do not correspond to a known mode and, second, the number of duplicate detections that an algorithm makes. Duplicate detections are when there are two or more detections for a single known mode.

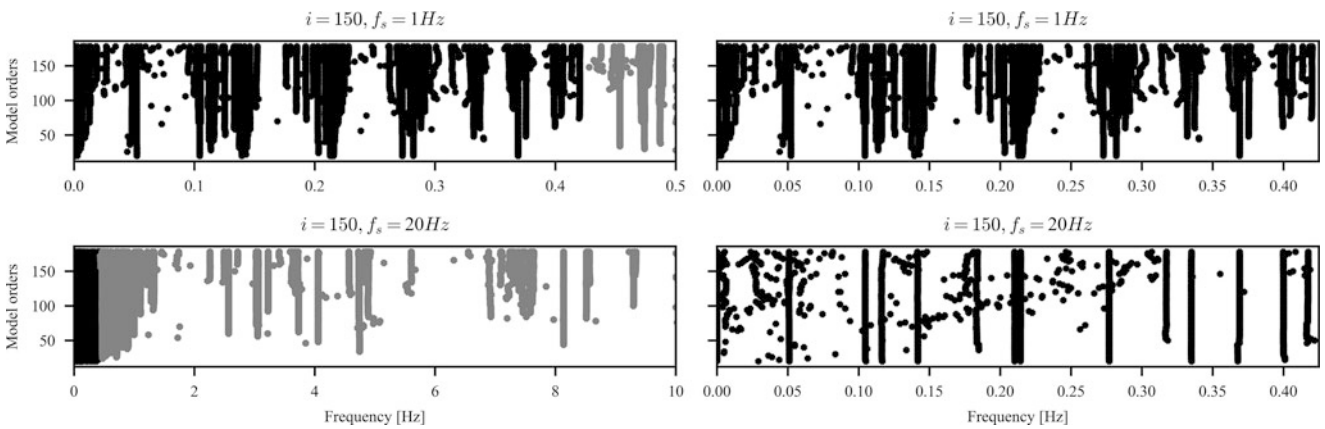

Fig. 22.1 Example of the impact of different sampling frequencies on the output of cov-SSI. The same dataset is analysed for a constant number of block-rows in the Hankel matrix and sampling frequencies of 1 Hz and 20 Hz. The left column shows the full frequency range of the detected poles, and the right column shows a zoom into the frequency range of interest

Table 22.1 Summary of known modal properties of the Hardanger Bridge

Mode number	Numerical frequency [Hz]	Mode shape description	Experimental detection [ref] [Hz]	Tolerance range [Hz]
1	0.05	Horizontal	0.052	[0.049, 0.055]
2	0.098	Horizontal	0.105	[0.099, 0.107]
3	0.11	Vertical	0.119	[0.111, 0.124]
4	0.14	Vertical	0.142	[0.139, 0.145]
5	0.169	Horizontal	0.183	[0.177, 0.186]
6	0.197	Vertical	0.206	[0.201, 0.209[
7	0.21	Vertical	0.212	[0.209, 0.216]
8	0.233	Horizontal + cables, lateral	0.230	[0.227, 0.234]
9	0.272	Vertical	0.276	[0.273, 0.279]
10	0.293	Horizontal	0.318	[0.308, 0.323]
11	0.33	Vertical	0.333	[0.328, 0.338]
12	0.36	Torsional	0.374	[0.362, 0.376]
13	0.394	Vertical	0.401	[0.396, 0.406]
14	0.406	Horizontal + cables, lateral	0.418	[0.412, 0.420]

The analysis is performed twice. The first analysis is done by maintaining the number of block-rows constant and equal to $i = 150$ in the Hankel matrix. This means lower sampling frequencies have a longer time lag in the system identification compared to the higher sampling frequencies. A longer time lag means that cov-SSI returns a more precise modal parameter estimation, as it has more periods in the input signal to analyse. The second analysis is made at a constant maximal time lag of $t_{\text{lag, max}} = 40$ [s]. This alleviates the precisions issues of the first analysis, but at the cost of increasing the size of the block-Hankel matrix significantly for higher sampling frequencies. It is not possible to analyse the sampling rate of $f_s = 100$ [Hz] for the second analysis due to memory issues associated with the size of the block-Hankel matrix. The number of block rows in the Hankel matrix are 20, 40, 100, 200, and 400, for sampling frequencies of 1 Hz, 2 Hz, 5 Hz, 10 Hz, and 20 Hz. For both analyses, the recorded datasets of 30 minutes in length are cut into three 10-minute samples, and only the middle 10-minute recording is analysed.

22.4 Results

Table 22.2 summarises the overall consistency rate of each algorithm for both analysis scenarios and all sampling frequencies. It also contains the combined number of errors made for each case. The three selected algorithms have previously been shown to have similar performance levels [7], and as expected, the consistency rates of the algorithms are similar for each given analysis case. The worst consistency rates are found for the constant number of block-rows scenario for a sampling rate of 100 Hz. Intuitively, this makes sense, as, first, the sampling frequency does not seem in adequation to the frequency range of interest, being about 100 times higher than the highest expected modal frequency, and second, because of the very short time lag included in the system identification. The maximal time lag of $t_{\text{lag,max}} = \frac{(2i+1)}{f_s} = \frac{301}{f_s} = 3$ [s] is far inferior to the longest modal period of close to 20 seconds and within the same order of magnitude as the shortest expected modal periods. Such a short time lag does not permit a good estimate of the modal properties, when multiple periods of a given mode are normally required. The bad estimates present too much scatter for them to be recognised as a cluster by the AOMA algorithms.

Disregarding the 100 Hz sample rate case, the consistency rates increase with increased sampling frequency in both analysis scenarios and reach a high plateau for sample rates of 10 Hz and 20 Hz. The increase is more marked for the constant block-row case, starting around 0.45 for 1 Hz sampling and reaching around 0.75 for 10 Hz and 20 Hz sampling rates. The constant time-lag analysis has a consistency of 0.6 for the lowest sampling rate and reaches 0.8 for the two highest sampling rates. The higher consistency rates are likely due to the constant time-lag scenario having better system identification parameters for all sampling rates compared to the constant block-row scenario. These results corroborate the theoretical hypothesis that a too-low sampling rate leads to too much noise being introduced into the frequency range of interest and thus diminishing the performance of AOMA algorithms.

The error committed by the algorithms are also within the expected range based on previous research [7] for sampling frequencies of 5 Hz and above. For the Magalhaes 2009 and Kvåle 2020 algorithms, the error rate decreases with increased sampling rate until increasing again for the 100 Hz analysis case. These two algorithms are known to mostly make direct

Table 22.2 Average consistency rates and number of errors per sampling frequency and algorithm

Sampling frequency [Hz]		Constant $i = 150$			Time lag: 40 s		
		Magalhaes 2009	Neu 2017	Kvåle 2020	Magalhaes 2009	Neu 2017	Kvåle 2020
1	Consistency	0.51	0.47	0.39	0.44	0.73	0.63
	# Errors	6.14	14.96	3.31	1.44	20.35	3.11
2	Consistency	0.68	0.61	0.60	0.68	0.66	0.73
	# Errors	5.55	15.64	4.55	2.05	12.49	2.65
5	Consistency	0.76	0.68	0.70	0.78	0.64	0.74
	# Errors	1.92	10.99	2.20	1.22	9.67	1.76
10	Consistency	0.80	0.72	0.76	0.81	0.74	0.76
	# Errors	1.07	10.08	1.34	1.02	10.20	1.53
20	Consistency	0.79	0.68	0.75	0.83	0.75	0.76
	# Errors	1.00	9.20	1.39	0.98	10.47	1.31
100	Consistency	0.35	0.25	0.27	–		
	# Errors	3.17	4.96	3.59			

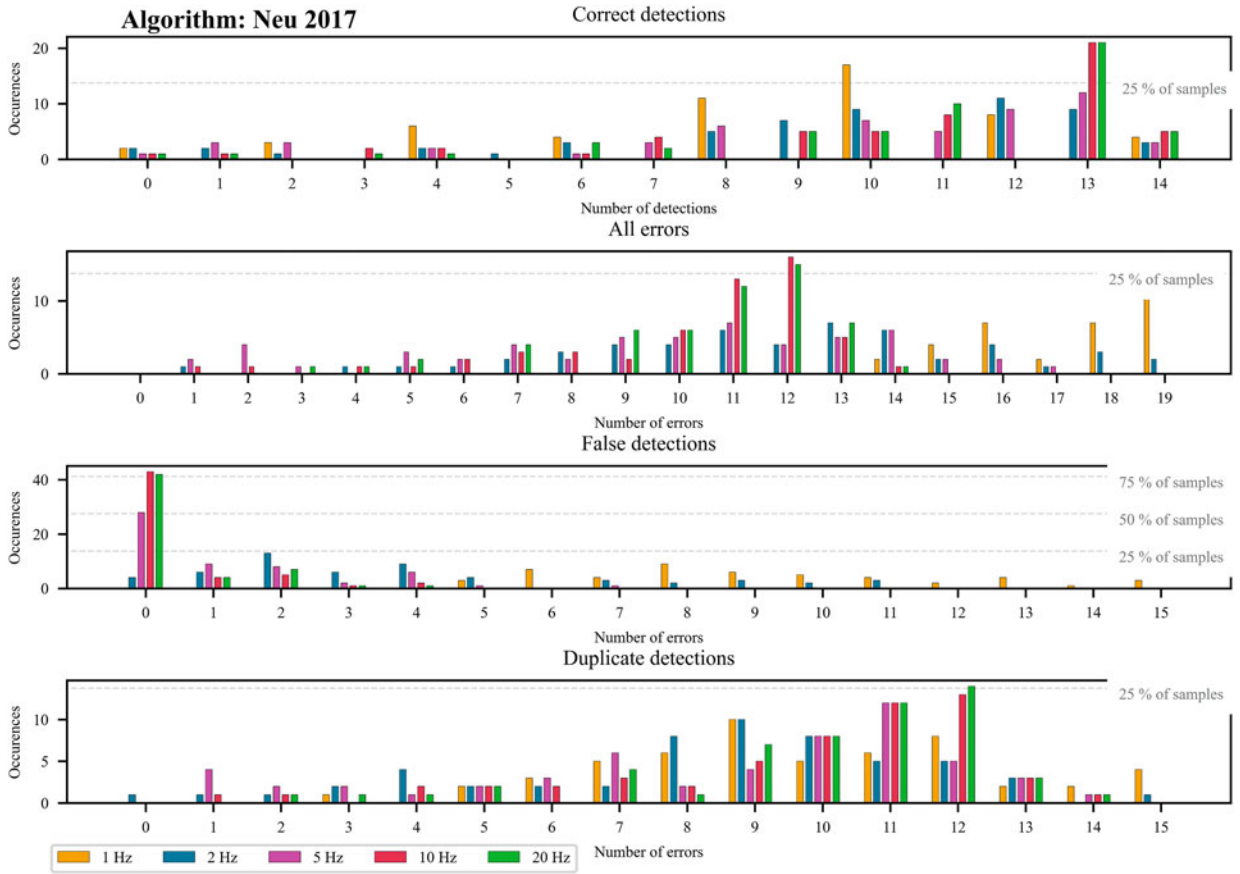

Fig. 22.2 Distribution of consistency rates and the number of errors made per dataset. The total number of errors and a breakdown into false and duplicate detections are shown for the Neu 2017 algorithm in the constant time-lag analysis case

errors and few duplicate errors. The algorithms are prone to selecting noise clusters as structural modes for low sampling frequencies due to the amount of noise concentrated into the frequency range of interest. The system identification estimates suffer from poor quality for the very high sampling rate case, leading to the algorithm detections being classified as errors due to this poor quality. In the case of the Neu 2017 algorithm, known to make few direct errors but many duplicate errors, the error rate continues to decrease for the 100 Hz case. As fewer modes are present in the frequency range of interest of the algorithm, it cannot make as many duplicate detections. Figure 22.2 shows the distribution of correct detections and errors made by the Neu 2017 algorithm across all samples in the constant time-lag analysis scenario. The third graph, illustrating

the distribution of direct errors per processed dataset, shows that in 75% of the cases, the sampling frequencies of 10 Hz and 20 Hz lead to no direct errors, while no other sampling frequency gets close to the same score. The fourth graph shows that most errors are due to duplicate detections and that these happen similarly at all sampling frequencies.

22.5 Discussion

Low sampling rates lead to worse modal detection results, with more errors being committed by AOMA algorithms in the two analyses performed in this study. Although this can seem counter-intuitive because one generally selects a sampling frequency to correspond to the frequency range of interest of the problem at hand. In the case of AOMA, it is better to increase the sampling frequency rate so that the inevitable noise and spurious modal detections generated in the system identification process do not get concentrated in the frequency range of interest. In this case, the ideal sampling frequency is 10 to 20 times higher than the minimum frequency needed to detect all modes of interest. This difference of one order of magnitude is in the same range as the difference between the expected number of modes to detect (14 in this case) and the actual number of poles detected (fixed by the model order, ranging from 20 to 180). As mathematical poles are uniformly randomly generated across the full range of detection frequencies, having a range of frequencies an order of magnitude larger than strictly necessary leads to, on average, only a few mathematical poles within the frequency range of interest. This noise level is then within most AOMA algorithms' filtering capabilities.

Overall, the constant time-lag analysis leads to better results than the constant number of block-rows analysis. This is mostly due to the increased system identification precision, which comes with having a longer time lag included in the block-Hankel matrix. The chosen time lag is twice the length of the longest modal period and roughly 15 times as long as the shortest modal period of interest. This is sufficient for precise detection of the modal frequency to be made. But needing to combine a time lag this large with a sampling frequency an order of magnitude larger than strictly necessary means that the block-Hankel matrix must be large, leading to memory and computational issues in the extreme cases on most normal computers. For this reason, it is often simpler to set up an analysis with a fixed number of block-rows, as one directly controls the size of the matrix at the cost of detection precision. This work shows that it is possible to achieve good results from AOMA even when using a fixed number of block-rows and a sampling frequency an order of magnitude larger than theoretically necessary.

All algorithms tested show similar levels of performance across all analyses and sampling frequencies, in line with their performance levels previously reported. The robustness of the algorithms to changes in sampling frequency being very similar, the choice of algorithm for a given investigation only needs to be based on the intrinsic performance characteristics of the AOMA algorithm.

22.6 Conclusion

The performance of automatic operational modal analysis algorithms is influenced by the sampling frequency of the acceleration data analysed. Contrary to intuition, it is necessary to select a sampling frequency in an order of magnitude larger than the highest modal frequency to be detected to obtain the best AOMA results for the Hardanger Bridge monitoring project. This helps spread most of the spurious pole detection made by cov-SSI be outside the frequency range of interest, diminishing the filtering and interpretation work necessary by the AOMA algorithms. Varying the block-Hankel matrix size to ensure a sufficient time lag in the system identification procedure leads to better and more consistent results from the AOMA algorithms, but often at the cost of higher computation complexity and larger memory needs. All three tested algorithms performed similarly across all sampling frequencies and to their expected functionality level in the best-case scenarios. No algorithm is more sensitive to sampling frequency than another.

References

1. Magalhães, F., Cunha, Á., Caetano, E.: Online automatic identification of the modal parameters of a long span arch bridge. Mech. Syst. Signal Process. **23**(2), 316–329 (2009). https://doi.org/10.1016/j.ymssp.2008.05.003
2. Reynders, E., Houbrechts, J., De Roeck, G.: Fully automated (operational) modal analysis. Mech. Syst. Signal Process. **29**, 228–250 (2012). https://doi.org/10.1016/j.ymssp.2012.01.007

3. Zhang, G., Ma, J., Chen, Z., Wang, R.: Automated eigensystem realisation algorithm for operational modal analysis. J. Sound Vib. **333**(15), 3550–3563 (2014). https://doi.org/10.1016/j.jsv.2014.03.024
4. Neu, E., Janser, F., Khatibi, A.A., Orifici, A.C.: Fully automated operational modal analysis using multi-stage clustering. Mech. Syst. Signal Process. **84**, 308–323 (2017). https://doi.org/10.1016/j.ymssp.2016.07.031
5. Yang, X.M., Yi, T.H., Qu, C.X., Li, H.N., Liu, H.: Automated Eigensystem realization algorithm for operational modal identification of bridge structures. J. Aerosp. Eng. **32**(2) (2019). https://doi.org/10.1061/(ASCE)AS.1943-5525.0000984
6. Kvåle, K.A., Øiseth, O.: Automated operational modal analysis of an end-supported pontoon bridge using covariance-driven stochastic subspace identification and a density-based hierarchical clustering algorithm. In: IABMAS Conf., No. 1996 (2020)
7. Dederichs, A.C., Øiseth, O., Petersen, Ø.W., Kvåle, K.A.: Comparison of automated operational modal analysis algorithms for long-span bridge applications. In: BT – Topics in Modal Analysis & Parameter Identification, vol. 8, pp. 27–35. Springer International Publishing, Cham (2023)
8. Van Overschee, P., De Moor, B.: Subspace Identification for Linear Systems. Springer (1996)
9. Rainieri, C., Fabbrocino, G.: Operational Modal Analysis of Civil Engineering Structures. Springer New York, New York (2014)
10. Petersen, Ø.W., Øiseth, O., Lourens, E.M.: Estimation of the dynamic response of a slender suspension bridge using measured acceleration data. Proc. Eng. **199**, 3047–3052 (2017). https://doi.org/10.1016/j.proeng.2017.09.547
11. Fenerci, A., Andreas Kvåle, K., Wiig Petersen, Ø., Rønnquist, A., Øiseth, O.: Data set from long-term wind and acceleration monitoring of the Hardanger bridge. J. Struct. Eng. **147**(5), 2–10 (2021). https://doi.org/10.1061/(asce)st.1943-541x.0002997

Chapter 23
Comparison of Two Possible Dynamic Models for Gear Dynamic Analysis

Fabio Bruzzone and Carlo Rosso

Abstract Several gear dynamics models are available in the literature, each with its unique application. In this chapter, a comparison between two models will be discussed. While the source of excitation in both models will come from the time-varying mesh stiffness caused by the static transmission error, the first model aims to estimate the dynamic overloads due to the meshing with a simple one-dimensional approach, neglecting other flexibilities. The second one instead includes the flexibilities of the shafts as well as bearings and the gearbox housing, with the possibility of being extended to multistage transmissions. Both models are quick and can give useful insight in the design process of a geared transmission. A simple test case will be detailed highlighting the different capabilities of the models and providing several key results such as dynamic forces and displacements which can help designers to define better components.

Keywords Gear dynamics · Static transmission error · Dynamic model · Gear tooth stiffness · Gear contact

23.1 Introduction

As reported in [1], many dynamic models have been proposed in the literature. Tuplin first defined the natural frequency of the engagement in the earlier dynamic model ever proposed. A great number of studies were reported in the extensive review by [2]. The same authors proposed the model described in [3] and visible in Fig. 23.1. This model is the "father" of a series of variants. One of the most important is the one in [4] but where the distinction between Static Transmission Error and Dynamic Transmission Error was introduced. Another "son" is the one proposed in [5, 6], where nonlinear behavior of the mesh stiffness and its harmonic nature was introduced. In particular, in this approach, the STE is considered as a sinusoidal signal characterized by its own frequency and the variation of the external torque presented a fundamental frequency different from the one of the STE, and the complex ones of those variations make up the excitation sources. In order to affine the model, the authors inserted in the model also the compliance of the shafts and the clearances in the bearings.

Generally speaking, the equation of motion for the model proposed in [5, 6] can be written as

$$m\ddot{x} + c\dot{x} + k_m x = \frac{T_1}{d_{b,1}} + e(t), \tag{23.1}$$

where the equivalent mass is $m = m_{eq} = I_1 I_2/(I_1 r_1^2 + I_2 r_2^2)$ computed starting from the inertias I_1 and I_2 of the pinion and gear, respectively, and their base radii r_1 and r_2. k_m represents the mesh stiffness, T_1 is the applied torque that can be static or dynamic, and c is the proportional damping. According to the standard definition, $x = r_2\theta_1 + r_1\theta_2$ is the DTE and $e(t)$ is the excitation source described above. Another approach was proposed in [7]. The elements involved in the model are almost the same, but in this methodology an external excitation source is not directly defined and the excitation of the system is intrinsic into the fluctuation of one of the parameters, namely the Time-Varying Mesh Stiffness ($TVMS$), where mesh stiffness $k_m(t)$ is computed from the STE at different torque levels. Thus, the parametrically excited system equation of motion can hence be written as

F. Bruzzone (✉) · C. Rosso
Department of Mechanical and Aerospace Engineering, Politecnico di Torino, Torino, Italy

GeDy TrAss company, Torino, Italy
e-mail: fabio.bruzzone@polito.it; carlo.rosso@polito.it

B. J. Dilworth et al. (eds.), *Topics in Modal Analysis & Parameter Identification, Volume 9*, Conference Proceedings of the Society for Experimental Mechanics Series, https://doi.org/10.1007/978-3-031-34942-3_23

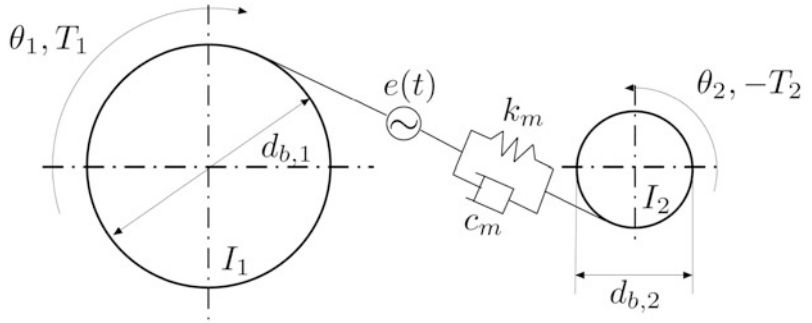

Fig. 23.1 Ozguven and Houser dynamic model as detailed in [3]

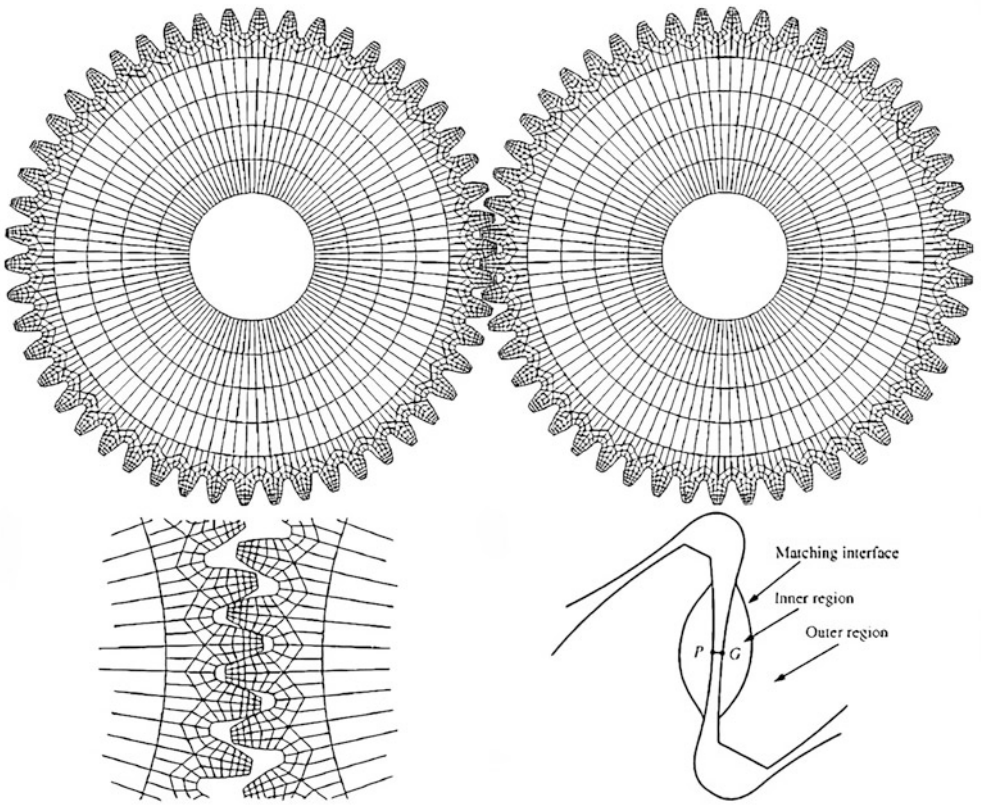

Fig. 23.2 Coupled FE/Contact mechanics model from [7]

$$m\ddot{x} + c\dot{x} + k_m(t)x = \frac{T_1}{d_{b,1}}. \tag{23.2}$$

On the basis of this 1D models, other scholars researched more accurate results using more complex models, principally involving the Finite Element Technique. Parker and Vijayakar [7] (Fig. 23.2) coupled an FE model with a detailed analytical contact model in order to compute the variation of mesh stiffness.

As a consequence, the same approach was applied to the frequency domain in [8]. The more a model is accurate, the more is high the computational effort requested, so many improvements were researched to reduce them in [9] and [10] still maintaining all the possible sources of nonlinearities and the influence of flexibilities. In [11], the effects of tooth profile modifications were investigated using the above cited methodology. On the basis of this model, the Hybrid Analytical–Computational technique was developed in [12]. The authors precompute a Force Deflection Function (Fig. 23.3) building a map in which tooth deflection is a function of various loads across the pitch. This mesh-dependent stiffness was applied to a lumped parameters model obtaining accurate results with lower computational efforts. For particularly thin web and ring gears, Cooley and Parker introduced a methodology for simulating the flexibilities of gears through a rotating elastic

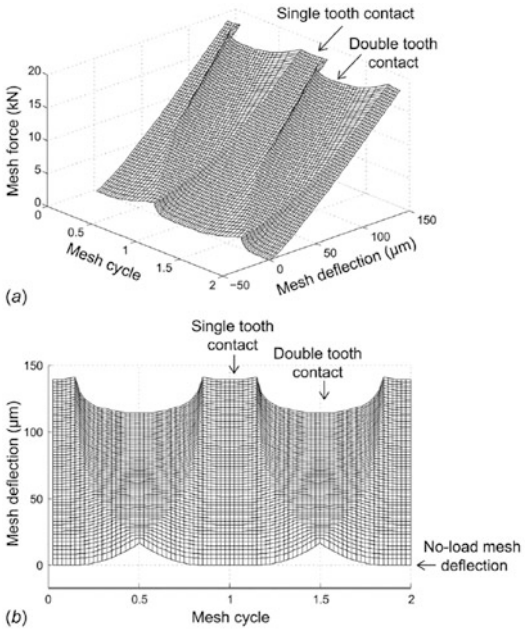

Fig. 23.3 Force Deflection Function from [12]

ring coupled to constant space-fixed foundations [13, 14] and a study on the parametric instabilities was indeed performed introducing variable mesh stiffness values [15]. The analytical nature of their model allows them to derive closed-form solutions for the eigenvalues including rotor dynamics effects and study in detail veering and instability phenomena. As depicted in the literature review [1], more complex approaches were implemented by scholars and software houses, but the simulation time is a key factor in the development of a new gearbox. So, in the present chapter, the authors investigate the main difference in two different approaches for studying the gear dynamics. They compare a 1D model based on TVMS methodology with a 3D evolution of the previous one, in order to highlight the main difference and the limit of application of the two strategies.

23.2 Materials and Methods

In this section, the two compared models are briefly described.

23.2.1 1D Model

Based on [7] approach, the authors modified the 1D model as detailed in [16]. In that approach, the $TVMS$ is enriched in order to take into account also the loss of contact and the backside contact. This means that nonlinearities in the contact grow of importance and this require a modification of the motion equation. As the first step, the motion equation is rearranged as

$$\ddot{p(t)} = \frac{T(t)}{r_b \cdot m_{eq}} - \frac{K(t)}{m_{eq}} p(t) - \frac{c}{m_{eq}} \dot{p(t)}, \tag{23.3}$$

where $T(t)$ is the torque, which can vary with respect to the time, $K(t)$ is the stiffness that varies according to a gear mating model, and c is the damping, set at a constant value as in the literature.

In Fig. 23.4, the Simulink implementation of Eq. 23.3 is shown. In the big sum symbol, five addends are converging. One is related to the damping force (lower arrow), one to the inertia fore (the arrow with plus sign), and the other three arrows to the stiffness forces. In the nonlinear scheme depicted in Table 23.1, the three contributions are described. The three outputs are always generated, but only the contribution of one of them is really summed. By defining p as the dynamic displacement along the Line of Action (LOA) and by checking the relative value with respect to the dead zone generated by the backlash b, the correct contact condition is defined. On the basis of this check, a multiplication for 0 or 1 selects the right contribution to the dynamic force.

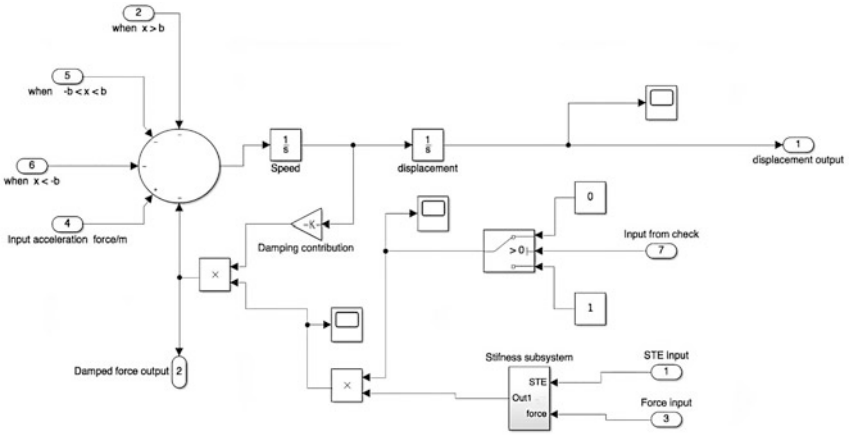

Fig. 23.4 Simulink implementation of the numerical integration of motion equation

Table 23.1 Displacement check for nonlinear modeling

Condition	Contact
$p > b$	Proper contact, stiffness evaluated by means of the lookup table
$-b \leq p \leq b$	Absence of contact
$p < -b$	Backside contact, stiffness evaluated by means of the lookup table

23.2.2 3D Model

The proposed methodology is depicted in [17] and implemented in the software GeDy TrAss. The peculiarity of that approach is the capability to evaluate the meshing stiffness by considering all the compliances involved in the gearbox. The dynamic model of a gearbox involves several elements. One of the most important contribution to the deformation is the shaft on which the gears are mounted. In addition casing and bearings can deeply affect the dynamic behavior of the gearbox, so their compliances have to be considered. In the proposed methodology, the abovementioned elements will be modeled as a Timoshenko beam [18] with 6 Degrees Of Freedom (x, y, z, θ_x, θ_y, θ_z) and a 12 X 12 diagonal matrix that takes into account the 6-direction of action of the bearings. The Mass $\mathbf{M_s}$ and stiffness $\mathbf{K_s}$ matrices are built depending on the geometry and the discretization of the system. The casing is typically inserted in the model by means of a reduced model order technique taking into account the main interaction points with the rest of the gearbox. In order to build the dynamic model, at least a shaft (beam element) is connected to one gear in one of its nodes and on the other to a bearing. The gear element is modeled as a connection to the other shafts by means of a kinematic link. The pinion gear is defined by means of a node O_1 located on the shaft and another node T_1 that represents the engagement law. According to gear theory [19], T_1 is the tangent point between the Line Of Action (LOA) and the base circle of the gear, and C is the pitch point. The point C is a virtual node, as the two coincident virtual nodes ($T_{1,1}$ and $T_{1,2}$) added at point T_1. Nodes $T_{1,1}$ and O_1 are connected by means of a Rigid Body Element (RBE) in a master–slave relationship. As shown in Fig. 23.5, a rigid link is also created between the repeated node $T_{1,2}$ and the C node. With this scheme, the motion along the line of action is guaranteed. The same approach is used for the gear. In C, a spring connects the two rigid elements of the two mating gears, finally simulating the engagement. The stiffness value of such spring is computed by means of the approach depicted in [20]. The instantaneous stiffness value $k_{n,z}$ depending on the nth gear pair and zth position along the pitch, Eq. 23.4, is used for each time instant.

$$k_{n,z} = \frac{T(t)}{S.T.E.r_b}, \tag{23.4}$$

where r_b is the base radius of the pinion.

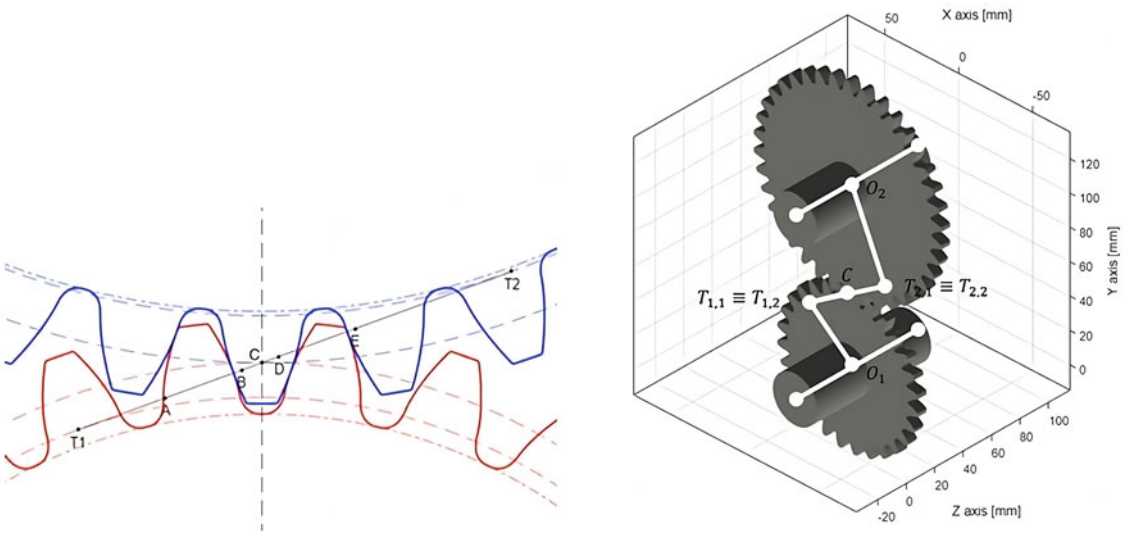

Fig. 23.5 Scheme for links between shafts that depicts the gear set

23.2.3 Dynamic Solution

As presented in [17], an iterative integration scheme is performed. Newmark [21] scheme with constant acceleration is adopted. By rearranging the terms of motion equation, the following expression is evaluated for the ith time step:

$$\ddot{\mathbf{u}}_\mathbf{i} = \mathbf{S}_{\mathbf{i}\delta\mathbf{r}_\mathbf{i}}, \tag{23.5}$$

where

$$\mathbf{S_i} = \mathbf{M_z} + \Delta t_i \mathbf{C_z} + \Delta t_i^2 \alpha_{NM} \left(\mathbf{K_z} + \mathbf{K_{c,i}}\right) \tag{23.6}$$

and $\mathbf{M_z}$, $\mathbf{C_z}$, and $\mathbf{K_z}$, are the mass, damping, and stiffness matrices of the structures, whereas $\mathbf{K_{c,i}}$ is the connection stiffness matrix. α_{NM} is fixed equal to 1/4 and Δt_i is the time step.

The residual vector is then evaluated as

$$\delta\mathbf{r_i} = \mathbf{f} + (-\mathbf{K_z} + \mathbf{K_{c,i}})_\mathbf{i}\mathbf{u_{i-1}} - (\mathbf{C_z} + \Delta t_i \mathbf{K_z} + \mathbf{K_{c,i}})_\mathbf{i}\dot{\mathbf{u}}_\mathbf{i-1} + \mathbf{A_i}\ddot{\mathbf{u}}_\mathbf{i-1}, \tag{23.7}$$

where

$$\mathbf{A_i} = -\mathbf{C_z}(1 - \delta_{NM})\Delta t_i - \left(\mathbf{K_z} + \mathbf{K_{c,i}}\right)\left(\frac{1}{2} - \alpha_{NM}\right)\Delta t_i^2 \tag{23.8}$$

and δ_{NM} is set equal to 1/2.

As Newmark prescribes, $\mathbf{u_{i-1}}$, $\dot{\mathbf{u}}_\mathbf{i-1}$, and $\ddot{\mathbf{u}}_\mathbf{i-1}$ are the displacements, velocities, and accelerations vectors at the previous time instant. The vector $\mathbf{f}$ represents the external forces and it is assumed constant in the single time instant and the unique value different from zero will be the torque T applied to the θ_z DOF of the input shaft. This procedure allows to take into account the variation of the engagement stiffness and the torque during the mesh cycle, but obviously in the single time instant they remain constant. In such a way, the complete integration scheme can follow the nonlinear behavior of the gear mating.

23.3 Results and Discussion

In this paragraph, a gearbox with three shafts and an idle gear is considered. Results are obtained by means of two different models. A particular attention is focused on the comparison of the dynamic force among the gear contact. The tested gearbox is shown in Fig. 23.6 and the data are listed in Table 23.2. The input gear (Z1) is supported by a shaft with a complex geometry due to the presence of spline coupling and 5 bearings. The input torque is equal to 115 Nm, and it is directed as depicted in Fig. 23.6. The idle gear (Z2) is a simple disk that is supported by two bearings and the output gear (Z3) has a short shaft and it is supported by two bearings. In such a model, the casing is not considered, only shafts and bearing flexibilities are introduced. In particular, the stiffness of the bearing is set according to Table 23.3. Bearings with axial stiffness are considered as hinges, and the others are considered as supports. The stiffnesses of the shafts are computed according to the actual geometrical properties and setting a Young modulus of 200 GPa and a density of 7800 kg/m^3.

In Figs. 23.7 and 23.8, the STE of the two stages of the gearbox are presented. Comparison is made by considering only teeth deflection or shaft and bearing compliances.

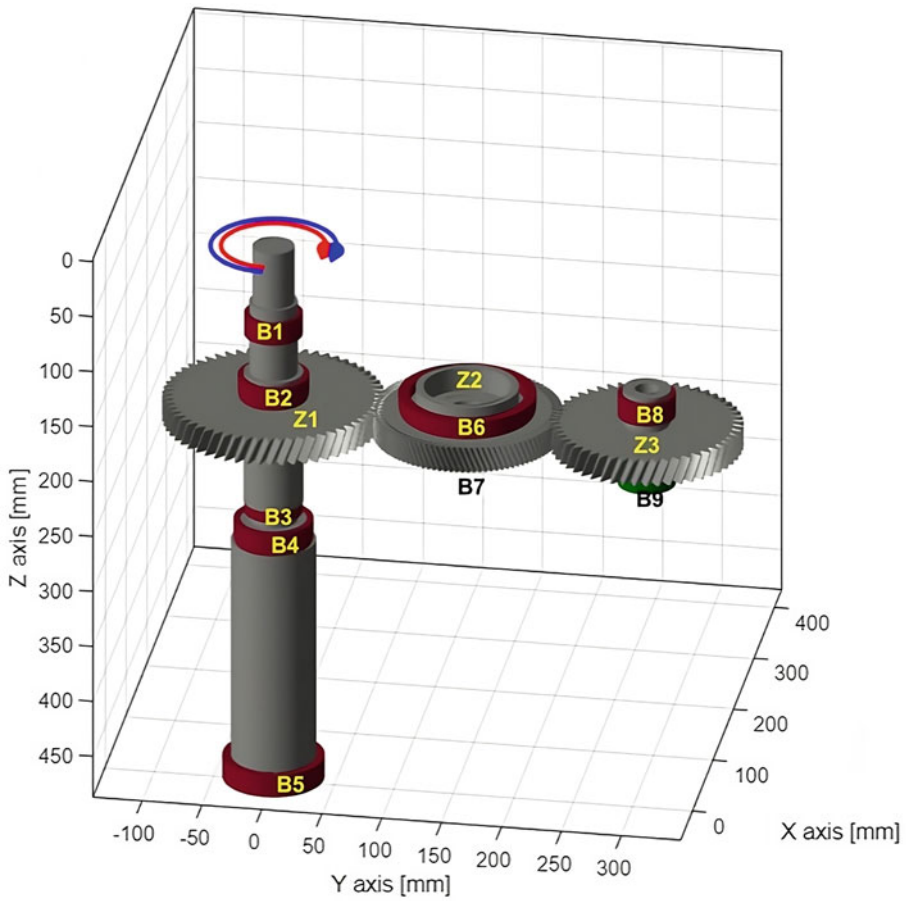

Fig. 23.6 Image of the gearbox model

Table 23.2 Mating gear main parameters.

	Quantity	Name	Units
Input gear	Number of teeth	Z1	61
Idle gear	Number of teeth	Z2	51
Output gear	Number of teeth	Z2	53
All the gear	Module	2.54	mm
All the gear	Pressure angle	20	°
All the gear	Helix angle	20	°
All the gear	Face width	20	mm
All the gear	Reference rack	ISO 53/A	

Table 23.3 Bearing stiffness

Name	Radial N/mm	Axial N/mm
B1	245,000	0
B2	280,000	171,000
B3	250,000	0
B4	250,000	0
B5	250,000	0
B6	380,000	0
B7	180,000	80,000
B8	223,000	0
B9	250,000	390,000

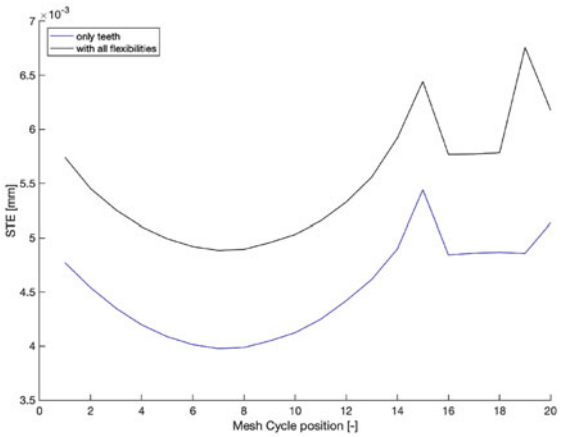

Fig. 23.7 STE of the first stage, comparison between the two models

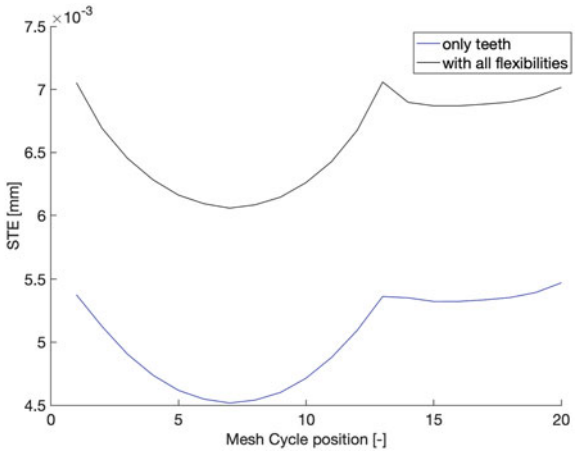

Fig. 23.8 STE of the second stage, comparison between the two models

Both 1D and 3D models compute the meshing force during a speed-up maneuver from 0 to 2500 RPM. The 1D model can only estimate the meshing force, whereas the 3D model also provides results concerning the bearing reactions. In Fig. 23.9a, the dynamic force on the first stage is shown by considering as input the STE computed with only the tooth compliance, the same, and in Fig. 23.9b, the meshing force on the second stage is presented.

In Fig. 23.10a and b, the same results but computed with the STE obtained considering all the flexibilities.

It can be noted that the presence of the shafts and bearing compliances changes the behavior of the meshing force, and in particular a reduction of the natural frequency of gear meshing can be highlighted. On the first stage, an increment of the force can be registered.

The same analysis is conducted using the 3D model. In this case, the model considers all the flexibilities, but the meshing stiffness is derived on the basis of the two different STEs of Figs. 23.7 and 23.8. In Fig. 23.11, the results related to the first and second stages are reported considering the meshing stiffness due to the tooth compliance. In Fig. 23.12, the results by

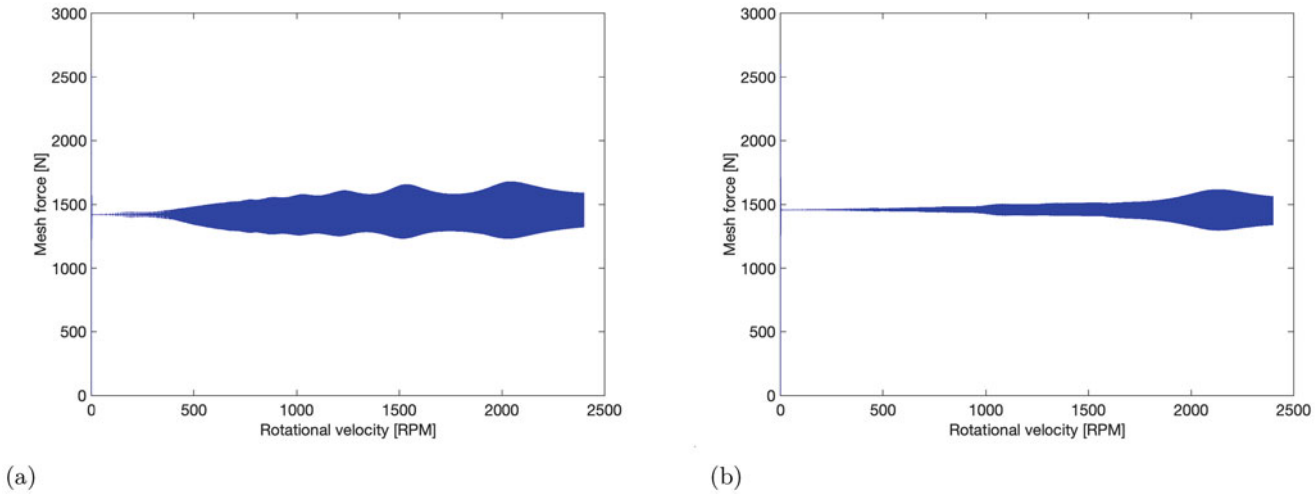

Fig. 23.9 Meshing force computed with 1D model considering the tooth deflection. (**a**) First stage. (**b**) Second stage

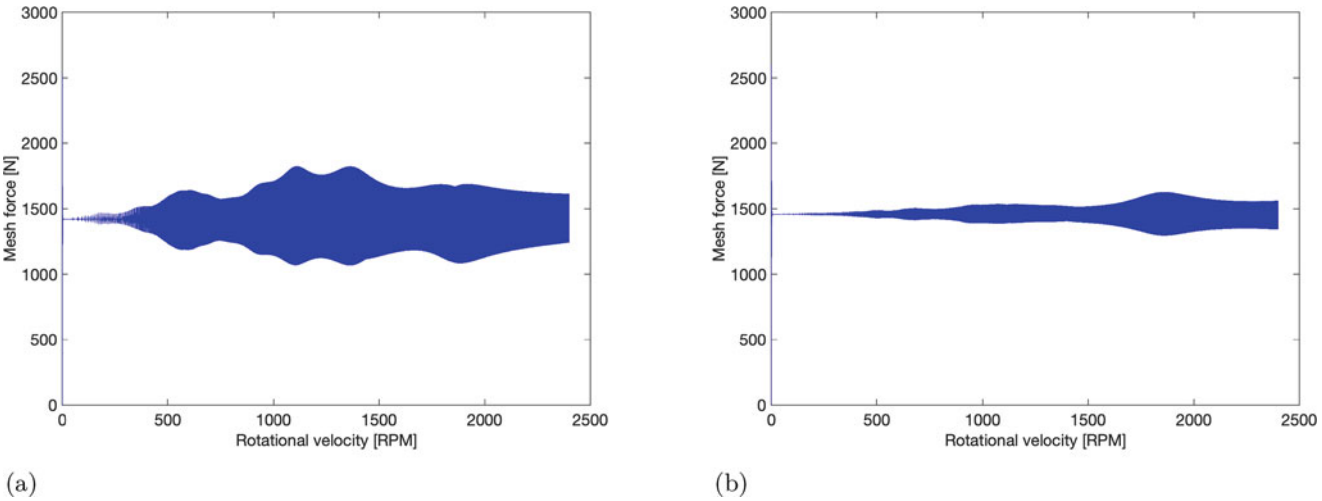

Fig. 23.10 Meshing force computed with 1D model considering the shaft and bearing compliances. (**a**) First stage. (**b**) Second stage

considering the meshing stiffness computed with the addiction of shaft and bearing are shown. By comparing the results, it is evident that considering all the flexibilities produces an increase of the exchanged force, and this is particularly evident in the first stage in the speed range over 1500 RPM. In addition, the 1D model highlights the contribution of the tooth compliance to the meshing force, whereas the 3D model allows to evaluate the contribution of all the flexibilities to the meshing force. As a matter of fact, the meshing forces computed by 1D and 3D models for the first stage show the same trend in particular between 1000 and 1500 RPM. It is possible to conclude that the trend of the two peaks are directly correlated to the meshing properties of the first stage. On the contrary, the peak near 2000 RPM is referred to the second stage meshing properties, but it is evident that, due to the higher flexibilities of the first shaft, the effect of the second mesh is higher on the first stage than on the second. As the 1D model is performed, no interaction between stages is considered, whereas the 3D model takes into account the whole system, so by the comparison of the results of the two models, it is possible to understand mutual interaction and forces of vibrations. In particular, from the 1D model, the contribution of the tooth compliance to the meshing force can be highlighted, whereas in the 3D model, the mutual effects can be evaluated.

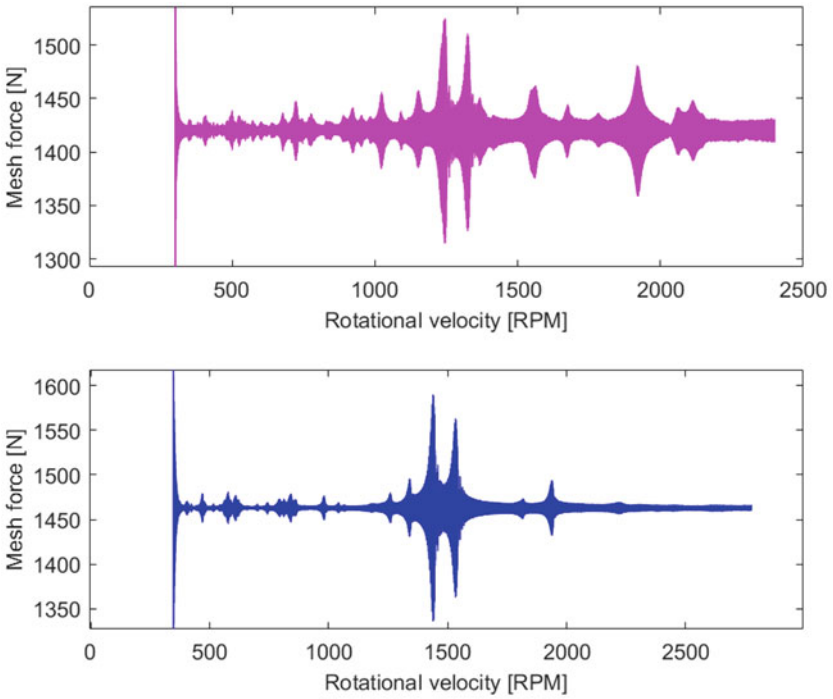

Fig. 23.11 Meshing force in stages 1 and 2 considering only the meshing stiffness due to tooth compliance

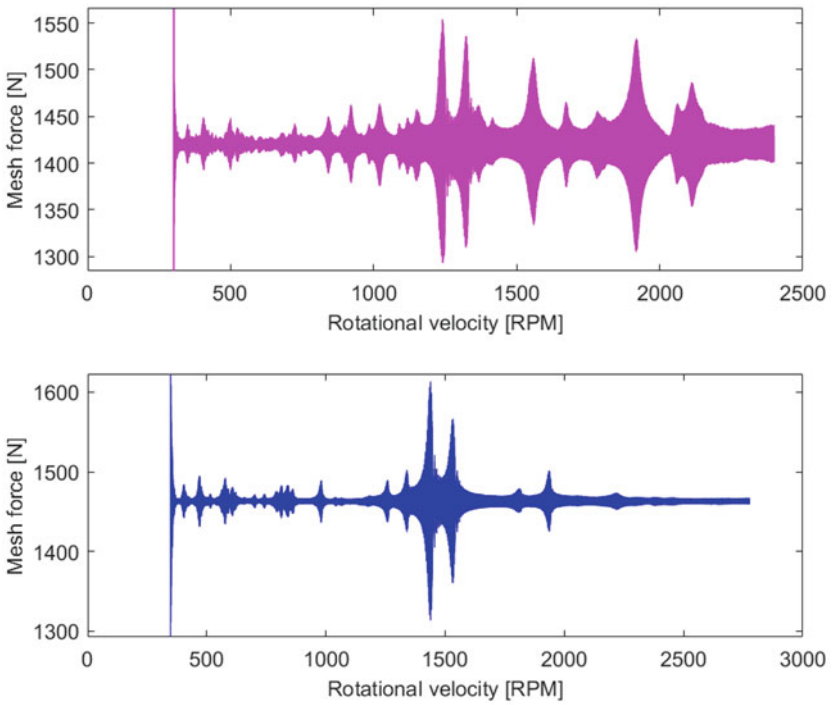

Fig. 23.12 Meshing force in stage 1 and 2 considering the meshing stiffness due to tooth, shaft and bearing compliances

23.4 Conclusion

In this chapter, two different approaches to compute the meshing force of a geared transmission are discussed. The first model is a simplified 1D model which can be useful for evaluating the contribution of the meshing properties. The 3D model here described presents higher accuracy and also richness of results, and it is useful for evaluating the mutual effects of the different stages of the gearbox. The same models were analyzed considering two different excitation sources: the first one obtained considering only the tooth compliance and the second considering all the shaft and bearing flexibilities. It is evident that considering all the flexibilities, both the models highlighted an increment in the exchanged forces, proving the importance to study the gear dynamics with an accurate model that takes into account all the flexibilities.

References

1. Bruzzone, F., Rosso, C.: Sources of excitation and models for cylindrical gear dynamics: a review. Machines **8**(3), 37 (2020)
2. Ozguven, H.N., Houser, D.R.: Mathematical models used in gear dynamics—a review. J. Sound Vib. **121**, 383–411 (1988)
3. Ozguven, H.N., Houser D.R.: Dynamic analysis of high speed gears by using the loaded static transmission error. J. Sound Vib. **125**, 71–83 (1988)
4. Umezawa, K., Suzuki, T., Sato, T.: Vibration of power transmission helical gears: approximate equation of tooth stiffness. Bull. JSME **29**, 1605–1611 (1986)
5. Kahraman, A., Singh, R.: Non-linear dynamics of a spur gear pair. J. Sound Vib. **142**, 45–79 (1990)
6. Kahraman, A., Singh, R.: Interactions between time-varying mesh stiffness and clearance non-linearities in a geared system. J. Sound Vib. **146**, 135–156 (1991)
7. Parker, R.G., Vijayakar, S.M., Imajo, T.: Non-linear dynamic response of a spur gear pair: Modelling and experimental comparisons. J. Sound Vib. **237**, 435–455 (2000)
8. Cooley, C.G., Parker, R.G., Vijayakar, S.M.: A frequency domain finite element approach for three-dimensional gear dynamics. In: Proceedings of the ASME 2009 IDETC/CIE, pp. DETC2009–87525(1–11) (2009)
9. Eritnel, T., Parker, R.G.: Three-dimensional nonlinear vibration of gear pairs. J. Sound Vib. **331**, 3628–3648 (2012)
10. Eritnel, T., Parker, R.G.: An investigation of tooth mesh nonlinearity and partial contact loss in gear pairs using a lumped-parameter model. Mech. Mach. Theory **56**, 28–51 (2012)
11. Eritnel, T., Parker, R.G.: Nonlinear vibration of gears with tooth surface modifications. J. Vib. Acoust. **135**, 051005 (2013)
12. Dai, X., Cooley, C.G., Parker, R.G.: An efficient hybrid analytical-computational method for nonlinear vibration of spur gear pairs. J. Vib. Acoust. **141**, 011006 (2018)
13. Cooley, C.G., Parker, R.G.: Vibration of high-speed rotating rings coupled to spatial space-fixed stiffness. J. Sound Vib. **333**, 2631–2648 (2014)
14. Cooley, C.G., Parker, R.G.: Limitations of an inextensible model for the vibration of high-speed rotating elastic rings with attached space-fixed discrete stiffness. Eur. J. Mech. A/Solids **54**, 187–197 (2015)
15. Liu, C., Cooley, C.G., Parker, R.G.: Parametric instability of spinning elastic rings excited by fluctuating space-fixed stiffnesses. J. Sound Vib. **400**, 533–549 (2017)
16. Rosso, C., Bruzzone, F., Maggi, T., Marcellini, C.: Influence of micro geometry modification on gear dynamics. SAE Technical Paper 2020-01-1323, 2020
17. Bruzzone, F., Rosso, C.: Effect of web flexibility in gear engagement: a proposal of analysis strategy. Vibration **5**(2), 200–212 (2022)
18. Cowper, G.R.: The shear coefficient in Timoshenko's beam theory. J. Appl. Mech. **33**, 335–340 (1966)
19. Litvin, F.L.: Gear Geometry and Applied Theory. P. T. R. Prentice Hall (1994)
20. Bruzzone, F., Maggi, T., Marcellini, C., Rosso, C.: Gear teeth deflection model for spur gears: Proposal of a 3d nonlinear and non-hertzian approach. Machines **9**(10), 223 (2021)
21. Newmark, N.M.: A method of computation for structural dynamics. J. Eng. Mech. Div. **85**, 67–94 (1959)

Chapter 24
Influence of Gearbox Flexibilities on Dynamic Overloads

Fabio Bruzzone and Carlo Rosso

Abstract Geared transmissions are prone to harmful vibrations and annoying noise emissions. The sources of excitation of those vibrations are many and different in nature, starting from torque fluctuations from the engine or the unsteady aerodynamics in wind turbines, for example. However, the main source of excitation comes from an intrinsic characteristic of meshing gears and is the time-varying mesh stiffness which is generated by the transmission error. Several flexibilities can be accounted for the calculation of the transmission error depending on the complexity of the model employed. In this chapter, the importance of including shaft flexibilities is highlighted. A nonlinear semi-analytical model is applied to the study of a simple test case with and without the misalignment caused by the inflection of the shafts under load, and several results, such as the static transmission error and the contact pressure maps, are shown and discussed.

Keywords Gear dynamics · Static transmission error · Dynamic overloads · Gear tooth stiffness · Gear contact

24.1 Introduction

The main source of excitation and cause of failure in geared transmissions are load and stiffness fluctuations [1, 2, 3]. At the end of the twentieth century, Japanese researchers highlighted the complex dynamic features of gears analyzing their torsional behavior including other sources such as profile errors or modifications [4, 5, 6, 7, 8]. In [9], the Dynamic Factor (DF) was introduced for explaining certain failures by comparing the dynamic loads in operation with those under static conditions. Machine characteristics rule the input torques, and they can certainly be origin of vibrations and impacts [10, 11, 12], but the Time-Varying Mesh Stiffness (TVMS) was quickly found to be a key player [13]. Since the stiffness of mating gear pair varies during gear rotation, self-excited vibrations are generated, and for that reason, many researches are conducted on the Transmission Error (TE). Several methods have been proposed, starting from integral approaches [14, 15] or discrete ones [16, 17] in order to take into account the tooth stiffness. Experimental methods were also proposed to study the Static Transmission Error (STE) [18, 19, 20], while others included mounting and manufacturing deviations to estimate the Manufacturing Transmission Error (MTE) [21, 22, 23, 24]. More recently, the Finite Element (FE) models were introduced for studying the problem, but its computational effort and difficulty to set up made it applicable to limited aspects such as tooth root stresses and its structural behavior [25, 26, 27], crack propagation [28, 29, 30, 31, 32], or generally as a validation tool for other proposed models. In addition, the Hertzian theory [33] of cylinder-to-cylinder contact is normally used to predict the contact behavior of the teeth flanks, avoiding to consider some peculiar aspects of the gears, such as the continuously varying curvature and the presence of sharp edges. When contact is not neglected, it is generally introduced as an addition to the elastic behavior of the mating teeth, but still under Hertz's hypotheses [34, 35, 36, 37, 38], while other works included non-Hertzian properties but neglected the flexibility under load of the teeth. Hybrid approaches coupling

F. Bruzzone (✉) · C. Rosso
Department of Mechanical and Aerospace Engineering, Politecnico di Torino, Torino, Italy

GeDy TrAss Company, Torino, Italy
e-mail: fabio.bruzzone@polito.it; fabio.bruzzone@polito.it

B. J. Dilworth et al. (eds.), *Topics in Modal Analysis & Parameter Identification, Volume 9*, Conference Proceedings of the Society for Experimental Mechanics Series, https://doi.org/10.1007/978-3-031-34942-3_24

an FE model with a Semi-Analytical (SA) contact model have also been proposed [39] with great success. In [40], a combination of some of the presented approaches will be used to accurately estimate the STE and the contact conditions including the influence of the micro-geometrical modifications of the teeth flanks both along its height and along the face width. In addition, a technique for taking into account the flexibilities of other gearbox components was developed and is presented here.

24.2 Methodology

The reader can find deeper details on the methodology used here for computing the tooth stiffness in [40]. For the sake of simplicity, the flow chart of the nonlinear and non-Hertzian procedure is reported here (Fig. 24.1) and briefly described. Once the gear parameters are set in terms of a number of teeth, module, angle of pressure and helix, profile shift and geometry of the generating rack, the procedure generates the flank geometry and applies to them all the possible micro modifications (an example is reported in Fig. 24.2a and b). In such a way, the teeth characteristics are defined, and the stiffnesses of the

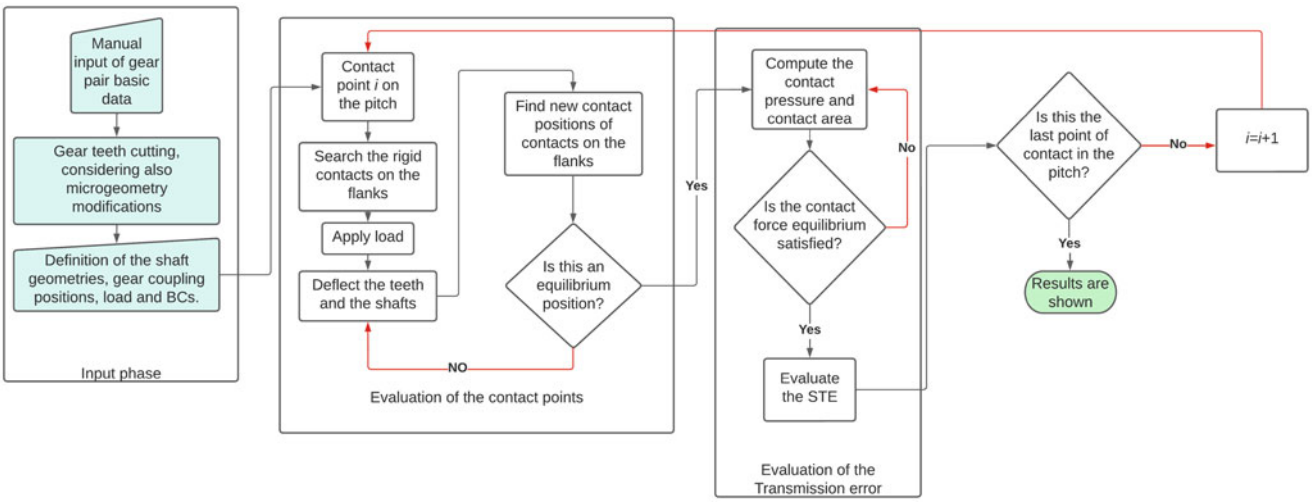

Fig. 24.1 Flowchart of the numerical procedure

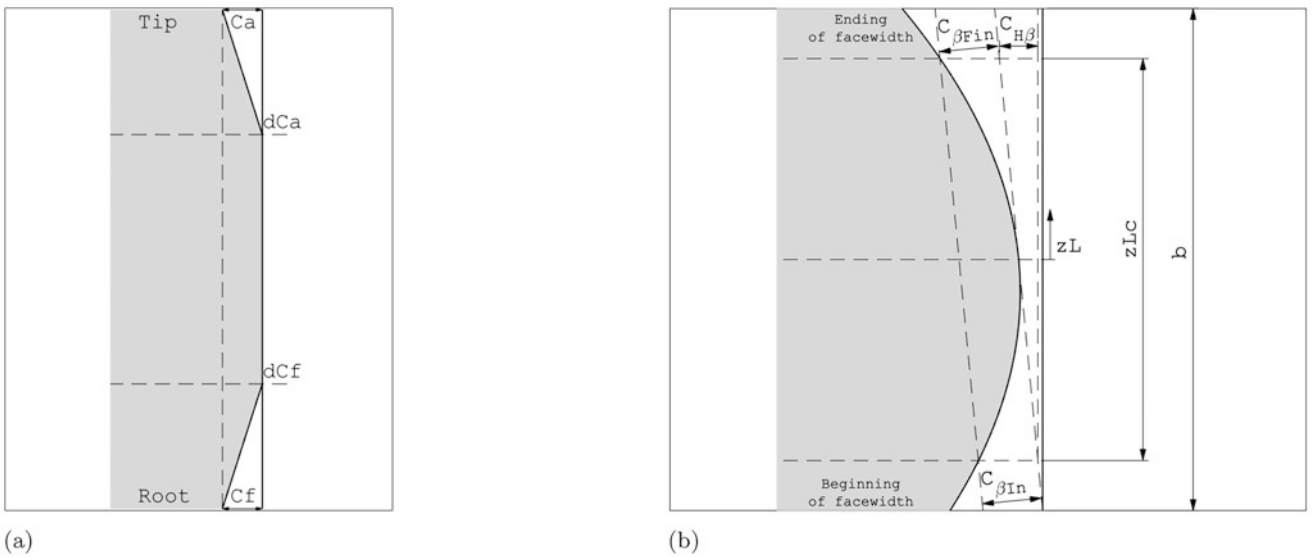

Fig. 24.2 Tooth profile modifications. (**a**) Tip and root relief. (**b**) Crowning

tooth, contact, and gears can be computed. By defining a gearbox layout, the size of shafts, the position of the gear sets and the position of bearing, and their connection to the housing, the procedure applies the torque to the input shaft and starts computing the deflection of gearbox. A first contact position is selected as the starting point of the meshing evolution. This position is first defined according to the static and kinematic gear contact. As no a priori assumptions are made regarding the location of the contact point as well as the number of mating tooth pairs, the load and the load sharing among them are computed by the procedure in order to evaluate the actual contact point. This methodology considers a Semi-Analytical model based on [17] in order to determine the stiffness of the different contacting pairs. By taking into account, in a simplified finite element model, all the flexibilities involved (shafts, bearing, casing), the contact point is estimated according to the actual deformation of the gearbox. In such a way, any possible misalignment due to gearbox flexibilities can be considered, and the contact point is more accurate. The non-Hertzian algorithm allows, hence, to evaluate any possible edge or point contact due to the non-perfect alignment of the mating gears. The continuously changing curvature of the flanks, the effects of the profile modifications, and discontinuities can be solved by means of a numerical rough frictionless non-Hertzian contact model. The contact problem is derived according to the Hertz–Signorini–Moreau problem [41, 42, 43]. In particular, the proposed contact model has been implemented following the elastic half-space theory and hence implies that in any transverse section a plane state of deformations is respected. Side and tip mirroring corrections are introduced to relieve the stresses on the free surfaces of the finite-length bodies in contact allowing accurate representation of the varying curvature and discontinuities of the flanks. Such methodology allows us to take into account any possible Tooth Profile Modifications (TPMs). The entire process is iterative and the procedure stops when the force gap with the previously computed force is within a certain tolerance. Then, a new contact point in the mesh cycle is investigated. When all the selected points in which the pitch is divided are investigated, the procedure ends.

24.2.1 Misalignment Evaluation

The misalignment can be due to the manufacturing process or to the elastic deformation of the gearbox components. The proposed methodology is capable to consider both. Since the misalignment due to the elastic deformation is the most important in the design phase, in this chapter, only this effect is considered. If manufacturing errors are known, but usually in the design phase they are not, the imposed displacement can be taking into account directly adding to the computed displacement. In order to evaluate the misalignment, the compliances of all the elements involved in the gearbox are considered. In particular, the shafts are modeled as a Timoshenko beams; the bearings are, at the moment (but in near future a nonlinear model will be proposed), depicted as linear springs by means of 12×12 diagonal matrices and the casing is represented by a reduced stiffness matrix according to a model order reduction technique starting from the actual CAD model and the consequent FE model. All those elements are assembled, together with the gears in a finite element model, which is solved by applying the constraints and load conditions. In such a way, the 3D displacement of the gear pair is evaluated as the deformation of the shafts where gears are mounted and that value is used to move the position of the gear center, thus altering the position of the contacting flanks in an $Oxyz$ Cartesian reference frame. After this static calculation and the application of the so computed displacement to the positions of the gears, the calculation of the Static Transmission Error is performed as previously described.

24.2.2 Gear Stiffness

According to the procedure depicted in [44], in the proposed methodology it is possible to take into account also the flexibility of the gear body. In particular, a shaft is connected to the connection points on the casing by means of the bearing matrices and to the other shafts by means of the gears. The gear connection can be described according to gear theory [45]. Two notable points can be defined: T_1, the tangent point between the Line Of Action (LOA) and the base circle of the gear, and C, the pitch point. As shown in Fig. 24.3, a rigid link is created between the node T_1 and the C node, in order to guarantee connection and motion along the line of action. The gear body can be inserted as a reduced matrix in between the previously identified nodes, and in particular the reduced matrix has a node for the connection to the shaft and a node to the connection to the rigid link in T1. The same reasoning is made for the mating gear, and in the common C point, the stiffness depicting the teeth behavior is placed.

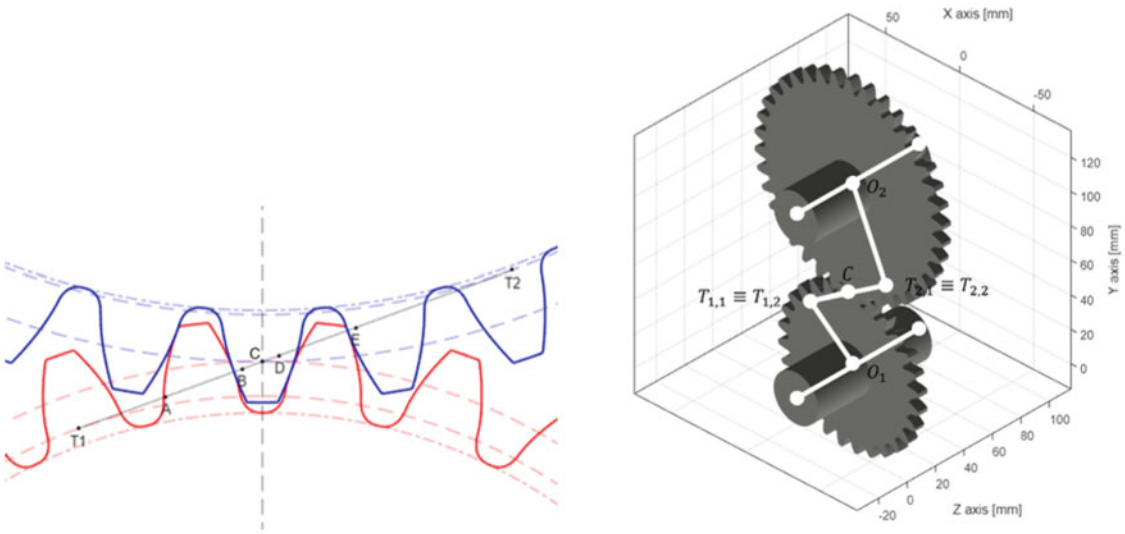

Fig. 24.3 Scheme for links between shafts that depicts the gear set

24.2.3 Dynamic Solution

As presented in [44], the previously assembled stiffness matrix is coupled with a coherent mass matrix that depicts the inertia properties of the gearbox, and by means of a Newmark integration scheme, the time evolution of the system is evaluated. The particular scheme adopted takes into account the actual value of the meshing stiffness on the basis of the previous integration step force and mesh position. In such a way, the integration algorithm is capable to follow the variation of stiffness due to the nonlinear contact problem, and it formally becomes a nonlinear integration scheme. Using this approach, it is possible to compute the time evolution considering a varying mesh stiffness and indeed the variation of the torque input.

24.3 Results and Discussion

In this paragraph, a gearbox with three shafts and an idle gear is considered. Results are obtained by means of two different models: one that only considers the teeth flexibilities and one with all the elements considered as flexible. A particular attention is paid to the comparison of the dynamic answer of the gearbox. The tested gearbox is shown in Fig. 24.4, and the data are listed in Table 24.1. The input gear (Z1) is supported by a shaft with a complex geometry due to the presence of spline coupling and 5 bearings. The input torque is equal to 100 Nm, and it is directed as depicted in Fig. 24.4. The idle gear (Z2) is a simple disk that is supported by two bearings, and the output gear (Z3) has a short shaft and it is supported by two bearings. In such a model, the casing is not considered, and only shafts and bearing flexibilities are introduced. In particular, the stiffness of the bearing is set according to Table 24.2. Bearings with axial stiffness are considered as hinges, and the others are considered as support. The stiffnesses of the shafts are computed according to the actual geometrical properties and setting a Young modulus of 200 GPa and a density of 7800 kg/m^3.

Two analyses are conducted: the first just considering only the teeth flexibilities and the second integrating the compliances of the shafts and bearings. In the following, the comparison of the results of the two models is reported. The first comparison is conducted on the Static Transmission Error (STE), and in Fig. 24.5, the STE of the first stage of the gearbox is presented. In Fig. 24.6, the same result is shown for the second stage. The short shafts for second and third gears give a high stiffness to the system, so great differences cannot be highlighted in the two STEs. In particular, the shape is quite similar, but the harmonic content is higher for the second case as will be evident later.

In Figs. 24.7 and 24.8, the contact patches of the two engagement are shown. It is not evident a great change because shafts are short and so they are stiff enough to guide the contact in a proper way. In any case, some differences in the shape of the contact and values of pressure can be highlighted; in particular, a little reduction of the pressure values can be seen in the second stage.

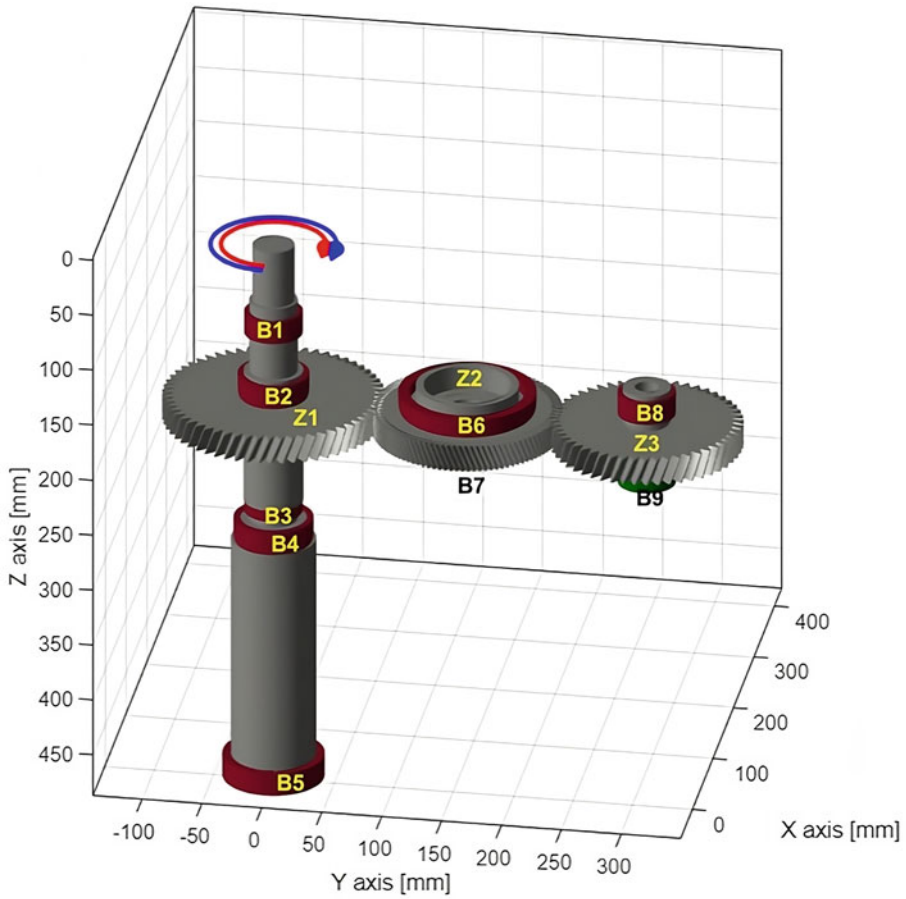

Fig. 24.4 Image of the gearbox model

Table 24.1 Mating gear main parameters

	Quantity	Name	Units
Input gear	Number of teeth	Z1	61
Idle gear	Number of teeth	Z2	51
Output gear	Number of teeth	Z2	53
All the gear	Module	2.54	mm
All the gear	Pressure angle	20	°
All the gear	Helix angle	20	°
All the gear	Face width	20	mm
All the gear	Reference rack	ISO 53/A	

Table 24.2 Bearing stiffness

Name	Radial (N/mm)	Axial (N/mm)
B1	245,000	0
B2	280,000	171,000
B3	250,000	0
B4	250,000	0
B5	250,000	0
B6	380,000	0
B7	180,000	80,000
B8	223,000	0
B9	250,000	390,000

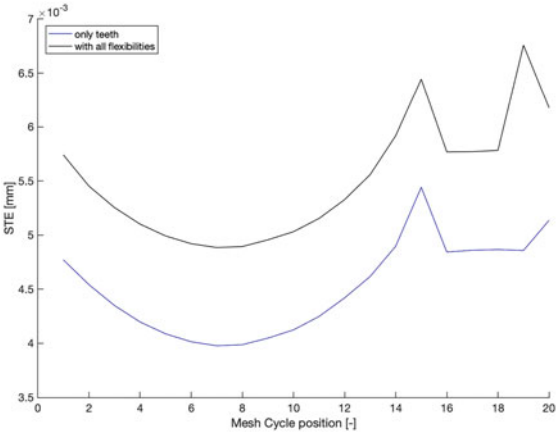

Fig. 24.5 STE of the first stage, comparison between the two models

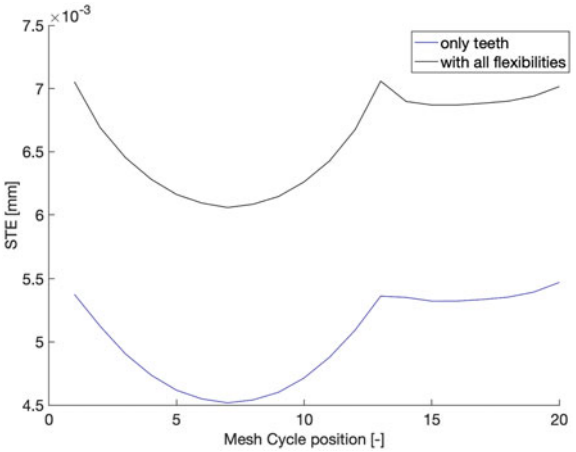

Fig. 24.6 STE of the second stage, comparison between the two models

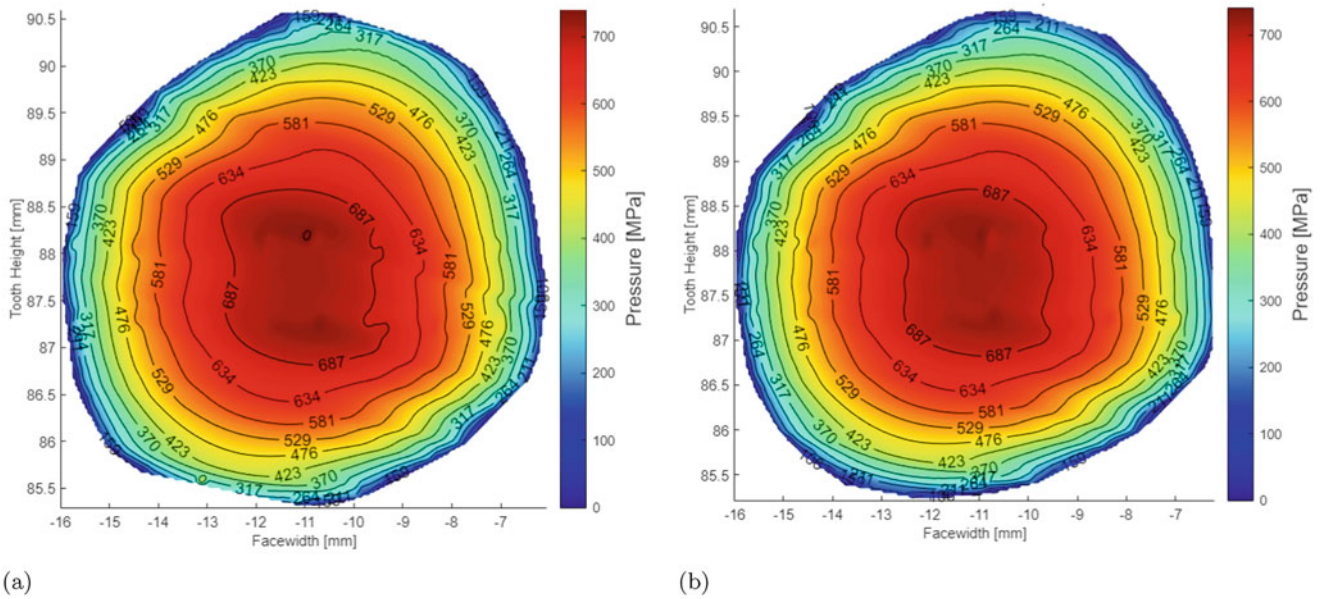

Fig. 24.7 Contact patch of the Z1/Z2 engagement @100 Nm. (**a**) With only tooth flexibility. (**b**) With tooth, bearing and shafts flexibilities

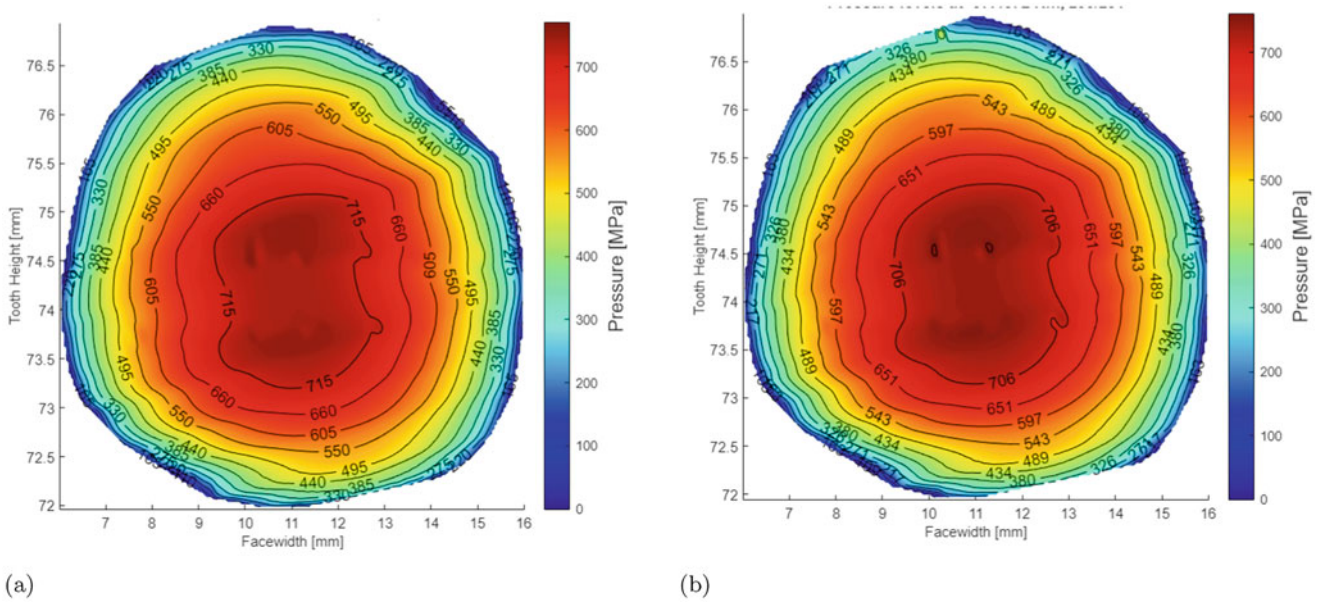

Fig. 24.8 Contact patch of the Z2/Z3 engagement @100 Nm. (**a**) With only tooth flexibility. (**b**) With tooth, bearing and shafts flexibilities

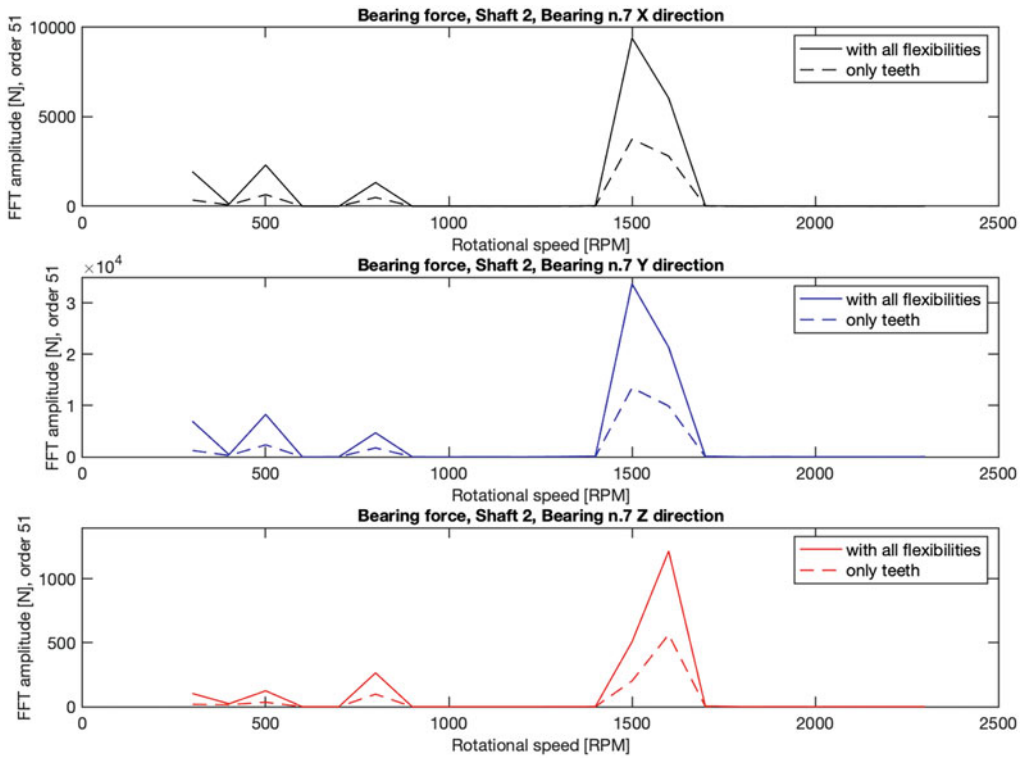

Fig. 24.9 Comparison between the dynamic overload on the bearing $n'7$ in the three directions predicted for the two different models

In Figs. 24.9 and 24.10, the dynamic overload on bearings is highlighted. In particular, the increment of load on bearing can be really important in the region of 1500 RPM. Thanks to an industrial partner, the data obtained are compared with experimental results revealing a good agreement.

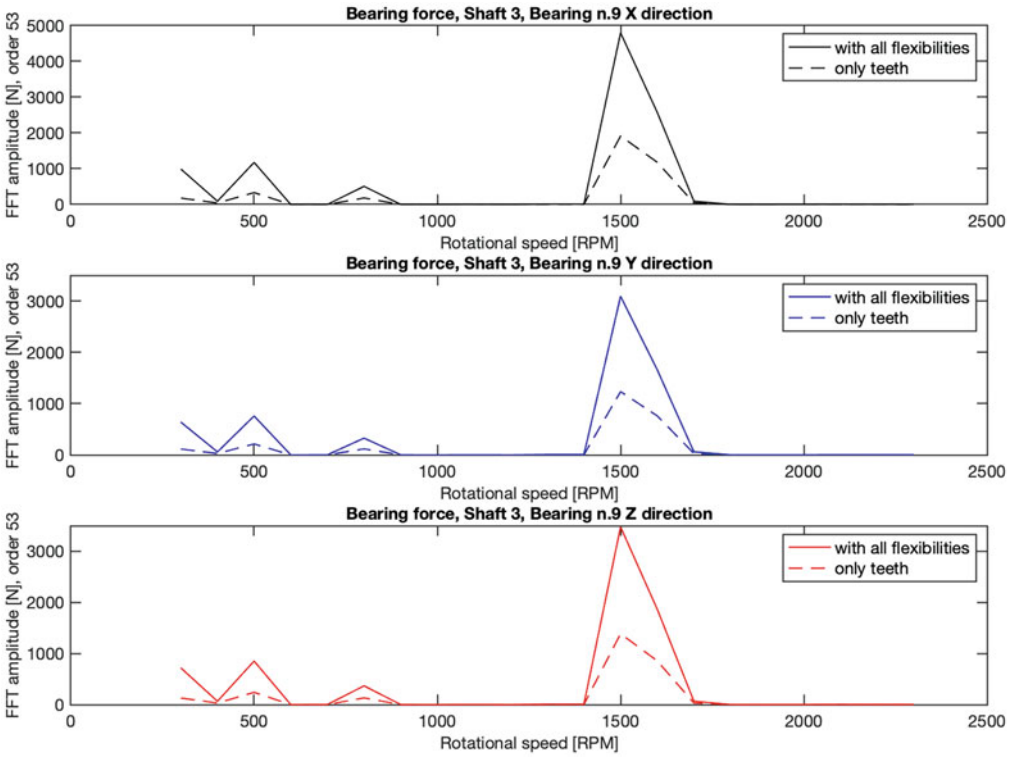

Fig. 24.10 Comparison between the dynamic overload on the bearing $n'9$ in the three directions predicted for the two different models

24.4 Conclusion

In the present chapter, flexibility of shafts and bearing were considered in order to highlight the effect of the compliance of those components. The flexibility of the components emphasizes the misalignment effect on the contact patch and STE. In particular, a greater influence of the flexibilities on the dynamic overloads is underlined. For that reason, it is really important to take into account all the flexibilities involved in the gearbox. At the moment, this is quite complicated because the traditional strategies are long to set and computationally heavy to solve. A quick and efficient strategy for modeling the dynamic behavior is here used, and it proves to be effective to forecast the dynamic overloads in gearboxes. In such a way, during the design phase, accurate checks on possible dynamic overload can be performed, speeding up the time to market and achieving more reliable solutions.

References

1. Abersek, B., Flasker, J., Glodez, S.: Review of mathematical and experimental models for determination of service life of gears. Eng. Fract. Mech. **71**, 439–453 (2004)
2. Prasil, L., Mackerle, J.: Finite element analyses and simulations of gears and gear drives a bibliography 1997–2006. Int. J. Comput.-Aided Eng. Softw. **25**, 196–219 (2008)
3. Bruzzone, F., Rosso, C.: Sources of excitation and models for cylindrical gear dynamics: a review. Machines **8**(3), 37 (2020)
4. Sato, T., Umezawa, K., Ishikawa, J.: Effects of contact ratio and profile correction on gear rotational vibration. Bull. Jpn. Soc. Mech. Eng. **26**, 2010–2016 (1983)
5. Umezawa, K., Sato, T., Ishikawa, J.: Simulation on rotational vibration of spur gears. Bull. Jpn. Soc. Mech. Eng. **27**, 102–109 (1984)
6. Umezawa, K., Ajima, T., Houhoh, H.: Vibration of three axes gear system (in Japanese). Bull. Jpn. Soc. Mech. Eng. **29**, 950–957 (1986)
7. Kubo, A., Kiyono, S., Fujino, M.: On analysis and prediction of machine vibration caused by gear meshing (1st report, nature of gear vibration and the total vibrational excitation). Bull. Jpn. Soc. Mech. Eng. **29**, 4424–4429 (1986)
8. Yang, D.C.H., Lin, J.Y.: Hertzian damping, tooth friction and bending elasticity in gear impact dynamics. Trans. Am. Soc. Mech. Eng. J. Mech. Transm. Autom. Design **109**, 189–196 (1986)
9. Ozguven, H.N., Houser, D.R.: Mathematical models used in gear dynamics—a review. J. Sound Vib. **121**, 383–411 (1988)

10. Kadmiri, Y., Perret-Liaudet, J., Rigaud, E., Le Bot, A., Vary, L.: Influence of multiharmonics excitation on rattle noise in automotive gearboxes. Adv. Acoust. Vib. **2011**, 659797 (2011)
11. Bel Mabrouk, I., El Hami, A., Walha, L., Zghal, B.: Dynamic vibrations in wind energy systems: application to vertical axis wind turbine. Mech. Syst. Signal Process. **85**, 396–414 (2017)
12. Garambois, P., Donnard, G., Rigaud, E., Perret-Liaudet, J.: Multiphysics coupling between periodic gear mesh excitation and input/output fluctuating torques: application to a roots vacuum pump. J. Sound Vib. **405**, 158—174 (2017)
13. Harris, S.L.: Dynamic loads on teeth of spur gears. Proc. Inst. Mech. Eng. **172**, 87–112 (1958)
14. Weber, C.: The deformation of load gears and the effect on their load-carrying capacity. technical report n.3. British Department of Scientific and Industrial Research (1949)
15. Weber, C., Banaschek, K.: Formänderung und profilrücknahme bei gerad-und schragverzahnten antriebstechnik. F. Vieweg (1953)
16. Cornell, R.W., Westervelt, W.W.: Dynamic tooth loads and stressing for high contact ratio spur gears. Trans. Am. Soc. Mech. Eng. J. Mech. Design **100**, 69–76 (1978)
17. Cornell, R.W.: Compliance and stress sensitivity of spur gear teeth. J. Mech. Design **103**, 447–459 (1981)
18. Chi, C.W., Howard, I., Wang, J.D.: An Experimental Investigation of the Static Transmission Error and Torsional Mesh Stiffness of Nylon Gears. Volume 7: 10th International Power Transmission and Gearing Conference, pp. 207–216 (2007)
19. Raghuwanshi, N.K., Parey, A.: Experimental measurement of gear mesh stiffness of cracked spur gear by strain gauge technique. Measurement **86**, 266–275 (2016)
20. Raghuwanshi, N.K., Parey, A.: Experimental measurement of mesh stiffness by laser displacement sensor technique. Measurement **128**, 63–70 (2018)
21. Wei, J., Sun, W., Wang, L.: Effect of flank deviation on load distributions for helical gear. J. Mech. Sci. Technol. **25**, 1781–1789 (2011)
22. Zhang, Y., Wang, Q., Ma, H., Huang, J., Zhao, C.: Dynamic analysis of three-dimensional helical geared rotor system with geometric eccentricity. J. Mech. Sci. Technol. **27**, 3231—3242 (2013)
23. Inalpolat, M., Handschuh, M., Kahraman, A.: Influence of indexing errors on dynamic response of spur gear pairs. Mech. Syst. Signal Process. **60–61**, 391—405 (2015)
24. Wang, Q., Zhang, Y.: A model for analyzing stiffness and stress in a helical gear pair with tooth profile errors. J. Vib. Control **23**, 272–289 (2017)
25. Deng, G., Nakanishi, T., Inoue, K.: Bending load capacity enhancement using an asymmetric tooth profile. JSME Int. J. Series C **46**, 1171–1177 (2003)
26. Lin, T., Ou, H., Li, R.: A finite element method for 3d static and dynamic contact/impact analysis of gear drives. Comput. Methods Appl. Mech. Eng. **196**, 1716–1728 (2007)
27. Pedersen, N.L., Jorgenses, M.F.: On gear tooth stiffness evaluation. Comput. Struct. **135**, 109–117 (2014)
28. Ural, A., Heber, G., Wawrzynek, P.A., Ingraffea, A.R., Lewicki, D.G., Neto, J.B.: Three-dimensional, parallel, finite element simulation of fatigue crack growth in a spiral bevel pinion gear. Eng. Fract. Mech. **72**(8), 1148–1170 (2005)
29. Chaari, F., Fakhfakh, T., Haddar, M.: Analytical modelling of spur gear tooth crack and influence on gear mesh stiffness. Eur. J. Mech. A Solids **28**(3), 461–468 (2009)
30. Qin, W.J., Guan,C.Y.: An investigation of contact stresses and crack initiation in spur gears based on finite element dynamics analysis. Int. J. Mech. Sci. **83**, 96–103 (2014)
31. Cura, F., Mura, A., Rosso, C.: Effect of rim and web interaction on crack propagation paths in gears by means of XFEM technique. Fatigue Fract. Eng. Mater. Struct. **38**(10), 1237–1245 (2015)
32. Cura, F., Mura, A., Rosso, C.: Investigation about crack propagation paths in thin rim gears. Frattura e Integrita Strutturale **30**, 446–453 (2014)
33. Hertz, H.R.: On contact between elastic bodies. Collected Works, 1, 1895
34. Hu, W., Chen, Z.: A multi-mesh MPM for simulating the meshing process of spur gears. Comput. Struct. **81**, 1991–2002 (2003)
35. Wang, J.D., Howard, I.M.: Error analysis of finite element modeling of involute spur gears. J. Mech. Design **128**, 90–97 (2006)
36. He, S., Gunda, R., Singh, R.: Effect of sliding friction on the dynamics of spur gear pair with realistic time-varying stiffness. J. Sound Vib. **301**, 927–949 (2007)
37. Tesfahuneng, A.Y., Rosa, F., Gorca, C.: The effects of the shape of tooth profile modifications on the transmission error, bending and contact stress of spur gears. Proc. Inst. Mech. Eng. C: J. Mech. Eng. Sci. **224**, 1749–1758 (2010)
38. Nikolic, V., Dolicanin, C., Dimitrijevic, D.: Dynamic model for the stress and strain state analysis of a spur gear transmission. J. Mech. Eng. **58**, 56–67 (2012)
39. Parker, R.G., Vijayakar, S.M., Imajo, T.: Non-linear dynamic response of a spur gear pair: modelling and experimental comparisons. J. Sound Vib. **237**, 435–455 (2000)
40. Bruzzone, F., Maggi, T., Marcellini, C., Rosso, C.: Gear teeth deflection model for spur gears: proposal of a 3d nonlinear and non-hertzian approach. Machines **9**(10) (2021)
41. Johnson, K.L.: Contact Mechanics. Cambridge University Press, Cambridge (1985)
42. Kalker, J.J.: Three-Dimensional Elastic Bodies in Rolling Contact. Springer Netherlands (1990)
43. Wriggers, P.: Computational Contact Mechanics. Springer, Berlin (2002)
44. Bruzzone, F., Rosso, C.: Effect of web flexibility in gear engagement: a proposal of analysis strategy. Vibration **5**(2), 200–212 (2022)
45. Litvin, F.L.: Gear Geometry and Applied Theory. P. T. R. Prentice Hall (1994)

Chapter 25
Experimental Modal Analysis and Operational Deflection Shape Analysis of a Cantilever Plate in a Wind Tunnel with Finite Element Model Verification

David T. Will and Weidong Zhu

Abstract Experimental methods are used across all engineering domains to study a system's response to some specified input or forcing function. This work explores the response of a structural member in a wind tunnel containing a cantilever plate attached to a cylinder, under an impact excitation. The computer-aided design (CAD) model and finite element analysis (FEA) modal simulation of the experimental setup are introduced. Two experimental techniques used in this research are discussed – an accelerometer-based experimental modal analysis (EMA) method and a non-contact, full-field digital image correlation (DIC) operational deflection shape (ODS) analysis method. The FEA and experimental results of the first five mode shapes and natural frequencies of the cantilever plate are presented and compared. The modal assurance criterion (MAC) between FEA-based mode shapes and EMA-based mode shapes is at least 0.935 for each mode. Absolute values of percent errors between EMA-based and FEA-based natural frequency results are less than 5% for each mode, while absolute values of percent errors between ODS analysis and FEA-based natural frequency results are less than 11% for each natural frequency. When comparing the EMA method with the ODS analysis method, there is less than 2% difference between each mode's natural frequency.

Keywords Modal analysis · Cantilever plate · Wind tunnel

25.1 Introduction

Cantilever plates, or flexible splitter plates, have been proposed for use as passive noise-reduction and vibration suppression devices in aerodynamic and hydrodynamic flow fields, as they act to disrupt natural vortex shedding that occurs behind bluff bodies immersed in flow fields [1–3]. Flexible splitter plates have also been used to model biological applications such as a soft palate vibrating within the pharynx of a human airway, which is known to cause snoring and sleep apnea [4]. Other applications include energy harvesting [5] and flexible membrane wings for greater aerodynamic efficiency in micro-air-vehicle flight [6]. These diverse fluid-structure interaction (FSI) applications inspire the need to study various measurement and analysis techniques for cantilever plate vibration.

In the analysis of vibration of rectangular plates, it is well known that the differential equation describing the motion of a plate cannot be solved directly for most boundary condition cases [7, 8]. In the system of eight boundary condition equations with eight unknown coefficients, the determinant of the eight-by-eight matrix of boundary condition terms is equal to zero. Thus, the matrix of boundary condition terms has linearly dependent rows or columns, and there are no unique solutions for the unknown coefficients. To overcome this issue, several approaches to solving for approximate solutions of rectangular cantilever plates have been developed, including variational methods, such as the Rayleigh-Ritz method, Galerkin's method, and Vlasov's method, and finite element methods [9]. Warburton [10] used the Rayleigh-Ritz method to calculate frequency equation coefficients for every combination of boundary conditions of a rectangular plate. This allows for an approximation of mode frequencies and subsequent prediction of the displacement at any point on the plate under free vibration. Leissa [11] compiled a survey of literature on analytical and numerical solutions for vibrations of plates, including circular, rectangular, and anisotropic plates, and plates of variable thicknesses. With modern computers, analysis is usually performed with finite element methods using commercially available software such as Nastran, ANSYS, and Abaqus.

D. T. Will · W. Zhu (✉)
Department of Mechanical Engineering, University of Maryland Baltimore County, Baltimore, MD, USA
e-mail: wzhu@umbc.edu

B. J. Dilworth et al. (eds.), *Topics in Modal Analysis & Parameter Identification, Volume 9*, Conference Proceedings of the Society for Experimental Mechanics Series, https://doi.org/10.1007/978-3-031-34942-3_25

Methods of EMA have evolved from contact-based impact hammer [12] or shaker excitation [13] and accelerometer response measurement [14], to non-contact speaker excitation [15] and laser vibrometer [16], photogrammetry [17], or DIC response measurement [15], to any combination of these excitation and response measurement techniques. Gülbahçe and Çelik [18] developed a roving shaker, fixed accelerometer approach to plate excitation and response measurement and found that this approach had higher correlation to FEA results than the roving hammer technique. Improvements in modal parameter estimation have also been made, with the PolyMAX algorithm [19] developed by LMS International, now acquired by Siemens, considered to be a high-performance algorithm in terms of producing clear stabilization diagrams, accurate results, and computational efficiency [18]. Whalen et al. [20] used non-contact photogrammetry to investigate FSI between hypersonic flow and a plate clamped on all sides. Among other interesting findings, the researchers noted mode shapes correlated well with expected results from the classical plate theory, but natural frequencies shifted with changes in the shock-wave/boundary-layer interaction intensity due to subsequent temperature changes in the plate. As the cost of high-speed cameras continues to decrease, more DIC-based ODS analysis research becomes available. Yu and Pan developed a lower-cost DIC technique that used a single high-speed camera with four mirrors for viewing a test object via two separate optical paths [21], and they successfully demonstrated the single-camera DIC technique on a rotating structure [22]. Xie et al. [23] studied the vibration of a flexible splitter plate behind a cylinder in a wind tunnel using single-camera high-speed stereo-DIC. Warren et al. [12] compared frequency response functions (FRFs) of a cantilever plate captured using DIC, three-dimensional (3D) point tracking, 3D laser vibrometer, and accelerometer measurements. Results showed high correlation to an FEA-based modal analysis. More recently, Frankovský et al. [24] developed an application module for DIC that generates FRFs of a structure using excitation data from an impact hammer, and response data collected from high-speed cameras. This application module allowed for estimation of modal parameters of the structure, such as natural frequencies, mode shapes, and damping values.

In this work, the design of the experimental test structure will be introduced, including its CAD model, finite element model (FEM), and FEA simulation setup. Then, the EMA experimental setup and testing in the wind tunnel will be discussed, followed by the ODS analysis experimental setup and testing. Next, the EMA and FEA results and analysis will be presented, followed by the ODS analysis and FEA results analysis. The EMA and ODS analysis results will be presented and compared. Finally, a discussion on the presence of a 608.262 Hz peak in the EMA FRF curve fit plot and ODS analysis fast Fourier transform (FFT) plot will be presented.

25.2 Background

25.2.1 Design, Modeling, and Simulation

The design for the experimental setup was developed using Siemens NX CAD software, given size constraints for the experiment in an AEROLAB Educational Wind Tunnel whose test section was 304.8 mm wide and 304.8 mm tall, and whose length was 609.6 mm long. Mounting provisions inside the test section were limited, and the surrounding structure was not perfectly rigid, and the boundary conditions in the wind tunnel were imperfect. A 152.4 mm tall, 152.4 mm wide, and 2.54 mm thick aluminum 2024-T3 cantilever plate clamped between two 6061-T6 half-cylinders with a diameter of 31.75 mm was modeled. One half-cylinder was threaded, and the other half-cylinder had counterbored thru-holes to allow 300-series stainless steel fasteners to pass through the plate and provide clamping forces to the plate. After assembly, the exposed plate surface was 152.4 mm tall and 128.5875 mm wide. Upper and lower brackets were modeled to securely fasten the cylinder to the test section. At the lower boundary condition, an aluminum 6061-T6 rectangular bracket, 12.7 mm tall, 43.307 mm wide, and 93.0148 mm long, with counterbored thru-holes allowed for fastening the two half-cylinders to the bracket with 300-series stainless steel fasteners, which was then fastened to the base of the test section with 300-series stainless steel fasteners. At the upper boundary condition, a 44.45 mm tall, 44.45 mm wide, and 596.9 mm long aluminum 6061-T6 angle bracket with thru-holes allowed for fastening the two half-cylinders to the bracket with 300-series stainless steel fasteners, which was then fastened to the top of the test section with 300-series stainless steel fasteners. For the EMA scenario, accelerometers were added to the structure model to account for their masses, while in the ODS analysis scenario, the accelerometers were removed from the structure model. The presence of accelerometers in the EMA scenario allowed for model updating of the FEA by slightly tuning the accelerometer model masses to account for masses from the accelerometer cables and adhesive wax. The CAD model of the experimental setup is shown in Fig. 25.1. A simplified model of the experimental setup was developed, which eliminated the upper and lower mounting brackets, as shown in Fig. 25.2.

A simplified FEA-based modal analysis of a cantilever plate, with perfect fixed-free-free-free boundary conditions, mounted to a cylinder with perfect fixed-fixed boundary conditions, was performed to model the simplified structure using the

Fig. 25.1 CAD model of the experimental setup that includes the cantilever plate, two half-cylinders, upper- and lower-cylinder mounting brackets, and fastening hardware

Fig. 25.2 CAD model of the simplified experimental setup that includes the cantilever plate, two half-cylinders, and fastening hardware

Siemens NX Pre/Post application FEA software. A 3D tetrahedral mesh with a 2.54 mm element edge length was generated for each individual FEM part, including the cantilever plate, two half-cylinders, and fastening hardware. The surface-to-surface gluing simulation object type was used to mate all simulation parts in the analysis. Figure 25.3 shows the simplified CAD model, FEM with meshing, and simulation model of the cylinder with fixed-fixed boundary conditions and surface-to-surface gluing of the two half-cylinders with the plate. The simulation was run, and the first five modes of the simplified structure were captured.

25.2.2 EMA Experimental Setup

All experimental setup parts were machined per the design and assembled using common tools. Then, the finished structure was installed into the AEROLAB Educational Wind Tunnel using common tools. The upper- and lower-cylinder boundary

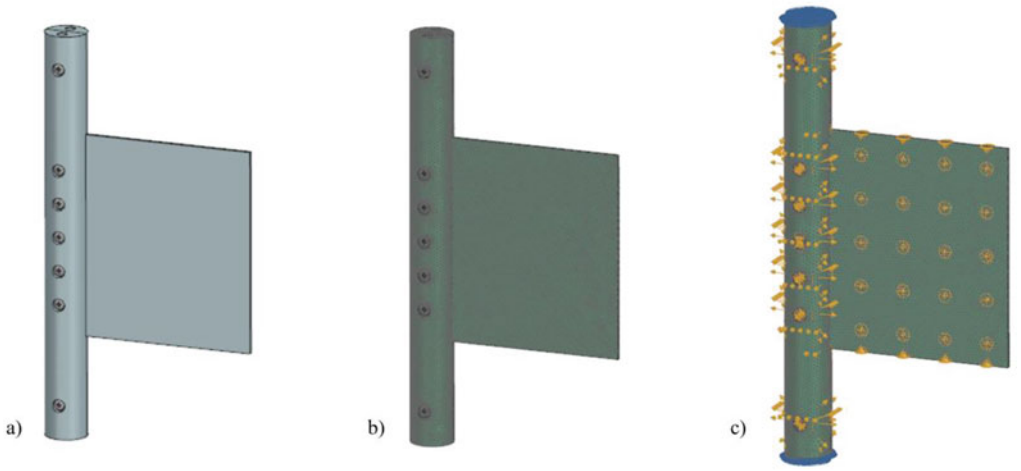

Fig. 25.3 From left to right: (**a**) the CAD model of the simplified experimental setup, (**b**) its FEM with tetrahedral meshing, and (**c**) its simulation model showing fixed-fixed cylinder boundary conditions and the surface-to-surface gluing simulation object

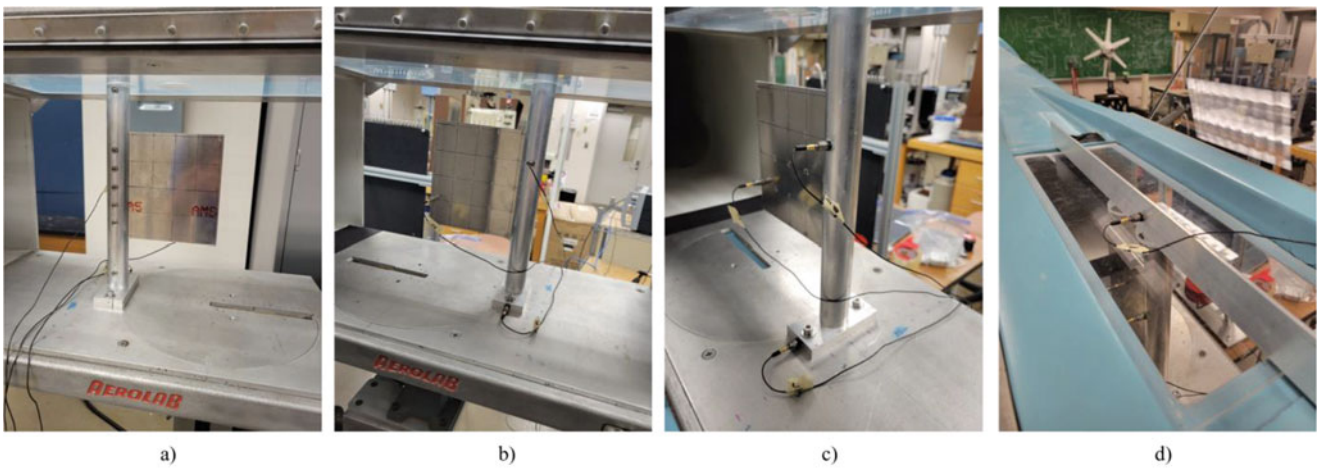

Fig. 25.4 Experimental setup in the lab. From left to right: (**a**) the impact side of the cantilever plate, (**b**) the accelerometer side of the cantilever plate, (**c**) a close-up view of three of the accelerometers – one attached to the lower boundary condition, one attached to the cylinder, and one attached to the cantilever plate, (**d**) a close-up view of the fourth accelerometer attached to the upper boundary condition

conditions were not considered perfectly fixed due to the imperfect rigidity and relatively low mass of the surrounding composite wind tunnel structure to which the cylinder and its mounting brackets were fastened. To gain a complete understanding of the structure's natural frequencies and mode shapes, one PCB Piezotronics, Inc. 352C66 accelerometer was placed on each component of the structure. The experimental setup installed in the wind tunnel and with accelerometers attached for EMA testing is shown in Fig. 25.4.

EMA testing was performed using an LMS SCADAS III (SC-316W), a PCB Piezotronics, Inc. modally tuned impact hammer (086C01) with nylon tip, a quantity of four PCB Piezotronics, Inc. accelerometers (352C66), a quantity of four PCB Piezotronics, Inc. adhesive mounting bases (080A15), adhesive wax (080A109), and Siemens Testlab 18.2 software. Several components of the test equipment are shown in Fig. 25.5.

A roving hammer test was performed by using a total of 37 impact locations, or nodes, for the EMA testing – 25 on the cantilever plate, 4 on the cylinder, 5 on the upper boundary condition, and 3 on the lower boundary condition. Each node was impacted three times to compute an average of three FRFs, for a total of 111 hammer impacts on the structure. The nodes and accelerometer locations on the structure are shown in Fig. 25.6. Previous testing revealed that the roving accelerometer

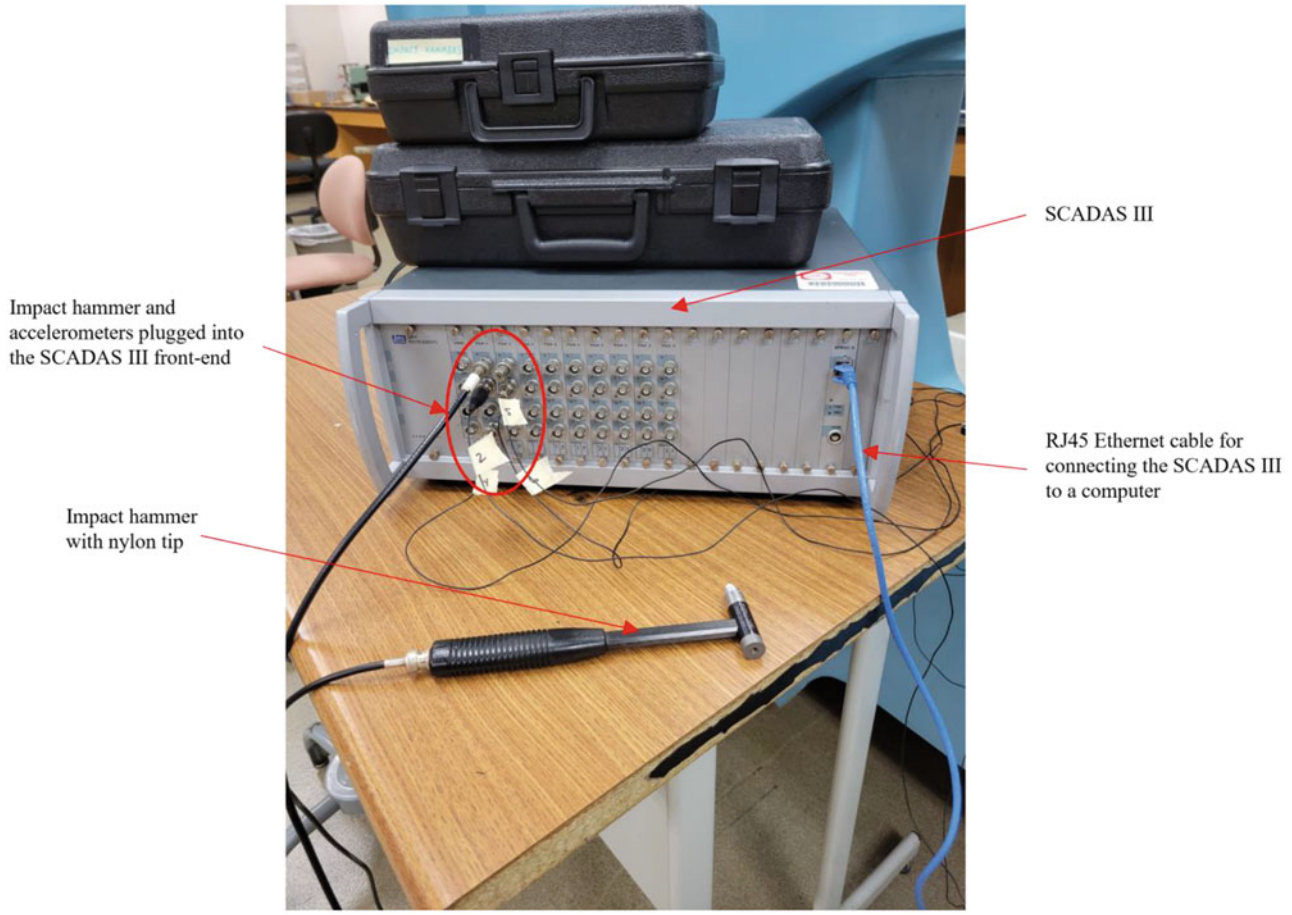

Fig. 25.5 Test equipment used in EMA testing including an LMS SCADAS III (SC-316W) and a PCB Piezotronics, Inc. modally tuned impact hammer (086C01). The four PCB Piezotronics, Inc. accelerometers (352C66) and PCB Piezotronics, Inc. modally tuned impact hammer are plugged into the front-end of the SCADAS III. The blue RJ45 Ethernet cable plugs directly into a computer running Siemens Testlab 18.2 software

technique resulted in poor results due to changes in mass loading between hammer impacts on the relatively thin cantilever plate. The Siemens Testlab 18.2 impact settings were chosen using the software's suggested values based on several test impacts. The Testlab settings used are given in Table 25.1.

25.2.3 ODS Analysis Experimental Setup

An ODS analysis of the cantilever plate was performed using a Correlated Solutions, Inc. DIC system, a non-contact optical measurement tool using stereo high-speed digital cameras that track speckle patterns on an object's surface. The equipment used was two Phantom V2640 high-speed cameras with Tokina 100 mm lenses mounted on a Moog tripod, two HEDLER light-emitting diode (LED) lamps, a computer with Advanced Micro Devices, Inc. 3970x Threadripper central processing unit, 128 GB Double Data Rate 4 memory, 1 TB solid-state drive, 8 TB hard disk drive, and VIC-3D software. The cantilever plate was prepared for ODS analysis testing by application of a thin coat of flat white paint followed by a speckle pattern using an ink stamp. The speckled cantilever plate is shown in Fig. 25.7, and the experimental setup with DIC equipment is shown in Fig. 25.8. A PCB Piezotronics, Inc. modally tuned impact hammer (086C01) was used to impact the cantilever plate one time on the side opposite the speckled surface, as shown in Fig. 25.7, while the high-speed digital cameras recorded

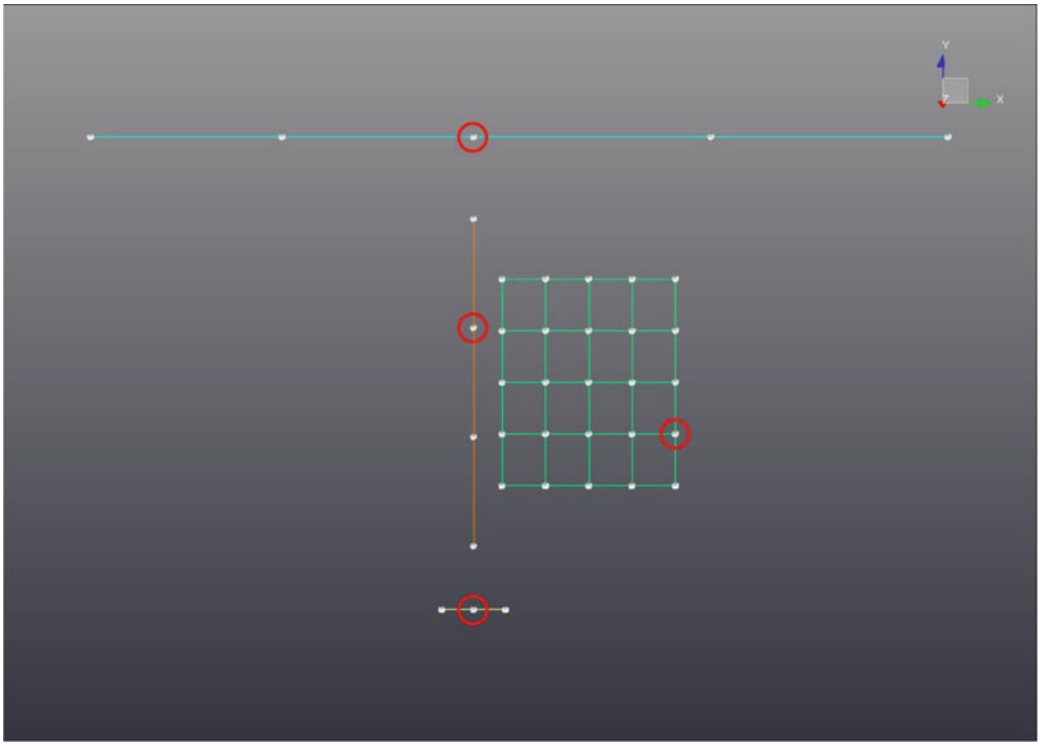

Fig. 25.6 Siemens Testlab 18.2 test geometry showing all roving hammer impact nodes on the cantilever plate, cylinder, and upper and lower boundary conditions. Accelerometers were placed at the circled nodes on the far side of the structure

Table 25.1 Siemens Testlab 18.2 "Impact Setup" menu test settings

Setting	Value
Input range	2 V
Trigger level	0.080 V
Pre-trigger	0.0025 s
Span	2500 Hz
Spectral lines	1600
Acquisition time	0.64 s
Resolution	1.56 Hz
Input exponential window	100% (no windowing)
Response exponential window	100% (no windowing)

at 5000 frames per second. Note that the DIC system was not able to measure excitation force from the impact hammer as a standalone system. Therefore, FRFs could not be generated and modal parameters such as mode shapes and damping were not estimated. However, natural frequencies were estimated by performing an FFT on the displacement versus time data, velocity versus time data, and acceleration versus time data captured by the DIC system.

25.3 Results and Analysis

25.3.1 EMA and FEA Results

After completion of the roving hammer test, Siemens Testlab 18.2 software's PolyMAX algorithm calculated a curve fit of the captured FRFs and the first five cantilever plate modes were selected, as shown in Fig. 25.9. A simplified case was considered in the EMA results where only the modes of the cantilever plate were considered. Any mode shapes that did not primarily involve vibration of the cantilever plate were ignored. The first five measured cantilever plate mode shapes from EMA testing are shown in Fig. 25.10. The Siemens Testlab 18.2 modal data was exported to Siemens NX where the test

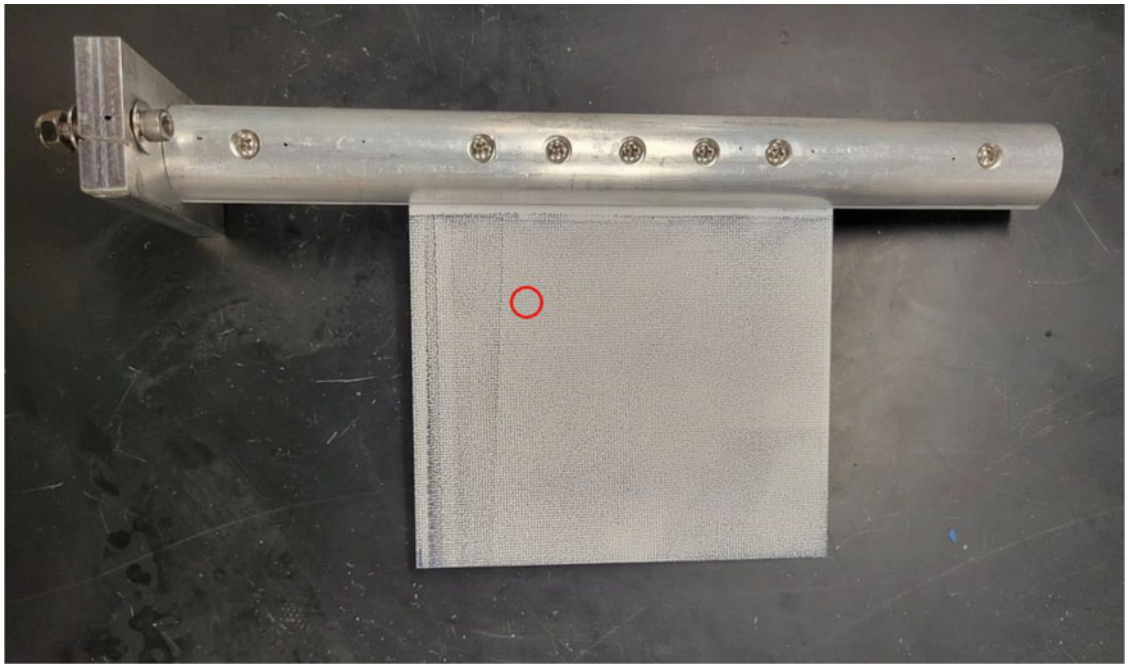

Fig. 25.7 The cantilever plate after application of a thin coat of flat white paint and subsequent ink stamp speckle pattern. The hammer impact occurred at the circled location on the far side of the cantilever plate

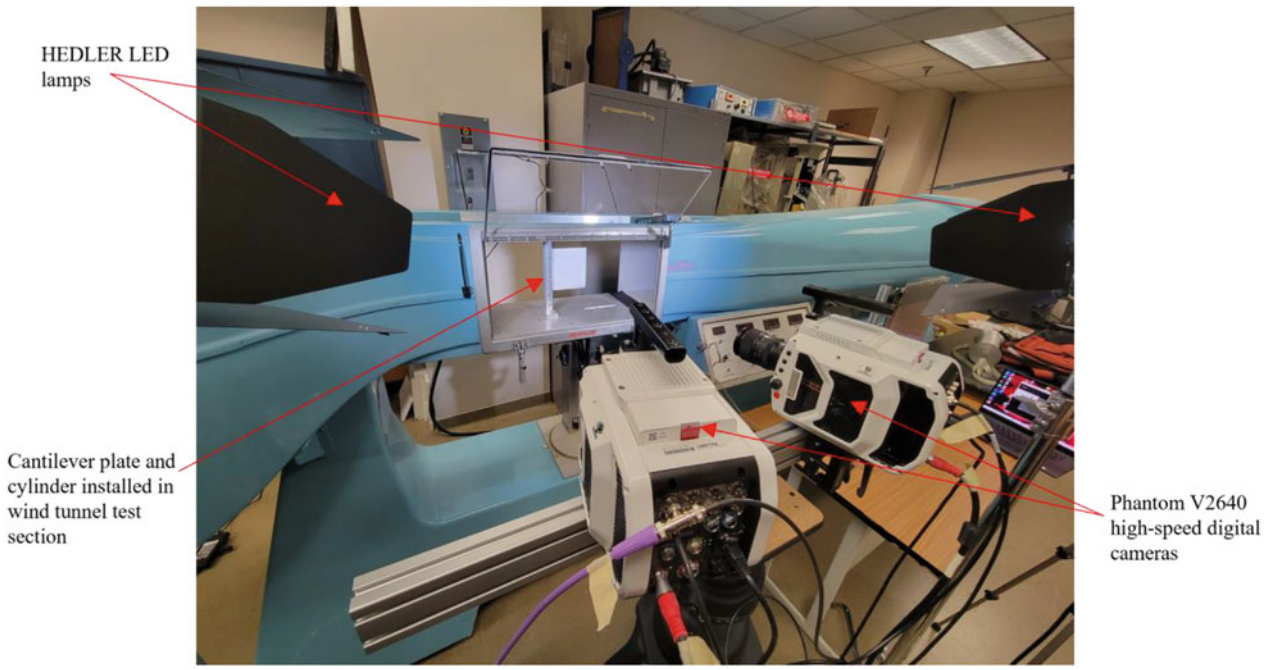

Fig. 25.8 The DIC test equipment used in ODS analysis testing in the laboratory, including two Phantom V2640 high-speed digital cameras, and two HEDLER LED lamps. The cantilever plate and cylinder can be seen mounted in the wind tunnel test section

geometry was overlaid with the FEA simulation model, as shown in Fig. 25.11, allowing a direct comparison between the EMA-based and FEA-based mode shapes. Figure 25.12 shows a side-by-side comparison of the first five cantilever plate modes as captured by EMA testing and FEA results.

Table 25.2 presents the first five natural frequencies of the cantilever plate, as captured by the EMA and FEA results. The absolute values of the percent errors between the EMA and FEA results are less than 5% for each mode and the average percent error of the absolute values over the first five cantilever plate modes is 2.065%. Furthermore, a MAC analysis

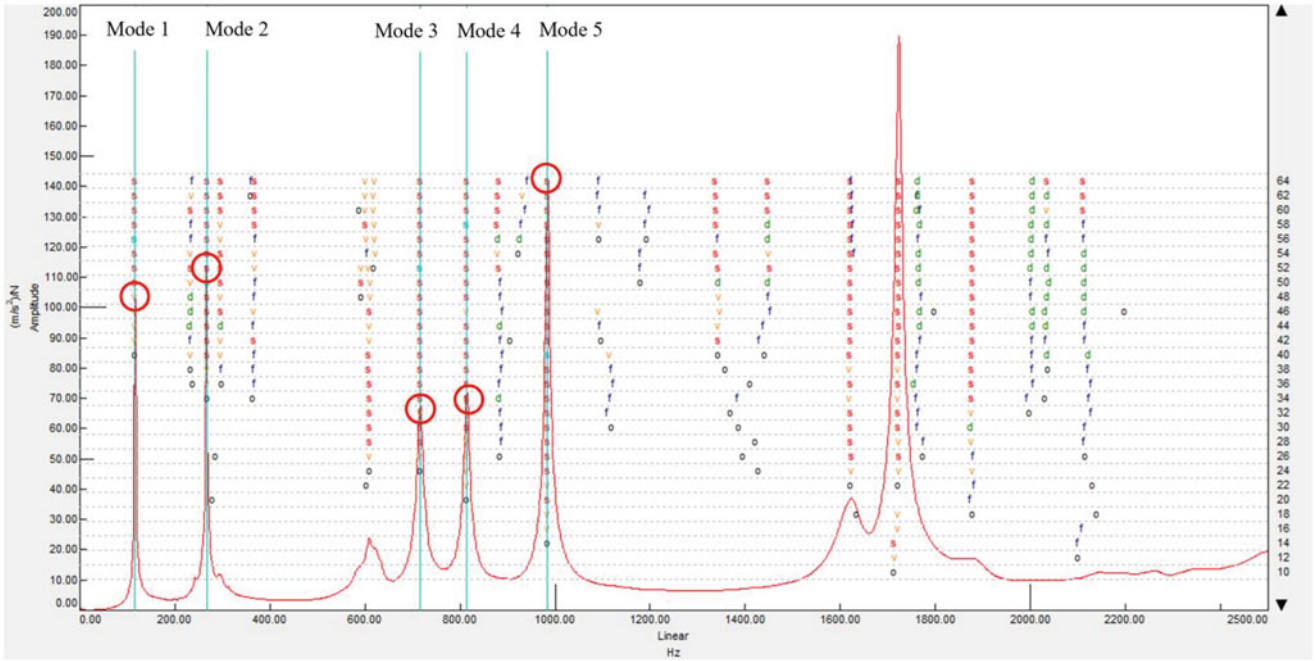

Fig. 25.9 The FRF curve fitting and stabilization diagram using the Siemens Testlab 18.2 PolyMAX algorithm. Only the first five cantilever plate modes were selected for analysis

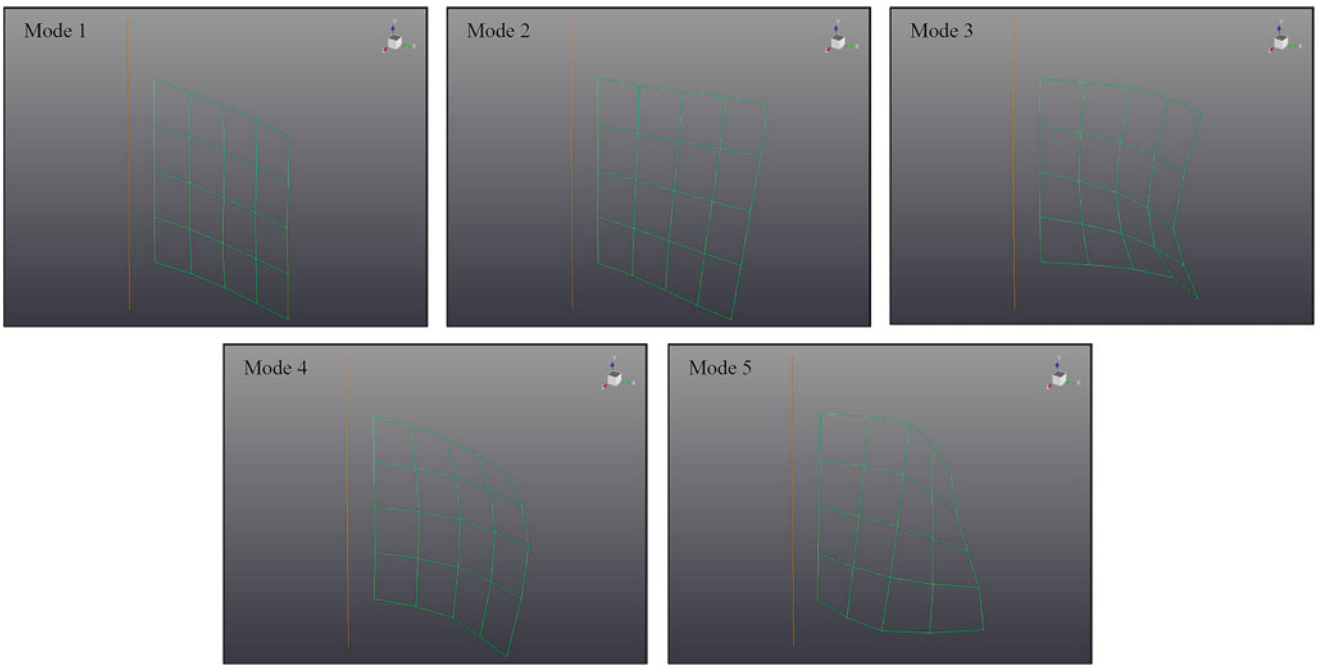

Fig. 25.10 The first five cantilever plate mode shapes captured from EMA using Siemens Testlab 18.2

was performed which determines how well the FEA-based mode shapes correlate with the EMA-based mode shapes. FEA modes that are compared with their corresponding EMA modes (diagonal) should be close to one, while FEA modes that are compared with differing EMA modes (off-diagonal) should be close to zero. The MAC numbers on the diagonal are at least 0.935, meaning the FEA results correlate very well with the EMA results. The largest off-diagonal term is 0.167, meaning that the FEA modes compared with differing EMA modes do not correlate well, as expected. The MAC data is presented in tabular form in Table 25.3 and in graphical form in Fig. 25.13.

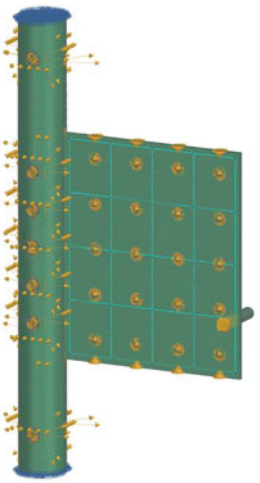

Fig. 25.11 The simulation model of the simplified experimental setup with overlaid Siemens Testlab 18.2 test geometry. The Siemens Testlab 18.2 test geometry is given by the 5×5 grid on the cantilever plate

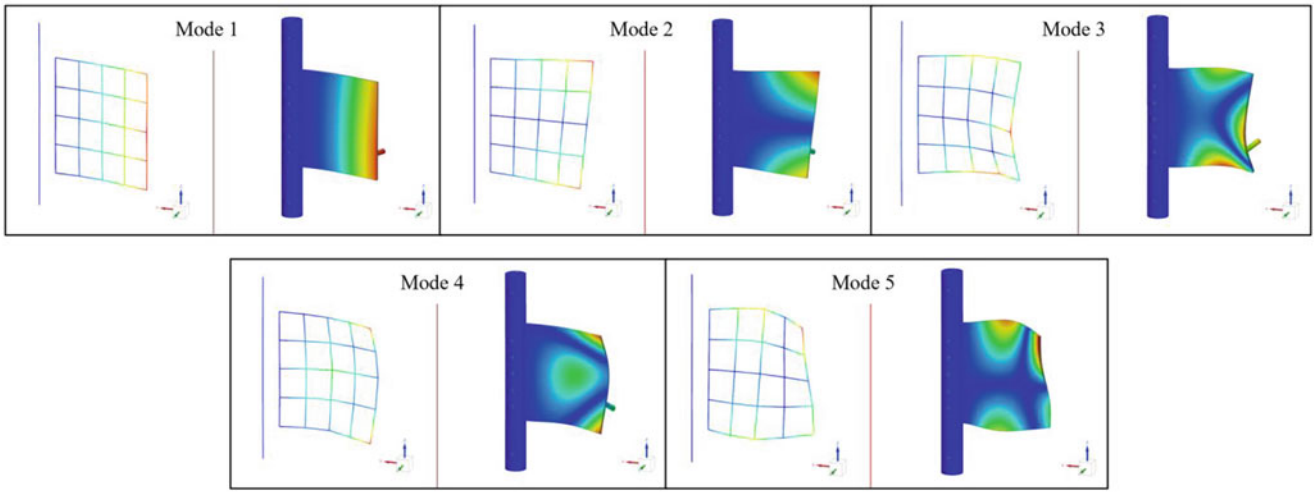

Fig. 25.12 The EMA-based mode shapes (left) as imported from Siemens Testlab 18.2 into Siemens NX and FEA-based mode shapes (right) for the first five cantilever plate modes

Table 25.2 The first five natural frequencies of the cantilever plate determined by EMA and FEA. The percent errors are reported with the EMA test data taken as the reference frequencies

Mode	EMA (Reference) (Hz)	FEA (Hz)	Percent error (%)
1	116.333	118.865	2.177
2	266.597	265.814	−0.294
3	715.333	681.647	−4.709
4	814.372	799.453	−1.832
5	984.343	997.283	1.315

Table 25.3 MAC correlation metrics between EMA test data and FEA results for the first five cantilever plate modes

FEA \ EMA	Mode 1	Mode 2	Mode 3	Mode 4	Mode 5
Mode 1	0.996	0.002	0.007	0.118	0.009
Mode 2	0.013	0.994	0.000	0.009	0.050
Mode 3	0.023	0.011	0.935	0.032	0.000
Mode 4	0.080	0.003	0.167	0.976	0.001
Mode 5	0.022	0.006	0.001	0.012	0.955

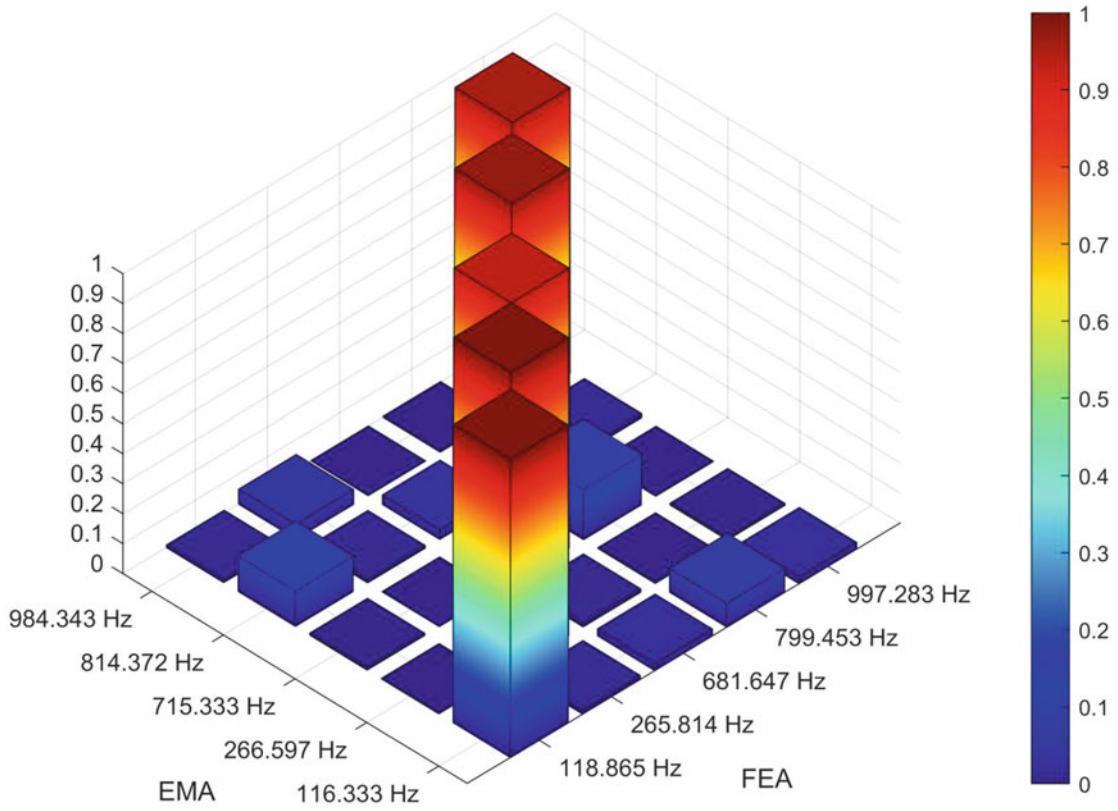

Fig. 25.13 MAC between EMA test data and FEA results for the first five cantilever plate modes

25.3.2 ODS Analysis and FEA Results

After completion of the single impact test with DIC, the Correlated Solutions, Inc. VIC-3D software performed an FFT of the time-series data and generated the acceleration versus frequency plot shown in Fig. 25.14. The first five cantilever plate ODSs were selected from the FFT plot using the peak-picking method. Again, a simplified case was considered in the ODS analysis results where only the ODSs of the cantilever plate were considered. Any ODSs that did not primarily involve vibration of the cantilever plate were ignored. The first five measured cantilever plate ODSs are shown in Fig. 25.15, and they match very well with the EMA-based mode shapes and the FEA-based mode shapes shown in Figs. 25.10 and 25.12. Also as expected, the shape of the ODS analysis FFT plot of acceleration versus frequency in Fig. 25.14 agrees well with the Siemens Testlab 18.2 FRF curve fit and stabilization diagram given in Fig. 25.9.

Table 25.4 presents the first five natural frequencies of the cantilever plate, as captured by the ODS analysis and FEA results. Note that the FEA natural frequencies in Table 25.4 are higher than the FEA natural frequencies in Table 25.2 because of the removal of the accelerometer masses from the FEA model for the DIC test scenario. The absolute values of the percent errors between the ODS analysis and FEA results are less than 11% for each natural frequency and the average percent error of the absolute values over the first five cantilever plate natural frequencies is 4.444%. Although the first natural frequency percent error of 10.801% is relatively large, the first natural frequency error is only 12.640 Hz.

25.3.3 EMA and ODS Analysis Results

Table 25.5 presents the first five natural frequencies of the cantilever plate, as captured by the EMA and ODS analysis results. The percent differences between the EMA and ODS analysis results are less than 2% for each natural frequency and

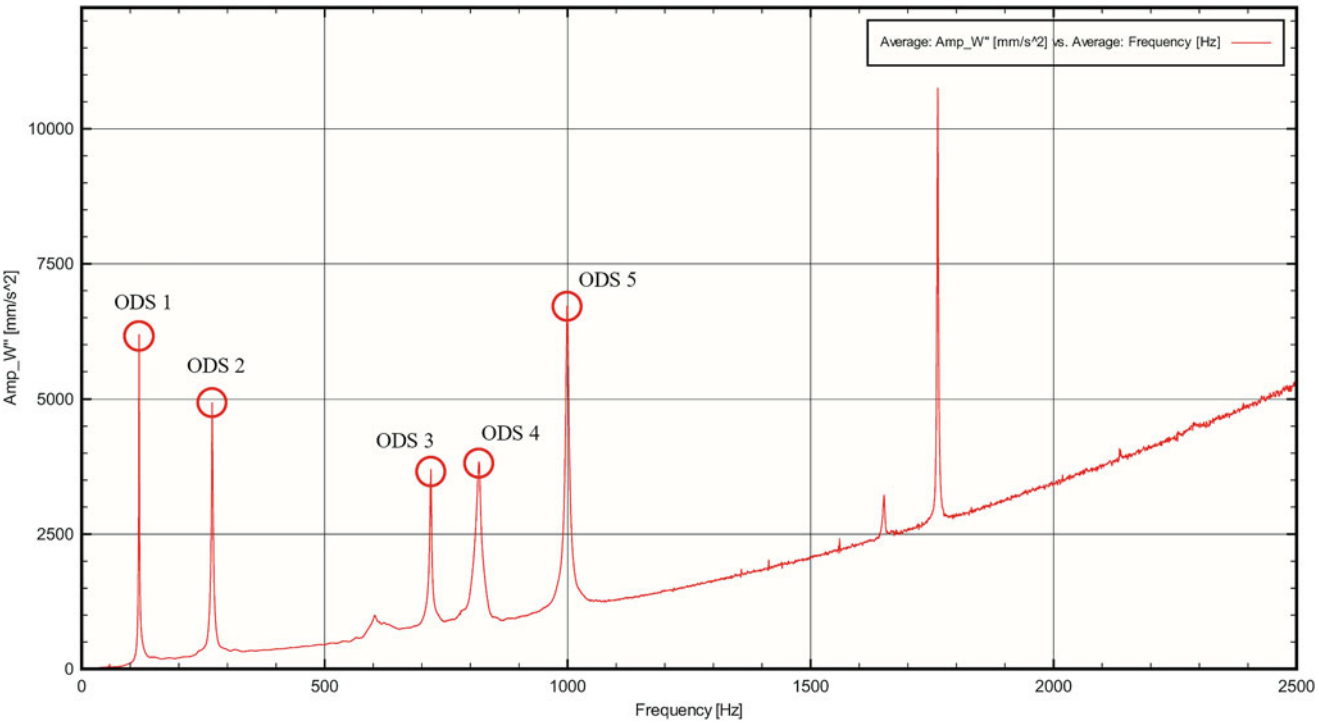

Fig. 25.14 The acceleration versus frequency plot of the cantilever plate captured using DIC. The frequencies at the peaks indicate the cantilever plate's natural frequencies

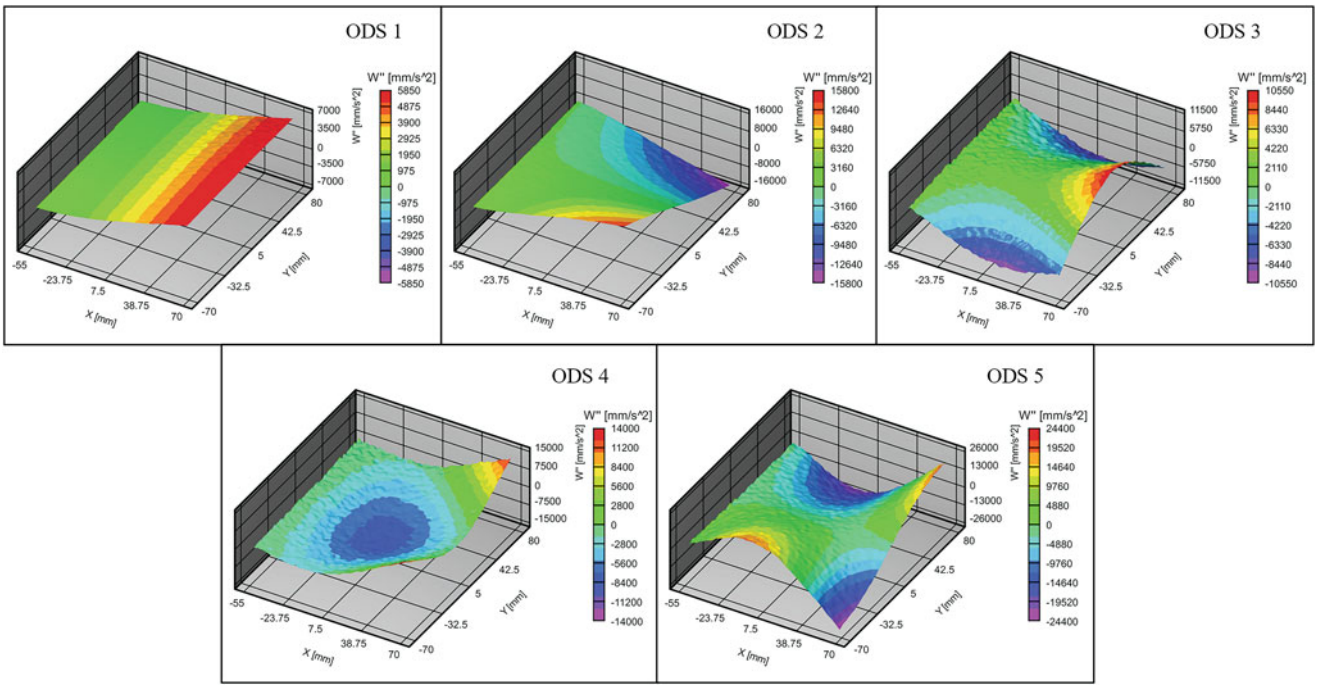

Fig. 25.15 The ODSs for the first five cantilever plate natural frequencies captured using DIC

Table 25.4 The first five natural frequencies of the cantilever plate determined by ODS analysis and FEA. The percent errors are reported with the ODS analysis test data taken as the reference frequencies

Natural frequencies	ODS (Reference) (Hz)	FEA (Hz)	Percent error (%)
1	117.021	129.661	10.801
2	269.504	278.225	3.236
3	719.858	727.488	1.060
4	817.243	828.523	1.380
5	999.523	1056.9	5.740

Table 25.5 The first five natural frequencies of the cantilever plate determined by EMA and ODS analysis and their percent differences

Natural frequencies	EMA (Hz)	ODS analysis (Hz)	Percent difference (%)
1	116.333	117.021	0.590
2	266.597	269.504	1.084
3	715.333	719.858	0.631
4	814.372	817.243	0.352
5	984.343	999.523	1.530

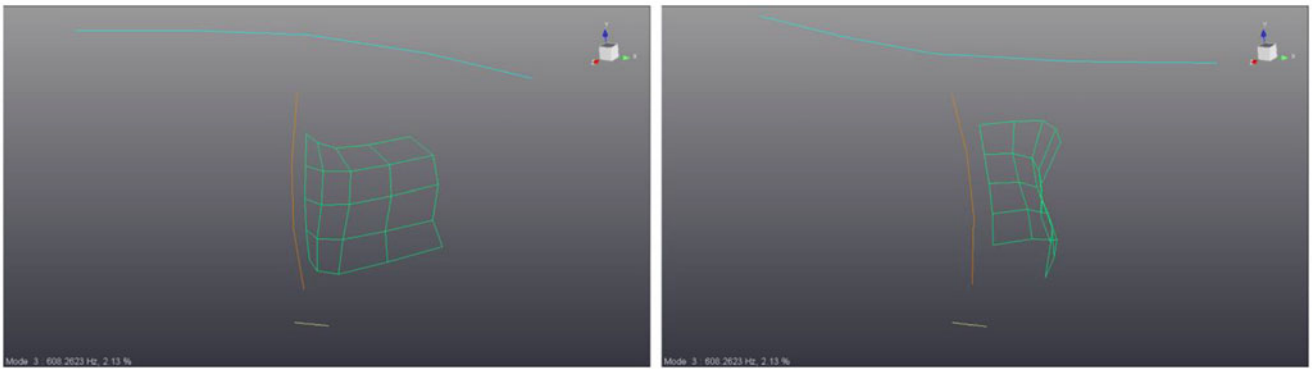

Fig. 25.16 The mode shape at 608.262 Hz involved vibration of the complete structure, including the cylinder, the upper mounting bracket, and the cantilever plate. Note the large deflections in the upper mounting bracket and cylinder

the average percent difference over the first five cantilever plate natural frequencies is 0.837%. The ODS analysis natural frequencies are greater than the EMA-based natural frequencies because of the removal of the accelerometers from the experimental setup for the DIC test scenario. As the mass of a system decreases, the natural frequency of the system increases per the natural frequency equation [8] given in Eq. (25.1), where ω_n is the natural frequency of a mass-spring system, k is the system's spring constant, and m is the system's mass.

$$\omega_n = \sqrt{\frac{k}{m}} \tag{25.1}$$

25.3.4 608.262 Hz Peak

The small peak at 608.262 Hz in Fig. 25.9 and the small peak at 608.262 Hz in Fig. 25.14 were a mode shape and ODS, respectively, involving the entire experimental setup, including the cylinder, upper mounting bracket, and cantilever plate. As shown by the EMA-based mode shape in Fig. 25.16, the cylinder and upper mounting bracket had large deflections at 608.262 Hz, and therefore the EMA-based mode shape was not primarily a cantilever plate mode.

Additionally, this 608.262 Hz mode was seen to have a large influence from the upper boundary condition and cylinder where they have large peaks at 608.262 Hz, as shown by their EMA-based FRFs in Fig. 25.17. Due to the large FRF influence from the upper boundary and cylinder, as well as the large deflections, the 608.262 Hz mode shape and ODS were not considered in the analysis results.

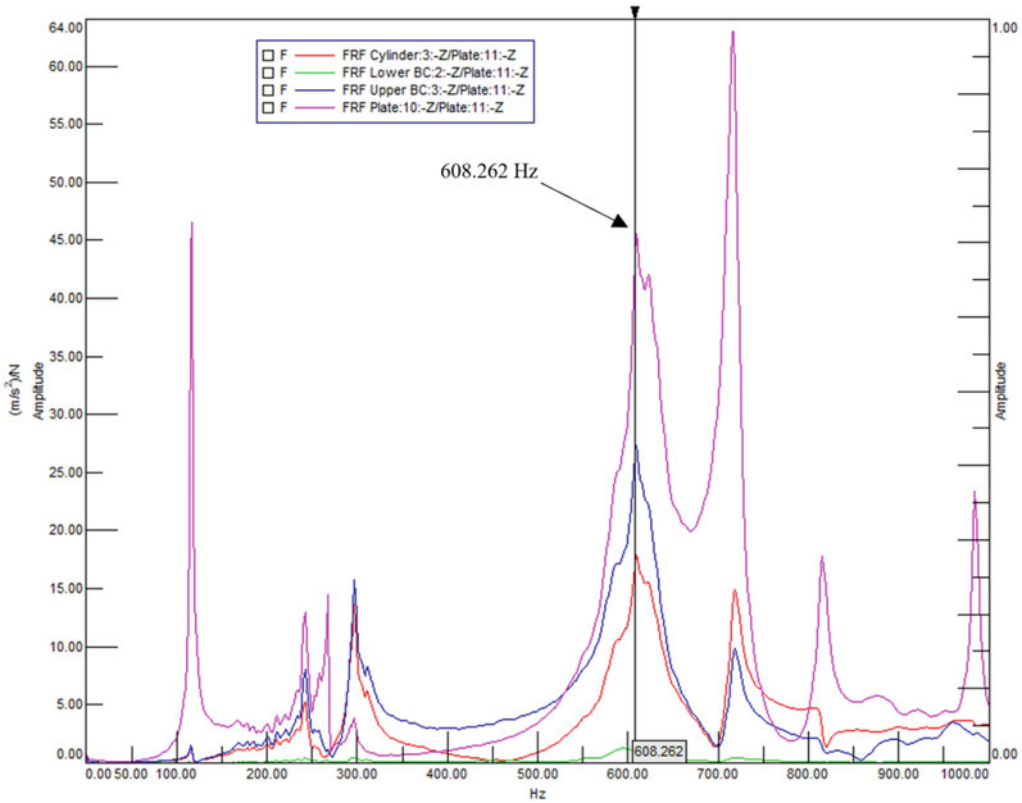

Fig. 25.17 The FRFs at the lower mounting bracket (green), upper mounting bracket (blue), cylinder (red), and cantilever plate (pink) for a hammer impact on the cantilever plate

25.4 Conclusion

The purpose of this work was to employ experimental techniques on a cantilever plate by performing EMA and ODS analysis methods in the lab. A CAD model of the experimental setup was first introduced, followed by a simplified model of the fixed-fixed cylinder with cantilever plate. The FEM and simulation setup were discussed, including mesh parameters and boundary conditions. Then, the experimental setup in the lab was introduced, including impact hammer and accelerometer equipment as well as the DIC system. The results and analysis using each experimental method were presented and compared to the FEA results. The absolute values of the percent errors between the EMA-based and FEA-based results were less than 5% for each mode's natural frequency. The MAC between EMA-based modes and FEA-based modes were at least 0.935 on the diagonal for each mode. For the ODS method, the absolute values of the percent errors between the ODS analysis and FEA-based results were less than 11% for each natural frequency. The EMA and ODS analysis results were also compared, and there was less than a 2% difference between each corresponding natural frequency. Finally, a brief discussion on a structure mode at 608.262 Hz involving the cylinder, the upper mounting bracket, and the cantilever plate, and why it was not considered in the analysis results was provided.

Acknowledgments The authors would like to thank the Siemens team for their guidance and technical support throughout the completion of this work, including Frank Poradek, Chris Sensor, Peter Schaldenbrand, Scott Beebe, Ramana Kappagantu, and Kin Hong. The authors would also like to thank Micah Simonsen and Alistair Tofts of Correlated Solutions, Inc. for their training and technical assistance with DIC testing.

References

1. Wu, J., Shu, C., Zhao, N.: Numerical study of flow control via the interaction between a circular cylinder and a flexible plate. J. Fluids Struct. **49**, 594–613 (2014)

2. Duan, F., Wang, J.: Fluid–structure–sound interaction in noise reduction of a circular cylinder with flexible splitter plate. J. Fluid Mech. **920**, A6, 1–A6,44 (2021)
3. Oruç, V.: Strategies for the applications of flow control downstream of a bluff body. Flow Meas. Instrum. **53**, 204–214 (2016)
4. Balint, T.S., Lucey, A.D.: Instability of a cantilevered flexible plate in viscous channel flow. J. Fluids Struct. **20**(7), 893–912 (2005)
5. Yu, Y., Liu, Y.: Flapping dynamics of a piezoelectric membrane behind a circular cylinder. J. Fluids Struct. **55**, 347–363 (2015)
6. Bleischwitz, R., de Kat, R., Ganapathisubramani, B.: Aeromechanics of membrane and rigid wings in and out of ground-effect at moderate Reynolds Numbers. J. Fluids Struct. **62**, 318–331 (2016)
7. Meirovitch, L.: Vibration of plates. In: Principles and Techniques of Vibrations, pp. 451–457. Prentice-Hall, Inc, Upper Saddle River (1997)
8. Inman, D.J.: Vibration of membranes and plates. In: Engineering Vibration, pp. 556–562. Pearson India Education Services Pvt. Ltd (2014)
9. Szilard, R.: Theories and Applications of Plate Analysis: Classical, Numerical and Engineering Methods. Wiley, Hoboken (2004)
10. Warburton, G.B.: The vibration of rectangular plates. Proc. Inst. Mech. Eng. **168**(1), 371–384 (1954)
11. Leissa, A.W.: The free vibration of rectangular plates. J. Sound Vib. **31**(3), 257–293 (1973)
12. Warren, C., Niezrecki, C., Avitabile, P., Pingle, P.: Comparison of FRF measurements and mode shapes determined using optically image based, laser, and accelerometer measurements. Mech. Syst. Signal Process. **25**(6), 2191–2202 (2011)
13. Kalybek, M., Bocian, M., Pakos, W., Grosel, J., Nikitas, N.: Performance of camera-based vibration monitoring systems in input-output modal identification using shaker excitation. Remote Sens. **13**(17), 3471 (2021)
14. Ewins, D.J.: Modal Testing: Theory, Practice and Application, 2nd edn. Research Studies Press Ltd., Baldock, Hertfordshire (2000)
15. Hu, Y., Guo, W., Zhu, W., Xu, Y.: Local damage detection of membranes based on Bayesian operational modal analysis and three-dimensional digital image correlation. Mech. Syst. Signal Process. **131**, 633–648 (2019)
16. Xu, Y.F., Chen, D.-M., Zhu, W.D.: Damage identification of beam structures using free response shapes obtained by use of a continuously scanning laser Doppler vibrometer system. Mech. Syst. Signal Process. **92**, 226–247 (2017)
17. Gwashavanhu, B., Oberholster, A.J., Heyns, P.S.: Rotating blade vibration analysis using photogrammetry and tracking laser Doppler vibrometry. Mech. Syst. Signal Process. **76–77**, 174–186 (2016)
18. Gülbahçe, E., Çelik, M.: Experimental modal analysis for the plate structures with roving inertial shaker method approach. J. Low Freq. Noise Vib. Active Control. **41**(1), 27–40 (Sep. 2021)
19. Peeters, B., Van der Auweraer, H., Guillaume, P., Leuridan, J.: The Polymax frequency-domain method: a new standard for modal parameter estimation? Shock. Vib. **11**(3–4), 395–409 (2004)
20. Whalen, T.J., Schöneich, A.G., Laurence, S.J., Sullivan, B.T., Bodony, D.J., Freydin, M., Dowell, E.H., Buck, G.M.: Hypersonic fluid–structure interactions in compression corner shock-wave/boundary-layer interaction. AIAA J. **58**(9), 4090–4105 (2020)
21. Yu, L., Pan, B.: Single-camera high-speed stereo-digital image correlation for full-field vibration measurement. Mech. Syst. Signal Process. **94**, 374–383 (2017)
22. Yu, L., Pan, B.: High-speed stereo-digital image correlation using a single color high-speed camera. Appl. Opt. **57**(31), 9257–9269 (2018)
23. Xie, R., Yu, L., Zhu, W., Pan, B.: Experimental study on flow-induced full-field vibration of a flexible splitter plate behind a cylinder using stereo-digital image correlation. J. Vib. Acoust. **143**(3) (2020)
24. Frankovský, P., Delyová, I., Sivák, P., Bocko, J., Živčák, J., Kicko, M.: Modal analysis using digital image correlation technique. Materials. **15**(16), 5658–5672 (2022)